frontiers | Research Topics

Extracellular matrix dynamics in biology, bioengineering, and pathology, volume II

Edited by
Rajprasad Loganathan, Hiromi Yanagisawa, Charles D. Little,
Eileen Gentleman and Jeffrey A. Weiss

Published in
Frontiers in Cell and Developmental Biology
Frontiers in Bioengineering and Biotechnology
Frontiers in Physics
Frontiers in Cardiovascular Medicine

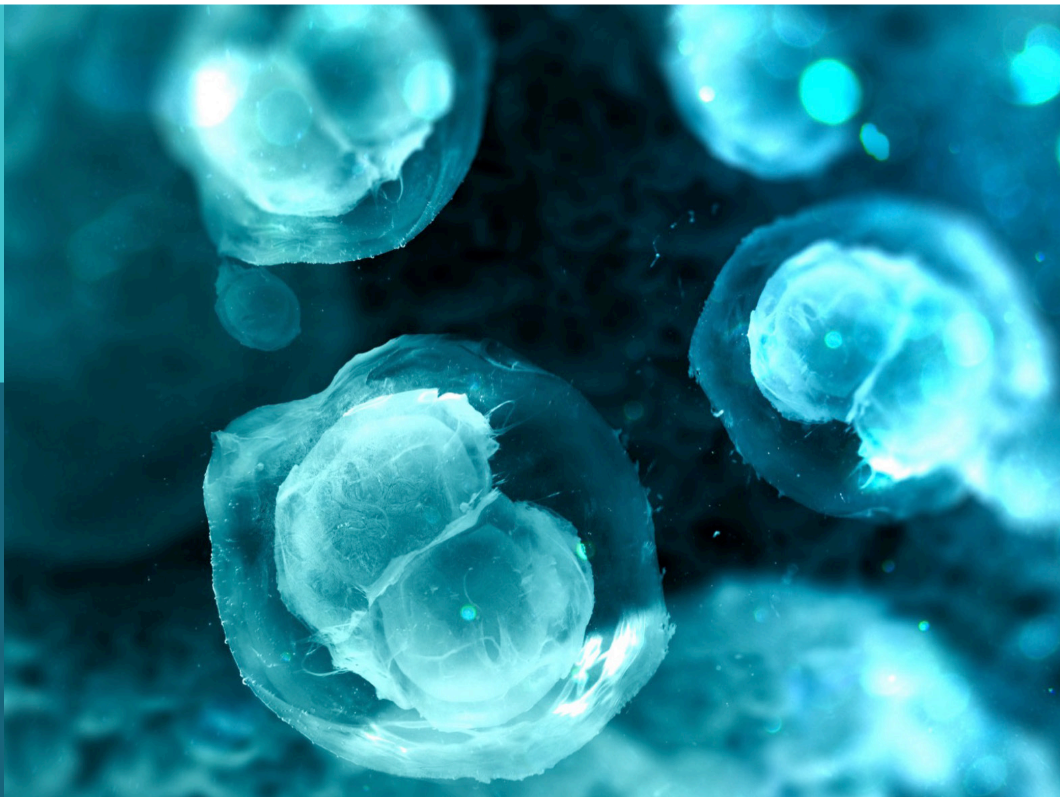

ISSN 1664-8714
ISBN 978-2-83251-078-0
DOI 10.3389/978-2-83251-078-0

About Frontiers

Frontiers is more than just an open access publisher of scholarly articles: it is a pioneering approach to the world of academia, radically improving the way scholarly research is managed. The grand vision of Frontiers is a world where all people have an equal opportunity to seek, share and generate knowledge. Frontiers provides immediate and permanent online open access to all its publications, but this alone is not enough to realize our grand goals.

Frontiers journal series

The Frontiers journal series is a multi-tier and interdisciplinary set of open-access, online journals, promising a paradigm shift from the current review, selection and dissemination processes in academic publishing. All Frontiers journals are driven by researchers for researchers; therefore, they constitute a service to the scholarly community. At the same time, the *Frontiers journal series* operates on a revolutionary invention, the tiered publishing system, initially addressing specific communities of scholars, and gradually climbing up to broader public understanding, thus serving the interests of the lay society, too.

Dedication to quality

Each Frontiers article is a landmark of the highest quality, thanks to genuinely collaborative interactions between authors and review editors, who include some of the world's best academicians. Research must be certified by peers before entering a stream of knowledge that may eventually reach the public - and shape society; therefore, Frontiers only applies the most rigorous and unbiased reviews. Frontiers revolutionizes research publishing by freely delivering the most outstanding research, evaluated with no bias from both the academic and social point of view. By applying the most advanced information technologies, Frontiers is catapulting scholarly publishing into a new generation.

What are Frontiers Research Topics?

Frontiers Research Topics are very popular trademarks of the *Frontiers journals series*: they are collections of at least ten articles, all centered on a particular subject. With their unique mix of varied contributions from Original Research to Review Articles, Frontiers Research Topics unify the most influential researchers, the latest key findings and historical advances in a hot research area.

Find out more on how to host your own Frontiers Research Topic or contribute to one as an author by contacting the Frontiers editorial office: frontiersin.org/about/contact

Extracellular matrix dynamics in biology, bioengineering, and pathology, volume II

Topic editors

Rajprasad Loganathan — Wichita State University, United States
Hiromi Yanagisawa — University of Tsukuba, Japan
Charles D. Little — University of Kansas Medical Center, United States
Eileen Gentleman — King's College London, United Kingdom
Jeffrey A. Weiss — The University of Utah, United States

Citation

Loganathan, R., Yanagisawa, H., Little, C. D., Gentleman, E., Weiss, J. A., eds. (2023). *Extracellular matrix dynamics in biology, bioengineering, and pathology, volume II.* Lausanne: Frontiers Media SA. doi: 10.3389/978-2-83251-078-0

Table of contents

frontiers | Frontiers in Cell and Developmental Biology

TYPE Editorial
PUBLISHED 02 December 2022
DOI 10.3389/fcell.2022.1105566

EDITED AND REVIEWED BY
Akihiko Ito,
Kindai University, Japan

*CORRESPONDENCE
Rajprasad Loganathan,
raj.logan@wichita.edu

SPECIALTY SECTION
This article was submitted to Cell Adhesion and Migration,
a section of the journal
Frontiers in Cell and Developmental Biology

RECEIVED 22 November 2022
ACCEPTED 24 November 2022
PUBLISHED 02 December 2022

CITATION
Loganathan R, Yanagisawa H, Gentleman E, Little CD and Weiss JA (2022), Editorial: Extracellular matrix dynamics in biology, bioengineering, and pathology, volume II.
Front. Cell Dev. Biol. 10:1105566.
doi: 10.3389/fcell.2022.1105566

Editorial: Extracellular matrix dynamics in biology, bioengineering, and pathology, volume II

Rajprasad Loganathan[1]*, Hiromi Yanagisawa[2], Eileen Gentleman[3], Charles D. Little[4] and Jeffrey A. Weiss[5]

[1]Developmental and Integrative Systems Biology Lab, Department of Biological Sciences, Wichita State University, Wichita, KS, United States, [2]Life Science Center for Survival Dynamics, TARA, University of Tsukuba, Tsukuba, Japan, [3]Centre for Craniofacial and Regenerative Biology, King's College London, London, United Kingdom, [4]Department of Cell Biology and Physiology, University of Kansas Medical Center, Kansas City, KS, United States, [5]Department of Biomedical Engineering, The University of Utah, Salt Lake City, UT, United States

KEYWORDS

ECM, biology, bioengineering, pathology, network, dynamics

Editorial on the Research Topic
Extracellular matrix dynamics in biology, bioengineering, and pathology—Volume II

Introduction

The current volume of articles focused on extracellular matrix (ECM) presents some recent developments in biology, bioengineering, and pathology that reiterate the central theme of our previous volume. Collectively, these articles provide multidisciplinary evidence that the ECM operates as a highly dynamic functional framework in physiology and pathology. Furthermore, they underscore the opportunities available for future explorations that can help develop more robust models of ECM structure and function for human health and disease.

Biology

Petzold and Gentleman offer a comprehensive review of mechanical cues and their impact on stem cells and embryogenesis. Their article contrasts the effects of mechanotransduction from intrinsic cues vs. extrinsic cues for cell differentiation. ECM mechanical properties and topography take the central stage in their discussion of cellular response to mechanotransduction. The authors also provide a coherent summary of the bidirectional structural changes that occur in the cell and the ECM mediated by a robust cytoskeletal signaling network. Furthermore, their discussion extends to the mechanoregulation of embryogenesis and the novel methods that have emerged in this field for the measurement of embryonic stiffness.

Few models of tendon developmental biology are available. Moreover, models of tendon development that allow investigation of craniofacial muscles have yet to be explored. Korntner et al. test the capacity of chick embryos to offer a system for the study of craniofacial tendon development. Using the jaw-closing tendon of the musculus adductor mandibulate externus and the jaw-opening tendon of the musculus depressor mandibulae, they characterize the developmental trajectory of cell and ECM morphology. They discover that several markers implicated in limb tendon formation are also present in embryonic jaw tendon. Their morphological and molecular biological characterizations of the developmental program directing chick jaw muscle tendon assembly provide a basis for future modeling of the developmental program shaping human masticatory tendons.

The study by López-Mengual et al. illustrates the critical role played by mechanical cues in the developing nervous system. Using the mouse embryonic explant system for the study of slices of developing brain in Matrigel preparations, the authors complement the methods of classical developmental biology with atomic force microscopy and traction force microscopy measurements to demonstrate differential tissue stiffness of the developing brain and its immediate effects on Cajal-Retzius cell migration and ultimate effect on neocortical development.

Bioengineering

Bioengineering researchers have long provided an ever-expanding toolkit of methods to investigate cell and ECM mechanobiology. In that tradition, Scholp et al. present their design of a custom force-bioreactor that uses fibroblast-seeded fibrin gels to allow microscopy-based documentation of force generation in response to drug treatment. Lu et al. describe their findings on the use of pulmonary visceral pleura (PVP) as a potential biomaterial for tissue repair and reconstruction. They test PVP processed from both swine and bovine lungs to determine its structural characteristics, mechanical properties, cytotoxicity, and biocompatibility for rat sciatic nerve and skin repair.

ECM structural organization has long remained a fertile ground for investigations from diverse scientific fields. An application of methods from condensed matter physics to detect changes in collagen fiber organization in colorectal cancer is tested by Despotović and Ćosić. Their work shows that the collagen fiber straightness quantified using theoretical methods as a measure of ECM remodeling can be a useful indicator of the early stages in the development of colorectal cancer.

Pathology

Knutsen et al. report on the therapeutic effects of K_{ATP} channel opener Minoxidil for the treatment of individuals with William-Beuren Syndrome (WBS), which occurs as a result of loss of one copy of the elastin gene ultimately causing large artery vasculopathy. After confirming the similarities in pathophysiological features of elastin heterozygous null mice with those of children with WBS they demonstrate partial remedy of cardiovascular features in mice. Their results provide the necessary evidence to suggest consideration of Minoxidil therapy under strict cardiac size monitoring as an adjunct to surgical intervention for humans with WBS cardiovascular pathology.

In addition to gene loss targeting the ECM architecture, defects of the cardiovascular system are also caused by the effects of aging on the ECM morphology. In their mini-review, Mammoto et al. describe the ECM changes that occur in aging aorta with a particular focus on the fragmentation of elastic fibers and excessive deposition and crosslinking of collagens as major drivers of aging-induced aortic dysfunction. Cardiac pathology is the focus of yet another investigation published in this Research Topic. Studying a rodent model of heart hypoplasia induced by congenital diaphragmatic hernia, Watson et al. suggest that changes in environmental cues such as ECM stiffness and mechanical force may underlie the pathological progression of heart hypoplasia by affecting the balance between cardiomyocyte cell proliferation and maturation.

From experiments showing the unexpected effects of prophylactically administered drugs on ECM functional organization in a rat model of elbow injury and *in vitro* collagen gel assay, David et al. report that simvastatin may be a suitable prophylactic drug therapy for preventing or mitigating post-traumatic joint contracture.

In their study on the effects of ECM on nerve injury and regeneration, Bauch et al., using a cerebellar slice culture model of demyelination/remyelination, provide evidence for the inhibitory effects of tenascin-C and tenascin-R on remyelination. Collectively, their results show the relevance of oligodendrocyte physiology and ECM dynamics for gaining a better understanding of debilitating pathologies, e.g., multiple sclerosis.

Summary

As co-editors of this Research Topic, we thoroughly enjoyed learning about the aforementioned recent developments in ECM dynamics. We hope the readers of this Research Topic would also feel the same way.

Author contributions

All authors listed have made a substantial, direct, intellectual contribution to the work and approved it for publication.

Conflict of interest

The authors declare that the research was conducted in the absence of any commercial or financial relationships that could be construed as a potential conflict of interest.

Publisher's note

frontiers in Cell and Developmental Biology

REVIEW
published: 08 November 2021
doi: 10.3389/fcell.2021.761871

Intrinsic Mechanical Cues and Their Impact on Stem Cells and Embryogenesis

*Jonna Petzold and Eileen Gentleman**

Centre for Craniofacial and Regenerative Biology, King's College London, London, United Kingdom

Although understanding how soluble cues direct cellular processes revolutionised the study of cell biology in the second half of the 20th century, over the last two decades, new insights into how mechanical cues similarly impact cell fate decisions has gained momentum. During development, extrinsic cues such as fluid flow, shear stress and compressive forces are essential for normal embryogenesis to proceed. Indeed, both adult and embryonic stem cells can respond to applied forces, but they can also detect intrinsic mechanical cues from their surrounding environment, such as the stiffness of the extracellular matrix, which impacts differentiation and morphogenesis. Cells can detect changes in their mechanical environment using cell surface receptors such as integrins and focal adhesions. Moreover, dynamic rearrangements of the cytoskeleton have been identified as a key means by which forces are transmitted from the extracellular matrix to the cell and *vice versa.* Although we have some understanding of the downstream mechanisms whereby mechanical cues are translated into changes in cell behaviour, many of the signalling pathways remain to be defined. This review discusses the importance of intrinsic mechanical cues on adult cell fate decisions, the emerging roles of cell surface mechano-sensors and the cytoskeleton in enabling cells to sense its microenvironment, and the role of intracellular signalling in translating mechanical cues into transcriptional outputs. In addition, the contribution of mechanical cues to fundamental processes during embryogenesis such as apical constriction and convergent extension is discussed. The continued development of tools to measure the biomechanical properties of soft tissues *in vivo* is likely to uncover currently underestimated contributions of these cues to adult stem cell fate decisions and embryogenesis, and may inform on regenerative strategies for tissue repair.

Keywords: mechanotransduction, stem cell, embryogenesis, stiffness, development

Edited by:
Florian Rehfeldt,
University of Bayreuth, Germany

Reviewed by:
Joe Swift,
The University of Manchester,
United Kingdom
Bipul R. Acharya,
University of Virginia, United States

***Correspondence:**
Eileen Gentleman
eileen.gentleman@kcl.ac.uk

Specialty section:
This article was submitted to
Cell Adhesion and Migration,
a section of the journal
Frontiers in Cell and Developmental Biology

Received: *20 August 2021*
Accepted: *14 October 2021*
Published: *08 November 2021*

Citation:
Petzold J and Gentleman E (2021)
Intrinsic Mechanical Cues and Their Impact on Stem Cells and Embryogenesis.
Front. Cell Dev. Biol. 9:761871.
doi: 10.3389/fcell.2021.761871

INTRODUCTION

Over a century ago, tissue formation was often described in terms of mechanical cues. For example, the German surgeon Julius Wolff noted that bone adapts its inner structure in response to mechanical loading (Wolff, 1892). Later observational studies from scientists such as Eben Carey and Alfred Glücksmann concluded that the convex and concave aspects of developing bone are exposed to varying mechanical stresses, which impacted cartilage and bone formation (Carey, 1922a; Glucksmann, 1942). However, in the subsequent decades of the 20th century, much emphasis was put on understanding how highly intricate soluble biochemical cues, molecule-receptor binding interactions and their downstream transcriptional outputs control tissue formation, which together now govern much of our understanding of biology. It could be said that as a consequence, the importance of the less specific physical cues in the cellular microenvironment was somewhat overlooked.

Yet, despite these insights, it is now recognised that growth factor, chemotactic and cytokine signals alone are insufficient to explain many biological phenomena. Indeed, a cell's mechanical landscape plays a vital role in regulating functions such as proliferation, differentiation and migration, in some cases even overriding the contribution of biochemical cues. The mechanisms whereby cells translate mechanical information from their environment into signals that alter their behaviour is termed "mechanotransduction" (Discher, 2005; DuFort et al., 2011; Walters and Gentleman, 2015). In comparison to many well characterised biochemical signals that govern cell behaviour and function, our understanding of the impact of mechanical cues on cells remains in its infancy. Despite this, the significance of tissue mechanics, and in particular matrix stiffness, in health and disease is now widely recognised (Janmey and Miller, 2011; Astudillo, 2020).

This commentary discusses the importance of intrinsic mechanical cues on adult cell fate decisions, with a focus on mesenchymal stem cells (MSC). Although externally applied extrinsic cues also play important roles in MSC differentiation, these are only briefly referred to here, but have been reviewed previously (Steward and Kelly, 2015; Vining and Mooney, 2017). Specifically, we discuss the following important questions: How do cell surface receptors such as integrins enable a cell to sense mechanical cues from its microenvironment? What is the importance of the cytoskeleton in the cellular response to mechanical cues? How do intracellular signalling pathways enable the translation of biomechanical cues into transcriptional outputs, and what is the contribution of the nucleus itself? Lastly, to put the importance of intrinsic mechanical cues into an *in vivo* biological context, a brief historical view of mechanotransduction in embryogenesis and the impact of intrinsic cues on embryonic development is outlined.

THE ROLE OF MECHANICAL CUES IN DRIVING CELL FATE

A growing body of evidence suggests that cells are able to interact with and respond to physical changes in their microenvironment (Vollrath et al., 2007; D'Angelo et al., 2011; Wisdom et al., 2018). Both extrinsic and intrinsic mechanical signals are known to regulate cell differentiation (**Figure 1A**). For simplicity, in this review extrinsic cues are categorised as externally applied forces that include fluid flow, compression, hydrostatic pressure and tension, whilst cell shape, density, extracellular matrix (ECM) stiffness and topography are given as examples of intrinsic cues. Importantly the mechanical landscape within organisms is highly complex and extrinsic and intrinsic cues often interrelate and cannot be decoupled from one another. Cells perceive mechanical signals in their surroundings via integrins and other cell surface molecules (Sun et al., 2016). This prompts the cellular cytoskeleton to respond by increasing or decreasing contractility to counter-balance the forces acting on the cell. Changes in cytoskeletal tension can activate downstream signalling pathways which lead to transcriptional changes that direct cell behaviour, including cell fate decisions. Direct interactions between the cytoskeleton and the nucleus also play an important role in mechanotransduction. For example, the nuclear protein lamin A accumulates in cells on stiff ECM, protecting against DNA damage (Swift and Discher, 2014; Cho et al., 2019). However, this protective effect is inhibited when the cytoskeleton is disrupted. Thus, mechanotransduction does not function as a "one-way street" and signals from the nucleus can be transferred back to the cytoskeleton to alter the way a cell perceives mechanical cues, creating a transcriptional feedback loop (**Figure 1B**; Swift et al., 2013; Mason et al., 2019).

Many studies in mechanobiology use bone marrow or adipose tissue-derived MSC as a model (Gomez-Salazar et al., 2020). It is important to note that despite their name, MSC do not completely fulfil the criteria of *bona fide* stem cells. Thus, MSC have also been referred to as "mesenchymal progenitor cells," "multipotent adult stem cells" and "multipotent stromal cells" (Jiang et al., 2002; Zimmermann et al., 2003; Beltrami et al., 2007; Gomez-Salazar et al., 2020). MSC are reported to able to differentiate into several cell types such as osteoblasts, myoblasts, adipocytes and chondrocytes (Pittenger et al., 1999; McBeath et al., 2004; Deng et al., 2006; Engler et al., 2006). Their multipotency makes MSC a particularly attractive candidate for the rapidly advancing field of regenerative medicine and is the driving factor behind much of the research into this cell population.

Cell Shape and Cell Density

The direct effect of shape on cell behaviour was observed over 40 years ago by Folkman and Moscona (1978) who developed polymer-based culture systems to alter cell shape *in vitro*. Endothelial cells cultured on thin and highly adhesive polymer layers were more spread and synthesised DNA at a faster rate compared to rounder cells cultured on thicker polymer layers (Folkman and Moscona, 1978). The development of patterned PDMS stamps, which force cells to adopt a certain morphology, identified that shape also regulates cell growth (Singhvi et al., 1994). Individual hepatocytes cultured on small adhesive islands have a round morphology, proliferate slowly and undergo apoptosis, whilst culture on larger islands promotes cell spreading and proliferation. Indeed, only 3% of hepatocytes on the smallest islands ($<1{,}600\ \mu m^2$) entered S phase (Singhvi et al., 1994).

More recent studies have used micropatterned substrates, in which cell shape can be tightly controlled at the micro- and nano-meter scale *in vitro* (Chen et al., 1997; Engler A. J. et al., 2004; Kumar et al., 2006). The impact of shape on cell fate was demonstrated when examining the adipogenic-osteogenic differentiation potential of MSC (McBeath et al., 2004; Engler et al., 2006; Dupont et al., 2011; Halder et al., 2012). Culture of MSC on small ECM-coated islands promotes a round cell shape and adipogenic differentiation, whilst cells spread and activate osteogenic differentiation programmes on larger islands (McBeath et al., 2004). Geometrically driven cell fate change was later confirmed by Kilian et al. (2010), who plated MSC

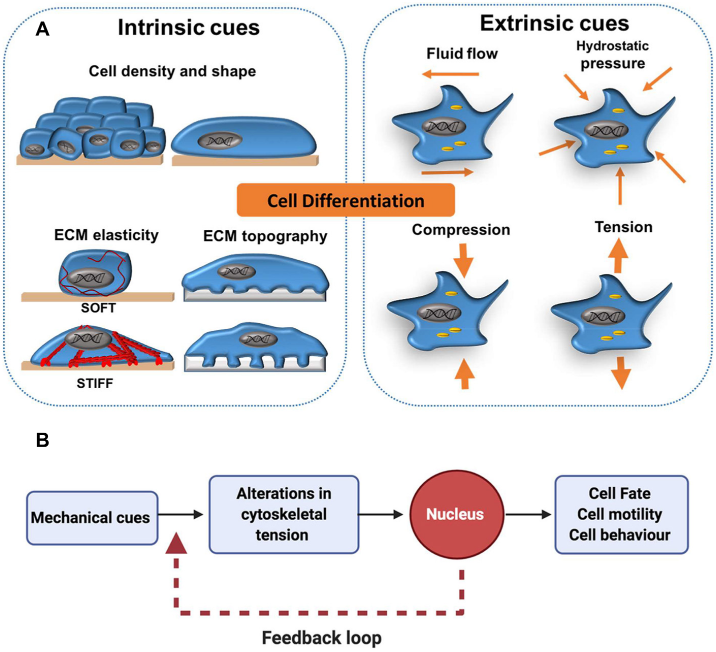

FIGURE 1 | Extrinsic and intrinsic cues in mechanotransduction. **(A)** Cell differentiation has been shown to be affected by mechanical forces external to the cell (extrinsic) such as shear stress from fluid flow and more local mechanical cues (intrinsic) such as cell density, shape and elasticity of the surrounding extracellular matrix (ECM). **(B)** As a general concept, mechano-transduction involves the transfer of mechanical cues from the cell surface to the nucleus via the cytoskeleton. This activates downstream cell signalling cascades, which can influence cell fate decisions. In addition, a transcriptional feedback loop allows cells to maintain a cytoskeletal equilibrium that is responsive to changes in their mechano-environment. This is particularly important for processes like cell migration, in which continual cytoskeletal remodelling is required for persistent cell motility.

on micropatterned surface shapes with varying cell area. Here, lipid droplets were observed in smaller, rounder cells, whilst alkaline phosphatase (ALP) expression was increased in spread cells on larger islands (Kilian et al., 2010). Importantly, the shape of these cells reflects their specialised functions *in vivo;* the round morphology of adipocytes enhances their lipid storage capabilities in adipose tissue, whereas spreading of osteoblasts maximises deposition of matrix (Parfitt, 1984; McBeath et al., 2004). In addition, cells' aspect ratio is an important determinant of fate. Specifically, the rate of osteogenesis is ∼20% higher in MSC cultured on rectangular micro-patterns with a 4:1 aspect ratio compared to a 1:1 aspect ratio, despite the cell area remaining constant (Kilian et al., 2010). In addition, a high degree of curvature at the cell edge (flower-shaped micro-patterns) promotes adipogenesis, whilst straight cell edges (star-shaped micro-patterns) stimulates osteogenic differentiation (Kilian et al., 2010).

Cell shape and density are closely intertwined. Cells cultured at a low density have space to spread, whereas high density cultures are compact, promoting a rounded cell morphology (McBride and Knothe Tate, 2008; Wada et al., 2011). Changes in cell density directly impact on cell fate. MSC cultured at low density tend to express the osteogenic marker alkaline phosphatase (ALP), whilst high density culture promotes adipogenesis (McBeath et al., 2004). Importantly, initial plating density was found to drive lineage commitment independently of later densities; a 4-day high-density culture of MSC showed suppressed osteogenesis after re-plating at a lower density (McBeath et al., 2004). Cell density also controls morphogenesis and cell proliferation in sheets of epithelial and endothelial cells cultured *in vitro* (Nelson et al., 2005; Halder et al., 2012). Increased density at the centre of cell monolayers cultured on round FN-coated islands prevents proliferation, whilst sparsely spaced cells at island edges undergo rapid cell proliferation (Nelson et al., 2005). This difference in cell-cycle progression was attributed to a gradient of traction forces generated by cells according to their location, whereby those at the edge of the islands applied more force than cells in the centre (Nelson et al., 2005). Taken together, these studies outline the impact that cell area, aspect-ratio and density can have in determining fate.

Effects of Extracellular Matrix Elasticity

The ECM provides both chemical and physical signals which impact on cell behaviour and fate (Eroshenko et al., 2013). Specifically, both the viscoelasticity (discussed in Section "Summary and Outlook") and elasticity of the cellular microenvironment are known to modulate various cellular characteristics, such as shape, proliferation, differentiation and migration (Lo et al., 2000; Engler et al., 2008; Winer et al., 2008; Evans et al., 2009; Dupont et al., 2011; Kumar et al., 2017; Chaudhuri et al., 2020). "Stiffness" describes the ability of an elastic material to resist deformation when force is applied (Evans and Gentleman, 2014). In effect, this constitutes the resistance felt by a cell when it deforms its surrounding matrix (Engler et al., 2006). Stiffness is often quantified by measuring the Young's modulus (units: pascal; Pa) of a material (Evans and Gentleman, 2014). Importantly, the Young's modulus is a fundamental property of a material and remains the same even when the size of a material changes. Here, the terms "stiffness," "elasticity" and "compliance" are used interchangeably to describe the same concept (Norman et al., 2021).

To better understand the effect of ECM stiffness on cell behaviour, several studies have attempted to recapitulate relevant *in vivo* stiffnesses *in vitro* by using 2D tunable polymer matrices (Engler et al., 2006; Dupont et al., 2011; Zhang et al., 2017; Zhou et al., 2017; Sun et al., 2018). A common strategy is to use polyacrylamide (PAA) hydrogels, in which varying concentrations of acrylamide and bis-acrylamide are combined to generate hydrogel matrices of varying stiffness (Pelham and Wang, 1997; Flanagan et al., 2002; Chin et al., 2020). The first well-characterised study using PAA hydrogels identified that fibroblasts and epithelial cells were less spread, irregularly shaped and lacked focal adhesions (FA) on more compliant matrices (Pelham and Wang, 1997). This finding provided early evidence that cells elicit a compliance-specific response, and provided the basis for studies that later showed stem cells to differentiate most readily on surfaces with stiffnesses that were physiologically relevant for the particular cell type (McBeath et al., 2004; Kumar et al., 2006; Venugopal et al., 2018).

The compliance of a cell's environment modulates its morphology. In general, stiffer matrices promote cell spreading and softer matrices induce rounded cell phenotypes (**Figure 1**; Engler et al., 2006; McBride et al., 2008; El-Mohri et al., 2017). Cells residing in more compliant environments can easily deform their surrounding matrix and do not need to generate a large amount of force to counter-balance their matrix, thus they remain round (Knothe Tate et al., 2008). Less compliant environments resist cellular forces and are not easily deformed. Therefore, cells generate tension and respond by spreading over their matrix (McBride et al., 2008). Cell proliferation is also coupled to substrate compliance and many cells proliferate at a slower rate on softer matrices (Engler et al., 2006; Ghosh et al., 2007; Winer et al., 2008; Dupont et al., 2011; Provenzano and Keely, 2011; Wood et al., 2011). Winer et al. showed that MSC cultured on collagen I-coated PAA gels recapitulating the stiffness of bovine bone marrow (250 Pa) underwent cell cycle arrest and a reduction in DNA synthesis (Winer et al., 2008). This phenomenon has biological relevance, as this may be a mechanism by which MSC retain their stemness within the bone marrow microenvironment (Winer et al., 2008).

Stem cell differentiation and/or self-renewal has also been shown to be dependent on matrix elasticity and can be promoted on substrates with tissue-specific compliance (Engler A. et al., 2004; Georges and Janmey, 2005; Venugopal et al., 2018). For example, MSC preferentially express skeletal muscle-like myosin striations on micro-patterned substrates with a matrix compliance 8–11 kPa (Engler A. et al., 2004). This is in keeping with Atomic Force Microscopy (AFM) force spectroscopy measurements performed *ex vivo* on digitorum longus muscles in mice that identified a Young's modulus of ∼12 kPa. Moreover, Gilbert and colleagues were able to show that the self-renewal of muscle stem cells could be enhanced on 12 kPa substrates that matched the stiffness of the native tissue (Gilbert et al., 2010). Thus, by recapitulating the mechanical compliance of the *in vivo* cellular matrix *in vitro*, a specific cellular response could be promoted.

Along similar lines, neuronal or adipogenic differentiation of MSC was found to be enhanced on softer matrices, whilst stiffer ECM promoted myocyte and osteoblast differentiation (McBeath et al., 2004; Engler et al., 2006; Dupont et al., 2011). Specifically, substrate compliances between 0.1 and 1 kPa (*in vivo* elasticity of brain tissue) promoted branched morphologies and B3 tubulin expression typical of neurons (Flanagan et al., 2002; McBeath et al., 2004), 8–17 kPa promoted striated muscle morphologies and expression of the myogenic transcription factor myogenic differentiation 1 (*MYOD1*) (Engler A. et al., 2004), and 25–40 kPa promoted osteogenic morphologies and expression of the early osteogenic transcription factor *RUNX2* (Engler et al., 2006). In fact, if MSC are pre-incubated on neurogenic matrices (0.1–1 kPa) for three weeks before switching to myogenic or osteogenic media, inductive signals from the media are over-ridden and MSC maintain a neurogenic fate (Engler et al., 2006; Halder et al., 2012). Taken together ECM elasticity and the associated cell shape changes are sufficient to drive MSC fate independently of soluble factors, although addition of induction media can further enhance this response.

"Micropillars" of varying heights have also been developed to modulate the cell's perceived stiffness of its substrate, whilst directly controlling the number of cell-ECM contacts *in vitro* (**Figure 2**; Andersson et al., 2003; Nikkhah et al., 2012; Lee et al., 2013). In general, the behaviour of cells on short pillars mirrors that on stiff PAA gels, whilst cells cultured on tall, bendable pillars behave as they would on soft ECM (Nikkhah et al., 2012). Fu et al. showed that much like on stiff surfaces, short rigid microposts promote MSC spreading, actin stress fibre assembly and the formation of large FA. In contrast, cells maintain a rounded phenotype and disorganised actin structure on longer microposts (Fu et al., 2010). Here, micropillar-induced specification did not occur in normal differentiation medium, but when supplemented with adipo-osteogenic differentiation factors, rigid pillars promoted osteogenic and soft pillars enhanced adipogenic differentiation.

It is important to note that cellular responses to ECM stiffness are not universal. Although for many cell types, differentiation is enhanced on tissue-specific ECM stiffnesses, this is not always the case. For instance, it has been reported that the expansion of undifferentiated embryonic fibroblasts occurs independently of substrate stiffness (Ali et al., 2015). In addition, human blood cells such as neutrophils appear to be insensitive to the compliance of their environment and spread equally on a range of matrix stiffnesses from 180 Pa to 2.8 kPa (Discher, 2005; Yeung et al., 2005). Lastly, the differentiation state of cells may play a role in how responsive they are to mechanical cues (Eroshenko et al., 2013). Although mature fibroblasts and endothelial cells alter their shape when exposed to different ECM stiffnesses, this is not the case in undifferentiated ESC. Here, no change in undifferentiated ESC shape was observed within 12 h of culture on matrices with varying compliance (Eroshenko et al.,

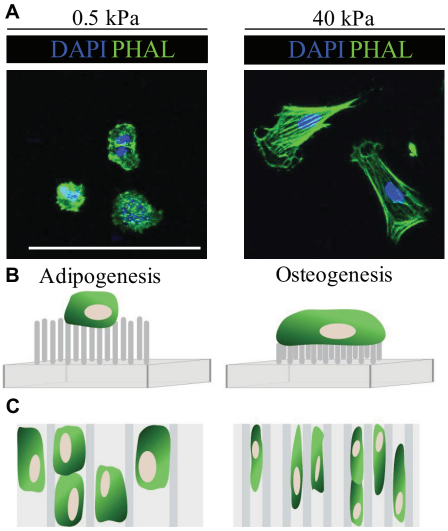

FIGURE 2 | Summary of cell responses to ECM elasticity, topography and micropillars. **(A)** Fluorescence microscopy images show typical cell response on soft (0.5 kPa) and stiff (40 kPa) substrates. In general, cells (in this case embryonic neural crest cells) on soft (0.5 kPa) substrates remain rounded, whilst those on stiff (40 kPa) ECM spread and have organised F-actin fibres, as seen by the phalloidin staining (PHAL, green). **(B)** Typically, MSC cultured on long flexible micropillars respond similarly as they would on soft ECM and have a rounded morphology, whilst those on short inflexible micropillars behave as they would on stiff ECM and spread. **(C)** In general, MSC cultured on wider microgrooves show enhanced adipogenesis, whilst those on stiff substrates have an elongated morphology which promotes osteogenesis (Fu et al., 2010; Nikkhah et al., 2012; Abagnale et al., 2015). Scale bar 100 μm.

2013). Taken together, cell responses to ECM elasticity appear to be fundamentally different depending on the cell type, so conclusions one cannot necessarily be extrapolated to other cell populations.

Extracellular Matrix Topography

In addition to ECM stiffness and geometry, topographic changes to the cellular environment impact on cell behaviour and fate (Chen et al., 2012; Eroshenko et al., 2013; Abagnale et al., 2017, 2015). Thus far, we have discussed cellular responses to the mechanical properties of flat 2D surfaces; however, during embryogenesis and adult homeostasis, cells are likely to encounter a varying topographic landscape (Abagnale et al., 2017; Murakami et al., 2017). Micro-and nano-printing techniques using microgrooves, ridges and thin polymer fibres, have helped to delineate the impact of surface topography on cell differentiation (Chen et al., 2012; Chen and Zhu, 2013). In general, the presence of grooves and ridges increases cell attachment, proliferation and alignment in comparison with flat controls (Peerani et al., 2007; Yim et al., 2007; Chen et al., 2012; Goetzke et al., 2018). For example, using microgrooved polyimide substrates, Abagnale et al. report that MSC cultured on wider grooves (15 μm) undergo adipogenesis, whilst those on thinner grooves (2 μm) differentiate into osteoblasts (**Figure 2**; Abagnale et al., 2015). Notably, altering ridge width was not sufficient to induce terminal differentiation in MSC *per se*, but directed differentiation toward a particular lineage. In this case, soluble growth factors were required to fully induce adipogenic or osteogenic fate (Abagnale et al., 2015).

Notably, defined and straight microgrooves are unlikely to replicate the complexity of the *in vivo* environment, a problem partly overcome by the development of nanorough surfaces. Here, reactive ion etching is used to generate nanorough surfaces, with a surface roughness between 1 and 150 nm (Chen et al., 2012). In one study, 7-day culture on nanorough surfaces stimulated ESC differentiation, as indicated by a reduction in the number of Oct3/4 positive cells from 93% on smooth glass to 37% on 150 nm nanorough glass (Chen et al., 2012). Not only is cell morphology and differentiation sensitive to surface topography, the release of cytokines to fight bacterial infection is also affected. Epithelial cells seeded onto microgrooves or nanopillars released fewer proinflammatory cytokines and chemokines in comparison to flat controls, despite identical surface chemistry between conditions (Andersson et al., 2003). This highlights the far-reaching impact of the topographical environment. As with cell shape and ECM stiffness, cell responses to topological cues appears to be cell-type dependent, thus conclusions from one cell type cannot be extrapolated to another.

MECHANISMS OF MECHANOTRANSDUCTION – MECHANOSENSORS

Section 3 described the behavioural responses of cells to intrinsic mechanical cues. However, the intracellular mechanisms by which mechanical cues are translated into transcriptional outputs are less well understood. In general, mechanical signals are initially perceived by membrane-embedded proteins acting as "stiffness-sensors" such as integrins, FA, G-protein coupled receptors (GPCR), cadherins and ion channels (Aragona et al., 2013; Dasgupta and McCollum, 2019). This activates Rho-ROCK, FAK and integrin-mediated signalling pathways. Subsequently, the cytoskeleton responds by changing its structure to increase or decrease cellular contractility. Ultimately, these cytoskeletal changes activate downstream signalling pathways, such as YAP/TAZ and MRTF-SRF signalling, leading to changes in cell behaviour and fate. **Figure 3** provides an overview of some of the most important mechano-transduction pathways identified to date.

Integrin and Focal Adhesion Signalling

Integrins are transmembrane receptors that consist of non-covalently bonded α and ß subunits at the cell membrane, which directly tether the cytoskeleton to the ECM. Many changes to the mechanical properties of the ECM will be perceived by these transmembrane receptors. For instance, if the rigidity of the ECM is increased, this is felt via integrin receptors on the cell surface. These integrin receptors are associated with the actin cytoskeleton via the "integrin adhesome," which consists of several proteins (Winograd-Katz et al., 2014). Thus, the integrin adhesome enables changes in the cellular microenvironment to be transmitted to the cytoskeleton and *vice versa* (Ingber, 2006;

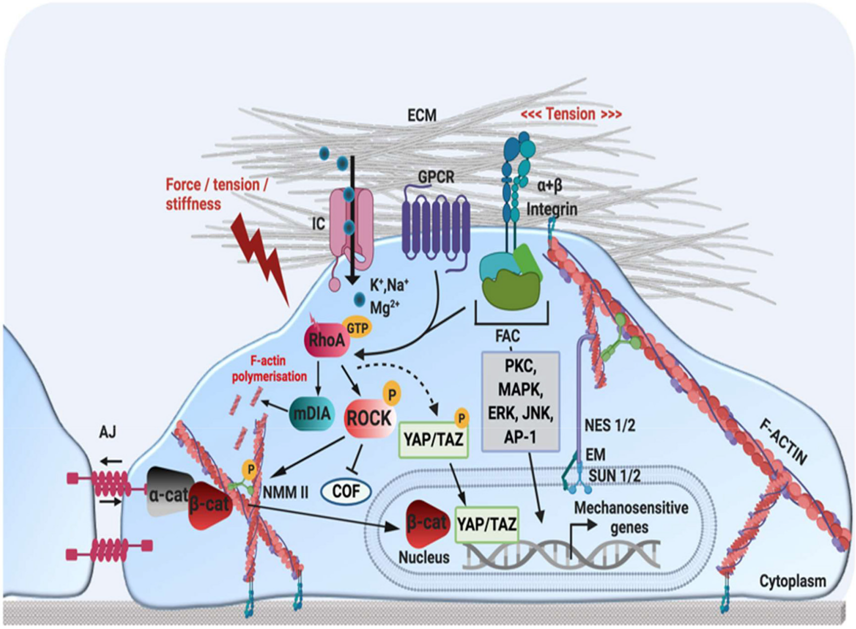

FIGURE 3 | Schematic representation of mechanotransduction pathways. Mechanical stimuli are perceived by mechano-sensors at the cellular-ECM interface, such as integrin-FA complexes, GPCR, AJ and stretch-activated ion channels. This activates several cellular signalling pathways involving kinases or transcription factors (MAPK, ERK, JNK, PKC, AP-1), as well as Rho small GTPases (RhoA). RhoA-GTP regulates actin structure by (1) activating mDia to promote actin polymerisation (2) activating ROCK, which enhances actin contractility by activating NMM II phosphorylation, and (3) preventing actin disassembly by inhibiting the actin-severing protein COF. The remodelling of F-actin and increased cytoskeletal tension also regulates YAP/TAZ, which translocate to the nucleus in response to mechanical strain. At AJ, cadherin-actomyosin connections form via α-cat and ß-cat. An increase in tension at cell-cell contacts induces unfolding of α-cat, which promotes recruitment of AJ-stabilisation proteins such as vinculin. In response to a loss of cell-cell adhesion or mechanical stimulation, ß-cat can translocate to the nucleus, to activate mechanosensitive genes. Nuclear mechano-transduction occurs via the LINC complex, which directly couples the nuclear envelope to the cytoskeleton. NES 1/2 form a link between actin and SUN 1/2 proteins in the perinuclear space, which interact with the nuclear lamina via EM and lamin A. Nesprin proteins also connect the nuclear lamina with intermediate filaments and microtubules (not depicted here). JNK, c-Jun N-terminal kinase; PKC, protein kinase C; AP-1, activator protein 1; FAC, focal adhesion complex; GCPR, G-protein coupled receptor; IC, ion channel; ECM, extracellular matrix; AJ, adherens junction; α-cat, alpha-catenin; ß-cat, beta-catenin; YAP, yes associated protein; TAZ, WW domain-containing transcription regulator protein 1 NES 1/2, nesprin-1/2; SUN 1/2, sun-domain containing protein 1/2; EM, emerin; AP-1, activator protein 1; ERK, extracellular-receptor kinase; ROCK, rho-associated protein kinase; RhoA, ras homolog family member A; COF, cofillin; NMM II, non-muscle myosin II. Created using BioRender.com.

Kumar et al., 2006). In stiff microenvironments, the cell responds by re-arranging its actin cytoskeleton and strengthening its stress fibres to balance out the forces exerted by the ECM (Ingber, 2006). This maintains a tensional equilibrium between the cell and its surrounding microenvironment, whereby stiffness-induced changes in cytoskeletal tension are transmitted back to the ECM via FA and integrin receptors, enabling cells to remodel their surrounding matrix (Ingber, 2006).

FA are the main site of interaction between ECM-bound integrins and the actin cytoskeleton, providing a form of molecular bridge between the ECM and the cell (Matthews et al., 2004; Martino et al., 2018). This enables integrins and FA to mediate several processes such as cell adhesion, migration, cell-ECM force transmission, cytoskeletal re-arrangements and signal transduction (Kanchanawong et al., 2010; Bays and DeMali, 2017; Martino et al., 2018). To date, over 50 proteins have been associated with FA sites; some of the most well-characterised components of FA complexes include the non-receptor tyrosine kinase focal adhesion kinase (FAK), the adaptor proteins paxillin, talin, vinculin, zyxin, vasodilator–stimulated phosphoprotein (VASP) and the microfilament protein α-actinin (Bays and DeMali, 2017; Burridge, 2017). Using 3D super-resolution fluorescence microscopy, Kanchanawong et al. identified three vertical FA layers; the uppermost "integrin signalling layer," the central "force transduction layer," and the innermost "actin regulatory layer," each composed of different interacting proteins (**Figure 4**; Kanchanawong et al., 2010). This "integrin adhesome" spans 20 nm across the plasma membrane and provides a "snapshot" view of the position of FA proteins (Kanchanawong et al., 2010). Later evidence shows that when activated, some proteins such as vinculin and zyxin are mobilised from their position in one layer (in this case the signalling layer) to another (in this case actin regulatory layer). This active redistribution of proteins helps to propagate mechanical signals from the ECM to the cytoskeleton (Yoshigi et al., 2005; Case et al., 2015; Sun et al., 2016).

FA proteins are highly sensitive to the cellular microenvironment, and are readily recruited and assembled at the integrin binding site in response to an increase in ECM stiffness (Smith et al., 2013). This stabilises the strain site and reinforces the cytoskeleton (Smith et al., 2013). Seong et al. visualised FAK activity using a FAK-FRET biosensor in various

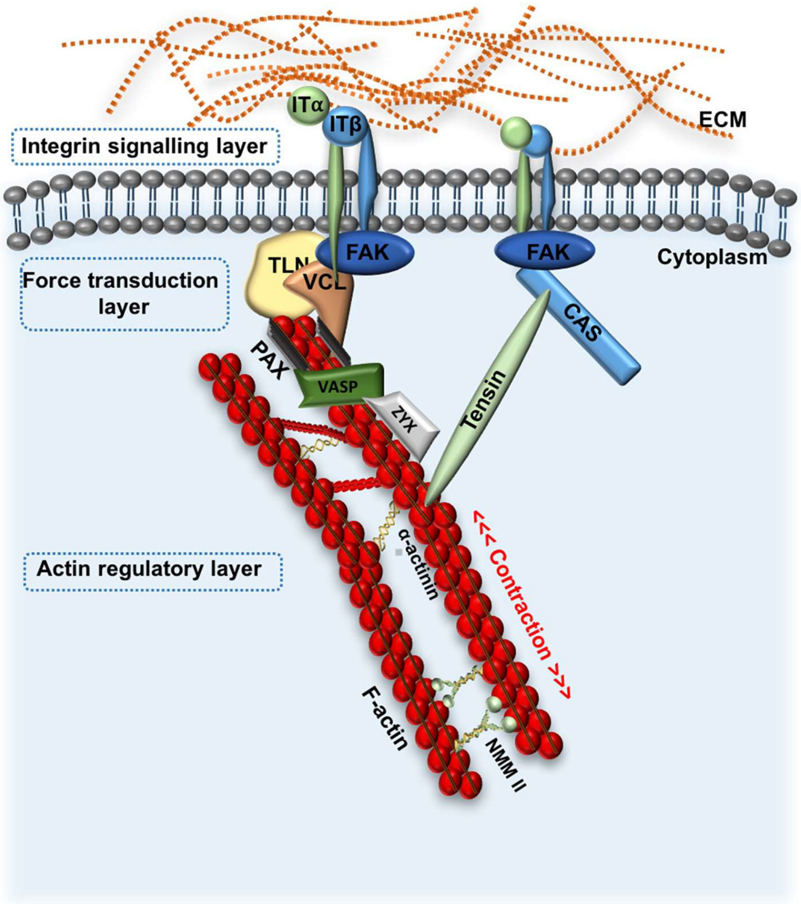

FIGURE 4 | Schematic representation of focal adhesion kinase signalling. FA signalling: FAK is recruited to integrin clusters at the cell-ECM boundary in response to changes to ECM stiffness, or other physical cues. This initiates formation of the FA complex by recruitment of various proteins such as TLN and VCL and CAS, which transduce mechanical stimuli from the ECM to the cellular cytoskeleton. VASP, Zyx and α-actinin directly regulate actin assembly. Three general FA layers are depicted, including the integrin signalling layer, force transduction layer and actin regulatory layer. FA, focal adhesion; ECM, extracellular matrix; ITα;ITß, integrin subunit α and ß; FAK, focal adhesion kinase; TLN, talin; VCL, vinculin; Zyz, zyxin; NMM II, non-muscle myosin II; VASP, vasodilator-stimulated phosphoprotein.

tumour cell lines cultured on surfaces with varying stiffnesses and concluded that FAK activity is directly proportional to increasing substrate stiffness (Seong et al., 2013). This was correlated with increased cell traction, confirming that cells in stiffer environments exert a higher traction to interact with their less compliant surroundings (Seong et al., 2013). The recruitment of the adaptor protein paxillin to FA sites is also known to be tension sensitive; a lack of tension reduces paxillin at FA and prevents actin polymerisation, leading to a lack of stress fibre repair and stress fibre breaks (Smith et al., 2013; Martino et al., 2018). Thus, effective recruitment of FA proteins is essential for the reinforcement of the cytoskeleton in response to mechanical cues.

In addition to recruitment of FA adaptor proteins, application of force can induce conformational changes to promote their interaction. Indeed, vinculin forms a link between talin and actin, which is essential for cells to strengthen their FA and generate traction forces (Atherton et al., 2015; Martino et al., 2018). The adhesion protein talin has several vinculin binding sites, but these remain unavailable to vinculin in the absence of force (Rahikainen et al., 2017). However, by computationally inducing changes to the stability of talin, Rahikainen et al. showed that mechanical forces are transmitted through talin as the FA site matures, which promotes unfolding of the protein. As a result, binding sites for vinculin are made available and subsequent vinculin accumulation strengthens the adhesion complex (Rahikainen et al., 2017).

FA and their associated adaptor proteins play an important role in creating the ECM–cytoskeleton–nuclear signalling axis. As mentioned, several FA proteins, such as zyxin, VASP and vinculin can be redistributed to actin stress fibres within the cell when mechanical force is applied (Yoshigi et al., 2005; Case et al., 2015). Some reports show that zyxin and paxillin can detach from FA sites and translocate directly to the nucleus to initiate specific gene expression changes (Cattaruzza et al., 2004; Zhou et al., 2017). For instance, in vascular smooth muscle cells, zyxin dissociates and shuttles to the nucleus when cyclic stretch is applied to cells *in vitro*, modulating mechano-responsive genes such as those for endothelin B and tenascin-C (Cattaruzza et al., 2004). In addition, nuclear transport of paxillin is known to promote DNA synthesis and cell proliferation in cervical cancer cells (Dong et al., 2009). Taken together, these studies demonstrate the important role integrins and FA play in the transmission of mechanical cues and their translation into biochemical responses.

The Cytoskeleton

The cytoskeleton is a dynamic structure composed of F-actin stress fibres, microtubules and intermediate filaments, which control cell movement, shape and homeostasis (Fletcher et al., 2010; Hoffman et al., 2011; Martino et al., 2018). Contraction of the cytoskeleton is mediated by F-actin fibres and NMM II contractile units, which form direct links with integrins and FA at the cell membrane to transmit forces from the ECM to the cell and *vice versa* (Engler et al., 2006; Naumanen et al., 2008; Kilian et al., 2010). The cytoskeleton exerts tension in a similar way to which muscles contract; as NMM II contracts, actomyosin filaments slide over one-another and contract (Steward and Kelly, 2015). As such, the cytoskeleton can "feel" and counterbalance extracellular forces applied to the cell by generating intracellular tension. Subsequently, this increases or decreases the traction forces applied by the cell to its surrounding matrix, a phenomenon described as "mechano-sensing" (Evans and Gentleman, 2014).

Changes in ECM stiffness have a striking effect on F-actin structure and assembly. Cells on stiff ECM cannot deform their matrix and generate highly organised linear arrays of F-actin fibres, whilst cells on soft ECM deform their surrounding matrix and do not exhibit pronounced cytoskeletal F-actin fibres (Georges and Janmey, 2005; Engler et al., 2006; Ghosh et al., 2007; Seong et al., 2013; Evans and Gentleman, 2014). For instance, human dermal fibroblasts cultured on stiff PAA gels (∼5 kPa) have highly organised F-actin fibres, whilst F-actin filaments are irregular in cells cultured on soft matrices (550 Pa) (Ghosh et al., 2007). This study also characterised the traction forces generated by fibroblasts on their ECM by dissociating fibroblasts from PAA hydrogels and measuring the subsequent displacement of 40 nm fluorescent beads embedded within the substrates. The traction forces exerted by the fibroblasts on their matrix as well as the stiffness of the cells themselves increased as the matrix became less compliant (Ghosh et al., 2007). Changes to ECM topography also impact on F-actin assembly (Halder et al., 2012). This is particularly noticeable in cells cultured on micro-patterned linear grooves where F-actin fibres arrange themselves parallel to the grooves (Engler A. et al., 2004; Halder et al., 2012). Notably, F-actin stress fibre size, strength, and curvature are directly linked to the number and spatial distribution of cell-ECM adhesion sites (Théry et al., 2006). This matrix-specific cytoskeletal response allows cells to appropriately interact with and deform their surrounding matrix.

Small molecule cytoskeletal inhibitors have helped to elucidate the role of the cytoskeleton in propagating mechanical signals *in vitro*. Common inhibitors include blebbistatin (inhibits NMM II), Y-27632 (inhibits Rho kinase; ROCK) and Latrunculin A (inhibits actin polymerisation). These inhibitors have helped identify the role of cytoskeletal tension in cell lineage specification (Engler A. et al., 2004; Engler et al., 2006; Kumar et al., 2006). For instance, treatment with blebbistatin prevents the stiffness-induced differentiation of MSC, which demonstrates the integral role of the cytoskeleton in mediating the mechano-sensory response of MSC (Engler et al., 2006). As mentioned previously, MSC cultured on flower- or star-shaped patterns promote adipogenic (72%) or osteogenic (67%) cell fates, respectively (Kilian et al., 2010). However, when cytoskeletal tension is inhibited, adipogenic differentiation is favoured on both shapes (Kilian et al., 2010). In contrast, osteogenesis is promoted independently of cell shape when actomyosin contractility is pharmacologically enhanced (Kilian et al., 2010). Cytoskeletal inhibitors have also proven fundamental in determining the longevity of tension-mediated cell fate changes (Fu et al., 2010). Indeed, a 12-h Y27632-treatment of MSC on ridged micro-pillars suppressed osteogenic differentiation for up to 7-days post-treatment (Fu et al., 2010). The studies discussed here indicate that the cellular cytoskeleton, traction forces and cell stiffness act in a feedback loop and respond to changes in substrate dynamics to create an equilibrium between cell and matrix tension (Ghosh et al., 2007).

Rho/Rho-Associated Protein Kinase/Non-muscle Myosin II Signalling

Rho/ROCK signalling is one of the main pathways mediating the cytoskeletal responses described above. This Rho family of GTPases (RhoA, Rac and Cdc42) is responsible for the organisation of actin cytoskeletal stress fibres and the formation of lamellipodia and filopodia (Nobes and Hall, 1999; Amano et al., 2010). Rho and ROCK can directly associate with actin stress fibres and when Rho is active (Rho-GTP), it signals via ROCK to increase cytoskeletal contraction in response to force (Leung et al., 1996; Amano et al., 1997; Katoh et al., 2011). When ROCK is active, stress fibres and FA are well-defined whilst ROCK inhibition disrupts F-actin stress fibres and reduces contractile tension after just 1 h (Katoh et al., 2001).

ROCK induces and maintains stress fibre contraction via various mechanisms (Amano et al., 2010; Katoh et al., 2011, 2001; Julian and Olson, 2014). For instance, ROCK phosphorylates myosin II light chain (MLC) and activates myosin ATPase, which mediates the interaction between MLC and F-actin to induce actomyosin contractility (Julian and Olson, 2014). Furthermore, ROCK inactivates myosin phosphatase, which prevents this kinase from dephosphorylating MLC, maintaining the activity of MLC (Julian and Olson, 2014). ROCK kinases also phosphorylate LIM kinases and subsequently inactivate cofilin, preventing this protein from depolymerising actin filaments (Sumi et al., 2001). Thus, inhibition of cofilin results in an overall increase in the number of cellular actin filaments and cytoskeletal tension (Sumi et al., 2001). In summary, Rho, ROCK and MLC work together to modulate force-induced actomyosin contraction.

Rho/ROCK signalling has been implicated in cell fate decisions in multiple cell types (Sordella et al., 2003; McBeath et al., 2004; Woods et al., 2005). Indeed, the fundamental role of ROCK signalling in MSC differentiation in response to cell shape was identified in 2004. Here, transfection of MSC with active ROCK was sufficient to induce osteogenic fate independently of cell shape (McBeath et al., 2004). In addition, pharmacological inhibition of ROCK prevented stress fibre formation and osteogenesis. Interestingly, the authors conclude that both cell shape and RhoA signalling are necessary, but that neither is sufficient to drive cell fate in MSC (McBeath et al., 2004). Later studies in human fibroblasts confirmed that high ROCK activity is associated with stiff ECM and osteogenesis, whilst soft matrix is associated with low ROCK activity and adipogenic fate (Katoh et al., 2011). Rho/ROCK signalling also plays an important role in chondrogenesis. Inhibition of RhoA or ROCK increases glycosaminoglycan production and mRNA expression of the chondrogenic marker *SOX9* in MSC cultured *in vitro* (Woods et al., 2005). Moreover, ROCK inhibition in the chondrogenic cell line ATDC5 promotes a round cell morphology and an increase in cortical actin, which are typical hallmarks of the chondrogenic phenotypes (Woods et al., 2005). In a later study, the hypoxia-mediated enrichment of chondrogenic markers on soft PAA gels was prevented by inhibition of ROCK (Foyt et al., 2019). This suggests that Rho/ROCK signalling may underpin the effects of hypoxia in this context.

Rho signalling has also been implicated in the switch between adipogenic and myogenic differentiation programmes in MSC (Sordella et al., 2003; McBeath et al., 2004). Several findings support the notion that Rho activity promotes myogenesis, whilst RhoA inhibition induces adipogenesis. MSC cultured in ROCK inhibitor promoted adipogenesis (Sordella et al., 2003); however, expression of a constitutionally active Rho GTPase (RhoV14), which acts upstream of ROCK, reduces adipogenesis. This effect is mediated by the insulin growth factor (IGF) pathway, whereby IGF-1 promotes Rho activation which drives myogenesis. Mechanical cues such as oscillatory fluid flow have been shown to directly activate RhoA and downstream ROCK in murine MSC, and induce the expression of the osteogenic marker *Runx2*. Inhibition of RhoA and ROCK independently of one another, found that both are required for flow-induced *Runx2* expression (Arnsdorf et al., 2009). In conclusion, these studies illustrate the integral role that RhoA/ROCK signalling plays in the transmission of mechanical cues to drive cell differentiation.

Yes-Associated Protein/TAZ Signalling

The protein homologues yes-associated protein (YAP) and WW domain-containing transcription regulator protein 1 (TAZ) are key components of the HIPPO signalling cascade, which regulates organ size, cell proliferation, differentiation and migration in several systems (Dupont, 2016; Hindley et al., 2016; Manning et al., 2020). When Hippo signalling is active, YAP and TAZ are phosphorylated by large tumour suppressor kinase 1/2 (LATS1/2), which induces YAP/TAZ ubiquitination and degradation and/or sequesters the proteins to the cytoplasm. When the HIPPO signalling is inactive, YAP and TAZ are not phosphorylated and translocate to the nucleus, where they bind to TEAD regulatory elements and activate transcriptional programmes to promote cell growth and proliferation (**Figure 5**). In principle, nuclear YAP/TAZ promotes proliferation whilst contact inhibition induces cytoplasmic and transcriptionally inactive YAP/TAZ, reducing proliferation (Piccolo et al., 2014). In reality, nuclear-cytoplasmic shuttling of YAP/TAZ is more complex and occurs via multiple regulatory pathways. For instance, these proteins can be phosphorylated by other kinases, for example protein kinase B (AKT) and c-Jun N-terminal kinases (JNK) and are regulated by the ß-catenin degradation complex during WNT signalling (Basu et al., 2003; Azzolin et al., 2014; Piccolo et al., 2014). In addition, YAP/TAZ activity has been found to be regulated via HIPPO-dependent and HIPPO-independent mechanisms (**Figure 6**; Zhao et al., 2008; Dupont et al., 2011; Aragona et al., 2013; Dobrokhotov et al., 2018).

In 2011, pioneering work by Dupont et al. categorised YAP and TAZ as "mechano-sensors." They identified that in MSC, the localisation of YAP/TAZ changes in response to mechanical cues such as shape, density, ECM stiffness and cytoskeletal tension (Dupont et al., 2011). Specifically, small micro-patterned islands, low ECM stiffness, high cell density and a rounded shape promoted cytoplasmic retention of YAP/TAZ, while larger islands, a high matrix stiffness, sparse cell density and spreading promoted nuclear accumulation of YAP/TAZ (Dupont et al., 2011). Moreover, YAP/TAZ localisation impacted MSC fate. Nuclear YAP was found to promote osteogenesis, while cytoplasmic localisation drove adipogenesis (Dupont et al., 2011; Dupont, 2016). Importantly, overexpression of YAP/TAZ *in vitro* promotes osteogenic differentiation and cell proliferation in cells on soft ECM, and is thus sufficient to "trick" cells into behaving as they would on a stiff matrix (Dupont et al., 2011). In short, YAP/TAZ sense mechanical cues and also mediate the cellular response to mechanical stimulation, a mechanism which is conserved across multiple cell types (Engler et al., 2006; Dupont et al., 2011; Wada et al., 2011; Halder et al., 2012; Aragona et al., 2013; Galarza Torre et al., 2018; Meng et al., 2018).

Wada et al. (2011) reported that actomyosin tension regulates YAP/TAZ through LATS1/2-dependent phosphorylation of YAP. It was proposed that signals from F-actin stress fibres either directly inhibit or function upstream of LATS 1/2, which prevents YAP/TAZ phosphorylation (Wada et al., 2011). In endothelial cells, pharmacological disruption of F-actin led to a decrease in nuclear YAP localisation. However, when endothelial cells were transfected with a kinase-defective form of LATS2 and F-actin was inhibited, nuclear YAP was maintained. The authors conclude that stress fibres regulate YAP via HIPPO signalling, although the possibility that F-actin also functions independently of HIPPO could not be excluded. Stiff ECM also activates a FAK signalling pathway (β1-integrin–FAK–Src–PI3K–PDK1), which directly inhibits LATS1/2 activity and promotes nuclear YAP localisation (Dobrokhotov et al., 2018; Lachowski et al., 2018).

However, YAP/TAZ have also been found to be modulated via cytoskeletal tension, cell shape, density and ECM stiffness *independently* of HIPPO signalling pathways (Aragona et al., 2013; Dobrokhotov et al., 2018). This phenomenon has been reported in MSC, mouse embryonic fibroblasts, keratinocytes and mammary epithelial cells (Dupont et al., 2011; Halder et al., 2012). Disruption of actomyosin tension inactivates YAP/TAZ and promotes their cytoplasmic localisation, which suggests these proteins are directly regulated by the cytoskeleton (Dupont et al., 2011; Wada et al., 2011; Zhao et al., 2012). YAP/TAZ

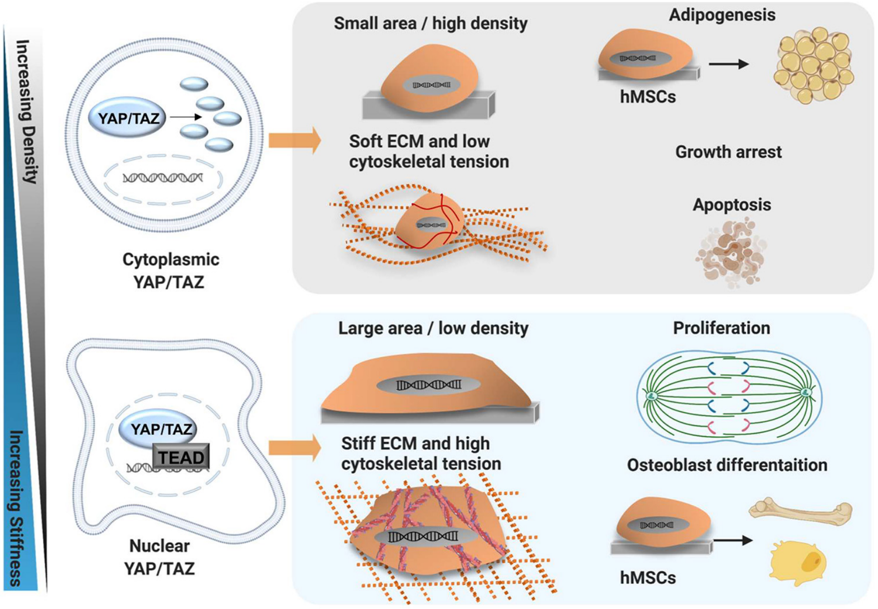

FIGURE 5 | YAP/TAZ mechanism of action. Schematic showing mechanical regulation of YAP/TAZ activity and modulation of cell behaviour by YAP/TAZ in MSC. Osteogenesis and skeletal muscle fates are promoted by stiff ECM and a low cell density, allowing MSC to spread and generate cytoskeletal tension via F-actin stress fibres. The stiff matrix promotes stress fibre formation and YAP/TAZ nuclear translocation. Conversely, adipogenic fates are promoted by soft ECM and high cell-cell contact. The soft matrix prevents stress fibre formation, thus MSC cannot generate tension and display only cortical actin. As such, YAP/TAZ are retained in the cytoplasm, undergo proteasomal degradation and are rendered inactive, promoting adipogenesis. Created using Biorender.com.

expression can be modulated by F-actin capping and severing proteins, which prevent actin polymerisation; siRNA-mediated knock-out of the actin-capping proteins reactivated mRNA expression of the YAP/TAZ target genes on soft matrices and in dense cultures (Aragona et al., 2013). In addition, LATS1/2 knockdown did not restore nuclear YAP/TAZ activity in cells treated with a cytoskeletal inhibitor, or cells cultured on soft ECM (Dupont et al., 2011; Aragona et al., 2013). This suggests that mechanical control of YAP/TAZ activity is predominantly regulated by cytoskeletal signals, which may dominate over HIPPO-dependent signalling. Moreover, physical cues and F-actin structure can also alter the responsiveness of YAP/TAZ to inputs from WNT or GPCR signalling (Aragona et al., 2013). Ultimately, this implies that cells require an appropriate cytoskeletal structure to control YAP/TAZ transcriptional activity; however, the exact mechanisms are not yet well characterised (Piccolo et al., 2014).

Additional regulators of YAP/TAZ activity such as calveolin-1 (CAV1), as well as the nucleus itself have recently been described (Elosegui-Artola et al., 2017; Meng et al., 2018; Moreno-Vicente et al., 2018). CAV1 controls YAP via a HIPPO-independent mechanism; mouse embryonic fibroblasts deficient of CAV1 exhibit a disorganised actin cytoskeleton, cytoplasmic YAP and reduced expression of YAP targets (Moreno-Vicente et al., 2018). CAV1 was also found to directly control the response of YAP/TAZ to cytoskeletal tension via direct interaction with YAP (Moreno-Vicente et al., 2018). In addition, stiff ECM has been found to drive YAP/TAZ into the nucleus by opening nuclear pores which can occur independently of cytoskeletal contraction (see Section "Nuclear Mechanotransduction"; Elosegui-Artola et al., 2017; Dobrokhotov et al., 2018).

Serum Response Factor Signalling and Myocardin-Related Transcription Factors

Myocardin-related transcription factors (MRTF) and serum response factor (SRF) also play important roles in modulating gene expression in response to biophysical cues (Olson and Nordheim, 2010; Costa et al., 2012). MRTFs bind to nuclear SRF, which activates downstream SRF-responsive genes, many of which are involved in the regulation of the cellular actomyosin structure. MRTFs are normally sequestered to the cytoplasm when bound to G-actin in the presence of low actin polymerisation (Sotiropoulos et al., 1999; Posern et al., 2002). However, when cells are mechanically stimulated, MRTF is released from G-actin and translocates to the nucleus, where it directly interacts with SRF (Sotiropoulos et al., 1999; Miano et al., 2007; Olson and Nordheim, 2010). The downstream targets of SRF are not limited to cytoskeletal genes. SRF also regulates smooth muscle differentiation by binding to the CArg box element of myocardin (MYOCD) (Miano et al., 2007). Several stretch-sensitive signalling pathways, such as the ERK1/2 pathway have been implicated in smooth muscle differentiation. ERK1/2 mediates its responses by phosphorylating ternary complex factors, which bind to SRF and activate early smooth muscle gene-expression (Ball and Price, 1995; Hellstrand and Albinsson, 2005).

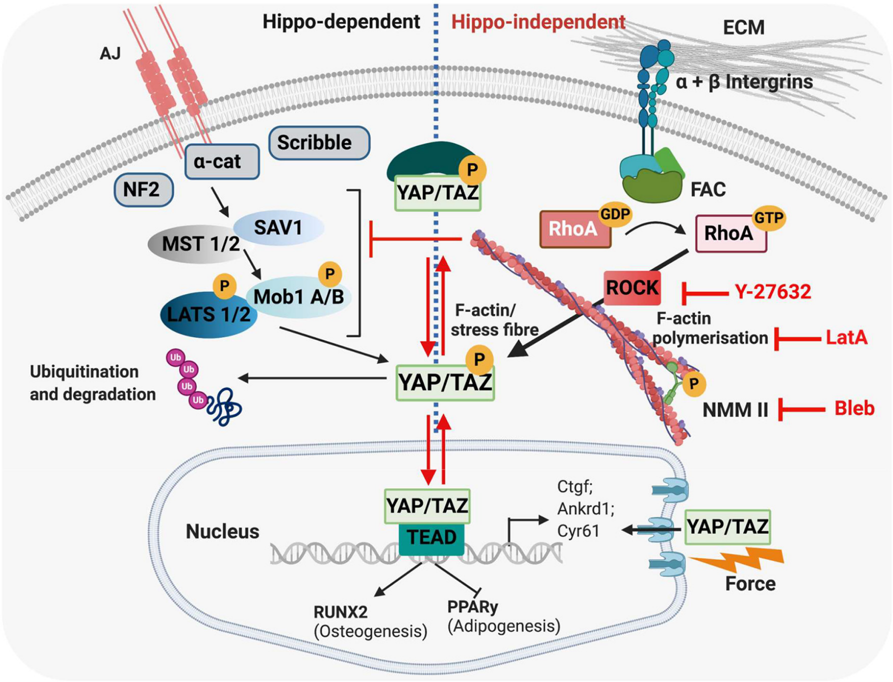

FIGURE 6 | Hippo-dependent and Hippo-independent regulation of YAP/TAZ. YAP/TAZ are known to be regulated via the HIPPO signalling pathway and by a mechanically regulated HIPPO-independent mechanism. **(Left)** HIPPO control of YAP and TAZ. The HIPPO pathway regulates organ growth as well as cell proliferation, migration and differentiation. In tightly packed tissues, proliferation is regulated by contact inhibition via the HIPPO pathway. Tight junctions and adherens junctions between cells interact with and activate MST1/2, which recruit SAV1, and subsequently phosphorylate LATS1/2. This phosphorylation is facilitated by the scaffold proteins MOB1 A/B and NF2. In turn, LATS1/2 phosphorylate YAP/TAZ, leading to cytoplasmic sequestering of these proteins, and their eventual ubiquitination/degradation. F-actin has been proposed to regulate YAP/TAZ localisation via the HIPPO pathway by inhibiting LATS1/2 and/or upstream factors, thus preventing phosphorylation and cytoplasmic retention of YAP/TAZ. **(Right)** ECM stiffness also regulates YAP/TAZ in a HIPPO-independent mechanism. Cells interact with their ECM via integrins; in stiff environments, focal adhesion assembly is promoted, which activates Rho-ROCK signalling, which in turn activates F-actin stress fibre formation and translocation of YAP/TAZ to the nucleus, where these proteins regulate gene expression via activation of TEAD1-4. External application of force to the nucleus has also been shown to open nuclear pores and allow increased YAP/TAZ entry into the nucleus. Cytoskeletal inhibitors affect different parts of the mechanotransduction pathway; Y-27632 inhibits ROCK, Latrunculin A inhibits F-actin polymerisation and Blebbistatin inhibits Myosin (all depicted in red). MST1/2, mammalian ste-20-like kinases 1/2; SAV1, salvador family WW domain containing protein 1; LATS1/2, large tumour suppressors 1/2; MOB1 A/B, MOB kinase activator 1A; NF2, neurofibromatosis type 2; TEAD1-4, TEA domain family member 1-4; FAC, focal adhesion kinase. Created using Biorender.com.

Nuclear Mechanotransduction

The "LINC complex" (linker of nucleoskeleton and cytoskeleton) directly links cytoskeletal components to the nuclear surface and has received much attention in recent years for its role in the direct transmission of ECM force to the nucleus (Crisp et al., 2006; Neelam et al., 2015; Martino et al., 2018). This complex contains several proteins including sun-domain containing protein 1/2 (SUN 1/2), nesprin and lamins, which directly anchor cytoskeletal elements such as microtubules, intermediate filaments and F-actin to the nuclear envelope (Crisp et al., 2006; Wang et al., 2009; Swift et al., 2013; Neelam et al., 2015). Mechanosensitive proteins, such as nuclear lamins, are responsible for driving many cellular responses to stiffness by either changing their confirmation, undergoing post-translational modifications or altering their subcellular localisation (Buxboim et al., 2014; Cho et al., 2019). For instance, increases in matrix stiffness and subsequent changes to myosin II activity lead to increased dephosphorylation of the nucleoskeletal protein lamin A, which regulates its turnover and the properties of the nuclear envelope (Buxboim et al., 2014).

Nuclear shape is also important in mechanotransduction. For example, micropipette-induced deformation of nuclear shape can be enhanced when cells are treated with inhibitors of intermediate filaments (Neelam et al., 2015). This suggests that intermediate filaments aid in the control of nuclear deformation (Neelam et al., 2015). Changes to cytoskeletal structure are known to directly impact on nuclear membrane shape, ion channels and the structure of nuclear pores, which in turn affects gene expression (Feldherr and Akin, 1990; Wang et al., 2009). However, the mechanisms through which mechanical cues are translated to the nucleus via the cytoskeleton are not yet well understood. A recent report proposes that force transmission to the nucleus occurs independently of the cytoskeleton. Indeed, cells cultured on stiff ECM had flatter and stretched nuclei, which in turn stretched nuclear pores and increased nuclear YAP import (Elosegui-Artola et al., 2017). Interestingly, force application to the nucleus via AFM was sufficient to translocate

YAP to the nucleus independently of FA and when components of the cytoskeleton were inhibited (Elosegui-Artola et al., 2017). Thus, direct force transmission from the ECM to the nucleus is a novel and alternative mechanism for controlling gene expression.

THE ROLE OF INTRINSIC MECHANICAL FORCES IN EMBRYONIC DEVELOPMENT

Brief Historical View of Mechanoregulation in Embryogenesis

Almost a century ago, the concept that mechanical forces regulate embryonic development was gaining momentum. For example, while it had been previously widely believed that smooth muscle cells self-differentiated, by the 1920s the idea that tensional stress-induced elongation of mesenchymal cells was an important stimulus for smooth muscle differentiation in tissues such as the oesophagus was picking up speed (Carey, 1922b). Indeed, Carey et al. suggested that the spiral growth pattern of the epithelium as it expands to form the oesophageal lumen exposed the mesenchyme to extrinsic force which promoted mesenchymal cell elongation and stimulated smooth muscle differentiation (Carey, 1922a). It was later reported that mechanical stress may be important for blood vessel formation and subsequent nutrient supply in developing tissues (Loeschke and Weinhold, 1922; Glucksmann, 1942).

A putative role for mechanically driven processes in embryogenesis was further supported by early observations that embryonic limb explants cultured *in vitro* developed into identifiable bones and joints, but were often incomplete. Indeed, cultured long bones formed a recognisable morphology, but failed to develop a marrow cavity *ex vivo* (Fell, 1925; Thorogood, 1983). These observations led several researchers to suggest that mechanical cues *in vivo* were important in controlling such developmental processes and raised questions about the role of the environment adjacent to the developing bone during morphogenesis (Fell, 1925; Murray, 1926; Drachman and Sokoloff, 1966). Such questions were explored as early as the 1920s when the developing pig femur was used to show preferential osteoblast differentiation in regions under tensile stress (Carey, 1922a). Indeed, during limb rotation, muscular activity causes bending of the femur. As a result, bone is first deposited on the convex aspect of the femoral shaft, which is under high tensile stress, whilst osteoblast differentiation on the concave aspect is secondary. These findings were later confirmed in the chick in the early 1940s when Glucksmann et al., showed that osteogenesis is promoted by tension in chick bone rudiments cultured *in vitro.* Here, the authors cultured chick tibiae rudiments, which naturally became enclosed in a fibrous capsule during the culture period. The fibrous capsule contracted during cultivation and pulled the rudiments together, which altered forces in the capsule, and drove new bone deposition in the direction of increased tension forces (Glucksmann, 1942). Later landmark studies in the 1990s investigated the effect of pharmacologically paralysing both avian and murine embryos at various stages (Hall and Herring, 1990; Rodríguez et al., 1992). Immobilised embryos were shown to have smaller and lighter skeletal bones and less surrounding muscle compared to untreated controls (Hall and Herring, 1990; Rodríguez et al., 1992). Notably, areas with the greatest reduction in musculature, such as around the clavicle, were correlated with a more significant reduction in bone growth, suggesting an integral role for muscle contraction in bone development (Hall and Herring, 1990). Collectively these studies demonstrate that mechanical load is important for both bone development and achieving proper tissue size (Pai, 1965; Hall and Herring, 1990; Rodríguez et al., 1992).

Early studies of cartilage and joint development also used paralysis models to gain insights into the role of mechanical cues in their formation (Fell and Canti, 1934; Murray and Smiles, 1965; Drachman and Sokoloff, 1966; Hall, 1979). For instance, secondary cartilage was found not to form in the quadratojugal bone of immobilised 10-day old chick embryos *in ovo* (Hall, 1979). The authors concluded that continued differentiation of the progenitor pool into chondroblasts as opposed to osteoblasts requires biomechanical signals in the form of muscle contraction. In this case, a lack of movement reduced the mitotic activity of periosteal progenitor cells, which depleted the available pool of progenitor cells with the potential to undergo chondrogenesis (Hall, 1979). This was supported by further studies in mammals which similarly showed that although cartilage formation in the mandible could be initiated in the absence of normal *in vivo* mechanical cues, the maintenance of secondary cartilage required mechanical stimulation. Indeed, in the absence of mechanical stimulation cartilage in *ex vivo* cultured mandibles disappeared as the progenitor cells switched to osteogenesis (Fang and Hall, 1997). Evidence from the 1960s also showed that muscle contraction was indispensable for joint cavity formation; *in ovo* treatment of chick embryos with neuromuscular blocking agents, or complete removal of the lumbosacral spinal cord resulted in absent knee and ankle joint cavities (Drachman and Sokoloff, 1966). Instead, the interzone between articular elements was filled with vascular connective tissue, which eventually became compact and fibrous.

Intrinsic Forces in Embryonic Development

In addition to extrinsic forces, intrinsic forces such as cell density, shape and ECM compliance also control morphogenesis and cell differentiation within the embryo (McBride et al., 2008; Chevalier et al., 2016a). For instance, mesenchymal condensations are necessary for the development of muscle, bone, cartilage, lung, hair follicles and kidney, and can affect both the physical and biochemical cellular environment (Dunlop and Hall, 1995; McBride et al., 2008). These two elements are often intertwined; for example, an increase in cell density and subsequent round morphology promotes cell-cell adhesion and increases paracrine signalling (Dunlop and Hall, 1995; Knothe Tate et al., 2008). Importantly, each cell within the condensing mesenchyme is likely to encounter a unique set of biophysical cues, as mesenchymal cells are not a homogenous population due to the asymmetry of condensation boundaries (Knothe Tate et al., 2008).

Moreover, just as cell shape and density are important for driving MSC fate decisions, cells receive similar cues during condensation events in embryogenesis, which also act as important regulators of fate. Condensation can occur as an "aggregation" event, in which mesenchymal cells become compressed around a central point, or as an "expansion" event in which a central mitotic mesenchymal pool increases the cell number within a given space (Knothe Tate et al., 2008). During osteogenesis, condensation events are key for increasing the number of pre-osteoblasts, which then differentiate and deposit bone matrix (Dunlop and Hall, 1995). Mesenchymal condensation is also critical for odontogenesis (Mammoto et al., 2011). During the bud stage of tooth formation, neural crest cell (NCC)-derived mesenchyme rapidly proliferates, creating a compact mass of cells with a round morphology (Mammoto et al., 2011). Culture of primary murine NCC isolated from the first pharyngeal arch on micro-patterned substrates revealed that a round cell shape is sufficient to upregulate the odontogenic marker paired box 9 (*Pax9*) independently of cell-cell contact. Specifically, the rounded cell shape suppressed RhoA and cytoskeletal pre-stress within the cell, promoting Pax9-mediated osteogenesis (Mammoto et al., 2011).

Intrinsic biophysical cues also impact on processes such as neurulation. The genetic basis of neural tube closure is relatively well-characterised and to date over 300 genes have been implicated, including Shh, GLI family zinc finger 3 (Gli3), VANGL planar cell polarity protein 2 (Vangl2), zic family member 2 (Zic2), and LDL receptor related protein 2 (Lrp2) (Copp and Greene, 2013; Kur et al., 2014; Galea et al., 2018, 2017; Juriloff and Harris, 2018). Mutations in these genes can predispose sufferers to a range of neural tube defects, such as anencephaly and spina bifida (Galea et al., 2017; Nikolopoulou et al., 2017). In addition to these genetic factors, mechanical cues are required to convert the flat ectoderm into a round tube (Vijayraghavan and Davidson, 2017). Two mechanical processes particularly important for effective neurogenesis are convergent extension (CE) and apical constriction (AC) (Inoue et al., 2016; Nikolopoulou et al., 2017). The neural plate is shaped via CE, which increases the embryonic length in the anterior-posterior direction relative to its medio-lateral width (Vijayraghavan and Davidson, 2017). In late gastrula stage *Xenopus*, the stiffness of dorsal neural tube explants increases from 13 to 85 Pa during CE (Zhou et al., 2009). Treatment of the dorsal neural tube isolates with a ROCK inhibitor resulted in a 50% reduction in tissue stiffness (Zhou et al., 2009). This suggests that cytoskeletal tension accounts for some, but not all, of the stiffness increase that occurs during CE. The same group later generated force-maps of the dorsal explants during CE by using a gel force sensor system, in which explants were embedded into agarose gels containing fluorescent beads. The forces produced by the explant as it underwent CE were inferred by measuring the bead displacement and degree of agarose gel deformation (Zhou et al., 2015). The greatest agarose deformation was observed at the anterior and posterior regions of the dorsal explants. Furthermore, when explants were cultured in stiffer agarose gels, the stress produced by the dorsal explant itself also increased. Thus, the dorsal neural tube is able to respond to and counterbalance changes to its surrounding mechanical environment (Zhou et al., 2015).

Apical constriction (AC) events are critical for driving processes such as gastrulation, neural tube closure, the formation of the salivary glands and inner ear (Sawyer et al., 2010; Inoue et al., 2016; Hartl et al., 2019). During AC, the apical side of the cell contracts, creating cells with a wedge-like morphology. In addition, actin and NMM II accumulate at the cell apex and at cell-cell junctions (Sai and Ladher, 2008; Galea et al., 2017; Vijayraghavan and Davidson, 2017; Butler et al., 2019). Numerous studies in *Xenopus* and vertebrates state that AC and actomyosin contractility are required to regulate the bending and folding of the neural plate and formation of the medial hingepoint (Zhou et al., 2009; Inoue et al., 2016; Nikolopoulou et al., 2017; Suzuki et al., 2017; Butler et al., 2019; Karpińska et al., 2020). The posterior neuropore (PNP) at the most caudal end of the neural tube is known to be under tension during closure. Galea et al. (2017) identified the presence of a F-actin cable around the borders of the neural folds. Laser ablation of the PNP zippering point caused the neuropore to widen and the neural folds to move further apart (Galea et al., 2017). The same group later reported that *ex vivo* ROCK inhibition of E9.5 embryos slows PNP closure by reducing the accumulation of apical F-actin in the neuroepithelium and along the neural folds (Butler et al., 2019). Laser ablation of F-actin cables at the PNP zippering point confirmed that lateral tissue recoil in ROCK-inhibited embryos was greatly reduced compared to controls, therefore ROCK inhibition decreases the tensions that normally act on the neural folds (Butler et al., 2019). In addition, the absence of ROCK activity prevented AC, as quantified by an increase in the apical size of neuroepithelial cells in Y-27632-treated embryos (Butler et al., 2019).

Both contraction of the apical cell surface via actomyosin interactions and removal of the surface membrane are required for effective AC. Several studies have identified proteins such as vinculin and MARCKS that mediate the actomyosin contractility during neural tube closure (Morriss-Kay and Tuckett, 1985; Stumpo et al., 1995; Xu et al., 1998). For instance, the protein Catulin A is a key player in Rho-mediated AC; *Catulin A-/-* mutants are embryonically lethal at E10.5 and neural tube fusion fails to occur at the hindbrain/cervical boundary (Karpińska et al., 2020). Apical actin and nestin filaments did not form in the neuroepithelium of mutants, which was correlated with a lack of active RhoA signalling (Karpińska et al., 2020). A recent study identified the endocytic receptor Lrp2 as an integral mediator of membrane remodelling during AC. Indeed, a striking increase in apical surface area, defective neural fold morphogenesis and mis-localisation of the planar cell polarity protein Vangl2 were all observed in Lrp2 mutants (Kowalczyk et al., 2021).

Measuring Embryonic Stiffnesses *in vivo*

In vivo, ECM and cellular stiffness can affect cell fate decisions and techniques for measuring these nano- and micro-scale tissue elasticities are advancing. However, measuring mechanical properties *in vivo* is very challenging and few studies have directly quantified stiffness within the embryo (Barriga et al., 2018; Wozniak and Chen, 2009;

Efremov et al., 2011; Marturano et al., 2013; Chevalier et al., 2016b). The Young's modulus of a tissue can be indirectly estimated via micropipette aspiration assays, in which several cells within a tissue are sucked into a micropipette. Using this approach, the length of the aspirated tissue at a given suction pressure can be used to infer cellular mechanical properties (Majkut et al., 2013; Daza et al., 2019). For example, Majkut et al. (2013), demonstrated that *in vivo,* mouse heart tissue stiffens over time, which is important for contraction of cardiomyocytes. The same study showed that *in vitro* culture of primary cardiomyocytes from E4 embryos on collagen I substrates that closely resemble the stiffness of the heart at this stage (1–2 kPa) initiated their contraction.

Measurement of cell and ECM stiffness *in vivo* is also possible via AFM force spectroscopy (Thurner, 2009; Iwashita et al., 2014; Chevalier et al., 2016b; Koser et al., 2016). AFM measures the deflection of a laser beam focussed on the back of a cantilever as it indents the surface of a tissue (Alonso and Goldmann, 2003). The deflections are captured by a photodiode and used to infer stiffness. A hallmark study in chick identified that the stiffness of the embryonic tendon significantly increased over time at both the nano- and micro-scale between stage HH38 and HH43. Inhibition of enzymatic collagen cross-linking identified that this decrease correlated with an increase in collagen cross-linking and was necessary for tendon development (Marturano et al., 2013). In the same year, Iwashita and colleagues reported a correlation between matrix stiffness and cell fate in the murine cortical brain. From E12.5 to E18.5, the stiffness of each cortical brain layer significantly increased as neuronal differentiation progressed. This shift in stiffness was attributed to both cellular and matrix origins, as *in vitro* AFM measurements confirmed neuronal and matrix stiffness changes independently (Iwashita et al., 2014).

SUMMARY AND OUTLOOK

In summary, mechanical cues play a fundamental role in driving both adult and embryonic cell fate decisions. Despite significant progress in understanding the molecular mechanisms that govern mechanotransduction, many of the signalling pathways remain to be defined. Extrinsic cues such as fluid flow and compression as well as local intrinsic cues such as cell shape and density are "felt" by mechano-sensors at the cellular-ECM interface. This activates various downstream signalling pathways including Rho/ROCK signalling, which promotes actomyosin rearrangements and allows cells to counteract the forces from their surrounding microenvironment. Although the cytoskeleton is known to play an integral role in translating cues from the ECM to the cell and *vice versa*, the intricacies of nuclear mechanotransduction are only now becoming apparent. Moreover, the discovery that the nucleus can deform independently of the cytoskeleton in response to directly applied forces, thereby increasing nuclear entry of factors such as YAP, demonstrates the far-reaching effects of mechanical stimuli (Elosegui-Artola et al., 2017).

Understanding the impact of intrinsic mechanical cues, such as stiffness, during embryogenesis is somewhat limited by the tools available to study very soft tissues. Indeed, for embryonic tissues, experimental measurements of stiffness can be limited by challenges regarding sample preparation and immobilisation, as slicing can often disrupt tissue integrity and structure (Viji Babu and Radmacher, 2019). In addition, embryonic samples are composed of highly heterogeneous morphological structures, which can hinder accurate measurements of tissue stiffness using techniques such as AFM (Galluzzi et al., 2018). Despite this, several recent reports describe how AFM can be optimised to measure the stiffness of soft culture surfaces and tissues (Galluzzi et al., 2018; Babu et al., 2019; Norman et al., 2021).

With the development of new techniques such as the standardised nanomechanical AFM procedure, which standardises AFM calibration and protocols between laboratories, reproducible data acquisition, particularly on soft tissue samples should become the norm (Schillers et al., 2017). Recent advancements also include magnetic devices capable of measuring the viscoelastic properties of entire 3D structures up to the size of an E10.5 mouse embryo (Zhu et al., 2020). The device generates a magnetic field to displace magnetic beads injected into the developing mouse limb bud, and has been used to uncover the presence of a mesodermal stiffness gradient (Zhu et al., 2020). In addition to improving our understanding of mechanical cues in embryonic development, measuring tissue stiffness is likely to play an increasingly important role in non-invasive diagnosis of cancer (including extent of invasion), liver fibrosis and primary biliary cholangitis (Corpechot et al., 2021; Li and Wu, 2021; Shao et al., 2021). For instance, shear wave elastography ultrasound imaging can detect increases in the Young's modulus of tissues induced by malignant tumours and is being optimised for use clinically through the addition of colour mapping functionality (Lee et al., 2020).

In recent years, there have also been growing efforts to re-create mechanical cues experienced by living tissues in 3D engineered tissue constructs grown *in vitro*. However, whilst specific elasticities can often be engineered into polymer scaffolds, matching the mechanical cues experienced by cells within native tissues is often more challenging. This is because many tissue do not behave elastically, but rather display time-dependent and non-linear responses (Chaudhuri et al., 2020; Elosegui-Artola, 2021). For example, rather than immediately returning to their original shape when an applied strain is removed, tissues are viscoelastic and exhibit a time-dependent response (Chaudhuri et al., 2020; Efremov et al., 2020; Pogoda et al., 2021). To create materials that better reflect these tissue responses, hydrogels with dynamic cross-links between polymers have been developed (Chaudhuri et al., 2020). For example, within these materials, covalent thioester exchange and/or hydrozone bonds allow for investigation of time-dependent rearrangements of bonds (Brown et al., 2018; Marozas et al., 2019).

Finally, gaining a better understanding of the cellular response to local matrix compliance and topography has important implications for improving *in vitro* differentiation assays. This will in turn improve the design of physiologically relevant materials for tissue repair. This has particular relevance in orthopaedic applications, such as knee arthroplasty for osteoarthritis patients. Here, appropriate implant structure and mechanical stimulation may be necessary to promote its anchorage within the bone (Li et al., 2018). The upcoming challenge in tissue engineering will be not only to understand the complexity of the cellular response to mechanical cues, but also to develop scaffolds that accurately capture and recapitulate *in vivo* environments.

AUTHOR CONTRIBUTIONS

Both authors listed have made a substantial, direct and intellectual contribution to the work, and approved it for publication.

FUNDING

JP acknowledges the London Interdisciplinary Doctoral Programme, which is funded by the BBSRC.

ACKNOWLEDGMENTS

We would like to acknowledge helpful discussions with Professor Philippa Francis-West, Steve Allen, Johanna Engel, and Mohamed Zein, which contributed to this review.

REFERENCES

Abagnale, G., Sechi, A., Steger, M., Zhou, Q., Kuo, C.-C., Aydin, G., et al. (2017). Surface topography guides morphology and spatial patterning of induced pluripotent stem cell colonies. *Stem Cell Rep.* 9, 654–666. doi: 10.1016/j.stemcr.2017.06.016

Abagnale, G., Steger, M., Nguyen, V. H., Hersch, N., Sechi, A., Joussen, S., et al. (2015). Surface topography enhances differentiation of mesenchymal stem cells towards osteogenic and adipogenic lineages. *Biomaterials* 61, 316–326. doi: 10.1016/j.biomaterials.2015.05.030

Ali, S., Wall, I. B., Mason, C., Pelling, A. E., and Veraitch, F. S. (2015). The effect of Young's modulus on the neuronal differentiation of mouse embryonic stem cells. *Acta Biomater.* 25, 253–267. doi: 10.1016/j.actbio.2015.07.008

Alonso, J. L., and Goldmann, W. H. (2003). Feeling the forces: atomic force microscopy in cell biology. *Life Sci.* 72, 2553–2560. doi: 10.1016/S0024-3205(03)00165-6

Amano, M., Chihara, K., Kimura, K., Fukata, Y., Nakamura, N., Matsuura, Y., et al. (1997). Formation of actin stress fibers and focal adhesions enhanced by Rho-kinase. *Science* 275, 1308–1311. doi: 10.1126/science.275.5304.1308

Amano, M., Nakayama, M., and Kaibuchi, K. (2010). Rho-Kinase/ROCK: a key regulator of the cytoskeleton and cell polarity. *Cytoskeleton (Hoboken)* 67, 545–554. doi: 10.1002/cm.20472

Andersson, A.-S., Bäckhed, F., von Euler, A., Richter-Dahlfors, A., Sutherland, D., and Kasemo, B. (2003). Nanoscale features influence epithelial cell morphology and cytokine production. *Biomaterials* 24, 3427–3436. doi: 10.1016/S0142-9612(03)00208-4

Aragona, M., Panciera, T., Manfrin, A., Giulitti, S., Michielin, F., Elvassore, N., et al. (2013). A mechanical checkpoint controls multicellular growth through yap/taz regulation by actin-processing factors. *Cell* 154, 1047–1059. doi: 10.1016/j.cell.2013.07.042

Arnsdorf, E. J., Tummala, P., Kwon, R. Y., and Jacobs, C. R. (2009). Mechanically induced osteogenic differentiation – the role of RhoA, ROCKII and cytoskeletal dynamics. *J. Cell Sci.* 122, 546–553. doi: 10.1242/jcs.036293

Astudillo, P. (2020). Extracellular matrix stiffness and Wnt/β-catenin signaling in physiology and disease. *Biochem. Soc. Trans.* 48, 1187–1198. doi: 10.1042/BST20200026

Atherton, P., Stutchbury, B., Wang, D.-Y., Jethwa, D., Tsang, R., Meiler-Rodriguez, E., et al. (2015). Vinculin controls talin engagement with the actomyosin machinery. *Nat. Commun.* 6:10038. doi: 10.1038/ncomms10038

Azzolin, L., Panciera, T., Soligo, S., Enzo, E., Bicciato, S., Dupont, S., et al. (2014). YAP/TAZ incorporation in the β-catenin destruction complex orchestrates the Wnt response. *Cell* 158, 157–170. doi: 10.1016/j.cell.2014.06.013

Babu, P. K. V., Rianna, C., Mirastschijski, U., and Radmacher, M. (2019). Nano-mechanical mapping of interdependent cell and ECM mechanics by AFM force spectroscopy. *Sci. Rep.* 9, 1–19. doi: 10.1038/s41598-019-48566-7

Ball, J. L., and Price, T. (1995). *Chesneys Radiographic Imaging*, 6th Edn. Cambridge, MA: John Wiley & Sons, Oxford.

Barriga, E. H., Franze, K., Charras, G., and Mayor, R. (2018). Tissue stiffening coordinates morphogenesis by triggering collective cell migration in vivo. *Nature* 554, 523–527. doi: 10.1038/nature25742

Basu, S., Totty, N. F., Irwin, M. S., Sudol, M., and Downward, J. (2003). Akt phosphorylates the Yes-associated protein, YAP, to induce interaction with 14-3-3 and attenuation of p73-mediated apoptosis. *Mol. Cell* 11, 11–23. doi: 10.1016/S1097-2765(02)00776-1

Bays, J. L., and DeMali, K. A. (2017). Vinculin in cell–cell and cell–matrix adhesions. *Cell. Mol. Life Sci.* 74, 2999–3009. doi: 10.1007/s00018-017-2511-3

Beltrami, A. P., Cesselli, D., Bergamin, N., Marcon, P., Rigo, S., Puppato, E., et al. (2007). Multipotent cells can be generated *in vitro* from several adult human organs (heart, liver, and bone marrow). *Blood* 110, 3438–3446. doi: 10.1182/blood-2006-11-055566

Brown, T. E., Carberry, B. J., Worrel, B. T., Dudaryeva, O. Y., McBride, M. K., Bowman, C. N., et al. (2018). Photopolymerized dynamic hydrogels with tunable viscoelastic properties through thioester exchange. *Biomaterials* 178, 496–503. doi: 10.1016/j.biomaterials.2018.03.060

Burridge, K. (2017). Focal adhesions: a personal perspective on a half century of progress. *FEBS J.* 284:3355. doi: 10.1111/febs.14195

Butler, M. B., Short, N. E., Maniou, E., Alexandre, P., Greene, N. D. E., Copp, A. J., et al. (2019). Rho kinase-dependent apical constriction counteracts M-phase apical expansion to enable mouse neural tube closure. *J. Cell Sci.* 132:jcs230300. doi: 10.1242/jcs.230300

Buxboim, A., Swift, J., Irianto, J., Spinler, K. R., Dingal, P. C. D. P., Athirasala, A., et al. (2014). Matrix elasticity regulates lamin-A,C phosphorylation and turnover with feedback to actomyosin. *Curr. Biol.* 24, 1909–1917. doi: 10.1016/j.cub.2014.07.001

Carey, E. J. (1922a). Direct observations on the transformation of the mesenchyme in the thigh of the pig embryo (*Sus scrofa*), with especial reference to the genesis of the thigh muscles, of the knee- and hip-joints, and of the primary bone of the femur. *J. Morphol.* 37, 1–77. doi: 10.1002/jmor.1050370102

Carey, E. J. (1922b). Tension of differential growth as a stimulus to myogenesis. Tension of differential growth as a stimulus to myogenesis. *J. Gen. Physiol.* 2, 357–371.

Case, L. B., Baird, M. A., Shtengel, G., Campbell, S. L., Hess, H. F., Davidson, M. W., et al. (2015). Molecular mechanism of vinculin activation and nanoscale spatial organization in focal adhesions. *Nat. Cell Biol.* 17, 880–892. doi: 10.1038/ncb3180

Cattaruzza, M., Lattrich, C., and Hecker, M. (2004). Focal adhesion protein zyxin is a mechanosensitive modulator of gene expression in vascular smooth muscle cells. *Hypertension* 43, 726–730. doi: 10.1161/01.HYP.0000119189.82659.52

Chaudhuri, O., Cooper-White, J., Janmey, P. A., Mooney, D. J., and Shenoy, V. B. (2020). Effects of extracellular matrix viscoelasticity on cellular behaviour. *Nature* 584, 535–546. doi: 10.1038/s41586-020-2612-2

Chen, C. S., Mrksich, M., Huang, S., Whitesides, G. M., and Ingber, D. E. (1997). Geometric control of cell life and death. *Science* 276, 1425–1428. doi: 10.1126/science.276.5317.1425

Chen, W., and Zhu, C. (2013). Mechanical regulation of T-cell functions. *Immunol. Rev.* 256, 160–176. doi: 10.1111/imr.12122

Chen, W., Villa-Diaz, L. G., Sun, Y., Weng, S., Kim, J. K., Lam, R. H. W., et al. (2012). Nanotopography influences adhesion, spreading, and self-renewal of human embryonic stem cells. *ACS Nano* 6, 4094–4103. doi: 10.1021/nn3004923

Chevalier, N. R., Gazguez, E., Bidault, L., Guilbert, T., Vias, C., Vian, E., et al. (2016a). How tissue mechanical properties affect enteric neural crest cell migration. *Sci. Rep.* 6:20927. doi: 10.1038/srep20927

Chevalier, N. R., Gazquez, E., Dufour, S., and Fleury, V. (2016b). Measuring the micromechanical properties of embryonic tissues. *Methods* 94, 120–128. doi: 10.1016/j.ymeth.2015.08.001

Chin, M. H. W., Norman, M. D. A., Gentleman, E., Coppens, M.-O., and Day, R. M. (2020). A hydrogel-integrated culture device to interrogate T cell activation with physicochemical cues. *ACS Appl. Mater. Interfaces* 12, 47355–47367. doi: 10.1021/acsami.0c16478

Cho, S., Vashisth, M., Abbas, A., Majkut, S., Vogel, K., Xia, Y., et al. (2019). Mechanosensing by the lamina protects against nuclear rupture, DNA damage, and cell-cycle arrest. *Dev. Cell* 49, 920–935.e5. doi: 10.1016/j.devcel.2019.04.020

Copp, A. J., and Greene, N. D. E. (2013). Neural tube defects – disorders of neurulation and related embryonic processes. *Wiley Interdiscip. Rev. Dev. Biol.* 2, 213–227. doi: 10.1002/wdev.71

Corpechot, C., Heurgue, A., Decraecker, M., Tanne, F., Potier, P., Hanslik, B., et al. (2021). Non-invasive diagnosis and follow-up of primary biliary cholangitis. *Clin. Res. Hepatol. Gastroenterol.* doi: 10.1016/j.clinre.2021.101770 [Epub ahead of print].

Costa, P., Almeida, F. V. M., and Connelly, J. T. (2012). Biophysical signals controlling cell fate decisions: how do stem cells really feel? *Int. J. Biochem. Cell Biol.* 44, 2233–2237. doi: 10.1016/j.biocel.2012.09.003

Crisp, M., Liu, Q., Roux, K., Rattner, J. B., Shanahan, C., Burke, B., et al. (2006). Coupling of the nucleus and cytoplasm. *J. Cell Biol.* 172, 41–53. doi: 10.1083/jcb.200509124

D'Angelo, F., Tiribuzi, R., Armentano, I., Kenny, J. M., Martino, S., and Orlacchio, A. (2011). Mechanotransduction: tuning stem cells fate. *J. Funct. Biomater.* 2, 67–87. doi: 10.3390/jfb2020067

Dasgupta, I., and McCollum, D. (2019). Control of cellular responses to mechanical cues through YAP/TAZ regulation. *J. Biol. Chem.* 294, 17693–17706. doi: 10.1074/jbc.REV119.007963

Daza, R., González-Bermúdez, B., Cruces, J., De la Fuente, M., Plaza, G. R., Arroyo-Hernández, M., et al. (2019). Comparison of cell mechanical measurements provided by atomic force microscopy (AFM) and micropipette aspiration (MPA). *J. Mech. Behav. Biomed. Mater.* 95, 103–115. doi: 10.1016/j.jmbbm.2019.03.031

Deng, J., Petersen, B. E., Steindler, D. A., Jorgensen, M. L., and Laywell, E. D. (2006). Mesenchymal stem cells spontaneously express neural proteins in culture and are neurogenic after transplantation. *Stem Cells* 24, 1054–1064. doi: 10.1634/stemcells.2005-0370

Discher, D. E. (2005). Tissue cells feel and respond to the stiffness of their substrate. *Science* 310, 1139–1143. doi: 10.1126/science.1116995

Dobrokhotov, O., Samsonov, M., Sokabe, M., and Hirata, H. (2018). Mechanoregulation and pathology of YAP/TAZ via hippo and non-hippo mechanisms. *Clin. Transl. Med.* 7:23. doi: 10.1186/s40169-018-0202-9

Dong, J. M., Lau, L. S., Ng, Y. W., Lim, L., and Manser, E. (2009). Paxillin nuclear-cytoplasmic localization is regulated by phosphorylation of the LD4 motif: evidence that nuclear paxillin promotes cell proliferation. *Biochem. J.* 418, 173–184. doi: 10.1042/BJ20080170

Drachman, D. B., and Sokoloff, L. (1966). The role of movement in embryonic joint development. *Dev. Biol.* 14, 401–420. doi: 10.1016/0012-1606(66)90022-4

DuFort, C. C., Paszek, M. J., and Weaver, V. M. (2011). Balancing forces: architectural control of mechanotransduction. *Nat. Rev. Mol. Cell Biol.* 12, 308–319. doi: 10.1038/nrm3112

Dunlop, L. L. T., and Hall, B. K. (1995). Relationships between cellular condensation, preosteoblast formation and epithelial-mesenchymal interactions in initiation of osteogenesis. *Int. J. Dev. Biol.* 39, 357–371.

Dupont, S. (2016). Role of YAP/TAZ in cell-matrix adhesion-mediated signalling and mechanotransduction. *Exp. Cell Res.* 343, 42–53. doi: 10.1016/j.yexcr.2015.10.034

Dupont, S., Morsut, L., Aragona, M., Enzo, E., Giulitti, S., Cordenonsi, M., et al. (2011). Role of YAP/TAZ in mechanotransduction. *Nature* 474, 179–183. doi: 10.1038/nature10137

Efremov, Y. M., Okajima, T., and Raman, A. (2020). Measuring viscoelasticity of soft biological samples using atomic force microscopy. *Soft Matter.* 16, 64–81. doi: 10.1039/c9sm01020c

Efremov, Y. M., Pukhlyakova, E. A., Bagrov, D. V., and Shaitan, K. V. (2011). Atomic force microscopy of living and fixed *Xenopus laevis* embryos. *Micron* 42, 840–852. doi: 10.1016/j.micron.2011.05.010

El-Mohri, H., Wu, Y., Mohanty, S., and Ghosh, G. (2017). Impact of matrix stiffness on fibroblast function. *Mater. Sci. Eng.* 74, 146–151. doi: 10.1016/j.msec.2017.02.001

Elosegui-Artola, A. (2021). The extracellular matrix viscoelasticity as a regulator of cell and tissue dynamics. *Curr. Opin. Cell Biol.* 72, 10–18.

Elosegui-Artola, A., Andreu, I., Beedle, A. E. M., Lezamiz, A., Uroz, M., Kosmalska, A. J., et al. (2017). Force triggers YAP nuclear entry by regulating transport across nuclear pores. *Cell* 171, 1397–1410.e14. doi: 10.1016/j.cell.2017.10.008

Engler, A. J., Carag-Krieger, C., Johnson, C. P., Raab, M., Tang, H.-Y., Speicher, D. W., et al. (2008). Embryonic cardiomyocytes beat best on a matrix with heart-like elasticity: scar-like rigidity inhibits beating. *J. Cell Sci.* 121, 3794–3802. doi: 10.1242/jcs.029678

Engler, A. J., Griffin, M. A., Sen, S., Bönnemann, C. G., Sweeney, H. L., and Discher, D. E. (2004). Myotubes differentiate optimally on substrates with tissue-like stiffness. *J. Cell Biol.* 166, 877–887. doi: 10.1083/jcb.200405004

Engler, A. J., Sen, S., Sweeney, H. L., and Discher, D. E. (2006). Matrix elasticity directs stem cell lineage specification. *Cell* 126, 677–689. doi: 10.1016/j.cell.2006.06.044

Engler, A., Bacakova, L., Newman, C., Hategan, A., Griffin, M., and Discher, D. (2004). Substrate compliance versus ligand density in cell on gel responses. *Biophys. J.* 86, 617–628.

Eroshenko, N., Ramachandran, R., Yadavalli, V. K., and Rao, R. R. (2013). Effect of substrate stiffness on early human embryonic stem cell differentiation. *J. Biol. Eng.* 7:7. doi: 10.1186/1754-1611-7-7

Evans, N. D., and Gentleman, E. (2014). The role of material structure and mechanical properties in cell–matrix interactions. *J. Mater. Chem. B* 2, 2345–2356. doi: 10.1039/C3TB21604G

Evans, N. D., Minelli, C., Gentleman, E., LaPointe, V., Patankar, S. N., Kallivretaki, M., et al. (2009). Substrate stiffness affects early differentiation events in embryonic stem cells. *Eur. Cells Mater.* 18, 1–14. doi: 10.22203/eCM.v018a01

Fang, J., and Hall, B. K. (1997). Chondrogenic cell differentiation from membrane bone periostea. *Anat. Embryol.* 196, 349–362. doi: 10.1007/s004290050104

Feldherr, C. M., and Akin, D. (1990). The permeability of the nuclear envelope in dividing and nondividing cell cultures. *J. Cell Biol.* 111, 1–8.

Fell, H. B. (1925). The histogenesis of cartilage and bone in the long bones of the embryonic fowl. *J. Morphol.* 40, 417–459. doi: 10.1002/jmor.1050400302

Fell, H. B., and Canti, R. B. (1934). Experiments on the development in vitro of the avian knee joint. *Proc. R. Soc. Lond. Ser. B Biol. Sci.* 116, 316–315.

Flanagan, L. A., Ju, Y.-E., Marg, B., Osterfield, M., and Janmey, P. A. (2002). Neurite branching on deformable substrates. *Neuroreport* 13, 2411–2415. doi: 10.1097/01.wnr.0000048003.96487.97

Fletcher, J. M., Lalor, S. J., Sweeney, C. M., Tubridy, N., and Mills, K. H. G. (2010). T cells in multiple sclerosis and experimental autoimmune encephalomyelitis. *Clin. Exp. Immunol.* 162, 1–11. doi: 10.1111/j.1365-2249.2010.04143.x

Folkman, J., and Moscona, A. (1978). Role of cell shape in growth control. *Nature* 273, 345–349. doi: 10.1038/273345a0

Foyt, D. A., Taheem, D. K., Ferreira, S. A., Norman, M. D. A., Petzold, J., Jell, G., et al. (2019). Hypoxia impacts human MSC response to substrate stiffness during chondrogenic differentiation. *Acta Biomater.* 89, 73–83. doi: 10.1016/j.actbio.2019.03.002

Fu, J., Wang, Y.-K., Yang, M. T., Desai, R. A., Yu, X., Liu, Z., et al. (2010). Mechanical regulation of cell function with geometrically modulated elastomeric substrates. *Nat. Methods* 7, 733–736. doi: 10.1038/nmeth.1487

Galarza Torre, A., Shaw, J. E., Wood, A., Gilbert, H. T. J., Dobre, O., Genever, P., et al. (2018). An immortalised mesenchymal stem cell line maintains mechano-responsive behaviour and can be used as a reporter of substrate stiffness. *Sci. Rep.* 8:8981. doi: 10.1038/s41598-018-27346-9

Galea, G. L., Cho, Y.-J., Galea, G., Molè, M. A., Rolo, A., Savery, D., et al. (2017). Biomechanical coupling facilitates spinal neural tube closure in mouse embryos. *Proc. Natl. Acad. Sci. U.S.A.* 114, E5177–E5186. doi: 10.1073/pnas.1700934114

Galea, G. L., Nychyk, O., Mole, M. A., Moulding, D., Savery, D., Nikolopoulou, E., et al. (2018). Vangl2 disruption alters the biomechanics of late spinal neurulation leading to spina bifida in mouse embryos. *Dis. Models Mech.* 11:dmm032219. doi: 10.1242/dmm.032219

Galluzzi, M., Tang, G., Biswas, C. S., Zhao, J., Chen, S., and Stadler, F. J. (2018). Atomic force microscopy methodology and AFMech suite software for nanomechanics on heterogeneous soft materials. *Nat. Commun.* 9:3584. doi: 10.1038/s41467-018-05902-1

Georges, P. C., and Janmey, P. A. (2005). Cell type-specific response to growth on soft materials. *J. Appl. Physiol.* 98, 1547–1553. doi: 10.1152/japplphysiol.01121.2004

Ghosh, K., Pan, Z., Guan, E., Ge, S., Liu, Y., Nakamura, T., et al. (2007). Cell adaptation to a physiologically relevant ECM mimic with different viscoelastic properties. *Biomaterials* 28, 671–679. doi: 10.1016/j.biomaterials.2006.09.038

Gilbert, P., Havenstrite, K., Magnusson, K., Sacco, A., Leonardi, N., Kraft, P., et al. (2010). Substrate elasticity regulates skeletal muscle stem cell self-renewal in culture. *Science* 329, 1078–1081. doi: 10.1126/science.1191035

Glucksmann, A. (1942). The role of mechanical stresses in bone formation in vitro. *J. Anat.* 76, 231–239.

Goetzke, R., Sechi, A., De Laporte, L., Neuss, S., and Wagner, W. (2018). Why the impact of mechanical stimuli on stem cells remains a challenge. *Cell. Mol. Life Sci.* 75, 3297–3312. doi: 10.1007/s00018-018-2830-z

Gomez-Salazar, M., Gonzalez-Galofre, Z. N., Casamitjana, J., Crisan, M., James, A. W., and Péault, B. (2020). Five decades later, are mesenchymal stem cells still relevant? *Front. Bioeng. Biotechnol.* 8:148. doi: 10.3389/fbioe.2020.00148

Halder, G., Dupont, S., and Piccolo, S. (2012). Transduction of mechanical and cytoskeletal cues by YAP and TAZ. *Nat. Rev. Mol. Cell Biol.* 13, 591–600. doi: 10.1038/nrm3416

Hall, B. K. (1979). Selective proliferation and accumulation of chondroprogenitor cells as the mode of action of biomechanical factors during secondary chondrogenesis. *Teratology* 20, 81–91. doi: 10.1002/tera.1420200112

Hall, B. K., and Herring, S. W. (1990). Paralysis and growth of the musculoskeletal system in the embryonic chick. *J. Morphol.* 206, 45–56. doi: 10.1002/jmor.1052060105

Hartl, L., Huelsz-Prince, G., van Zon, J., and Tans, S. J. (2019). Apical constriction is necessary for crypt formation in small intestinal organoids. *Dev. Biol.* 450, 76–81. doi: 10.1016/j.ydbio.2019.03.009

Hellstrand, P., and Albinsson, S. (2005). Stretch-dependent growth and differentiation in vascular smooth muscle: role of the actin cytoskeleton. *Can. J. Physiol. Pharmacol.* 83, 869–875. doi: 10.1139/y05-061

Hindley, C. J., Condurat, A. L., Menon, V., Thomas, R., Azmitia, L. M., Davis, J. A., et al. (2016). The Hippo pathway member YAP enhances human neural crest cell fate and migration. *Sci. Rep.* 6, 1–9. doi: 10.1038/srep23208

Hoffman, B. D., Grashoff, C., and Schwartz, M. A. (2011). Dynamic molecular processes mediate cellular mechanotransduction. *Nature* 475, 316–323. doi: 10.1038/nature10316

Ingber, D. E. (2006). Cellular mechanotransduction: putting all the pieces together again. *Fed. Am. Soc. Exp. Biol. J.* 20, 811–827. doi: 10.1096/fj.05-5424rev

Inoue, Y., Suzuki, M., Watanabe, T., Yasue, N., Tateo, I., Adachi, T., et al. (2016). Mechanical roles of apical constriction, cell elongation, and cell migration during neural tube formation in *Xenopus. Biomech. Modelling Mechanobiol.* 15, 1733–1746. doi: 10.1007/s10237-016-0794-1

Iwashita, M., Kataoka, N., Toida, K., and Kosodo, Y. (2014). Systematic profiling of spatiotemporal tissue and cellular stiffness in the developing brain. *Development* 141, 3793–3798. doi: 10.1242/dev.109637

Janmey, P. A., and Miller, R. T. (2011). Mechanisms of mechanical signaling in development and disease. *J. Cell Sci.* 124, 9–18. doi: 10.1242/jcs.071001

Jiang, Y., Jahagirdar, B. N., Reinhardt, R. L., Schwartz, R. E., Keene, C. D., Ortiz-Gonzalez, X. R., et al. (2002). Pluripotency of mesenchymal stem cells derived from adult marrow. *Nature* 418, 41–49. doi: 10.1038/nature00870

Julian, L., and Olson, M. F. (2014). Rho-associated coiled-coil containing kinases (ROCK): structure, regulation, and functions. *Small GTPases* 5:e29846. doi: 10.4161/sgtp.29846

Juriloff, D. M., and Harris, M. J. (2018). Insights into the etiology of mammalian neural tube closure defects from developmental, genetic and evolutionary studies. *J. Dev. Biol.* 6:22. doi: 10.3390/jdb6030022

Kanchanawong, P., Shtengel, G., Pasapera, A. M., Ramko, E. B., Davidson, M. W., Hess, H. F., et al. (2010). Nanoscale architecture of integrin-based cell adhesions. *Nature* 468, 580–584. doi: 10.1038/nature09621

Karpińska, K., Cao, C., Yamamoto, V., Gielata, M., and Kobielak, A. (2020). Alpha-catulin, a new player in a Rho dependent apical constriction that contributes to the mouse neural tube closure. *Front. Cell Dev. Biol.* 8:154. doi: 10.3389/fcell.2020.00154

Katoh, K., Kano, Y., Amano, M., Onishi, H., Kaibuchi, K., and Fujiwara, K. (2001). Rho-kinase–mediated contraction of isolated stress fibers. *J. Cell Biol.* 153, 569–584.

Katoh, K., Kano, Y., and Noda, Y. (2011). Rho-associated kinase-dependent contraction of stress fibres and the organization of focal adhesions. *J. R. Soc. Interface* 8, 305–311. doi: 10.1098/rsif.2010.0419

Kilian, K. A., Bugarija, B., Lahn, B. T., and Mrksich, M. (2010). Geometric cues for directing the differentiation of mesenchymal stem cells. *Proc. Natl. Acad. Sci. U.S.A.* 107, 4872–4877. doi: 10.1073/pnas.0903269107

Knothe Tate, M. L., Falls, T. D., McBride, S. H., Atit, R., and Knothe, U. R. (2008). Mechanical modulation of osteochondroprogenitor cell fate. *Int. J. Biochem. Cell Biol.* 40, 2720–2738. doi: 10.1016/j.biocel.2008.05.011

Koser, D. E., Thompson, A. J., Foster, S. K., Dwivedy, A., Pillai, E. K., Sheridan, G. K., et al. (2016). Mechanosensing is critical for axon growth in the developing brain. *Nat. Neurosci.* 19, 1592–1598. doi: 10.1038/nn.4394

Kowalczyk, I., Lee, C., Schuster, E., Hoeren, J., Trivigno, V., Riedel, L., et al. (2021). Neural tube closure requires the endocytic receptor Lrp2 and its functional interaction with intracellular scaffolds. *Development* 148:dev195008. doi: 10.1242/dev.195008

Kumar, A., Placone, J. K., and Engler, A. J. (2017). Understanding the extracellular forces that determine cell fate and maintenance. *Development* 144, 4261–4270. doi: 10.1242/dev.158469

Kumar, S., Maxwell, I. Z., Heisterkamp, A., Polte, T. R., Lele, T. P., Salanga, M., et al. (2006). Viscoelastic retraction of single living stress fibers and its impact on cell shape, cytoskeletal organization, and extracellular matrix mechanics. *Biophys. J.* 90, 3762–3773. doi: 10.1529/biophysj.105.071506

Kur, E., Mecklenburg, N., Cabrera, R. M., Willnow, T. E., and Hammes, A. (2014). LRP2 mediates folate uptake in the developing neural tube. *J. Cell Sci.* 127, 2261–2268. doi: 10.1242/jcs.140145

Lachowski, D., Cortes, E., Robinson, B., Rice, A., Rombouts, K., and Hernández, A. E. D. R. (2018). FAK controls the mechanical activation of YAP, a transcriptional regulator required for durotaxis. *Fed. Am. Soci. Exp. Biol. J.* 32, 1099–1107. doi: 10.1096/fj.201700721R

Lee, H., Kim, K., and Lee, Y. (2020). Development of stiffness measurement program using color mapping in shear wave elastography. *Diagnostics (Basel)* 10:362. doi: 10.3390/diagnostics10060362

Lee, J. M., Kim, J., Borana, J., Chung, B. H., and Chung, B. G. (2013). Dual-micropillar-based microfluidic platform for single embryonic stem cell-derived neuronal differentiation. *Electrophoresis* 13, 1931–1938. doi: 10.1002/elps.201200578

Leung, T., Chen, X. Q., Manser, E., and Lim, L. (1996). The p160 RhoA-binding kinase ROK alpha is a member of a kinase family and is involved in the reorganization of the cytoskeleton. *Mol. Cell Biol.* 16, 5313–5327.

Li, Y., and Wu, S. (2021). Liver stiffness measured with two-dimensional shear wave elastography comparable to histopathology falls dominantly on the severe liver fibrosis. *Clin. Hemorheol. Microcirc.* doi: 10.3233/CH-211223 [Epub ahead of print].

Li, Z., Müller, R., and Ruffoni, D. (2018). Bone remodeling and mechanobiology around implants: insights from small animal imaging. *J. Orthop. Res.* 36, 584–593. doi: 10.1002/jor.23758

Lo, C. M., Wang, H. B., Dembo, M., and Wang, Y. L. (2000). Cell movement is guided by the rigidity of the substrate. *Biophys. J.* 79, 144–152.

Loeschke, H., and Weinhold, H. (1922). Tiber den einfluss von druck und entspannung auf das knochenwachstum des hirnschadels. *Beitr. Pathol. Anat.* 70, 406–439.

Majkut, S., Idema, T., Swift, J., Krieger, C., Liu, A., and Discher, D. E. (2013). Heart-specific stiffening in early embryos parallels matrix and myosin expression to optimize beating. *Curr. Biol.* 23, 2434–2439. doi: 10.1016/j.cub.2013.10.057

Mammoto, T., Mammoto, A., Torisawa, Y., Tat, T., Gibbs, A., Derda, R., et al. (2011). Mechanochemical control of mesenchymal condensation and embryonic tooth organ formation. *Dev. Cell* 21, 758–769. doi: 10.1016/j.devcel.2011.07.006

Manning, S. A., Kroeger, B., and Harvey, K. F. (2020). The regulation of yorkie, YAP and TAZ: new insights into the hippo pathway. *Development* 147:dev179069. doi: 10.1242/dev.179069

Marozas, I. A., Anseth, K. S., and Cooper-White, J. J. (2019). Adaptable boronate ester hydrogels with tunable viscoelastic spectra to probe timescale dependent mechanotransduction. *Biomaterials* 223:119430. doi: 10.1016/j.biomaterials.2019.119430

Martino, F., Perestrelo, A. R., Vinarskı, V., Pagliari, S., and Forte, G. (2018). Cellular mechanotransduction: from tension to function. *Front. Physiol.* 9:824. doi: 10.3389/fphys.2018.00824

Marturano, J. E., Arena, J. D., Schiller, Z. A., Georgakoudi, I., and Kuo, C. K. (2013). Characterization of mechanical and biochemical properties of developing embryonic tendon. *Proc. Natl. Acad. Sci. U.S.A.* 110, 6370–6375. doi: 10.1073/pnas.1300135110

Mason, D. E., Collins, J. M., Dawahare, J. H., Nguyen, T. D., Lin, Y., Voytik-Harbin, S. L., et al. (2019). YAP and TAZ limit cytoskeletal and focal adhesion maturation to enable persistent cell motility. *J. Cell Biol.* 218, 1369–1389. doi: 10.1083/jcb.201806065

Matthews, B. D., Overby, D. R., Alenghat, F. J., Karavitis, J., Numaguchi, Y., Allen, P. G., et al. (2004). Mechanical properties of individual focal adhesions probed with a magnetic microneedle. *Biochem. Biophys. Res. Commun.* 313, 758–764. doi: 10.1016/j.bbrc.2003.12.005

McBeath, R., Pirone, D. M., Nelson, C. M., Bhadriraju, K., and Chen, C. S. (2004). Cell shape, cytoskeletal tension, and RhoA regulate stem cell lineage commitment. *Dev. Cell* 6, 483–495. doi: 10.1016/S1534-5807(04)00075-9

McBride, S. H., and Knothe Tate, M. L. (2008). Modulation of stem cell shape and fate a: the role of density and seeding protocol on nucleus shape and gene expression. *Tissue Eng. Part A* 14, 1561–1572. doi: 10.1089/ten.tea.2008.0112

McBride, S. H., Falls, T., and Knothe Tate, M. L. (2008). Modulation of stem cell shape and fate b: mechanical modulation of cell shape and gene expression. *Tissue Eng. Part A* 14, 1573–1580. doi: 10.1089/ten.tea.2008.0113

Meng, Z., Qiu, Y., Lin, K. C., Kumar, A., Placone, J. K., Fang, C., et al. (2018). RAP2 mediates mechanoresponses of the hippo pathway. *Nature* 560, 655–660. doi: 10.1038/s41586-018-0444-0

Miano, J. M., Long, X., and Fujiwara, K. (2007). Serum response factor: master regulator of the actin cytoskeleton and contractile apparatus. *Am. J. Physiol. Cell Physiol.* 292, C70–C81. doi: 10.1152/ajpcell.00386.2006

Moreno-Vicente, R., Pavón, D. M., Martín-Padura, I., Català-Montoro, M., Díez-Sánchez, A., Quílez-Álvarez, A., et al. (2018). Caveolin-1 modulates mechanotransduction responses to substrate stiffness through actin-dependent control of YAP. *Cell Rep.* 25, 1622–1635.e6. doi: 10.1016/j.celrep.2018.10.024

Morriss-Kay, G., and Tuckett, F. (1985). The role of microfilaments in cranial neurulation in rat embryos: effects of short-term exposure to cytochalasin D. *Development* 88, 333–348.

Murakami, F., Ando, Y., Miyagi, A., Sugita, S., Ueno, N., and Matsumoto, T. (2017). Measurement of surface topography and stiffness distribution on cross-section of *Xenopus laevis* tailbud for estimation of mechanical environment in embryo. *Dev. Growth Differ.* 59, 434–443. doi: 10.1111/dgd.12372

Murray, P. D. F. (1926). An experimental study of the development of the limbs of the chick. *Protoc. Proc. Linn. Soc.* 51, 187–263.

Murray, P. D. F., and Smiles, M. (1965). Factors in the evocation of adventitious (secondary) cartilage in the chick embryo. *Aust. J. Zool.* 13, 351–382. doi: 10.1071/zo9650351

Naumanen, P., Lappalainen, P., and Hotulainen, P. (2008). Mechanisms of actin stress fibre assembly. *J. Microsc.* 231, 446–454. doi: 10.1111/j.1365-2818.2008.02057.x

Neelam, S., Chancellor, T. J., Li, Y., Nickerson, J. A., Roux, K. J., Dickinson, R. B., et al. (2015). Direct force probe reveals the mechanics of nuclear homeostasis in the mammalian cell. *Proc. Natl. Acad. Sci. U.S.A.* 112, 5720–5725. doi: 10.1073/pnas.1502111112

Nelson, C. M., Jean, R. P., Tan, J. L., Liu, W. F., Sniadecki, N. J., Spector, A. A., et al. (2005). Emergent patterns of growth controlled by multicellular form and mechanics. *Proc. Natl. Acad. Sci. U.S.A.* 102, 11594–11599. doi: 10.1073/pnas.0502575102

Nikkhah, M., Edalat, F., Manoucheri, S., and Khademhosseini, A. (2012). Engineering microscale topographies to control the cell–substrate interface. *Biomaterials* 33, 5230–5246. doi: 10.1016/j.biomaterials.2012.03.079

Nikolopoulou, E., Galea, G. L., Rolo, A., Greene, N. D. E., and Copp, A. J. (2017). Neural tube closure: cellular, molecular and biomechanical mechanisms. *Development* 144, 552–566. doi: 10.1242/dev.145904

Nobes, C. D., and Hall, A. (1999). Rho GTPases control polarity, protrusion, and adhesion during cell movement. *J. Cell Biol.* 144, 1235–1244. doi: 10.1083/jcb.144.6.1235

Norman, M. D. A., Ferreira, S. A., Jowett, G. M., Bozec, L., and Gentleman, E. (2021). Measuring the elastic modulus of soft culture surfaces and three-dimensional hydrogels using atomic force microscopy. *Nat. Protoc.* 16, 2418–2449. doi: 10.1038/s41596-021-00495-4

Olson, E. N., and Nordheim, A. (2010). Linking actin dynamics and gene transcription to drive cellular motile functions. *Nat. Rev. Mol. Cell Biol.* 11, 353–365. doi: 10.1038/nrm2890

Pai, A. C. (1965). Developmental genetics of a lethal mutation, muscular dysgenesis (mdg), in the mouse: II. Developmental analysis. *Dev. Biol.* 11, 93–109. doi: 10.1016/0012-1606(65)90039-4

Parfitt, A. M. (1984). Age-related structural changes in trabecular and cortical bone: cellular mechanisms and biomechanical consequences. *Calcif. Tissue Int.* 36, S123–S128. doi: 10.1007/BF02406145

Peerani, R., Rao, B. M., Bauwens, C., Yin, T., Wood, G. A., Nagy, A., et al. (2007). Niche-mediated control of human embryonic stem cell self-renewal and differentiation. *EMBO J.* 26, 4744–4755. doi: 10.1038/sj.emboj.7601896

Pelham, R. J., and Wang, Y. (1997). Cell locomotion and focal adhesions are regulated by substrate flexibility. *Proc. Natl. Acad. Sci. U.S.A.* 94, 13661–13665.

Piccolo, S., Dupont, S., and Cordenonsi, M. (2014). The biology of YAP/TAZ: hippo signaling and beyond. *Physiol. Rev.* 94, 1287–1312. doi: 10.1152/physrev.00005.2014

Pittenger, M. F., Mackay, A. M., Beck, S. C., Jaiswal, R. K., Douglas, R., Mosca, J. D., et al. (1999). Multilineage potential of adult human mesenchymal stem cells. *Science* 284, 143–147. doi: 10.1126/science.284.5411.143

Pogoda, K., Charrier, E. E., and Janmey, P. A. (2021). A novel method to make polyacrylamide gels with mechanical properties resembling those of biological tissues. *Bio Protoc.* 11:e4131. doi: 10.21769/BioProtoc.4131

Posern, G., Sotiropoulos, A., and Treisman, R. (2002). Mutant actins demonstrate a role for unpolymerized actin in control of transcription by serum response factor. *Mol. Biol. Cell* 13, 4167–4178. doi: 10.1091/mbc.02-05-0068

Provenzano, P. P., and Keely, P. J. (2011). Mechanical signaling through the cytoskeleton regulates cell proliferation by coordinated focal adhesion and Rho GTPase signaling. *J. Cell Sci.* 124, 1195–1205. doi: 10.1242/jcs.067009

Rahikainen, R., von Essen, M., Schaefer, M., Qi, L., Azizi, L., Kelly, C., et al. (2017). Mechanical stability of talin rod controls cell migration and substrate sensing. *Sci. Rep.* 7:3571. doi: 10.1038/s41598-017-03335-2

Rodríguez, J. I., Palacios, J., Ruiz, A., Sanchez, M., Alvarez, I., and Demiguel, E. (1992). Morphological changes in long bone development in fetal akinesia deformation sequence: an experimental study in curarized rat fetuses. *Teratology* 45, 213–221. doi: 10.1002/tera.1420450215

Sai, X., and Ladher, R. K. (2008). FGF signaling regulates cytoskeletal remodeling during epithelial morphogenesis. *Curr. Biol.* 18, 976–981. doi: 10.1016/j.cub.2008.05.049

Sawyer, J. M., Harrell, J. R., Shemer, G., Sullivan-Brown, J., Roh-Johnson, M., and Goldstein, B. (2010). Apical constriction: a cell shape change that can drive morphogenesis. *Dev. Biol.* 341, 5–19. doi: 10.1016/j.ydbio.2009.09.009

Schillers, H., Rianna, C., Schäpe, J., Luque, T., Doschke, H., Wälte, M., et al. (2017). Standardized nanomechanical atomic force microscopy procedure (SNAP) for measuring soft and biological samples. *Sci. Rep.* 7:5117. doi: 10.1038/s41598-017-05383-0

Seong, J., Tajik, A., Sun, J., Guan, J.-L., Humphries, M. J., Craig, S. E., et al. (2013). Distinct biophysical mechanisms of focal adhesion kinase mechanoactivation by different extracellular matrix proteins. *Proc. Natl. Acad. Sci. U.S.A.* 110, 19372–19377. doi: 10.1073/pnas.1307405110

Shao, J., Shi, G., Qi, Z., Zheng, J., and Chen, S. (2021). Advancements in the application of ultrasound elastography in the cervix. *Ultrasound Med. Biol.* 47, 2048–2063. doi: 10.1016/j.ultrasmedbio.2021.04.009

Singhvi, R., Kumar, A., Lopez, G. P., Stephanopoulos, G. N., Wang, D. I., Whitesides, G. M., et al. (1994). Engineering cell shape and function. *Science* 264, 696–698. doi: 10.1126/science.8171320

Smith, M. A., Blankman, E., Deakin, N. O., Hoffman, L. M., Jensen, C. C., Turner, C. E., et al. (2013). LIM Domains target actin regulators paxillin and zyxin to sites of stress fiber strain. *PLoS One* 8:e69378. doi: 10.1371/journal.pone.0069378

Sordella, R., Jiang, W., Chen, G.-C., Curto, M., and Settleman, J. (2003). Modulation of Rho GTPase signaling regulates a switch between adipogenesis and myogenesis. *Cell* 113, 147–158. doi: 10.1016/s0092-8674(03)00271-x

Sotiropoulos, A., Gineitis, D., Copeland, J., and Treisman, R. (1999). Signal-regulated activation of serum response factor is mediated by changes in actin dynamics. *Cell* 98, 159–169. doi: 10.1016/S0092-8674(00)81011-9

Steward, A. J., and Kelly, D. J. (2015). Mechanical regulation of mesenchymal stem cell differentiation. *J. Anat.* 227, 717–731. doi: 10.1111/joa.12243

Stumpo, D. J., Bock, C. B., Tuttle, J. S., and Blackshear, P. J. (1995). MARCKS deficiency in mice leads to abnormal brain development and perinatal death. *Proc. Natl. Acad. Sci. U.S.A.* 92, 944–948.

Sumi, T., Matsumoto, K., and Nakamura, T. (2001). Specific activation of LIM kinase 2 via phosphorylation of threonine 505 by ROCK, a Rho-dependent protein kinase. *J. Biol. Chem.* 276, 670–676. doi: 10.1074/jbc.M007074200

Sun, M., Chi, G., Xu, J., Tan, Y., Xu, J., Lv, S., et al. (2018). Extracellular matrix stiffness controls osteogenic differentiation of mesenchymal stem cells mediated by integrin α5. *Stem Cell Res. Ther.* 9:52. doi: 10.1186/s13287-018-0798-0

Sun, Z., Guo, S. S., and Fässler, R. (2016). Integrin-mediated mechanotransduction. *J. Cell Biol.* 215, 445–456. doi: 10.1083/jcb.201609037

Suzuki, M., Sato, M., Koyama, H., Hara, Y., Hayashi, K., Yasue, N., et al. (2017). Distinct intracellular Ca 2+ dynamics regulate apical constriction and differentially contribute to neural tube closure. *Development* 144, 1307–1316. doi: 10.1242/dev.141952

Swift, J., and Discher, D. E. (2014). The nuclear lamina is mechano-responsive to ECM elasticity in mature tissue. *J. Cell Sci.* 127, 3005–3015. doi: 10.1242/jcs.149203

Swift, J., Ivanovska, I. L., Buxboim, A., Harada, T., Dingal, P. C. D. P., Pinter, J., et al. (2013). Nuclear Lamin-A scales with tissue stiffness and enhances matrix-directed differentiation. *Science* 341:1240104. doi: 10.1126/science.1240104

Théry, M., Pépin, A., Dressaire, E., Chen, Y., and Bornens, M. (2006). Cell distribution of stress fibres in response to the geometry of the adhesive environment. *Cell Motil. Cytoskeleton* 63, 341–355. doi: 10.1002/cm.20126

Thorogood, P. V. (1983). "Morphogenesis of cartilage," in *Cartilage, Development, Differentiation and Growth*, Vol. 2, ed. B. K. Hall (New York, NY: Academic Press), 223–254.

Thurner, P. J. (2009). Atomic force microscopy and indentation force measurement of bone: AFM and indentation force measurement of bone. *Wiley Interdiscip. Rev.* 1, 624–649. doi: 10.1002/wnan.56

Venugopal, B., Mogha, P., Dhawan, J., and Majumder, A. (2018). Cell density overrides the effect of substrate stiffness on human mesenchymal stem cells' morphology and proliferation. *Biomater. Sci.* 6, 1109–1119. doi: 10.1039/c7bm00853h

Vijayraghavan, D. S., and Davidson, L. A. (2017). Mechanics of neurulation: from classical to current perspectives on the physical mechanics that shape, fold, and form the neural tube. *Birth Defects Res.* 109, 153–168. doi: 10.1002/bdra.23557

Viji Babu, P. K., and Radmacher, M. (2019). Mechanics of brain tissues studied by atomic force microscopy: a perspective. *Front. Neurosci.* 13:600. doi: 10.3389/fnins.2019.00600

Vining, K. H., and Mooney, D. J. (2017). Mechanical forces direct stem cell behaviour in development and regeneration. *Nat. Rev. Mol. Cell Biol.* 18, 728–742. doi: 10.1038/nrm.2017.108

Vollrath, M. A., Kwan, K. Y., and Corey, D. P. (2007). The micromachinery of mechanotransduction in hair cells. *Annu. Rev. Neurosci.* 30, 339–365. doi: 10.1146/annurev.neuro.29.051605.112917

Wada, K.-I., Itoga, K., Okano, T., Yonemura, S., and Sasaki, H. (2011). Hippo pathway regulation by cell morphology and stress fibers. *Development* 138, 3907–3914. doi: 10.1242/dev.070987

Walters, N. J., and Gentleman, E. (2015). Evolving insights in cell-matrix interactions: elucidating how non-soluble properties of the extracellular niche direct stem cell fate. *Acta Biomater.* 11, 3–16. doi: 10.1016/j.actbio.2014.09.038

Wang, N., Tytell, J. D., and Ingber, D. E. (2009). Mechanotransduction at a distance: mechanically coupling the extracellular matrix with the nucleus. *Nat. Rev. Mol. Cell Biol.* 10, 75–82. doi: 10.1038/nrm2594

Winer, J. P., Janmey, P. A., McCormick, M. E., and Funaki, M. (2008). Bone marrow-derived human mesenchymal stem cells become quiescent on soft substrates but remain responsive to chemical or mechanical stimuli. *Tissue Eng. Part A* 15, 147–154. doi: 10.1089/ten.tea.2007.0388

Winograd-Katz, S. E., Fässler, R., Geiger, B., and Legate, K. R. (2014). The integrin adhesome: from genes and proteins to human disease. *Nat. Rev. Mol. Cell Biol.* 15, 273–288. doi: 10.1038/nrm3769

Wisdom, K. M., Adebowale, K., Chang, J., Lee, J. Y., Nam, S., Desai, R., et al. (2018). Matrix mechanical plasticity regulates cancer cell migration through confining microenvironments. *Nat. Commun.* 9:4144. doi: 10.1038/s41467-018-06641-z

Wolff, J. (1892). *Das gesetz Der Transformation Der Knochen*. Berlin: Verlag von August Hirschwald.

Wood, J. A., Shah, N. M., McKee, C. T., Hughbanks, M. L., Liliensiek, S. J., Russell, P., et al. (2011). The role of substratum compliance of hydrogels on vascular endothelial cell behavior. *Biomaterials* 32, 5056–5064. doi: 10.1016/j.biomaterials.2011.03.054

Woods, A., Wang, G., and Beier, F. (2005). RhoA/ROCK signaling regulates sox9 expression and actin organization during chondrogenesis. *J. Biol. Chem.* 280, 11626–11634. doi: 10.1074/jbc.M409158200

Wozniak, M. A., and Chen, C. S. (2009). Mechanotransduction in development: a growing role for contractility. *Nat. Rev. Mol. Cell Biol.* 10, 34–43. doi: 10.1038/nrm2592

Xu, W., Baribault, H., and Adamson, E. D. (1998). Vinculin knockout results in heart and brain defects during embryonic development. *Development* 125, 327–337.

Yeung, T., Georges, P. C., Flanagan, L. A., Marg, B., Ortiz, M., Funaki, M., et al. (2005). Effects of substrate stiffness on cell morphology, cytoskeletal structure, and adhesion. *Cell Motil.* 60, 24–34. doi: 10.1002/cm.20041

Yim, E. K. F., Pang, S. W., and Leong, K. W. (2007). Synthetic nanostructures inducing differentiation of human mesenchymal stem cells into neuronal lineage. *Exp. Cell Res.* 313, 1820–1829. doi: 10.1016/j.yexcr.2007.02.031

Yoshigi, M., Hoffman, L. M., Jensen, C. C., Yost, H. J., and Beckerle, M. C. (2005). Mechanical force mobilizes zyxin from focal adhesions to actin filaments and regulates cytoskeletal reinforcement. *J. Cell Biol.* 171, 209–215. doi: 10.1083/jcb.200505018

Zhang, T., Lin, S., Shao, X., Zhang, Q., Xue, C., Zhang, S., et al. (2017). Effect of matrix stiffness on osteoblast functionalization. *Cell Prolif.* 50:e12338. doi: 10.1111/cpr.12338

Zhao, B., Li, L., Wang, L., Wang, C.-Y., Yu, J., and Guan, K.-L. (2012). Cell detachment activates the hippo pathway via cytoskeleton reorganization to induce anoikis. *Genes Dev.* 26, 54–68. doi: 10.1101/gad.173435.111

Zhao, B., Ye, X., Yu, J., Li, L., Li, W., Li, S., et al. (2008). TEAD mediates YAP-dependent gene induction and growth control. *Genes Dev.* 22, 1962–1971. doi: 10.1101/gad.1664408

Zhou, D. W., Lee, T. T., Weng, S., Fu, J., and García, A. J. (2017). Effects of substrate stiffness and actomyosin contractility on coupling between force transmission and vinculin–paxillin recruitment at single focal adhesions. *Mol. Biol. Cell* 28, 1901–1911. doi: 10.1091/mbc.e17-02-0116

Zhou, J., Kim, H. Y., and Davidson, L. A. (2009). Actomyosin stiffens the vertebrate embryo during crucial stages of elongation and neural tube closure. *Development* 136, 677–688. doi: 10.1242/dev.026211

Zhou, J., Pal, S., Maiti, S., and Davidson, L. A. (2015). Force production and mechanical accommodation during convergent extension. *Development* 142, 692–701. doi: 10.1242/dev.116533

Zhu, M., Tao, H., Samani, M., Luo, M., Wang, X., Hopyan, S., et al. (2020). Spatial mapping of tissue properties in vivo reveals a 3D stiffness gradient in the mouse limb bud. *Proc. Natl. Acad. Sci. U.S.A.* 117, 4781–4791.

Zimmermann, S., Voss, M., Kaiser, S., Kapp, U., Waller, C. F., and Martens, U. M. (2003). Lack of telomerase activity in human mesenchymal stem cells. *Leukemia* 17, 1146–1149. doi: 10.1038/sj.leu.2402962

Conflict of Interest: The authors declare that the research was conducted in the absence of any commercial or financial relationships that could be construed as a potential conflict of interest.

frontiers
in Cell and Developmental Biology

MINI REVIEW
published: 21 February 2022
doi: 10.3389/fcell.2022.822561

Extracellular Matrix in Aging Aorta

Akiko Mammoto[1,2]*, *Kienna Matus*[1] *and Tadanori Mammoto*[1,3]*

[1]*Department of Pediatrics, Milwaukee, WI, United States,* [2]*Department of Cell Biology, Neurobiology and Anatomy, Milwaukee, WI, United States,* [3]*Department of Pharmacology and Toxicology, Medical College of Wisconsin, Milwaukee, WI, United States*

The aging population is booming all over the world and arterial aging causes various age-associated pathologies such as cardiovascular diseases (CVDs). The aorta is the largest elastic artery, and transforms pulsatile flow generated by the left ventricle into steady flow to maintain circulation in distal tissues and organs. Age-associated structural and functional changes in the aortic wall such as dilation, tortuousness, stiffening and losing elasticity hamper stable peripheral circulation, lead to tissue and organ dysfunctions in aged people. The extracellular matrix (ECM) is a three-dimensional network of macromolecules produced by resident cells. The composition and organization of key ECM components determine the structure-function relationships of the aorta and therefore maintaining their homeostasis is critical for a healthy performance. Age-associated remodeling of the ECM structural components, including fragmentation of elastic fibers and excessive deposition and crosslinking of collagens, is a hallmark of aging and leads to functional stiffening of the aorta. In this mini review, we discuss age-associated alterations of the ECM in the aortic wall and shed light on how understanding the mechanisms of aortic aging can lead to the development of efficient strategy for aortic pathologies and CVDs.

Keywords: extracellular matrix, aging, aorta, stiffness, elastin, collagen

Edited by:
Hiromi Yanagisawa,
University of Tsukuba, Japan

Reviewed by:
Yoshito Yamashiro,
University of Tsukuba, Japan
Elena MacFarlane,
Johns Hopkins Medicine,
United States

***Correspondence:**
Akiko Mammoto
amammoto@mcw.edu
Tadanori Mammoto
tmammoto@mcw.edu

Specialty section:
This article was submitted to
Cell Adhesion and Migration,
a section of the journal
Frontiers in Cell and Developmental
Biology

Received: *25 November 2021*
Accepted: *07 February 2022*
Published: *21 February 2022*

Citation:
Mammoto A, Matus K and
Mammoto T (2022) Extracellular Matrix
in Aging Aorta.
Front. Cell Dev. Biol. 10:822561.
doi: 10.3389/fcell.2022.822561

INTRODUCTION

The aging population is booming worldwide. At present, those aged over 65 years old constitute 16.5% of the population in the United States (US), and this number is expected to rise to 22% by 2050 (https://www.census.gov/content/dam/Census/library/publications/2020/demo/p25-1146.pdf).
Aging is associated with structural and functional alterations in tissues and organs that over time, lead to various age-associated pathologies (Donato et al., 2018; Franceschi et al., 2018). The arteries transport circulating cells, oxygen and nutrients to local tissues and organs. The structure and function of the arteries are significantly altered during aging, which makes aging a major risk factor for cardiovascular diseases (CVDs) (Heidenreich et al., 2011; North and Sinclair, 2012; Paneni et al., 2017). Arterial aging is characterized by increased stiffness, reduced elasticity, impaired distensibility, endothelial dysfunction, and deregulated vascular tone (Paneni et al., 2015; Sun, 2015). To develop more efficient treatment to slow down arterial aging and prevent age-associated pathologies, it is necessary to comprehensively understand the structural and functional alterations in the aging arteries.

The extracellular matrix (ECM) is a three-dimensional network of macromolecules that determines morphological and physical properties of the tissues and organs (Frantz et al., 2010; Theocharis et al., 2016). Homeostasis of the ECM network is critical for maintaining tissue structure-functional relationships, and aberrant ECM remodeling contributes to various pathological conditions in the aging population (Birch, 2018; Theocharis et al., 2019). ECM proteins such as elastin, collagens, and soluble proteoglycans are the major components of the arterial wall (Jana et al.,

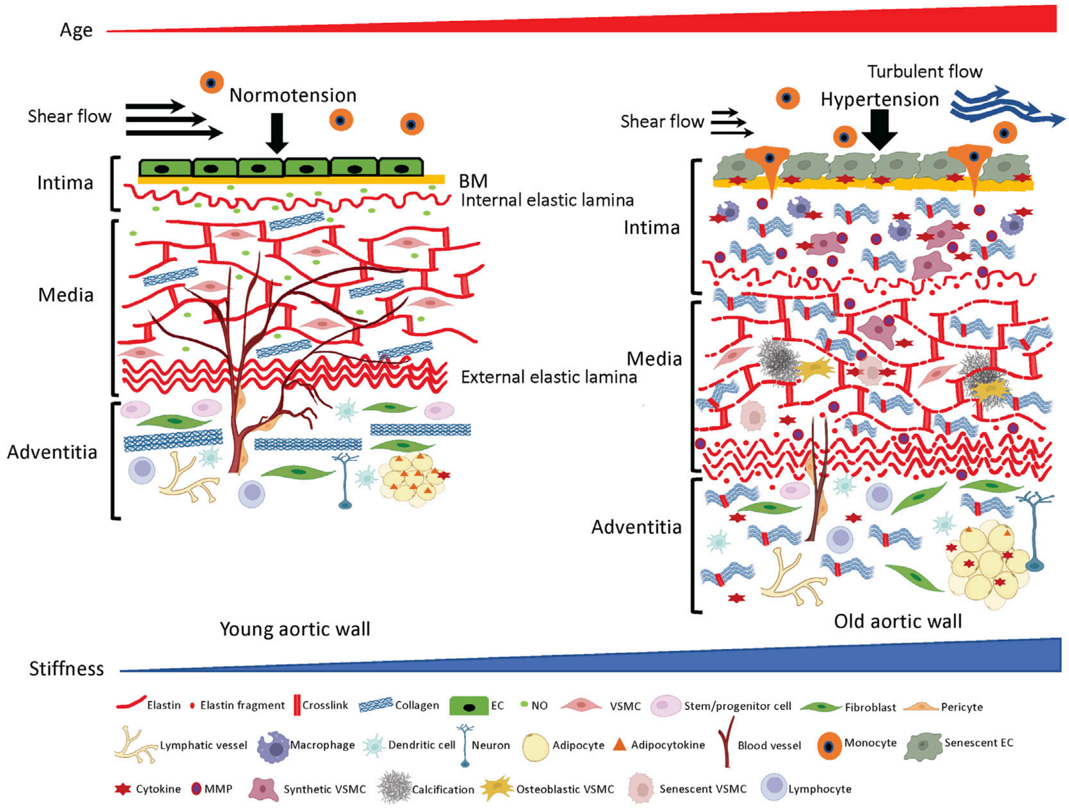

FIGURE 1 | ECM structures and cellular components in the aortic wall. Young aortic wall (*left*): In intima, endothelial cells (ECs) maintain homeostasis of the wall by forming seamless barrier structure over the basement membrane (BM) and producing vasoprotective factors such as nitric oxide (NO). In media, key ECM molecules (e.g., elastin, collagen) and vascular smooth muscle cells (VSMCs) create the contractile units to maintain vascular tone and compliance. In adventitia, collagen fibers support the aortic wall to prevent overexpansion, and various adventitial cellular and non-cellular ECM components maintain homeostasis of the aortic wall. Aged aortic wall (*right*): Aging induces senescence of the ECs, which leads to chronic low-grade inflammation and subsequent aberrant ECM remodeling (fragmentation of elastin, excess deposition of collagen and their crosslinking) in the intima and media. Adventitial fibroblasts directly or indirectly stiffen the aortic wall by depositing excessive collagens.

2019). In large arteries, the ECM provides a structural framework, which not only withstands a wide range of tensile stresses, but also preserves its shape and functionality (Wagenseil and Mecham, 2009; Beenakker et al., 2012). In addition to structure, the ECM provides signaling cues that regulate proliferation and differentiation of resident cells [vascular smooth muscle cells (VSMCs), endothelial cells (ECs)] in the arterial wall (Davis and Senger, 2008; Nakayama et al., 2014).

The aorta is the largest elastic artery and the ascending region is anatomically positioned at the top of the left ventricle, which then arches (aortic arch) and branches into smaller arteries (right and left carotid and subclavian), before descending into the abdominal area. Elasticity of the aorta facilitates distension and recoil of the aortic wall during cardiac cycles to transform pulsatile flow generated by the left ventricle into steady flow to maintain local circulation in tissues and organs (Belz, 1995; Westerhof et al., 2009). The ECM composition and its three-dimensional structure determine morphology, mechanical property and functionality of the aorta (Wagenseil and Mecham, 2009). For example, elastic fibers and associated microfibrils and proteoglycans in the media (Halper and Kjaer, 2014; Hedtke et al., 2019; Halabi and Kozel, 2020) allow the aorta to expand and recoil during cardiac cycles (Cocciolone et al., 2018). On the other hand, fibrillar collagens (predominantly collagen I and III) in the media and adventitia are responsible for the tensile strength of the aortic wall to withstand the axial pressure created by the beating left ventricle (Wagenseil and Mecham, 2009). Along aging, elastic fibers in the aortic wall are progressively fragmented and lose their original elastic properties due to the life-long mechanical loads and low-grade chronic inflammation (Antonicelli et al., 2007; Duca et al., 2016; Heinz, 2021). Morphologically, the aortic aging is characterized by dilation, tortuousness and wall thickening in the intima and media layers (Gariepy et al., 1998; Lakatta and Levy, 2003), predominantly resulting from structural remodeling of the ECM and deregulated behaviors of VSMCs (Collins et al., 2014b). Fragmentation of the elastic fibers, aberrant collagen deposition and excess crosslinking of these ECM molecules lead to loss of elasticity and stiffening of the aortic wall (Qiu et al., 2007; Kohn et al., 2015; Duca et al., 2016). Aortic stiffness is known to parallel aortic aging and has

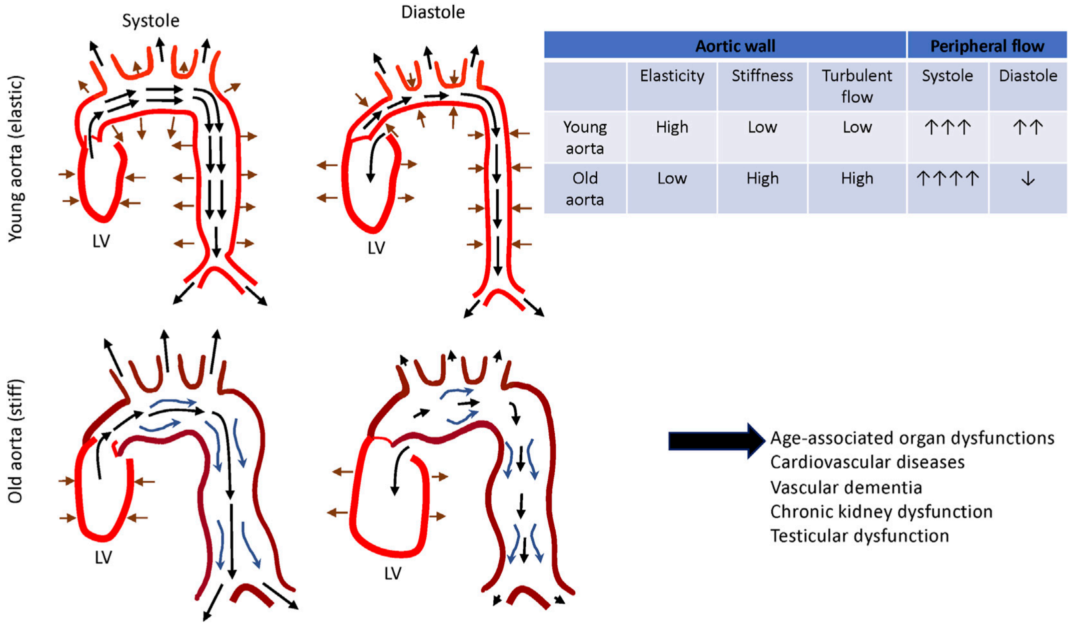

	Aortic wall			Peripheral flow	
	Elasticity	Stiffness	Turbulent flow	Systole	Diastole
Young aorta	High	Low	Low	↑↑↑	↑↑
Old aorta	Low	High	High	↑↑↑↑	↓

FIGURE 2 | Changes in aortic functions during aging. Aortic wall stores energy generated by the left ventricle during systole and release the energy during diastole by returning to its initial dimension. This facilitates smooth and constant circulation in the peripheral tissues and organs (*top*). Aged aorta becomes dilated and tortuous. Together with these morphological changes, thickening and stiffening of the aging aortic wall disturb the local circulation, which leads to the tissue and organ dysfunction (*bottom*).

been regarded as an independent predictor of morbidity and mortality of CVDs in the aging population (Mceniery et al., 2007; Wallace et al., 2007; Mitchell et al., 2010); aortic stiffening precedes clinical hypertension and is considered as the earliest predictor of hypertension (Liao et al., 1999; Dernellis and Panaretou, 2005; Peralta et al., 2010; Sun, 2015). In this mini review, we discuss the role of aberrant ECM remodeling in aging aorta and the underlying mechanism.

ANATOMY OF AORTA

Intima

The intima is the innermost layer of the aortic wall composed of a single layer of ECs, basement membrane (BM) and subendothelial space (**Figure 1**, left panel). ECs form a seamless monolayer over the BM, a thin pliable ECM membrane mainly consisting of laminin, collagen IV, fibronectin, perlecan, and heparan sulfate proteoglycans (Hallmann et al., 2005; Yurchenco, 2011). The BM plays crucial roles in the signaling events that regulate migration, proliferation, survival and barrier functions of resident vascular ECs (Davis and Senger, 2005). The vascular endothelium regulates homeostasis of the vessel by producing various vasoprotective factors such as nitric oxide (NO) to maintain vascular tone and blood flow (Sandoo et al., 2010; Kruger-Genge et al., 2019). The single layer of internal elastic lamina not only physically supports ECs and the BM, but also acts as a barrier structure between intima and media to prevent infiltration of circulating factors and media-derived cells that may trigger pathogenesis.

Media

The media layer of the vessel is predominantly composed of the lamellar units of elastic fibers, collagen fibers and VSMCs (Clark and Glagov, 1985; Tsamis et al., 2013) (**Figure 1**, left panel) and determines the elastic properties of the aortic wall (Taghizadeh et al., 2015). Elastic fibers and VSMCs create a highly organized media layer within the vessel wall. VSMCs synthesize tropoelastin, which is a water-soluble precursor to elastin (Ozsvar et al., 2021). Tropoelastin monomers generated by VSMCs undergo extensive cross-linking to create mature elastin (Sandberg et al., 1981; Krettek et al., 2003), which is assembled into elastic fibers to form the elastin-contractile units around the VSMCs in the media. VSMCs are heterogenous and exhibit a high degree of plasticity (Alexander and Owens, 2012). In the media layer, VSMCs are the most abundant cell type and play key roles in maintaining structure and functions of the aorta (Lacolley et al., 2017). Upon circumferential stretching, the elastic fibers within the aortic wall store the energy created from the pumping left ventricle during systole and release the energy during diastole by returning to their initial dimension (**Figure 2**, upper panel). This is indispensable for maintaining a regular and efficient circulation in the peripheral tissues and organs during the cardiac cycle (Belz, 1995). Collagens closely associate with elastic fibers in the media (Dingemans et al., 2000) and contribute to aortic wall stiffness and strength (Wagenseil and Mecham, 2009; Wang et al., 2021). Collagen types I and III are enriched within the aortic wall; type I collagen localizes around the VSMCs, while type III collagen exists alongside the multiple layers of external elastic lamella in the media layer (Shekhonin et al., 1987). These series of cellular and ECM structural units in the media are the major determinants of the elastic properties of the aortic wall.

Adventitia

The outermost layer of the aortic wall is the adventitia, composed of stem/progenitor cells, fibroblasts, pericytes, vasa vasorum (VV), lymphatic vessels, inflammatory cells (e.g., macrophages, dendritic cells, mast cells, T cells, and B cells), perivascular neurons, and adipocytes that are distributed in the collagen-rich connective tissue (**Figure 1**, left panel). ECM structures in the adventitia determine physical strengths of the aortic wall (Beenakker et al., 2012; Stenmark et al., 2013), which bears over half of the mechanical load to protect the aortic wall from overdistension. Importantly, adventitia is a regulatory center for vascular injury, and a pathological adventitia structure contributes to age-related vascular disease (Majesky et al., 2012; Stenmark et al., 2013; Tinajero and Gotlieb, 2020). Several types of stem/progenitor cells that reside adjacent to the media have the capacity to differentiate into VSMCs, ECs, chondrocytes, adipocytes, macrophages and myofibroblasts to maintain homeostasis of the aortic wall in response to physiological and pathological stimuli (Majesky et al., 2011; Majesky et al., 2012; Jolly et al., 2021). Fibroblasts that are absent in the intima and media are dispersed within the adventitia, where they serve to deposit collagen fibrils (Ross and Glomset, 1973; Kohn et al., 2015). VV is a specialized microvasculature that transports nutrients and oxygen to the adventitia and two-thirds of the media layer within the aortic wall. Adventitial lymphatic vessels modulate inflammation of the aortic wall by draining interstitial fluid and trafficking the immune cells through the aortic wall (Kutkut et al., 2015; Yeo et al., 2021). Perivascular innervation in the adventitia modulates functions of VSMCs and ECs to regulate vascular tone (Nava and Llorens, 2019). Perivascular adipose tissue (PVAT) also plays important roles in homeostasis of the aortic wall by releasing adipocytokines, chemokines and growth factors to determine inflammation status and stiffness of the aortic wall (Ozen et al., 2015; Nava and Llorens, 2019).

DISCUSSION

Aging of Intima and Media

With aging, anti-aging factors (e.g., GDF11, IGF-1, klotho, oxytocin, nitric oxide (NO)) decrease, while pro-aging factors (e.g., β2-microglobulin, oxidized low-density lipoproteins) increase in the circulating blood (Ozen et al., 2015; Smith et al., 2015; Cannata et al., 2017; Yang et al., 2017; Sahu et al., 2018; Kang and Yang, 2020; Kiss et al., 2020; Rybtsova et al., 2020). ECs that cover the surface of blood vessels orchestrate arterial homeostasis by mediating vascular tone, coagulation, immune response, inflammation, metabolism and angiogenesis (Michiels, 2003; Busse and Fleming, 2006; Pober et al., 2009; Falkenberg et al., 2019; Kruger-Genge et al., 2019), and are constantly exposed to pro- and anti-aging factors in the blood. In concert with age-associated hemodynamic challenges (e.g., hypertension, decreased shear flow and increased turbulent flow resulting from dilated and tortuous aged aorta) (Lantz et al., 2015; Buford, 2016; Ha et al., 2018) and intrinsic cellular aging programs (Hohensinner et al., 2016; Morgan et al., 2018), degenerative imbalances in anti- and pro-aging factors directly or indirectly accelerate endothelial senescence in the aortic wall (Erusalimsky and Kurz, 2006). Senescent ECs mitotically halt and become dysfunctional (Donato et al., 2015; Bhayadia et al., 2016) (**Figure 1** right panel), while exhibiting pro-inflammatory phenotypes (Wang et al., 2014a; Wang et al., 2014b; Pantsulaia et al., 2016) such as attenuated endothelial NO production, increased endothelin-1 (ET-1) release, production of inflammatory cytokines [e.g., IL-1, IL-6, IL-8, TNF-α, monocyte chemoattractant protein-1 (MCP-1)] (Maier et al., 1990; Pantsulaia et al., 2016), activation of surface adhesion receptors (e.g., ICAM-1, VCAM-1) and disruption of barrier function (Krouwer et al., 2012). Consequently, circulating immune cells are activated and adhere to the surface of dysfunctional ECs, which promotes their infiltration through the endothelium and into the subendothelial space (Trott et al., 2018) (**Figure 1**, right panel). Activated macrophages also release pro-inflammatory cytokines such as TNF-α, IL-1b, IL-6 and INF-γ (Wang et al., 2007; Lesniewski et al., 2011a; Lesniewski et al., 2011b) and chronic, low-grade sterile inflammation ensues in the aortic wall (Wang et al., 2014a; Wang et al., 2014b; Duca et al., 2016) (**Figure 1**, right panel). In response to the age-associated proinflammatory microenvironment, degenerative ECM remodeling (e.g., degradation of BM, fragmentation of internal elastic laminae, excessive deposition and crosslinking of collagens) (Bruel and Oxlund, 1996; Tsamis et al., 2013; Steppan et al., 2019) leads to thickening and stiffening of the ECM network within the subendothelial space (Guyton et al., 1983; Lakatta and Levy, 2003) (**Figure 1**, right panel). As a result, ECs sense the substrate stiffness (Collins et al., 2014a), which in turn, further aggravates endothelial dysfunction (Fels et al., 2012). For example, stiffening of the subendothelial space due to aberrant ECM remodeling sensitizes ECs to oxidative stress, accelerates EC senescence (Urbano et al., 2019), and disrupts EC barrier function to further promote infiltration of activated immune cells (Huynh et al., 2011). Aberrant cell-ECM interactions also reduce NO bioavailability and impair endothelial-dependent vasodilation (Paar et al., 2014). Decreased NO bioavailability also stimulates activation of MMPs (Nascimento et al., 2019), which further degrades the matrix composition of the aortic wall, particularly within collagen and elastic fibers (Tronc et al., 2000; Upchurch et al., 2001; Zaragoza et al., 2002).

These changes in the intima layer contribute to aortic aging and pathogenesis of CVDs (inside-out theory: inner layer triggers remodeling of aortic wall) (Donato et al., 2015; Yin and Pickering, 2016). Physiological crosstalk between ECs, immune cells, ECM and VSMCs maintains homeostasis of the healthy aorta, while age-associated changes lead to deregulated crosstalk and aberrant aortic wall remodeling (Mendez-Barbero et al., 2021). Aged ECs and disorganized underlying ECM structures also synergistically stimulate migration of medial VSMCs into the intima (Li et al., 1999; Miller et al., 2007). These VSMCs aberrantly remodel native

ECM structures in the intima (Schwartz et al., 1995) (**Figure 1**, right panel). Decreased expression of contractile proteins (Bochaton-Piallat et al., 1993; Bochaton-Piallat et al., 2001; Moon et al., 2003; Ferlosio et al., 2012) and increased expression of pro-inflammatory and migratory factors such as MMPs (Moon et al., 2003), MCP-1 (Spinetti et al., 2004) and PDGFR (Wang et al., 2012) in the VSMCs contribute to the intimal remodeling in the aging aorta (Li et al., 1999). These synthetic VSMCs further degrade elastic fibers, while deposit and crosslink collagens that are 100–1000 times stiffer than elastin between the fragmented elastic fibers in intima and media (Hays et al., 2018) (**Figure 1**, right panel). In the aging aorta, deregulated collagen deposition and crosslinking lead to fibrosis and thickening of the aortic wall (Movat et al., 1958; Spina and Garbin, 1976; Mccullagh et al., 1980; Toda et al., 1980; Andreotti et al., 1985; Shekhonin et al., 1987; Wang et al., 2006; Lyck Hansen et al., 2015). Aged ECs generate excess reactive oxygen species (ROS) through mitochondrial respiratory chain, NADPH oxidases and down regulation of antioxidant enzymes (Donato et al., 2015) to create chronic oxidative stress and subsequent low-grade inflammatory phenotype in the aortic wall (Ungvari et al., 2008), which leads to severe aortic pathologies such as atherosclerosis and abdominal aneurysm (AAA) (Ungvari et al., 2010; Peshkova et al., 2016; Golledge, 2019) in aged people. AAA is a 15th-leading cause of overall death in the United States and is an age-associated CVD (prevalence of men over 65 years is 4–8 percent) (Sakalihasan et al., 2018). The prevalence of aortic atherosclerosis also significantly increases along aging (Jaffer et al., 2002; Oyama et al., 2008; Chen et al., 2013) and causes serious CVDs such as coronary artery disease and stroke (Kronzon and Tunick, 2006; Di Tullio et al., 2008).

The heart beats over 100,000 times a day and each cardiac cycle induces pulsatile strain to the elastic fibers within the aortic wall. In the aged aorta, relatively quiescent elastic fibers in the media (Avolio et al., 1998) are mechanically fragmented and those fragmented elastic fibers are stabilized and stiffened by excessive deposition of collagens and their crosslinking in the pro-inflammatory environment (Duca et al., 2016). The fragmentation of the elastic fibers in the media with aging also enhances its proteolysis by specific elastases (i.e., elastolysis), which in turn generates short peptides known as elastin-derived peptides (Le Page et al., 2019). These peptides subsequently stimulate VSMC proliferation and differentiation into osteoblast-like cells (Simionescu et al., 2005) to accelerate inflammation and calcification of the aortic wall (Simionescu et al., 2005; Maurice et al., 2013; Dale et al., 2016). Importantly, exposure of the resident cells to the elastin-derived peptide further sustains chronic low-grade inflammation of the aortic wall (Le Page et al., 2019). Senescence of aged VSMCs (Monk and George, 2015) also accelerates aortic wall inflammation through the senescence-associated secretory phenotype (Chi et al., 2019) and osteoblast-like differentiation, which leads to calcium deposition in the media by upregulation of synthesis of alkaline phosphatase (ALP), bone morphogenetic protein (BMP), osteopontin (OPN), calpain-1, runt-related transcription factor (Runx-2) and collagens (Nakano-Kurimoto et al., 2009; Jiang et al., 2012; Fakhry et al., 2017). Calcium deposition around the elastic fibers is markedly increased in the aortic wall with aging (Lansing et al., 1950; Derlin et al., 2015), which further stiffens the medial layer and enhances aortic wall dysfunction (Laurent et al., 1996; Aronson, 2003).

Although arterial stiffening has historically been associated with changes in the native ECM structures, additional evidence suggests that stiffening of the resident cells [e.g., ECs and VSMCs (Gao et al., 2014; Nicholson et al., 2017; Morales-Quinones et al., 2020)] also contributes to overall stiffness of the aortic wall (Qiu et al., 2010; Sehgel et al., 2013; Sehgel et al., 2015; Leloup et al., 2019). The activity of the contractile filaments as well as the molecular signaling pathways that regulate actin polymerization and focal adhesion signaling in the VSMCs contribute to the age-associated vascular stiffening (Nicholson et al., 2018). Interactions between VSMCs and aberrant ECM structures also play key roles in these cellular events (Zhu et al., 2012; Ribeiro-Silva et al., 2021). Excessively deposited collagens progressively acquire crosslinks (Aronson, 2003) in the intima and media, altering their structural and functional properties. Thus, disorganized ECM structures, deregulated cell-ECM interactions, and increased cellular stiffness collectively contribute to the aortic wall stiffening phenotype.

Aging of Adventitia

Adventitia not only provides structural support to the aortic wall, but also maintains its homeostasis (Tinajero and Gotlieb, 2020). Collagen fibers in the adventitia layer provide tensile strength and resilience to the cyclic deformation of the aortic wall caused by the beating heart (Thompson et al., 2002; Tsamis et al., 2013). As an axial load is placed on the vessel wall, the collagen fibers deform and straighten, exhibiting their high tensile strength. Adventitial fibroblasts synthesize and deposit collagen I and III, and these collagens increase with age and are also accompanied by stiffening of the aorta (Fleenor et al., 2010). While it is widely accepted that various adventitial cells (e.g., stem/progenitor cells, fibroblasts, arterial and lymphatic ECs, pericytes, immune cells, adipocytes, neuronal cells) and adventitial ECM molecules maintain homeostasis of the aortic wall, and deregulation of these adventitial components are proposed to contribute to pathological remodeling of the aortic wall such as atherosclerosis and AAA (outside-in theory: outer layer triggers remodeling of the aortic wall) (Stefanadis et al., 1995; Majesky et al., 2012; Majesky, 2015; Doderer et al., 2018; Tinajero and Gotlieb, 2020), the effects of aging on structure and functions of aortic adventitia have not been well-characterized compared to intima and media. A comprehensive analysis of cellular and non-cellular constituents of adventitia in young and aging aorta will be necessary to understand how they interact and crosstalk to maintain homeostasis of the aortic wall.

Perspective

Life-long mechanical loads generated by the beating left ventricle and chronic low-grade inflammation stiffen the aortic wall with age, which accelerates EC dysfunction, and subsequent remodeling of the aortic wall. Importantly, normally aging aortic wall (**Figure 1**) is not pathological, but this is predisposed to CVDs such as atherosclerosis (e.g., formation of atheromatous plaque and foam cells) and AAA (e.g., medial necrosis, dissection and rupture). To prevent the aorta from progressing into these pathological conditions, it is critical to understand the structural and functional alterations of the aging aorta. These spiral cycles lead to impaired peripheral circulation, organ failure and cardiovascular events during aging (Thorin-Trescases and Thorin, 2016) (**Figure 2**). Several anti-aging remedies have been explored to prevent this over the decades. For example, anti-hypertensive medications, regular aerobic exercise habits or specific diets such as Mediterranean diet may slow down the vicious cycles and decrease the risk of CVDs (Vaitkevicius et al., 1993; Seals et al., 2008; Kanaki et al., 2013; Liu et al., 2013; Santos-Parker et al., 2014; Larocca et al., 2017; Upala et al., 2017). Although these anti-aging remedies may exert the beneficial effects by attenuating chronic low-grade inflammation (Chrysohoou et al., 2004; Lesniewski et al., 2011a; Lesniewski et al., 2011b; Woods et al., 2012), more comprehensive mechanisms of age-associated aortic wall remodeling need to be explored to develop more efficient anti-aortic aging strategies. Since stiffness of the aorta, which is determined by the structures of ECM and stiffness of the resident cells, can be measured in non-invasive ways using pulse-wave-velocity (PWV) (Cavalcante et al., 2011; Laurent et al., 2016; Salvi et al., 2019), more efficient anti-aortic aging strategies such as combination of medications, fitness program and diet instruction could be rigorously explored at the clinic level.

SUMMARY

Age-associated ECM alterations play crucial roles in the progression of aortic aging. Targeting altered ECM structures and cell-ECM interactions in the aortic wall using combinations of ECM and cytoskeleton modifiers can be a promising therapeutic strategy for aortic pathologies. Further functional characterization of the ECM alterations and cell-ECM interactions in the aged aorta will provide a new framework to develop more efficient therapies for aortic aging and CVDs.

AUTHOR CONTRIBUTIONS

All authors listed have made a substantial, direct, and intellectual contribution to the work and approved it for publication.

FUNDING

This work was supported by funds from NIH R21AG054830 (to AM, to TM), R01HL139638 (to AM, to TM), R21AG062893 (to AM, to TM), R01HL142578 (to AM, to TM), and AHA 18TPA34170129 (to AM).

ACKNOWLEDGMENTS

The authors thank Joy Lincoln for critical review of the manuscript.

REFERENCES

Alexander, M. R., and Owens, G. K. (2012). Epigenetic Control of Smooth Muscle Cell Differentiation and Phenotypic Switching in Vascular Development and Disease. *Annu. Rev. Physiol.* 74, 13–40. doi:10.1146/annurev-physiol-012110-142315

Andreotti, L., Bussotti, A., Cammelli, D., Di Giovine, F., Sampognaro, S., Sterrantino, G., et al. (1985). Aortic Connective Tissue in Ageing-A Biochemical Study. *Angiology* 36, 872–879. doi:10.1177/000331978503601206

Antonicelli, F., Bellon, G., Debelle, L., and Hornebeck, W. (2007). Elastin-Elastases and Inflamm-Aging. *Curr. Top. Dev. Biol.* 79, 99–155. doi:10.1016/s0070-2153(06)79005-6

Aronson, D. (2003). Cross-linking of Glycated Collagen in the Pathogenesis of Arterial and Myocardial Stiffening of Aging and Diabetes. *J. Hypertens.* 21, 3–12. doi:10.1097/00004872-200301000-00002

Avolio, A., Jones, D., and Tafazzoli-Shadpour, M. (1998). Quantification of Alterations in Structure and Function of Elastin in the Arterial media. *Hypertension* 32, 170–175. doi:10.1161/01.hyp.32.1.170

Beenakker, J.-W. M., Ashcroft, B. A., Lindeman, J. H. N., and Oosterkamp, T. H. (2012). Mechanical Properties of the Extracellular Matrix of the Aorta Studied by Enzymatic Treatments. *Biophysical J.* 102, 1731–1737. doi:10.1016/j.bpj.2012.03.041

Belz, G. G. (1995). Elastic Properties and Windkessel Function of the Human Aorta. *Cardiovasc. Drug Ther.* 9, 73–83. doi:10.1007/bf00877747

Bhayadia, R., Schmidt, B. M. W., Melk, A., and Hömme, M. (2016). Senescence-Induced Oxidative Stress Causes Endothelial Dysfunction. *Gerona* 71, 161–169. doi:10.1093/gerona/glv008

Birch, H. L. (2018). Extracellular Matrix and Ageing. *Subcell Biochem.* 90, 169–190. doi:10.1007/978-981-13-2835-0_7

Bochaton-Piallat, M.-L., Clowes, A. W., Clowes, M. M., Fischer, J. W., Redard, M., Gabbiani, F., et al. (2001). Cultured Arterial Smooth Muscle Cells Maintain Distinct Phenotypes when Implanted into Carotid Artery. *Atvb* 21, 949–954. doi:10.1161/01.atv.21.6.949

Bochaton-Piallat, M. L., Gabbiani, F., Ropraz, P., and Gabbiani, G. (1993). Age Influences the Replicative Activity and the Differentiation Features of Cultured Rat Aortic Smooth Muscle Cell Populations and Clones. *Arterioscler Thromb.* 13, 1449–1455. doi:10.1161/01.atv.13.10.1449

Brüel, A., and Oxlund, H. (1996). Changes in Biomechanical Properties, Composition of Collagen and Elastin, and Advanced Glycation Endproducts of the Rat Aorta in Relation to Age. *Atherosclerosis* 127, 155–165. doi:10.1016/s0021-9150(96)05947-3

Buford, T. W. (2016). Hypertension and Aging. *Ageing Res. Rev.* 26, 96–111. doi:10.1016/j.arr.2016.01.007

Busse, R., and Fleming, I. (2006). Vascular Endothelium and Blood Flow. *Handb Exp. Pharmacol.* 176, 43–78. doi:10.1007/3-540-36028-x_2

Cannatà, A., Marcon, G., Cimmino, G., Camparini, L., Ciucci, G., Sinagra, G., et al. (2017). Role of Circulating Factors in Cardiac Aging. *J. Thorac. Dis.* 9, S17–S29. doi:10.21037/jtd.2017.03.95

Cavalcante, J. L., Lima, J. A. C., Redheuil, A., and Al-Mallah, M. H. (2011). Aortic Stiffness. *J. Am. Coll. Cardiol.* 57, 1511–1522. doi:10.1016/j.jacc.2010.12.017

Chen, M. A., Kawakubo, M., Colletti, P. M., Xu, D., Labree Dustin, L., Detrano, R., et al. (2013). Effect of Age on Aortic Atherosclerosis. *J. Geriatr. Cardiol.* 10, 135–140. doi:10.3969/j.issn.1671-5411.2013.02.005

Chi, C., Li, D.-J., Jiang, Y.-J., Tong, J., Fu, H., Wu, Y.-H., et al. (2019). Vascular Smooth Muscle Cell Senescence and Age-Related Diseases: State of the Art. *Biochim. Biophys. Acta (Bba) - Mol. Basis Dis.* 1865, 1810–1821. doi:10.1016/j.bbadis.2018.08.015

Chrysohoou, C., Panagiotakos, D. B., Pitsavos, C., Das, U. N., and Stefanadis, C. (2004). Adherence to the Mediterranean Diet Attenuates Inflammation and

Coagulation Process in Healthy Adults. *J. Am. Coll. Cardiol.* 44, 152–158. doi:10.1016/j.jacc.2004.03.039

Clark, J. M., and Glagov, S. (1985). Transmural Organization of the Arterial media. The Lamellar Unit Revisited. *Arteriosclerosis* 5, 19–34. doi:10.1161/01.atv.5.1.19

Cocciolone, A. J., Hawes, J. Z., Staiculescu, M. C., Johnson, E. O., Murshed, M., and Wagenseil, J. E. (2018). Elastin, Arterial Mechanics, and Cardiovascular Disease. *Am. J. Physiology-Heart Circulatory Physiol.* 315, H189–H205. doi:10.1152/ajpheart.00087.2018

Collins, C., Osborne, L. D., Guilluy, C., Chen, Z., O'Brien, E. T., 3rd, Reader, J. S., et al. (2014a). Haemodynamic and Extracellular Matrix Cues Regulate the Mechanical Phenotype and Stiffness of Aortic Endothelial Cells. *Nat. Commun.* 5, 3984. doi:10.1038/ncomms4984

Collins, J. A., Munoz, J.-V., Patel, T. R., Loukas, M., and Tubbs, R. S. (2014b). The Anatomy of the Aging Aorta. *Clin. Anat.* 27, 463–466. doi:10.1002/ca.22384

Dale, M. A., Xiong, W., Carson, J. S., Suh, M. K., Karpisek, A. D., Meisinger, T. M., et al. (2016). Elastin-Derived Peptides Promote Abdominal Aortic Aneurysm Formation by Modulating M1/M2 Macrophage Polarization. *J.I.* 196, 4536–4543. doi:10.4049/jimmunol.1502454

Davis, G. E., and Senger, D. R. (2005). Endothelial Extracellular Matrix. *Circ. Res.* 97, 1093–1107. doi:10.1161/01.res.0000191547.64391.e3

Davis, G. E., and Senger, D. R. (2008). Extracellular Matrix Mediates a Molecular Balance between Vascular Morphogenesis and Regression. *Curr. Opin. Hematol.* 15, 197–203. doi:10.1097/moh.0b013e3282fcc321

Derlin, T., Janssen, T., Salamon, J., Veldhoen, S., Busch, J. D., Schön, G., et al. (2015). Age-related Differences in the Activity of Arterial mineral Deposition and Regional Bone Metabolism: a 18F-Sodium Fluoride Positron Emission Tomography Study. *Osteoporos. Int.* 26, 199–207. doi:10.1007/s00198-014-2839-6

Dernellis, J., and Panaretou, M. (2005). Aortic Stiffness Is an Independent Predictor of Progression to Hypertension in Nonhypertensive Subjects. *Hypertension* 45, 426–431. doi:10.1161/01.hyp.0000157818.58878.93

Di Tullio, M. R., Homma, S., Jin, Z., and Sacco, R. L. (2008). Aortic Atherosclerosis, Hypercoagulability, and Stroke. *J. Am. Coll. Cardiol.* 52, 855–861. doi:10.1016/j.jacc.2008.04.062

Dingemans, K. P., Teeling, P., Lagendijk, J. H., and Becker, A. E. (2000). Extracellular Matrix of the Human Aortic media: an Ultrastructural Histochemical and Immunohistochemical Study of the Adult Aortic media. *Anat. Rec.* 258, 1–14. doi:10.1002/(sici)1097-0185(20000101)258:1<1::aid-ar1>3.0.co;2-7

Doderer, S. A., Gäbel, G., Kokje, V. B. C., Northoff, B. H., Holdt, L. M., Hamming, J. F., et al. (2018). Adventitial Adipogenic Degeneration Is an Unidentified Contributor to Aortic wall Weakening in the Abdominal Aortic Aneurysm. *J. Vasc. Surg.* 67, 1891–1900. doi:10.1016/j.jvs.2017.05.088

Donato, A. J., Machin, D. R., and Lesniewski, L. A. (2018). Mechanisms of Dysfunction in the Aging Vasculature and Role in Age-Related Disease. *Circ. Res.* 123, 825–848. doi:10.1161/circresaha.118.312563

Donato, A. J., Morgan, R. G., Walker, A. E., and Lesniewski, L. A. (2015). Cellular and Molecular Biology of Aging Endothelial Cells. *J. Mol. Cell Cardiol.* 89, 122–135. doi:10.1016/j.yjmcc.2015.01.021

Duca, L., Blaise, S., Romier, B., Laffargue, M., Gayral, S., El Btaouri, H., et al. (2016). Matrix Ageing and Vascular Impacts: Focus on Elastin Fragmentation. *Cardiovasc. Res.* 110, 298–308. doi:10.1093/cvr/cvw061

Erusalimsky, J. D., and Kurz, D. J. (2006). Endothelial Cell Senescence. *Handb Exp. Pharmacol.* 106, 213–248. doi:10.1007/3-540-36028-x_7

Fakhry, M., Roszkowska, M., Briolay, A., Bougault, C., Guignandon, A., Diaz-Hernandez, J. I., et al. (2017). TNAP Stimulates Vascular Smooth Muscle Cell Trans-differentiation into Chondrocytes through Calcium Deposition and BMP-2 Activation: Possible Implication in Atherosclerotic Plaque Stability. *Biochim. Biophys. Acta (Bba) - Mol. Basis Dis.* 1863, 643–653. doi:10.1016/j.bbadis.2016.12.003

Falkenberg, K. D., Rohlenova, K., Luo, Y., and Carmeliet, P. (2019). The Metabolic Engine of Endothelial Cells. *Nat. Metab.* 1, 937–946. doi:10.1038/s42255-019-0117-9

Fels, J., Jeggle, P., Kusche-Vihrog, K., and Oberleithner, H. (2012). Cortical Actin Nanodynamics Determines Nitric Oxide Release in Vascular Endothelium. *PLoS One* 7, e41520. doi:10.1371/journal.pone.0041520

Ferlosio, A., Arcuri, G., Doldo, E., Scioli, M. G., De Falco, S., Spagnoli, L. G., et al. (2012). Age-related Increase of Stem Marker Expression Influences Vascular Smooth Muscle Cell Properties. *Atherosclerosis* 224, 51–57. doi:10.1016/j.atherosclerosis.2012.07.016

Fleenor, B. S., Marshall, K. D., Durrant, J. R., Lesniewski, L. A., and Seals, D. R. (2010). Arterial Stiffening with Ageing Is Associated with Transforming Growth Factor-B1-Related Changes in Adventitial Collagen: Reversal by Aerobic Exercise. *J. Physiol.* 588, 3971–3982. doi:10.1113/jphysiol.2010.194753

Franceschi, C., Garagnani, P., Morsiani, C., Conte, M., Santoro, A., Grignolio, A., et al. (2018). The Continuum of Aging and Age-Related Diseases: Common Mechanisms but Different Rates. *Front. Med.* 5, 61. doi:10.3389/fmed.2018.00061

Frantz, C., Stewart, K. M., and Weaver, V. M. (2010). The Extracellular Matrix at a Glance. *J. Cel Sci* 123, 4195–4200. doi:10.1242/jcs.023820

Gao, Y. Z., Saphirstein, R. J., Yamin, R., Suki, B., and Morgan, K. G. (2014). Aging Impairs Smooth Muscle-Mediated Regulation of Aortic Stiffness: a Defect in Shock Absorption Function? *Am. J. Physiology-Heart Circulatory Physiol.* 307, H1252–H1261. doi:10.1152/ajpheart.00392.2014

Gariepy, J., Salomon, J., Denarie´, N., Laskri, F., Me´gnien, J. L., Levenson, J., et al. (1998). Sex and Topographic Differences in Associations between Large-Artery Wall Thickness and Coronary Risk Profile in a French Working Cohort. *Atvb* 18, 584–590. doi:10.1161/01.atv.18.4.584

Golledge, J. (2019). Abdominal Aortic Aneurysm: Update on Pathogenesis and Medical Treatments. *Nat. Rev. Cardiol.* 16, 225–242. doi:10.1038/s41569-018-0114-9

Guyton, D. L., Lindsay, K. L., and Dao, D. T. (1983). Pediatric Ophthalmology. *Ophthalmology* 90, 234–246. doi:10.1016/s0161-6420(83)80140-7

Ha, H., Ziegler, M., Welander, M., Bjarnegård, N., Carlhäll, C.-J., Lindenberger, M., et al. (2018). Age-Related Vascular Changes Affect Turbulence in Aortic Blood Flow. *Front. Physiol.* 9, 36. doi:10.3389/fphys.2018.00036

Halabi, C. M., and Kozel, B. A. (2020). Vascular Elastic Fiber Heterogeneity in Health and Disease. *Curr. Opin. Hematol.* 27, 190–196. doi:10.1097/moh.0000000000000578

Hallmann, R., Horn, N., Selg, M., Wendler, O., Pausch, F., and Sorokin, L. M. (2005). Expression and Function of Laminins in the Embryonic and Mature Vasculature. *Physiol. Rev.* 85, 979–1000. doi:10.1152/physrev.00014.2004

Halper, J., and Kjaer, M. (2014). Basic Components of Connective Tissues and Extracellular Matrix: Elastin, Fibrillin, Fibulins, Fibrinogen, Fibronectin, Laminin, Tenascins and Thrombospondins. *Adv. Exp. Med. Biol.* 802, 31–47. doi:10.1007/978-94-007-7893-1_3

Hays, T. T., Ma, B., Zhou, N., Stoll, S., Pearce, W. J., and Qiu, H. (2018). Vascular Smooth Muscle Cells Direct Extracellular Dysregulation in Aortic Stiffening of Hypertensive Rats. *Aging Cell* 17, e12748. doi:10.1111/acel.12748

Hedtke, T., Schräder, C. U., Heinz, A., Hoehenwarter, W., Brinckmann, J., Groth, T., et al. (2019). A Comprehensive Map of Human Elastin Cross-linking during Elastogenesis. *FEBS J.* 286, 3594–3610. doi:10.1111/febs.14929

Heidenreich, P. A., Trogdon, J. G., Khavjou, O. A., Butler, J., Dracup, K., Ezekowitz, M. D., et al. (2011). Forecasting the Future of Cardiovascular Disease in the United States: a Policy Statement from the American Heart Association. *Circulation* 123, 933–944. doi:10.1161/cir.0b013e31820a55f5(

Heinz, A. (2021). Elastic Fibers during Aging and Disease. *Ageing Res. Rev.* 66, 101255. doi:10.1016/j.arr.2021.101255

Hohensinner, P. J., Kaun, C., Buchberger, E., Ebenbauer, B., Demyanets, S., Huk, I., et al. (2016). Age Intrinsic Loss of Telomere protection via TRF1 Reduction in Endothelial Cells. *Biochim. Biophys. Acta (Bba) - Mol. Cel Res.* 1863, 360–367. doi:10.1016/j.bbamcr.2015.11.034

Huynh, J., Nishimura, N., Rana, K., Peloquin, J. M., Califano, J. P., Montague, C. R., et al. (2011). Age-related Intimal Stiffening Enhances Endothelial Permeability and Leukocyte Transmigration. *Sci. Transl Med.* 3, 112ra122. doi:10.1126/scitranslmed.3002761

Jaffer, F. A., O'Donnell, C. J., Larson, M. G., Chan, S. K., Kissinger, K. V., Kupka, M. J., et al. (2002). Age and Sex Distribution of Subclinical Aortic Atherosclerosis. *Atvb* 22, 849–854. doi:10.1161/01.atv.0000012662.29622.00

Jana, S., Hu, M., Shen, M., and Kassiri, Z. (2019). Extracellular Matrix, Regional Heterogeneity of the Aorta, and Aortic Aneurysm. *Exp. Mol. Med.* 51, 1–15. doi:10.1038/s12276-019-0286-3

Jiang, L., Zhang, J., Monticone, R. E., Telljohann, R., Wu, J., Wang, M., et al. (2012). Calpain-1 Regulation of Matrix Metalloproteinase 2 Activity in Vascular Smooth Muscle Cells Facilitates Age-Associated Aortic wall Calcification and Fibrosis. *Hypertension* 60, 1192–1199. doi:10.1161/hypertensionaha.112.196840

Jolly, A. J., Lu, S., Strand, K. A., Dubner, A. M., Mutryn, M. F., Nemenoff, R. A., et al. (2021). Heterogeneous Subpopulations of Adventitial Progenitor Cells Regulate Vascular Homeostasis and Pathological Vascular Remodeling. *Cardiovasc. Res.* 14, cvab174. doi:10.1093/cvr/cvab174

Kanaki, A. I., Sarafidis, P. A., Georgianos, P. I., Kanavos, K., Tziolas, I. M., Zebekakis, P. E., et al. (2013). Effects of Low-Dose Atorvastatin on Arterial Stiffness and central Aortic Pressure Augmentation in Patients with Hypertension and Hypercholesterolemia. *Am. J. Hypertens.* 26, 608–616. doi:10.1093/ajh/hps098

Kang, J. S., and Yang, Y. R. (2020). Circulating Plasma Factors Involved in Rejuvenation. *Aging (Albany NY)* 12, 23394–23408. doi:10.18632/aging.103933

Kiss, T., Tarantini, S., Csipo, T., Balasubramanian, P., Nyúl-Tóth, Á., Yabluchanskiy, A., et al. (2020). Circulating Anti-geronic Factors from Heterochonic Parabionts Promote Vascular Rejuvenation in Aged Mice: Transcriptional Footprint of Mitochondrial protection, Attenuation of Oxidative Stress, and rescue of Endothelial Function by Young Blood. *Geroscience* 42, 727–748. doi:10.1007/s11357-020-00180-6

Kohn, J. C., Lampi, M. C., and Reinhart-King, C. A. (2015). Age-related Vascular Stiffening: Causes and Consequences. *Front. Genet.* 06, 112. doi:10.3389/fgene.2015.00112

Krettek, A., Sukhova, G. K., and Libby, P. (2003). Elastogenesis in Human Arterial Disease. *Atvb* 23, 582–587. doi:10.1161/01.atv.0000064372.78561.a5

Kronzon, I., and Tunick, P. A. (2006). Aortic Atherosclerotic Disease and Stroke. *Circulation* 114, 63–75. doi:10.1161/circulationaha.105.593418

Krouwer, V. J. D., Hekking, L. H. P., Langelaar-Makkinje, M., Regan-Klapisz, E., and Post, J. (2012). Endothelial Cell Senescence Is Associated with Disrupted Cell-Cell Junctions and Increased Monolayer Permeability. *Vasc. Cel* 4, 12. doi:10.1186/2045-824x-4-12

Krüger-Genge, A., Blocki, A., Franke, R. P., and Jung, F. (2019). Vascular Endothelial Cell Biology: An Update. *Int. J. Mol. Sci.* 20, 4411. doi:10.3390/ijms20184411

Kutkut, I., Meens, M. J., Mckee, T. A., Bochaton-Piallat, M.-L., and Kwak, B. R. (2015). Lymphatic Vessels: an Emerging Actor in Atherosclerotic Plaque Development. *Eur. J. Clin. Invest.* 45, 100–108. doi:10.1111/eci.12372

Lacolley, P., Regnault, V., Segers, P., and Laurent, S. (2017). Vascular Smooth Muscle Cells and Arterial Stiffening: Relevance in Development, Aging, and Disease. *Physiol. Rev.* 97, 1555–1617. doi:10.1152/physrev.00003.2017

Lakatta, E. G., and Levy, D. (2003a). Arterial and Cardiac Aging: Major Shareholders in Cardiovascular Disease Enterprises. *Circulation* 107, 139–146. doi:10.1161/01.cir.0000048892.83521.58

Lansing, A. I., Alex, M., and Rosenthal, T. B. (1950). Calcium and Elastin in Human Arteriosclerosis. *J. Gerontol.* 5, 112–119. doi:10.1093/geronj/5.2.112

Lantz, J., Renner, J., Länne, T., and Karlsson, M. (2015). Is Aortic wall Shear Stress Affected by Aging? an Image-Based Numerical Study with Two Age Groups. *Med. Eng. Phys.* 37, 265–271. doi:10.1016/j.medengphy.2014.12.011

Larocca, T. J., Martens, C. R., and Seals, D. R. (2017). Nutrition and Other Lifestyle Influences on Arterial Aging. *Ageing Res. Rev.* 39, 106–119. doi:10.1016/j.arr.2016.09.002

Laurent, S., Lacolley, P., Girerd, X., Boutouyrie, P., Bezie, Y., and Safar, M. (1996). Arterial Stiffening: Opposing Effects of Age- and Hypertension-Associated Structural Changes. *Can. J. Physiol. Pharmacol.* 74, 842–849. doi:10.1139/y96-075

Laurent, S., Marais, L., and Boutouyrie, P. (2016). The Noninvasive Assessment of Vascular Aging. *Can. J. Cardiol.* 32, 669–679. doi:10.1016/j.cjca.2016.01.039

Le Page, A., Khalil, A., Vermette, P., Frost, E. H., Larbi, A., Witkowski, J. M., et al. (2019). The Role of Elastin-Derived Peptides in Human Physiology and Diseases. *Matrix Biol.* 84, 81–96. doi:10.1016/j.matbio.2019.07.004

Leloup, A. J. A., Van Hove, C. E., De Moudt, S., De Meyer, G. R. Y., De Keulenaer, G. W., and Fransen, P. (2019). Vascular Smooth Muscle Cell Contraction and Relaxation in the Isolated Aorta: a Critical Regulator of Large Artery Compliance. *Physiol. Rep.* 7, e13934. doi:10.14814/phy2.13934

Lesniewski, L. A., Durrant, J. R., Connell, M. L., Folian, B. J., Donato, A. J., and Seals, D. R. (2011a). Salicylate Treatment Improves Age-Associated Vascular Endothelial Dysfunction: Potential Role of Nuclear Factor B and Forkhead Box O Phosphorylation. *Journals Gerontol. Ser. A: Biol. Sci. Med. Sci.* 66A, 409–418. doi:10.1093/gerona/glq233

Lesniewski, L. A., Durrant, J. R., Connell, M. L., Henson, G. D., Black, A. D., Donato, A. J., et al. (2011b). Aerobic Exercise Reverses Arterial Inflammation with Aging in Mice. *Am. J. Physiology-Heart Circulatory Physiol.* 301, H1025–H1032. doi:10.1152/ajpheart.01276.2010

Li, Z., Froehlich, J., Galis, Z. S., and Lakatta, E. G. (1999). Increased Expression of Matrix Metalloproteinase-2 in the Thickened Intima of Aged Rats. *Hypertension* 33, 116–123. doi:10.1161/01.hyp.33.1.116

Liao, D., Arnett, D. K., Tyroler, H. A., Riley, W. A., Chambless, L. E., Szklo, M., et al. (1999). Arterial Stiffness and the Development of Hypertension. *Hypertension* 34, 201–206. doi:10.1161/01.hyp.34.2.201

Liu, M., Li, G.-L., Li, Y., and Wang, J.-G. (2013). Effects of Various Antihypertensive Drugs on Arterial Stiffness and Wave Reflections. *Pulse* 1, 97–107. doi:10.1159/000354108

Lyck Hansen, M., Beck, H. C., Irmukhamedov, A., Jensen, P. S., Olsen, M. H., and Rasmussen, L. M. (2015). Proteome Analysis of Human Arterial Tissue Discloses Associations between the Vascular Content of Small Leucine-Rich Repeat Proteoglycans and Pulse Wave Velocity. *Atvb* 35, 1896–1903. doi:10.1161/atvbaha.114.304706

Maier, J. A. M., Voulalas, P., Roeder, D., and Maciag, T. (1990). Extension of the Life-Span of Human Endothelial Cells by an Interleukin-1αAntisense Oligomer. *Science* 249, 1570–1574. doi:10.1126/science.2218499

Majesky, M. W. (2015). Adventitia and Perivascular Cells. *Arterioscler Thromb. Vasc. Biol.* 35, e31–5. doi:10.1161/ATVBAHA.115.306088

Majesky, M. W., Dong, X. R., Hoglund, V., Daum, G., and Mahoney, Jr., W. M., Jr. (2012). The Adventitia: a Progenitor Cell Niche for the Vessel wall. *Cells Tissues Organs* 195, 73–81. doi:10.1159/000331413

Majesky, M. W., Dong, X. R., Hoglund, V., Mahoney, W. M., Jr., and Daum, G. (2011). The Adventitia. *Arterioscler Thromb. Vasc. Biol.* 31, 1530–1539. doi:10.1161/atvbaha.110.221549

Maurice, P., Blaise, S., Gayral, S., Debelle, L., Laffargue, M., Hornebeck, W., et al. (2013). Elastin Fragmentation and Atherosclerosis Progression: the Elastokine Concept. *Trends Cardiovasc. Med.* 23, 211–221. doi:10.1016/j.tcm.2012.12.004

Mccullagh, K. G., Duance, V. C., and Bishop, K. A. (1980). The Distribution of Collagen Types I, III and V (AB) in normal and Atherosclerotic Human Aorta. *J. Pathol.* 130, 45–55. doi:10.1002/path.1711300107

Mceniery, C. M., Wilkinson, I. B., and Avolio, A. P. (2007). Age, Hypertension and Arterial Function. *Clin. Exp. Pharmacol. Physiol.* 34, 665–671. doi:10.1111/j.1440-1681.2007.04657.x

Méndez-Barbero, N., Gutiérrez-Muñoz, C., and Blanco-Colio, L. M. (2021). Cellular Crosstalk between Endothelial and Smooth Muscle Cells in Vascular Wall Remodeling. *Int. J. Mol. Sci.* 22, 7284. doi:10.3390/ijms22147284

Michiels, C. (2003). Endothelial Cell Functions. *J. Cel. Physiol.* 196, 430–443. doi:10.1002/jcp.10333

Miller, S. J., Watson, W. C., Kerr, K. A., Labarrere, C. A., Chen, N. X., Deeg, M. A., et al. (2007). Development of Progressive Aortic Vasculopathy in a Rat Model of Aging. *Am. J. Physiology-Heart Circulatory Physiol.* 293, H2634–H2643. doi:10.1152/ajpheart.00397.2007

Mitchell, G. F., Hwang, S.-J., Vasan, R. S., Larson, M. G., Pencina, M. J., Hamburg, N. M., et al. (2010). Arterial Stiffness and Cardiovascular Events. *Circulation* 121, 505–511. doi:10.1161/circulationaha.109.886655

Monk, B. A., and George, S. J. (2015). The Effect of Ageing on Vascular Smooth Muscle Cell Behaviour - A Mini-Review. *Gerontology* 61, 416–426. doi:10.1159/000368576

Moon, S.-K., Cha, B.-Y., and Kim, C.-H. (2003). *In Vitro* cellular Aging Is Associated with Enhanced Proliferative Capacity, G1 Cell Cycle Modulation, and Matrix Metalloproteinase-9 Regulation in Mouse Aortic Smooth Muscle Cells. *Arch. Biochem. Biophys.* 418, 39–48. doi:10.1016/s0003-9861(03)00402-8

Morales-Quinones, M., Ramirez-Perez, F. I., Foote, C. A., Ghiarone, T., Ferreira-Santos, L., Bloksgaard, M., et al. (2020). LIMK (LIM Kinase) Inhibition Prevents Vasoconstriction- and Hypertension-Induced Arterial Stiffening and Remodeling. *Hypertension* 76, 393–403. doi:10.1161/hypertensionaha.120.15203

Morgan, R. G., Donato, A. J., and Walker, A. E. (2018). Telomere Uncapping and Vascular Aging. *Am. J. Physiology-Heart Circulatory Physiol.* 315, H1–H5. doi:10.1152/ajpheart.00008.2018

Movat, H. Z., More, R. H., and Haust, M. D. (1958). The Diffuse Intimal Thickening of the Human Aorta with Aging. *Am. J. Pathol.* 34, 1023–1031.

Nakano-Kurimoto, R., Ikeda, K., Uraoka, M., Nakagawa, Y., Yutaka, K., Koide, M., et al. (2009). Replicative Senescence of Vascular Smooth Muscle Cells Enhances the Calcification through Initiating the Osteoblastic Transition. *Am. J. Physiology-Heart Circulatory Physiol.* 297, H1673–H1684. doi:10.1152/ajpheart.00455.2009

Nakayama, K. H., Hou, L., and Huang, N. F. (2014). Role of Extracellular Matrix Signaling Cues in Modulating Cell Fate Commitment for Cardiovascular Tissue Engineering. *Adv. Healthc. Mater.* 3, 628–641. doi:10.1002/adhm.201300620

Nascimento, R. A., Possomato-Vieira, J. S., Bonacio, G. F., Rizzi, E., and Dias-Junior, C. A. (2019). Reductions of Circulating Nitric Oxide Are Followed by Hypertension during Pregnancy and Increased Activity of Matrix Metalloproteinases-2 and -9 in Rats. *Cells* 8, 1402. doi:10.3390/cells8111402

Nava, E., and Llorens, S. (2019). The Local Regulation of Vascular Function: From an Inside-Outside to an Outside-Inside Model. *Front. Physiol.* 10, 729. doi:10.3389/fphys.2019.00729

Nicholson, C. J., Singh, K., Saphirstein, R. J., Gao, Y. Z., Li, Q., Chiu, J. G., et al. (2018). Reversal of Aging-Induced Increases in Aortic Stiffness by Targeting Cytoskeletal Protein-Protein Interfaces. *J. Am. Heart Assoc.* 7, e008926. doi:10.1161/JAHA.118.008926

Nicholson, C. J., Seta, F., Lee, S., and Morgan, K. G. (2017). MicroRNA-203 Mimics Age-Related Aortic Smooth Muscle Dysfunction of Cytoskeletal Pathways. *J. Cel. Mol. Med.* 21, 81–95. doi:10.1111/jcmm.12940

North, B. J., and Sinclair, D. A. (2012). The Intersection between Aging and Cardiovascular Disease. *Circ. Res.* 110, 1097–1108. doi:10.1161/circresaha.111.246876

Oyama, N., Gona, P., Salton, C. J., Chuang, M. L., Jhaveri, R. R., Blease, S. J., et al. (2008). Differential Impact of Age, Sex, and Hypertension on Aortic Atherosclerosis. *Atvb* 28, 155–159. doi:10.1161/atvbaha.107.153544

Ozen, G., Daci, A., Norel, X., and Topal, G. (2015). Human Perivascular Adipose Tissue Dysfunction as a Cause of Vascular Disease: Focus on Vascular Tone and wall Remodeling. *Eur. J. Pharmacol.* 766, 16–24. doi:10.1016/j.ejphar.2015.09.012

Ozsvar, J., Yang, C., Cain, S. A., Baldock, C., Tarakanova, A., and Weiss, A. S. (2021). Tropoelastin and Elastin Assembly. *Front. Bioeng. Biotechnol.* 9, 643110. doi:10.3389/fbioe.2021.643110

Paar, M., Pavenstädt, H., Kusche-Vihrog, K., Drüppel, V., Oberleithner, H., and Kliche, K. (2014). Endothelial Sodium Channels Trigger Endothelial Salt Sensitivity with Aging. *Hypertension* 64, 391–396. doi:10.1161/hypertensionaha.114.03348

Paneni, F., Costantino, S., and Cosentino, F. (2015). Molecular Pathways of Arterial Aging. *Clin. Sci. (Lond)* 128, 69–79. doi:10.1042/cs20140302

Paneni, F., Diaz Cañestro, C., Libby, P., Lüscher, T. F., and Camici, G. G. (2017). The Aging Cardiovascular System. *J. Am. Coll. Cardiol.* 69, 1952–1967. doi:10.1016/j.jacc.2017.01.064

Pantsulaia, I., Ciszewski, W. M., and Niewiarowska, J. (2016). Senescent Endothelial Cells: Potential Modulators of Immunosenescence and Ageing. *Ageing Res. Rev.* 29, 13–25. doi:10.1016/j.arr.2016.05.011

Peralta, C. A., Adeney, K. L., Shlipak, M. G., Jacobs, D., Jr., Duprez, D., Bluemke, D., et al. (2010). Structural and Functional Vascular Alterations and Incident Hypertension in Normotensive Adults: the Multi-Ethnic Study of Atherosclerosis. *Am. J. Epidemiol.* 171, 63–71. doi:10.1093/aje/kwp319

Peshkova, I. O., Schaefer, G., and Koltsova, E. K. (2016). Atherosclerosis and Aortic Aneurysm - Is Inflammation a Common Denominator? *FEBS J.* 283, 1636–1652. doi:10.1111/febs.13634

Pober, J. S., Min, W., and Bradley, J. R. (2009). Mechanisms of Endothelial Dysfunction, Injury, and Death. *Annu. Rev. Pathol. Mech. Dis.* 4, 71–95. doi:10.1146/annurev.pathol.4.110807.092155

Qiu, H., Depre, C., Ghosh, K., Resuello, R. G., Natividad, F. F., Rossi, F., et al. (2007). Mechanism of Gender-specific Differences in Aortic Stiffness with Aging in Nonhuman Primates. *Circulation* 116, 669–676. doi:10.1161/circulationaha.107.689208

Qiu, H., Zhu, Y., Sun, Z., Trzeciakowski, J. P., Gansner, M., Depre, C., et al. (2010). Short Communication: Vascular Smooth Muscle Cell Stiffness as a Mechanism for Increased Aortic Stiffness with Aging. *Circ. Res.* 107, 615–619. doi:10.1161/circresaha.110.221846

Ribeiro-Silva, J. C., Nolasco, P., Krieger, J. E., and Miyakawa, A. A. (2021). Dynamic Crosstalk between Vascular Smooth Muscle Cells and the Aged Extracellular Matrix. *Int. J. Mol. Sci.* 22, 10175. doi:10.3390/ijms221810175

Ross, R., and Glomset, J. A. (1973). Atherosclerosis and the Arterial Smooth Muscle Cell. *Science* 180, 1332–1339. doi:10.1126/science.180.4093.1332

Rybtsova, N., Berezina, T., Kagansky, A., and Rybtsov, S. (2020). Can Blood-Circulating Factors Unveil and Delay Your Biological Aging? *Biomedicines* 8, 615. doi:10.3390/biomedicines8120615

Sahu, A., Mamiya, H., Shinde, S. N., Cheikhi, A., Winter, L. L., Vo, N. V., et al. (2018). Age-related Declines in α-Klotho Drive Progenitor Cell Mitochondrial Dysfunction and Impaired Muscle Regeneration. *Nat. Commun.* 9, 4859. doi:10.1038/s41467-018-07253-3

Sakalihasan, N., Michel, J.-B., Katsargyris, A., Kuivaniemi, H., Defraigne, J.-O., Nchimi, A., et al. (2018). Abdominal Aortic Aneurysms. *Nat. Rev. Dis. Primers* 4, 34. doi:10.1038/s41572-018-0030-7

Salvi, P., Scalise, F., Rovina, M., Moretti, F., Salvi, L., Grillo, A., et al. (2019). Noninvasive Estimation of Aortic Stiffness through Different Approaches. *Hypertension* 74, 117–129. doi:10.1161/hypertensionaha.119.12853

Sandberg, L. B., Soskel, N. T., and Leslie, J. G. (1981). Elastin Structure, Biosynthesis, and Relation to Disease States. *N. Engl. J. Med.* 304, 566–579. doi:10.1056/nejm198103053041004

Sandoo, A., Veldhuijzen van Zanten, J. J. C. S., Metsios, G. S., Carroll, D., and Kitas, G. D. (2010). The Endothelium and its Role in Regulating Vascular Tone. *Tocmj* 4, 302–312. doi:10.2174/1874192401004010302

Santos-Parker, J. R., Larocca, T. J., and Seals, D. R. (2014). Aerobic Exercise and Other Healthy Lifestyle Factors that Influence Vascular Aging. *Adv. Physiol. Educ.* 38, 296–307. doi:10.1152/advan.00088.2014

Schwartz, S. M., Deblois, D., and O'Brien, E. R. M. (1995). The Intima. *Circ. Res.* 77, 445–465. doi:10.1161/01.res.77.3.445

Seals, D. R., Desouza, C. A., Donato, A. J., and Tanaka, H. (2008). Habitual Exercise and Arterial Aging. *J. Appl. Physiol.* 105, 1323–1332. doi:10.1152/japplphysiol.90553.2008

Sehgel, N. L., Vatner, S. F., and Meininger, G. A. (2015). "Smooth Muscle Cell Stiffness Syndrome"-Revisiting the Structural Basis of Arterial Stiffness. *Front. Physiol.* 6, 335. doi:10.3389/fphys.2015.00335

Sehgel, N. L., Zhu, Y., Sun, Z., Trzeciakowski, J. P., Hong, Z., Hunter, W. C., et al. (2013). Increased Vascular Smooth Muscle Cell Stiffness: a Novel Mechanism for Aortic Stiffness in Hypertension. *Am. J. Physiology-Heart Circulatory Physiol.* 305, H1281–H1287. doi:10.1152/ajpheart.00232.2013

Shekhonin, B. V., Domogatsky, S. P., Idelson, G. L., Koteliansky, V. E., and Rukosuev, V. S. (1987). Relative Distribution of Fibronectin and Type I, III, IV, V Collagens in normal and Atherosclerotic Intima of Human Arteries. *Atherosclerosis* 67, 9–16. doi:10.1016/0021-9150(87)90259-0

Simionescu, A., Philips, K., and Vyavahare, N. (2005). Elastin-derived Peptides and TGF-B1 Induce Osteogenic Responses in Smooth Muscle Cells. *Biochem. Biophysical Res. Commun.* 334, 524–532. doi:10.1016/j.bbrc.2005.06.119

Smith, L. K., He, Y., Park, J.-S., Bieri, G., Snethlage, C. E., Lin, K., et al. (2015). β2-microglobulin Is a Systemic Pro-aging Factor that Impairs Cognitive Function and Neurogenesis. *Nat. Med.* 21, 932–937. doi:10.1038/nm.3898

Spina, M., and Garbin, G. (1976). Age-related Chemical Changes in Human Elastins from Non-atherosclerotic Areas of Thoracic Aorta. *Atherosclerosis* 24, 267–279. doi:10.1016/0021-9150(76)90082-4

Spinetti, G., Wang, M., Monticone, R., Zhang, J., Zhao, D., and Lakatta, E. G. (2004). Rat Aortic MCP-1 and its Receptor CCR2 Increase with Age and Alter Vascular Smooth Muscle Cell Function. *Atvb* 24, 1397–1402. doi:10.1161/01.atv.0000134529.65173.08

Stefanadis, C., Vlachopoulos, C., Karayannacos, P., Boudoulas, H., Stratos, C., Filippides, T., et al. (1995). Effect of Vasa Vasorum Flow on Structure and Function of the Aorta in Experimental Animals. *Circulation* 91, 2669–2678. doi:10.1161/01.cir.91.10.2669

Stenmark, K. R., Yeager, M. E., El Kasmi, K. C., Nozik-Grayck, E., Gerasimovskaya, E. V., Li, M., et al. (2013). The Adventitia: Essential Regulator of Vascular wall Structure and Function. *Annu. Rev. Physiol.* 75, 23–47. doi:10.1146/annurev-physiol-030212-183802

Steppan, J., Wang, H., Bergman, Y., Rauer, M. J., Tan, S., Jandu, S., et al. (2019). Lysyl Oxidase-like 2 Depletion Is Protective in Age-Associated Vascular Stiffening. *Am. J. Physiology-Heart Circulatory Physiol.* 317, H49–H59. doi:10.1152/ajpheart.00670.2018

Sun, Z. (2015). Aging, Arterial Stiffness, and Hypertension. *Hypertension* 65, 252–256. doi:10.1161/hypertensionaha.114.03617

Taghizadeh, H., Tafazzoli-Shadpour, M., Shadmehr, M., and Fatouraee, N. (2015). Evaluation of Biaxial Mechanical Properties of Aortic Media Based on the Lamellar Microstructure. *Materials* 8, 302–316. doi:10.3390/ma8010302

Theocharis, A. D., Manou, D., and Karamanos, N. K. (2019). The Extracellular Matrix as a Multitasking Player in Disease. *FEBS J.* 286, 2830–2869. doi:10.1111/febs.14818

Theocharis, A. D., Skandalis, S. S., Gialeli, C., and Karamanos, N. K. (2016). Extracellular Matrix Structure. *Adv. Drug Deliv. Rev.* 97, 4–27. doi:10.1016/j.addr.2015.11.001

Thompson, R. W., Geraghty, P. J., and Lee, J. K. (2002). Abdominal Aortic Aneurysms: Basic Mechanisms and Clinical Implications. *Curr. Probl. Surg.* 39, 110–230. doi:10.1067/msg.2002.121421

Thorin-Trescases, N., and Thorin, E. (2016). Lifelong Cyclic Mechanical Strain Promotes Large Elastic Artery Stiffening: Increased Pulse Pressure and Old Age-Related Organ Failure. *Can. J. Cardiol.* 32, 624–633. doi:10.1016/j.cjca.2015.12.022

Tinajero, M. G., and Gotlieb, A. I. (2020). Recent Developments in Vascular Adventitial Pathobiology. *Am. J. Pathol.* 190, 520–534. doi:10.1016/j.ajpath.2019.10.021

Toda, T., Tsuda, N., Nishimori, I., Leszczynski, D. E., and Rummerow, F. A. (1980). Morphometrical Analysis of the Aging Process in Human Arteries and Aorta. *Acta Anatomica* 106, 35–44. doi:10.1159/000145167

Tronc, F., Mallat, Z., Lehoux, S., Wassef, M., Esposito, B., and Tedgui, A. (2000). Role of Matrix Metalloproteinases in Blood Flow-Induced Arterial Enlargement: Interaction with NO. *Arterioscler Thromb. Vasc. Biol.* 20, E120–E126. doi:10.1161/01.atv.20.12.e120

Trott, D. W., Henson, G. D., Ho, M. H. T., Allison, S. A., Lesniewski, L. A., and Donato, A. J. (2018). Age-related Arterial Immune Cell Infiltration in Mice Is Attenuated by Caloric Restriction or Voluntary Exercise. *Exp. Gerontol.* 109, 99–107. doi:10.1016/j.exger.2016.12.016

Tsamis, A., Krawiec, J. T., and Vorp, D. A. (2013). Elastin and Collagen Fibre Microstructure of the Human Aorta in Ageing and Disease: a Review. *J. R. Soc. Interf.* 10, 20121004. doi:10.1098/rsif.2012.1004

Ungvari, Z., Kaley, G., De Cabo, R., Sonntag, W. E., and Csiszar, A. (2010). Mechanisms of Vascular Aging: New Perspectives. *Journals Gerontol. Ser. A: Biol. Sci. Med. Sci.* 65A, 1028–1041. doi:10.1093/gerona/glq113

Ungvari, Z., Labinskyy, N., Gupte, S., Chander, P. N., Edwards, J. G., and Csiszar, A. (2008). Dysregulation of Mitochondrial Biogenesis in Vascular Endothelial and Smooth Muscle Cells of Aged Rats. *Am. J. Physiology-Heart Circulatory Physiol.* 294, H2121–H2128. doi:10.1152/ajpheart.00012.2008

Upala, S., Wirunsawanya, K., Jaruvongvanich, V., and Sanguankeo, A. (2017). Effects of Statin Therapy on Arterial Stiffness: A Systematic Review and Meta-Analysis of Randomized Controlled Trial. *Int. J. Cardiol.* 227, 338–341. doi:10.1016/j.ijcard.2016.11.073

Upchurch, G. R., Jr., Ford, J. W., Weiss, S. J., Knipp, B. S., Peterson, D. A., Thompson, R. W., et al. (2001). Nitric Oxide Inhibition Increases Matrix Metalloproteinase-9 Expression by Rat Aortic Smooth Muscle Cells *In Vitro*. *J. Vasc. Surg.* 34, 76–83. doi:10.1067/mva.2001.115598

Urbano, R. L., Swaminathan, S., and Clyne, A. M. (2019). Stiff Substrates Enhance Endothelial Oxidative Stress in Response to Protein Kinase C Activation. *Appl. Bionics Biomech.* 2019, 6578492. doi:10.1155/2019/6578492

Vaitkevicius, P. V., Fleg, J. L., Engel, J. H., O'connor, F. C., Wright, J. G., Lakatta, L. E., et al. (1993). Effects of Age and Aerobic Capacity on Arterial Stiffness in Healthy Adults. *Circulation* 88, 1456–1462. doi:10.1161/01.cir.88.4.1456

Wagenseil, J. E., and Mecham, R. P. (2009). Vascular Extracellular Matrix and Arterial Mechanics. *Physiol. Rev.* 89, 957–989. doi:10.1152/physrev.00041.2008

Wallace, S. M. L., YasminMceniery, C. M., McEniery, C. M., Mäki-Petäjä, K. M., Booth, A. D., Cockcroft, J. R., et al. (2007). Isolated Systolic Hypertension Is Characterized by Increased Aortic Stiffness and Endothelial Dysfunction. *Hypertension* 50, 228–233. doi:10.1161/hypertensionaha.107.089391

Wang, M., Fu, Z., Wu, J., Zhang, J., Jiang, L., Khazan, B., et al. (2012). MFG-E8 Activates Proliferation of Vascular Smooth Muscle Cells via Integrin Signaling. *Aging Cell* 11, 500–508. doi:10.1111/j.1474-9726.2012.00813.x

Wang, M., Jiang, L., Monticone, R. E., and Lakatta, E. G. (2014a). Proinflammation: the Key to Arterial Aging. *Trends Endocrinol. Metab.* 25, 72–79. doi:10.1016/j.tem.2013.10.002

Wang, M., Monticone, R. E., and Lakatta, E. G. (2014b). Proinflammation of Aging central Arteries: a Mini-Review. *Gerontology* 60, 519–529. doi:10.1159/000362548

Wang, M., Zhang, J., Jiang, L.-Q., Spinetti, G., Pintus, G., Monticone, R., et al. (2007). Proinflammatory Profile within the Grossly normal Aged Human Aortic wall. *Hypertension* 50, 219–227. doi:10.1161/hypertensionaha.107.089409

Wang, M., Zhao, D., Spinetti, G., Zhang, J., Jiang, L.-Q., Pintus, G., et al. (2006). Matrix Metalloproteinase 2 Activation of Transforming Growth Factor-B1 (TGF-B1) and TGF-β1-type II Receptor Signaling within the Aged Arterial Wall. *Atvb* 26, 1503–1509. doi:10.1161/01.atv.0000225777.58488.f2

Wang, R., Yu, X., and Zhang, Y. (2021). Mechanical and Structural Contributions of Elastin and Collagen Fibers to Interlamellar Bonding in the Arterial wall. *Biomech. Model. Mechanobiol* 20, 93–106. doi:10.1007/s10237-020-01370-z

Westerhof, N., Lankhaar, J.-W., and Westerhof, B. E. (2009). The Arterial Windkessel. *Med. Biol. Eng. Comput.* 47, 131–141. doi:10.1007/s11517-008-0359-2

Woods, J. A., Wilund, K. R., Martin, S. A., and Kistler, B. M. (2012). Exercise, Inflammation and Aging. *Aging Dis.* 3, 130–140.

Yang, R., Fu, S., Zhao, L., Zhen, B., Ye, L., Niu, X., et al. (2017). Quantitation of Circulating GDF-11 and β2-MG in Aged Patients with Age-Related Impairment in Cognitive Function. *Clin. Sci. (Lond)* 131, 1895–1904. doi:10.1042/cs20171028

Yeo, K. P., Lim, H. Y., and Angeli, V. (2021). Leukocyte Trafficking via Lymphatic Vessels in Atherosclerosis. *Cells* 10, 1344. doi:10.3390/cells10061344

Yin, H., and Pickering, J. G. (2016). Cellular Senescence and Vascular Disease: Novel Routes to Better Understanding and Therapy. *Can. J. Cardiol.* 32, 612–623. doi:10.1016/j.cjca.2016.02.051

Yurchenco, P. D. (2011). Basement Membranes: Cell Scaffoldings and Signaling Platforms. *Cold Spring Harb Perspect. Biol.* 3, a004911. doi:10.1101/cshperspect.a004911

Zaragoza, C., Balbín, M., López-Otín, C., and Lamas, S. (2002). Nitric Oxide Regulates Matrix Metalloprotease-13 Expression and Activity in Endothelium. *Kidney Int.* 61, 804–808. doi:10.1046/j.1523-1755.2002.00224.x

Zhu, Y., Qiu, H., Trzeciakowski, J. P., Sun, Z., Li, Z., Hong, Z., et al. (2012). Temporal Analysis of Vascular Smooth Muscle Cell Elasticity and Adhesion Reveals Oscillation Waveforms that Differ with Aging. *Aging Cell* 11, 741–750. doi:10.1111/j.1474-9726.2012.00840.x

Conflict of Interest: The authors declare that the research was conducted in the absence of any commercial or financial relationships that could be construed as a potential conflict of interest.

frontiers
in Bioengineering and Biotechnology

ORIGINAL RESEARCH
published: 21 February 2022
doi: 10.3389/fbioe.2022.803403

Pleiotropic Effects of Simvastatin and Losartan in Preclinical Models of Post-Traumatic Elbow Contracture

*Michael A. David[1], Alex J. Reiter[1], Chelsey L. Dunham[2], Ryan M. Castile[1], James A. Abraham[1], Leanne E. Iannucci[2], Ishani D. Shah[1], Necat Havlioglu[3], Aaron M. Chamberlain[4] and Spencer P. Lake[1,2,4]**

[1]Department of Mechanical Engineering and Materials Science, Washington University in St. Louis, St. Louis, MO, United States, [2]Department of Biomedical Engineering, Washington University in St. Louis, St. Louis, MO, United States, [3]Department of Pathology, John Cochran VA Medical Center, St. Louis, MO, United States, [4]Department of Orthopaedic Surgery, Washington University in St. Louis, St. Louis, MO, United States

Edited by:
Jeffrey A. Weiss,
The University of Utah, United States

Reviewed by:
Darren Player,
University College London,
United Kingdom
Jay Trivedi,
Rhode Island Hospital, United States
Salomi Desai,
Rhode Island Hospital, United States

***Correspondence:**
Spencer P. Lake
lake.s@wustl.edu

Specialty section:
This article was submitted to Biomechanics,
a section of the journal Frontiers in Bioengineering and Biotechnology

Received: *27 October 2021*
Accepted: *04 January 2022*
Published: *21 February 2022*

Citation:
David MA, Reiter AJ, Dunham CL, Castile RM, Abraham JA, Iannucci LE, Shah ID, Havlioglu N, Chamberlain AM and Lake SP (2022) Pleiotropic Effects of Simvastatin and Losartan in Preclinical Models of Post-Traumatic Elbow Contracture.
Front. Bioeng. Biotechnol. 10:803403.
doi: 10.3389/fbioe.2022.803403

Elbow trauma can lead to post-traumatic joint contracture (PTJC), which is characterized by loss of motion associated with capsule/ligament fibrosis and cartilage damage. Unfortunately, current therapies are often unsuccessful or cause complications. This study aimed to determine the effects of prophylactically administered simvastatin (SV) and losartan (LS) in two preclinical models of elbow PTJC: an *in vivo* elbow-specific rat injury model and an *in vitro* collagen gel contraction assay. The *in vivo* elbow rat (n = 3–10/group) injury model evaluated the effects of orally administered SV and LS at two dosing strategies [i.e., low dose/high frequency/short duration (D1) vs. high dose/low frequency/long duration (D2)] on post-mortem elbow range of motion (*via* biomechanical testing) as well as capsule fibrosis and cartilage damage (*via* histopathology). The *in vitro* gel contraction assay coupled with live/dead staining (n = 3–19/group) evaluated the effects of SV and LS at various concentrations (i.e., 1, 10, 100 μM) and durations (i.e., continuous, short, or delayed) on the contractibility and viability of fibroblasts/myofibroblasts [i.e., NIH3T3 fibroblasts with endogenous transforming growth factor-beta 1 (TGFβ1)]. *In vivo*, no drug strategy prevented elbow contracture biomechanically. Histologically, only SV-D2 modestly reduced capsule fibrosis but maintained elevated cellularity and tissue hypertrophy, and both SV strategies lessened cartilage damage. SV modest benefits were localized to the anterior region, not the posterior, of the joint. Neither LS strategy had meaningful benefits in capsule nor cartilage. *In vitro*, irrespective of the presence of TGFβ1, SV (≥10 μM) prevented gel contraction partly by decreasing cell viability (100 μM). In contrast, LS did not prevent gel contraction or affect cell viability. This study demonstrates that SV, but not LS, might be suitable prophylactic drug therapy in two preclinical models of elbow PTJC. Results provide initial insight to guide future preclinical studies aimed at preventing or mitigating elbow PTJC.

Keywords: post-traumatic joint contracture, rat elbow, gel contraction, simvastatin, losartan

---

Abbreviations: PTJC, post-traumatic joint contracture; SV, simvastatin; LS, losartan; D1, dosing strategy 1 of low dose/high frequency/short duration; D2, dosing strategy 2 of high dose/low frequency/long duration; SV-D1, simvastatin dosing strategy 1; SV-D2, simvastatin dosing strategy 2; LS-D1, losartan dosing strategy 1; LS-D2, losartan dosing strategy 2; INJ, injury no drug; Control, uninjured, age-matched; TGFβ1, transforming growth factor-beta 1.

1 INTRODUCTION

Elbow trauma can lead to the debilitating condition of post-traumatic joint contracture (PTJC) in ~8–50% of afflicted elbows (Anakwe et al., 2011; Myden and Hildebrand, 2011; Monument et al., 2013; Wessel et al., 2019; Hildebrand et al., 2021). An elbow affected by PTJC becomes contracted and stiff, leading to reduced range of motion and function (Anakwe et al., 2011; Myden and Hildebrand, 2011; Monument et al., 2013; Wessel et al., 2019; David et al., 2021; Hildebrand et al., 2021). Elbow PTJC is largely associated with capsule fibrosis, but can involve injury to other soft tissues like muscle, ligament, and cartilage (Monument et al., 2013; David et al., 2021; Hildebrand et al., 2021; Pooley and Van der Linden, 2021). When severe elbow PTJC develops, procedures removing the fibrotic capsule (i.e., capsulotomy) or treating arthritic cartilage (e.g., joint fusion or arthroplasty) serve as surgical options to improve forearm function (Monument et al., 2013; David et al., 2021; Hildebrand et al., 2021; Papadopoulos et al., 2021; Pooley and Van der Linden, 2021). However, the prognosis of these strategies is largely unpredictable, and these strategies are often unsuccessful in restoring full-motion/function and/or are associated with surgical revisions or complications (Monument et al., 2013; David et al., 2021; Hildebrand et al., 2021; Papadopoulos et al., 2021; Pooley and Van der Linden, 2021). Importantly, these approaches fail to address the biological underpinnings of PTJC, especially during the immediate-early biological response post-trauma (Monument et al., 2013; David et al., 2021; Hildebrand et al., 2021). Thus, novel disease-modifying strategies are needed to prevent or mitigate elbow PTJC.

Successful preventative treatments for elbow PTJC will likely depend on the disease severity at the time of intervention and the soft tissues (e.g., capsule and cartilage) responding to the aberrant biomechanical and biochemical stimuli post-trauma. Further, since these stimuli can cause joint-wide changes, it is important to consider the impact of injury and treatment on spatial changes in soft tissues at tissue and cellular levels. Similar to other fibrotic diseases, these aberrant stimuli are thought to drive a sustained increase in the number of myofibroblasts in the capsule that contract the tissue and deposit fibrotic matrix (e.g., collagen and proteoglycan), leading to fibrosis, stiffness, and loss of elbow motion (Monument et al., 2013; David et al., 2021; Hildebrand et al., 2021). In the cartilage, aberrant stimuli post-trauma might drive chondrocytes to overproduce proinflammatory, profibrotic, and catabolic factors, as well as activate chondrocyte proliferation and death (Zuscik et al., 2008; Anderson et al., 2011; Goldring, 2012; David et al., 2017). Consequentially, irreversible changes can occur to cartilage composition (e.g., loss of proteoglycan) and structure (e.g., surface fibrillation), leading to cartilage erosions (Zuscik et al., 2008; Anderson et al., 2011; Goldring, 2012; David et al., 2017). Taken together, preventative strategies modulating the immediate-to-early injury response of fibroblasts/myofibroblasts and chondrocytes in the capsule and cartilage, respectively, will reduce soft tissue damage and elbow contracture.

In the search for preventative treatments for elbow PTJC, two FDA-approved drugs, namely simvastatin (SV) and losartan (LS), offer potential options because of their pleiotropic effects in multiple organs and diseases. Classically, SV targets the mevalonate pathway, which is an essential pathway for cell health and metabolism (Stancu and Sima, 2001); whereas LS is an antagonist for the angiotensin II receptor type 1 (Bernasconi and Nyström, 2018), which modulates the renin-angiotensin physiologic system. These properties have led to the primary clinical use of SV and LS to treat hypercholesterolemia and hypertension, respectively, although these drugs have recently been considered for treating arthritis due to their potential ability to suppress inflammation in the joint capsule and synovial fluid, resulting in reduced cartilage damage (Cojocaru et al., 2013; Veronese et al., 2019; Wu et al., 2019, 2020). Additional preclinical studies show benefits of administration of both drugs in other diseases, including cartilage damage and joint swelling in the knee (Price et al., 2007; Yudoh and Karasawa, 2010; Aktas et al., 2011; Chen R. et al., 2015; Hamilton et al., 2018; Huard et al., 2018; Utsunomiya et al., 2020; Logan et al., 2021) and tissue fibrosis in the knee (Baranowski et al., 2019), lungs (Bagnato et al., 2013; Guo et al., 2015), muscle (Bedair et al., 2008; Burks et al., 2011; Kobayashi et al., 2013; Davis et al., 2015; Whitehead et al., 2015; Huard et al., 2018), and heart (Varo et al., 1999; Spurney et al., 2011; Sun et al., 2015; Böckmann et al., 2019; Kuo et al., 2019). Collectively, the aforementioned studies in the knee and other soft-tissues holistically suggest that both drugs might modulate fibroblasts/myofibroblasts and chondrocytes biology in the elbow joint post-trauma. Despite these pleiotropic benefits in other organ-tissues and diseases, both SV and LS's impact on elbow PTJC remains unknown.

Therefore, this study aimed to evaluate the effects of SV and LS in two established preclinical models of contracture. Two SV and LS dosing strategies were tested in an elbow-specific rat injury model *in vivo*, which normally causes loss of elbow function, capsule fibrosis, and mild arthritis (Lake et al., 2016; Dunham et al., 2017a; Dunham et al., 2017b; Dunham et al., 2018a; Dunham et al., 2018b; Dunham et al., 2019; Dunham et al., 2020; Dunham et al., 2021; Reiter et al., 2019; Reiter et al., 2021a; Reiter et al., 2021b). The *in vivo* model provides translatability of SV and LS therapy and joint-wide impact on multiple soft tissues (i.e., capsule and cartilage). Additionally, SV and LS were evaluated in a collagen gel contraction model *in vitro,* serving to mimic elbow capsule contraction *in vivo* (Hildebrand et al., 2014). The *in vitro* model allows for manipulation of experimental conditions on capsule cells of interest (i.e., fibroblasts/myofibroblasts). Overall, we hypothesized that SV and LS would prevent: 1) elbow contracture, capsule fibrosis, and cartilage damage *in vivo*; and 2) gel contraction of fibroblasts/myofibroblasts *in vitro*.

2 METHODS

2.1 *In Vivo* Rat Elbow Injury Model

2.1.1 Animals, Surgery, and Drug Strategies

In this IACUC-approved study, male Long-Evans rats (n = 35; 330–370 g; Charles River Laboratories International, Wilmington, MA) were subjected to an established elbow

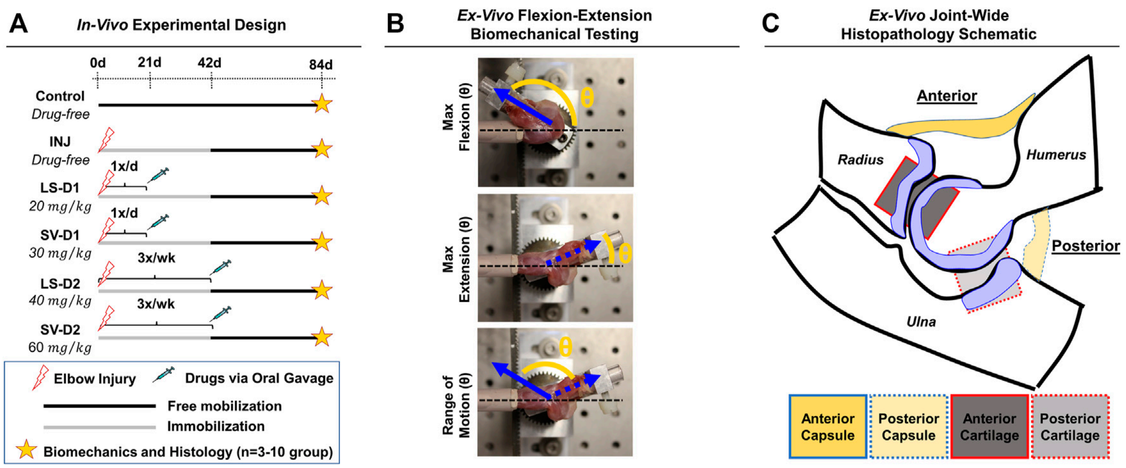

FIGURE 1 | Experimental design for *in vivo* rat elbow injury model. **(A)** Summary of experimental groups, timeline, and post-mortem analysis. Control is uninjured, age-matched animals. For drug strategies, INJ is an injury with no treatment, while losartan (LS) and simvastatin (SV) represent injury plus LS and SV, respectively; dosage strategy 1 (D1) and dosing strategy 2 (D2) represents the treatment strategies of low dose/high frequency/short duration vs. high dose/low frequency/long duration, respectively. **(B)** Images depicting the *ex vivo* flexion-extension biomechanical testing set-up and the quantitative angular measurements obtained. In this elbow injury model, elbow contracture is characterized by i) decrease in the total range of motion, ii) increase in max extension angle (which translates into decreased elbow extension), and iii) unaltered max flexion. The total range of motion is calculated by determining the angle difference between max extension and max flexion. **(C)** Schematic of an elbow mid-sagittal section with the corresponding anatomical location of the capsule and cartilage for histopathology.

injury model (Lake et al., 2016; Dunham et al., 2017b); male rats were selected because this PTJC model was developed using males and few sex-based differences have been observed (Reiter et al., 2021b). Briefly, unilateral elbows were subjected to anterior capsulotomy and transection of the lateral collateral ligament followed by a period of immobilization (0–42 days post-injury *via* bandage/wraps) and then free mobilization (i.e., unrestricted cage activity; 42–84 days post-injury) (**Figure 1A**). Immediately after injury, rats received either no drugs (INJ; *n* = 9) or one of two drug dosing strategies (D1 or D2; *n* = 3–5/group) administered *via* oral gavage: 1) LS-D1; 2) SV-D1; (iii); LS-D2; and 4) SV-D2. For D1, each drug was given 1x/daily for 3 weeks at 20 mg/kg and 30 mg/kg for LS and SV, respectively. For D2, each drug was given 3x/week for 6 weeks at 40 mg/kg and 60 mg/kg for LS and SV, respectively. Based on previous preclinical studies (Varo et al., 1999; Bedair et al., 2008; Aktas et al., 2011; Burks et al., 2011; Spurney et al., 2011; Bagnato et al., 2013; Kobayashi et al., 2013; Davis et al., 2015; Guo et al., 2015), the respective low and high doses were chosen, and the dosing strategies were categorized by either a low dose/high frequency/short duration (D1) or high dose/low frequency/long duration (D2); due to the difference in doses for each drug, no direct comparison between drug-treated groups is evaluated herein. Oral gavage was chosen as the delivery route to better control for the drug dose administered at a given time. Powdered forms of SV and LS were mixed with sterile water and adjusted for the weight of each rat. Elbows from uninjured, age-matched rats served as controls (Control; *n* = 10). After the free mobilization period, rats were humanely euthanized, and elbows were harvested for post-mortem biomechanical and histopathological analysis.

2.1.2 Biomechanical Testing

Biomechanical analysis on *ex vivo* elbows from Control (*n* = 10), INJ (*n* = 9), D1 (*n* = 5/drug), and D2 (*n* = 3/drug) was performed as described previously (Lake et al., 2016; Dunham et al., 2017b; Reiter et al., 2019). Elbows were tested in flexion-extension to measure the maximum flexion, maximum extension, and range of motion (ROM), which collectively describe elbow motion (**Figure 1B**).

2.1.3 Capsule and Cartilage Histological Semi-Quantitative Scoring

Following biomechanical testing, elbows (*n* = 3/group) were histologically processed for paraffin embedding, sectioned (mid-sagittal), and then stained with hematoxylin and eosin (H&E) and toluidine-blue (Tol-Blue) as previously performed (Lake et al., 2016; Dunham et al., 2017b, 2018a). Each section (*n* = 3 sections/stain/elbow) was blinded and semi-quantitatively scored by a musculoskeletal histopathologist (N.H.) using an adaptation of published metrics (Branchet-Gumila et al., 1999; Lake et al., 2016; Dar et al., 2017; Dunham et al., 2017b, 2018a). The semi-quantitative assessment of capsule and cartilage (**Supplementary Table S1**) included the characterization of cellular (e.g., cell number and type) and tissue (e.g., adhesions, fibrosis, thickness, and proteoglycans) level changes in both anterior and posterior anatomical joint regions (**Figure 1C**). For each histological section, a semi-quantitative metric was derived from a musculoskeletal histopathologist assessment. After evaluation, numerical scores for each elbow and group were averaged, converted into symbolic representation (–, +, ++, +++, or ++++), and then used for comparisons among groups.

2.1.4 Cartilage Histomorphometry

Cartilage histomorphometry on the humerus was deployed using a method derived from previous techniques (Fukui et al., 2014; Dar et al., 2017; David et al., 2017). Briefly, sections ($n = 1$ representative section/elbow; chosen due to minimal slide to slide variation in histology scoring) were scanned under identical settings at 20x magnification (460 nm/pixel) using the NanoZoomer 2.0-HT System slide scanner (C9600-12; Hamamatsu, Shizuoka, Japan). Cartilage regions were defined in, and exported from, NanoZoomer Digital Pathology software (NDP-view2, Hamamatsu) and then processed through a semi-automatic script in MATLAB (Mathworks, Natick, MA). The following parameters were determined within the articular and calcified cartilages: 1) the number of chondrocytes; 2) the number of proteoglycan-rich chondrocytes (i.e., chondrocytes with intense pericellular Tol-Blue$^+$ staining); 3) the number of empty lacunae; 4) the cartilage area; and 5) the proteoglycan-rich cartilage area (Tol-Blue$^+$ staining). To obtain proteoglycan-rich cartilage, images were first color normalized to account for histological staining variation (i.e., scaled to each image's white background and subchondral bone intensity) and then thresholded to remove non-proteoglycan rich pixels (based on average RGB pixel intensities for the subchondral bone). Proteoglycan amount was quantified by exploiting Tol-Blue's metachromatic staining properties, where a darker Tol-Blue stain (i.e., lower average RGB pixel intensity) indicates more proteoglycan (Sridharan and Shankar, 2012).

2.2 *In Vitro* Gel Contraction and Live/Dead Assays

2.2.1 Cell and Gel Culture

NIH3T3 fibroblasts (Sigma, St. Louis, MO) and transforming growth factor-beta one (TGFβ1; R&D Systems, Minneapolis, MN) were used as the cell line and profibrotic/contraction stimuli, respectively. This model system is routinely used to study the transdifferentiation of fibroblasts into myofibroblasts (Abdalla et al., 2013; Gutiérrez et al., 2015; Negmadjanov et al., 2015). Further, NIH3T3 fibroblasts were chosen in this study because primary capsule cells from rat or human tissue are not easily obtained, isolated, and expanded for high-throughput analysis. Briefly, NIH3T3 fibroblasts were cultured in media comprised of DMEM/High Glucose +10% fetal bovine serum and 1% penicillin-streptomycin (Fisher Scientific, Waltham, MA). Upon reaching ~80% confluency, NIH3T3 fibroblasts were trypsinized and mixed into neutralized (pH 7; 300 mOsm) rat-tail collagen solution (collagen concentration of 1.5 mg/ml) at a density of 5×10^5 cells/ml following previous methods (Cross et al., 2010; Iannucci et al., 2019). The collagen-cell mixture (500 μL) was then cast into uncoated 24-well plates (Midwest Scientific, Valley Park, MO) and polymerized for 1 h at 37°C before adding fresh media. After 24 h, gels were released from the wells using a sterile spatula to initiate spontaneous, free-floating gel contraction (**Figure 2A**). Immediately after releasing gels, SV or LS was added (1, 10, or 100 μM) with and without TGFβ1 (10 ng/ml) 1) every day (continuous), 2) for the first 2 days only (short), or 3) every day after a 2-days delay (delayed) (**Figure 2B**; $n = 3–12$ gels/group). These concentrations were chosen based on previous preclinical work and to test a range of concentrations several orders of magnitudes apart (Watson et al., 1998; Fürst et al., 2002; Porter et al., 2004; Watts et al., 2005; Benoit et al., 2008; Monzack et al., 2009; Burks et al., 2011; Copaja et al., 2011; Jia et al., 2016; Olschewski et al., 2018). Gels cultured in drug-free media with and without TGFβ1 served as controls ($n = 12–19$ gels/group). Culture media was changed every 2 days. Powdered SV, LS, and TGFβ1 were mixed into culture media following manufacture guidelines. A subset of gels ($n = 2–3$ gels/group) in drug-free media were supplemented with only the reconstitution solvents for SV (i.e., 0.001% dimethyl sulfoxide) and TGFβ1 (i.e., 0.002 mM hydrochloric acid) to verify that these solvents without drugs did not alter gel contraction.

2.2.2 Collagen Gel Contraction Dynamics

Gels were imaged daily to monitor changes in gel contraction (i.e., gel area) by positioning an iPhone 5s (Apple, Cupertino, CA) below the culture plate resting on a custom-built stand (**Figure 2A**). Gel area was quantified using a custom MATLAB script, with results shown as a fraction of the initial gel area (**Figure 2B**).

2.2.3 Cell Viability in Collagen Gels

After 6 days of continuous drug treatment with or without TGFβ1, gels ($n = 4–11$ gels/group) were stained with calcein-AM (2 μM; Fisher Scientific, Waltham, MA; FITC filter cube), ethidium homodimer-1 (4 μM; Fisher Scientific; TRITC filter cube), and Hoescht (2.5 μg/ml; Fisher Scientific; DAPI filter cube) dyes to identify live, dead, and total cells, respectively (**Figure 2C**). Gels were imaged within the gel interior (depths of ~40 and ~100 μm) at ×10 magnification (PlanFluor DLL 10x 0.30/16.00 mm; Nikon, Calgary, Canada) using an epifluorescent microscope (BZ-X810; Keyence, Itasca, IL). Cell number and viability at each gel depth was quantified and then averaged to obtain a representative gel value using a custom MATLAB script.

2.3 Statistics

Biomechanical data for INJ and Control were published previously and included for comparison (Reiter et al., 2019) but their histological sections were subjected to the analysis protocol herein (Dunham et al., 2017b). Statistical analysis was performed using GraphPad Prism 9 (GraphPad Software, San Diego, CA). For *in vivo* data, one-way ANOVA with Dunnett's post-hoc test was performed to detect differences in biomechanical and cartilage histomorphometry parameters between INJ and drug-treated groups compared to Control. Of note, samples from LS-D2 were excluded from semi-quantitative scoring ($n = 1$) and histomorphometry ($n = 2$) because of histological processing errors and section folding. For *in vitro* data analysis, one-way ANOVA with Dunnett's post-hoc test (against the respective drug-free condition) was performed for each parameter. Statistical significance was set at $p \leq 0.05$, while trends were identified as $0.05 < p \leq 0.10$.

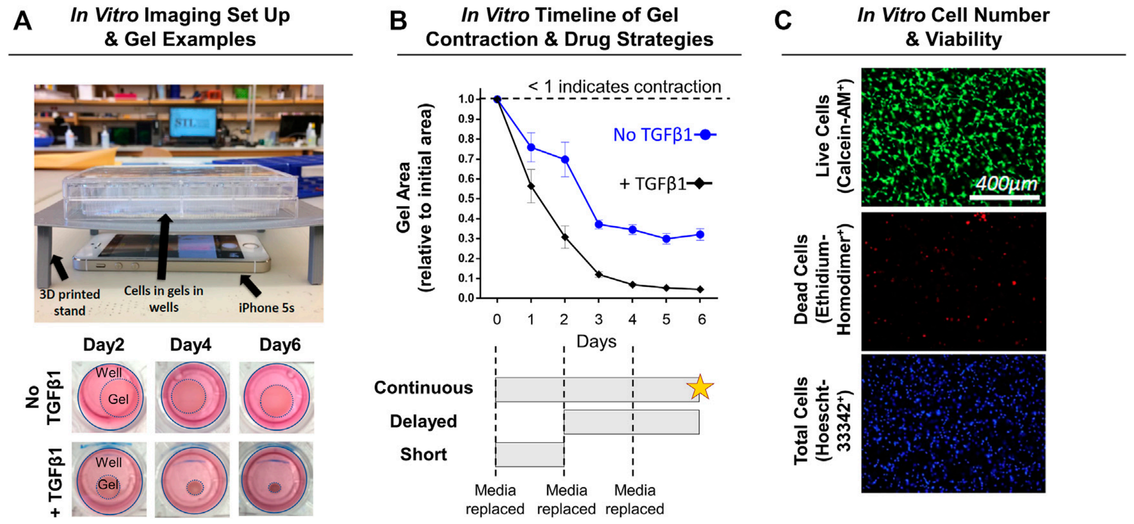

FIGURE 2 | Experimental design for *in vitro* NIH3T3 fibroblast-embedded gel contraction. **(A)** Imaging set-up used to monitor gel contraction. Representative images of collagen gel (1.5 mg/ml) contraction by embedded NIH3T3 fibroblasts (5×10^5 cells/ml) with and without TGFβ1 (10 ng/ml) over time. Note: Day 0 is not shown as the gels are approximately the same size as the well, and intermediate timepoints are sizes in between the days shown. **(B)** Quantification of gel contraction and drug dosing strategies used. Results are shown as average ± SEM ($n = 12$ for No TGFβ1; $n = 19$ for + TGFβ1). Note: star = live/dead assay. **(C)** Representative images of live, dead, and total cell staining used to quantify cell number (# of nuclei) and viability (% viable).

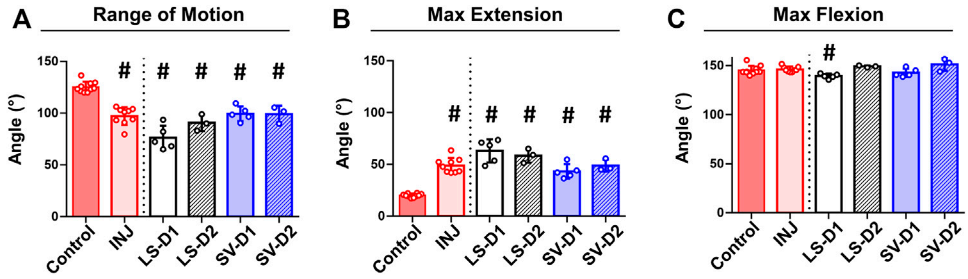

FIGURE 3 | No drug strategy prevented biomechanical measures of elbow contracture. Biomechanical parameters of decreased range of motion **(A)** and increased max extension (i.e., decreased elbow extension) **(B)** demonstrate significant elbow contracture in all groups compared to Control; no treatment strategy prevented or improved elbow contracture. Max flexion **(C)** was largely unaffected by injury and treatment compared to Control. Results are shown as average ± SD; # indicates $p < 0.05$ significant difference from Control (one way-ANOVA with Dunnett's post-hoc). Note: Control = uninjured, age-matched; INJ = injury no drug; LS-D1 = losartan dosing strategy 1; LS-D2 = losartan dosing strategy 2; SV-D1 = simvastatin dosing strategy 1; and SV-D2 = simvastatin dosing strategy 2.

3 RESULTS

3.1 *In Vivo* Rat Injury Model

3.1.1 Rat Health and Elbow Biomechanics

No visible adverse side effects assessed by a veterinarian nor differences in rat weights among groups were observed (data not shown). Biomechanical testing revealed significantly decreased elbow range of motion (~22%; **Figure 3A**) and extension motion (i.e., larger maximum extension values; ~145%; **Figure 3B**) in INJ compared to Control. All drug strategies displayed similar changes in the range of motion and extension motion as in INJ compared to Control (**Figures 3A,B**). There were no differences in maximum flexion between any experimental group and Control except for LS-D1 (~5%; **Figure 3C**). These biomechanics results indicate elbow contracture is not mitigated by drug treatments.

3.1.2 Anterior and Posterior Capsule Histopathology

Histopathology analysis revealed that all groups displayed different injury-induced responses at the tissue and cellular level in both the anterior (**Table 1**; **Figure 4**) and posterior (**Table 1**; **Supplementary Figure S1**) capsule. In the anterior capsule, INJ increased tissue-level parameters of capsule thickness, fibrosis, adhesion, and proteoglycans compared to Control (**Table 1**; **Figure 4**). With both LS treatments, similar tissue-level changes occurred in the INJ, except both resulted in a thickened, more fibrotic anterior capsule; LS-D2 also slightly reduced proteoglycans (**Table 1**; **Figure 4**). Similarly, both SV treatments had a different response to that observed in INJ (**Table 1**; **Figure 4**). SV-D2 slightly reduced fibrosis, proteoglycans, and adhesions compared to INJ, although these metrics were still elevated compared to Control (**Table 1**;

TABLE 1 | Histological semi-quantitative scoring of the anterior and posterior capsule highlighted altered tissue and cellular properties post-injury and treatment. In the anterior capsule, INJ induced tissue-level thickening, proteoglycan deposition, and development of fibrosis and adhesions; SV-D2 is the only treatment that modestly reduced proteoglycans, adhesions, and fibrosis, albeit with increased tissue thickness, cellularity (predominantly fibroblasts/myofibroblasts), and synovial proliferation. Similar observations were made in the posterior capsule; however, SV-D2 no longer had capsular benefits in reducing tissue fibrosis, adhesions, or proteoglycans. In both anterior and posterior capsules, there was no change in vascularity or the number of mast cells and mononuclear inflammatory cells in any group compared to Control. Note: Histological parameters were semi-quantitatively assessed and given a symbol of either –, +, ++, +++, or ++++, where increases in the number of symbols (+vs. ++++) indicate worse disease severity; details on grading scheme is found in **Supplementary Table S1**; Control = uninjured, age-matched; INJ = injury no drug; LS-D1 = losartan dosing strategy 1; LS-D2 = losartan dosing strategy 2; SV-D1 = simvastatin dosing strategy 1; and SV-D2 = simvastatin dosing strategy 2.

Level	**Parameter**	**Anterior Capsule**						**Posterior Capsule**					
		Control	INJ	LS-D1	LS-D2	SV-D1	SV-D2	Control	INJ	LS-D1	LS-D2	SV-D1	SV-D2
Tissue	Thickness	–	++	++++	+++	++	++	+	+++	+++	++++	++++	++++
	Adhesions	–	++	++	++	++	+	–	++	+++	+++	+++	+++
	Fibrosis	–	++	+++	++	++	+	–	++	++	++	+++	+++
	Proteoglycan Amount	–	+	+	–	+	–	–	+	+	++	+	+
	Vascularity	+	+	+	+	+	+	+	+	+	+	+	+
Cellular	Cellularity	+	+	+++	++	+++	++	+	+	+++	++	+++	++
	Synovial Proliferation	–	–	+	+	+	+	–	+	+	+	+	+
	Fibroblasts/myofibrobasts	+	+	+++	++	+++	++	+	+	++	+	++	++
	Mast Cells	+	+	+	+	+	+	+	+	+	+	+	+
	Mononuclear Inflammatory Cells	+	+	+	+	+	+	+	+	+	+	+	+

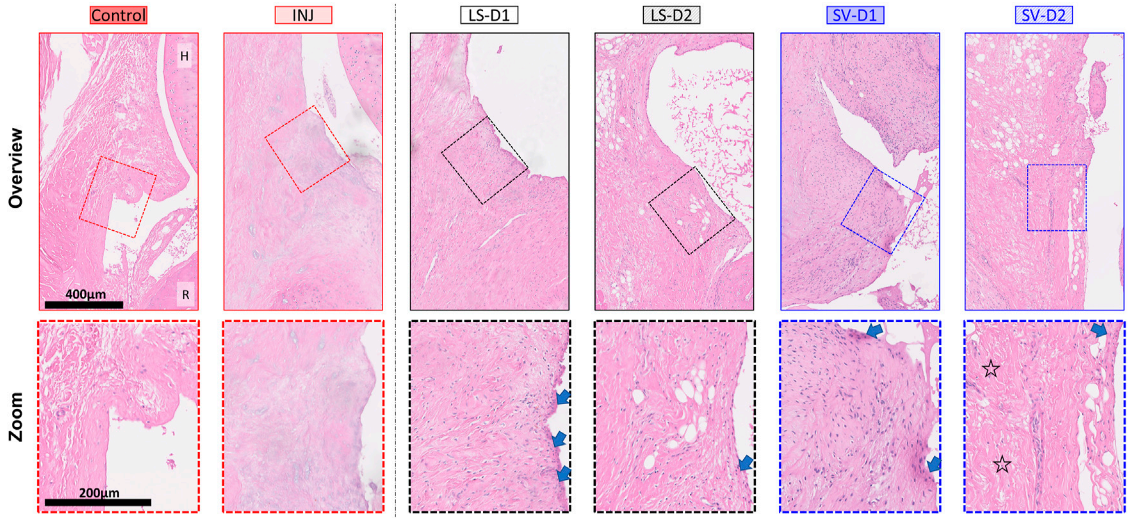

FIGURE 4 | SV, but not LS, modestly reduced capsule fibrosis anteriorly, albeit with increased tissue thickness and cellularity. Qualitative histopathology assessment on H&E midsagittal sections of the anterior capsule highlights changes in the overall capsule tissue and cellular morphology. Control capsule displays loosely packed and disorganized tissue with minimal cellularity, whereas injury caused thickened tissue and fibrosis with minimal cells. Treatments displayed increased thickness, cellularity (mostly fibroblasts/myofibroblasts), synovial proliferation (arrows), and fibrosis. However, SV-D2 was the only group able to modestly reduce capsule fibrosis (open star). Note: H = humerus; R = radius; Control = uninjured, age-matched; INJ = injury no drug; LS-D1 = losartan dosing strategy 1; LS-D2 = losartan dosing strategy 2; SV-D1 = simvastatin dosing strategy 1; and SV-D2 = simvastatin dosing strategy 2.

Figure 4). There was no change in vascularity between groups (**Table 1**).

At the cellular level of the anterior capsule, no differences were observed in total cellularity, synovial proliferation, and types of cells (fibroblasts/myofibroblasts, mast cells, or mononuclear inflammatory) in INJ compared to Control (**Table 1**; **Figure 4**). In contrast, every drug strategy led to increased cellularity, fibroblasts/myofibroblasts, and synovial proliferation compared to Control (**Table 1**; **Figure 4**). No drug strategy resulted in changes to mast or mononuclear inflammatory cells at the time point evaluated (**Table 1**).

For the posterior capsule, every drug strategy exhibited similar trends but increased scores at the tissue and cellular level compared to the anterior capsule (**Table 1**; **Supplementary Figure S1**). Notably,

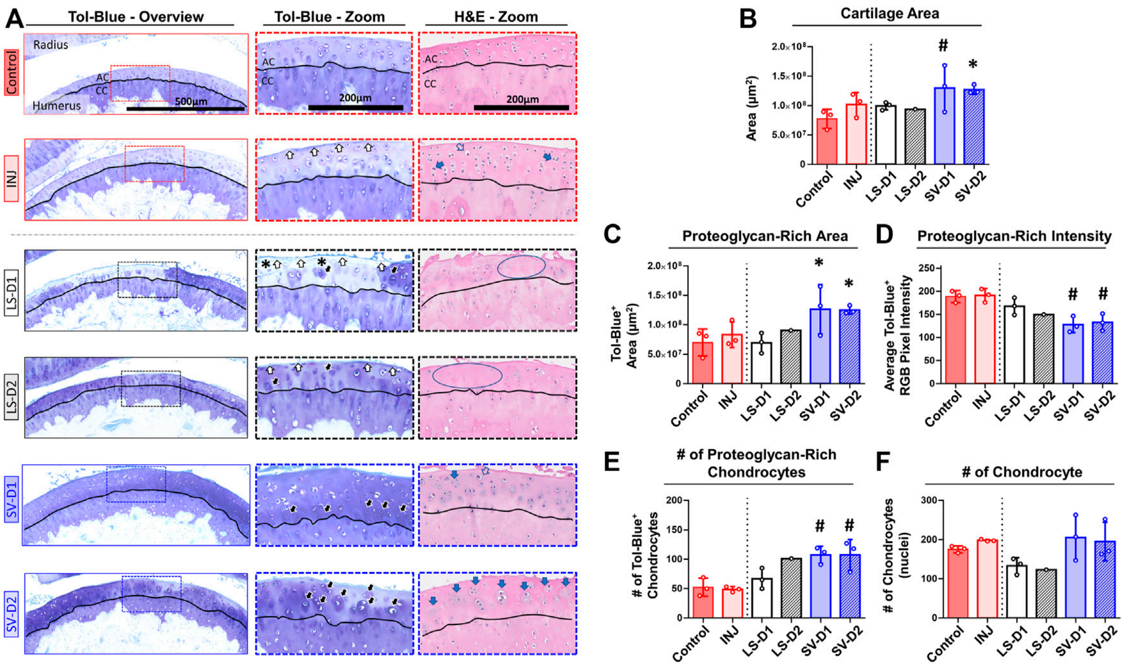

FIGURE 5 | SV, but not LS, reduced cartilage surface irregularities and enhanced proteoglycan content anteriorly. **(A)** Qualitative histopathology assessment on toluidine blue (Tol-Blue) and hematoxylin and eosin (H&E) midsagittal sections of anterior humerus articular cartilage (AC) and calcified cartilage (CC) demonstrate minor cartilage surface-level fibrillations (white-filled arrow) with injury alone (INJ) compared to Control. Treatment with either LS strategy caused worse visible structural and modest proteoglycan loss (asterisks) changes. In contrast, both SV treatments appeared to reduce the severity of this damage and increased cartilage thickness, proteoglycan content, and proteoglycan-rich chondrocytes (black-filled arrow), as seen in Tol-Blue images. Note the minor loss of chondrocytes (blue circle) and the drastic change in chondrocyte morphology with an enlargement (open arrow) and cloning/clustering (blue-filled arrow) of chondrocytes in the articular cartilage, as seen in H&E images. **(B–F)** Quantitative cartilage histomorphometry of the humerus articular cartilage at the tissue level largely confirms these qualitative assessments while providing additional insight into cellular level changes in the number of chondrocytes and those with enriched pericellular proteoglycan. Results are shown as mean ± SD; # indicates $p \leq 0.05$ significant difference and * indicates $0.05 < p \leq 0.10$ trending significance from Control (one-way ANOVA with Dunnett's post-hoc). Note: Control = uninjured, age-matched; INJ = injury no drug; LS-D1 = losartan dosing strategy 1; LS-D2 = losartan dosing strategy 2; SV-D1 = simvastatin dosing strategy 1; and SV-D2 = simvastatin dosing strategy 2.

TABLE 2 | Histological semi-quantitative scoring of the anterior and posterior cartilage demonstrated altered tissue and cellular properties post-injury and treatment. In both anterior and posterior cartilage, INJ caused minor surface irregularities compared to Control. In the anterior cartilage, both SV strategies could slightly prevent these minor surface irregularities, whereas LS had no benefit and even caused a loss of proteoglycan matrix staining. Posteriorly, no strategy provided cartilage protection; in fact, SV strategies worsened the severity of cartilage damage. Note: Histological parameters were semi-quantitatively assessed and given a symbol of either –, +, ++, +++, or ++++, where increases in the number of symbols (+vs. ++++) indicate worse disease severity; details on grading scheme is found in **Supplementary Table S1**; Control = uninjured, age-matched; INJ = injury no drug; LS-D1 = losartan dosing strategy 1; LS-D2 = losartan dosing strategy 2; SV-D1 = simvastatin dosing strategy 1; and SV-D2 = simvastatin dosing strategy 2.

Level	**Parameter**	**Anterior Cartilage**						**Posterior Cartilage**					
		Control	INJ	LS-D1	LS-D2	SV-D1	SV-D2	Control	INJ	LS-D1	LS-D2	SV-D1	SV-D2
Tissue	Structural Damage	–	+	+	+	–	–	–	+	+	+	+	++
	Proteoglycan Loss	–	–	+	+	–	–	–	+	+	+	+	+
	Tidemark Integrity	–	–	–	–	–	–	–	–	–	–	–	–
Cellular	Cellularity	–	–	–	–	–	–	–	–	–	+	–	–

SV-D2 did not reduce fibrosis and adhesions in the posterior capsule as was seen in the anterior capsule (**Table 1**; **Supplementary Figure S1**). Collectively, these results indicate that only SV had modest benefits in capsule pathology (i.e., decreased fibrosis, adhesions, and thickening) through modulating the population of fibroblasts/myofibroblasts in the anterior region and not the posterior region.

3.1.3 Anterior and Posterior Cartilage Histopathology

Histopathology assessment of the cartilage highlighted drastic changes at the tissue and cellular level depending on the anatomical location and the drug strategy. In the anterior region of INJ compared to Control, qualitative (**Figure 5A**) and semi-quantitative scores (**Table 2**) revealed mild cartilage damage in the form of surface irregularities, but without either a loss of proteoglycans, compromise in the tidemark integrity, or cellular morphological changes. Both LS strategies had a similar level of cartilage damage as INJ, except there was an additional loss of proteoglycans (**Table 2**; **Figure 5A**). On the contrary, SV-treated groups showed modestly reduced cartilage damage (**Table 2**; **Figure 5A**). While semi-quantitative metrics indicated no drastic changes in chondrocyte cellularity across entire cartilage (**Table 2**), qualitatively it appeared that injury with or without drug treatments induced subtle yet notable localized cellular morphology changes in the articular cartilage of the humerus (**Figure 5A**). Chondrocyte hypertrophy and cloning/clustering was observed in localized regions in INJ compared to Control (**Figure 5A**). For treatments, chondrocytes were somewhat absent in both LS groups while being enlarged and displaying clustering/cloning in both SV strategies (**Figure 5A**). Histomorphometry of the humerus cartilage revealed that INJ did not alter any parameter compared to Control (**Figures 5B–F**). However, SV strategies largely increased the overall cartilage area (**Figure 5B**), the distribution (i.e., area; **Figure 5C**) and amount (i.e., staining intensity; **Figure 5D**) of proteoglycan, and the number of proteoglycan-rich chondrocytes (**Figure 5E**). In contrast, LS strategies exerted no appreciable changes. For all groups, no appreciable changes in humerus cartilage histomorphometry were seen in the number of chondrocytes (**Figure 5F**) and empty lacunae (data not shown) in the articular cartilage or in any metric in the calcified cartilage (data not shown).

Histopathology assessment of the posterior cartilage revealed mostly similar observations to the anterior cartilage. Qualitative (**Supplementary Figure S2A**) and semi-quantitative analyses (**Table 2**) showed posterior cartilage damage in INJ and both LS treatment groups compared to Control, including surface fibrillations and loss of proteoglycans; additional diffuse hypercellularity was seen in the LS-D2 group. Contrary to semi-quantitative observations in the anterior cartilage, both SV strategies caused significant cartilage erosions and loss of proteoglycan in the posterior region (**Table 2**). Qualitative assessment did not reveal striking changes in chondrocyte morphology in most groups, except the slight appearance of empty lacunae with both SV strategies (**Supplementary Figure S2A**). Articular cartilage histomorphometry (**Supplementary Figures S2B–F**) largely confirmed these qualitative and semi-quantitative observations with no changes in any parameter evaluated; however, despite erosions and loss of proteoglycan observed qualitatively and semi-quantitatively, there was no overall change in cartilage area or proteoglycans quantitatively. No appreciable cellular and tissue-level cartilage histomorphometry changes were observed in the posterior calcified cartilage (data not shown). Taken together, these results indicate that only SV had modest cartilage protection anteriorly through changes in chondrocyte appearance and extracellular matrix of the articular cartilage and not calcified cartilage.

3.2 *In Vitro* Gel Contraction

3.2.1 Fibroblasts/Myofibroblasts Cell Contractility and Viability

In vitro studies detected differences across groups in the degree of gel contraction (**Figures 6A–C**). On day 6 of culture, drug-free gels decreased in area from the initial size without (~30%) and with (~95%) TGFβ1 (**Figures 6A,B**). Irrespective of TGFβ1, continuous SV treatment prevented (i.e., no decreased area; **Figures 6A,B**) gel contraction at concentrations ≥10 μM compared to drug-free control. In contrast, no concentration of LS prevented gel contraction. Since only SV prevented gel contraction, a subset of SV- and TGFβ1-treated only gels were used to test the effect of timing and duration of SV. Similar inhibition of contraction occurred if SV was delayed and given for a short duration (**Figure 6C**); however, 10 μM SV no longer inhibited contraction if applied for a short duration. On day 6 after continuous drug treatment with and without TGFβ1, 100 μM SV significantly reduced cell number (~70–80%; **Figures 6D,E**) and viability (~35–45%; **Figures 6F,G**). In a subset of gels, there was no impact of reconstitution solvents for SV and TGFβ1 on gel contraction (**Supplementary Figure S3**). Overall, these results indicate that only SV could prevent gel contraction at moderate to high concentrations through modulation of NIH3T3 fibroblasts/myofibroblasts health and contractility.

4 DISCUSSION

4.1 Overview

Currently, an unmet clinical need exists for novel therapies to prevent the development of elbow PTJC. Thus, this study tested the effects of prophylactically administered SV and LS in two preclinical models of elbow PTJC. In the rat elbow PTJC model *in vivo*, SV and LS did not prevent the onset of elbow contracture as indicated from post-mortem biomechanics (**Figure 3**). However, both drugs modulated capsule and cartilage biology on a region-dependent cellular and tissue level as indicated histologically (**Tables 1**, **2**; **Figures 4**, **5**; **Supplementary Figures S1, S2**). SV drug delivery appeared to decrease capsule fibrosis and cartilage damage in the joint anteriorly, yet increased damage severity in the posterior region. This observed location-dependent phenotype suggests a complex injury-drug response by which altering the anterior region of the joint with drugs might impact the biological activity in multiple tissues throughout the elbow. Neither LS dose showed any benefits and appeared to increase disease severity in both cartilage and capsule. *In vitro*, concentrations of SV, but not LS, inhibited fibroblasts/myofibroblast contractility (**Figure 6**). Considering the *in vitro* and *in vivo* data together suggests that both SV and LS can modulate the biological activity and tissue-level properties of capsule and cartilage. However, it appears that drug-induced cellular and tissue level changes do not necessarily translate to the functional level, at least at the single timepoint evaluated, which might have implications for future clinical and preclinical studies of elbow PTJC. Overall, these data provide a foundation of knowledge to understand better SV and LS potential as

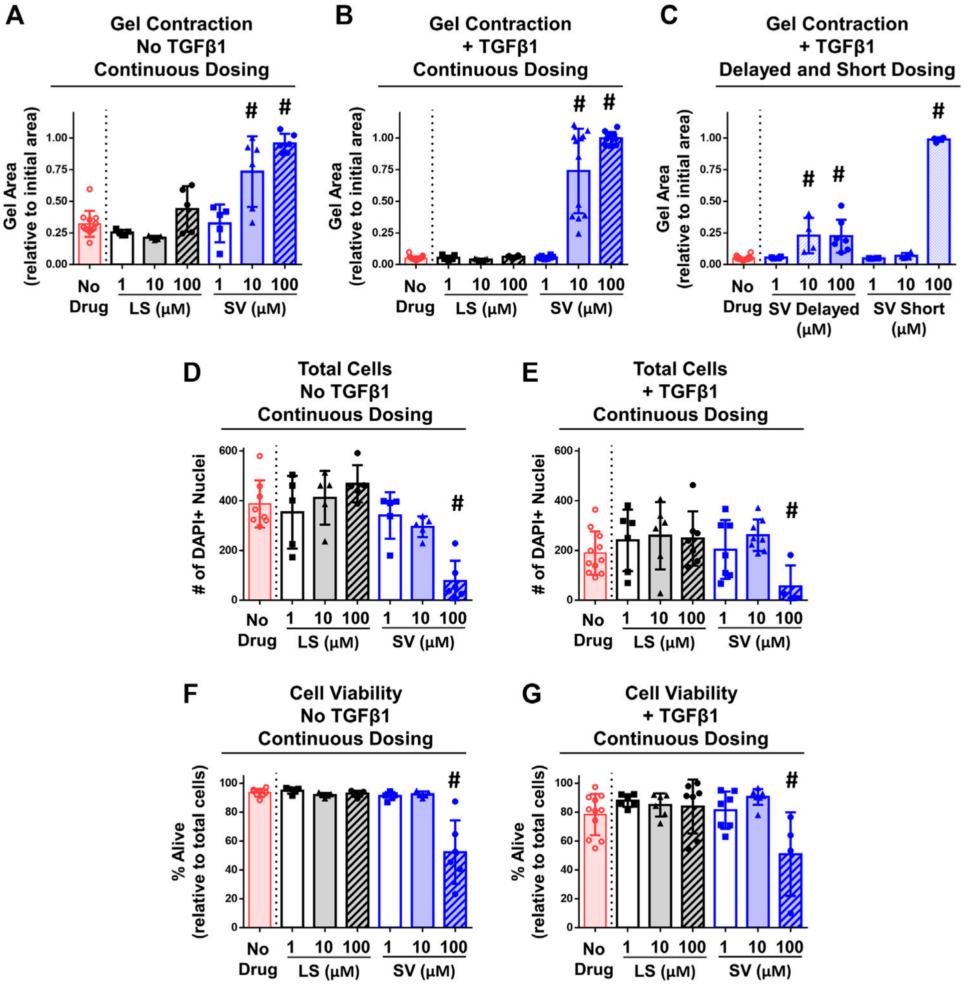

FIGURE 6 | SV, but not LS, reduced fibroblasts/myofibroblasts contractility and viability *in vitro.* **(A–C)** Quantitative assessment of gel contraction area demonstrated that continuous, delayed, and short application of SV, but not LS, reduced contraction without and with TGFβ1 after 6 days. **(D–G)** Assessment of cell number and viability demonstrated that only continuous 100 µM SV treatment reduced cell number and viability without and with TGFβ1 after 6 days. Results are shown as mean ± SD; # indicates $p < 0.05$ significant difference from drug-free controls (one way-ANOVA with Dunnett's post-hoc).

disease-modifying drugs for elbow PTJC and to guide the future optimization of dosing and delivery strategies.

4.2 SV and LS Induces Pleiotropic Effects on Capsule Biology *In Vivo*

Elbow PTJC is primarily driven by capsule fibrosis; hence, a study goal was to prevent capsule fibrosis post-trauma, particularly in the anterior region of the elbow since it is the location where the surgically induced injury occurs in the *in vivo* model (Lake et al., 2016; Dunham et al., 2017b). Indeed, SV given at dosing strategy 2 (60 mg/kg given 3 days/wk for 6 weeks), but not dosing strategy 1 (30 mg/kg given daily for 3 weeks), modestly reduced anterior capsule fibrosis/adhesions, although the capsule was still thick and displayed increased cellularity compared to Control (**Figure 4**; **Table 1**). At the cellular level, fibroblasts and/or myofibroblasts were histologically identified as the predominant cell type in the capsule at the timepoint evaluated (**Table 1**). This is in opposition to inflammatory cells (e.g., monocytes and mast cells) that are commonly implicated in knee contracture (Monument et al., 2013; David et al., 2021), yet shifts in these cell populations could occur at other timepoints post-injury or the signaling between such cells might be altered. It is unclear why SV's effects were localized anteriorly; however, since the anterior capsule is the primary tissue of interest driving elbow contracture in this model and clinically, the increased disease severity in the posterior joint location may not be as critical. Despite modest benefits of SV, LS given at either dosing strategy 1 (20 mg/kg given daily for 3 weeks) or strategy 2 (40 mg/kg given 3 days/week for 6 weeks) failed to decrease the severity of capsule fibrosis, cartilage damage, or contracture. Given the limited timepoints following trauma and drug therapies assessed herein, it remains unknown if decreased capsule fibrosis, adhesions, and proteoglycans associated with elevated tissue thickness and cellularity indicates a delay or reduction in capsule fibrosis or tissue regeneration.

Since limited knowledge exists regarding elbow specific PTJC, as well as the use of SV and LS for PTJC in other musculoskeletal joints (e.g., knee), careful considerations should be taken when comparing this study to the literature. Nevertheless, our mixed multi-scale results somewhat align with a study by Baranowski et al., that evaluated the effects of orally administered losartan (30 mg/kg/day) and statins (in this case, atorvastatin; 15 mg/kg/day) on capsule fibrosis and joint contracture in a rat knee model of PTJC (Baranowski et al., 2019). Similar to our results, they found no functional benefit, yet both drugs still altered the capsule tissue and cellular properties. At the tissue level, atorvastatin and LS decreased and increased capsular thickness, respectively, while both drugs reduced the total cellularity and proportion of myofibroblasts at the cellular level. The efficacy discrepancy between studies could be due to the joint type, soft-tissue damage from traumatic injury, dosing strategies, timepoints evaluated, or analysis technique. Nevertheless, it appears that SV and LS can modulate the capsule's biological activity and tissue-level properties of the elbow in a dosing strategy and anatomical location-dependent manner.

4.3 SV, but not LS, Prevents Fibroblasts/Myofibroblasts-Mediated Gel Contraction *In Vitro*

In this study, the gel contraction model utilizing NIH3T3 fibroblasts and TGFβ1 as a profibrotic factor (Abdalla et al., 2013; Gutiérrez et al., 2015; Negmadjanov et al., 2015) was performed to simulate *in vivo* capsule contraction (Hildebrand et al., 2014) and evaluate SV and LS's direct effects on fibroblasts and myofibroblasts. SV, but not LS, reduced gel contraction under conditions with and without TGFβ1 in NIH3T3 fibroblasts/myofibroblasts (**Figure 6**). SV at higher concentration (100 μM) inhibited gel contraction mostly due to cell death, while SV at a moderate concentration (10 μM) likely altered cell contractility (assessed *via* extent of gel contraction; **Figure 6**). Notably, the effects of SV were transient because the gel contraction response was not altered when SV was only given for a short duration (**Figure 6**). Delayed application of SV (≥10 μM) led to a complete halt in gel contraction, albeit with about ~60% contraction still occurring prior to applying SV (**Figure 6**). Generally, our results align with SV's known influence on the mevalonate pathway (Stancu and Sima, 2001) and fibroblasts/myofibroblasts (i.e., reduced proliferation, viability, and contractility with ≤10 μM) (Fürst et al., 2002; Porter et al., 2004; Watts et al., 2005; Monzack et al., 2009; Burks et al., 2011; Copaja et al., 2011; Kuo et al., 2019). Further, our *in vitro* gel findings might explain/support the ability of SV to have a potential reduction in anterior capsule fibrosis by modulating fibroblasts/myofibroblasts phenotype (i.e., contractility), metabolism (e.g., deposition of fibrotic matrix), and signaling (e.g., autocrine/paracrine signaling). However, given the systemic administration of drugs in this study, SV's impacts *in vivo* might extend beyond the direct effects on fibroblasts/myofibroblasts observed *in vitro* (e.g., modulating inflammatory cell health and signaling). Surprisingly, LS did not reduce gel contraction *in vitro* despite its known anti-fibrotic properties (Bedair et al., 2008; Burks et al., 2011; Spurney et al., 2011; Bagnato et al., 2013; Kobayashi et al., 2013; Guo et al., 2015; Huard et al., 2018; Baranowski et al., 2019; Böckmann et al., 2019). Other studies have reported similarly mixed effects, where LS inhibited gel contraction in some culture conditions (Watson et al., 1998; Benoit et al., 2008; Jia et al., 2016) yet also increased cell adhesions/invasion and proliferation (Olschewski et al., 2018). Such mixed results could be due to *in vitro* vs. *in vivo* study designs, culture conditions (e.g., collagen and cellular densities), cell type (e.g., primary vs. cell line), use of a single profibrotic factor (e.g., TGFβ1 vs. angiotensin II) and/or the presence of LS target receptor [i.e., angiotensin II type 1, which NIH3T3 fibroblasts minimally express (Heemskerk et al., 1999; De Paolis et al., 2002)]. In a subset of separate gels, angiotensin II (i.e., 10 and 100 ng/ml) was applied and had no impact on gel contraction (**Supplementary Figure S3**), suggesting a minimal influence of angiotensin II on NIH3T3 fibroblasts/myofibroblasts contractility. However, angiotensin II and LS might exert effects in other cellular activity of NIH3T3 fibroblasts/myofibroblasts that extend beyond gel contraction studied herein (e.g., production of growth factors/cytokines, proliferation, and adhesions/invasion). Collectively, these *in vitro* findings suggest SV, but not LS, can directly modulate cellular contractility and health of fibroblasts/myofibroblasts embedded within collagen gels, but whether SV can directly impact these cellular processes *in vivo* remains unknown.

4.4 SV and LS Induces Pleiotropic Effects on Cartilage Biology *In Vivo*

Elbow trauma can cause damage to other soft tissues in the elbow like cartilage; hence, this study evaluated changes to cartilage in the rat injury model of elbow post-trauma. Similar to the capsule, cartilage exhibited location- and drug-dependent changes. In both the joint's anterior and posterior region, all cartilage changes occurred in the articular and not calcified cartilage, suggesting direct and localized effects to chondrocytes in the articular cartilage; however, this does not rule out the possibility of intracellular signaling between articular and calcified cartilage with other elbow tissues such as the capsule or subchondral bone. In both the anterior and posterior region, injury alone caused mild surface fibrillations/irregularities (**Table 2**; **Figure 5**; **Supplementary Figure S2**). Surface irregularities in the posterior region was unexpected since the injury model herein causes soft tissue damage to the anterior region of the joint (Lake et al., 2016; Dunham et al., 2017b); this suggests joint-wide changes not previously appreciated in this injury model of PTJC. With treatments, cartilage damage in the anterior region was slightly prevented (e.g., reduced surface irregularities/fibrillation) with both SV strategies, whereas both LS strategies caused further damage (e.g., erosions) (**Table 2**; **Figure 5**). There were notable focal regions of chondrocytes in SV treated groups that displayed enhanced clustering (**Figure 5A**), though this was not a widespread phenomenon across all articular cartilage. Collectively, histological observations of SV cartilage protection might be due to an overall increase in cartilage area combined with enhanced proteoglycan matrix composition in both the extracellular and pericellular matrices around chondrocytes (**Figure 5**). These observations in SV-treated joints suggest chondrocyte-driven attempts to repair, regeneration, and/or anabolism (Zuscik et al., 2008; Anderson et al., 2011; Goldring, 2012). However, since only one time point was evaluated post-trauma, it is unclear if this chondrocyte response would continue to be beneficial long term. Despite providing modest benefits anteriorly, both SV strategies led to articular cartilage erosions posteriorly (**Table 2**; **Supplementary Figure S2**). Although erosions developed, histomorphometric analysis revealed that the total cartilage area did not change; suggesting that the remaining non-eroded articular cartilage increases in area, as seen anteriorly, and could indicate tissue adaptation. Contrary to SV, LS was unable to provide any surface-level protection and led to areas devoid of chondrocytes (**Table 2**; **Supplementary Figure S2**).

Given the limited *a priori* knowledge of elbow-specific cartilage biology, studies from the literature utilizing SV and LS for preventing arthritis in other joints (e.g., the knee) can help interpret this study's findings. For example, SV is thought to prevent cartilage damage by enhancing chondrogenesis (e.g., increased proteoglycan synthesis) and reducing chondrocyte production of harmful biochemical factors (e.g., inflammatory cytokines and matrix-degrading enzymes) (Yudoh and Karasawa, 2010; Aktas et al., 2011). LS appears to provide similar cartilage structure protection in the knee (Chen R. et al., 2015; Huard et al., 2018; Utsunomiya et al., 2020; Logan et al., 2021) but can also accelerate chondrocyte enlargement/hypertrophy in the growth plate (Chen S. et al., 2015). Contrary to the structural/composition benefits (e.g., prevention of fibrillations and erosions) of drug treatment on cartilage seen in these previous preclinical studies, there was no robust tissue-level improvement with most SV and LS strategies in this study. However, recent work has shown LS at higher dosages can halt cartilage repair and induce cartilage damage in healthy cartilage (Logan et al., 2021), which somewhat aligns with the deleterious effects of LS strategies in this study. Collectively, these discrepancies could be due to the dosing strategy, joint location (e.g., anterior vs. posterior), joint studied (e.g., elbow vs. knee), type of arthritis (e.g., rheumatoid arthritis vs. post-trauma osteoarthritis), and type of traumatic insult (e.g., trauma, immobilization, chemical, or combinations). Furthermore, it is unclear whether the cartilage response was directly or indirectly modulated by capsule biology, or vice versa. Nevertheless, our findings suggest that SV and LS impact the chondrocyte/cartilage injury response, but the full extent of these drugs' impact on cartilage requires further investigations.

4.5 Future Work

While these data are insightful, many questions remain to be answered that will require further evaluation. Future work could increase sample sizes, modify the dosing strategies, and evaluate other drug toxicity parameters [e.g., pain, liver dysfunction, and muscle damage (MacDonald and Halleck, 2004; Schachter, 2005; Sica et al., 2005)], functional deficiencies [e.g., gait and grip strength (Reiter et al., 2019)], elbow motions [i.e., pronation and supination (Dunham et al., 2017a)], and time points post-trauma. Further, although only male rats were included in this study and previous work showed minor sex-dependent progression of PTJC (Reiter et al., 2021b), the effect of drug treatment in female rats could be different and should be considered. Since drugs were given systemically, knowledge about the pharmacokinetics and bioavailability of drugs within the elbow's synovial space would be critical for understanding the drug mechanisms of action and optimizing and choosing alternative dosing and delivery strategies (e.g., use of nanoparticles, intra-articular injections, drinking water, or topical application). It is also important to consider that the bioavailability and effects of each drug herein and using alternative dosing and delivery strategies could also be impacted by the *in vivo* half-life of each drug [e.g., about 1–5 h in humans (MacDonald and Halleck, 2004; Schachter, 2005; Sica et al., 2005)]. Additionally, *in vivo* work should also evaluate drug concentrations and critical biomarkers of disease (e.g., TGFβ1, matrix degrading enzymes, and proinflammatory cytokines assessed *via* immunohistochemistry or other analysis techniques) in the cartilage and capsule, as well as the elbow's synovial space and systemic blood serum. Beyond future *in vivo* work, the *in vitro* gel contraction assay would be more impactful if primary cells from the elbow capsule are used and co-culture studies are performed using other cells (e.g., macrophages and mast cells) that might communicate to fibroblasts/myofibroblasts *in vivo* (Monument et al., 2013; Hildebrand et al., 2014). Finally, understanding the underlying drug mechanism(s) driving capsule and cartilage biology changes will prove vital to fully determining the therapeutic potential of these treatment strategies.

5 CONCLUSION

In conclusion, this study demonstrated that SV, but not LS, can prevent capsule fibrosis and cartilage damage *in vivo* and cell contractility *in vitro*. In the rat elbow contracture model, orally administered SV altered histopathological evaluations at the cellular and tissue level in the capsule and cartilage but did not ultimately improve joint function at the single time point evaluated. In the gel contraction assay, SV transiently altered fibroblasts/myofibroblasts contractility. Both preclinical models demonstrated that the success of SV as a treatment for elbow PTJC will be dependent on the dosing strategy. Unfortunately, LS did not elicit a beneficial change in either the *in vivo* or *in vitro* system. Overall, results from this study support further investigation and optimization of SV dosing and delivery strategies to serve as a preventative therapy for elbow PTJC.

DATA AVAILABILITY STATEMENT

The original contributions presented in the study are included in the article/**Supplementary Material**, further inquiries can be directed to the corresponding author.

ETHICS STATEMENT

The animal study was reviewed and approved by Institutional Animal Care and Use Committee, Washington University in St. Louis.

AUTHOR CONTRIBUTIONS

MD, AR, CD, and SL designed the study. MD, AR, CD, RC, NH, and AC performed research associated with the *in vivo* rat injury model. MD, JA, LI, and IS performed research associated with the *in vitro* gel contraction assay. MD and SL analyzed and interpreted the data. MD and SL wrote the manuscript. All authors reviewed the manuscript.

FUNDING

This work was supported by National Institutes of Health (NIH R01 AR071444). Histopathology processing was assisted by the Washington University Musculoskeletal Research Center (NIH P30 AR074992). Histopathology slide digitalization was supported by the Alafi Neuroimaging Laboratory, the Hope Center for Neurological Disorders, and NIH Shared Instrumentation Grant (NIH S10 RR027552) to Washington University. AC has received support for work outside of the submitted manuscript from Zimmer-Biomet, DePuy, Arthrex, and Wright Medical.

SUPPLEMENTARY MATERIAL

The Supplementary Material for this article can be found online at: https://www.frontiersin.org/articles/10.3389/fbioe.2022.803403/full#supplementary-material

REFERENCES

Abdalla, M., Goc, A., Segar, L., and Somanath, P. R. (2013). Akt1 Mediates α-Smooth Muscle Actin Expression and Myofibroblast Differentiation via Myocardin and Serum Response Factor. *J. Biol. Chem.* 288, 33483–33493. doi:10.1074/jbc.M113.504290

Aktas, E., Sener, E., and Gocun, P. U. (2011). Mechanically Induced Experimental Knee Osteoarthritis Benefits from Anti-inflammatory and Immunomodulatory Properties of Simvastatin via Inhibition of Matrix Metalloproteinase-3. *J. Orthopaed. Traumatol.* 12, 145–151. doi:10.1007/s10195-011-0154-y

Anakwe, R. E., Middleton, S. D., Jenkins, P. J., McQueen, M. M., and Court-Brown, C. M. (2011). Patient-Reported Outcomes after Simple Dislocation of the Elbow. *J. Bone Jt. Surg.* 93, 1220–1226. doi:10.2106/JBJS.J.00860

Anderson, D. D., Chubinskaya, S., Guilak, F., Martin, J. a., Oegema, T. R., Olson, S. a., et al. (2011). Post-traumatic Osteoarthritis: Improved Understanding and Opportunities for Early Intervention. *J. Orthop. Res.* 29, 802–809. doi:10.1002/jor.21359

Bagnato, G., Bitto, A., Pizzino, G., Irrera, N., Sangari, D., Cinquegrani, M., et al. (2013). Simvastatin Attenuates the Development of Pulmonary and Cutaneous Fibrosis in a Murine Model of Systemic Sclerosis. *Rheumatology* 52, 1377–1386. doi:10.1093/rheumatology/ket144

Baranowski, A., Schlemmer, L., Förster, K., Slotina, E., Mickan, T., Truffel, S., et al. (2019). Effects of Losartan and Atorvastatin on the Development of Early Posttraumatic Joint Stiffness in a Rat Model. *Dddt* Vol. 13, 2603–2618. doi:10.2147/DDDT.S204135

Bedair, H. S., Karthikeyan, T., Quintero, A., Li, Y., and Huard, J. (2008). Angiotensin II Receptor Blockade Administered after Injury Improves Muscle Regeneration and Decreases Fibrosis in Normal Skeletal Muscle. *Am. J. Sports Med.* 36, 1548–1554. doi:10.1177/0363546508315470

Benoit, C., Gu, Y., Zhang, Y., Alexander, J., and Wang, Y. (2008). Contractility of Placental Vascular Smooth Muscle Cells in Response to Stimuli Produced by the Placenta: Roles of ACE vs. Non-ACE and AT1 vs. AT2 in Placental Vessel Cells. *Placenta* 29, 503–509. doi:10.1016/j.placenta.2008.03.002

Bernasconi, R., and Nyström, A. (2018). Balance and Circumstance: The Renin Angiotensin System in Wound Healing and Fibrosis. *Cel. Signal.* 51, 34–46. doi:10.1016/j.cellsig.2018.07.011

Böckmann, I., Lischka, J., Richter, B., Deppe, J., Rahn, A., Fischer, D.-C., et al. (2019). FGF23-Mediated Activation of Local RAAS Promotes Cardiac Hypertrophy and Fibrosis. *Ijms* 20, 4634. doi:10.3390/ijms20184634

Branchet-Gumila, M. C., Boisnic, S., Le Charpentier, Y., Nonotte, I., Montastier, C., and Breton, L. (1999). Neurogenic Modifications Induced by Substance P in an Organ Culture of Human Skin. *Skin Pharmacol. Physiol.* 12, 211–220. doi:10.1159/000066245

Burks, T. N., Andres-Mateos, E., Marx, R., Mejias, R., Van Erp, C., Simmers, J. L., et al. (2011). Losartan Restores Skeletal Muscle Remodeling and Protects against Disuse Atrophy in Sarcopenia. *Sci. Transl. Med.* 3, 82ra37. doi:10.1126/scitranslmed.3002227

Chen, R., Mian, M., Fu, M., Zhao, J. Y., Yang, L., Li, Y., et al. (2015a). Attenuation of the Progression of Articular Cartilage Degeneration by Inhibition of TGF-β1 Signaling in a Mouse Model of Osteoarthritis. *Am. J. Pathol.* 185, 2875–2885. doi:10.1016/j.ajpath.2015.07.003

Chen, S., Grover, M., Sibai, T., Black, J., Rianon, N., Rajagopal, A., et al. (2015b). Losartan Increases Bone Mass and Accelerates Chondrocyte Hypertrophy in Developing Skeleton. *Mol. Genet. Metab.* 115, 53–60. doi:10.1016/j.ymgme.2015.02.006

Cojocaru, L., Rusali, A. C., Şuţa, C., Rădulescu, A. M., Şuţa, M., and Craiu, E. (2013). The Role of Simvastatin in the Therapeutic Approach of Rheumatoid Arthritis. *Autoimmune Dis.* 2013, 1–7. doi:10.1155/2013/326258

Copaja, M., Venegas, D., Aránguiz, P., Canales, J., Vivar, R., Catalán, M., et al. (2011). Simvastatin Induces Apoptosis by a Rho-dependent Mechanism in Cultured Cardiac Fibroblasts and Myofibroblasts. *Toxicol. Appl. Pharmacol.* 255, 57–64. doi:10.1016/j.taap.2011.05.016

Cross, V. L., Zheng, Y., Won Choi, N., Verbridge, S. S., Sutermaster, B. A., Bonassar, L. J., et al. (2010). Dense Type I Collagen Matrices that Support Cellular Remodeling and Microfabrication for Studies of Tumor Angiogenesis and Vasculogenesis *In Vitro*. *Biomaterials* 31, 8596–8607. doi:10.1016/j.biomaterials.2010.07.072

Dar, Q.-A., Schott, E. M., Catheline, S. E., Maynard, R. D., Liu, Z., Kamal, F., et al. (2017). Daily Oral Consumption of Hydrolyzed Type 1 Collagen Is Chondroprotective and Anti-inflammatory in Murine Posttraumatic Osteoarthritis. *PLoS One* 12, e0174705. doi:10.1371/journal.pone.0174705

David, M. A., Smith, M. K., Pilachowski, R. N., White, A. T., Locke, R. C., and Price, C. (2017). Early, Focal Changes in Cartilage Cellularity and Structure Following Surgically Induced Meniscal Destabilization in the Mouse. *J. Orthop. Res.* 35, 537–547. doi:10.1002/jor.23443

David, M. A., Chamberlain, A. M., and Lake, S. P. (2021). Preclinical Models of Elbow Injury and Pathology. *Ann. Jt.* 6, 12. doi:10.21037/aoj.2020.02.09

Davis, M. E., Korn, M. A., Gumucio, J. P., Harning, J. A., Saripalli, A. L., Bedi, A., et al. (2015). Simvastatin Reduces Fibrosis and Protects against Muscle Weakness after Massive Rotator Cuff Tear. *J. Shoulder Elbow Surg.* 24, 280–287. doi:10.1016/j.jse.2014.06.048

De Paolis, P., Porcellini, A., Savoia, C., Lombardi, A., Gigante, B., Frati, G., et al. (2002). Functional Cross-Talk between Angiotensin II and Epidermal Growth Factor Receptors in NIH3T3 Fibroblasts. *J. Hypertens.* 20, 693–699. doi:10.1097/00004872-200204000-00027

Dunham, C. L., Castile, R. M., Chamberlain, A. M., Galatz, L. M., and Lake, S. P. (2017a). Pronation-Supination Motion Is Altered in a Rat Model of Post-Traumatic Elbow Contracture. *J. Biomech. Eng.* 139, 071011. doi:10.1115/1.4036472

Dunham, C. L., Castile, R. M., Havlioglu, N., Chamberlain, A. M., Galatz, L. M., and Lake, S. P. (2017b). Persistent Motion Loss after Free Joint Mobilization in a Rat Model of post-traumatic Elbow Contracture. *J. Shoulder Elbow Surg.* 26, 611–618. doi:10.1016/j.jse.2016.09.059

Dunham, C. L., Castile, R. M., Havlioglu, N., Chamberlain, A. M., and Lake, S. P. (2018a). Temporal Patterns of Motion in Flexion-Extension and Pronation-Supination in a Rat Model of Posttraumatic Elbow

Contracture. *Clin. Orthop. Relat. Res.* 476, 1878–1889. doi:10.1097/CORR.0000000000000388

Dunham, C. L., Chamberlain, A. M., Meyer, G. A., and Lake, S. P. (2018b). Muscle Does Not Drive Persistent Posttraumatic Elbow Contracture in a Rat Model. *Muscle Nerve* 58, 843–851. doi:10.1002/mus.26344

Dunham, C. L., Castile, R. M., Chamberlain, A. M., and Lake, S. P. (2019). The Role of Periarticular Soft Tissues in Persistent Motion Loss in a Rat Model of Posttraumatic Elbow Contracture. *J. Bone Jt. Surg.* 101, e17. doi:10.2106/JBJS.18.00246

Dunham, C., Havlioglu, N., Chamberlain, A., Lake, S., and Meyer, G. (2020). Adipose Stem Cells Exhibit Mechanical Memory and Reduce Fibrotic Contracture in a Rat Elbow Injury Model. *FASEB j.* 34, 12976–12990. doi:10.1096/fj.202001274R

Dunham, C. L., Steenbock, H., Brinckmann, J., Reiter, A. J., Castile, R. M., Chamberlain, A. M., et al. (2021). Increased Volume and Collagen Crosslinks Drive Soft Tissue Contribution to Post-Traumatic Elbow Contracture in an Animal Model. *J. Orthop. Res.* 39, 1800–1810. doi:10.1002/jor.24781

Fürst, J., Haller, T., Chwatal, S., Wöll, E., Dartsch, P., Gschwentner, M., et al. (2002). Simvastatin Inhibits Malignant Transformation Following Expression of the *Ha-Ras* Oncogene in NIH 3T3 Fibroblasts. *Cel. Physiol. Biochem.* 12, 19–30. doi:10.1159/000047823

Fukui, T., Kitamura, N., Kurokawa, T., Yokota, M., Kondo, E., Gong, J. P., et al. (2014). Intra-Articular Administration of Hyaluronic Acid Increases the Volume of the Hyaline Cartilage Regenerated in a Large Osteochondral Defect by Implantation of a Double-Network Gel. *J. Mater. Sci. Mater. Med.* 25, 1173–1182. doi:10.1007/s10856-013-5139-3

Goldring, M. B. (2012). Chondrogenesis, Chondrocyte Differentiation, and Articular Cartilage Metabolism in Health and Osteoarthritis. *Ther. Adv. Musculoskelet.* 4, 269–285. doi:10.1177/1759720X12448454

Guo, F., Sun, Y., Su, L., Li, S., Liu, Z., Li, J., et al. (2015). Losartan Attenuates Paraquat-Induced Pulmonary Fibrosis in Rats. *Hum. Exp. Toxicol.* 34, 497–505. doi:10.1177/0960327114543840

Gutiérrez, J., Droppelmann, C. A., Contreras, O., Takahashi, C., and Brandan, E. (2015). RECK-Mediated β1-Integrin Regulation by TGF-β1 Is Critical for Wound Contraction in Mice. *PLoS One* 10, e0135005. doi:10.1371/journal.pone.0135005

Hamilton, K., Dunning, L., Ferrell, W. R., Lockhart, J. C., and MacKenzie, A. (2018). Endothelium-derived Contraction in a Model of Rheumatoid Arthritis Is Mediated via Angiotensin II Type 1 Receptors. *Vasc. Pharmacol.* 100, 51–57. doi:10.1016/j.vph.2017.11.001

Heemskerk, F. M. J., Zorad, S., Xu, N., Gutkind, S. J., and Saavedra, J. M. (1999). Characterization of AT2 Receptor Expression in NIH 3T3 Fibroblasts. *Cel. Mol. Neurobiol.* 19, 277–288. doi:10.1023/a:1006985329240

Hildebrand, K. A., Zhang, M., Befus, A. D., Salo, P. T., and Hart, D. A. (2014). A Myofibroblast-Mast Cell-Neuropeptide axis of Fibrosis in Post-Traumatic Joint Contractures: An *In Vitro* Analysis of Mechanistic Components. *J. Orthop. Res.* 32, 1290–1296. doi:10.1002/jor.22676

Hildebrand, K. A., Ademola, A., and Hart, D. A. (2021). Nonsurgical Treatments for post-traumatic Elbow Contractures: Approaches for the Prevention of Their Development and Progression. *Ann. Jt.* 6, 8. doi:10.21037/aoj-20-62

Huard, J., Bolia, I., Briggs, K., Utsunomiya, H., Lowe, W. R., and Philippon, M. J. (2018). Potential Usefulness of Losartan as an Antifibrotic Agent and Adjunct to Platelet-Rich Plasma Therapy to Improve Muscle Healing and Cartilage Repair and Prevent Adhesion Formation. *Orthopedics* 41, E591–E597. doi:10.3928/01477447-20180806-05

Iannucci, L. E., Boys, A. J., McCorry, M. C., Estroff, L. A., and Bonassar, L. J. (2019). Cellular and Chemical Gradients to Engineer the Meniscus-to-Bone Insertion. *Adv. Healthc. Mater.* 8, 1800806. doi:10.1002/adhm.201800806

Jia, X., Gu, Y., Groome, L. J., Al-Kofahi, M., Alexander, J. S., Li, W., et al. (2016). 1,25(OH)2D3 Induces Placental Vascular Smooth Muscle Cell Relaxation by Phosphorylation of Myosin Phosphatase Target Subunit 1Ser507: Potential Beneficial Effects of Vitamin D on Placental Vasculature in Humans1. *Biol. Reprod.* 94, 1–8. doi:10.1095/biolreprod.116.138362

Kobayashi, T., Uehara, K., Ota, S., Tobita, K., Ambrosio, F., Cummins, J. H., et al. (2013). The Timing of Administration of a Clinically Relevant Dose of Losartan Influences the Healing Process after Contusion Induced Muscle Injury. *J. Appl. Physiol.* 114, 262–273. doi:10.1152/japplphysiol.00140.2011

Kuo, H.-F., Hsieh, C.-C., Wang, S.-C., Chang, C.-Y., Hung, C.-H., Kuo, P.-L., et al. (2019). Simvastatin Attenuates Cardiac Fibrosis via Regulation of Cardiomyocyte-Derived Exosome Secretion. *Jcm* 8, 794. doi:10.3390/jcm8060794

Lake, S. P., Castile, R. M., Borinsky, S., Dunham, C. L., Havlioglu, N., and Galatz, L. M. (2016). Development and Use of an Animal Model to Study post-traumatic Stiffness and Contracture of the Elbow. *J. Orthop. Res.* 34, 354–364. doi:10.1002/jor.22981

Logan, C. A., Gao, X., Utsunomiya, H., Scibetta, A. C., Talwar, M., Ravuri, S. K., et al. (2021). The Beneficial Effect of an Intra-articular Injection of Losartan on Microfracture-Mediated Cartilage Repair Is Dose Dependent. *Am. J. Sports Med.* 49, 2509–2521. doi:10.1177/03635465211008655

MacDonald, J. S., and Halleck, M. M. (2004). The Toxicology of HMG-CoA Reductase Inhibitors: Prediction of Human Risk. *Toxicol. Pathol.* 32, 26–41. doi:10.1080/01926230490462057

Monument, M. J., Hart, D. A., Salo, P. T., Hildebrand, K. A., and Dean Befus, A. (2013). Posttraumatic Elbow Contractures: Targeting Neuroinflammatory Fibrogenic Mechanisms. *J. Orthop. Sci.* 18, 869–877. doi:10.1007/s00776-013-0447-5

Monzack, E. L., Gu, X., and Masters, K. S. (2009). Efficacy of Simvastatin Treatment of Valvular Interstitial Cells Varies with the Extracellular Environment. *Atvb* 29, 246–253. doi:10.1161/ATVBAHA.108.179218

Myden, C., and Hildebrand, K. (2011). Elbow Joint Contracture after Traumatic Injury. *J. Shoulder Elbow Surg.* 20, 39–44. doi:10.1016/j.jse.2010.07.013

Negmadjanov, U., Godic, Z., Rizvi, F., Emelyanova, L., Ross, G., Richards, J., et al. (2015). TGF-β1-Mediated Differentiation of Fibroblasts Is Associated with Increased Mitochondrial Content and Cellular Respiration. *PLoS One* 10, e0123046. doi:10.1371/journal.pone.0123046

Olschewski, D. N., Hofschröer, V., Nielsen, N., Seidler, D. G., Schwab, A., and Stock, C. (2018). The Angiotensin II Type 1 Receptor Antagonist Losartan Affects NHE1-Dependent Melanoma Cell Behavior. *Cel. Physiol. Biochem.* 45, 2560–2576. doi:10.1159/000488274

Papadopoulos, D., Papatheodorou, L. K., and Sotereanos, D. G. (2021). Elbow Contracture Release. *Ann. Jt.* 6, 7. doi:10.21037/aoj-19-180

Pooley, J., and Van der Linden, D. (2021). Clinical and Pathological Perspectives on Elbow Arthritis and Arthroplasty. *Ann. Jt.* 6, 9. doi:10.21037/aoj-19-178

Porter, K., Turner, N. A., O'Regan, D. J., Balmforth, A. J., and Ball, S. G. (2004). Simvastatin Reduces Human Atrial Myofibroblast Proliferation Independently of Cholesterol Lowering via Inhibition of RhoA. *Cardiovasc. Res.* 61, 745–755. doi:10.1016/j.cardiores.2003.11.032

Price, A., Lockhart, J. C., Ferrell, W. R., Gsell, W., McLean, S., and Sturrock, R. D. (2007). Angiotensin II Type 1 Receptor as a Novel Therapeutic Target in Rheumatoid Arthritis: *In Vivo* Analyses in Rodent Models of Arthritis and *Ex Vivo* Analyses in Human Inflammatory Synovitis. *Arthritis Rheum.* 56, 441–447. doi:10.1002/art.22335

Reiter, A. J., Kivitz, G. J., Castile, R. M., Cannon, P. C., Lakes, E. H., Jacobs, B. Y., et al. (2019). Functional Measures of Grip Strength and Gait Remain Altered Long-Term in a Rat Model of Post-Traumatic Elbow Contracture. *J. Biomech. Eng.* 141, 071001. doi:10.1115/1.4043433

Reiter, A. J., Castile, R. M., Schott, H. R., Kivitz, G. J., Chamberlain, A. M., and Lake, S. P. (2021a). Investigating the Effects of Physical Therapy Timing, Intensity and Duration on Post-Traumatic Joint Contracture in a Rat Elbow Model. *Muscle Ligaments Tendons J.* 11, 547. doi:10.32098/mltj.03.2021.20

Reiter, A. J., Schott, H. R., Castile, R. M., Cannon, P. C., Havlioglu, N., Chamberlain, A. M., et al. (2021b). Females and Males Exhibit Similar Functional, Mechanical, and Morphological Outcomes in a Rat Model of Posttraumatic Elbow Contracture. *J. Orthop. Res.* 39, 2062–2072. doi:10.1002/jor.24918

Schachter, M. (2005). Chemical, Pharmacokinetic and Pharmacodynamic Properties of Statins: an Update. *Fundam. Clin. Pharmacol.* 19, 117–125. doi:10.1111/j.1472-8206.2004.00299.x

Sica, D. A., Gehr, T. W. B., and Ghosh, S. (2005). Clinical Pharmacokinetics of Losartan. *Clin. Pharmacokinet.* 44, 797–814. doi:10.2165/00003088-200544080-00003

Spurney, C. F., Sali, A., Guerron, A. D., Iantorno, M., Yu, Q., Gordish-Dressman, H., et al. (2011). Losartan Decreases Cardiac Muscle Fibrosis and Improves Cardiac Function in Dystrophin-Deficient Mdx Mice. *J. Cardiovasc. Pharmacol. Ther.* 16, 87–95. doi:10.1177/1074248410381757

Sridharan, G., and Shankar, A. (2012). Toluidine Blue: A Review of its Chemistry and Clinical Utility. *J. Oral Maxillofac. Pathol.* 16, 251–255. doi:10.4103/0973-029X.99081

Stancu, C., and Sima, A. (2001). Statins: Mechanism of Action and Effects. *J. Cell. Mol. Med.* 5, 378–387. doi:10.1111/j.1582-4934.2001.tb00172.x

Sun, F., Duan, W., Zhang, Y., Zhang, L., Qile, M., Liu, Z., et al. (2015). Simvastatin Alleviates Cardiac Fibrosis Induced by Infarction via Up-Regulation of TGF-β Receptor III Expression. *Br. J. Pharmacol.* 172, 3779–3792. doi:10.1111/bph.13166

Utsunomiya, H., Gao, X., Deng, Z., Cheng, H., Nakama, G., Scibetta, A. C., et al. (2020). Biologically Regulated Marrow Stimulation by Blocking TGF-β1 with Losartan Oral Administration Results in Hyaline-like Cartilage Repair: A Rabbit Osteochondral Defect Model. *Am. J. Sports Med.* 48, 974–984. doi:10.1177/0363546519898681

Varo, N., Etayo, J. C., Zalba, G., Beaumont, J., Iraburu, M. J., Montiel, C., et al. (1999). Losartan Inhibits the post-transcriptional Synthesis of Collagen Type I and Reverses Left Ventricular Fibrosis in Spontaneously Hypertensive Rats. *J. Hypertens.* 17, 107–114. doi:10.1097/00004872-199917010-00016

Veronese, N., Koyanagi, A., Stubbs, B., Cooper, C., Guglielmi, G., Rizzoli, R., et al. (2019). Statin Use and Knee Osteoarthritis Outcomes: A Longitudinal Cohort Study. *Arthritis Care Res.* 71, 1052–1058. doi:10.1002/acr.23735

Watson, S., Burnside, T., and Carver, W. (1998). Angiotensin II-Stimulated Collagen Gel Contraction by Heart Fibroblasts: Role of the AT1 Receptor and Tyrosine Kinase Activity. *J. Cel. Physiol.* 177, 224–231. doi:10.1002/(sici)1097-4652(199811)177:2<224:aid-jcp4>3.0.co;2-p

Watts, K. L., Sampson, E. M., Schultz, G. S., and Spiteri, M. A. (2005). Simvastatin Inhibits Growth Factor Expression and Modulates Profibrogenic Markers in Lung Fibroblasts. *Am. J. Respir. Cel. Mol. Biol.* 32, 290–300. doi:10.1165/rcmb.2004-0127OC

Wessel, L. E., Gu, A., Richardson, S. S., Fufa, D. T., and Osei, D. A. (2019). Elbow Contracture Following Operative Fixation of Fractures about the Elbow. *JSES Open Access* 3, 261–265. doi:10.1016/j.jses.2019.09.004

Whitehead, N. P., Kim, M. J., Bible, K. L., Adams, M. E., and Froehner, S. C. (2015). A New Therapeutic Effect of Simvastatin Revealed by Functional Improvement in Muscular Dystrophy. *Proc. Natl. Acad. Sci. USA* 112, 12864–12869. doi:10.1073/pnas.1509536112

Wu, Y., Lu, X., Li, M., Zeng, J., Zeng, J., Shen, B., et al. (2019). Renin-angiotensin System in Osteoarthritis: A New Potential Therapy. *Int. Immunopharmacol.* 75, 105796. doi:10.1016/j.intimp.2019.105796

Wu, Y., Li, M., Zeng, J., Feng, Z., Yang, J., Shen, B., et al. (2020). Differential Expression of Renin-Angiotensin System-Related Components in Patients with Rheumatoid Arthritis and Osteoarthritis. *Am. J. Med. Sci.* 359, 17–26. doi:10.1016/j.amjms.2019.10.014

Yudoh, K., and Karasawa, R. (2010). Statin Prevents Chondrocyte Aging and Degeneration of Articular Cartilage in Osteoarthritis (OA). *Aging* 2, 990–998. doi:10.18632/aging.100213

Zuscik, M. J., Hilton, M. J., Zhang, X., Chen, D., and O'Keefe, R. J. (2008). Regulation of Chondrogenesis and Chondrocyte Differentiation by Stress. *J. Clin. Invest.* 118, 429–438. doi:10.1172/JCI34174

Conflict of Interest: The authors declare that the research was conducted in the absence of any commercial or financial relationships that could be construed as a potential conflict of interest.

frontiers
in Cell and Developmental Biology

ORIGINAL RESEARCH
published: 15 March 2022
doi: 10.3389/fcell.2022.819967

Tenascins Interfere With Remyelination in an Ex Vivo Cerebellar Explant Model of Demyelination

Juliane Bauch, Sina Vom Ort, Annika Ulc and Andreas Faissner*

Department of Cell Morphology and Molecular Neurobiology, Ruhr-University Bochum, Bochum, Germany

Oligodendrocytes form myelin membranes and thereby secure the insulation of axons and the rapid conduction of action potentials. Diseases such as multiple sclerosis highlight the importance of this glial cell population for brain function. In the adult brain, efficient remyelination following the damage to oligodendrocytes is compromised. Myelination is characterized by proliferation, migration, and proper integration of oligodendrocyte precursor cells (OPCs). These processes are among others controlled by proteins of the extracellular matrix (ECM). As a prominent representative ECM molecule, tenascin-C (Tnc) exerts an inhibitory effect on the migration and differentiation of OPCs. The structurally similar paralogue tenascin-R (Tnr) is known to promote the differentiation of oligodendrocytes. The model of lysolecithin-induced demyelination of cerebellar slice cultures represents an important tool for the analysis of the remyelination process. *Ex vivo* cerebellar explant cultures of *Tnc*$^{-/-}$ and *Tnr*$^{-/-}$ mouse lines displayed enhanced remyelination by forming thicker myelin membranes upon exposure to lysolecithin. The inhibitory effect of tenascins on remyelination could be confirmed when demyelinated wildtype control cultures were exposed to purified Tnc or Tnr protein. In that approach, the remyelination efficiency decreased in a dose-dependent manner with increasing concentrations of ECM molecules added. In order to examine potential roles in a complex *in vivo* environment, we successfully established cuprizone-based acute demyelination to analyze the remyelination behavior after cuprizone withdrawal in SV129, *Tnc*$^{-/-}$, and *Tnr*$^{-/-}$ mice. In addition, we documented by immunohistochemistry in the cuprizone model the expression of chondroitin sulfate proteoglycans that are inhibitory for the differentiation of OPCs. In conclusion, inhibitory properties of Tnc and Tnr for myelin membrane formation could be demonstrated by using an *ex vivo* approach.

Keywords: extracellular matrix (ECM), tenascin-C, tenascin-R, myelin, myelin lesion, oligodendrocyte, regeneration

Edited by:
Eileen Gentleman,
King's College London,
United Kingdom

Reviewed by:
Pavle R. Andjus,
University of Belgrade, Serbia
Pablo Hector Horacio Lopez,
Medical Research Institute Mercedes and Martín Ferreyra (INIMEC),
Argentina

***Correspondence:**
Andreas Faissner
andreas.faissner@rub.de

Specialty section:
This article was submitted to Cell Adhesion and Migration, a section of the journal Frontiers in Cell and Developmental Biology

Received: 22 November 2021
Accepted: 24 February 2022
Published: 15 March 2022

Citation:
Bauch J, Ort SV, Ulc A and Faissner A (2022) Tenascins Interfere With Remyelination in an Ex Vivo Cerebellar Explant Model of Demyelination.
Front. Cell Dev. Biol. 10:819967.
doi: 10.3389/fcell.2022.819967

INTRODUCTION

Neurons, astrocytes, oligodendrocytes, and microglia form part of the four determining cell types of the central nervous system (CNS), whose interactions are necessary for memory formation (Hertz and Chen, 2016). Oligodendrocytes are the myelin membrane–forming cells of the CNS (Bradl and Lassmann, 2010). Due to the formation of myelin membranes, oligodendrocytes facilitate the rapid nerve conduction and insulation of axons (Hughes and Appel, 2016). In this context, conduction rates of up to 200 m/s can be reached, which are used for the complex information transfer in the

CNS (Nave, 2010). A single oligodendrocyte can form up to 40 myelin membranes, which isolate many axons (Miron et al., 2011). Oligodendrocytes are postmitotic cells, and their development is characterized by proliferation of oligodendrocyte precursor cells (OPCs) (Goldman and Kuypers, 2015), migration toward target axons (Miller, 2002), and differentiation into myelin membrane–forming cells (Zhang, 2001). Furthermore, the oligodendrocyte-dependent myelination influences survival and development of neurons. Due to the importance of intact myelin, acute demyelination entails serious neurological diseases like multiple sclerosis (MS) (Franklin and Ffrench-Constant, 2017). MS is a chronic inflammatory and demyelinating disease that affects the CNS, highlighted by a demyelination of axons (Franklin and Ffrench-Constant, 2008; Hagemeier et al., 2012). MS belongs to autoimmune diseases (Sospedra, 2018), involving T-lymphocytes and activated macrophages that attack and demyelinate myelin membranes and also damage axons. Recently, it became clear that B-cells play an important role in MS by activating T-cells (Sospedra 2018). Although remyelination processes occur in the demyelinated CNS, it does not suffice for a complete regeneration (Patani et al., 2007). With regard to the clinical picture of MS, we focus on two toxicity-based demyelination models: the cuprizone and the lysolecithin demyelination model (Birgbauer et al., 2004; Kipp et al., 2009). Both models induce a reversible demyelination of axons in the absence of an immune reaction. This allows analyzing mechanisms of remyelination or factors relevant to a higher remyelination efficiency in more detail. Cuprizone is a toxic copper chelator and induces demyelination, especially in the corpus callosum and hippocampus of the CNS of rodents. Due to a reversible demyelination after withdrawal of cuprizone, a remyelination can be observed (Matsushima and Morell, 2001; Kipp et al., 2009; Ransohoff, 2012). Within the *ex vivo* model, lysolecithin induces a reversible demyelination in cerebellar slice cultures and a remyelination ensues (Miron et al., 2013). In the context of oligodendrocyte development, molecules of the extracellular matrix (ECM) have been described to alter oligodendrocyte differentiation and migration (Jakovcevski et al., 2013; Wheeler and Fuss, 2016). The ECM allows cohesion of tissue and organs and is synthesized and released by the individual cells. The matrix influences cell development, survival, proliferation, morphology, migration, and differentiation (Dityatev et al., 2010; Barros et al., 2011; Faissner and Reinhard, 2015). Earlier studies revealed that the extracellular glycoprotein Tnc has an inhibitory effect on migration and differentiation of OPCs (Kiernan et al., 1996; Czopka et al., 2009b). In demyelinated MS plaques, which are characterized by demyelination of axons, an upregulation of Tnc may mediate inhibitory influences on oligodendrocytes (Zhao et al., 2009). Along these lines, when experimental allergic encephalomyelitis (EAE) was elicited in Tnc$^{-/-}$ mice, the disease course was less severe than that in the wildtype. Furthermore, proinflammatory cytokine levels and the stimulation of Th1 and Th17 cells in response to myelin oligodendrocyte glycoprotein (MOG) were less than those in the control (Momcilovic et al., 2017). In humans, tenascins belong to the glycoproteins of the ECM, with the four members of tenascin-C, tenascin-R, tenascin-X, and tenascin-W (Tucker et al., 2006). Tnc has a hexameric structure and is synthesized in early postnatal stages of CNS by neural stem cells and immature astrocytes (Bartsch et al., 1992; Garwood et al., 2004; Karus et al., 2011). The glycoprotein tenascin-R (Tnr) has a similar structure and forms dimers and trimers (Rathjen and Hodge, 2020). In contrast to Tnc, Tnr is expressed during late postnatal development of CNS in neurons and oligodendrocytes (Bartsch et al., 1992; Becker et al., 2000; Czopka et al., 2009b). Tnr promotes cell adhesion and cell differentiation of oligodendrocytes but also blocks migration of OPCs (Pesheva et al., 1997). Both tenascins exert an inhibitory influence on formation of myelin membranes. However, they act antagonistically on differentiation of oligodendrocytes. Tnc blocks differentiation, whereas Tnr is necessary for the temporal differentiation *in vitro* (Czopka et al., 2009b). Up to now, less is known about the function of Tnr. Therefore, we wanted to analyze the influence of Tnr on remyelination efficiency and on differentiation of oligodendrocytes. Here, within both demyelination models, *Tnc*$^{-/-}$ and *Tnr*$^{-/-}$ mice are used for the first time. We show that both demyelination models can be performed with *Tnc*$^{-/-}$ and *Tnr*$^{-/-}$ mice. Both glycoproteins Tnc and Tnr revealed an inhibitory influence on remyelination efficiency of oligodendrocytes in *ex vivo* explants. Furthermore, the known inhibitory effect of chondroitin sulfate on differentiation of OPCs (Karus et al., 2016; Keough et al., 2016) proved consistent with the expression pattern observed in this study.

MATERIALS AND METHODS

All experiments performed conform to the relevant regulatory standards.

Animals and Genotyping

Tnc$^{-/-}$ and *Tnr*$^{-/-}$ knockout mouse (*Mus musculus*) lines were derived and maintained in the animal facility of the Faculty of Biology and Biotechnology, Ruhr University Bochum, as described (Czopka et al., 2009b). For cerebellar explant cultures, mice heterozygous for the *Tnc* and *Tnr* genes were mated, and their homozygous wildtype and *Tnc*$^{-/-}$- and *Tnr*$^{-/-}$-deficient litters were genotyped at the age of 0–3 days. In order to isolate genomic DNA, mouse tail tips were lysed in 200 µl DirectPCR® Lysis Reagent Tail (Peqlab, VWR Life Science; Cat. No. 31-101-T) containing Proteinase K (Thermo Fisher Scientific; Cat. No. EO0491) at 55°C for 30 min and centrifuged at 16,000 g for 10 **s. 1** µl of lysed genomic DNA was used as a template for PCR analysis. On the one hand, the Tnc wildtype was amplified by a Tnc primer (5′-CTGCCA GGCATCTTTCTAGC-3′) and Tnc Exon 1 primer (5′-TTCTGCAGGTTGGA GGCAAC-3′), resulting in a PCR product of 420 bp. The amplification of the mutant allele with the Tnc primer combined with a Tnc Neo primer (5′-CTGCTC TTTACTGAAGGCTC-3′) resulted in a PCR product of 340 bp. On the other hand, the *Tnr* wildtype was amplified by a *Tnr*

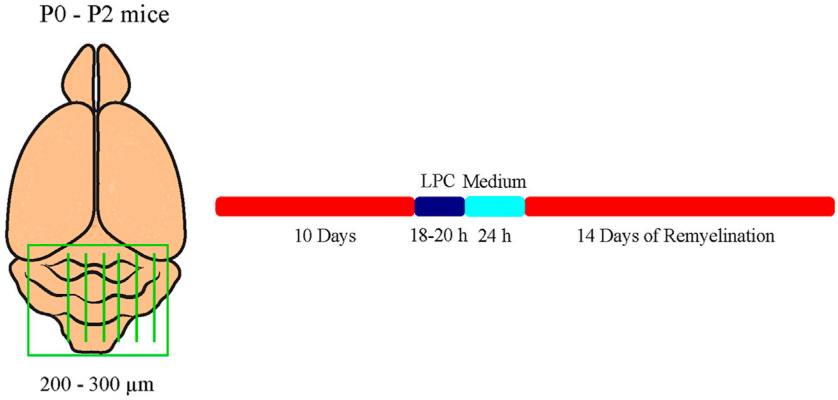

FIGURE 1 | Experimental setup of the cerebellar explant cultures. Cerebella of newborn tenascin-C and tenascin-R knockout and wildtype mice pups were cut into 250–300 µm thick sagittal sections and cultivated in slice culture medium. Demyelination was induced by administration of 0.5 mg/ml lysolecithin to the medium for 16-18 h. For remyelination analysis, explants were cultivated for further 14 days. Untreated control explants (C) were kept for the whole duration of the experiment.

primer (5′-AACTCCATGCTGGCTACCAC-3′) and an *Tnr* Exon 1 primer (5′-TTTT GGGGAGGTTGATCTTG-3′), resulting in a PCR product of 420 bp. The amplification of the mutant allele with the *Tnr* primer combined with a *Tnr* Neo primer (5′-ACCGCTTCCTCGTGCTT-3′) resulted in a PCR product of approximately 429 bp. *Tnc* and *Tnr* wildtype mice will be referred to as *Tnc*$^{+/+}$ and *Tnr*$^{+/+}$, whereas *Tnc* and *Tnr* knockout mice will be referred to as *Tnc*$^{-/-}$ and *Tnr*$^{-/-}$. For cerebellar slice cultures in the presence of purified Tnr protein, homozygous NMRI-mice were used. For de- and remyelination studies in the cuprizone model, homozygous *Tnc*$^{-/-}$ and *Tnr*$^{-/-}$ mice were compared to in-house bred SV129 wildtype mice (129S2/SvPasCrl) (Charles River, Sulzfeld, Germany). All experiments and animal handling were approved by LANUV, North Rhine-Westphalia, Germany (license AZ 84-02.04-2014.A332), and conducted according to German animal protection laws.

Lysolecithin-Induced Demyelination Model (*Ex Vivo* Model)

To analyze myelination and especially remyelination efficiency dependent on Tnc and Tnr, cerebellar slice cultures of newborn *Tnc*$^{+/+}$, *Tnc*$^{-/-}$, *Tnr*$^{+/+}$, and *Tnr*$^{-/-}$ pups were prepared as described previously (Miron et al., 2011; Zhang et al., 2011). This method represents an *ex vivo* model which allows for the application of compounds into the culture medium. In this model, the application of 0.5 mg/ml lysolecithin (Sigma-Aldrich; Cat. No. 9008-30-4) induces the demyelination of cerebellar axons (Birgbauer et al., 2004). Briefly, newborn pups were decapitated, and the brains were isolated and dissected. The cerebellum with the attached hindbrain was cut into 200–300 µm thick sagittal slices using an MCIIwain tissue chopper. Slices were placed on Millicell cell culture inserts (Merck KGaA) in slice culture medium (50% (v/v) MEM (Gibco Minimum Essential Media, Thermo Fisher Scientific; Cat. No. 15188319), 25% (v/v) Earle's Balanced Salt Solution (EBSS, Sigma-Aldrich; Cat. No. E2888), 25% (v/v) heat-inactivated horse serum (Sigma-Aldrich; Cat. No. S9135), Pen/Strep 10 µl/ml (Sigma-Aldrich; Cat. No. P4333), and 6.5 mg/ml D-Glucose (Serva Electrophoresis GmbH; Cat. No. 22700)) in six-well culture plates. The membrane of those inserts allows gas exchange with the area and with the slice culture medium. The media were changed every 2 days. In our experimental design, two cerebellar slices a time were cultivated for each of the conditions of myelination, demyelination, remyelination, and control. After 10 days in culture, myelinated slices were fixed for staining. Demyelination was induced by administration of 0.5 mg/ml lysolecithin to the medium for 16–18 h. Thereafter, inserts of the demyelinated condition were washed and transferred to fresh medium. After an additional cultivation of 24 h, demyelinated slices were fixed. For remyelination analysis, slices were cultivated for further 14 days (**Figure 1**).

Treatment of Cerebellar Slice Cultures With Exogenous Purified Tnc and Tnr

In the *ex vivo* model, remyelination efficiency was analyzed by application of purified Tnc and Tnr [diluted in phosphate-buffered saline (PBS)] in NMRI-mice to analyze its potential inhibitory influence in detail. Tnc was gained by immunoaffinity chromatography as described (Faissner and Kruse, 1990; Czopka et al., 2009b). To specify the impact on the remyelination process, Tnc was applied in a high concentration of 50 µg/ml PBS to the culture after demyelination. Regarding the concentration of Tnc in the perturbation experiments, we used 50 µg/ml to make sure that we operate in an efficient range. Concentrations down to 15 µg/ml were used in previous studies; however, these were performed with single cells, not with explants (Moritz et al., 2008). As we use Tnc purified from the postnatal mouse brain, the supplies are limited, and we could not carry out dose-response studies in this case. Therefore, we aimed at the assumed endpoint to probe the decisive issue, namely, whether Tnc interferes with remyelination. Tnr was gained by immunoaffinity purification from adult *Tnr*$^{+/+}$ mouse brains as described (Czopka et al., 2009b). To determine the impact on the remyelination process, Tnr was applied in concentrations of 10 μg/ml and 20 μg/ml PBS to the cultures after demyelination. Tnr was isolated from the adult mouse CNS and was also only available in limited amounts. Cultivation was performed as described above, but Tnr was part of the medium during the remyelination period. For internal control, purified Tnc and Tnr were also applied to untreated explants. For further external control, we used an additional culture plate with application of 1x PBS instead of Tnr. The concentrations of tenascins are difficult to compare as Tnr occurs in dimers and trimers, whereas Tnc occurs as trimers and hexamers. If we assume that Tnr trimers (Mr 480 kD) and Tnc hexamers (Mr 1000 kD) prevailed in our samples, the multimers were used in comparable nanomolar ranges at the concentrations we applied. We assume that we saturated the inhibitory effect under these conditions.

Imaging of Cerebellar Slices

Confocal images were obtained by using a Zeiss LSM 510 Meta microscope. Images of at least three different areas of the cerebellum were taken, whereas in the z-plane, six images were recorded at intervals of 1 μm. The ImageJ Plugin JaCoP (Bolte and Cordelieres, 2006) was used to identify Manders' overlap coefficient (MOC), which reflects the intensities of colocalized pixels in relation to the intensities of either all red pixels or all green pixels. Moreover, we compared the measured M2 values (De Santis et al., 2021) of the different genotypes $Tnc^{+/+}$, $Tnc^{-/-}$, $Tnr^{+/+}$, and $Tnr^{-/-}$ to exclude the possibility that changed myelin formation was due to the influence of the tenascins on the axons (**Supplementary Figure S2**). The M2 signal therein corresponded to the red fluorescence and reflected the density of axon surfaces in the explants.

Cuprizone-Induced Demyelination Model (*In Vivo* Model)

For myelination studies *in vivo*, eight-week-old male SV129, $Tnc^{-/-}$, and $Tnr^{-/-}$ mice were fed 0.2% (w/w) cuprizone (Sigma-Aldrich; Cat. No. 370-81-0) mixed with powdered chow for six weeks to induce demyelination (Hillis et al., 2016), followed by a diet without cuprizone for one or two weeks (Albrecht et al., 2016) to allow for remyelination, as described previously (Ulc et al., 2019). Control mice received powdered chow without cuprizone. Four different experimental groups of mice were used. At the end of the experiment, mice of each group were perfused intracardially with 20 ml PBS in deep anesthesia (800 μl 0.9% (w/v) NaCl (Thermo Fisher Scientific; Cat. No. 7647-14-5), 50 μl Xylavet (xylazine) (10 mg/ml weight) (CP-Pharma, Handelsgesellschaft mbH; Cat. No. 1205), and 150 μl ketamine (150 mg/ml weight) (CP-Pharma, Handelsgesellschaft mbH; Cat. No. 1202)), and brains were removed and cut sagittally in two halves. Then, one hemisphere was fixed with 4% (w/v) paraformaldehyde (PFA) (Carl Roth; Cat. No. 4235.1) in PBS at 4°C for 48 h, before embedding in tissue-freezing medium for cryosectioning and following immunohistochemical staining. The second hemisphere was frozen in liquid nitrogen for RNA analysis.

Immunohistochemistry

Immunological Reagents

The following primary antibodies were used: APC (clone CC1, mouse IgG2b, IF: 1:100, Abcam (Ab16794) RRID:AB_443473; Cambridge, UK), MBP (mouse IgG, IF: 1:50, Bio-Rad (MCA409) RRID:AB_325004, Millipore, Eschborn, Deutschland), NF200 (rabbit polyclonal, IgG, IF: 1:200, Sigma-Aldrich (N4142) RRID:AB_477272, Chemie GmbH, Munich Germany), Olig2 (rabbit polyclonal IgG, IF: 1:500, Merck (AB9610) RRID: AB_570666, Millipore), and 473HD (rat, IgM monoclonal, IF: 1:100, Hybridoma-technique) (Faissner et al., 1994a). Species-specific secondary antibodies coupled to Cy2 AF488 (1:250) and Cy3 (1:500) were obtained from Dianova GmbH (Hamburg, Germany).

Immunohistochemical Staining

After 2 days, PFA-fixed brain halves were dehydrated in 30% (w/v) sucrose (J.T. Baker; Cat. No. 4072-01) before embedding in tissue-freezing medium (Leica Biosystems; Cat. No. 14020108926) on dry ice. For immunohistochemical staining, cryosections with a slice thickness of 14 μm were used. Here, we focused sagittal sections on the area of the corpus callosum (CC). To permeabilize the tissue, brain sections were first boiled with blocking solution in 0.01 M citrate buffer before incubation (PBS+ 1% (w/v) BSA (Carl Roth GmbH & Co. KG; Cat. No. 8076.2) + 0.1% (v/v) Triton-X 100 (AppliChem; Cat. No. A4975,0500) + 5% (v/v) goat serum (Abcam; Cat. No. ab7481)) for 1 h at RT in a humid chamber. Individual primary antibodies (MBP, 473HD, Olig2, and CC1) were diluted in blocking solution and incubated at 4°C overnight. After three consecutive washing steps in PBS, secondary antibodies were diluted in PBS/A (PBS + 0.1% (w/v) BSA) and incubated for 2 h at RT. Finally, stained cryosections were washed three times with PBS and mounted using ImmuMount. For luxol fast blue–periodic acid Schiff's reagent staining (LFB–PAS-staining), LFB (Thermo Fisher Scientific; Cat. No. 1328-51-4) was used to stain myelin blue and PAS to stain axons red. At the beginning, *in vivo* sections were dehydrated in a graded alcohol series (30% (v/v), 70% (v/v), 90% (v/v), 96% (v/v) ethanol) and stained in 1% LFB solution in 96% (v/v) ethanol (Carl Roth; Cat. No. 64-17-5) for 24 h at 60°C. Afterward, cryosections were rinsed in 96% (v/v) ethanol followed by incubation in 0.05% (w/v) lithium carbonate ($LiCO_3$) (Sigma-Aldrich; Cat. No. 554-13-2) for 30 s. Next, the sections were washed in 70% (v/v) ethanol for 30 s, which reduces the background staining, and in A. dest. for 5 min to block differentiation. Then, staining was followed with 1% (w/v) periodic acid (7 min) and afterward with Schiff's reagent (Carl Roth; Cat. No. 1789) for 20 min. Subsequently, the sections were washed three times with A. dest. before they were stained in hematoxylin for 3 min for making the cell nuclei in tissue visible. After further dehydration in a graded alcohol series, cryosections were mounted using Euparal mounting medium (Carl Roth; Cat. No. 1993). For the immunohistochemical staining of cerebellar explant cultures, slices were fixed in 4% (w/v) PFA in PBS for 1 h at RT and afterward rinsed three times in PBS for 10 min. For staining, slices were permeabilized and blocked in 3% (v/v) heat-inactivated horse serum (HS), 2% BSA (w/v), and 0.5% (v/v) Triton-X 100 (blocking buffer) for 1 h at RT. Primary antibodies were diluted in blocking buffer and incubated at 4°C overnight. Secondary antibodies were diluted for 3 h at RT, followed by two washes in PBS for 10 min and one wash in PBS for 1 h. Slices were mounted on glass slides using ImmuMount. Confocal images were collected by using a Zeiss LSM 510 Meta microscope at intervals of 1 μm. The ImageJ Plugin JaCoP (Bolte and Cordelieres, 2006) was used to identify the individual Manders' coefficient, which describes the intensity of colocalized pixels in relation to the intensity of all red pixels. Here, the myelination index describes the percentage of myelinated axons in relation to all axons.

Molecular Biology

RNA Isolation, cDNA Synthesis, and qRT-PCR

In order to monitor myelin-specific genes in the corpus callosum, the anatomical region was prepared from partially frozen brain halves of cuprizone-treated mice. Prior to RNA extraction, the isolated corpus callosum tissue was stored at −80°C. Total RNA from the corpus callosum was isolated using the GeneElute™ Mammalian Total RNA MiniPrep Kit (Sigma-Aldrich by Merck KGaA; Cat. No. RTN350) according to the manufacturer's instructions. 0.5 μg RNA was transcribed into cDNA in a volume of 40 μl using the First Strand cDNA Synthesis Kit (Thermo Fisher Scientific; Cat. No. K1622). 6.25 ng cDNA in total was used for each qRT-PCR. All qRT-PCRs were performed on LightCycler96 (Hoffmann-La Roche AG) using the FastStart Essential DNA Green Master Kit (Hoffmann-La Roche AG; Cat. No. 064027120 01). For each condition (control, demyelination, one-week remyelination, two-weeks remyelination), cDNA samples from three different animals were prepared in triplicate. For each RT-PCR, only one myelin gene was analyzed (β-actin and ribosomal protein lateral stalk subunit P0 (RPLP0) as controls, myelin basic protein (MBP) and proteolipid protein 1 (PLP1) as myelin genes). The following primers were used: β-actin forward: 5′-ctaaggccaaccgtgaaaag-3′, β-actin reverse: 5′-accagaggcatacagggaca-3′, RPLP0 forward: 5′-cgacctggaagtccaactac-3′, RPLP0 reverse: 5′-atctgctgcatctgctg-3′, PLP1 forward: 5′-caagacctctgccagtatag-3′, PLP1 reverse: 5′-agc tcagaacttggtgcctc-3′, MBP forward: 5′-agccgaggtcccattgtt-3′, and MBP reverse: 5′-cctcagaggacagagtgatgtgttt-3′. In each sample, three technical replicates were measured and normalized to the expression of stably expressed genes (β-actin and RPLP0). qPCR data were analyzed with the program LightCycler® 96 and given as values. Evaluating the primer efficiency and relative gene expression was performed with Rest 2009.

Statistics

All results are provided as mean ± SEM if not declared otherwise. The number of performed experiments and the type of statistical tests are indicated in figure legends. The two-way ANOVA and the subsequent Tukey's multiple-comparisons test were performed for the comparison of more than two samples. All statistical tests were run using the GraphPad Prism 7 program (GraphPad Software, San Diego, United States) and were considered as significantly different when $p \leq 0.05$; p-values are indicated with * for $p \leq 0.05$, ** for $p \leq 0.01$, and *** for $p \leq 0.001$.

RESULTS

Faster Remyelination in Cerebella Slice Cultures of *Tnc*$^{-/-}$ Mice

Earlier studies had revealed that Tnc and Tnr regulate the differentiation of oligodendrocytes *in vitro* (Czopka et al., 2009b; Czopka et al., 2010). In order to examine whether this is also the case in a more complex setting closer to the *in vivo* situation, we studied their impact on de- and remyelination in a live cerebellar explant system (Zhang et al., 2011) (**Figure 1**). To this end, remyelination in cerebellar slice cultures of *Tnc*$^{+/+}$, *Tnc*$^{-/-}$, *Tnr*$^{+/+}$, and *Tnr*$^{-/-}$ mice was studied. Immunohistochemical staining with NF200 and MBP was performed in four conditions, namely, myelinated (M), demyelinated (DM), remyelinated (RM), and control (C) (**Figures 2–5**). The degree of myelination was assessed according to MBP-labeling along neurofilament-positive axons and developed during the first 10 days of cultivation (M, **Figure 2**). Upon application of lysolecithin after 10 days of cultivation, a drastic demyelination (DM) was obvious and could be observed in all genotypes studied, where MBP-staining appeared highly reduced (**Figure 2**) (Ulc et al., 2019). Upon withdrawal of lysolecithin, an initial remyelination (RM) was observable in both genotypes that progressed over 14 days, the endpoint of the experiment. Progressively myelinated axons were visible in the control condition (C), explants that were kept unperturbed over 25 days. To investigate the difference between *Tnc*$^{+/+}$ and *Tnc*$^{-/-}$ slices, we performed a quantification of the myelination indices. After 10 days, the *Tnc*$^{-/-}$ explants presented a higher percentage of myelinated axons compared to the wildtype that proved statistically significant (M, *Tnc*$^{+/+}$: 18.56% ± 7.33%, *Tnc*$^{-/-}$: 24.56% ± 7.9%, $p = 0.003$). Demyelination was successful (**Figures 2A,B**), presenting the lowest myelination grade for both genotypes (DM, *Tnc*$^{+/+}$: 2.64% ± 1.64%, *Tnc*$^{-/-}$: 3.51% ± 2.50%). Successful remyelination occurred in both genotypes, with an apparent advantage in *Tnc*$^{-/-}$ compared with *Tnc*$^{+/+}$ cultures that did not, however, achieve statistical significance (RM, *Tnc*$^{+/+}$: 24.37% ± 9.97%, *Tnc*$^{-/-}$: 31.71% ± 7.34%). The control condition (C) that had not been exposed to lysolecithin revealed an ongoing increase of myelination compared to the demyelinated condition. Interestingly, myelination in the absence of Tnc appeared comparable to the WT (C, *Tnc*$^{+/+}$: 26.80% ± 5.95%, *Tnc*$^{-/-}$: 29.35% ± 9.79%). A change in the degree of myelin formation could result from the reduced availability of axons as a consequence of fasciculation. To exclude the influence of axon fasciculation on the myelination degree, we also measured the percentage of NF200-positive fluorescence in the explants. As our results demonstrated, axon signals were only significantly increased during myelination in *Tnc*$^{-/-}$ tissue (M, *Tnc*$^{+/+}$: 19.83%, *Tnc*$^{-/-}$: 40.59%, $p = 0.0013$) (**Supplementary Figure S2B**). No significant differences

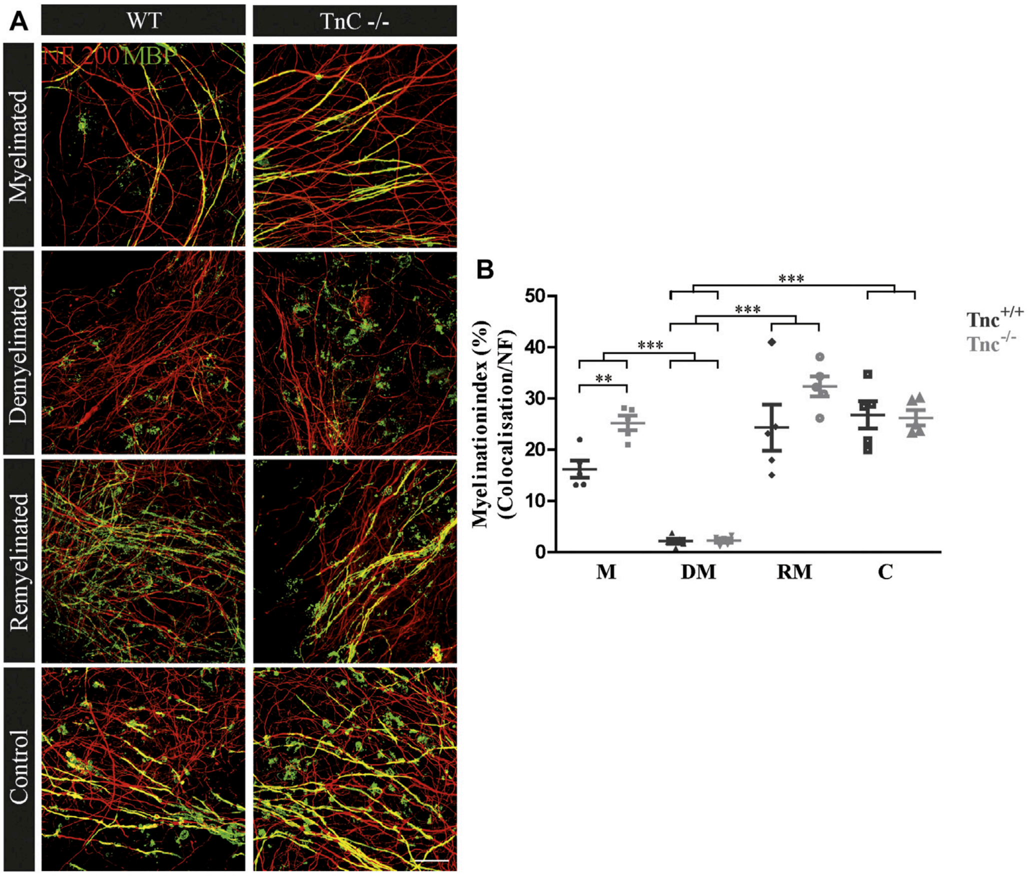

FIGURE 2 | (A,B) Comparison of myelination and remyelination in live cerebellar explant cultures of *Tnc*$^{+/+}$ and *Tnc*$^{-/-}$ mice. **(A)** *Tnc*$^{+/+}$ and *Tnc*$^{-/-}$ cerebellar explant cultures of the conditions myelinated (M), demyelinated (DM), remyelinated (RM), and control (C) were labeled with antibodies against NF200 (red) and MBP (green) to visualize the wrapping of myelin membranes around nerve fibers. Colocalization of neurofilament and MBP appeared as yellow staining. Demyelination nearly eliminated MBP-labeling. The myelinated condition shows a highly distinctive MBP staining. An initiating remyelination is visible for both genotypes. **(B)** Quantification of myelination indices of each condition in the comparison of *Tnc*$^{+/+}$ and *Tnc*$^{-/-}$ explant cultures (M, myelinated; DM, demyelinated; RM, remyelinated; C, control). For the demyelinated condition, the quantification shows a significant reduction of the myelination index compared to the other conditions. Overall, both myelination and remyelination appeared more extensive in the absence of Tnc. All data are provided as mean ± SEM. Statistical significance was assessed using the two-way ANOVA (*$p \leq 0.05$, **$p \leq 0.01$, ***$p \leq 0.001$) and Tukey's multiple-comparisons test. Scale bars: 20 µm. Six independent experiments (N = 6) were performed, and three explants (*n* = 3) were analyzed per experiment for each condition.

considering the axon signals were detectable in the control condition (C, *Tnc*$^{+/+}$: 41.3%, *Tnc*$^{-/-}$: 45.3%), or during demyelination (DM, *Tnc*$^{+/+}$: 30.6%, *Tnc*$^{-/-}$: 45.98%). In the latter case, a large scatter of values obliterated the significance of the seeming difference (**Supplementary Figure S2B**). Moreover, during the successful remyelination, there were still no significant differences considering the axon signals detectable (RM, *Tnc*$^{+/+}$: 40.08%, *Tnc*$^{-/-}$: 43.81%). Therefore, the availability of axon surfaces for ensheathment by myelin was comparable in the different experimental samples.

Purified Tnc Interferes With Remyelination in the Cerebellar Explant Assay

The data seemed to indicate a weak but visible retarding effect of Tnc on myelination, whereas demyelination per se was not modified by the absence of Tnc. To test this interpretation, demyelinated WT explants were directly exposed to purified Tnc isolated from the postnatal CNS (**Figure 3**). After lysolecithin withdrawal, 50 µg/ml Tnc was added in soluble form to the slice cultures and cultivated for 14 days (**Figure 3A**). This concentration range had proven efficient for stimulating cells with soluble Tnc in previous studies (Haage et al., 2019). Myelination indices were evaluated for untreated and treated remyelination and control groups (**Figure 3B**). No differences from the untreated group were measured by adding Tnc to the control group (C, w/o Tnc: 20.13% ± 2.66%, +Tnc: 18.53% ± 12.26%) (**Figures 3A-B, A-B'**). However, remyelination efficiency was significantly decreased when Tnc was added to the remyelination group in comparison with the untreated remyelination group (RM, w/o Tnc: 17.82% ± 1.61%, +Tnc: 11.15% ± 1.01%, p = 0.0029) (**Figures 3A-A, A-A'**). In the presence of Tnc, the remyelination appeared strongly impeded (**Figure 3B**).

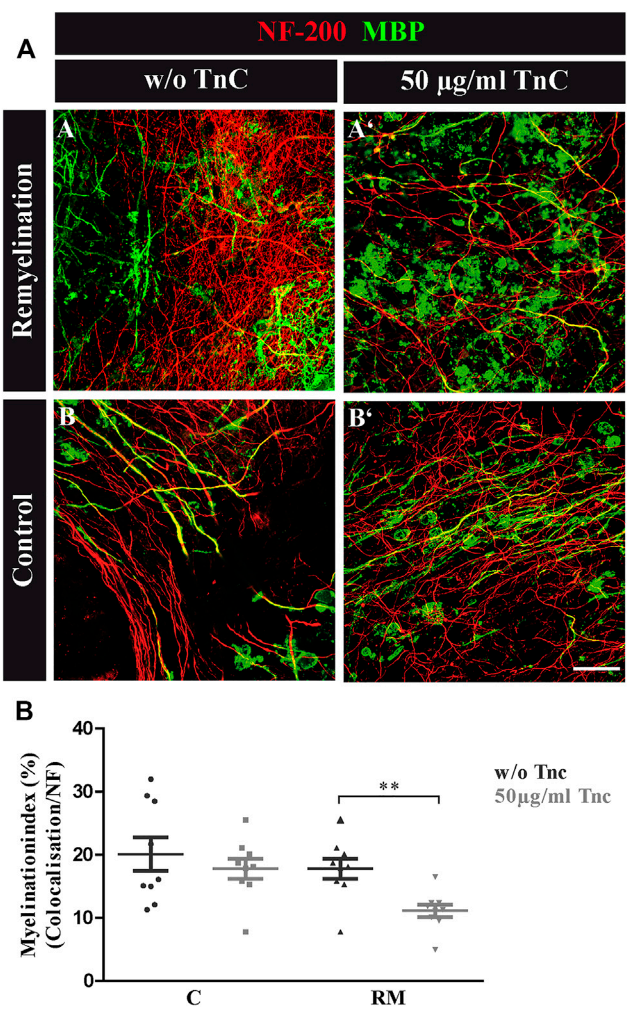

FIGURE 3 | (A,B) Tnc inhibits remyelination in cerebellar slice cultures. **(A,A′,B,B′)** Exemplary cerebellar explants cultivated in the absence **(A,B)** or presence **(A′,B′)** of Tnc. Slices were stained for NF-200 and MBP. Tnc-treated remyelinated cultures displayed myelin membranes that did not wrap the axons throughout the whole cerebellar slice. Scale bar: 20 µm. **(B)** Evaluation of myelination index, defined as the proportion of colocalized area among the areas of complete neurofilament staining. These results indicate an impaired remyelination in Tnc-treated cultures. Data are presented as mean ± SEM, and statistical significance was assessed using an unpaired two-tailed Student's t-test for each group (remyelinated and control). Six independent (N = 6) experiments were performed, and three explants (*n* = 3) were analyzed per experiment for each condition.

Accelerated Remyelination in Cerebellar Slice Cultures of *Tnr*$^{-/-}$ Mice

The inhibitory effects of Tnc on remyelination were in agreement with studies showing that Tnc reduces oligodendrocyte membrane extension *in vitro*. The paralogue Tnr is structurally related to Tnc and had analogous effects in that cell biological assay (Czopka et al., 2009b). Therefore, we examined the consequences of *Tnr* gene ablation in the cerebellar remyelination assay (**Figure 1**). To assess the difference between *Tnr*$^{+/+}$ and *Tnr*$^{-/-}$ explants (**Figure 4A**), we performed a quantification of the myelination indices. Here, the myelinated condition represented a slightly higher, although not statistically significant percentage of myelinated axons compared to the control group (M, *Tnr*$^{+/+}$: 23.20% ± 9.71%, *Tnr*$^{-/-}$: 24.66% ± 11.21%; **Figure 4**). This was not observed in the untreated control explants (*Tnr*$^{+/+}$: 16.11% ± 3.68%, *Tnr*$^{-/-}$: 15.58% ± 4.41%). As reflected in the myelination indices, demyelination by lysolecithin was successful (**Figure 4B**) and presented the lowest myelination grade in the demyelinated condition for both genotypes (DM, *Tnr*$^{+/+}$: 5.60 %± 1.5%, *Tnr*$^{-/-}$: 4.92% ± 2.12%). Moreover, a successful remyelination could be observed which, remarkably, appeared stronger in *Tnr*$^{-/-}$ than *Tnr*$^{+/+}$ cultures (RM, *Tnr*$^{+/+}$: 9.11% ± 3.2%, *Tnr*$^{-/-}$: 15.21% ± 6.1%, p = 0.0165). This observation suggested a clear inhibitory effect of *Tnr* on the remyelination process. Furthermore, we have analyzed the fraction of axon-dependent fluorescence in the different conditions, and as our results demonstrated, the intensity of NF200-positive signals in *Tnr*$^{-/-}$ mice was significantly increased in the demyelination condition (DM, *Tnr*$^{+/+}$: 29.83%, *Tnr*$^{-/-}$: 45.09%, p = 0.0003) (**Supplementary Figure S2C**). Under untreated control condition, no significant differences considering the axon signals in both genotypes were detectable (C, *Tnr*$^{+/+}$: 44.19%, *Tnr*$^{-/-}$: 54.54%). Moreover, the results showed that Tnr seemed to exert no influence on axon signals under myelination (M, *Tnr*$^{+/+}$: 45.35%, *Tnr*$^{-/-}$: 45.53%) and remyelination conditions (RM, *Tnr*$^{+/+}$: 40.08%, *Tnr*$^{-/-}$: 43.91%). In view of the apparent inhibitory effect, we tested the purified Tnr protein directly in the explant remyelination assay.

Purified Tnr Reduces Remyelination in the Cerebellar Explant Assay

Cerebellar explants were kept in culture for 10 days, demyelinated, and subsequently remyelinated as indicated (**Figure 1**). To assess the impact on myelination, Tnr was added at 10 µg/ml or 20 µg/ml purified protein to the culture medium, while plain PBS instead of ECM protein was used as the control (**Figure 5A**). During the first 10 days of cultivation, quantification revealed a higher percentage of myelinated axons in the PBS-control compared to Tnr-treated groups (M; PBS-C: 23.07% ± 8.42%, 10 µg Tnr: 11.37% ± 3.09%, p = 0.0142, 20 µg Tnr: 15.12% ± 1.47%, p = 0.0176). Explants kept in the presence of 10 µg Tnr represented the least degree of myelination of axons, and this apparent retardation of myelination during the initial cultivation phase was highly significant (**Figure 5**). Demyelination upon application of lysolecithin was successful, as evidenced by a reduction of MBP-staining (DM; PBS-C: 5.16 ± 2.34%, 10 µg Tnr: 6.50% ± 3.69%, 20 µg Tnr: 9.56% ± 2.51%). Remyelination could be observed but differed between these three groups. The highest percentage of remyelinated axons was obtained in the PBS-control situation, whereas the least percentage was recorded for explants confronted with 20 µg/ml Tnr. Interestingly, in that latter situation, the myelination

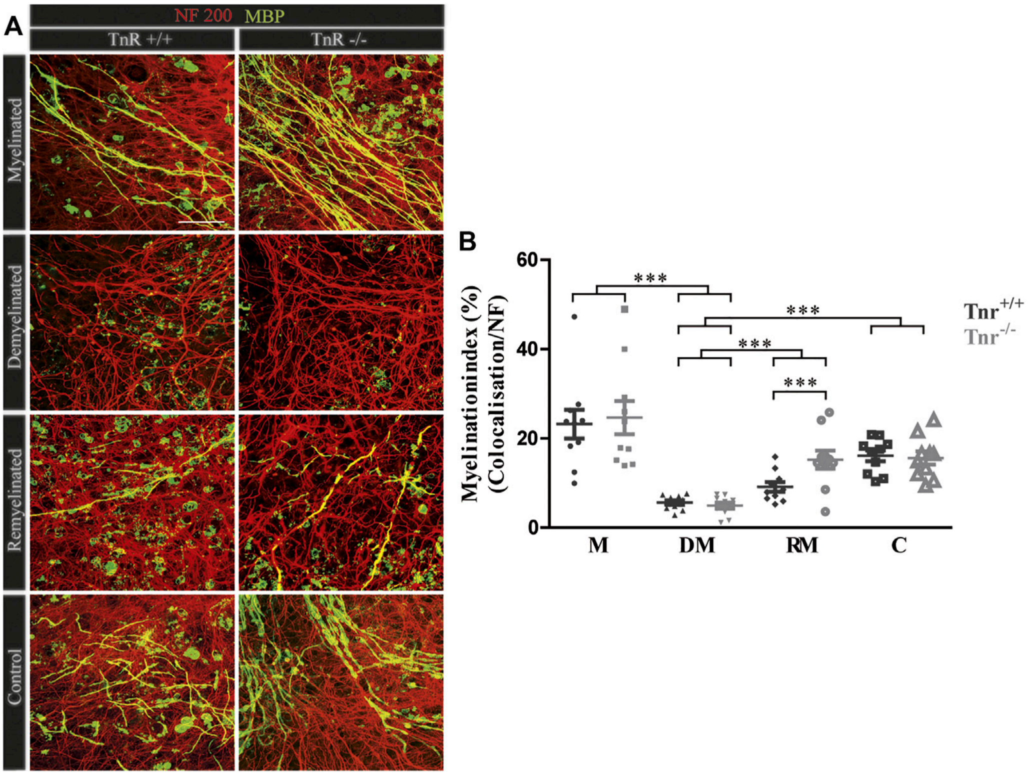

FIGURE 4 | (A,B) Comparison of myelination and remyelination in live cerebellar explant cultures of *Tnr*$^{+/+}$ and *Tnr*$^{-/-}$ mice. **(A)** *Tnr*$^{+/+}$ and *Tnr*$^{-/-}$ cerebellar explant cultures of the conditions myelinated (M), demyelinated (DM), remyelinated (RM), and control (C) were immunohistochemically labeled with antibodies against NF200 (red) and MBP (green) to visualize the wrapping of myelin membranes around nerve fibers. Colocalization of neurofilament and MBP appeared as yellow staining. Demyelination nearly eliminated MBP-labeling. The myelinated condition shows a highly distinctive MBP staining. An initiating remyelination is visible for both genotypes. **(B)** Quantification of myelination indices of each condition in the comparison of *Tnr*$^{+/+}$ and *Tnr*$^{-/-}$ explant cultures (M, myelinated; DM, demyelinated; RM, remyelinated; C, control). For the demyelinated condition, the quantification shows a significant reduction of the myelination index compared to the other conditions. Overall, both myelination and remyelination appeared more extensive in the absence of Tnr. All data are provided as mean ± SEM. Statistical significance was assessed using the two-way ANOVA (*$p \le 0.05$, **$p \le 0.01$, ***$p \le 0.001$) and Tukey's multiple-comparisons test. Scale bars: 50 µm. Nine independent experiments were performed (N = 9), and three explants (*n* = 3) were analyzed per experiment for each condition and each slice culture group.

index was nearly the same for the remyelinated condition compared to the demyelinated condition (RM; PBS-C: 20.45% ± 7.26%, 10 µg Tnr: 13.03% ± 2.29%, 20 µg Tnr: 9.97% ± 3.30%). As a further support of Tnr-dependent inhibition, the PBS-control displayed a significant increase of remyelination compared to demyelination. In the control condition for all groups, the highest percentage of myelinated axons was noted when the explants were exposed neither to lysolecithin nor to Tnr protein (C; PBS-C: 25.75% ± 8.35%, 10 µg/ml Tnr: 23.84% ± 7.09%, 20 µg/ml Tnr: 20.37% ± 4.80%, $p = 0.0053$). Overall, these observations clearly suggest that Tnr protein reduced myelination in the cerebellar explant assay. Considering the remyelination condition, it is noteworthy that the myelination indices in the presence of Tnr did not differ from the demyelination condition, while a significantly recovery could be detected when the explants were treated with plain PBS (**Figure 5B**). We interpret this result as indicating that Tnr delayed recovery of myelin to some extent by maintaining the demyelination level (**Figure 5B**).

LFB–PAS-Staining and MBP-Staining Reveal Successful Demyelination and Remyelination in the Different Genotypes in the Cuprizone Model *In Vivo*

The outcome of the studies with cerebellar explants strongly suggested an inhibitory role of Tnc and Tnr in remyelination *in vitro*. This prompted the question whether these glial-derived ECM constituents interfere with the remyelination process *in vivo*. In order to study this issue, demyelination was induced in wildtype and transgenic mice by administration of a cuprizone-rich diet over a period of 6 weeks, following an established protocol (Ulc et al., 2019). To assess the myelination grade in the corpus callosum of SV129, *Tnc*$^{-/-}$, and *Tnr*$^{-/-}$ mice in the conditions "control," "demyelination," "one-week remyelination," and "two-weeks remyelination," we performed LFB–PAS- and MBP-staining of tissue sections. LFB detects phospholipids/lipoproteins in myelin, and PAS marks glycoproteins in the axons (Xiang et al., 2005; Lindner et al., 2008). In contrast, labeling for MBP focuses on the

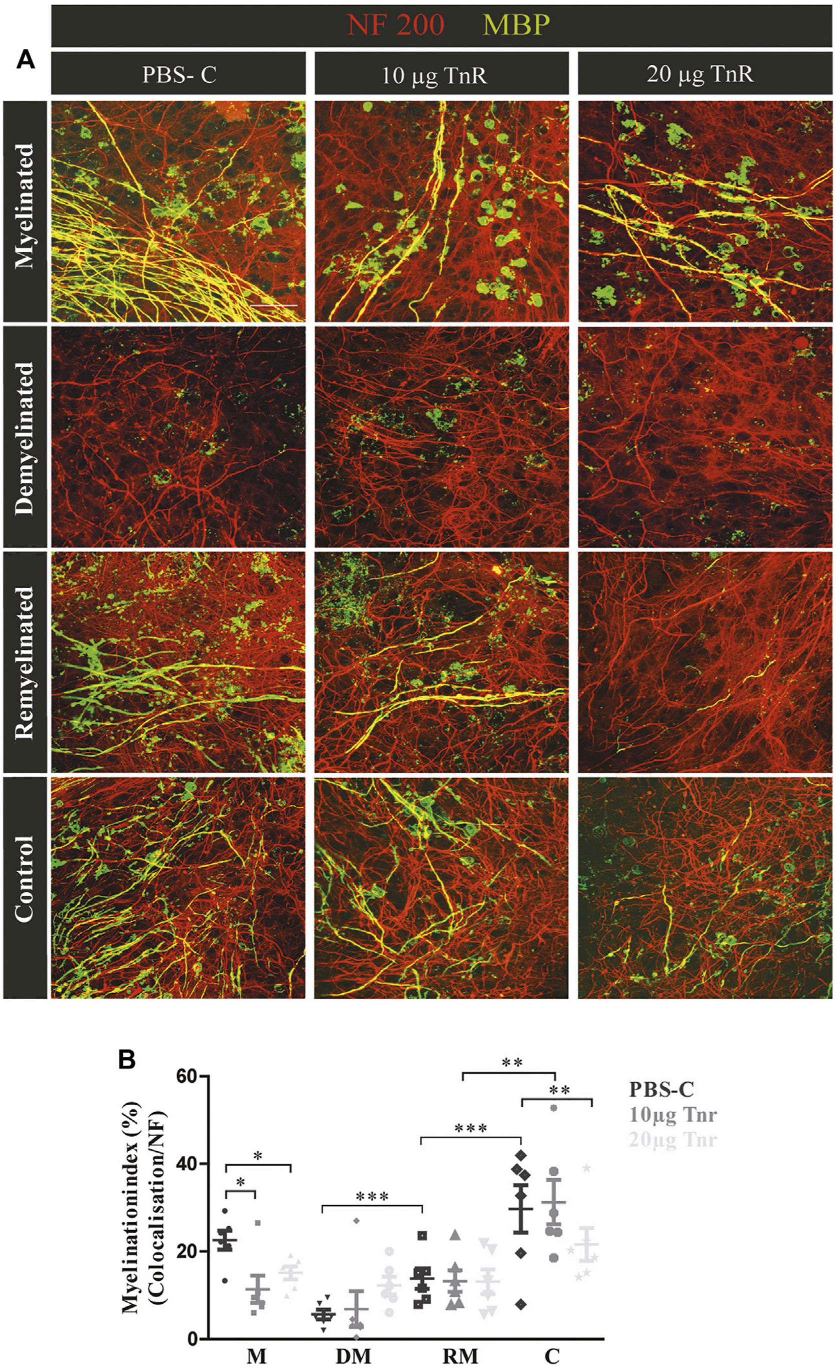

FIGURE 5 | (A,B) Comparison of remyelination efficiency in cerebellar cultures from NMRI-mice in the presence of purified Tnr. **(A)** Labeling for neurofilament (red) and MBP (green) of live cerebellar explants kept under four different conditions: myelinated, demyelinated, remyelinated, and control. Explants were complemented either with plain PBS (control), with 10 µg, or with 20 µg immunopurified Tnr applied to the explant culture medium. MBP labeling indicates the degree of myelination under the different conditions. **(B)** The graph displays the quantification of myelination indices of the distinct conditions PBS-control (PBS-C), 10 µg Tnr, and 20 µg Tnr as applied to explant cultures kept in the different conditions (M, myelinated; DM, demyelinated; RM, remyelinated; C, control). All data are provided as mean ± SEM. Statistical significance was assessed using the two-way ANOVA (*$p \le 0.05$, **$p \le 0.01$, ***$p \le 0.001$) and Tukey's multiple-comparisons test. Scale bars: 50 µm. Five independent experiments (N = 5) were carried out, and three ($n = 3$) explants per experiment were analyzed for each condition and each slice culture group.

specific myelin compartment. In all genotypes, the histochemical staining revealed more pronounced myelin in the control as compared to the demyelinated condition. The reduced intensity of myelin staining in the demyelinated condition could be explained by a successful cuprizone-induced demyelination. However, some residual LFB- and

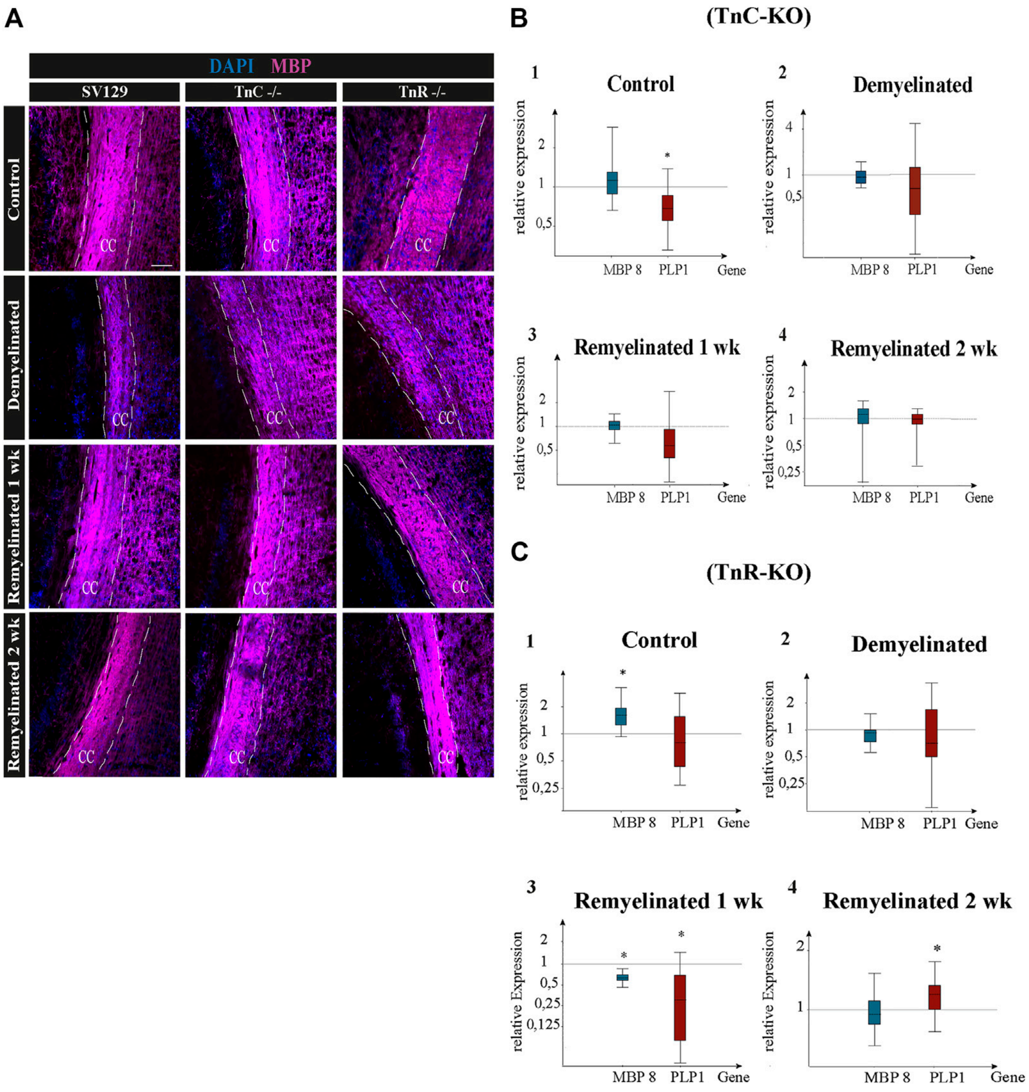

FIGURE 6 | (A–C) Immunolabeling for MBP and gene expression analysis of the myelin genes PLP1 and MBP8 in the corpus callosum of SV129, $Tnc^{-/-}$, and $Tnr^{-/-}$ mice under control, demyelinated, and remyelinated conditions. **(A)** Immunohistochemistry with antibodies against MBP (violet) for visualizing the myelination grade in the corpus callosum of SV129, $Tnc^{-/-}$, and $Tnr^{-/-}$ mice. Four conditions were compared: control, one-week demyelinated (1 wk DM), one-week remyelinated (1 wk RM), and two-weeks remyelinated (2 wk RM). DAPI-staining (blue) shows the cell nuclei in the field of vision. The immunohistochemical staining illustrates an increased intensity of MBP in the area of the corpus callosum in the control condition for the three genotypes. In comparison with the untreated control, MBP-staining of the demyelinated condition was reduced in all genotypes, revealing efficient demyelination by cuprizone. The different genotypes behaved similarly in all four conditions. Scale bars: 100 µm. Using qPCR **(B)**, the expression analysis of the myelin genes MBP and PLP1 was carried out in corpus callosum samples of $Tnc^{-/-}$ and SV129 mice in "control," "demyelinated," "one-week remyelinated (1 wk)," and "two-weeks remyelinated (2 wk)" conditions and was represented graphically with box plots. The expression of MBP and PLP1 was normalized with reference to the control genes RPLP0 and β-actin. The expression of myelin genes in SV129 mice was set as 1. The control condition exhibited nearly unchanged expression of MBP but significantly reduced expression of PLP1 in $Tnc^{-/-}$ samples compared to the SV129 wildtype. The demyelinated condition revealed a downregulation of both myelin genes in $Tnc^{-/-}$ in comparison with SV129 samples. After one week of remyelination, PLP1 was also downregulated in $Tnc^{-/-}$ samples, while MBP expression remained unchanged. After two weeks of remyelination, both genotypes did not differ. **(C)** The expression of both myelin genes in $Tnr^{-/-}$ and SV129 mice was normalized with reference to the control genes RPLP0 and β-actin. The analysis of all data and statistical significance were assessed using LightCycler® 96 and Rest 2009 (*$p \leq 0.05$, **$p \leq 0.01$, ***$p \leq 0.001$). At least three animals were included in each group (N = 3) and genotype ($n = 500$ cells).

MBP-staining was still visible in demyelinated tissue, although demyelination had occurred. Additionally, LFB-staining revealed a reduction of myelin also outside the corpus callosum (**Supplementary Figure S1B**), which suggested effective demyelination in the telencephalon. After one week of remyelination, MBP-staining increased compared to the demyelinated condition (**Figure 6A**). In contrast, LFB-staining did not detect differences between one-week remyelination and the demyelinated condition. Interestingly, brain sections of $Tnc^{-/-}$ and $Tnr^{-/-}$ mice displayed a higher intensity of MBP-labeling after one week of remyelination compared to the wildtype SV129 sections. The histochemical staining intensity increased further after two weeks, clearly suggestive of remyelination. According to histochemistry and to immunohistochemical analysis for MBP, we established successfully the cuprizone model in *Tnc*$^{-/-}$ and *Tnr*$^{-/-}$ mutant mice. Because histological studies relying on LFB–PAS- and MBP-staining did not allow for precise quantification, the expression of two important myelin genes was studied on the mRNA level.

Monitoring Cuprizone-Dependent Myelin Remodeling With Oligodendrocyte Markers

Quantitative PCR was used to analyze the expression of the myelin-specific genes *MBP8* and *PLP1* from the corpus callosum of *Tnc*$^{-/-}$ and *Tnr*$^{-/-}$ mice in the conditions "control," "demyelinated," "one-week remyelinated," and "two weeks remyelinated" (**Figure 6**). The gene expression of *MBP8* and *PLP1* was normalized to the gene expression of the housekeeping genes *RPLP0* and *β-actin* (**Figures 6B,C**). The expression of *MBP8* (relative expression: 1.24) in *Tnc*$^{-/-}$ compared to SV129 samples did not change and was nearly the same in each condition (**Figure 6B**). For *PLP1*, on the contrary, the control (**Figures 6A,B**) was significantly reduced in the corpus callosum of *Tnc*$^{-/-}$ compared to SV129 mice (p = 0.017). In the demyelination condition, a downregulation for both myelin genes was detectable. However, there were hardly any differences between *Tnc*$^{-/-}$ and SV129 mice (relative expression of *MBP8*: 0.952, *PLP1*: 0.679). After one week of remyelination, only a higher expression of *MBP8* (1.051) could be observed (**Figures 6B,C**), whereas *PLP1* was downregulated in *Tnc*$^{-/-}$ compared to SV129 samples (relative expression: 0.626). In comparison with SV129, after two weeks of remyelination, there were no significant differences in myelination-specific expression in the *Tnc*$^{-/-}$ samples (**Figures 6B–D**). In comparison with the SV129 wildtype, a significant upregulation of *MBP8* in the control condition of the *Tnr*$^{-/-}$ mice could be noted. The *PLP1* gene, on the contrary, was weakly downregulated (relative expression of PLP1: 0.80). The demyelinated condition also showed a reduced expression for *MBP8*, whereas *PLP1* was weakly downregulated (relative expression of *MBP8*: 0.910, *PLP1*: 0.812). In the condition "one-week remyelinated," the myelin genes *MBP8* and *PLP1* in the corpus callosum of *Tnr*$^{-/-}$ mice were significantly downregulated (**Figure 6C**) compared to SV129 (*MBP8*, p = 0.001; *PLP1*, p = 0.004). The comparison of the two myelin genes in the *Tnr*$^{-/-}$ genotype yielded a higher expression for *MBP8* compared to *PLP1* (relative expression of *MBP8*: 0.611, *PLP1*: 0.257). After two weeks of remyelination, the expression of *MBP8* in *Tnr*$^{-/-}$ samples appeared reduced (**Figures 6C,D**) compared to the SV129 samples (relative expression: 0.936). For *PLP1*, on the contrary, after two weeks of remyelination, a significantly increased expression (relative expression: 1.183) could be observed in *Tnr*$^{-/-}$ samples compared to SV129 samples (p = 0.036). Overall, for the myelinating gene *PLP1*, in the control condition and after one and two weeks of remyelination, a higher expression in all genotypes compared to *MBP8* was evident.

Comparison of OPCs and Mature Oligodendrocytes in the Cuprizone Model

To gain insight into the oligodendrocyte lineage, studies using the markers Olig2 and CC1 were performed (**Figure 7**). For an individual quantification of mature oligodendrocytes, we carried out Olig2/CC1 double immunostaining to investigate the differentiation process of OPCs dependent on tenascins. Immunopositive cells were counted comparatively in SV129, *Tnc*$^{-/-}$, and *Tnr*$^{-/-}$ mice. In the demyelinated condition, we observed (**Figure 7C**) cells that were Olig2/CC1-positive (demyelination; SV129: 56.10% ± 13.08%, *Tnc*$^{-/-}$: 44.33% ± 21.27%, *Tnr*$^{-/-}$: 50.02% ± 7.27%) compared to the control condition (SV129: 89.31% ± 1.92%, *Tnc*$^{-/-}$: 73.8% ± 15.75%, *Tnr*$^{-/-}$: 79.92% ± 4.11%). The quantitative analysis of Olig2-positive cells confirmed the presence of oligodendroglia in the demyelinated condition for all genotypes (**Figure 7B**). A complete elimination of oligodendroglia, however, could not be detected upon demyelination. The knockout of both tenascins did not substantially modify Olig2- or Olig2/CC1-positive populations in the untreated control condition (C; **Figures 7B,C**). Olig2- and Olig2/CC1-positive OPCs and oligodendrocytes, respectively, were monitored upon demyelination and after one and two weeks of remyelination. Possibly due to the variability of the system, no statistical significance could be achieved in most of the comparisons (**Figures 7A,B**). To accentuate the effects, a more extended exposure to cuprizone might be necessary. Interestingly, after one week of remyelination, however, in comparison with the demyelinated condition, *Tnc*$^{-/-}$ sections presented a significant increase of Olig2-positive cells (**Figure 7B**) and a significant increase of mature oligodendrocytes (*Tnc*$^{-/-}$: 86.41 % ± 2.10%, p = 0.0194) (**Figure 7C**). After two weeks of remyelination, the significant increase of Olig2/CC1-positive cells compared to the demyelinated condition persisted in the *Tnc*$^{-/-}$ knockout (RM2; *Tnc*$^{-/-}$: 84.13% ± 4.24%, p = 0.0330). This might reflect the inhibitory effect of Tnc on OPC migration and maturation, so that, in the absence of Tnc, the immigration of OPCs is favored. This is in agreement with an earlier report showing enhanced invasion of OPCs into the *Tnc*$^{-/-}$ optic nerve (Garcion et al., 2001).

Expression of the DSD-1/Phosphacan Proteoglycan in the Cuprizone Model

A previous study had shown that chondroitin sulfate regulates the proliferative maintenance of OPCs and inhibits further differentiation toward mature oligodendrocytes (Karus et al., 2016). In order to trace a potential inhibitory influence of chondroitin sulfate, we performed immunohistochemical staining of brain sections of SV129, *Tnc*$^{-/-}$, and *Tnr*$^{-/-}$ mice using the markers Olig2 and 473HD. The mAb 473HD reacts with the particular DSD-1-chondroitin sulfate epitope (Faissner et al., 1994a; Clement et al., 1998). To measure the expression level, the corrected total cell fluorescence (CTCF) of the 473HD-positive area in the corpus callosum was determined. In the absence of treatment (**Figure 8**), immunostaining revealed a

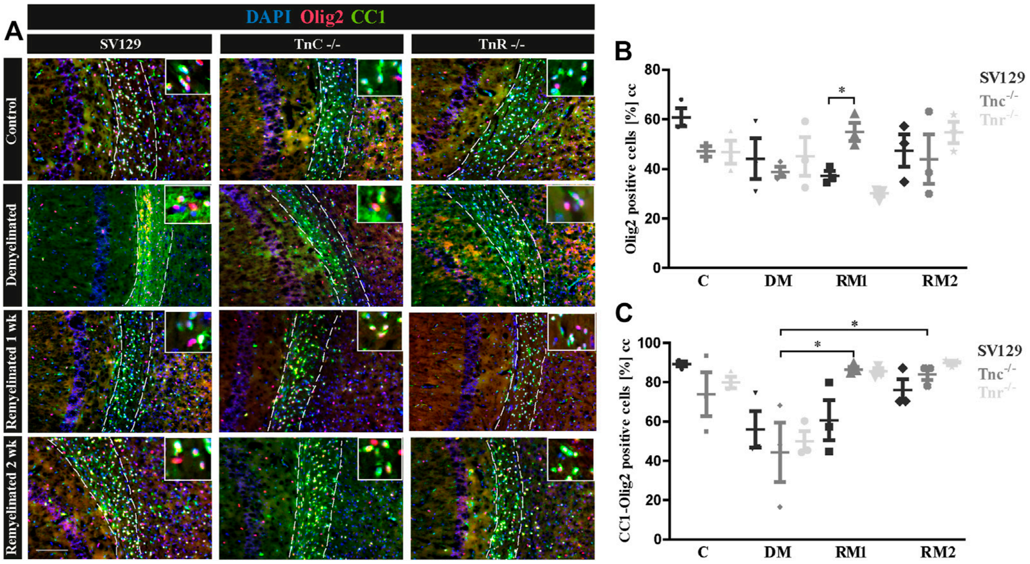

FIGURE 7 | (A–C) Comparison of Olig2/CC1-double immunolabeling in the corpus callosum of SV129, $Tnc^{-/-}$, and $Tnr^{-/-}$ mice under control, demyelinated, and remyelinated conditions. **(A)** Using immunohistochemical labeling with antibodies against Olig2 (detects all oligodendroglia) and CC1 (detects mature oligodendrocytes), the percentage of mature oligodendrocytes in the corpus callosum of *SV129*, $Tnc^{-/-}$, and $Tnr^{-/-}$ mice was compared. The four conditions "control," "demyelinated," "one-week remyelinated," and "two-weeks remyelinated" were examined. DAPI-staining marks cell nuclei in blue color. Olig2 is nucleus-based staining, and CC1 is located in the cytosol. In the absence of treatment, a strong labeling of CC1-positive cells (green) was detectable in the corpus callosum (CC) of all genotypes. Mature CC1/Olig2-positive cells were reduced in the demyelinated condition. **(B)** Quantification of Olig2-positive cells in the particular conditions (C: control, DM: demyelinated, RM1: one-week remyelinated, RM2: two-weeks remyelinated). **(C)** Quantification of CC1/Olig2-double immunopositive cells. The quantification confirms a lower percentage of mature oligodendrocytes in the demyelinated condition compared to the control for all genotypes. All data are provided as mean ± SEM. The statistical significance was assessed by using the two-way ANOVA ($^*p \le 0.05$, $^{**}p \le 0.01$, $^{***}p \le 0.001$) and Tukey's multiple-comparisons test. The micrograph of the illustration was captured via Axiophot. Scale bars: illustration: 100 µm detail, pictures: 50 µm; at least $N = 3$ animals were used for each group and genotype, and at least $n = 500$ cells were evaluated for each individual animal.

higher intensity of 473HD in $Tnc^{-/-}$ and $Tnr^{-/-}$ sections compared to wildtype SV129 (C; SV129: 6442954.67 ± 591709.4, $Tnc^{-/-}$: 8716938.67 ± 3131031.83, $Tnr^{-/-}$: 8495473.33 ± 946020.84, $p = 0.0333$). In contrast, in the demyelinated condition, $Tnc^{-/-}$ and $Tnr^{-/-}$ sections presented a significantly reduced 473HD-staining and fluorescent intensity than those observed in the SV129 WT (DM; SV129: 9264336 ± 149233.09, $Tnc^{-/-}$: 6727202.67 ± 656442.63, $p = 0.0028$, $Tnr^{-/-}$: 8148442.67 ± 164110.66, $p = 0.0010$). Under remyelinated conditions, the intensity of immunostaining in SV129 WT seemed slightly elevated in comparison with that in $Tnc^{-/-}$ and $Tnr^{-/-}$. However, this could not be reflected in measurements of the fluorescence intensity (RM1; SV129: 8811688 ± 284248, $Tnc^{-/-}$: 8906437.33 ± 2579201.47, $Tnr^{-/-}$: 9285434.67 ± 868391.98). After two weeks of remyelination, no differences between the genotypes could be detected (RM2; SV129: 7769445.33 ± 164110.66, $Tnc^{-/-}$: 10327677.33 ± 5335489.68, $Tnr^{-/-}$: 8811688 ± 752049.52). Relating to an increased 473HD-staining and measured fluorescent intensity in $Tnr^{-/-}$ sections under control condition, these results suggest that Tnr has an inhibitory influence on chondroitin sulfates in the absence of treatment. These results are consistent with an inhibitory influence of chondroitin sulfate on oligodendrocyte differentiation. However, in the demyelinated condition, the fluorescence intensity of 473HD in both $Tnc^{-/-}$ and $Tnr^{-/-}$ mice was significantly decreased, which suggests that both tenascins at least in the inflammatory environment are essential for the normal expression of oligodendrocyte precursors.

DISCUSSION

In the present study, we investigated the influence of the glycoproteins Tnc and especially Tnr on the differentiation and remyelination efficiency of oligodendrocytes. Previous studies of the laboratory had revealed that the Tnc protein of the tenascin family of EM glycoproteins exerts inhibitory effects on the differentiation of oligodendrocyte precursor cells *in vitro* (Kiernan et al., 1996; Czopka et al., 2009b). While Tnc is expressed by neural stem cells and astrocyte precursors and downregulated postnatally, Tnr is upregulated during the postnatal period and clearly expressed by a subpopulation of neurons and maturing oligodendrocytes (Czopka et al., 2009b; Faissner et al., 2017). When comparing the $Tnc^{+/+}$ and $Tnc^{-/-}$ explant cultures, the highest degree of myelination was observed in the untreated situation. Overall, the $Tnc^{-/-}$ explants seem to acquire a higher degree of myelination. The addition of lysolecithin led to a strong demyelination, and successful remyelination was achieved upon removal of the compound. In all conditions tested, more myelin was observable in $Tnc^{-/-}$ explants. Tnc inhibits the migration and differentiation of OPCs

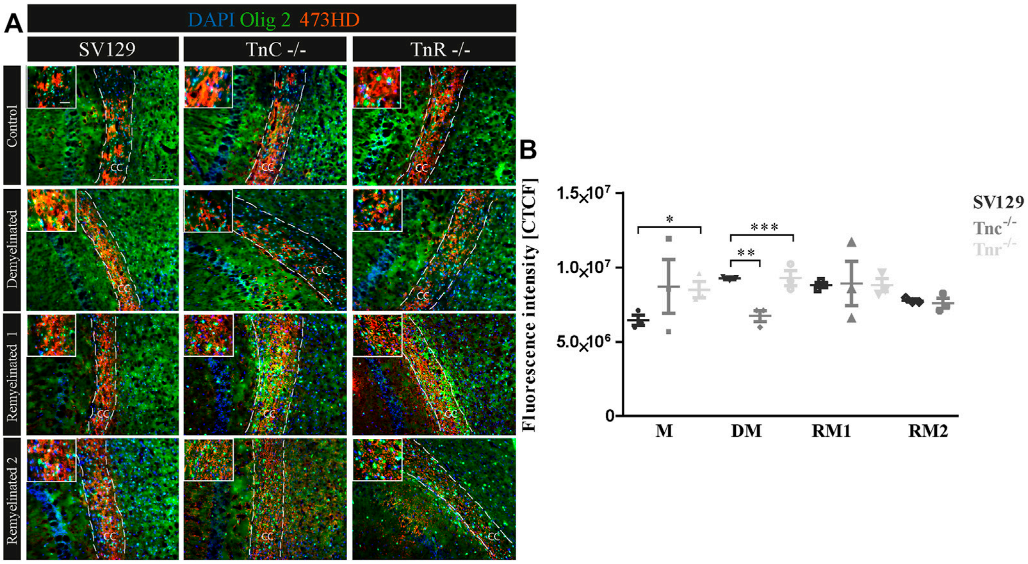

FIGURE 8 | (A,B) Comparative analysis of Olig2/473HD-staining in the corpus callosum of SV129, *Tnc*$^{-/-}$, and *Tnr*$^{-/-}$ mice under control, demyelinated, and remyelinated conditions. Immunohistochemical labeling **(A)** with antibodies against Olig2 (detects all oligodendroglia) and 473HD (detects chondroitin sulfate) of SV129, *Tnc*$^{-/-}$, and *Tnr*$^{-/-}$ brain sections under different conditions (control, demyelinated, one-week remyelinated, two-weeks remyelinated) is shown. **(B)** Quantitative analysis of the 473HD fluorescence intensity (CTCF) in the corpus callosum above the region of the hippocampus. The fluorescence intensity was significantly reduced within the corpus callosum of *Tnr*$^{-/-}$ in control and demyelinated conditions. DAPI stains cell nuclei in blue. Scale bar: illustration: 100 µm, detail pictures: 50 µm. *N* = 3 animals were used for each group and genotype, and at least *n* = 500 cells were evaluated for each individual animal.

after demyelination and thereby reduces the remyelination of demyelinated axons. Alternatively, a Tnc-dependent activation of astrocytes may result in reduced myelination of axons (Nash et al., 2011). Tnc accumulation in demyelinated plaques thus might prevent successful remyelination (Gutowski et al., 1999; Czopka et al., 2009b; Zhao et al., 2009). The comparison of *Tnr*$^{+/+}$ and *Tnr*$^{-/-}$ explant cultures displayed the highest degree of myelination in the untreated situation. In particular, the *Tnr*$^{-/-}$ explants displayed the most extensive myelination. Upon demyelination by addition of lysolecithin, a strong reduction of myelin could be obtained. Compared to normal development, newly formed myelin membranes are thinner upon remyelination (Dubois-Dalcq et al., 2008). After demyelination, a strong increase in the proliferation rate of OPCs ensues in the explants. The OPCs subsequently differentiate into mature oligodendrocytes and myelinate the demyelinated axons (Zhang et al., 2011). Altogether, the *Tnr*$^{-/-}$ explants were characterized by a higher degree of myelination and remyelination than the *Tnr*$^{+/+}$ wildtype. By comparing the several conditions from each genotype in view of myelinated and control conditions, it is noticeable that the myelination index in the control condition is higher than that in the myelinated condition. This is not what one firstly expected because a longer cultivation time might favor ongoing myelination. However, in organotypic slice culture, a timing of myelin onset in white matter lesions was reported, and it was shown that the number of MBP-positive oligodendrocytes was after 9 div higher than after 13 div (Dean et al., 2011). This is consistent with studies reporting that the highest degree of myelination can be observed after 12 div (Zhang et al., 2011; Shen and Yuen, 2020).

As previously reported, the knockout of *Tnc* leads to better myelination and remyelination rates through an interplay of increased migration and differentiation rates (Czopka et al., 2009b; Zhao et al., 2009; Zhang et al., 2011). The analogous inhibitory effect of Tnr on the formation of new myelin membranes and remyelination can be explained by structural similarities between Tnr and Tnc as members of the tenascin gene family. Interestingly, both Tnc and Tnr interfere with the formation of myelin membranes *in vitro* (Czopka et al., 2009b). The inhibitory property of Tnr could explain the comparatively faster remyelination observed in *Tnr*$^{-/-}$ explants. The inhibitory effect of Tnc on OPC migration could be ascribed to FNIII domains 7 and 8 (Kiernan et al., 1996). The corresponding domain responsible in Tnr has not been localized yet. However, previous studies have revealed that both Tnc and Tnr interfere with the activation of RhoA GTPase, which results in an impaired formation of myelin membranes (Wenk et al., 2000; Czopka et al., 2009b). Accordingly, it could be expected that the deletion of Tnr or Tnc unleashes the RhoA GTPase which has a positive effect on the formation of myelin membranes. Along these lines, thicker and more extensive myelin membranes were generated in *Tnr*$^{-/-}$ in comparison with wildtype mice. The myelination process can be divided into two phases: first, the extension of oligodendrocyte processes toward axons and, subsequently, the wrapping of axons with several layers of myelin membranes (Zuchero et al., 2015). Myelin basic protein (MBP) activates actin-degrading proteins such as cofilin and gelsolin, which promotes actin degradation and thereby may support the process of myelin wrapping (Zuchero et al., 2015). However, in the explant paradigm, the expression of MBP did not significantly vary between the wildtype, *Tnc*$^{-/-}$, and *Tnr*$^{-/-}$ tissues.

It is known that ECM components are upregulated after CNS injury, which leads to the formation of a glial scar resulting in an impairment of oligodendrocyte differentiation and remyelination (Lau et al., 2012; Jakovcevski et al., 2013; Deng et al., 2015; Roll and Faissner, 2019; Ghorbani and Yong, 2021). In *ex vivo* slices exposed to purified Tnc protein, the remyelination efficiency was significantly impaired. This is in line with previous studies showing that cultivation of OPCs on a Tnc substrate leads to an impaired differentiation toward MBP-positive oligodendrocytes effected via a reduced Fyn activity. This effect seems to be mediated by contactin-1 (Cntn1) whose activation results not only in a reduced Fyn activity but also in a tampered Sam68 expression. Both genes are required for MBP expression and oligodendrocyte differentiation (Czopka et al., 2010). Treatment of cerebellar explants with 20 μg/ml purified Tnr protein, on the contrary, confined remyelination to the level of the demyelinated situation. This was to be expected because remyelination was more effective in *Tnr*$^{-/-}$ compared to *Tnr*$^{+/+}$ explants and Tnr was known to tamper the formation of myelin membranes (Czopka et al., 2009b). Accordingly, when plain PBS was added to the explants, the interference with remyelination vanished. A straightforward explanation would be that the RhoA-signaling pathway is inhibited by the Tnr protein (Czopka et al., 2009b).

So far, four types of receptors have been identified for Tnc: cell adhesion molecules of the Ig-superfamily, integrins, heparan sulfate proteoglycans, and receptor tyrosine phosphatases (Czopka et al., 2010; Tucker and Chiquet-Ehrismann, 2015). Based on the structural resemblance between Tnr and Tnc, the aforementioned receptors are also conceivable for the ligand Tnr. For example, the cell adhesion molecule F3/F11 (also known as Cntn1) is a neuronal receptor of Tnr and implicated in the regulation of axonal growth (Xiao et al., 1996; Zacharias et al., 2002; Zacharias and Rauch, 2006). Interestingly, F3 is expressed by oligodendrocytes and might hence serve as the Tnr receptor in this cell type as well (Koch et al., 1997).

The outcome of the *in vitro* assays prompted us to investigate potential effects of tenascins on myelin formation *in vivo*. To this end, demyelination was induced with cuprizone, and the subsequent remyelination was studied using LFB–PAS-staining and immunohistochemistry for MBP. The cuprizone model had been successfully established in C57BL/6 mice (Torkildsen et al., 2008) and could also successfully be transferred to the *Tnc*$^{-/-}$ and *Tnr*$^{-/-}$ mice analyzed in our study. Extensive myelin was documented in the corpus callosum, which was expected because myelination is extensive there (Reyes-Haro et al., 2013). Successful demyelination was achieved by cuprizone added to the chow, as revealed by attenuated LFB–PAS-staining in- and outside of the corpus callosum, consistent with previous studies (Skripuletz et al., 2008). Residual myelin proteins and lipids after demyelination were detectable using these markers (Czopka et al., 2009a), as reported by others (Lindner et al., 2008).

The analysis of sequential expression of the myelin genes PLP1 and MBP by qPCR demonstrated successful de- and remyelination in the corpus callosum of SV129 wildtype, *Tnc*$^{-/-}$, and *Tnr*$^{-/-}$ mice and confirmed the successful functionality of the cuprizone model. For all genotypes, demyelination resulted in a significantly reduced expression of PLP1. The cholesterol-associated tetraspanin PLP1 is the major protein of CNS myelin and therefore serves as a reliable indicator of cuprizone-induced demyelination. Interestingly, in the situation of demyelination, PLP1 expression in *Tnc*$^{-/-}$ appeared reduced compared to the wildtype. It must be kept in mind that the degree of demyelination in the corpus callosum fluctuates (Sachs et al., 2014). Thus, more extensive demyelination occurs in the caudal area of the corpus callosum (Steelman et al., 2012), which may explain differences of expression between SV129 and *Tnc*$^{-/-}$ knockout mice.

After one week of remyelination, the expression of MBP remained unchanged, whereas the expression of PLP1 was reduced in *Tnc*$^{-/-}$ compared to the SV129 wildtype mice. As Tnc inhibits the differentiation of OPCs toward the MBP-expressing stage in culture (Kiernan et al., 1996; Czopka et al., 2009b), one would have expected an accelerated maturation of myelin in the *Tnc*$^{-/-}$ tissue, which was not the case. However, MBP and PLP1 merely represent two of the genes involved in myelin formation, which also strongly depends on neuron–glia interactions (Nave, 2010). Furthermore, RNA and protein expression are not always closely correlated. For example, housekeeping genes possess a stable RNA–protein ratio, whereas regulatory proteins are broken down quickly. Also, post-translational modifications may generate a considerable variety of proteins (Stark et al., 2006; Guo et al., 2008; Vogel and Marcotte, 2012). Therefore, a low level of message does not necessarily signify a minor protein amount of PLP1 and MBP in the corpus callosum.

MBP accounts for 30% of the protein amount contributed by PLP1 (Lindner et al., 2008). Post-translational modification of the classic 18.5 kDa MBP may result in the isoforms C1–C8 (Zhang et al., 2012; Harauz and Boggs, 2013). The primers used for qPCR in our case detect all these isoforms. Interestingly, the isoform MBP8 is upregulated in MS patients and would merit further study using isoform-specific primers (Boggs, 2006). In the assays using *ex vivo* cerebellar explants, the recovery of MBP in demyelinated tissue was significantly retarded in the *Tnr*$^{-/-}$ specimen after one week of remyelination. This is consistent with our former observation that Tnr promotes temporal differentiation of OPCs *in vitro* (Czopka et al., 2009b).

In order to address the differentiation process of OPCs dependent on tenascin proteins *in vivo*, the tissues were studied using the markers Olig2 and CC1 in combination. Demyelination by cuprizone caused a reduced proportion of immature oligodendrocytes and oligodendroglia in all genotypes compared to the untreated control. This reflects the fact that cuprizone disrupts the mitochondrial metabolism and thereby causes the death of oligodendrocytes (Lindner et al., 2008; Skripuletz et al., 2008; Torkildsen et al., 2008; Kipp et al., 2009; Sachs et al., 2014). The degree of demyelination, however, fluctuates and can vary in the tissue (Sachs et al., 2014). Therefore, the elimination of oligodendrocytes was not complete. After one week of remyelination, a significant increase of oligodendroglia could be noted, especially in *Tnc*$^{-/-}$ brain slices. Previous studies have pointed out that Tnc has an inhibitory effect on the migration and differentiation of OPCs (Kiernan et al., 1996; Garcion et al., 2001; Garwood et al., 2004; Czopka et al., 2009b; Jakovcevski et al., 2013; Brosicke and Faissner, 2015). Along these lines, our results are consistent with the interpretation that Tnc retards the differentiation of OPCs to mature oligodendrocytes. Therefore, it is conceivable that the OPCs migrate more efficiently to the demyelinated areas after demyelination in the $Tnc^{-/-}$ mice than in the wildtype mice. Altogether, we had the impression that remyelination was eased in $Tnc^{-/-}$ and $Tnr^{-/-}$ compared to SV129 wildtype brain slices. This effect, however, was weak and did not attain statistical significance after the short six weeks of exposure to cuprizone. Whether the observed inhibitory properties of tenascins on remyelination become more effective in a model of chronic demyelination has to be tested in future studies. Of note, the development of EAE was tampered in the $Tnc^{-/-}$ mice (Momcilovic et al., 2017).

Recent studies indicated that chondroitin sulfate proteoglycans (CSPGs) maintain OPCs in a proliferative state and inhibit further differentiation into mature oligodendrocytes (Karus et al., 2016; Keough et al., 2016). We have shown previously that OPCs express the DSD-1/phosphacan CSPG epitope recognized by the monoclonal antibody 473HD and used this marker and Olig2 to investigate CSPG expression by OPCs in our model (Faissner et al., 1994b; Garwood et al., 1999; Karus et al., 2016). The DSD-1-epitope is downregulated with maturation of OPCs which would result in reduced expression in maturing tissue. The observation that the epitope is well detectable in our models suggests that, in addition to oligodendrocytes, other cell types such as astrocytes secrete CSPGs into the ECM (Maeda et al., 2010; Okuda et al., 2014). An accelerated maturation of OPCs in $Tnc^{-/-}$ and $Tnr^{-/-}$ tissues after cuprizone-induced demyelination could be explained by the observation that OPCs mature faster in the absence of tenascins. Mature oligodendrocytes no longer secrete chondroitin sulfate (Galtrey and Fawcett, 2007). Along these lines, the increased proportion of CSPG in the demyelinated SV129 wildtype could be explained by the inhibitory effect of tenascins on the differentiation of OPCs. After remyelination, a lower level of CSPG in tenascin knockouts than in SV129 wildtype mice was detectable. This observation may indicate a greater remyelination efficiency in the absence of both tenascins. This may be a consequence of an increased transition of OPCs from the proliferative to the differentiative state. The co-labeling with the markers Olig2 and CC1 confirmed that more mature oligodendrocytes were formed in the absence of Tnc and Tnr in the remyelination condition after one week than in the wildtype, where a higher amount of CSPG was observed. Remyelination is promoted by inhibiting the synthesis of CSPGs (Keough et al., 2016; Pu et al., 2018). The presence of CSPGs retards the maturation of OPCs and prevents their further differentiation (Galtrey and Fawcett, 2007; Lau et al., 2012). Interestingly, both CSPGs and tenascins are upregulated after brain injuries, in particular also in MS lesions (Dauth et al., 2016). Our observations so far are in agreement with the asserted inhibitory influence of CSPGs on OPC differentiation and remyelination. The tenascins bind to the CSPGs aggrecan, phosphacan, neurocan, and versican (Perides et al., 1993; Jakovcevski et al., 2013). The joint occurrence of CSPGs and tenascins in the ECM of MS patients as well as the reduced 473HD labeling in $Tnc^{-/-}$ and $Tnr^{-/-}$ brain sections might indicate that an interaction between the two ECM molecules could cooperate with regard to the inhibitory effect on remyelination (Ghorbani and Yong, 2021).

Taken together, this study revealed that both Tnc and Tnr intervene in the remyelination capacity of oligodendrocytes. This could be shown by studying the remyelination behavior of WT and knockout specimens, and by adding the purified ECM proteins to lysolecithin-treated WT cerebellar explants. In order to examine their roles in an *in vivo* situation, the cuprizone model was successfully established in $Tnc^{-/-}$ and $Tnr^{-/-}$ mice, as confirmed by LFB- and MBP-staining. While demyelination and remyelination occurred as expected, the differences between the WT, $Tnc^{-/-}$, and $Tnr^{-/-}$ mouse lines were small and did not achieve statistical significance with respect to several parameters. This may be due to the duration of the exposure to cuprizone, which was limited to six weeks, reflecting an acute lesion situation. The tendencies observed may become relevant in a chronic setting, where cuprizone treatment could be extended to ten weeks. The roles of tenascins in the mimic of a chronic disease course remain to be explored in a future study.

DATA AVAILABILITY STATEMENT

The raw data supporting the conclusions of this article will be made available by the authors, without undue reservation.

ETHICS STATEMENT

The animal study was reviewed and approved by LANUV, North Rhine-Westfalia, Germany, license AZ 84-02.04-2014.A332.

AUTHOR CONTRIBUTIONS

AF designed and supervised the study. JB performed the experiments, quantified the data, and drafted the manuscript. AF and JB interpreted the data and revised the manuscript. All authors contributed to the article and approved the submitted version.

FUNDING

This work was funded by the German Research Foundation (DFG, FA 159/24-1 to AF). We acknowledge support from the DFG Open Access Publication Funds of Ruhr-Universität Bochum.

ACKNOWLEDGMENTS

We acknowledge Mrs. Marion Voelzkow and Stephanie Chun for technical support.

SUPPLEMENTARY MATERIAL

The Supplementary Material for this article can be found online at: https://www.frontiersin.org/articles/10.3389/fcell.2022.819967/full#supplementary-material

REFERENCES

Barros, C. S., Franco, S. J., and Muller, U. (2011). Extracellular Matrix: Functions in the Nervous System. *Cold Spring Harbor Perspect. Biol.* 3 (1), a005108. doi:10.1101/cshperspect.a005108

Bartsch, S., Bartsch, U., Dorries, U., Faissner, A., Weller, A., Ekblom, P., et al. (1992). Expression of Tenascin in the Developing and Adult Cerebellar Cortex. *J. Neurosci.* 12 (3), 736–749. doi:10.1523/JNEUROSCI.12-03-00736.1992

Becker, T., Anliker, B., Becker, C. G., Taylor, J., Schachner, M., Meyer, R. L., et al. (2000). Tenascin-R Inhibits Regrowth of Optic Fibers *In Vitro* and Persists in the Optic Nerve of Mice after Injury. *Glia* 29 (4), 330–346. doi:10.1002/(sici)1098-1136(20000215)29:4<330::aid-glia4>3.0.co;2-l

Birgbauer, E., Rao, T. S., and Webb, M. (2004). Lysolecithin Induces Demyelination *In Vitro* in a Cerebellar Slice Culture System. *J. Neurosci. Res.* 78 (2), 157–166. doi:10.1002/jnr.20248

Boggs, J. M. (2006). Myelin Basic Protein: a Multifunctional Protein. *Cell. Mol. Life Sci.* 63 (17), 1945–1961. doi:10.1007/s00018-006-6094-7

Bolte, S., and Cordelières, F. P. (2006). A Guided Tour into Subcellular Colocalization Analysis in Light Microscopy. *J. Microsc.* 224 (Pt 3), 213–232. doi:10.1111/j.1365-2818.2006.01706.x

Bradl, M., and Lassmann, H. (2010). Oligodendrocytes: Biology and Pathology. *Acta Neuropathol.* 119 (1), 37–53. doi:10.1007/s00401-009-0601-5

Brösicke, N., and Faissner, A. (2015). Role of Tenascins in the ECM of Gliomas. *Cell Adhes. Migration* 9 (1-2), 131–140. doi:10.1080/19336918.2014.1000071

Clement, A. M., Nadanaka, S., Masayama, K., Mandl, C., Sugahara, K., and Faissner, A. (1998). The DSD-1 Carbohydrate Epitope Depends on Sulfation, Correlates with Chondroitin Sulfate D Motifs, and Is Sufficient to Promote Neurite Outgrowth. *J. Biol. Chem.* 273 (43), 28444–28453. doi:10.1074/jbc.273.43.28444

Czopka, T., Hennen, E., von Holst, A., and Faissner, A. (2009a). Novel Conserved Oligodendrocyte Surface Epitope Identified by Monoclonal Antibody 4860. *Cell Tissue Res* 338 (2), 161–170. doi:10.1007/s00441-009-0868-9

Czopka, T., von Holst, A., ffrench-Constant, C., and Faissner, A. (2010). Regulatory Mechanisms that Mediate Tenascin C-dependent Inhibition of Oligodendrocyte Precursor Differentiation. *J. Neurosci.* 30 (37), 12310–12322. doi:10.1523/JNEUROSCI.4957-09.2010

Czopka, T., Von Holst, A., Schmidt, G., Ffrench-Constant, C., and Faissner, A. (2009b). Tenascin C and Tenascin R Similarly Prevent the Formation of Myelin Membranes in a RhoA-dependent Manner, but Antagonistically Regulate the Expression of Myelin Basic Protein via a Separate Pathway. *Glia* 57 (16), 1790–1801. doi:10.1002/glia.20891

Dauth, S., Grevesse, T., Pantazopoulos, H., Campbell, P. H., Maoz, B. M., Berretta, S., et al. (2016). Extracellular Matrix Protein Expression Is Brain Region Dependent. *J. Comp. Neurol.* 524 (7), 1309–1336. doi:10.1002/cne.23965

De Santis, I., Lorenzini, L., Moretti, M., Martella, E., Lucarelli, E., Calzà, L., et al. (2021). Co-Density Distribution Maps for Advanced Molecule Colocalization and Co-distribution Analysis. *Sensors* 21 (19), 6385. doi:10.3390/s21196385

Dean, J. M., Riddle, A., Maire, J., Hansen, K. D., Preston, M., Barnes, A. P., et al. (2011). An Organotypic Slice Culture Model of Chronic white Matter Injury with Maturation Arrest of Oligodendrocyte Progenitors. *Mol. Neurodegeneration* 6, 46. doi:10.1186/1750-1326-6-46

Deng, Y.-P., Sun, Y., Hu, L., Li, Z.-H., Xu, Q.-M., Pei, Y.-L., et al. (2015). Chondroitin Sulfate Proteoglycans Impede Myelination by Oligodendrocytes after Perinatal white Matter Injury. *Exp. Neurol.* 269, 213–223. doi:10.1016/j.expneurol.2015.03.026

Dityatev, A., Schachner, M., and Sonderegger, P. (2010). The Dual Role of the Extracellular Matrix in Synaptic Plasticity and Homeostasis. *Nat. Rev. Neurosci.* 11 (11), 735–746. doi:10.1038/nrn2898

Dubois-Dalcq, M., Williams, A., Stadelmann, C., Stankoff, B., Zalc, B., and Lubetzki, C. (2008). From Fish to Man: Understanding Endogenous Remyelination in central Nervous System Demyelinating Diseases. *Brain* 131 (Pt 7), 1686–1700. doi:10.1093/brain/awn076

Faissner, A., Scholze, A., and Götz, B. (1994b). Tenascin Glycoproteins in Developing Neural Tissues: Only Decoration? *Perspect. Dev. Neurobiol.* 2 (1), 53–66.

Faissner, A., Clement, A., Lochter, A., Streit, A., Mandl, C., and Schachner, M. (1994a). Isolation of a Neural Chondroitin Sulfate Proteoglycan with Neurite Outgrowth Promoting Properties. *J. Cell Biol* 126 (3), 783–799. doi:10.1083/jcb.126.3.783

Faissner, A., and Kruse, J. (1990). J1/tenascin Is a Repulsive Substrate for central Nervous System Neurons. *Neuron* 5 (5), 627–637. doi:10.1016/0896-6273(90)90217-4

Faissner, A., and Reinhard, J. (2015). The Extracellular Matrix Compartment of Neural Stem and Glial Progenitor Cells. *Glia* 63 (8), 1330–1349. doi:10.1002/glia.22839

Faissner, A., Roll, L., and Theocharidis, U. (2017). Tenascin-C in the Matrisome of Neural Stem and Progenitor Cells. *Mol. Cell Neurosci.* 81, 22–31. doi:10.1016/j.mcn.2016.11.003

Franklin, R. J. M., and Ffrench-Constant, C. (2017). Regenerating CNS Myelin - from Mechanisms to Experimental Medicines. *Nat. Rev. Neurosci.* 18 (12), 753–769. doi:10.1038/nrn.2017.136

Franklin, R. J. M., and Ffrench-Constant, C. (2008). Remyelination in the CNS: from Biology to Therapy. *Nat. Rev. Neurosci.* 9 (11), 839–855. doi:10.1038/nrn2480

Galtrey, C. M., and Fawcett, J. W. (2007). The Role of Chondroitin Sulfate Proteoglycans in Regeneration and Plasticity in the central Nervous System. *Brain Res. Rev.* 54 (1), 1–18. doi:10.1016/j.brainresrev.2006.09.006

Garcion, E., Faissner, A., and ffrench-Constant, C. (2001). Knockout Mice Reveal a Contribution of the Extracellular Matrix Molecule Tenascin-C to Neural Precursor Proliferation and Migration. *Development* 128 (13), 2485–2496. doi:10.1242/dev.128.13.2485

Garwood, J., Garcion, E., Dobbertin, A., Heck, N., Calco, V., ffrench-Constant, C., et al. (2004). The Extracellular Matrix Glycoprotein Tenascin-C Is Expressed by Oligodendrocyte Precursor Cells and Required for the Regulation of Maturation Rate, Survival and Responsiveness to Platelet-Derived Growth Factor. *Eur. J. Neurosci.* 20 (10), 2524–2540. doi:10.1111/j.1460-9568.2004.03727.x

Garwood, J., Schnädelbach, O., Clement, A., Schütte, K., Bach, A., and Faissner, A. (1999). DSD-1-proteoglycan Is the Mouse Homolog of Phosphacan and Displays Opposing Effects on Neurite Outgrowth Dependent on Neuronal Lineage. *J. Neurosci.* 19 (10), 3888–3899. doi:10.1523/JNEUROSCI.19-10-03888.1999

Ghorbani, S., and Yong, V. W. (2021). The Extracellular Matrix as Modifier of Neuroinflammation and Remyelination in Multiple Sclerosis. *Brain* 144, 1958–1973. doi:10.1093/brain/awab059

Goldman, S. A., and Kuypers, N. J. (2015). How to Make an Oligodendrocyte. *Development* 142 (23), 3983–3995. doi:10.1242/dev.126409

Guo, Y., Xiao, P., Lei, S., Deng, F., Xiao, G. G., Liu, Y., et al. (2008). How Is mRNA Expression Predictive for Protein Expression? A Correlation Study on Human Circulating Monocytes. *Acta Biochim. Biophys. Sinica* 40 (5), 426–436. doi:10.1111/j.1745-7270.2008.00418.x

Gutowski, N. J., Newcombe, J., and Cuzner, M. L. (1999). Tenascin-R and C in Multiple Sclerosis Lesions: Relevance to Extracellular Matrix Remodelling. *Neuropathol. Appl. Neurobiol.* 25 (3), 207–214. doi:10.1046/j.1365-2990.1999.00176.x

Haage, V., Elmadany, N., Roll, L., Faissner, A., Gutmann, D. H., Semtner, M., et al. (2019). Tenascin C Regulates Multiple Microglial Functions Involving TLR4 Signaling and HDAC1. *Brain Behav. Immun.* 81, 470–483. doi:10.1016/j.bbi.2019.06.047

Hagemeier, K., Brück, W., and Kuhlmann, T. (2012). Multiple Sclerosis - Remyelination Failure as a Cause of Disease Progression. *Histol. Histopathol* 27 (3), 277–287. doi:10.14670/HH-27.277

Harauz, G., and Boggs, J. M. (2013). Myelin Management by the 18.5-kDa and 21.5-kDa Classic Myelin Basic Protein Isoforms. *J. Neurochem.* 125 (3), 334–361. doi:10.1111/jnc.12195

Hertz, L., and Chen, Y. (2016). Editorial: All 3 Types of Glial Cells Are Important for Memory Formation. *Front. Integr. Neurosci.* 10, 31. doi:10.3389/fnint.2016.00031

Hillis, J. M., Davies, J., Mundim, M. V., Al-Dalahmah, O., and Szele, F. G. (2016). Cuprizone Demyelination Induces a Unique Inflammatory Response in the Subventricular Zone. *J. Neuroinflammation* 13 (1), 190. doi:10.1186/s12974-016-0651-2

Hughes, E. G., and Appel, B. (2016). The Cell Biology of CNS Myelination. *Curr. Opin. Neurobiol.* 39, 93–100. doi:10.1016/j.conb.2016.04.013

Jakovcevski, I., Miljkovic, D., Schachner, M., and Andjus, P. R. (2013). Tenascins and Inflammation in Disorders of the Nervous System. *Amino Acids* 44 (4), 1115–1127. doi:10.1007/s00726-012-1446-0

Karus, M., Denecke, B., ffrench-Constant, C., Wiese, S., and Faissner, A. (2011). The Extracellular Matrix Molecule Tenascin C Modulates Expression Levels and Territories of Key Patterning Genes during Spinal Cord Astrocyte Specification. *Development* 138 (24), 5321–5331. doi:10.1242/dev.067413

Karus, M., Ulc, A., Ehrlich, M., Czopka, T., Hennen, E., Fischer, J., et al. (2016). Regulation of Oligodendrocyte Precursor Maintenance by Chondroitin Sulphate Glycosaminoglycans. *Glia* 64 (2), 270–286. doi:10.1002/glia.22928

Keough, M. B., Rogers, J. A., Zhang, P., Jensen, S. K., Stephenson, E. L., Chen, T., et al. (2016). An Inhibitor of Chondroitin Sulfate Proteoglycan Synthesis Promotes central Nervous System Remyelination. *Nat. Commun.* 7, 11312. doi:10.1038/ncomms11312

Kiernan, B. W., Götz, B., Faissner, A., and ffrench-Constant, C. (1996). Tenascin-C Inhibits Oligodendrocyte Precursor Cell Migration by Both Adhesion-dependent and Adhesion-independent Mechanisms. *Mol. Cell Neurosci.* 7 (4), 322–335. doi:10.1006/mcne.1996.0024

Kipp, M., Clarner, T., Dang, J., Copray, S., and Beyer, C. (2009). The Cuprizone Animal Model: New Insights into an Old story. *Acta Neuropathol.* 118 (6), 723–736. doi:10.1007/s00401-009-0591-3

Koch, T., Brugger, T., Bach, A., Gennarini, G., and Trotter, J. (1997). Expression of the Immunoglobulin Superfamily Cell Adhesion Molecule F3 by Oligodendrocyte-Lineage Cells. *Glia* 19 (3), 199–212. doi:10.1002/(sici)1098-1136(199703)19:3<199::aid-glia3>3.0.co;2-v

Lau, L. W., Keough, M. B., Haylock-Jacobs, S., Cua, R., Döring, A., Sloka, S., et al. (2012). Chondroitin Sulfate Proteoglycans in Demyelinated Lesions Impair Remyelination. *Ann. Neurol.* 72 (3), 419–432. doi:10.1002/ana.23599

Lindner, M., Heine, S., Haastert, K., Garde, N., Fokuhl, J., Linsmeier, F., et al. (2008). Sequential Myelin Protein Expression during Remyelination Reveals Fast and Efficient Repair after central Nervous System Demyelination. *Neuropathol. Appl. Neurobiol.* 34 (1), 105–114. doi:10.1111/j.1365-2990.2007.00879.x

Maeda, N., Fukazawa, N., and Ishii, M. (2010). Chondroitin Sulfate Proteoglycans in Neural Development and Plasticity. *Front. Biosci.* 15, 626–644. doi:10.2741/3637

Matsushima, G. K., and Morell, P. (2001). The Neurotoxicant, Cuprizone, as a Model to Study Demyelination and Remyelination in the central Nervous System. *Brain Pathol.* 11 (1), 107–116. doi:10.1111/j.1750-3639.2001.tb00385.x

Miller, R. H. (2002). Regulation of Oligodendrocyte Development in the Vertebrate CNS. *Prog. Neurobiol.* 67 (6), 451–467. doi:10.1016/s0301-0082(02)00058-8

Miron, V. E., Boyd, A., Zhao, J.-W., Yuen, T. J., Ruckh, J. M., Shadrach, J. L., et al. (2013). M2 Microglia and Macrophages Drive Oligodendrocyte Differentiation during CNS Remyelination. *Nat. Neurosci.* 16 (9), 1211–1218. doi:10.1038/nn.3469

Miron, V. E., Kuhlmann, T., and Antel, J. P. (2011). Cells of the Oligodendroglial Lineage, Myelination, and Remyelination. *Biochim. Biophys. Acta (Bba) - Mol. Basis Dis.* 1812 (2), 184–193. doi:10.1016/j.bbadis.2010.09.010

Momčilović, M., Stamenković, V., Jovanović, M., Andjus, P. R., Jakovčevski, I., Schachner, M., et al. (2017). Tenascin-C Deficiency Protects Mice from Experimental Autoimmune Encephalomyelitis. *J. Neuroimmunology* 302, 1–6. doi:10.1016/j.jneuroim.2016.12.001

Moritz, S., Lehmann, S., Faissner, A., and von Holst, A. (2008). An Induction Gene Trap Screen in Neural Stem Cells Reveals an Instructive Function of the Niche and Identifies the Splicing Regulator Sam68 as a Tenascin-C-Regulated Target Gene. *Stem Cells* 26 (9), 2321–2331. doi:10.1634/stemcells.2007-1095

Nash, B., Thomson, C. E., Linington, C., Arthur, A. T., McClure, J. D., McBride, M. W., et al. (2011). Functional Duality of Astrocytes in Myelination. *J. Neurosci.* 31 (37), 13028–13038. doi:10.1523/JNEUROSCI.1449-11.2011

Nave, K.-A. (2010). Myelination and Support of Axonal Integrity by Glia. *Nature* 468 (7321), 244–252. doi:10.1038/nature09614

Okuda, H., Tatsumi, K., Morita, S., Shibukawa, Y., Korekane, H., Horii-Hayashi, N., et al. (2014). Chondroitin Sulfate Proteoglycan Tenascin-R Regulates Glutamate Uptake by Adult Brain Astrocytes. *J. Biol. Chem.* 289 (5), 2620–2631. doi:10.1074/jbc.M113.504787

Patani, R., Balaratnam, M., Vora, A., and Reynolds, R. (2007). Remyelination Can Be Extensive in Multiple Sclerosis Despite a Long Disease Course. *Neuropathol. Appl. Neurobiol.* 33 (3), 277–287. doi:10.1111/j.1365-2990.2007.00805.x

Perides, G., Erickson, H., Rahemtulla, F., and Bignami, A. (1993). Colocalization of Tenascin with Versican, a Hyaluronate-Binding Chondroitin Sulfate Proteoglycan. *Anat. Embryol.* 188 (5), 467–479. doi:10.1007/BF00190141

Pesheva, P., Gloor, S., Schachner, M., and Probstmeier, R. (1997). Tenascin-R Is an Intrinsic Autocrine Factor for Oligodendrocyte Differentiation and Promotes Cell Adhesion by a SulfatideMediated Mechanism. *J. Neurosci.* 17 (12), 4642–4651. doi:10.1523/JNEUROSCI.17-12-04642.1997

Pu, A., Stephenson, E. L., and Yong, V. W. (2018). The Extracellular Matrix: Focus on Oligodendrocyte Biology and Targeting CSPGs for Remyelination Therapies. *Glia* 66 (9), 1809–1825. doi:10.1002/glia.23333

Ransohoff, R. M. (2012). Animal Models of Multiple Sclerosis: the Good, the Bad and the Bottom Line. *Nat. Neurosci.* 15 (8), 1074–1077. doi:10.1038/nn.3168

Rathjen, F. G., and Hodge, R. (2020). Early Days of Tenascin-R Research: Two Approaches Discovered and Shed Light on Tenascin-R. *Front. Immunol.* 11, 612482. doi:10.3389/fimmu.2020.612482

Reyes-Haro, D., Mora-Loyola, E., Soria-Ortiz, B., and García-Colunga, J. (2013). Regional Density of Glial Cells in the Rat Corpus Callosum. *Biol. Res.* 46 (1), 27–32. doi:10.4067/S0716-97602013000100004

Roll, L., and Faissner, A. (2019). Tenascins in CNS Lesions. *Semin. Cell Developmental Biol.* 89, 118–124. doi:10.1016/j.semcdb.2018.09.012

Sachs, H. H., Bercury, K. K., Popescu, D. C., Narayanan, S. P., and Macklin, W. B. (2014). A New Model of Cuprizone-Mediated Demyelination/remyelination. *ASN Neuro* 6 (5), 175909141455195. doi:10.1177/1759091414551955

Shen, K., and Yuen, T. J. (2020). *Ex Vivo* Myelination and Remyelination in Cerebellar Slice Cultures as a Quantitative Model for Developmental and Disease-Relevant Manipulations. *JoVE* 160. doi:10.3791/61044

Skripuletz, T., Lindner, M., Kotsiari, A., Garde, N., Fokuhl, J., Linsmeier, F., et al. (2008). Cortical Demyelination Is Prominent in the Murine Cuprizone Model and Is Strain-dependent. *Am. J. Pathol.* 172 (4), 1053–1061. doi:10.2353/ajpath.2008.070850

Sospedra, M. (2018). B Cells in Multiple Sclerosis. *Curr. Opin. Neurol.* 31 (3), 256–262. doi:10.1097/WCO.0000000000000563

Stark, A. M., Pfannenschmidt, S., Tscheslog, H., Maass, N., Rösel, F., Mehdorn, H. M., et al. (2006). Reduced mRNA and Protein Expression of BCL-2 versus Decreased mRNA and Increased Protein Expression of BAX in Breast Cancer Brain Metastases: a Real-Time PCR and Immunohistochemical Evaluation. *Neurol. Res.* 28 (8), 787–793. doi:10.1179/016164106X110364

Steelman, A. J., Thompson, J. P., and Li, J. (2012). Demyelination and Remyelination in Anatomically Distinct Regions of the Corpus Callosum Following Cuprizone Intoxication. *Neurosci. Res.* 72 (1), 32–42. doi:10.1016/j.neures.2011.10.002

Torkildsen, Ø., Brunborg, L. A., Myhr, K.-M., and Bø, L. (2008). The Cuprizone Model for Demyelination. *Acta Neurol. Scand.* 117, 72–76. doi:10.1111/j.1600-0404.2008.01036.x

Tucker, R., Drabikowski, K., Hess, J., Ferralli, J., Chiquet-Ehrismann, R., and Adams, J. (2006). Phylogenetic Analysis of the Tenascin Gene Family: Evidence of Origin Early in the Chordate Lineage. *BMC Evol. Biol.* 6, 60. doi:10.1186/1471-2148-6-60

Tucker, R. P., and Chiquet-Ehrismann, R. (2015). Tenascin-C: Its Functions as an Integrin Ligand. *Int. J. Biochem. Cell Biol.* 65, 165–168. doi:10.1016/j.biocel.2015.06.003

Ulc, A., Zeug, A., Bauch, J., van Leeuwen, S., Kuhlmann, T., Ffrench-Constant, C., et al. (2019). The Guanine Nucleotide Exchange Factor Vav3 Modulates Oligodendrocyte Precursor Differentiation and Supports Remyelination in white Matter Lesions. *Glia* 67 (2), 376–392. doi:10.1002/glia.23548

Vogel, C., and Marcotte, E. M. (2012). Insights into the Regulation of Protein Abundance from Proteomic and Transcriptomic Analyses. *Nat. Rev. Genet.* 13 (4), 227–232. doi:10.1038/nrg3185

Wenk, M. B., Midwood, K. S., and Schwarzbauer, J. E. (2000). Tenascin-C Suppresses Rho Activation. *J. Cell Biol* 150 (4), 913–920. doi:10.1083/jcb.150.4.913

Wheeler, N. A., and Fuss, B. (2016). Extracellular Cues Influencing Oligodendrocyte Differentiation and (Re)myelination. *Exp. Neurol.* 283 (Pt B), 512–530. doi:10.1016/j.expneurol.2016.03.019

Xiang, Z., Nesterov, E. E., Skoch, J., Lin, T., Hyman, B. T., Swager, T. M., et al. (2005). Detection of Myelination Using a Novel Histological Probe. *J. Histochem. Cytochem.* 53 (12), 1511–1516. doi:10.1369/jhc.5A6704.2005

Xiao, Z.-c., Taylor, J., Montag, D., Rougon, G., and Schachner, M. (1996). Distinct Effects of Recombinant Tenascin-R Domains in Neuronal Cell Functions and Identification of the Domain Interacting with the Neuronal Recognition Molecule F3/11. *Eur. J. Neurosci.* 8 (4), 766–782. doi:10.1111/j.1460-9568.1996.tb01262.x

Zacharias, U., Leuschner, R., Norenberg, U., and Rathjen, F. G. (2002). Tenascin-R Induces Actin-Rich Microprocesses and Branches along Neurite Shafts. *Mol. Cell Neurosci.* 21 (4), 626–633. doi:10.1006/mcne.2002.1203

Zacharias, U., and Rauch, U. (2006). Competition and Cooperation between Tenascin-R, Lecticans and Contactin 1 Regulate Neurite Growth and Morphology. *J. Cell Sci* 119 (Pt 16), 3456–3466. doi:10.1242/jcs.03094

Zhang, C., Walker, A. K., Zand, R., Moscarello, M. A., Yan, J. M., and Andrews, P. C. (2012). Myelin Basic Protein Undergoes a Broader Range of Modifications in Mammals Than in Lower Vertebrates. *J. Proteome Res.* 11 (10), 4791–4802. doi:10.1021/pr201196e

Zhang, H., Jarjour, A. A., Boyd, A., and Williams, A. (2011). Central Nervous System Remyelination in Culture - A Tool for Multiple Sclerosis Research. *Exp. Neurol.* 230 (1), 138–148. doi:10.1016/j.expneurol.2011.04.009

Zhang, S.-C. (2001). Defining Glial Cells during CNS Development. *Nat. Rev. Neurosci.* 2 (11), 840–843. doi:10.1038/35097593

Zhao, C., Fancy, S. P. J., Franklin, R. J. M., and ffrench-Constant, C. (2009). Up-regulation of Oligodendrocyte Precursor Cell αV Integrin and its Extracellular Ligands during central Nervous System Remyelination. *J. Neurosci. Res.* 87 (15), 3447–3455. doi:10.1002/jnr.22231

Zuchero, J. B., Fu, M.-m., Sloan, S. A., Ibrahim, A., Olson, A., Zaremba, A., et al. (2015). CNS Myelin Wrapping Is Driven by Actin Disassembly. *Developmental Cell* 34 (2), 152–167. doi:10.1016/j.devcel.2015.06.011

Conflict of Interest: The authors declare that the research was conducted in the absence of any commercial or financial relationships that could be construed as a potential conflict of interest.

frontiers
in Bioengineering and Biotechnology

ORIGINAL RESEARCH
published: 30 March 2022
doi: 10.3389/fbioe.2022.796076

Pulmonary Visceral Pleura Biomaterial: Elastin- and Collagen-Based Extracellular Matrix

Xiao Lu, Ling Han and Ghassan S. Kassab *

California Medical Innovations Institute, San Diego, CA, United States

Objective: The goal of the study is to determine the structural characteristics, mechanical properties, cytotoxicity, and biocompatibility of the pulmonary visceral pleura (PVP).

Background: Collagen and elastin are the major components of the extracellular matrix. The PVP has an abundance of elastin and collagen that can serve as a potential biomaterial for clinical repair and reconstructions.

Methods: The PVP was processed from swine and bovine lungs. Chemical analyses were used to determine collagen and elastin contents in the PVPs. Immunofluorescence microscopy was used to analyze the structure of the PVP. The stress–strain relationships and stress relaxation were determined by using the planar uniaxial test. The cytotoxicity of the PVP was tested in cultured cells. In *in vivo* evaluations, the PVP was implanted in the sciatic nerve and skin of rats.

Results: Collagen and elastin contents are abundant in the PVP with larger proportions of elastin than in the bovine pericardium and porcine small intestinal submucosa. A microstructural analysis revealed that the elastin fibers were distributed throughout the PVP and the collagen was distributed mainly in the mesothelial basal lamina. The incremental moduli in stress–strain curves and relaxation moduli in the Maxwell–Wiechert model of PVP were approximately one-tenth of the bovine pericardium and small intestinal submucosa. The minimal cytotoxicity of the PVP was demonstrated. The axons proliferated in the PVP conduit guidance from proximal to distal sciatic nerves of rats. The neo-skin regenerated under the PVP skin substitute within 4 weeks.

Conclusions: The PVP is composed of abundant collagen and elastin. The structural characteristics and mechanical compliance of the PVP render a suitable biological material for repair/reconstruction.

Keywords: lung, structure, compliance, biomechanics, biocompatibility, nerve, skin

Edited by:
Jeffrey A. Weiss,
The University of Utah, United States

Reviewed by:
Karina Nakayama,
Oregon Health and Science University, United States
Anirudha Singh,
Johns Hopkins University, United States

***Correspondence:**
Ghassan S. Kassab
gkassab@calmi2.org

Specialty section:
This article was submitted to Biomaterials, a section of the journal Frontiers in Bioengineering and Biotechnology

Received: *15 October 2021*
Accepted: *28 February 2022*
Published: *30 March 2022*

Citation:
Lu X, Han L and Kassab GS (2022) Pulmonary Visceral Pleura Biomaterial: Elastin- and Collagen-Based Extracellular Matrix. Front. Bioeng. Biotechnol. 10:796076. doi: 10.3389/fbioe.2022.796076

INTRODUCTION

Biological tissues have several important advantages for prostheses over synthetic materials. The primary benefits include rapid and complete endothelialization, higher resistance to infection, and overall improved biocompatibility (Badylak et al., 1995; Lindberg and Badylak, 2001; Tamariz and Grinnell, 2002; Maestro et al., 2006; Waterhouse et al., 2011; Gauvin et al., 2013; Walters and Stegemann, 2014;

Sánchez et al., 2018; Lu et al., 2019; Lu et al., 2020). In biological tissues, collagen and elastin are two major components of the extracellular matrix (ECM). Collagen is the most abundant ECM protein and provides a highly biocompatible environment for cells. This high biocompatibility makes collagen a perfect biomaterial for implantable medical products and scaffolds for *in vitro* testing systems (Meyer, 2019). Elastin is also abundant in ECM and highly biocompatible for cellular proliferation. In comparison with collagen, elastin can render ECM more resilience due to its molecular coil structure. Elastin has advanced durability over collagen due to its resistance to proteases (Shapiro et al., 1991; Mecham, 2018). In biocompatibility, RGD (arginine–glycine–aspartate) in collagen is the dominant domain for cellular adhesion and proliferation (Tamariz and Grinnell, 2002; Walters and Stegemann, 2014). Specific domains in elastin, instead of RGD, however regulate cellular proliferation (Daamen et al., 2007; Waterhouse et al., 2011), which differentiates the function of elastin. In fact, both collagen and elastin are essential for the cellular environment and homeostasis. Therefore, the merits of both collagen and elastin ought to be brought into the ECM biomaterials.

The bovine pericardium (bPcm) and swine small intestinal submucosa (SIS) are popular biomaterials and broadly utilized in clinical practice. The bPcm and SIS are defined as collagen-based EMC since collagen is the dominant component and elastin is relatively minor (Badylak et al., 1995; Lindberg and Badylak, 2001; Maestro et al., 2006; Gauvin et al., 2013). Therefore, the ameliorations of elastin are insufficiently utilized in bPcm and SIS. It is known that the proportions of collagen and elastin are diverse in the ECM of various organs (Daamen et al., 2007; Meyer, 2019). A larger proportion of elastin in the ECM can result in more resilience. The lung is known as an elastic organ, and the proportion of elastin is much larger in the lung than in the bPcm and SIS (Oldmixon and Hoppin, 1984; Fraser et al., 2005; Mecham, 2018). Hence, the lung tissue ECM (e.g., pulmonary visceral pleura, PVP) includes the benefits of both collagen and elastin as a biomaterial. The PVP is a serous membrane that closely sheathes the surface of the lung (Oldmixon and Hoppin, 1984; Humphrey et al., 1986; Fraser et al., 2005). The PVP maintains key roles in preserving lung function (Ligas et al., 1984; Michailova, 1997; Fraser et al., 2005). The cyclical inflation and deflation during respiration tensions and relaxes the PVP and thereafter renders the potential of the PVP to resist cyclic deformation.

Despite the potentially advantageous properties, a detailed characterization of the PVP as an ECM biomaterial has not been previously described. The role for the PVP as an ECM biomaterial remains largely unexplored. Thus, we studied the structural and mechanical properties of swine and bovine PVP. The cytotoxicity and biocompatibility of the PVP were evaluated. The studies of *in vivo* implant were performed to identify the potential for the PVP as a novel biomaterial in tissue repair/reconstruction.

MATERIALS AND METHODS

Tissue Preparation

Swine lung ($n = 6$), bovine lungs ($n = 6$), bovine pericardium ($n = 6$), and swine small intestine ($n = 6$) were obtained from a local abattoir and transported in cool saline. All organs and tissues were processed within 4 h post-harvest. The PVP was isolated *via* blunt dissection from the pulmonary parenchyma. Following isolation of sections from the posterior lobe, the specimens were laid flat and rinsed with 4°C saline. The specimens of bovine pericardium (bPcm) were rinsed with 4°C saline. The specimens of swine small intestinal submucosa (SIS) were processed by removing the mucosa and muscle layers from the small intestine and then rinsed with 4°C saline. The overall approach is represented in **Figure 1A**. The specimen from each animal was cut with scissors into three samples, which were assigned to categories 1, 2, and 3 for various experiments, as given in **Table 1**. Briefly, the samples in category 1 were directly stored in cool saline for the analyses of collagen and elastin contents. The samples in category 2 were laid flat and fixed using 4% paraformaldehyde for immunofluorescence microscopy. The samples in category 3 were cross-linked in 0.625% buffered glutaraldehyde solution at 23°C for 24 h, and then divided into three pieces for mechanical tests, *in vitro* toxicity, and *in vivo* biocompatibility, respectively. Glutaraldehyde cross-link is routine to minimize immune rejection for heterogenous implants.

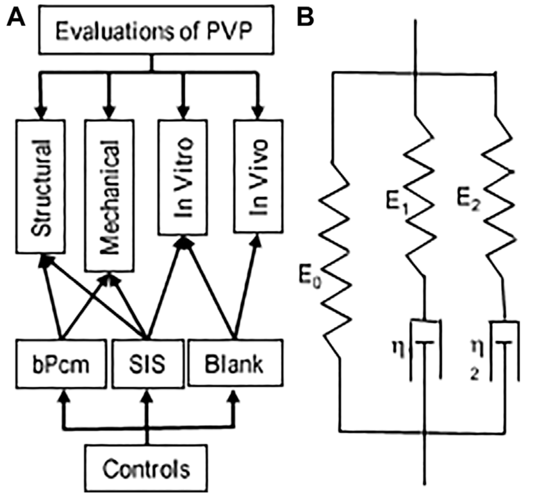

FIGURE 1 | Schematic representations of the evaluation and Maxwell–Wiechert model. **(A)** An overall picture of the evaluations. **(B)** Two Maxwell elements with moduli E_1 and E_2 and viscosities η_1 and η_2 provide a model with two relaxation times τ_1 and τ_2, respectively, that is, a fast-response element (E_1 and τ_1) and a slow-response element (E_2 and τ_2).

Collagen Content

The collagen analysis was based on the alkaline hydrolysis of samples to yield free hydroxyproline (Huszar et al., 1980). The released hydroxyproline is oxidized to form a reaction intermediate, which when further reacted forms brightly colored chromophore that can be detected at OD 550 nm (Kesava Reddy and Enwemeka, 1996). The collagen assay kit was obtained from Abcam (Total Collagen Assay Kit ab222942, Abcam, US) (da Silva et al., 2015). The tissue samples were prepared at 0.1–0.2 gm and hydrolyzed by alkaline solution. The

TABLE 1 | Distribution of various tissues for mechanical and biological tests.

	Category 1	Category 2	Category 3: 0.625% glutaraldehyde fixation			
	Ela and Col contents	Immunofluorescence	Mechanical test	*In vitro* toxicity	Biocompatibility in rats (*n = 12*)	
					Nerve, *n = 6*	Skin, *n = 6*
6 pigs, sPVP	*n = 6*	*n = 6*	*n = 6*	*n = 6*	*n = 6*	*n = 6*
6 pigs, SIS	*n = 6*	*n = 6*	*n = 6*	*n = 6*	--	--
6 cows, bPVP	*n = 6*	*n = 6*	*n = 6*	--	--	--
6 cows, bPcm	*n = 6*	*n = 6*	*n = 6*	--	--	--

assay kit employed a proprietary developer solution to accurately measure collagen in hydrolysates. The assay can detect as low as 0.5 µg collagen/well. The result was represented as micrograms (µg) of collagen per milligram (mg) of the tissue dry weight.

Elastin Content

We employed the acid hydrolysis and alkaline treatment for elastin evaluation. The acid hydrolysis converts all elastin in the tissue to soluble elastin by oxalic acid (hydrolytic solvent) (Partridge et al., 1955). The soluble elastin (tropoelastin, 50–70 kDa) is the precursor protein molecules to elastin, which is synthesized by the cell and cross-linked into elastin fibrils during their export into the extracellular matrix. These cross-linked elastin fibrils associate with fibrillin-containing microfibrils to form the elastic fiber, which is an insoluble and durable complex (Daamen et al., 2007; Wise et al., 2009). The soluble elastin can be evaluated by chemiluminescence using the dye reagent 5,10,15,20-tetraphenyl-21H,23H-porphine tetra-sulfonate (TPPS). The dye reagent binds to the "basic" and "non-polar" amino acid sequences found in mammalian tropoelastin (Kothapalli and Ramamurthi, 2009). The presence of other soluble proteins or complex carbohydrates does not interfere with the dye reagent. The commercialized kit (Fastin™ Elastin assay, Biocolor, UK) was used to evaluate the elastin in the tissues. The result was represented as micrograms (µg) of converted soluble elastin per milligram (mg) of the tissue dry weight.

The alkaline treatment is performed to use alkaline solvent to hydrolyze ECM, except elastin, for the evaluation of the insoluble elastin in the tissues. In alkaline treatment, the insoluble elastin in various tissues was retained due to its resistance to the hydrolysis during treatment with hot alkaline solution (Harkness et al., 1957; Wolinsky, 1970; Maestro et al., 2006). Briefly, the samples were trimmed to approximate 9 cm^2 and delipidated in chloroform/methanol (1:1 v/v). The delipidated samples were dried in room temperature and soaked in the lysis buffer (0.3% sodium dodecyl sulfate) for 12 h to remove cell proteins in the samples (Neethling et al., 2003). The remnant was minced and immersed in 0.1M NaOH solution (v/v: ~1/10), and heated at 100°C for 15 min. The ECM proteins except elastin were hydrolyzed by an alkaline solution, and the supernatant was discarded. The alkaline hydrolysis was repeated four times so that only insoluble elastin was retained in the remnant. The insoluble elastin was lyophilized. The dry insoluble elastin was weighed. The result was represented as micrograms (µg) of insoluble elastin per milligram (mg) of the tissue dry weight.

Immunofluorescence Microscopy for Collagen and Elastin Visualization

The samples (width × length: ~5 × 5 mm) were fixed in 4% paraformaldehyde overnight and subsequently sectioned with a cryostat. The sections were processed for immunofluorescence procedures; that is, blocking with phosphate-buffered solution (PBS, pH 7.4) contained 10% donkey serum for 1 h, permeabilization with PBS contained 0.25% Triton for 15 min, primary antibody incubation, and fluorescence secondary antibody incubation. The primary antibodies included anti-elastin (Cat. #sc17480, 1/30 dilution with PBS contained 0.25% Triton and 2.5% donkey serum, Santa Cruz Biotechnology) and collagen (Cat. #ab7778, 1/2530 dilution with PBS contained 0.25% Triton and 2.5% donkey serum, & ab6586, 1/20 dilution with PBS contained 0.25% Triton and 2.5% donkey serum, Abcam). The primary antibodies were incubated at 4°C overnight. The fluorescent dye-conjugated secondary antibodies (Cat. #A10040, A10036, A11081, & A11058, 1/100 dilution with PBS contained 0.25% Triton and 2.5% donkey serum, Thermo Fisher Scientific) were incubated at room temperature (22°C) for 1 h. The fluorescence reagent (Cat. #Hoechst 33342, 1/5000 dilution with PBS contained 0.25% Triton and 2.5% donkey serum, Life Technology) was used for cellular nuclei visualization. The fluorescent dyes were visualized using a fluorescence microscope (Eclipse Ts2R, Nikon).

Planar Uniaxial Stress–Strain Relation and Stress Relaxation

All samples for testing were trimmed to the dimensions of 22 × 55 mm (width × length) sheets. The thickness of the samples was measured in a no-load state. The samples were then secured in the clamps of a uniaxial device (Mark-10, NY). The loading rate was selected at 1.7 mm/s. The maximum stretch ratio for each sample was 1.5. The precondition was performed until repeatable loading forces were obtained (Zhao et al., 2014). The force–displacement relation was obtained from the loading curve following the precondition. The Cauchy stress and strain were computed to determine the stress–strain curve. In the stress relaxation test, the samples were elongated to a Cauchy strain of 0.3 at a speed of 3.3 mm/s. The stresses gradually decreased to a stable value in a period of approximate 300 s. We employed the Maxwell–Wiechert model for the analyses of viscoelastic properties of the tissues (**Figure 1B**). The relaxation modulus as a function of time for the Maxwell–Wiechert model can be expressed as follows:

$$\frac{\sigma(t)}{\varepsilon_0} = E_{\mathrm{Relax}}\ (t) = E_0 + E_1\ \exp\left(-\frac{t}{\tau_1}\right) + E_2\ \exp\left(-\frac{t}{\tau_2}\right),$$

where $\sigma(t)$ is stress (Cauchy stress) relaxation with time, ε_0 is the constant Cauchy strain during the stress relaxation test, $E_{relax}(t)$ is the time-dependent elastic modulus, and E_0 is the time-independent elastic modulus. The relaxation time τ_i of each Maxwell element is equal to the coefficient of viscosity of the dashpot (η_i) divided by the elastic modulus of the spring (E_i). The elastic modulus and relaxation times were obtained by fitting the stress–time data with the Maxwell–Wiechert model.

In Vitro Cytotoxicity

The samples of sPVP (n = 6) and SIS (n = 6) were rinsed, transferred to serum-free media, and placed into a shaking incubator at 37°C for 24 h. The samples were cut into 15 mm discs and placed into individual wells of a 24-well plate, in which the two wells coated with fibronectin served as blank. The wells were filled with full media (DMEM with 10% sterile filtered fetal bovine serum, 1% L-glutamine, and 1% penicillin/streptomycin). Confluent NIH 3T3 cells were released from tissue culture plates using 0.25% trypsin, spun, resuspended, and counted. Overall, 100,000 cells were added to each well in fresh full media and incubated at 37o̲C in 5% CO_2 for 1 day. Non-adherent cells were discarded. The wells containing adherent cells were filled with fresh full media and incubated at 37o̲C in 5% CO_2 for 5 days. The adherent cells on samples were released with 0.25% trypsin, spun, and resuspended in 1 ml Dulbecco's phosphate-buffered saline for cell counting. Fluorescent probes Calcein AM (ex/em: 485/530 nm) and ethidium homodimer (ex/em: 530/645 nm) were used to label living and dead cells. Reagents (LIVE/DEAD Viability/Cytotoxicity Kit, Invitrogen) were added in the cell suspension for the concentrations of 2 μM calcein AM and 4 μM ethidium homodimer. The suspension with the reagents was incubated at room temperature for 40 min. The fluorescent labeled cell suspensions were loaded to a hemocytometer (Bright-Line, Hausser Scientific). The number of living and dead cells in the hemocytometer was determined by counting using a fluorescence microscope (Ts2R, Nikon). Cell viability was calculated for the percentage of living cells in total cells (living plus dead cells).

Ethics Statement

We used rodent models to examine the biocompatibility of the PVP. All experimental procedures and protocols used in the investigations were approved by the Institutional Animal Care and Use Committee in accordance with the Guide for the Care and Use of Laboratory Animals. All protocols regarding the use of animals in the research were approved by California Medical Innovations Institute IACUC. The approved protocol numbers were CalMI2-013 and CalMI2-015.

In Vivo Evaluation as Nerve Guidance Conduit and Skin Substitute

Six swine PVPs (sPVPs) were constructed as hollow conduits (n = 6) to accommodate nerve regeneration in rodent sciatic nerve transection models (n = 6). Six Lewis rats of ages 5–6 months were anesthetized with 1.8% isoflurane. The hindquarters of rats were shaved and sterilized. The skin was cut parallel to the femur, and the sciatic nerve was exposed by means of a gluteal muscle slitting incision. With the help of a dissecting microscope, the sciatic nerve was excised over a span of approximate 12 mm between proximal and distal stumps. The PVP elastin conduit was placed near the two stumps of the sciatic nerve. The nerve stumps were inserted into the conduit and anchored to the conduit by means of 2–3 fine stiches with 10–0 monofilament suture. The proximal and distal nerve fibers were tension-free, while the conduit was implanted. The muscle was closed with running 6–0 absorbable suture, and the skin was closed with 5–0 prolene suture. Buprenorphine HCl (0.01–0.05 mg/kg) was administrated for postoperative pain control. The sciatic functional index (SFI) was evaluated biweekly. At the terminal study in 12 weeks, the distal muscle reinnervation was assessed. The contractile forces of the gastrocnemius muscle were measured during the tetanic stimulation (4 V, 100 Hz) by a bipolar electrode placed at the proximal end of the sPVP nerve guidance conduit. After a full rest, the bipolar electrode was moved to the distal end of the sPVP nerve guidance conduit. The contractile forces of the gastrocnemius muscle were measured again during the tetanic stimulation. The bipolar electrode was then placed on the contralateral non-traumatic sciatic nerve, and the tetanic contraction of the collateral gastrocnemius muscle was measured. The ratio of the ipsilateral tetanic contractions of sPVP nerve guidance conduit to the contralateral tetanic contractions was calculated. The ipsilateral and contralateral gastrocnemius muscles were weighed after euthanasia, and the weight ratio was calculated. The sPVP nerve guidance conduit and contralateral non-traumatic sciatic nerve were harvested for histologic and immunofluorescence analyses. The tissues were fixed with 4% paraformaldehyde and sectioned with a cryotome. Hematoxylin and eosin (HE) staining was performed. The sections were processed for immunofluorescence. The primary antibodies included anti-NF-L (neurofilament light polypeptide, Cat #: sc71678, 1/30 dilution with PBS contained 0.25% Triton and 2.5% donkey serum, Santa Cruz Biotechnology) and anti-MBP (myelin basic protein, Cat #: sc376995, 1/30 dilution with PBS contained 0.25% Triton and 2.5% donkey serum, Santa Cruz Biotechnology). The fluorescent secondary antibodies were visualized using a fluorescence microscope (Ts2R, Nikon). Each section was imaged by division into four squares. The myelinated axonal number and width in each division were counted and measured using image tool (ImageJ), respectively. The total number of myelinated axons in each section was the sum of the number in the four squares. The average of myelinated axonal width was calculated in the four squares. The mean and standard deviation were calculated from the data of six rats.

The sPVP was also used as skin substitute of an incised wound in rodent models (n = 6). Six Wistar rats of ages 5–6 months were anesthetized with 1–2% isoflurane. The hair on the dorsum was removed, and the skin was disinfected with Nolvasan, Betadine, and 70% alcohol. A piece of 2 × 4-cm dorsal skin was surgically excised to create a wound for repair. The sPVP was carefully

TABLE 2 | Dry weights of elastin and collagen in the tissues.

Unit: μg/mg	Elastin-CI	Elastin-IS	Collagen	E-CI/Col	E-IS/Col
bPVP	252.1 ± 30.1	361.4 ± 38.6	216.7 ± 27.9	1.18 ± 0.24	1.46 ± 0.51
sPVP	247.8 ± 27.3	325.7 ± 35.9	237.3 ± 29.1	1.06 ± 0.21	1.25 ± 0.39
bPcdm	9.3 ± 1.8*	54.8 ± 9.2*	410.3 ± 59.8*	0.02 ± 0.01*	0.09 ± 0.08*
SIS	61.2 ± 9.5#	19.5 ± 4.3#	373.5 ± 43.6#	0.17 ± 0.04#	0.11 ± 0.05#

*: p<*0.05 in comparison with the elastin in bPVP.*

#: p<*0.05 in comparison with the elastin in sPVP.*

bPVP, bovine pulmonary visceral pleura; sPVP, swine pulmonary visceral pleura; bPcdm, bovine pericardium. SIS, swine small intestine submucosa; elastin-CI, converted insoluble to soluble elastin to measure; elastin-IS, insoluble elastin was measured; E-CI/Col, ratio of elastin-CI to collagen; E-IS/Col, ratio of elastin-IS to collagen.

covered on the wound and sutured to the adjacent skin. Then, an antiseptic bandage was covered to protect the sPVP on the wound from infections. The rats survived for 4 weeks postoperation. The neo-dermal tissues were harvested after euthanasia. The tissues were fixed with 4% paraformaldehyde and sectioned with a cryotome. The HE stains were performed. The sections were processed for immunofluorescence. The primary antibodies included anti-collagen IV (Cat #: ab6586, 1/20 dilution with PBS contained 0.25% Triton and 2.5% donkey serum, Abcam) and anti-sialic acid (wheat germ agglutinin, Cat #: W11261, 1/100 dilution with PBS contained 0.25% Triton and 2.5% donkey serum, Thermo Fisher Scientific). The fluorescent secondary antibodies were visualized using a fluorescence microscope (Ts2R, Nikon).

Statistical analysis: The data were presented as mean ± SD, and significant differences between two groups were determined by Student's *t*-test (two-tailed distribution, two-sample unequal variance). Analysis of variance (ANOVA) was used to analyze the significant differences of mechanical tests among groups. A probability of $p < 0.05$ was indicative of a statistically significant difference.

RESULTS

Contents of Elastin and Collagen

The contents of collagen and elastin in the various tissues are summarized in **Table 2**. The collagen contents in bPcm and SIS were significantly higher than those in the bPVP and sPVP ($p < 0.05$). The elastin contents in bPVP and sPVP were on par with those of collagen. The elastin contents were somewhat lower/higher in the acid hydrolysis than those of alkaline treatment. The elastin contents in bPcm and SIS however were significantly lower than those in bPVP and sPVP with either the acid hydrolysis or alkaline treatment ($p < 0.05$). The ratio of elastin to collagen is 1.18 or 1.46 in bPVP and 1.06 or 1.25 in sPVP due to the different methods. The ratio of elastin to collagen is 0.02 or 0.09 in bPcm and 0.17 or 0.11 in SIS (**Table 2**).

Immunofluorescence Microscopy

Collagen and elastin in the various tissues were visualized under immunofluorescence microscopy. The collagen in bPVP and sPVP was denser on the mesothelial basal lamina and lesser in the middle and parenchyma sides (**Figures 2A,D**). The elastin was dense throughout the thickness of both bPVP and sPVP as robustly visualized (**Figures 2B,E**). The fluorescence images of collagen and elastin in bPVP and sPVP were merged and are shown in **Figures 2C,F**. The collagen in bPcm was evenly distributed throughout the thickness of the section, and the collagen fibers were easily observed (**Figure 2G**). The elastin fibers in bPcm were sparsely found in the middle and a little robust in the posterior (**Figure 2H**). The collagen was unevenly distributed in the SIS, that is, it was denser in the adjacent regions toward mucosa and muscularis externa than that in the middle region (**Figure 1J**). The elastin fibers were sparsely observed in SIS (**Figure 2K**). The fluorescence images of collagen and elastin in bPcm and SIS were merged and are represented in **Figures 1I,L**.

Uniaxial Mechanical Property

The Cauchy stress–stretch relations and stress relaxation of the PVP, SIS, and bPcm are represented in **Figure 3**. The stress–strain relation of the sPVP was close to the bPVP where the slope increased from 0 to 0.5 when stretched (**Figure 3A**). The stress of the bPVP at a strain of 0.49 was 262.8 ± 48.3 kPa, which was not significantly larger than 219.7 ± 38.9 kPa of the sPVP ($p > 0.05$). The stress–strain relations of the bPcm and SIS are represented in **Figure 3B**. The stress–strain relation of the bPcm was larger than the SIS in the range of strain 0–0.5 ($p < 0.05$, two-way ANOVA). The stress of the bPcm at strain 0.49 was 4,262.8 ± 657.3 kPa, which was significantly larger than the 2,516.3 ± 976.1 kPa of the SIS ($p < 0.05$). The stress of the SIS at strain 0.49 was approximately 10-fold of the stresses of the bPVP and sPVP.

The typical curves for stress relaxation are represented in **Figure 3C**, which differed for sPVP, bPVP, SIS, and bPcm. The time-independent elastic modulus (E_0), the modulus and relaxation–time pairs for a fast-response element (E_1 and t_1), and the modulus and relaxation–time pairs for a slow-response element (E_2 and t_2) are represented in **Table 2**. The goodness-of-fit parameter for the fitted curves (R^2) indicates a satisfactory representation of the data (**Table 3**). The viscoelastic parameters of sPVP and bPVP are significantly different from bPcm and SIS ($p < 0.05$). The $E_{relax}(t)$ for sPVP, bPVP, SIS, and bPcm is represented in **Figure 3D**, which shows that $E_{relax}(t)$ for bPcm and SIS is one order magnitude higher than that for sPVP and bPVP.

In Vitro Cytotoxicity

Cell viability (%) is represented in **Figure 4A**. Fibronectin-coated wells served as blanks of *in vitro* cytotoxicity. Cell viability on SIS and sPVP slightly decreased in the 5-day experimental period in

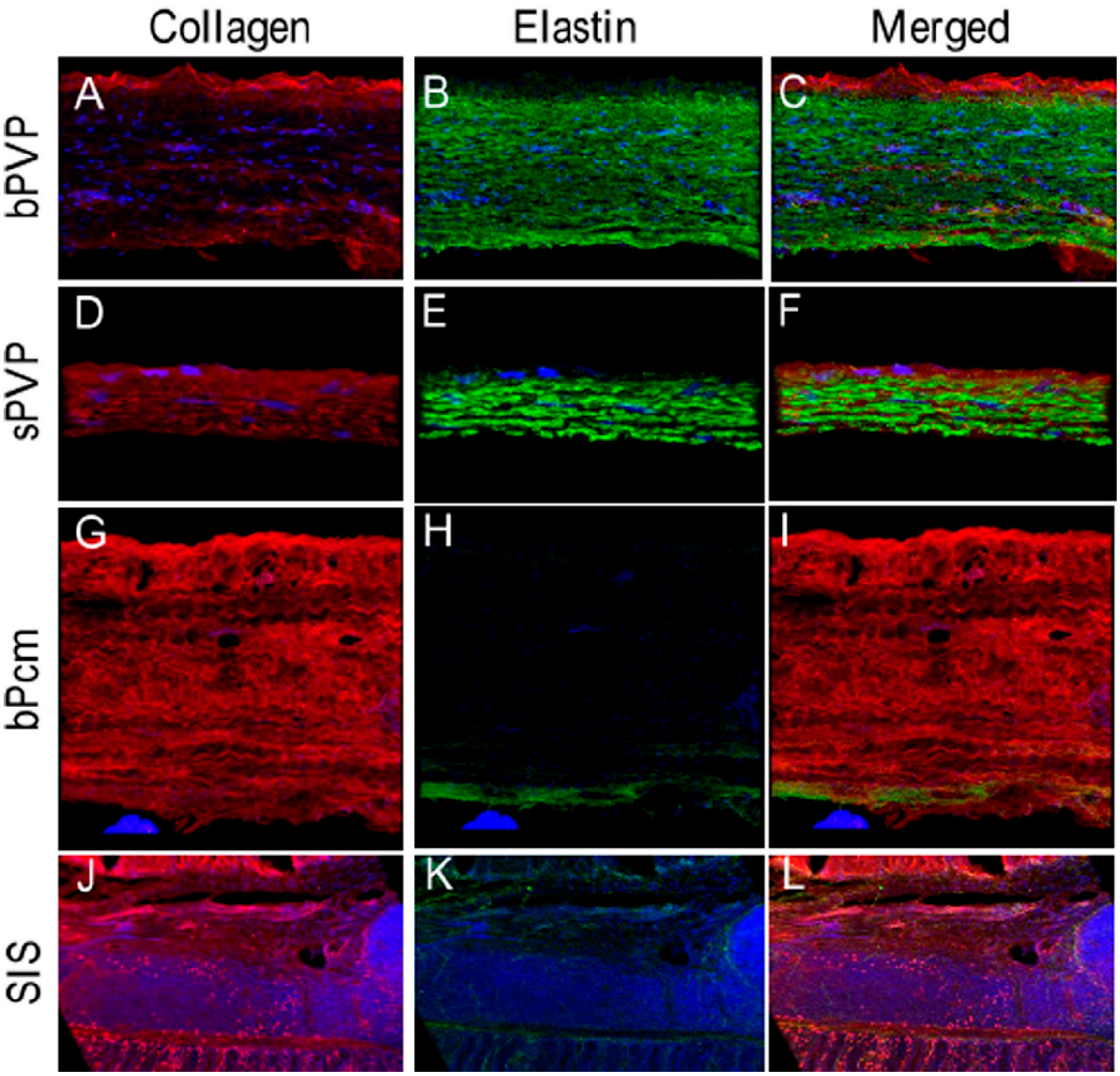

FIGURE 2 | Collagen and elastin fibers in bPVP, sPVP, bPcm, and SIS. **(A–C)** Collagen, elastin, and merged collagen and elastin in bPVP, respectively. **(D–F)** Collagen, elastin, and merged collagen and elastin in sPVP, respectively. **(G–I)** Collagen, elastin, and merged collagen and elastin in bPcm, respectively. **(J–L)** Collagen, elastin, and merged collagen and elastin in SIS. Red: anti-collagen; green: anti-elastin; blue: nuclei. Objective: ×60.

comparison with control ($p > 0.05$), that is, a negligible cytotoxicity in SIS and sPVP. **Figures 4B,C** show global views of the cells on the SIS and the PVP for 5 days, respectively. The living cells (green, calcein AM labeled) on the SIS and PVP are shown in **Figures 4D,E**, respectively.

In Vivo Biocompatibility

An example of conduit guidance before implantation and postop 12 weeks is shown in **Figures 5A,B**. The SFI slightly varied between −2 and −7 through postoperative 12 weeks (**Figure 5C**), when the sciatic nerve was not injured but only exposed (sham), and then the skin was closed (Wang et al., 2015b; Ma et al., 2014). The SFI decreased from −2.9 ± 4.1 for the non-injury of the sciatic nerve to −80.1 ± 5.1 for the transection of the sciatic nerve. The SFI after implanted PVP guidance conduit was slightly recovered to −58.9 ± 7.6 at postoperative 12 weeks ($p < 0.05$, **Figure 5C**). The recovery in SFI indicates that the sciatic nerve function was improved by the PVP guidance conduits. In contrast, the SFI slightly varied between −85 and −95 through postoperative 12 weeks (**Figure 5C**), when the sciatic nerve (~10 mm) was excised and no guidance conduit was implanted for the connection of two stumps (Ma et al., 2014; Wang et al., 2015b). The tetanic contraction of the gastrocnemius muscle (contractility) was represented as the ratio of the force in the ipsilateral sPVP nerve guidance conduit to the contralateral non-traumatic sciatic nerve (**Figure 5D**). There was no difference of the ratio for stimulation at proximal or distal ends of the sPVP nerve guidance conduit ($p > 0.05$). The ratio of wet gastrocnemius muscle mass is 0.50 ± 0.035. Based on immunofluorescence microscopy, the

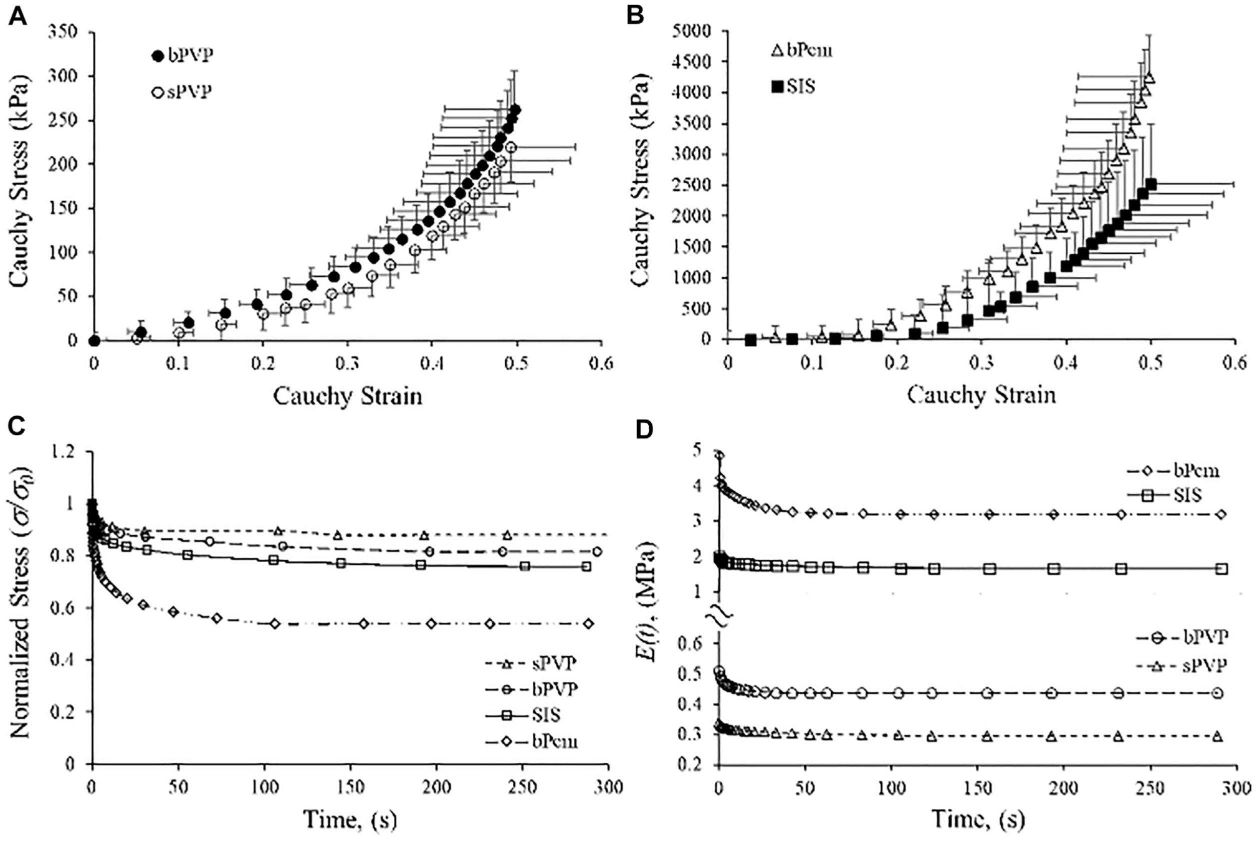

FIGURE 3 | Relationship of Cauchy stress-to-strain and stress relaxation of bPVP, sPVP, bPcm, and porcine SIS. **(A)** The relations of bPVP and sPVP. **(B)** The relations of bPcm and SIS. **(C)** Typical curves for stress relaxation of sPVP, bPVP, SIS, and bPcm. **(D)** Time-dependent modulus $E_{relax}(t)$ for sPVP, bPV, SIS, and bPcm.

TABLE 3 | Viscoelastic parameters of the tissues' best fit with the Maxwell–Wiechert model.

	E_0 (MPa)	E_1 (MPa)	E_2 (MPa)	τ_1 (s)	τ_2 (s)	R^2
sPVP	$0.31 \pm 0.11^{*\#}$	$0.02 \pm 0.01^{*\#}$	$0.03 \pm 0.01^{*\#}$	$2.57 \pm 1.65^{*\#}$	48.3 ± 18.5	0.99 ± 0.01
bPVP	$0.44 \pm 0.16^{*\#}$	$0.04 \pm 0.02^{*\#}$	$0.04 \pm 0.02^{\#}$	$1.73 \pm 1.15^{\#}$	47.3 ± 12.6	0.96 ± 0.04
SIS	1.7 ± 0.8	$0.18 \pm 0.15^{\#}$	$0.18 \pm 0.17^{\#}$	1.57 ± 0.15	46.3 ± 10.4	0.99 ± 0.01
bPcm	3.2 ± 1.8	0.72 ± 0.43	0.74 ± 0.46	0.67 ± 0.21	47.7 ± 11.2	0.99 ± 0.01

** $p < 0.05$ in comparison with SIS; #, $p < 0.05$ in comparison with bPcm.*

E_0: the time-independent elastic modulus. E_1 and τ_1: the modulus and relaxation–time pairs for a fast-response element.

E_2 and τ_2: the modulus and relaxation–time pairs for a slow-response element. R^2: the goodness-of-fit parameter for the fitted curves.

axonal numbers and width of myelinated axons (MA) were analyzed and are represented in **Figures 5E,F**. Histological analysis showed that the sPVP nerve guidance conduit was filled with regenerative tissues (**Figures 6C–H**), and **Figures 6A,B** show sciatic nerve fibers. The positive fluorescence signals of neurofilament light polypeptide and myelin basic proteins in the sPVP nerve guidance conduit confirm that the regeneration of axons bridges the proximal and distal stumps of the sciatic nerve (**Figures 7C–H**), and **Figures 7A,B** show sciatic nerve fibers.

In a skin substitute with sPVP, no infection or complications were observed in the rats postoperation. The neo-dermal regeneration under the sPVP had filled the wound at 4 weeks postoperative (**Figure 8A**). The immunofluorescence microscopy represented keratinocyte lining on the basal lamina of native skin (**Figure 8B**). Neo-keratinocyte lining on the basal lamina (collagen IV, red) was observed in the regenerative skin (**Figure 8C**), which implicates the epidermal layer was formed in the regenerative skin (**Figure 8C**). Based on immunofluorescence microscopy, the numbers of keratinocyte in unit length (mm) were 92 ± 31/mm for native skin and 106 ± 37/mm for neo-derma ($p > 0.1$).

DISCUSSION

We found that the bPVP and sPVP are composed of abundant collagen and elastin. Specifically, the elastin contents are

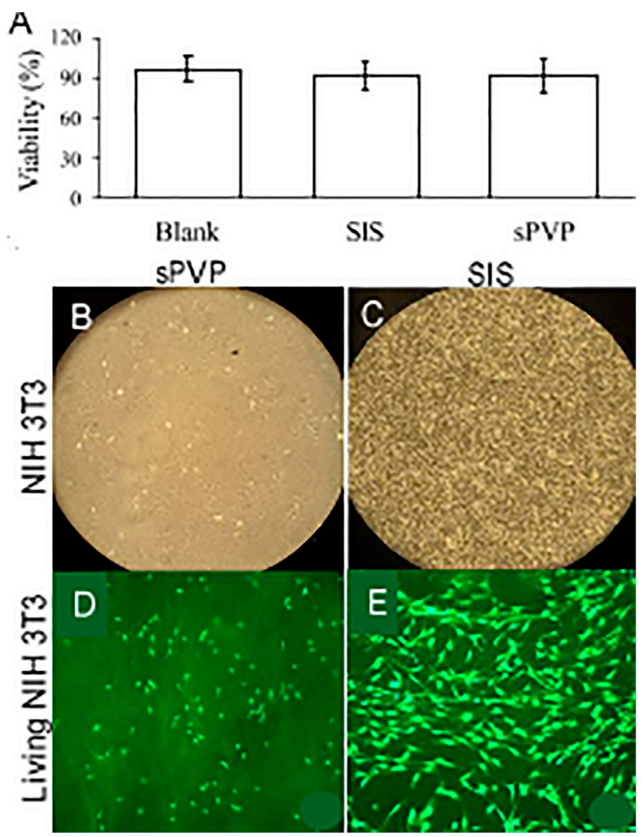

FIGURE 4 | *In vitro* cytotoxicity of sPVP in comparison with SIS. **(A)** Cellular viability (%). **(B–C)** NIH 3T3 cells on sPVP and SIS, respectively. Objective: ×4. **(D–E)** Calcein marked (green) NIH 3T3 cells on the PVP and SIS, respectively. Objective: ×60.

approximately equal to the collagen in the bPVP and sPVP. The thick and dense fibers of elastin were robustly observed in immunofluorescence microscopy. Therefore, the bPVP and sPVP can be defined as an elastin- and collagen-based ECM in comparison with primarily collagen-based ECM biomaterials such as swine SIS and bovine pericardium. The biomechanical analyses of stress–strain and stress relaxation confirm that the compliance of bPVP and sPVP is greater than bPcm and SIS. Furthermore, we found low cytotoxicity of PVP in the *in vitro* study and excellent biocompatibility in the *in vivo* implantation of the PVP as nerve guidance conduit and skin substitute.

Strengths of Elastin–Collagen ECM

Collagen and elastin are known as the critical ECM and regulate cellular proliferation and functionalization. Therefore, ECM is a desirable biomaterial in the reconstruction of organs or tissues, such as bPcm and SIS, which are known as collagen-based ECM and diversely utilized in the clinic. In the present study, we verified that the contents of elastin and collagen are approximately equivalent in the PVP. Therefore, we introduce PVP as an elastin- and collagen-based ECM, and expect that both collagen and elastin can enhance cellular proliferation and functionalization in organ or tissue

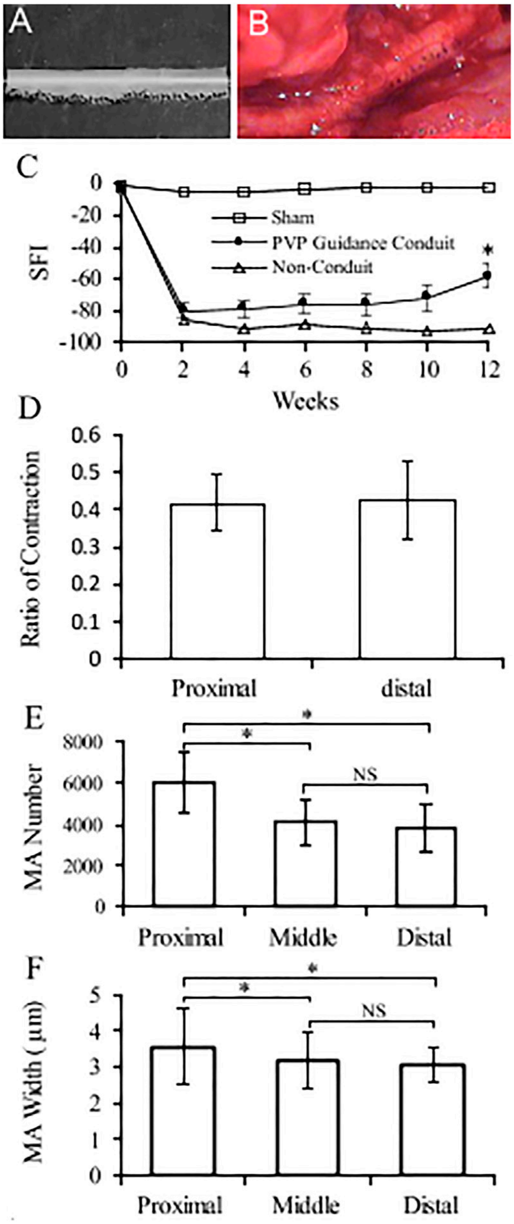

FIGURE 5 | Nerve conduit guidance and parameters of nerve regeneration in sciatic model of rats. **(A)** An example of conduit guidance before implantation. **(B)** An example of conduit guidance at postop 12 weeks. **(C)** Biweekly changes of SFI in rodent sciatic nerve. Sham: non-injury to the sciatic nerve during the sciatic nerve exposure and skin closure. PVP guidance conduit: The sPVP nerve guidance conduit implanted when the sciatic nerve excised. Non-conduit: no guidance conduit implanted when the sciatic nerve was excised. **(D)** Ratios of the ipsilateral tetanic contractions of sPVP nerve guidance conduit to contralateral tetanic contractions of the gastrocnemius muscle. Proximal and distal: a bipolar electrode was placed at the proximal or distal end of the sPVP nerve guidance conduit, respectively. **(E)** The number of myelinated axons in the proximal, middle, and distal regions of the sPVP nerve guidance conduit, respectively. **(F)** The average width of myelinated axons in the proximal, middle, and distal regions of the sPVP nerve guidance conduit, respectively. SFI: sciatic function index. MA: myelinated axons. *: $p < 0.05$. NS: $p > 0.05$.

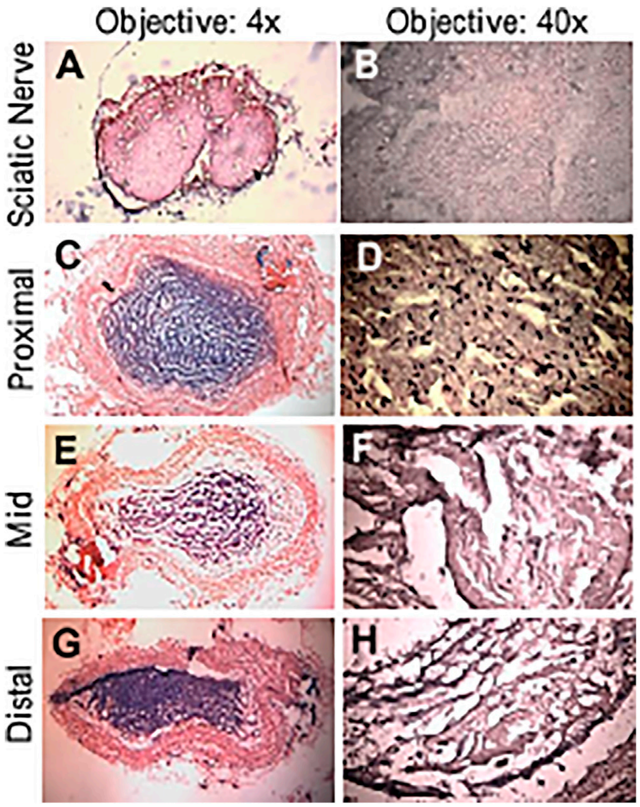

FIGURE 6 | HE of the sPVP nerve guidance conduit in sciatic model of rats. **(A)** Sciatic nerve fibers at low magnification (objective: ×4). **(C, E, and G)** The proximal, middle, and distal regions of the sPVP nerve guidance conduit at low magnification (objective: ×4), respectively. **(B)** Sciatic nerve fibers at high magnification (objective: ×40). **(D, F, and H)** The proximal, middle, and distal regions of the sPVP nerve guidance conduit at high magnification (objective: ×40), respectively.

reconstruction. It is well accepted that a biological material must be strong, flexible, and durable. Collagen-based ECM has manifested its excellent characteristics. Collagen may be further cross-linked to resist MMPs' degradation. Elastin fibers in the PVP further enhance the flexibility and durability of collagen-inherent characteristics. It is known that elastin fiber is extensively cross-linked in ECM, which renders elastin for the protein's insolubility and contributes to its longevity (Mecham, 2018). Shapiro et al. estimated the life span of elastin using aspartic acid racemization at 14°C that turnover to be ~80 years in humans (Shapiro et al., 1991). Studies using sensitive immunological techniques to measure elastin peptides in the blood or desmosine cross-links excreted in the urine suggest that <1% of the total body elastin pool turns over in a year (Starcher, 1986; Mecham, 2018). Another factor contributing to the longevity of mature elastin is its relative resistance to proteolysis. Since there are few lysine or arginine residues in the fully cross-linked protein, and few amino acids with large aromatic side chains, elastin is not degraded by trypsin- or chymotrypsin-like proteases. In the present study, the immunofluorescence microscopy reveals that the thick fibers of elastin densely distribute through the PVP (**Figures 2B,E**). The thick fibers of elastin may retain the elastic property of the PVPs for long term.

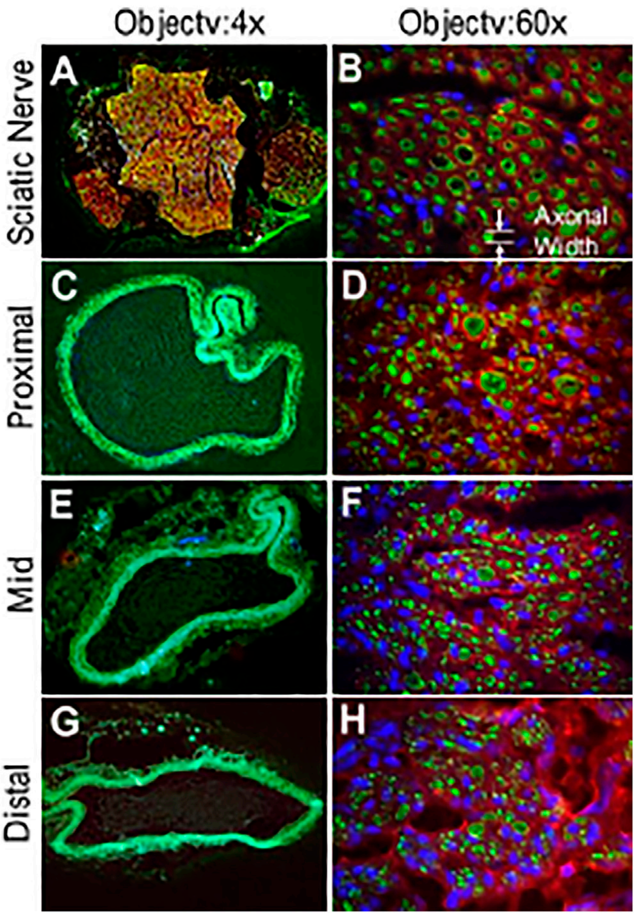

FIGURE 7 | Immunofluorescence images of the sPVP nerve guidance conduit in sciatic model of rats. **(A)** Sciatic nerve fibers at low magnification (objective: ×4). **(C, E, and G)** The proximal, middle, and distal regions of the sPVP nerve guidance conduit at low magnification (objective: ×4), respectively. **(B)** Sciatic nerve fibers at high magnification (objective: ×60). **(D, F, and H)** The proximal, middle, and distal regions of the sPVP nerve guidance conduit at high magnification (objective: ×60), respectively. Red: anti-MBP (myelin basic proteins); green: anti-NFLP (neurofilament light polypeptide); blue: nuclei of cells. Objective: ×60. The white lines and arrows indicate the measurement of axonal width.

Mechanical Mismatch

Mechanical property is a critical feature of biomaterials. Mechanical and structural mismatches between the biomaterial and native tissue may alter the local mechanical environment and contribute to abnormal growth and remodeling (Zilla et al., 2007; Shi and Tarbell, 2011). It is known that mechanical mismatch is a cause of poor performance of a vascular graft (Zilla et al., 2007; Sánchez et al., 2018). The compliance mismatch of the graft with an adjacent blood vessel can result in altered blood flow, platelet activation, and thrombus formation (Malek et al., 1999; Zilla et al., 2007). The reductions of intramural stress may mitigate propensity for mineralization such as in bioprosthetic heart valves (Munnelly et al., 2012). Therefore, the similarity of mechanical and structural properties of biomaterials and host is critical for successful tissue reconstruction (Zilla et al., 2007).

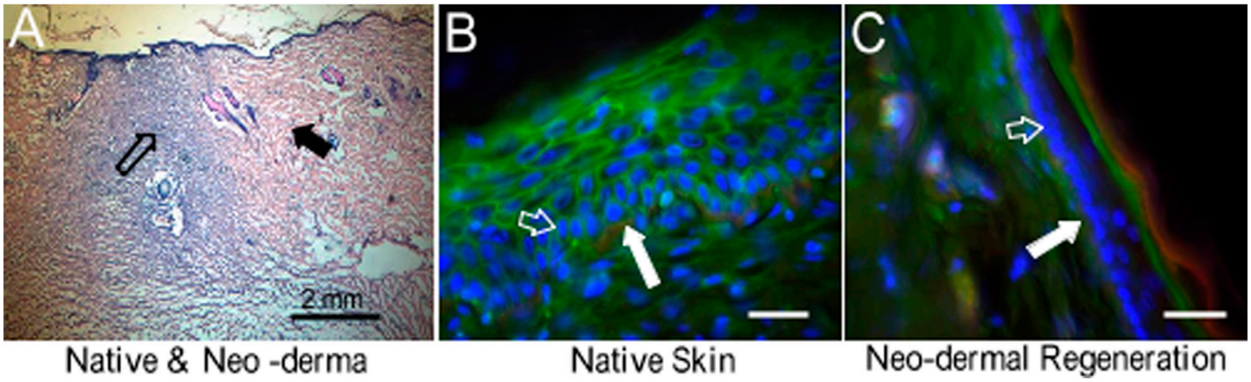

FIGURE 8 | HE staining and fluorescence microscopic images to represent skin regeneration after the wound created in rats. **(A)** HE stain of neo-dermal regeneration (black hollow arrow) and native skin (black solid arrow). Objective: ×4. **(B)** Native skin. **(C)** Neo-dermal regeneration filled in the wound. Objective: ×40. Red: green: sialic acid. Blue: nuclei. Collagen type IV. Bar: 50 μm. White solid arrows indicate collagen type IV in the basal lamina. White hollow arrows indicate keratinocytes which were proliferating during skin regeneration.

In this study, we verified that the incremental moduli in stress–strain curves and relaxation moduli in the Maxwell–Wiechert model of sPVP and bPVP were approximately one-tenth of bPcm and SIS. The prostheses made of sPVP and bPVP may mitigate some of the complications due to mechanical mismatch with biological tissues. The mechanical properties of fibrous tissues stem from their constituents, that is, collagen and elastin fibers (Lokshin and Lanir, 2009; Wang et al., 2015a). A proper content of elastin and collagen is necessary to render ideal mechanical properties for a biomaterial. Previous studies indicated that the PVP consists of more elastin (~25% dry weight) and maintains one-fifth as much collagen as the parenchyma, which serves the role of PVP mechanics (Oldmixon and Hoppin, 1984; Starcher, 1986; Fraser et al., 2005). The PVP has been viewed as a complex structure that adds to tissue disparity (Michailova, 1997). The immunofluorescence microscopy reveals the microstructure of PVP tissues, which is consistent with the macroscopic mechanical responses, where the stress–strain curve of the PVP becomes non-linear at a larger stretch ratio with higher stress level than at the lower loads as shown in **Figure 3A**. Specifically, the PVP microstructure and mechanical properties indicate that it is a highly compliant material. Hence, the PVP may be different for bioprosthetic applications, where the mechanical compliance needs to be adopted.

In Vivo Biocompatibility

There is no doubt that collagen and elastin have excellent biocompatibility because collagen and elastin are the major constituents of ECM and provide the mechanical environment of cell proliferation and biological functions. Therefore, it is not surprising that the cytotoxicity of the PVP is as low as that of SIS (**Figure 4**). It is well known that the *in vivo* experiment is the proper test for biocompatibility of biological prosthesis. In fact, the *in vivo* experiment is also an appreciated test for mechanical coupling of biomaterials to native tissues. In the present study, we designed *in vivo* nerve conduit guidance and skin substitute for the evaluation of the biocompatibility and mechanical coupling of the PVP. Although the autologous nerve graft remains the gold standard treatment for repair of peripheral nerve defects (Schmidt and Leach, 2003; Daly et al., 2012), there is a limitation of tissue harvest numbers and dimensions where extensive reconstruction is required (Schmidt and Leach, 2003). Nerve guidance conduit is used as an alternative autologous nerve graft for peripheral nerve repair. Although biological and synthetic materials are used for nerve guidance conduit, axonal regenerative capacity in existing nerve guidance conduit is often incomplete and functional recovery is limited. Novel biomaterials for nerve guidance conduit are needed to improve the functional and structural outcomes in nerve repair. The PVP mechanical compliance allows the PVP nerve guidance conduit to assimilate into adjacent tissues. Furthermore, both collagen and elastin are ameliorative to support nervous regeneration (Waitayawinyu et al., 2007; Whitlock et al., 2009; Hsueh et al., 2014). In the rodent model, we demonstrate that the PVP nerve guidance conduit is suitable for peripheral nerve repair/reconstruction.

The skin covers the body to provide protection and receive sensory stimuli from the external environment. Minor wounds can heal well, but severe wounds need rapid repair to prevent scar invasion and water loss. Although skin transplantation is the “gold standard” for repair/reconstruction, artificial skin is frequently used to repair wounds when an autologous donor is not available. Typical artificial skin is composed of collagen to promote regeneration of skin and accommodate epidermal cell migration and proliferation for re-epidermalization on the wound. Considering skin is an elastin-abundant organ, the abundant elastin in the PVP skin substitute can minimize the mechanical mismatch between the substitute and native skin. The abundant elastin can suppress the overgrowth of fibroblast during neo-dermal regeneration to mitigate scar formation because it has been demonstrated that scarring could be mitigated by controlling fibroblast plasticity (Plikus et al., 2015; Chan and Longaker, 2017). We demonstrated in rodent models that the PVP skin substitute promoted wound healing, and scars did not form during the period of the study.

Study Limitation

We employed acid hydrolysis plus TPPS dye and alkaline treatment for the analyses of elastin contents in various tissues. The variations of elastin contents in the same tissue require discussion. In acid hydrolysis, the thick fibers of insoluble elastin may diminish the efficacy to convert insoluble elastin to soluble elastin. Therefore, the elastin contents may be underestimated in the PVP since the insoluble elastin may not be completely converted to soluble elastin. In alkaline treatment, the microfibrils of insoluble elastin may be rinsed out from loose ECM such as the SIS, which may result in underestimation of insoluble elastin in the SIS. The mechanical property of the PVP in comparison with the bPcm and SIS may provide additional parameters to verify an abundant elastin in the PVP.

CONCLUSION

The abundant collagen and elastin contents in sPVP and bPVP confer the merits of an elastin- and collagen-based ECM, including the mechanical compliance, cytotoxicity, biocompatibility, and regulation of cellular proliferation. I*n vitro* studies indicate that the PVP has minimal cytotoxicity. *In vivo* studies indicate excellent PVP biocompatibility and minimal inflammation. Hence, the PVP is a suitable biological material for the repair/reconstruction of soft tissues due to its abundant collagen and elastin contents, structural characteristics, and mechanical compliance.

DATA AVAILABILITY STATEMENT

The original contributions presented in the study are included in the article/supplementary material; further inquiries can be directed to the corresponding author.

ETHICS STATEMENT

The animal study was reviewed and approved by the California Medical Innovations Institute (IACUC).

AUTHOR CONTRIBUTIONS

XL contributed to conception, design of the study, statistical analysis, and writing of the manuscript. LH contributed to experiments, data analyses, and writing of sections of the manuscript. GK contributed to concept, design of the study, and writing of the manuscript. All authors contributed to manuscript revision, read, and approved the submitted version.

FUNDING

The work was supported by the National Institute of Health (grant R43HL149455 and R43HL149418).

ACKNOWLEDGMENTS

We acknowledge the support from 3DT Holdings. We thank Cook for providing the cytotoxicity data in **Figure 4**.

REFERENCES

Badylak, S. F., Tullius, R., Kokini, K., Shelbourne, K. D., Klootwyk, T., Voytik, S. L., et al. (1995). The Use of Xenogeneic Small Intestinal Submucosa as a Biomaterial for Achille's Tendon Repair in a Dog Model. *J. Biomed. Mater. Res.* 29 (8), 977–985. doi:10.1002/jbm.820290809

Chan, C. K. F., and Longaker, M. T. (2017). Fibroblasts Become Fat to Reduce Scarring. *Science* 355 (6326), 693–694. doi:10.1126/science.aam6748

da Silva, C. M. L., Spinelli, E., and Rodrigues, S. V. (2015). Fast and Sensitive Collagen Quantification by Alkaline Hydrolysis/hydroxyproline Assay. *Food Chem.* 173, 619–623. doi:10.1016/j.foodchem.2014.10.073

Daamen, W., Veerkamp, J., Vanhest, J., and Vankuppevelt, T. (2007). Elastin as a Biomaterial for Tissue Engineering. *Biomaterials* 28, 4378–4398. doi:10.1016/j.biomaterials.2007.06.025

Daly, W., Yao, L., Zeugolis, D., Windebank, A., and Pandit, A. (2012). A Biomaterials Approach to Peripheral Nerve Regeneration: Bridging the Peripheral Nerve gap and Enhancing Functional Recovery. *J. R. Soc. Interf.* 9 (67), 202–221. doi:10.1098/rsif.2011.0438

Fraser, R. S. (2005). "Histology and Gross Anatomy of the Respiratory Tract," in *Physiologic Basis of Respiratory Disease. Hamilton (ON)*. Editors Q. Hamid, J. Shannon, and J. Martin (Hamilton, ON: B.C. Decker Inc.), 1–14.

Gauvin, R., Marinov, G., Mehri, Y., Klein, J., Li, B., Larouche, D., et al. (2013). A Comparative Study of Bovine and Porcine Pericardium to Highlight Their Potential Advantages to Manufacture Percutaneous Cardiovascular Implants. *J. Biomater. Appl.* 28, 552–565. doi:10.1177/0885328212465482

Harkness, M. L., Harkness, R. D., and Mcdonald, D. A. (1957). The Collagen and Elastin Content of the Arterial wall in the Dog. *Proc. R. Soc. Lond. B Biol. Sci.* 146, 541–551. doi:10.1098/rspb.1957.0029

Hsueh, Y.-S., Savitha, S., Sadhasivam, S., Lin, F.-H., and Shieh, M.-J. (2014). Design and Synthesis of Elastin-like Polypeptides for an Ideal Nerve Conduit in Peripheral Nerve Regeneration. *Mater. Sci. Eng. C* 38, 119–126. doi:10.1016/j.msec.2014.01.058

Humphrey, J. D., Vawter, D. L., and Vito, R. P. (1986). Mechanical Behavior of Excised Canine Visceral Pleura. *Ann. Biomed. Eng.* 14, 451–466. doi:10.1007/bf02367365

Huszar, G., Maiocco, J., and Naftolin, F. (1980). Monitoring of Collagen and Collagen Fragments in Chromatography of Protein Mixtures. *Anal. Biochem.* 105, 424–429. doi:10.1016/0003-2697(80)90481-9

Kesava Reddy, G., and Enwemeka, C. S. (1996). A Simplified Method for the Analysis of Hydroxyproline in Biological Tissues. *Clin. Biochem.* 29 (3), 225–229. doi:10.1016/0009-9120(96)00003-6

Kothapalli, C. R., and Ramamurthi, A. (2009). Biomimetic Regeneration of Elastin Matrices Using Hyaluronan and Copper Ion Cues. *Tissue Eng. A* 15 (1), 103–113. doi:10.1089/ten.tea.2007.0390

Ligas, J. R., Primiano, F. P., Jr., and Saidel, G. M. (1984). Static Mechanics of Excised Whole Lung: Pleural Mechanics. *Ann. Biomed. Eng.* 12, 437–448. doi:10.1007/bf02363915

Lindberg, K., and Badylak, S. F. (2001). Porcine Small Intestinal Submucosa (SIS): a Bioscaffold Supporting *In Vitro* Primary Human Epidermal Cell Differentiation and Synthesis of Basement Membrane Proteins. *Burns* 27 (3), 254–266. doi:10.1016/s0305-4179(00)00113-3

Lokshin, O., and Lanir, Y. (2009). Viscoelasticity and Preconditioning of Rat Skin under Uniaxial Stretch: Microstructural Constitutive Characterization. *J. Biomech. Eng.* 131, 031009. doi:10.1115/1.3049479

Lu, X., Han, L., Golts, E., Baradarian, S., and Kassab, G. S. (2020). Homologous and Heterologous Assessment of a Novel Biomaterial for Venous Patch. *J. Vasc. Surg. Venous Lymphatic Disord.* 8 (3), 458–469. doi:10.1016/j.jvsv.2019.09.011

Lu, X., Han, L., and Kassab, G. S. (2019). *In Vivo* self-assembly of Small Diameter Pulmonary Visceral Pleura Artery Graft. *Acta Biomater.* 83, 265–276. doi:10.1016/j.actbio.2018.11.001

Ma, F., Xiao, Z., Meng, D., Hou, X., Zhu, J., Dai, J., et al. (2014). Use of Natural Neural Scaffolds Consisting of Engineered Vascular Endothelial Growth Factor Immobilized on Ordered Collagen Fibers Filled in a Collagen Tube for Peripheral Nerve Regeneration in Rats. *Ijms* 15, 18593–18609. doi:10.3390/ijms151018593

Maestro, M. M., Turnay, J., Olmo, N., Fernández, P., Suárez, D., Páez, J. M. G., et al. (2006). Biochemical and Mechanical Behavior of Ostrich Pericardium as a New Biomaterial. *Acta Biomater.* 2, 213–219. doi:10.1016/j.actbio.2005.11.004

Malek, A. M., Alper, S. L., and Izumo, S. (1999). Hemodynamic Shear Stress and its Role in Atherosclerosis. *JAMA* 282, 2035–2042. doi:10.1001/jama.282.21.2035

Mecham, R. P. (2018). Elastin in Lung Development and Disease Pathogenesis. *Matrix Biol.* 73, 6–20. doi:10.1016/j.matbio.2018.01.005

Meyer, M. (2019). Processing of Collagen Based Biomaterials and the Resulting Materials Properties. *Biomed. Eng. Online* 18 (1), 24. doi:10.1186/s12938-019-0647-0

Michailova, K. N. (1997). Ultrastructural Observations on the Human Visceral Pleura. *Eur. J. Morphol.* 35, 125–135. doi:10.1076/ejom.35.2.125.13063

Munnelly, A. E., Cochrane, L., Leong, J., and Vyavahare, N. R. (2012). Porcine Vena Cava as an Alternative to Bovine Pericardium in Bioprosthetic Percutaneous Heart Valves. *Biomaterials* 33, 1–8. doi:10.1016/j.biomaterials.2011.09.027

Neethling, W. M. L., Hodge, A. J., and Glancy, R. (2003). Glutaraldehyde-fixed Kangaroo Aortic wall Tissue: Histology, Crosslink Stability and Calcification Potential. *J. Biomed. Mater. Res.* 66, 356–363. doi:10.1002/jbm.b.10015

Oldmixon, E. H., and Hoppin, F. G., Jr. (1984). Comparison of Amounts of Collagen and Elastin in Pleura and Parenchyma of Dog Lung. *J. Appl. Physiol.* 56, 1383–1388. doi:10.1152/jappl.1984.56.5.1383

Partridge, S. M., Davis, H. F., and Adair, G. S. (1955). The Chemistry of Connective Tissues. 2. Soluble Proteins Derived from Partial Hydrolysis of Elastin. *Biochem. J.* 61, 11–21. doi:10.1042/bj0610011

Plikus, M. V., Guerrero-Juarez, C. F., Treffeisen, E., and Gay, D. L. (2015). Epigenetic Control of Skin and Hair Regeneration after Wounding. *Exp. Dermatol.* 24, 167–170. doi:10.1111/exd.12488

Sánchez, P. F., Brey, E. M., and Briceño, J. C. (2018). Endothelialization Mechanisms in Vascular Grafts. *J. Tissue Eng. Regen. Med.* 12 (11), 2164–2178. doi:10.1002/term.2747

Schmidt, C. E., and Leach, J. B. (2003). Neural Tissue Engineering: Strategies for Repair and Regeneration. *Annu. Rev. Biomed. Eng.* 5, 293–347. doi:10.1146/annurev.bioeng.5.011303.120731

Shapiro, S. D., Endicott, S. K., Province, M. A., Pierce, J. A., and Campbell, E. J. (1991). Marked Longevity of Human Lung Parenchymal Elastic Fibers Deduced from Prevalence of D-Aspartate and Nuclear Weapons-Related Radiocarbon. *J. Clin. Invest.* 87, 1828–1834. doi:10.1172/jci115204

Shi, Z.-D., and Tarbell, J. M. (2011). Fluid Flow Mechanotransduction in Vascular Smooth Muscle Cells and Fibroblasts. *Ann. Biomed. Eng.* 39, 1608–1619. doi:10.1007/s10439-011-0309-2

Starcher, B. C. (1986). Elastin and the Lung. *Thorax* 41 (8), 577–585. doi:10.1136/thx.41.8.577

Tamariz, E., and Grinnell, F. (2002). Modulation of Fibroblast Morphology and Adhesion during Collagen Matrix Remodeling. *MBoC* 13, 3915–3929. doi:10.1091/mbc.e02-05-0291

Waitayawinyu, T., Parisi, D. M., Miller, B., Luria, S., Morton, H. J., Chin, S. H., et al. (2007). A Comparison of Polyglycolic Acid versus Type 1 Collagen Bioabsorbable Nerve Conduits in a Rat Model: an Alternative to Autografting. *J. Hand Surg.* 32 (10), 1521–1529. doi:10.1016/j.jhsa.2007.07.015

Walters, B. D., and Stegemann, J. P. J. P. (2014). Strategies for Directing the Structure and Function of Three-Dimensional Collagen Biomaterials across Length Scales. *Acta Biomater.* 10 (4), 1488–1501. doi:10.1016/j.actbio.2013.08.038

Wang, Y., Marshall, K. L., Baba, Y., Lumpkin, E. A., and Gerling, G. J. (2015). Compressive Viscoelasticity of Freshly Excised Mouse Skin Is Dependent on Specimen Thickness, Strain Level and Rate. *PLoS ONE* 10 (3), e0120897. doi:10.1371/journal.pone.0120897

Wang, Y., Wang, H., Mi, D., Gu, X., and Hu, W. (2015). Periodical Assessment of Electrophysiological Recovery Following Sciatic Nerve Crush via Surface Stimulation in Rats. *Neurol. Sci.* 36, 449–456. doi:10.1007/s10072-014-2005-0

Waterhouse, A., Wise, S. G., Ng, M. K., and Weiss, A. S. (2011). Elastin as a Nonthrombogenic Biomaterial. *Tissue Eng. Part. B Rev.* 17, 93–99. doi:10.1089/ten.TEB.2010.0432

Whitlock, E. L., Tuffaha, S. H., Luciano, J. P., Yan, Y., Hunter, D. A., Magill, C. K., et al. (2009). Processed Allografts and Type I Collagen Conduits for Repair of Peripheral Nerve Gaps. *Muscle Nerve* 39 (6), 787–799. doi:10.1002/mus.21220

Wise, S. G., Mithieux, S. M., and Weiss, A. S. (2009). Engineered Tropoelastin and Elastin-Based Biomaterials. *Rev. Adv Protein Chem Struct Biol* 78, 1–24. doi:10.1016/S1876-1623(08)78001-5

Wolinsky, H. (1970). Response of the Rat Aortic Media to Hypertension. *Circ. Res.* 26, 507–522. doi:10.1161/01.res.26.4.507

Zhao, X., Berwick, Z. C., Krieger, J. F., Chen, H., Chambers, S., and Kassab, G. S. (2014). Novel Design of Cruciform Specimens for Planar Biaxial Testing of Soft Materials. *Exp. Mech.* 54 (3), 343–356. doi:10.1007/s11340-013-9808-4

Zilla, P., Bezuidenhout, D., and Human, P. (2007). Prosthetic Vascular Grafts: Wrong Models, Wrong Questions and No Healing. *Biomaterials* 28 (34), 5009–5027. doi:10.1016/j.biomaterials.2007.07.017

Conflict of Interest: The authors declare that the research was conducted in the absence of any commercial or financial relationships that could be construed as a potential conflict of interest.

Frontiers in Cell and Developmental Biology

ORIGINAL RESEARCH
published: 16 May 2022
doi: 10.3389/fcell.2022.886110

Involvement of Mechanical Cues in the Migration of Cajal-Retzius Cells in the Marginal Zone During Neocortical Development

Ana López-Mengual[1,2,3,4], *Miriam Segura-Feliu*[1,2,3,4], *Raimon Sunyer*[5], *Héctor Sanz-Fraile*[5], *Jorge Otero*[5,6], *Francina Mesquida-Veny*[1,2,3,4], *Vanessa Gil*[1,2,3,4], *Arnau Hervera*[1,2,3,4], *Isidre Ferrer*[4,7,8], *Jordi Soriano*[9,10], *Xavier Trepat*[5,11,12,13], *Ramon Farré*[5,6,14], *Daniel Navajas*[5,6,15] and *José Antonio del Río*[1,2,3,4]*

[1]Molecular and Cellular Neurobiotechnology, Institute for Bioengineering of Catalonia (IBEC), Barcelona, Spain, [2]Department of Cell Biology, Physiology and Immunology, Universitat de Barcelona, Barcelona, Spain, [3]Network Centre of Biomedical Research of Neurodegenerative Diseases (CIBERNED), Institute of Health Carlos III, Madrid, Spain, [4]Institute of Neuroscience, University of Barcelona, Barcelona, Spain, [5]Unitat de Biofísica I Bioenginyeria, Universitat de Barcelona, Barcelona, Spain, [6]Centro de Investigación Biomédica en Red en Enfermedades Respiratorias, Madrid, Spain, [7]Senior Consultant, Bellvitge University Hospital, Hospitalet de Llobregat, Barcelona, Spain, [8]Department of Pathology and Experimental Therapeutics, University of Barcelona, Barcelona, Spain, [9]Departament de Física de La Matèria Condensada, Universitat de Barcelona, Barcelona, Spain, [10]University of Barcelona Institute of Complex Systems (UBICS), Barcelona, Spain, [11]Integrative Cell and Tissue Dynamics, Institute for Bioengineering of Catalonia (IBEC), Parc Científic de Barcelona, Barcelona, Spain, [12]Center for Networked Biomedical Research on Bioengineering, Biomaterials and Nanomedicine (CIBER-BBN), Madrid, Spain, [13]Institució Catalana de Recerca I Estudis Avançats, University of Barcelona, Barcelona, Spain, [14]Institut D'Investigacions Biomèdiques August Pi Sunyer, Barcelona, Spain, [15]Cellular and Respiratory Biomechanics, Institute for Bioengineering of Catalonia (IBEC), Barcelona, Spain

Edited by:
Rajprasad Loganathan,
Johns Hopkins Medicine,
United States

Reviewed by:
Yuki Hirota,
Keio University School of Medicine,
Japan
Achira Roy,
Jawaharlal Nehru Centre for
Advanced Scientific Research, India

***Correspondence:**
José Antonio del Río
jadelrio@ibecbarcelona.eu

Specialty section:
This article was submitted to Cell Adhesion and Migration, a section of the journal Frontiers in Cell and Developmental Biology

Received: *28 February 2022*
Accepted: *25 April 2022*
Published: *16 May 2022*

Citation:
López-Mengual A, Segura-Feliu M, Sunyer R, Sanz-Fraile H, Otero J, Mesquida-Veny F, Gil V, Hervera A, Ferrer I, Soriano J, Trepat X, Farré R, Navajas D and del Río JA (2022) Involvement of Mechanical Cues in the Migration of Cajal-Retzius Cells in the Marginal Zone During Neocortical Development. Front. Cell Dev. Biol. 10:886110. doi: 10.3389/fcell.2022.886110

Emerging evidence points to coordinated action of chemical and mechanical cues during brain development. At early stages of neocortical development, angiogenic factors and chemokines such as CXCL12, ephrins, and semaphorins assume crucial roles in orchestrating neuronal migration and axon elongation of postmitotic neurons. Here we explore the intrinsic mechanical properties of the developing marginal zone of the pallium in the migratory pathways and brain distribution of the pioneer Cajal-Retzius cells. These neurons are generated in several proliferative regions in the developing brain (e.g., the cortical hem and the pallial subpallial boundary) and migrate tangentially in the preplate/marginal zone covering the upper portion of the developing cortex. These cells play crucial roles in correct neocortical layer formation by secreting several molecules such as Reelin. Our results indicate that the motogenic properties of Cajal-Retzius cells and their perinatal distribution in the marginal zone are modulated by both chemical and mechanical factors, by the specific mechanical properties of Cajal-Retzius cells, and by the differential stiffness of the migratory routes. Indeed, cells originating in the cortical hem display higher migratory capacities than those generated in the pallial subpallial boundary which may be involved in the differential distribution of these cells in the dorsal-lateral axis in the developing marginal zone.

Keywords: Cajal-Retzius cells, cortical development, mechanical cues, marginal zone, atomic force microscopy, traction force microscopy

INTRODUCTION

Cajal-Retzius (CR) cells were first described by Santiago Ramón y Cajal and Gustaf Retzius (in 1890 and 1892, respectively) (Gil et al., 2014; Martinez-Cerdeno and Noctor, 2014). These cells are early-generated neurons located in cortical marginal zone/layer I that split from the embryonic preplate to form the marginal zone and the subplate when the cortical plate develops during early cortical development [(e.g., see (Soriano and Del Rio, 2005; Villar-Cervino and Marin, 2012; Kirischuk et al., 2014; Martinez-Cerdeno and Noctor, 2014; Marin-Padilla, 2015)]. Although several differences in CR cell phenotype, markers, physiology, and fate have been described in different mammals [e.g., (Cabrera-Socorro et al., 2007; Meyer, 2010; Meyer and Gonzalez-Gomez, 2018)], Reelin expressed by mouse CR cells during cortical development modulates the appropriate migration of cortical plate neurons, actively participating in neuronal network activity in developing marginal zone/layer I [e.g., (Soriano and Del Rio, 2005)]. In rodents, CR cells have the capacity to generate action potentials, establishing synaptic contacts in the marginal zone/layer I and receiving excitatory and GABAergic and non-GABAergic inputs (Frotscher et al., 2003; Soriano and Del Rio, 2005; Frotscher et al., 2009; Marin et al., 2010; Myakhar et al., 2011; Villar-Cervino and Marin, 2012; Quattrocolo and Maccaferri, 2013; Gesuita and Karayannis, 2021). Mouse CR cells are mainly generated in three neurogenic areas: the cortical hem (CH) (Takiguchi-Hayashi et al., 2004; Garcia-Moreno et al., 2007), the septum retrobulbar area (SR), and the pallial subpallial boundary (PSB) (Bielle et al., 2005). Shortly after generation, CR cells migrate through the preplate/marginal zone to populate the entire cortical surface following specific rostro-caudal and latero-tangential processes (De Carlos et al., 1995; Yamazaki et al., 2004; Bielle et al., 2005; Garcia-Moreno et al., 2007; Griveau et al., 2010; Miquelajauregui et al., 2010; Villar-Cervino et al., 2013). This dorsal-ventral migration of CR cells as well as subplate neurons thorough the preplate has been reported to play a crucial role in regionally defining the developing neocortex (Saito et al., 2019). Birthdates of cortical CR cells are between embryonic days 8.5 and 13.5 (E8.5-13.5) in the mouse, with a maximum between E9.5 and E12.5 (del Rio et al., 1995; Hevner et al., 2003; Gu et al., 2011), although a recent study points to a supply of CR cells from the olfactory bulb at protracted embryonic stages (de Frutos et al., 2016). During the first and second postnatal week, mouse CR cells disappear from layer I by programmed cell death [e.g., (Del Río et al., 1995; Del Rio et al., 1996)]. In fact, both their distribution and their differential disappearance play a role in neocortical regionalization and maturation (Ledonne et al., 2016; Riva et al., 2019).

Genetic screening of CR cells has revealed that a large number of factors are involved in their generation, migration, and maturation, such as *p73*, *p21*, *Zic1-3, Lhx5, and Fgf8*, *Tbr1, and 2*, *MDGA1*, *Emx1,* and *Emx2*, *Nectin1*, *Dmrt*, *Dbx1*, *Foxg1*, *Ebf2, Foxc1, LIM-homeobox* genes, and *miRNA9,* among others (Mallamaci et al., 1998; Hevner et al., 2001; Hevner et al., 2003; Muzio and Mallamaci, 2005; Zhao et al., 2006; Hanashima et al., 2007; Takeuchi et al., 2007; Abellan et al., 2010; Zimmer et al., 2010; Chiara et al., 2012; Zarbalis et al., 2012; Gil-Sanz et al., 2013; Hodge et al., 2013; Kikkawa et al., 2020). Concerning migration, several molecules have been identified as regulators of CR cell migration and distribution in the marginal zone, e.g., CXCL12, Eph/Ephrins, or Pax6 (Borrell and Marin, 2006; Paredes et al., 2006; Ceci et al., 2010; Villar-Cervino et al., 2013; Kaddour et al., 2020). In fact, CXCL12 (also termed Stromal Derived Factor 1, SDF-1), secreted by meningeal cells, is considered to be mainly responsible for CH-derived CR cell migration through CXCR4 and CXCR7 receptors expressed in CR cells. Surprisingly, the migration at the subpial position of CR cells in *CXCR4*–/–, *CXCR7*–/–, and *CXCL12*–/– mice, although affected, is largely maintained at dorsal pallial levels (Stumm et al., 2003). This is in contrast to other studies displaying relevant changes in CR cells location and cortical layering after the chemical removal of meningeal cells or genetic modification, suggesting that other factors associated with meninges are involved in CR cells migration and distribution (Super et al., 1997; Paredes et al., 2006; Dasgupta and Jeong, 2019). Angiogenic factors present in the outermost cortical blood vessels associated with meninges such as VEGF, Sema3E, and Ephrins have emerged as important cellular cues regulating the migration of CR cells, as is the case in other developmental processes [e.g., (Skaper et al., 2001; Mackenzie and Ruhrberg, 2012; Bribian et al., 2014)].

In addition, evidence emerging from recent research shows that, in parallel to chemical cues, neural morphogenesis, neuronal migration, and axon navigation are processes also governed by sensing the mechanical properties of the extracellular milieu (e.g., Young's modulus and topography) and neighboring cells during development [e.g., (Franze, 2013; Gangatharan et al., 2018; Javier-Torrent et al., 2021; Oliveri et al., 2021)]. These interactions influence the maturation and differentiation of particular neurons based on transduction of those external mechanical forces into intracellular biochemical signaling *via* a mechanical-transduction process (De Vincentiis et al., 2020; Javier-Torrent et al., 2021). This mechanical-transduction process involves the action of integrins and other elements linking extracellular matrix (ECM) to cellular cytoskeleton dynamics [see (Elosegui-Artola et al., 2018) for review]. In addition, specific signaling mechanisms such as mechanosensory receptors (e.g., Piezo1) and Hippo/YAP pathways are players in the mechanical transduction process in several cell types and tissues [e.g., (Nguyen-Lefebvre et al., 2021; Wu and Guan, 2021)], including neural tissue [e.g., (Sahu and Mondal, 2021)]. Considering matrix stiffness during mouse cortical development, Iwasita and coworkers measured, by means of Atomic Force Microscopy (AFM), the values for Young's/Elastic modulus (E) of the cortical plate (CP), the intermediate zone (IZ), the subventricular zone (SVZ), and the ventricular zone (VZ) in coronal sections of the prospective parietal cortex of the mouse at different postnatal stages (from E12.5 to E18.5) (Iwashita et al., 2014). In a broad sense, all values (for all cortical layers) increased from E12.5 with a peak at E16.5 and then decreasing (see **Figures 1**, **2** in (Iwashita et al., 2014)) at late (E18.5) embryonic stages. Young's modulus values ranked (for the CP) from 30.1 Pa at E12.5 to a maximum of 108.4 Pa (E16.5), decreasing to 57.4 Pa at E18.5. However, preplate and their

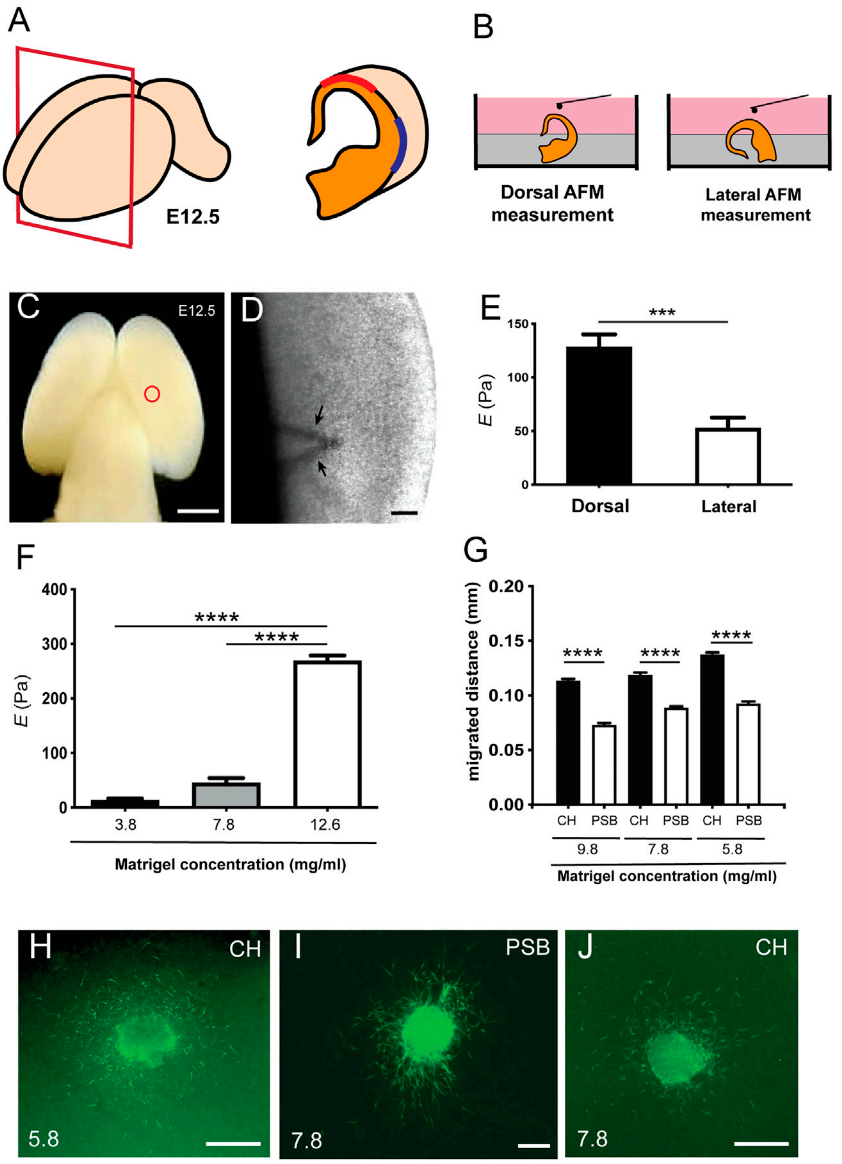

FIGURE 1 | Differential stiffness between dorsal and lateral regions of the pallial marginal zone in developing mouse embryos **(A)** Scheme illustrating the procedure of placement of the telencephalic hemispheres of the embryo (E12.5). **(B)** Illustration showing the procedure for Atomic Force Microscopy (AFM), in which the whole brain embryo was first embedded in agarose to obtain dorsal and lateral measurement using the BIO-AFM. **(C,D)** Scheme **(C)** and high magnification photograph **(D)** obtained from the BIO-AFM illustrating the location of the V-shaped cantilever (circle in **C** and arrows in **D**) in the surface of the marginal zone. **(E)** Histogram showing the results of the BIO-AFM experiments; *E* values are displayed in the *y* axis in Pa. **(F)** Rheometric values obtained after the analysis of three different hydrogels. The concentration of the total protein of the analyzed hydrogels is shown in the *x* axis. **(G)** Bar plots comparing the amount of differential migration of CR cells (obtained from CH or PSB) for gradually higher Matrigel™ concentrations **(H–J)** Examples of CH **(H–J)** and PSB **(I)** cultured explants in different Matrigel™ concentrations (5.8 and 7.8 mg/ml) immunostained against CALR to identify CR cells. CH: cortical hem; PSB: pallium subpallium boundary. Data in **(E,F,G)** are presented as mean ± s.e.m.; $^{***}p < 0.001$ and $^{****}p < 0.0001$. Scale bars: C = 1 mm, D = 500 µm, H and J = 300 µm and I = 300 µm.

derivatives: the molecular layer/layer I were not thoroughly analyzed in the study.

Concerning CR cell migration, a pioneer study described differences in the migratory properties of these cells depending on their origin (rostral *vs.* medial) after ectopic transplantation in different areas of the embryonic cortical hem (Ceci et al., 2010). Thus, the study revealed, for the first time, that the local environment in parallel to guidance molecules can modulate the migration of CH-derived CR cells (Ceci et al., 2010). In addition, Barber et al. (2015). demonstrated differences in migratory speed of subsets of CR cells. In fact, using *in vitro* experiments of the complete pallium, Barber et al. (2015). described how SR-derived and CH-derived CR cells migrate and then stop their migration at the dorsal pallium levels; whereas PSB derived CR cells migrate in the rostral caudal axis in the lateral part of the pallium (Barber et al., 2015).

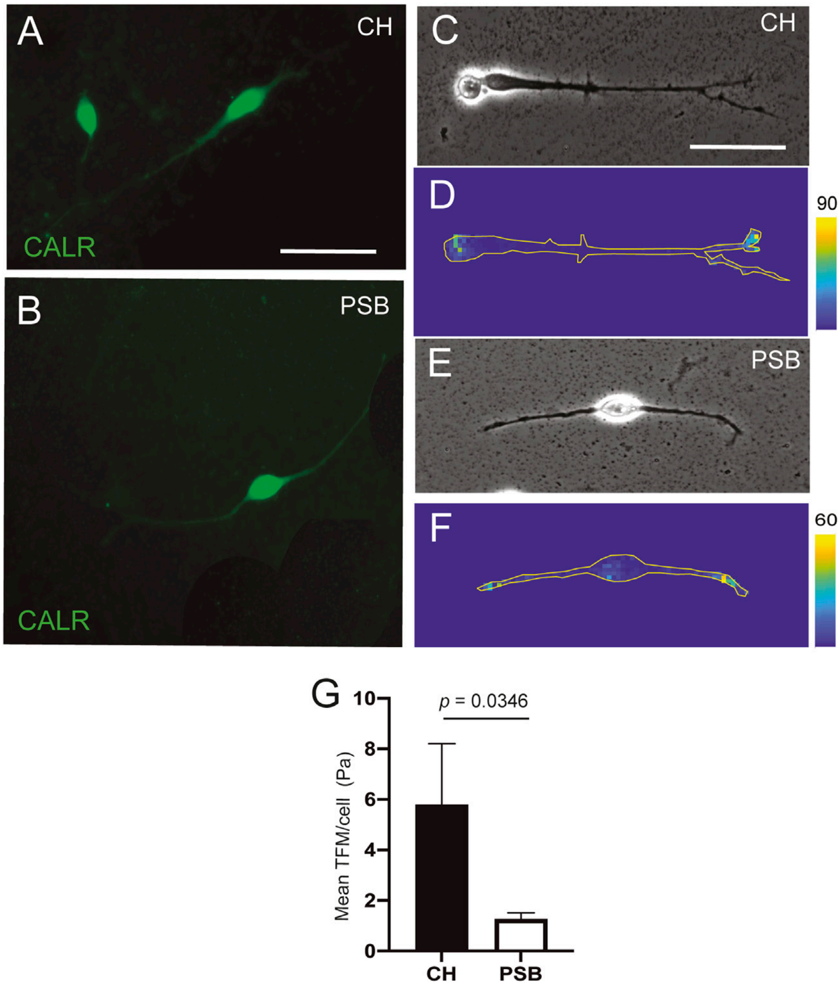

FIGURE 2 | TFM measurements of CH and PSB-derived CR cells in PAA gels **(A,B)** Examples of CR cells stained using CALR antibodies derived from CH **(A)** and PSB **(B)**. **(C–F)** Phase contrast (c and e) and constraint force maps (D and F) of CR cells derived from CH **(C,D)** and PSB **(E,F)** after TFM analysis. Forces triggered by the CR cells are color-coded according to their intensity. The shape of the CR cells is outlined with a yellow contour in the constraint maps to better visualize their extent. These maps reveals that the highest traction values are morphologically located at the tips of their neurites, for both CH- and PSB-derived CR cells **(G)** Results of the Traction Force Microscopy (TFM) analysis. The bar plots show the mean pressure (force per unit area) generated by the different CR cells. The pressure values are obtained by dividing the measured forces by the total area pixels occupied by the analyzed CR cells. CH: cortical hem; PSB: pallium-subpallium boundary. Data in (g) are presented as mean ± s.e.m.. The indicated *p* value was obtained by using the one-tail permutation test. Scale bars, A = 50 µm pertains to B, C = 50 µm pertains to **(D–F)**.

In this study, we aimed to explore whether putative differences in the mechanical properties between dorsal and lateral parts of the developing marginal zone/layer I also influenced the migration and distribution of CR cells derived from the CH and the PSB of the mouse. Our data reveal that both the stiffness differences between medial and lateral regions of the pallial marginal zone as well as the intrinsic mechanical properties of CR cells contribute to their migration from the CH and PSB in the dorsal and lateral parts of the developing neocortex.

MATERIAL AND METHODS

Animals

The following mice and rat strains were used in the present study: OF1 mice (E12.5) (RRID: MGI:5649743) and Sprague Dawley rats (E14.5) (RRID: MGI:5651135) were purchased from Charles River laboratories (Paris, France). In addition, the mTmG mice (ROSA$^{mT/mG}$; RRID: IMSR_JAX:007576; The Jackson Laboratories; Bar Harbor, ME, United States) were also used. *Plxnd1-eGFP* mice were obtained from the Mutant Mouse Regional Resource Center (MMRRC; RRID: MMRRC_015415-UCD; University of California, CA, United States). mTmG and *Plxnd1-eGFP* mouse genotypes were verified by observing a tail fragment under a fluorescence microscope (BX61; Olympus Corporation). In addition, CXCR4-eGFP transgenic mice (RRID: MMRRC_015859-UCD; kindly provided by J.H.R. Lubke [Germany) (Anstotz et al., 2014)] were used. All the animals were kept in the animal facility of the Faculty of Pharmacy at the University of Barcelona under controlled environmental conditions and were provided food and drink ad libitum. For AFM experiments, OF1 pregnant mice were housed in the animal facility of the Faculty of Medicine at the University of Barcelona. All the experiments were carried out following protocols of the Ethics Committee for Animal Experimentation (CEEA) of the University of Barcelona (OB47/19, C-007, 276/16, and 47/20).

CH and Pallial Subpallial Boundary Explant Dissection

In order to obtain CH and PSB regions, embryonic brains (E12.5) were covered with a mixture of L15 medium (31415-029, Invitrogen) containing 4% low melting point agarose (50111, Lonza) which was then allowed to solidify at 4°C for a few minutes. After gelation, 300 μm-thick coronal sections were obtained using a vibratome (VT1000S, Leica). Free-floating slices were collected in cold 0.1 M PBS containing 0.6% glucose and selected under a dissection microscope, and the explants of CH or PSB were dissected.

Culture of CH and Pallial Subpallial Boundary-Derived Explants on Hydrogels

For explants embedded in hydrogels, a sandwich procedure was used using a base of homemade rat tail type I collagen (Gil and del Rio, 2012) and a top of Matrigel™ (354434, Corning, Cultek). To prepare the Matrigel™ at different densities, cold Neurobasal™ media (21103-049, Invitrogen) was used to dilute Matrigel™ stock solution. One explant per preparation was placed on a homogeneous collagen base and then another layer of Matrigel™ was added on top. Before the Matrigel™ gels, explant position was verified and correctly positioned under the dissecting microscope. Once the explant was seeded, the gel was allowed to coagulate at 37°C, 5% CO_2 before adding the supplemented medium. At 2 days *in vitro* (DIV), explants were fixed for 1 h with cold 4% buffered paraformaldehyde (PFA) before washing with 0.1 M PBS, and then stored at 4°C prior to immunocytochemistry or photodocumentation. The number of cells that migrated out of the explants was counted, and the maximum distance migrated from the cell body to the explant edge was also determined using Fiji™ software, using as calibration pictures of a millimetric eyepiece at the same magnification. In some experiments, CH-derived explants were treated with 4 μg/ml of Cytochalasin D (C8273, Sigma-Aldrich), 10 μM Nocodazole (M1404, Sigma-Aldrich), or 0.5 μg/ml of Blebbistatin (1760, Tocris).

In vitro Transplantation of CH or Pallial Subpallial Boundary Explants in Telencephalic Slices

Brain slices were obtained from E12.5 wild-type mice and the CH and the PSB from E12.5 mTmG mouse embryos as described [see also (Bribian et al., 2014)]. Slices were transferred to collagen-coated culture membrane (PICM0RG50, Millipore) in 1.2 ml of medium BME-F12 1:1 (41010-026, Invitrogen), glutamine (25030-024, Invitrogen), 5% horse serum (26050-088; Invitrogen), penicillin, streptomycin (15140122, Invitrogen), and 5% bovine calf serum (12133C, Sigma-Aldrich). The CH and PSB from wild-type slices were removed and replaced with the dissected CH or the PSB from mTmG mice slices. After several hours, the medium was changed to Neurobasal™ medium supplemented as above and cultured for up to 48 h before analysis.

In situ Hybridization

In situ hybridization was carried out as described previously (Mingorance et al., 2004; Mata et al., 2018) on 50 μm vibratome fixed brain sections of E12.5 embryos. Both sense and antisense riboprobes against *Wnt2b* (provided by P. Bovolenta) and *Reln* (provided by T. Curran) were labelled with digoxigenin, according to the manufacturer's instructions (Roche Farma).

Immunocytochemical Methods

The processing of each *in vitro* model was determined by its culture characteristics (hydrogel, coverslip, or brain slice). Although the general procedure was similar for all conditions, the incubation times and mounting methods for analysis differed. The general procedure started with fixing the tissue samples with 4% PFA, then washing them with 0.1 M PBS and a blocking solution composed of 10% Fetal Bovine Serum (FBS; 10500064, Invitrogen) and 0.1 M PBS with Triton X-100 (Sigma-Aldrich) (concentration determined by each model). After washing with PBS-Triton X-100, the primary antibody was incubated with 7% FBS and PBS–0.2% gelatin and Triton X-100. This was followed by the Alexa-tagged secondary antibodies (Alexa 488; A21206, Invitrogen) diluted in 7% serum (FBS) and PBS 0.1 M containing gelatin 0.2% and 0.1% Triton X-100. Afterwards, nuclear staining was performed using Hoechst (1 μg/ml; B2261, Sigma-Aldrich). The antibody used for CR cell labeling was Calretinin (CALR; 1: 1,000; 7,697, Swant Antibodies). Details of the immunocytochemical procedures in each model are briefly explained below. For explant cultures growing in Matrigel™ 0.5% Triton X-100 was used in all steps and long incubation times were observed. After fixation for 1 h at 4°C with 4% buffered PFA and blockade for 4 h at room temperature, the primary antibody was incubated for 2 overnights at 4°C and the secondary antibody for 1 overnight at 4°C with gentle shaking. Finally, nuclear labeling with Hoechst was developed for 20 min before washing with 0.1 M PBS and mounting with Mowiol™ (475904, Calbiochem). For primary cultures of CH or PSB-derived CR cells growing on polyacrylamide (PAA) gels for Traction Force Microscopy (TFM) experiments, a short fixation time (5 min) with 2% buffered PFA (removing half of the medium), and 10 min in 4% buffered PFA at 4°C, was developed in selected preparations. Thereafter, fixed neurons were incubated at room temperature for 1 h with blocking solution, 2 h with primary antibodies, and 1 h for the secondary antibodies, at room temperature with gentle shaking. Hoechst staining was run for 10 min before washing with 0.1 M PBS after immunohistochemistry and photodocumentation. For slice cultures, coronal slices after CH or PSB transplantation (see above) were fixed for 1 h with 4% buffered PFA, and after this detached from the transwell membrane and free-floating processed with gentle agitation. All the immunohistological solutions contained 0.5% Triton X-100 and the samples were incubated for longer times. Thus, slices were treated with blocking solution for 4 h, incubated with primary antibodies for 48 h, and then for 12 h with secondary antibodies at 4°C with gentle shaking. Finally, the Hoechst solution was incubated for 20 min before washing with 0.1 M PBS and mounting with Mowiol™; double labelled CALR-mTmG-positive CR cells were photodocumented using a Zeiss SLM800 confocal microscopy.

Viscoelastic Properties of Matrigel™ Hydrogels Analysed With Rheometry

The different densities checked in the study were obtained from a Matrigel™ stock with known total protein concentration diluted in cold Neurobasal™ medium. The dilutions were different for different batches of Matrigel™: 12.72 mg/ml (Lot no: 9294006), 12.6 mg/ml (Lot no: 8015325), 11.95 mg/ml (Lot no: 9021221), and 9.8 mg/ml (Lot no: 9148009). To obtain the hydrogels, a minimum of 100 µl of mixture was needed per dish, carefully depositing the mixture and leaving it to gel for 2–4 h at 37°C. Once gelled, complete Neurobasal™ medium was added to cover, and left in an incubator at 37°C and 5% $CO_{2.}$ At 2 DIV the dishes were carefully lifted and placed on a rheometer plate previously heated to 37°C and calibrated. For rheometry measurement of the hydrogels, an ∅ 8 mm Peltier (Peltier plate Steel — 108990) coupled to a Discovery Hybrid Rheometer HR-2 (Discovery HR-2; 5,332-0316; TA instruments) was used. To prevent evaporation, rapeseed oil was used as a solvent-trap after applying loading gap to the sample and deleting medium and excess hydrogel. Finally, the geometry was taken to the gap to geometry and the chosen measurement began. With the TRIOS program (v. 5.0.0.44608) the Frequency sweep test using a gap of 0.5 mm (previously determined) was selected. To obtain the elastic modulus *E*, we first measured the storage and loss moduli in experiments at 1 Hz frequency sweep, which provided a strain modulus *G* given by the equation:

$$G = \sqrt{(G')^2 + (G'')^2}$$

Where G' corresponds to storage modulus and G'' to loss modulus. Once *G* was obtained, the elastic modulus *E* values were determined as equation:

$$E = 2G(1 + v)$$

Where v is the Poisson's ratio, defined as the ratio of transverse contraction strain to longitudinal extension strain, and that was assumed to be 0.5 for low stiffness hydrogels.

Atomic Force Microscopy Experiments

For *in situ* AFM measurements, whole E12.5 mouse embryonic brains were carefully dissected without damaging the cortical surface. Then, a 4% agarose (SeaPlaque™ GTGTM Agarose, 50111; Lonza) solution was prepared in 0.1M PBS and left at 45°C in a dry bath. The whole brain was dissected and examined at dorsal and lateral regions of the pallium for AFM analysis (**Figure 1**). Two brain orientations were generated in embedding the whole brain in specific orientation with agarose to achieve dorsal and lateral AFM measurements of the brain surface avoiding the supallial areas (**Figure 1B**). Briefly, a large plate, with a glass slide for AFM calibration, containing 2–3 mm thickness of 4% agarose, was prepared. Once jellified, one hemisphere was carefully placed over the agarose surface adding more agarose to embed the subpallial brain regions, leaving the dorsal pallial area to develop the dorsal AFM measurements (**Figure 1B**). In parallel experiments, the other whole hemisphere was placed laterally over the bottom agarose with the medial brain portion in contact with agarose, being leaving the lateral part of the pallium of the agarose-embedded brain for AFM measurement (**Figure 1B**). After gelling, the plate was covered with complete Neurobasal™ medium and placed in the incubation chamber at 37°C.

Measurements were carried out on a custom-made BIO-AFM mounted on an inverted optical microscope (TE 2000; Nikon). AFM was equipped with a V-shaped silicon nitride cantilever (0.01 N/m nominal spring constant) terminating in a 6 µm-radius borosilicate spherical tip (Novascan Technologies). The cantilever deflection was measured by using the optical lever method, and the sensitivity of the photodiode was calibrated prior to probing each sample by using the agarose semi-embedded glass slide in the preparation as reference. For each measurement (dorsal or lateral), 4 separate probing points were selected by laterally displacing the AFM probe 40 µm between measurements. For each probing point, the *E* modulus was calculated from the force-displacement curves by adjusting the Hertz model for the tip-surface contact (Alcaraz et al., 2018). From these 4 separate values, the average was calculated, and data were represented by mean ± standard error of the mean (s.e.m.) for each brain at the different positions.

Primary Cultures and Traction Force Microscopy Measurements of CH or Pallial Subpallial Boundary-Derived CR Cells

Pieces of CH and PSB were obtained as above and collected in cold dissection media (0.1M PBS (14200, Invitrogen) containing 0.65% glucose (G8769, Sigma-Aldrich)) and centrifuged for 5 min at 800 rpm. After removal of the dissection media, 3 ml of dissection medium containing 10X trypsin (15400-054, Invitrogen) at 37°C for 15 min was added. After digestion and inactivation with heat-inactivated normal horse serum (1:3 ratio); 10X DNase (AM2222, Ambion) diluted in fresh dissection media was added, and incubated for 15 min at 37°C. Finally, 10 ml of dissection medium was added and centrifuged for 5 min at 800 rpm. The pellet was resuspended in complete Neurobasal™ medium, and the cells were seeded on the plate. Then cell density was approximately 100,000 cells per 9.5 cm^2 plate. For acrylamide gels, a Matrigel™ coating (diluted 1:40) was made the day before and incubated at 37°C overnight. The next day, the surface was rinsed with Neurobasal™ medium. For the TFM assay, only isolated cells with clear morphology of CR cells (see below) were analysed to avoid interference from traction forces between different cells. PAA gels with different stiffness were generated by modifying the proportion of acrylamide 40% (1610140; BioRad) and Bis-acrylamide Solution (2% w/v;

10193523; ThermoFisher) and the level of crosslinking in the gel (between ≈40 Pa up to supraphysiological values) (Nocentini et al., 2012). To detect gel displacements due to CR cell mediated forces, the PAA gels was labelled with FluoSpheres® Carboxylate-Modified Microspheres 0.2 µm [(625/645) F8806; LifeTechnologies]. In order to generate a good homogeneous Matrigel™ coating for CR cells, the PAA gels were treated with SulfoSANPAH (803332; Sigma-Aldrich). Thus, 0.1 M PBS was removed and a mixture of SulfoSANPAH (and 20 µl of reagent diluted in 480 µl bidistilled water) was added. After two rinses with 0.1M PBS, treated gels were coated overnight at 37°C. The following day, coated gels were washed with the fresh culture medium and allowed to stabilize for a few minutes before seeding with CR cells. Once adhered to the PAA gel, isolated CR cells were selected (× 40 objective, inverted Olympus microscope I×71). For image acquisition and data processing, a Matlab™ script was used (see (Reginensi et al., 2015) for details), and the displacements were represented on the bright field image of the cell.

Calcium Analysis in Cultured CR Cells With Fluo4-AM

To develop analysis of the changes in Ca^{2+} levels in CR cells, CH-derived explants were cultured on Matrigel™ coated dishes as indicated above. In order to enhance explant adhesion and correct CR migration, culture media contained 1% methylcellulose. In previous experiments, we determined the appropriate concentration of methylcellulose maintaining the morphology of CALR-positive cells (**Supplementary Figure S1**). After 24 h of culturing, explants were incubated for 30 min with the cell–permeant calcium-sensitive dye Fluo4-AM (F14201, Molecular Probes). The culture was washed with fresh medium after incubation and finally placed in a recording chamber for observation. The recording chamber was mounted on an IX71 Olympus inverted microscope equipped with a Hamamatsu Orca Flash 4.0 CMOS camera (Hamamatsu Photonics). Cultures were recorded and images (1,024 × 1,024 pixels) were captured using a 20× objective and 470 nm wavelength (CoolLED's pE-300^{white}, Delta Optics) every 50 ms for 1 min using the CellSens™ software (Olympus). The recordings were analyzed offline using the Matlab™ toolbox NETCAL (www.itsnetcal.com). Identified CR cells were associated with a single region of interest (ROI). The average fluorescence $Fi\ (t)$ in each ROI (CR cell) i along the recording was then extracted, corrected for global drifts and artifacts, and finally normalized as $(Fi\ (t) - F_{(0,i)})\ /\ F_{(0,i)} = fi\ (t)$, where $F_{0,i}$ is the background fluorescence of the ROI. The time series of $fi\ (t)$ was analyzed with NETCAL to determine sharp calcium transients and that reveal neuronal activity. Obtained movies were edited in Fiji™ and the lockup table "physics" was applied. In this experiment, the mechanosensory channel inhibitor GsMTx-4 (ab141871, Abcam) was used at a final concentration of 10 µg/ml during video recording.

Statistical Analysis

Data in this manuscript are expressed as mean ± s.e.m. of at least four independent experiments unless specified. Means were compared using the Mann-Whitney U non-parametric test. The asterisks **, *** and **** indicate $p < 0.01$, $p < 0.001$ and $p < 0.0001$, respectively. For TFM and AFM analysis, a permutation test (one tail) was performed and *, ** indicate $p < 0.05$ and $p < 0.01$, respectively was considered statistically significant. Statistical test and graphical representation were performed with Prism v.8 (GraphPad Software), RStudio (RStudio, PBC), and R software (The R Foundation).

RESULTS

Dorsal to Lateral Stiffness (*E*) Differences are Present in Developing Marginal Zone of Developing Mouse Cortex

As a first set of experiments, we developed BIO-AFM measurements in dorsal and lateral parts of the pallial surface of embryonic mice (E12.5) (**Figure 1**). At this embryonic stage, a lateral growth of the pallium takes place (Jacobson and Rao, 2005) and CR cells tangentially migrate through the marginal zone and cover the entire pallial surface (see introduction for references). In our experiments we focused on the dorsal and lateral portions of the pallium, avoiding the most ventral/subpallial regions of the telencephalon. By placing the brain semi-embedded on agarose, we can immobilize the brain without disrupting the whole preparation and leaving a free-agarose zone for the BIO-AFM measurements (**Figure 1B**). A representation of the dorsal zone is showed in low magnification and at higher magnification the cantilever can be seen across the brain tissue (**Figures 1C,D**). Our BIO-AFM results indicate clear differences in stiffness between the dorsal and lateral portions of the pallial surface (dorsal: 128.1 ± 12.08 Pa *vs.* lateral: 52.46 ± 12.08 Pa, mean ± s.e.m., ***$p = 0.0002$) (**Figure 1E**) ($n = 9$ for each condition).

Differential Migration of CH and PSB-Derived CR Cells in Different Matrigel™ Concentrations

Next, we aimed to explore whether these stiffness differences might affect the migration of CR cells (**Figures 1F–J**). Classical studies analyzing CR cell migration used 3D-Matrigel™ hydrogels as a migration substrate [e.g., (Borrell and Marin, 2006; Bribian et al., 2014)]. In order to determine whether the stiffness of the environment could modulate the migration of CR cells in a region-specific manner, we first analyzed the stiffness of different Matrigel™ concentrations using rheometric analysis (**Figure 1F**). We selected the Matrigel™ concentrations taking into account the total protein level in the different batches obtained from the supplier (see Materials and Methods for details) in terms of the generation of a homogenous hydrogel at each of these concentrations [see (Gil and Del Rio, 2019) for example]. Data illustrate that, as expected, high Matrigel™ concentrations led to significantly higher Elastic moduli E (**Figure 1F**), with E decreasing from 12.6 mg/ml to 3.8 mg/ml Matrigel™ dilutions. Measured E at 1 Hz for 12.6 mg/ml was 268 ± 10.11 Pa ($n = 6$), for 7.8 mg/ml it was 45.39 ± 8.93 Pa ($n =$

5), and for 3.8 mg/ml it was 13.34 ± 3.02 Pa (*n* = 4), data as mean ± s.e.m. (**Figure 1F**). When comparing the elasticity of the hydrogels with those previously obtained in BIO-AFM, *E* values obtained using 12.6 mg/ml of Matrigel™ were around 2 times than those measured in the *in vivo* BIO-AFM. However, the data obtained using 7.8 mg/ml were similar to those observed in lateral regions of the apical surface and the values using 3.8 mg/ml were 4 times lower than the lateral telencephalic portion of the marginal zone. For this reason, we used three different concentrations of Matrigel™ ranging around physiological values as measured: 5.8 mg/ml, 7.8 mg/ml, and 9.8 mg/ml.

As indicated in several studies, CR cells derived from the CH and PSB showed an overlapping distribution in the developing marginal zone-layer I [e.g., (Barber and Pierani, 2016)]. Taking this into account, we cultured CH and PSB-derived explants in Matrigel™ hydrogels with different concentrations. CH-derived CR cells were able to migrate longer distances in 5.8 mg/ml, 7.8 mg/ml, and 9.8 mg/ml Matrigel™ dilutions (values for 9.8 mg/ml: CH = 113.4 ± 1.7 µm (*n* = 1632) *vs*. PSB = 72.86 ± 1.3 µm (*n* = 915). Values for 7.8 mg/ml: CH = 131.7 ± 2.1 µm (*n* = 1471) *vs*. PSB = 88.52 ± 1.4 µm (*n* = 1911). Values for 5.8 mg/ml: CH = 137.1 ± 2.2 µm (*n* = 1737) *vs*. PSB = 92.35 ± 2.2 µm (*n* = 1194); all mean ± s.e.m.) (**Figure 1G**; **Supplementary Materials movies S1, S2**). This suggests that 1) CH-derived CR cells have greater motogenic capacity than PSB-derived CR cells when migrating in hydrogels with the same *E* value, and 2) CH-derived CR cells are able to migrate greater distances in hydrogels displaying *E* values closer to those observed in the dorsal portion of the pallium in contrast to PSB-derived CR cells. In **Figures 1H–J** we offer some examples of the distribution of CALR-positive CR cells after completing their migration for 2 DIV in different Matrigel™ concentrations.

Hem-Derived CR Cells Displayed Greater Mechanical Forces Than PSB-Derived CR Cells in PAA Gels

In a next set of experiments, we aimed to determine whether these migratory differences could be attributed to intrinsic differences between CH- or PSB-derived CR cells in order to generate mechanical forces when cultured on PAA substrates. First, we generated PAA gels with very low *E* using the protocol published in (Sunyer et al., 2012; Sunyer et al., 2016). We obtained soft PAA gels with *E* values around ≈ 40–100 Pa. This *E* value is the lowest stiffness that allowed us to obtain good distribution of the nanoparticles used in TFM. Below these values the PAA is not stable and does not generate reliable TFM measurements. We aimed to analyze the behavior of CH- and PSB-derived CR cells when cultured on these low-Pa PAA gels. CR cells adhered to the PAA gel and did not migrate but generated forces on the substrate (**Figure 2**). In some cases, due to the absence of a 3D-hydrogel environment, CR cells modify their morphology from the typical unipolar to a more bipolar shape as also observed in other studies in 2D-cultures (Villar-Cervino et al., 2013). In previous experiments we also categorized the cell morphologies as CR cells in PAA gels using CALR immunostaining (**Figures 2A,B**). Thus, we developed the TFM measures in isolated CR cells with these morphologies (**Figures 2C, F**) and did not analyze TFM in cells with multipolar morphology nor did we group them to compare equal populations. TFM results demonstrated, as expected, that CR cells independently of their origin, do not generate large forces to the PAA substrates compared to other cell types [e.g., endothelial cells or fibroblasts, (Roca-Cusachs et al., 2017)]. TFM analysis reported that CH-derived CR cells can develop greater forces on the substrate when compared to PSB-derived ones (p = 0.0346, one tail permutation test, *n* = 18 and 14, respectively) (**Figure 2G**). This also points to differing intrinsic mechanical properties between CH and PSB-derived CR cells that might allow CR cells to sense the different stiffness of the marginal zone. One potential mechanism to sense stiffness is the expression of mechanosensory channels (Roca-Cusachs et al., 2017). To assess this, we developed a loss of function experiment using the mechanosensory channel inhibitor GsMTx-4 (Gnanasambandam et al., 2017) (**Figure 3**). This compound is a spider venom that inhibits cationic mechanosensitive channels. In fact, although the specific mechanisms of the drug have not been fully determined, when GsMTx-4 is applied to several cell types expressing mechanosensitive channels (e.g., Piezo channels) Ca^{2+} influx is blocked (Jacques-Fricke et al., 2006). Taking this into account, we cultured hem-derived explants, and after 40 h in order to obtain isolated CR cells, cultures were incubated with Fluo4-AM. After incubation, the changes in the Ca^{2+} waves in CR cells were analyzed using NETCAL Software (Orlandi et al., 2014). First, we checked the health status of cultured CR cells in 1% methylcellulose containing medium by analyzing their depolarization, using KCl (**Figures 3A–C**). After KCl treatment, an increase in the fluorescence $\Delta F/F0$ values was observed in all analyzed CR cells (**Figure 3C**). Next, we developed similar experiments, first incubating CR cells with the inhibitor GsMTx-4 and then after that with KCl (**Figure 3D–E**). Results demonstrated that treatment with GsMTx-4 transiently decrease intracellular calcium levels in CH-derived CR cells, reducing their migration (CH, Veh = 130, 8 ± 2.5; GsMTx-4 = 124, 4 ± 3.5, mean ± s.e.m., $**p = 0.0015$, *n* = 1,218 and 782, respectively) (**Figures 3E,F**). On the graph (**Figure 3E**) there is a first fluorescence increase by GsMTx-4 application by medium disruption, but after that, the cell senses the inhibitor and react with a second peak. As a result of the inhibitor entry, the cell decreases their calcium activity and decrease their levels under the baseline. For PSB, CR-cell migration was lower after incubation with the inhibitor but did not reach statistical significance (p = 0.063, *n* = 1,289 for GsMTx-4, and *n* = 382 for vehicle) (**Figure 3F**). In addition, we analyzed whether the blockage of cytoskeletal proteins and myosin II also impaired their migration. These experiments showed, as expected, that inhibiting tubulin (Nocodazole; $***p < 0.001$, *n* = 21) and myosin II (Blebbistatin; $**p$ = 0.0032, *n* = 22) almost blocked the migration of CR cells (**Figure 3G**). In addition, when inhibiting actin dynamics, we also achieved an inhibition of CH-derived CR cell migration (Cytochalasin D, 4 µg/ml; $**p$ = 0.0045, *n* = 9; **Figure 3G**). Taken together, the present data demonstrate that CR cells can

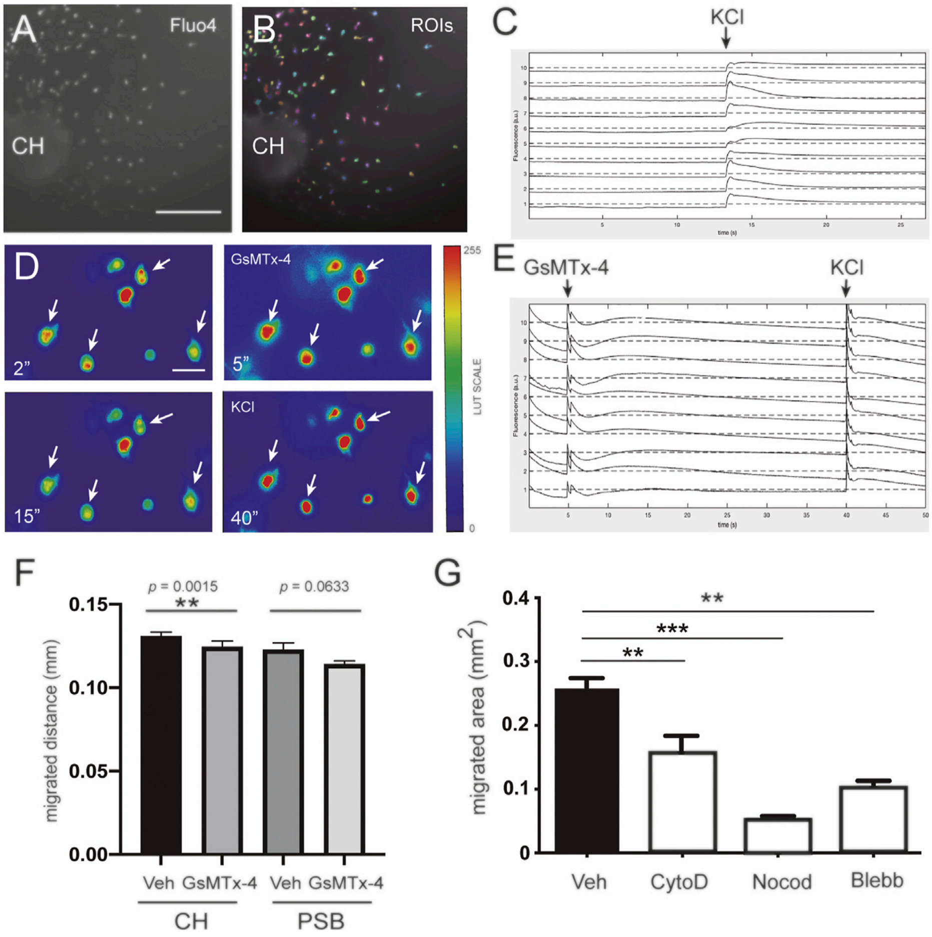

FIGURE 3 | Involvement of mechanosensory receptors in the migration of CH-derived CR cells **(A–C)** Fluorescent calcium imaging experiments demonstrating that CR cells are able to depolarize in the presence of KCl. The images in panel A corresponds to representative neuronal cultures of CH on methylcellulose-containing medium **(A)**. The same image is shown in panel B together with the detected regions of interest (ROIs, colored patches) and that ascribed as neuron **(B)**. **(C)** The application of 0.1 M KCl is indicated with an arrow. The abrupt increase in fluorescence reveals neuronal response to the chemical stimulation. **(D)** Fluorescence images at preset time points (2, 5, 15, and 40 s) from identified CR cells illustrating the changes in Ca^{2+} upon application of GsMTx4 (at 5 s) and KCl (at 40 s). Images were extracted from the **Supplementary Material Movie S3**). Fluorescence images were color edited to visually enhance the transient decrease in Ca^{2+} after GsMTx4 (at 5 s) and KCl (at 40 s). White arrows help identifying the fluorescence evolution of four neurons **(E)** Fluorescent traces for 10 representative neurons upon treatment with GsMTx4 (at 5 s) and KCl (at 40 s), highlighting their strong response to stimulation **(F)** Bar plots comparing the effect of GsMTx4 treatment on the migration of CH- and PSB-derived CR cells, and relative to untreated, control cells. CR cells exhibit a larger migration distance as compared to PSB ones **(G)** Bar plots comparing the migration capacity of control CR cells with those treated with cell-mobility blockers, namely cytochalasin D, Nocodazole, and Blebbistatin. For panels **(F,G)**, data are presented as mean ± s.e.m.. Veh: Vehicle; CytoD: Cytochalasin D; Noco: Nocodazole; Bleb: Blebbistatin; CH: cortical hem; PSB: pallium subpallium boundary. The specific *p* values are included in **(F)**, and $^{**}p < 0.01$ and $^{***}p < 0.001$ in **(F,G)**, respectively. Scale bar A = 300 μm pertains to B; D = 50 μm.

generate mechanical forces to the substrate (CH > PSB-derived CR cells), but that cytoskeletal disruption impairs their migration on Matrigel™ hydrogels.

Ectopic Transplantation of CH and PSB-Derived CR Cells Demonstrates Intrinsic Mechanical Properties *in Vitro*.

Due to the above illustrated data, we aimed to develop ectopic transplantation experiments in an *in vitro* preparation of telencephalic slices (see Materials and Methods for details) (**Figure 4**). Thus, coronal embryonic telencephalic slices (E12.5) from wild-type mice were cultured on transwells, essentially as described (Bribian et al., 2014), and the endogenous CH and PSB were removed, while the CH and PSB from mTmG reporter mice were transplanted (**Figure 4D**). Migrated CR cells generated after explant transplantation could be easily identified by their red fluorescence protein (tdTomato) expression, but also by using double labeling with CALR antibodies. Results demonstrated that CH-derived CR cells transplanted in their original position are able to migrate long distances tangentially in dorsal and medial marginal zones of the slices (mTmG CH in CH location = 565.7 ± 101.3 μm, *n* = 9, mean ± s.e.m) (**Supplementary Figure S2**). However, PSB-derived CR cells were unable to migrate longer distances in dorsal portions of the pallium (mTmG PSB in CH

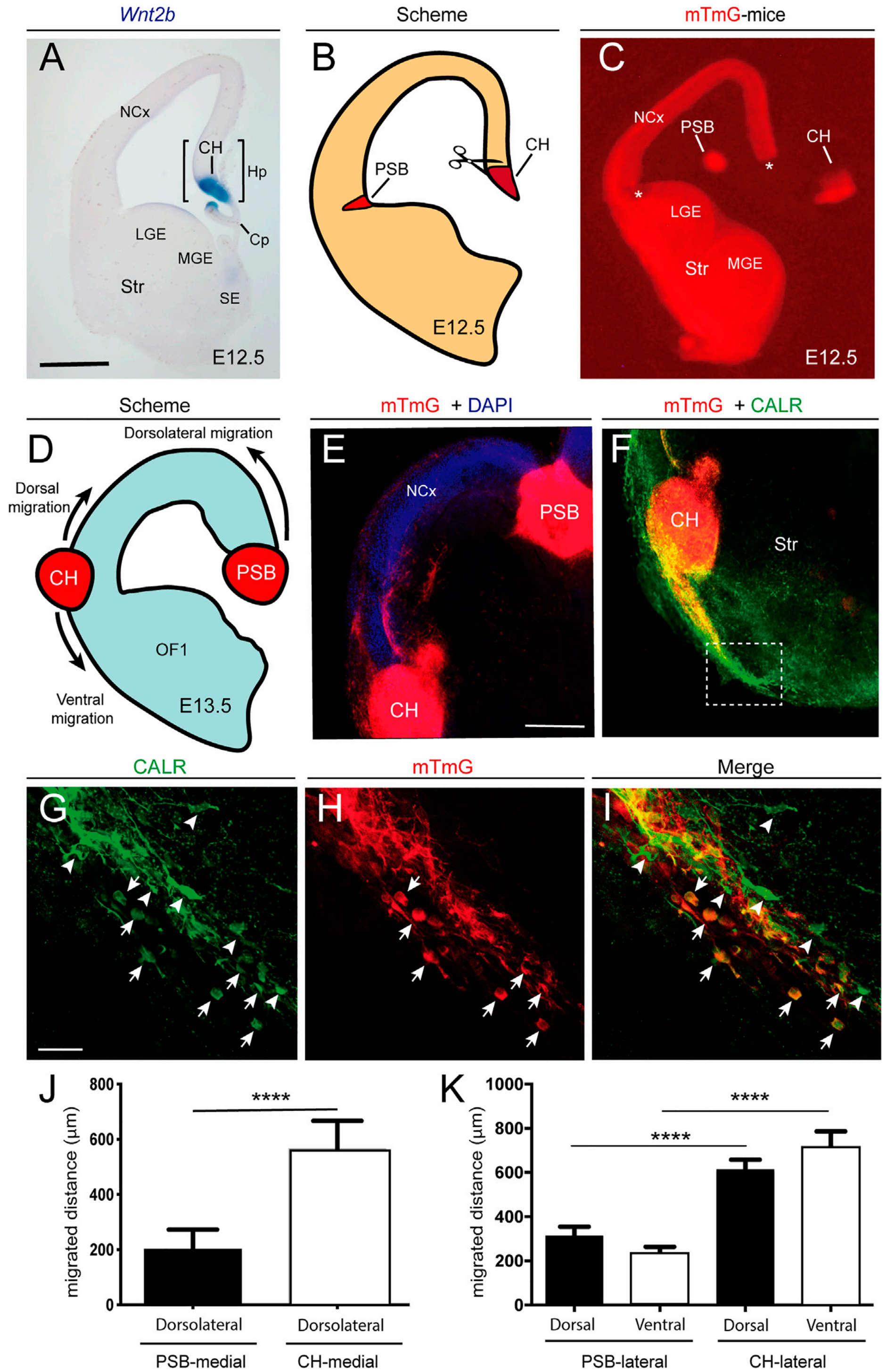

FIGURE 4 | Examples of the differential behavior of CH- and PSB-derived CR cells after transplantation experiments in telencephalic slices **(A)** Example of an E12.5 coronal section showing the location of the CH after *Wnt2b in situ* hybridization **(B,C)** Scheme **(B)** and low-power fluorescence photomicrographs **(C)** illustrating the microdissection procedure for the CH and the PSB using the reporter mTmG mice **(D,E)** Scheme **(D)** and confocal microcopy photomicrographs **(E)** illustrating the location of the transplanted CH and PSB in telencephalic slices **(F)** Photomicrographs illustrating the migratory stream of CH-derived CR cells after their lateral transplantation. The dashed labelled box is depicted in panels G-I **(G,I)** Representative images of double-labelled CR cells identified with CALR antibodies (left) and mTmG (center), together with the resulting combined image (right). White arrows mark cells that are both CALR- and mTmG-positive, while arrowheads point to CALR-positive cells. The panels highlight the large number of double-labelled cells that migrate ventrally to the transplanted CH, that contrasts with the fewer CALR-positive cells **(J)** Bar plots of the migration distance of double-labelled (CALR-mTmG) CR cells in transplantation experiments, comparing the extent of migration of PSB and CH-derived cells transplanted in the natural CH

(*Continued*)

FIGURE 4 | location **(K)** Bar plots of migration distance of double-labelled cells in the dorsal and ventral regions of the CH and PSB transplants after a lateral transplantation. Data on panels **(J,K)** are presented as mean ± s.e.m.. ****$p < 0.0001$. Abbreviations: Cp = choroid plexus; CH = cortical hem; Hp = hippocampal primordia; LGE and MGE = Lateral and medial ganglionic eminences; NCx = neocortex; SE = septal region; Str = striatum; PSB = pallial subpallial boundary. Scale bars, A = 300 μm pertains to C; E = 200 μm pertains to F and G = 50 μm pertains to **(F–I)**.

location = 200.7 ± 72.7 μm, $n = 12$; mean ± s.e.m.) (**Figures 4D–E**). In contrast, when mTmG CH explants were transplanted in the PSB location, a large number of double-labeled CR cells (mTmG + CALR) could migrate dorsally as well as towards ventral portions (mTmG CH in PSB location, lateral-dorsal migration = 603.1 ± 55.0 μm; lateral-ventral migration = 706.7 ± 79.5 μm; $n = 17$; mean ± s.e.m.) (**Figure 4F–K**). In parallel, mTmG PSB transplanted in the PSB location showed increased migration when compared after transplantation in the CH (mTmG PSB in PSB, dorsal migration = 310.5 ± 44.25 μm; ventral migration = 232.9 ± 30.94 μm; $n = 11$; mean ± s.e.m.) (**Figures 4J–K**). From these experiments we may conclude that PSB dorsal migration is ≈ 1.55 times greater when transplanted in PSB than in CH regions. In contrast, CH showed ≈ 1.25 times greater migration distances when transplanted in the PSB than in the CH. These data agree with previous TFM results indicating that CR cells originating from the CH were able to generate stronger mechanical forces to the substrate and they migrate in hydrogels ranking from 5.8 mg/ml to 9.8 mg/ml greater than PSB-derived CR cells. Thus, CH-derived CR cells, when transplanted in PSB, were able to strongly migrate both due to the lesser stiffness of the region (as compared to dorsal regions) and to their intrinsic mechanical properties. In contrast, PSB-derived CR cells migrate less towards or within dorsal pallial regions with increased stiffness. Taken together, the present data suggest that both the differing stiffness in marginal zone/layer I (dorsal *vs.* lateral) of the developing pallium and the intrinsic differences in the motogenic properties of the CR cells depending on their origin play a role in determining their distribution in the developing marginal zone as observed *in vivo*.

DISCUSSION

Several studies in the literature combines lineage analysis, *in vitro* cultures, and CR cell markers, and have revealed the migratory routes of CR cells in developing pallium have been revealed [see among others (Takiguchi-Hayashi et al., 2004; Bielle et al., 2005; Yoshida et al., 2006; Zhao et al., 2006; Garcia-Moreno et al., 2007; Imayoshi et al., 2008; Ceci et al., 2010; Gu et al., 2011; Villar-Cervino et al., 2013; Barber et al., 2015)]. To summarize these studies, CH-derived CR cells migrate in the marginal zone expanding to dorsal and medial parts of the neocortex with a preponderance in the medial level in the caudal axis [see (Barber and Pierani, 2016) as example], since the more rostral levels are mainly populated by SR-generated CR cells. In contrast, PSB-derived CR cells are more confined to lateral portions of the pallial marginal zone with a decreased presence in the medial and dorsal regions [see (Barber and Pierani, 2016) as example]. However, the limits of their distribution in the marginal zone are no hardly defined and these CR populations overlaps in their distribution.

Several groups have focused their attention on defining chemical factors that mediate the migration of the different sets of CR cells (see Introduction). Concerning migration properties of subsets of CR cells, an elegant study carried out by Barber et al. (2015). demonstrated *in vitro* using whole flattened cortical vesicles that CR cells originating in the CH showed increased migratory speed compared to PSB-derived CR cells. The difference (≈ 18%–20% at E10.5) was also associated with differences in VAMP3 expression (increased in CH-derived CR cells with respect to PSB-derived ones). VAMP3 is involved in endocytosis, a crucial process that modulates membrane dynamics at the leading edge of migrating neurons and axons (Kamiguchi and Yoshihara, 2001; Kawauchi, 2015) as occurs in other cell types (Llanses Martinez and Rainero, 2019). In addition, the authors showed that CH-derived CR cells migrate towards the dorsal pallium while PSB-derived CR cells migrate laterally in the rostro-caudal axis (Barber et al., 2015). Our current data corroborate these results.

Concerning expansion of the CR cells in marginal zones, several hypotheses have been proposed. For example, Villar-Cervino et al. (2013), indicated that the distribution of different CR cells is mediated by a contact repulsion process. These effects were not observed when they analyzed groups of CR cells growing in Matrigel™ (Bribian et al., 2014), nor were they seen in present results. However, Barber et al. (2015). suggested that, after analysis of their experiments and time-lapse results, factors other than contact repulsion might regulate CR cell expansion and trajectories in the developing pallium. Our present results are in line with their study, since we show that mechanical factors might contribute to the distribution of CR cells in the dorsal-lateral axis of the developing marginal zone. As indicated, emerging evidence demonstrates that, in parallel to chemical cues, mechanically-mediated processes play relevant roles in axonal guidance, neuronal migration, neurite growth, and brain development [e.g., (Franze, 2013; Gangatharan et al., 2018; Javier-Torrent et al., 2021)]. Concerning pallial morphogenesis, recently published studies from the Miyata's lab reported new results. In fact, a study of Nagasaka and Miyata (2021) analyzed the stiffness differences between the ventricular zone and the pallium and subpallial ganglionic eminence. Relevantly, in this study the authors reported greater E values in the pallial *vs.* the subpallial ventricle, which could be a factor involved in pallial folding (Nagasaka and Miyata, 2021). Our present results reinforce and expand these observations, demonstrating a significant difference for E values between the dorsal part of the marginal zone and the lateral regions of the pallium. However, we cannot rule out the possibility that these differences are also linked to those observed in the ventricular zone. From a developmental point of view, during the early stages of cortical development, the pallium expands in thickness with the addition of postmitotic neurons, generating the cortical plate in a lateral-to-medial gradient, but it also expands laterally [see (Bayer and Altman, 1991)]. Concerning the lateral-to-

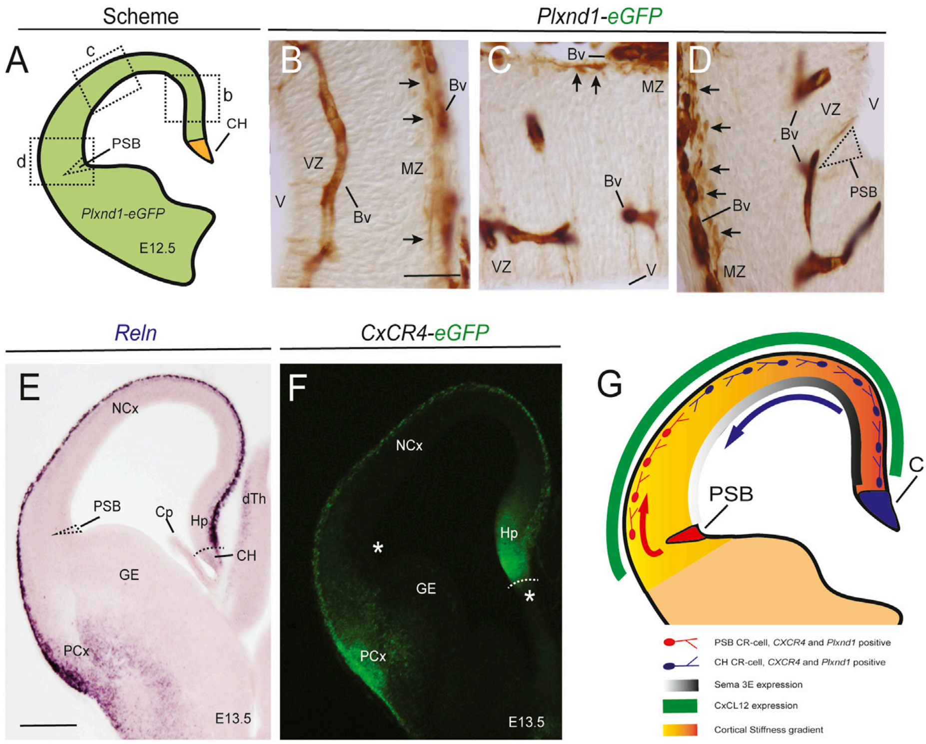

FIGURE 5 | Mechanical and chemical cues modulate the migration of PSB- and CH-derived CR cells. Data presented in this figure illustrate some of the cues involved in the CR-cell migration **(A–D)** Scheme **(A)** and eGFP immunostaining using immunoperoxidase methods of PlexinD1 in transgenic *Plxnd1*-eGFP mice. PlexinD1 is present in blood vessels as well as in CR cells in the complete marginal zone (arrows in B-D). The specific location of the PSB is labelled in **(D)** and illustrates the absence of PlexinD1 in this region. This demonstrates that its expression is postmitotic and linked to its position in marginal zone **(E,F)** *Reln in situ* hybridization **(E)** and eGFP fluorescence in CxCR4-eGFP mice **(F)**, respectively, illustrating their distribution in the developing pallium. Asterisks and dashed regions in **(F)** illustrate the absence of *Reln* and CXCR4 in the proliferative regions, especially the PSB **(G)** Scheme summarizing the results observed in our studies (see Discussion for details). Abbreviations as in **Figure 4** in addition to Bv = blood vessel; dTh = dorsal thalamus; GE = ganglionic eminence; MZ = marginal zone; PCx = piriform cortex; V = lateral ventricle; VZ = ventricular zone. Scale bars, B = 50 μm pertains to **(C,D)**; E = 300 μm pertains to **(F)**.

ventral expansion of the neocortex, a study by Saito et al. (2019). described how a migratory stream of the early generated (E10.5) dorsally preplate cells (mainly subplate cells) participated strongly in this lateral pallial expansion, as evidenced by a dorsal-to-lateral migration, and most probably acting on the orientation of radial glial cells and generating axon tensions at the level of subpallium, at E14.5 (Misson et al., 1988). The presence of these subplate corticofugal axons (labelled with anti-GABA antibodies or 1,1′-Dioctadecyl-3,3,3′,3′-Tetramethylindocarbocyanine Perchlorate (DiI) tracing) at E14.5 was also reported by a number of pioneering studies (De Carlos and O'Leary, 1992; Del Rio et al., 1992; Del Rio et al., 2000). Under this scenario, the lateral part of the pallium which is closest to the ganglionic eminence will allow the tangential migration of these preplate-derived cells (Saito et al., 2019). However, whether these early generated VZ-derived subplate cells with monopolar morphology also show mechanical differences with the non-monopolar cells located in the medial-dorsal portions of the subplate warrants further study and is of interest in fitting their functions and behavior into the stiffness differences observed in the developing pallium.

With respect to CR cells, these studies of Miyata's lab did not focus on this cell type. Our results demonstrate that CH-derived CR cells can migrate long distances in the marginal zone in both the lateral and the dorsal part of the pallium. Interestingly, they were able to migrate more in the lateral than the dorsal regions in our transplantation experiments. In contrast, PSB-derived CR cells showed reduced migration when transplanted into dorsal regions of the neocortex. This observation is likely related to their migratory properties in the differing stiffness of the dorsal *vs.* lateral parts of the marginal zone (BIO-AFM experiments) as corroborated in our Matrigel™ experiments. Taking this into account, our observations and those of Saito et al. (2019). suggest that the migration of CR cells follows the changes in cortical stiffness generated between E10.5 and E12.5. This is of relevance since in the absence of these coordinated actions, CR cell mechanical properties, dorsal-lateral *E* differences in the ventricular and marginal zones, as well as the described dorsal-lateral stream of preplate-derived cells, might trigger altered neocortical development. In fact, it is widely recognized that correct CR cell distribution in marginal zone-layer I is a crucial factor in both radial glia maintenance (Super et al., 2000) and neuronal radial migration (Rice and Curran, 2001). With altered CR cell distribution, changes in cortical plate development and layer specification might occur [e.g., (Super et al., 2000; Alcantara et al., 2006; Villar-Cervino et al., 2013)]. Our study describes for the first time how subsets of CR cells can also be characterized by their mechanical properties which, along with the differential dorsal-lateral stiffness of the marginal zone and additional chemical cues, allow the orchestrated dorsal-lateral migration of two different CR-cell populations (CH and PSB-derived) leading to a specific regional distribution that plays a role in cortical development and maturation.

Coordinated Action of Mechanical and Chemical Cues Modulates the Dorsal-Lateral Migration and Distribution of CH and PSB-Derived CR Cells: A Putative Scenario in Early Neocortical Development

In **Figure 5** we hypothesize a putative scenario for the dorsal-lateral CR-cell migration generated in the CH and the PSB. This summary includes results published by several research groups [among others (Bielle et al., 2005; Borrell and Marin, 2006; Bribian et al., 2014; Barber and Pierani, 2016)] and the present results. In this scheme, the dorsal-medial difference in pallial stiffness is illustrated (present results) and the presence of CXCL12 and Sema3E is illustrated. In addition, we include data related to the expression of CXCR4 as well as PlexinD1. In this hypothesis, during development, SR-, CH-, and PSB-derived CR cells are generated in parallel. However, neither the CH nor the PSB express PlexinD1 or CXCR4 (**Figures 5A–D,F**). In contrast, in the marginal zone, both CH- and PSB-derived CR cells express PlexinD1 and CXCR4, as well as Reelin (**Figures 5A–F**). Due to the differing stiffness of the pallium, PSB-derived CR cells can migrate in their lateral portions to the marginal zone, while being blocked in dorsal pallial regions displaying greater stiffness and increased Sema3E expression. In contrast, CH cells with greater mechanical properties can migrate in dorsal portions but are also progressively affected by the action of Sema3E (**Figure 5G**). Both CR-cell populations are positioned in the marginal zone by the action of CXCL12, and their final distribution in the dorsal-lateral axis is promoted by the inhibition of CXCL12/CXCR4 signaling by Sema3E, as demonstrated in (Bribian et al., 2014), along with their differences in intrinsic mechanical properties and the stiffness of the developing pallium (present results). In addition to this, other factors such as the expression of VAMP3 leading to intrinsic differences in CR-cell migration as well as other repulsive actions described in other studies play crucial roles in parallel to accomplish their regional distribution in the rostral-caudal and medial-lateral axis of the pallium (see Introduction for details).

DATA AVAILABILITY STATEMENT

The original contributions presented in the study are included in the article/**Supplementary Material**, further inquiries can be directed to the corresponding author.

ETHICS STATEMENT

The animal study was reviewed and approved by Ethics Committee for Animal Experimentation (CEEA) of the University of Barcelona (OB47/19, C-007, 276/16, and 47/20).

AUTHOR CONTRIBUTIONS

AL-M and JD planned and designed the study. AL-M, MS-F, HS-F, and VG performed experiments and analyzed data. AL-M and JD drafted the manuscript. JS, RS and JO provided essential advice on experimental design and contributed materials. All authors discussed the results and contributed to the final manuscript.

FUNDING

JD was supported by PRPSEM Project with ref. RTI 2018-099773-B-I00 and PRPCDEVTAU PID 2021-123714OB-I00 from MCINN/AEI/10.13039/501100011033/FEDER "Una manera de hacer Europa", the CERCA Programme, and the Generalitat de Catalunya (SGR 2017-648). The project leading to these results also received funding from "la Caixa" Foundation (ID 100010434) under the agreement LCF/PR/HR19/52160007 and the María de Maeztu Unit of Excellence (Institute of Neurosciences, University of Barcelona) MDM-2017-0729, to JD. JS was funded by Spanish Ministry for Science and Innovation (PID2019-108842GB-C21) and Generalitat de Catalunya (AGAUR, SGR-2017-1,061). RS is a Serra Hunter fellow, and was funded by the Spanish Ministry for Science and Innovation MICCINN/FEDER (RTI 2018–101256-J-I00). XT was funded by Generalitat de Catalunya (SGR-2017–01602), Spanish Ministry for Science and Innovation MICCINN/FEDER (PGC 2018–099645-B-I00), European Research Council (Adv-883739), Fundació la Marató de TV3 (project 201903-30-31-32) and La Caixa Foundation (LCF/PR/HR20/52400004). DN was financed by H2020 European Research and Innovation Programme under the Marie Skłodowska-Curie grant agreement "Phys2BioMed" contract no. 812772. AL-M. was supported by "La Caixa" Foundation and by FPI Programme (BES-2016-076893) supported by Spanish Ministry of Science and Innovation. FM-V was supported by FPU Programme (16/03992), from the Spanish Ministry of Universities. The funders had no role in study design, data collection and analysis, decision to publish, or preparation of the manuscript.

ACKNOWLEDGMENTS

The authors thank Tom Yohannan for his editorial advice and Jordi Ortín Rull for his help with rheometry measurements. The authors also thank all the members of the Del Río, Navajas, Farré, Trepat, Ferrer, and Soriano laboratories for their comments.

SUPPLEMENTARY MATERIAL

The Supplementary Material for this article can be found online at: https://www.frontiersin.org/articles/10.3389/fcell.2022.886110/full#supplementary-material

REFERENCE

Abellan, A., Menuet, A., Dehay, C., Medina, L., and Retaux, S. (2010). Differential Expression of LIM-Homeodomain Factors in Cajal-Retzius Cells of Primates, Rodents, and Birds. *Cereb. Cortex* 20 (8), 1788–1798. doi:10.1093/cercor/bhp242

Alcántara, S., Pozas, E., Ibañez, C. F., and Soriano, E. (2006). BDNF-modulated Spatial Organization of Cajal-Retzius and GABAergic Neurons in the Marginal Zone Plays a Role in the Development of Cortical Organization. *Cereb. Cortex* 16 (4), 487–499. doi:10.1093/cercor/bhi128

Alcaraz, J., Otero, J., Jorba, I., and Navajas, D. (2018). Bidirectional Mechanobiology between Cells and Their Local Extracellular Matrix Probed by Atomic Force Microscopy. *Seminars Cell. & Dev. Biol.* 73, 71–81. doi:10.1016/j.semcdb.2017.07.020

Anstötz, M., Cosgrove, K. E., Hack, I., Mugnaini, E., Maccaferri, G., and Lübke, J. H. R. (2014). Morphology, Input-Output Relations and Synaptic Connectivity of Cajal-Retzius Cells in Layer 1 of the Developing Neocortex of CXCR4-EGFP Mice. *Brain Struct. Funct.* 219 (6), 2119–2139. doi:10.1007/s00429-013-0627-2

Barber, M., Arai, Y., Morishita, Y., Vigier, L., Causeret, F., Borello, U., et al. (2015). Migration Speed of Cajal-Retzius Cells Modulated by Vesicular Trafficking Controls the Size of Higher-Order Cortical Areas. *Curr. Biol.* 25 (19), 2466–2478. doi:10.1016/j.cub.2015.08.028

Barber, M., and Pierani, A. (2016). Tangential Migration of Glutamatergic Neurons and Cortical Patterning during Development: Lessons from Cajal-Retzius Cells. *Devel Neurobio* 76 (8), 847–881. doi:10.1002/dneu.22363

Bayer, S. A., and Altman, J. (1991). *Neocortical Development*. New York: Raven Press.

Bielle, F., Griveau, A., Narboux-Nême, N., Vigneau, S., Sigrist, M., Arber, S., et al. (2005). Multiple Origins of Cajal-Retzius Cells at the Borders of the Developing Pallium. *Nat. Neurosci.* 8 (8), 1002–1012. doi:10.1038/nn1511

Borrell, V., and Marín, O. (2006). Meninges Control Tangential Migration of Hem-Derived Cajal-Retzius Cells via CXCL12/CXCR4 Signaling. *Nat. Neurosci.* 9 (10), 1284–1293. doi:10.1038/nn1764

Bribián, A., Nocentini, S., Llorens, F., Gil, V., Mire, E., Reginensi, D., et al. (2014). Sema3E/PlexinD1 Regulates the Migration of Hem-Derived Cajal-Retzius Cells in Developing Cerebral Cortex. *Nat. Commun.* 5, 4265. doi:10.1038/ncomms5265

Cabrera-Socorro, A., Hernandez-Acosta, N. C., Gonzalez-Gomez, M., and Meyer, G. (2007). Comparative Aspects of P73 and Reelin Expression in Cajal-Retzius Cells and the Cortical Hem in Lizard, Mouse and Human. *Brain Res.* 1132 (1), 59–70. doi:10.1016/j.brainres.2006.11.015

Ceci, M. L., López-Mascaraque, L., and de Carlos, J. A. (2010). The Influence of the Environment on Cajal-Retzius Cell Migration. *Cereb. Cortex* 20 (10), 2348–2360. doi:10.1093/cercor/bhp305

Chiara, F., Badaloni, A., Croci, L., Yeh, M. L., Cariboni, A., Hoerder-Suabedissen, A., et al. (2012). Early B-Cell Factors 2 and 3 (EBF2/3) Regulate Early Migration of Cajal-Retzius Cells from the Cortical Hem. *Dev. Biol.* 365 (1), 277–289. doi:10.1016/j.ydbio.2012.02.034

Dasgupta, K., and Jeong, J. (2019). Developmental Biology of the Meninges. *Genesis* 57 (5), e23288. doi:10.1002/dvg.23288

De Carlos, J. A., López-Mascaraque, L., and Valverde, F. (1995). The Telencephalic Vesicles Are Innervated by Olfactory Placode-Derived Cells: a Possible Mechanism to Induce Neocortical Development. *Neuroscience* 68 (4), 1167–1178. doi:10.1016/0306-4522(95)00199-s

De Carlos, J., and O'Leary, D. (1992). Growth and Targeting of Subplate Axons and Establishment of Major Cortical Pathways [published Erratum Appears in J Neurosci 1993 Mar;13(3):following Table of Contents]. *J. Neurosci.* 12 (4), 1194–1211. doi:10.1523/jneurosci.12-04-01194.1992

De Vincentiis, S., Falconieri, A., Scribano, V., Ghignoli, S., and Raffa, V. (2020). Manipulation of Axonal Outgrowth via Exogenous Low Forces. *Ijms* 21 (21), 8009. doi:10.3390/ijms21218009

Del Río, J. A., Heimrich, B., Supèr, H., Borrell, V., Frotscher, M., and Soriano, E. (1996). Differential Survival of Cajal-Retzius Cells in Organotypic Cultures of hippocampus and Neocortex. *J. Neurosci.* 16 (21), 6896–6907.

Del Rio, J. A., Martinez, A., Auladell, C., and Soriano, E. (2000). Developmental History of the Subplate and Developing White Matter in the Murine Neocortex. Neuronal Organization and Relationship with the Main Afferent Systems at Embryonic and Perinatal Stages. *Cereb. Cortex* 10 (8), 784–801. doi:10.1093/cercor/10.8.784

Del Río, J. A., Martinez, A., Fonseca, M., Auladell, C., and Soriano, E. (1995). Glutamate-like Immunoreactivity and Fate of Cajal-Retzius Cells in the Murine Cortex as Identified with Calretinin Antibody. *Cereb. Cortex* 5 (1), 13–21. doi:10.1093/cercor/5.1.13

Del Rio, J. A., Soriano, E., and Ferrer, I. (1992). Development of GABA-Immunoreactivity in the Neocortex of the Mouse. *J. Comp. Neurol.* 326 (4), 501–526. doi:10.1002/cne.903260403

de Frutos, C. A., Bouvier, G., Arai, Y., Thion, M. S., Lokmane, L., Keita, M., et al. (2016). Reallocation of Olfactory Cajal-Retzius Cells Shapes Neocortex Architecture. *Neuron* 92 (2), 435–448. doi:10.1016/j.neuron.2016.09.020

Elosegui-Artola, A., Trepat, X., and Roca-Cusachs, P. (2018). Control of Mechanotransduction by Molecular Clutch Dynamics. *Trends Cell. Biol.* 28 (5), 356–367. doi:10.1016/j.tcb.2018.01.008

Franze, K. (2013). The Mechanical Control of Nervous System Development. *Development* 140 (15), 3069–3077. doi:10.1242/dev.079145

Frotscher, M., Chai, X., Bock, H. H., Haas, C. A., Förster, E., and Zhao, S. (2009). Role of Reelin in the Development and Maintenance of Cortical Lamination. *J. Neural Transm.* 116 (11), 1451–1455. doi:10.1007/s00702-009-0228-7

Frotscher, M., Haas, C. A., and Forster, E. (2003). Reelin Controls Granule Cell Migration in the Dentate Gyrus by Acting on the Radial Glial Scaffold. *Cereb. Cortex* 13 (6), 634–640. doi:10.1093/cercor/13.6.634

Gangatharan, G., Schneider-Maunoury, S., and Breau, M. A. (2018). Role of Mechanical Cues in Shaping Neuronal Morphology and Connectivity. *Biol. Cell.* 110 (6), 125–136. doi:10.1111/boc.201800003

García-Moreno, F., López-Mascaraque, L., and De Carlos, J. A. (2007). Origins and Migratory Routes of Murine Cajal-Retzius Cells. *J. Comp. Neurol.* 500 (3), 419–432. doi:10.1002/cne.21128

Gesuita, L., and Karayannis, T. (2021). A 'Marginal' Tale: the Development of the Neocortical Layer 1. *Curr. Opin. Neurobiol.* 66, 37–47. doi:10.1016/j.conb.2020.09.002

Gil, V., and Del Río, J. A. (2012). Analysis of Axonal Growth and Cell Migration in 3D Hydrogel Cultures of Embryonic Mouse CNS Tissue. *Nat. Protoc.* 7 (2), 268–280. doi:10.1038/nprot.2011.445

Gil, V., and Del Río, J. A. (2019). Generation of 3-D Collagen-Based Hydrogels to Analyze Axonal Growth and Behavior during Nervous System Development. *JoVE* 148. doi:10.3791/59481

Gil, V., Nocentini, S., and Del Río, J. A. (2014). Historical First Descriptions of Cajalâ€"Retzius Cells: from Pioneer Studies to Current Knowledge. *Front. Neuroanat.* 8, 32. doi:10.3389/fnana.2014.00032

Gil-Sanz, C., Franco, S. J., Martinez-Garay, I., Espinosa, A., Harkins-Perry, S., and Müller, U. (2013). Cajal-Retzius Cells Instruct Neuronal Migration by Coincidence Signaling between Secreted and Contact-dependent Guidance Cues. *Neuron* 79 (3), 461–477. doi:10.1016/j.neuron.2013.06.040

Gnanasambandam, R., Ghatak, C., Yasmann, A., Nishizawa, K., Sachs, F., Ladokhin, A. S., et al. (2017). GsMTx4: Mechanism of Inhibiting Mechanosensitive Ion Channels. *Biophysical J.* 112 (1), 31–45. doi:10.1016/j.bpj.2016.11.013

Griveau, A., Borello, U., Causeret, F., Tissir, F., Boggetto, N., Karaz, S., et al. (2010). A Novel Role for Dbx1-Derived Cajal-Retzius Cells in Early Regionalization of the Cerebral Cortical Neuroepithelium. *PLoS Biol.* 8 (7), e1000440. doi:10.1371/journal.pbio.1000440

Gu, X., Liu, B., Wu, X., Yan, Y., Zhang, Y., Wei, Y., et al. (2011). Inducible Genetic Lineage Tracing of Cortical Hem Derived Cajal-Retzius Cells Reveals Novel Properties. *PLoS One* 6 (12), e28653. doi:10.1371/journal.pone.0028653

Hanashima, C., Fernandes, M., Hebert, J. M., and Fishell, G. (2007). The Role of Foxg1 and Dorsal Midline Signaling in the Generation of Cajal-Retzius Subtypes. *J. Neurosci.* 27 (41), 11103–11111. doi:10.1523/JNEUROSCI.1066-07.2007

Hevner, R. F., Neogi, T., Englund, C., Daza, R. A., and Fink, A. (2003). Cajal-Retzius Cells in the Mouse: Transcription Factors, Neurotransmitters, and Birthdays Suggest a Pallial Origin. *Brain Res. Dev. Brain Res.* 141 (1-2), 39–53. doi:10.1016/s0165-3806(02)00641-7

Hevner, R. F., Shi, L., Justice, N., Hsueh, Y.-P., Sheng, M., Smiga, S., et al. (2001). Tbr1 Regulates Differentiation of the Preplate and Layer 6. *Neuron* 29 (2), 353–366. doi:10.1016/s0896-6273(01)00211-2

Hodge, R. D., Garcia, A. J., 3rd, Elsen, G. E., Nelson, B. R., Mussar, K. E., Reiner, S. L., et al. (2013). Tbr2 Expression in Cajal-Retzius Cells and Intermediate Neuronal Progenitors Is Required for Morphogenesis of the Dentate Gyrus. *J. Neurosci.* 33 (9), 4165–4180. doi:10.1523/JNEUROSCI.4185-12.2013

Imayoshi, I., Shimogori, T., Ohtsuka, T., and Kageyama, R. (2008). Hes Genes and Neurogenin Regulate Non-neural versus Neural Fate Specification in the Dorsal Telencephalic Midline. *Development* 135 (15), 2531–2541. doi:10.1242/dev.021535

Iwashita, M., Kataoka, N., Toida, K., and Kosodo, Y. (2014). Systematic Profiling of Spatiotemporal Tissue and Cellular Stiffness in the Developing Brain. *Development* 141 (19), 3793–3798. doi:10.1242/dev.109637

Jacobson, M., and Rao, M. S. (2005). *Developmental Neurobiology*. New York: Kluwer Academic/Plenum.

Jacques-Fricke, B. T., Seow, Y., Gottlieb, P. A., Sachs, F., and Gomez, T. M. (2006). Ca2+ Influx through Mechanosensitive Channels Inhibits Neurite Outgrowth in Opposition to Other Influx Pathways and Release from Intracellular Stores. *J. Neurosci.* 26 (21), 5656–5664. doi:10.1523/JNEUROSCI.0675-06.2006

Javier-Torrent, M., Zimmer-Bensch, G., and Nguyen, L. (2021). Mechanical Forces Orchestrate Brain Development. *Trends Neurosci.* 44 (2), 110–121. doi:10.1016/j.tins.2020.10.012

Kaddour, H., Coppola, E., Di Nardo, A. A., Le Poupon, C., Mailly, P., Wizenmann, A., et al. (2020). Extracellular Pax6 Regulates Tangential Cajal-Retzius Cell Migration in the Developing Mouse Neocortex. *Cereb. Cortex* 30 (2), 465–475. doi:10.1093/cercor/bhz098

Kamiguchi, H., and Yoshihara, F. (2001). The Role of Endocytic L1 Trafficking in Polarized Adhesion and Migration of Nerve Growth Cones. *J. Neurosci.* 21 (23), 9194–9203. doi:10.1523/jneurosci.21-23-09194.2001

Kawauchi, T. (2015). Cellular Insights into Cerebral Cortical Development: Focusing on the Locomotion Mode of Neuronal Migration. *Front. Cell. Neurosci.* 9, 394. doi:10.3389/fncel.2015.00394

Kikkawa, T., Sakayori, N., Yuuki, H., Katsuyama, Y., Matsuzaki, F., Konno, D., et al. (2020). Dmrt Genes Participate in the Development of Cajal-Retzius Cells Derived from the Cortical Hem in the Telencephalon. *Dev. Dyn.* 249 (6), 698–710. doi:10.1002/dvdy.156

Kirischuk, S., Luhmann, H. J., and Kilb, W. (2014). Cajal-Retzius Cells: Update on Structural and Functional Properties of These Mystic Neurons that Bridged the 20th Century. *Neuroscience* 275, 33–46. doi:10.1016/j.neuroscience.2014.06.009

Ledonne, F., Orduz, D., Mercier, J., Vigier, L., Grove, E. A., Tissir, F., et al. (2016). Targeted Inactivation of Bax Reveals a Subtype-specific Mechanism of Cajal-Retzius Neuron Death in the Postnatal Cerebral Cortex. *Cell. Rep.* 17 (12), 3133–3141. doi:10.1016/j.celrep.2016.11.074

Llanses Martinez, M., and Rainero, E. (2019). Membrane Dynamics in Cell Migration. *Essays Biochem.* 63 (5), 469–482. doi:10.1042/EBC20190014

Mackenzie, F., and Ruhrberg, C. (2012). Diverse Roles for VEGF-A in the Nervous System. *Development* 139 (8), 1371–1380. doi:10.1242/dev.072348

Mallamaci, A., Iannone, R., Briata, P., Pintonello, L., Mercurio, S., Boncinelli, E., et al. (1998). EMX2 Protein in the Developing Mouse Brain and Olfactory Area. *Mech. Dev.* 77 (2), 165–172. doi:10.1016/s0925-4773(98)00141-5

MarÃn-Padilla, M. (2015). Human Cerebral Cortex Cajal-Retzius Neuron: Development, Structure and Function. A Golgi Study. *Front. Neuroanat.* 9, 21. doi:10.3389/fnana.2015.00021

Marin, O., Valiente, M., Ge, X., and Tsai, L.-H. (2010). Guiding Neuronal Cell Migrations. *Cold Spring Harb. Perspect. Biol.* 2 (2), a001834. doi:10.1101/cshperspect.a001834

MartÃnez-CerdeÃ±o, V., and Noctor, S. C. (2014). Cajal, Retzius, and Cajalâ€"Retzius Cells. *Front. Neuroanat.* 8, 48. doi:10.3389/fnana.2014.00048

Mata, A., Gil, V., Pérez-Clausell, J., Dasilva, M., González-Calixto, M. C., Soriano, E., et al. (2018). New Functions of Semaphorin 3E and its Receptor PlexinD1 during Developing and Adult Hippocampal Formation. *Sci. Rep.* 8 (1), 1381. doi:10.1038/s41598-018-19794-0

Meyer, G. (2010). Building a Human Cortex: the Evolutionary Differentiation of Cajal-Retzius Cells and the Cortical Hem. *J. Anat.* 217 (4), 334–343. doi:10.1111/j.1469-7580.2010.01266.x

Meyer, G., and González-Gómez, M. (2018). The Heterogeneity of Human Cajal-Retzius Neurons. *Seminars Cell. & Dev. Biol.* 76, 101–111. doi:10.1016/j.semcdb.2017.08.059

Mingorance, A., Fontana, X., Solé, M., Burgaya, F., Ureña, J. M., Teng, F. Y. H., et al. (2004). Regulation of Nogo and Nogo Receptor during the Development of the Entorhino-Hippocampal Pathway and after Adult Hippocampal Lesions. *Mol. Cell. Neurosci.* 26 (1), 34–49. doi:10.1016/j.mcn.2004.01.001

Miquelajauregui, A., Varela-Echavarria, A., Ceci, M. L., Garcia-Moreno, F., Ricano, I., Hoang, K., et al. (2010). LIM-homeobox Gene Lhx5 Is Required for Normal Development of Cajal-Retzius Cells. *J. Neurosci.* 30 (31), 10551–10562. doi:10.1523/JNEUROSCI.5563-09.2010

Misson, J.-P., Edwards, M. A., Yamamoto, M., and Caviness, V. S., Jr. (1988). Identification of Radial Glial Cells within the Developing Murine Central Nervous System: Studies Based upon a New Immunohistochemical Marker. *Dev. Brain Res.* 44 (1), 95–108. doi:10.1016/0165-3806(88)90121-6

Muzio, L., and Mallamaci, A. (2005). Foxg1 Confines Cajal-Retzius Neuronogenesis and Hippocampal Morphogenesis to the Dorsomedial Pallium. *J. Neurosci.* 25 (17), 4435–4441. doi:10.1523/JNEUROSCI.4804-04.2005

Myakhar, O., Unichenko, P., and Kirischuk, S. (2011). GABAergic Projections from the Subplate to Cajal-Retzius Cells in the Neocortex. *Neuroreport* 22 (11), 525–529. doi:10.1097/WNR.0b013e32834888a4

Nagasaka, A., and Miyata, T. (2021). Comparison of the Mechanical Properties between the Convex and Concave Inner/Apical Surfaces of the Developing Cerebrum. *Front. Cell. Dev. Biol.* 9, 702068. doi:10.3389/fcell.2021.702068

Nguyen-Lefebvre, A. T., Selzner, N., Wrana, J. L., and Bhat, M. (2021). The Hippo Pathway: A Master Regulator of Liver Metabolism, Regeneration, and Disease. *FASEB J.* 35 (5), e21570. doi:10.1096/fj.202002284RR

Nocentini, S., Reginensi, D., Garcia, S., Carulla, P., Moreno-Flores, M. T., Wandosell, F., et al. (2012). Myelin-associated Proteins Block the Migration of Olfactory Ensheathing Cells: an *In Vitro* Study Using Single-Cell Tracking and Traction Force Microscopy. *Cell. Mol. Life Sci.* 69 (10), 1689–1703. doi:10.1007/s00018-011-0893-1

Oliveri, H., Franze, K., and Goriely, A. (2021). Theory for Durotactic Axon Guidance. *Phys. Rev. Lett.* 126 (11), 118101. doi:10.1103/PhysRevLett.126.118101

Orlandi, J. G., Stetter, O., Soriano, J., Geisel, T., and Battaglia, D. (2014). Transfer Entropy Reconstruction and Labeling of Neuronal Connections from Simulated Calcium Imaging. *PLoS One* 9 (6), e98842. doi:10.1371/journal.pone.0098842

Paredes, M. F., Li, G., Berger, O., Baraban, S. C., and Pleasure, S. J. (2006). Stromal-derived Factor-1 (CXCL12) Regulates Laminar Position of Cajal-Retzius Cells in Normal and Dysplastic Brains. *J. Neurosci.* 26 (37), 9404–9412. doi:10.1523/JNEUROSCI.2575-06.2006

Quattrocolo, G., and Maccaferri, G. (2013). Novel GABAergic Circuits Mediating Excitation/inhibition of Cajal-Retzius Cells in the Developing hippocampus. *J. Neurosci.* 33 (13), 5486–5498. doi:10.1523/JNEUROSCI.5680-12.2013

Reginensi, D., Carulla, P., Nocentini, S., Seira, O., Serra-Picamal, X., Torres-Espín, A., et al. (2015). Increased Migration of Olfactory Ensheathing Cells Secreting the Nogo Receptor Ectodomain over Inhibitory Substrates and Lesioned Spinal Cord. *Cell. Mol. Life Sci.* 72 (14), 2719–2737. doi:10.1007/s00018-015-1869-3

Rice, D. S., and Curran, T. (2001). Role of the Reelin Signaling Pathway in Central Nervous System Development. *Annu. Rev. Neurosci.* 24, 1005–1039. doi:10.1146/annurev.neuro.24.1.1005

Riva, M., Genescu, I., Habermacher, C., Orduz, D., Ledonne, F., Rijli, F. M., et al. (2019). Activity-dependent Death of Transient Cajal-Retzius Neurons Is Required for Functional Cortical Wiring. *Elife* 8. doi:10.7554/eLife.50503

Roca-Cusachs, P., Conte, V., and Trepat, X. (2017). Quantifying Forces in Cell Biology. *Nat. Cell. Biol.* 19 (7), 742–751. doi:10.1038/ncb3564

Sahu, M. R., and Mondal, A. C. (2021). Neuronal Hippo Signaling: From Development to Diseases. *Dev. Neurobiol.* 81 (2), 92–109. doi:10.1002/dneu.22796

Saito, K., Okamoto, M., Watanabe, Y., Noguchi, N., Nagasaka, A., Nishina, Y., et al. (2019). Dorsal-to-Ventral Cortical Expansion Is Physically Primed by Ventral Streaming of Early Embryonic Preplate Neurons. *Cell. Rep.* 29 (6), 1555–1567. doi:10.1016/j.celrep.2019.09.075

Skaper, S. D., Moore, S. E., and Walsh, F. S. (2001). Cell Signalling Cascades Regulating Neuronal Growth-Promoting and Inhibitory Cues. *Prog. Neurobiol.* 65 (6), 593–608. doi:10.1016/s0301-0082(01)00017-x

Soriano, E., and Del Río, J. A. (2005). The Cells of Cajal-Retzius: Still a Mystery One Century after. *Neuron* 46 (3), 389–394. doi:10.1016/j.neuron.2005.04.019

Stumm, R. K., Zhou, C., Ara, T., Lazarini, F., Dubois-Dalcq, M., Nagasawa, T., et al. (2003). CXCR4 Regulates Interneuron Migration in the Developing Neocortex. *J. Neurosci.* 23 (12), 5123–5130. doi:10.1523/jneurosci.23-12-05123.2003

Sunyer, R., Conte, V., Escribano, J., Elosegui-Artola, A., Labernadie, A., Valon, L., et al. (2016). Collective Cell Durotaxis Emerges from Long-Range Intercellular Force Transmission. *Science* 353 (6304), 1157–1161. doi:10.1126/science.aaf7119

Sunyer, R., Jin, A. J., Nossal, R., and Sackett, D. L. (2012). Fabrication of Hydrogels with Steep Stiffness Gradients for Studying Cell Mechanical Response. *PLoS One* 7 (10), e46107. doi:10.1371/journal.pone.0046107

Super, H., Del Rio, J. A., Martinez, A., Perez-Sust, P., and Soriano, E. (2000). Disruption of Neuronal Migration and Radial Glia in the Developing Cerebral Cortex Following Ablation of Cajal-Retzius Cells. *Cereb. Cortex* 10 (6), 602–613. doi:10.1093/cercor/10.6.602

Supèr, H., Martínez, A., and Soriano, E. (1997). Degeneration of Cajal-Retzius Cells in the Developing Cerebral Cortex of the Mouse after Ablation of Meningeal Cells by 6-hydroxydopamine. *Dev. Brain Res.* 98 (1), 15–20. doi:10.1016/s0165-3806(96)00155-1

Takeuchi, A., Hamasaki, T., Litwack, E. D., and O'Leary, D. D. M. (2007). Novel IgCAM, MDGA1, Expressed in Unique Cortical Area- and Layer-specific Patterns and Transiently by Distinct Forebrain Populations of Cajal-Retzius Neurons. *Cereb. Cortex* 17 (7), 1531–1541. doi:10.1093/cercor/bhl064

Takiguchi-Hayashi, K., Sekiguchi, M., Ashigaki, S., Takamatsu, M., Hasegawa, H., Suzuki-Migishima, R., et al. (2004). Generation of Reelin-Positive Marginal Zone Cells from the Caudomedial Wall of Telencephalic Vesicles. *J. Neurosci.* 24 (9), 2286–2295. doi:10.1523/JNEUROSCI.4671-03.2004

Villar-Cerviño, V., and Marín, O. (2012). Cajal-Retzius Cells. *Curr. Biol.* 22 (6), R179. doi:10.1016/j.cub.2012.01.016

Villar-Cerviño, V., Molano-Mazón, M., Catchpole, T., Valdeolmillos, M., Henkemeyer, M., Martínez, L. M., et al. (2013). Contact Repulsion Controls the Dispersion and Final Distribution of Cajal-Retzius Cells. *Neuron* 77 (3), 457–471. doi:10.1016/j.neuron.2012.11.023

Wu, Z., and Guan, K.-L. (2021). Hippo Signaling in Embryogenesis and Development. *Trends Biochem. Sci.* 46 (1), 51–63. doi:10.1016/j.tibs.2020.08.008

Yamazaki, H., Sekiguchi, M., Takamatsu, M., Tanabe, Y., and Nakanishi, S. (2004). Distinct Ontogenic and Regional Expressions of Newly Identified Cajal-Retzius Cell-specific Genes during Neocorticogenesis. *Proc. Natl. Acad. Sci. U.S.A.* 101 (40), 14509–14514. doi:10.1073/pnas.0406295101

Yoshida, M., Assimacopoulos, S., Jones, K. R., and Grove, E. A. (2006). Massive Loss of Cajal-Retzius Cells Does Not Disrupt Neocortical Layer Order. *Development* 133 (3), 537–545. doi:10.1242/dev.02209

Zarbalis, K., Choe, Y., Siegenthaler, J. A., Orosco, L. A., and Pleasure, S. J. (2012). Meningeal Defects Alter the Tangential Migration of Cortical Interneurons in Foxc1hith/hith Mice. *Neural Dev.* 7, 2. doi:10.1186/1749-8104-7-2

Zhao, C., Guan, W., and Pleasure, S. J. (2006). A Transgenic Marker Mouse Line Labels Cajal-Retzius Cells from the Cortical Hem and Thalamocortical Axons. *Brain Res.* 1077 (1), 48–53. doi:10.1016/j.brainres.2006.01.042

Zimmer, C., Lee, J., Griveau, A., Arber, S., Pierani, A., Garel, S., et al. (2010). Role of Fgf8 Signalling in the Specification of Rostral Cajal-Retzius Cells. *Development* 137 (2), 293–302. doi:10.1242/dev.041178

Conflict of Interest: The authors declare that the research was conducted in the absence of any commercial or financial relationships that could be construed as a potential conflict of interest.

frontiers | Frontiers in Cardiovascular Medicine

ORIGINAL RESEARCH
published: 19 May 2022
doi: 10.3389/fcvm.2022.886813

Elastin Insufficiency Confers Proximal and Distal Pulmonary Vasculopathy in Mice, Partially Remedied by the K_{ATP} Channel Opener Minoxidil: Considerations and Cautions for the Treatment of People With Williams-Beuren Syndrome

Russell H. Knutsen [1]†, Leah M. Gober [1]†, Elise K. Kronquist [1], Maninder Kaur [1], Danielle R. Donahue [2], Danielle Springer [3], Zu Xi Yu [1], Marcus Y. Chen [1], Yi-Ping Fu [1], Feri Choobdar [1], My-Le Nguyen [1], Sharon Osgood [1], Joy L. Freeman [1], Neelam Raja [1], Mark D. Levin [1] and Beth A. Kozel [1]*

[1] National Heart, Lung, and Blood Institute, National Institutes of Health, Bethesda, MD, United States, [2] Mouse Imaging Facility, National Institute of Neurological Disorders and Stroke, National Institutes of Health, Bethesda, MD, United States, [3] Murine Phenotyping Core, National Heart Lung and Blood Institute, National Institutes of Health, Bethesda, MD, United States

OPEN ACCESS

Edited by:
Charles D. Little,
University of Kansas Medical Center,
United States

Reviewed by:
Matthew Bersi,
Washington University in St. Louis,
United States
Delphine Gomez,
University of Pittsburgh, United States

***Correspondence:**
Beth A. Kozel
Beth.Kozel@NIH.gov

†These authors have contributed equally to this work

Specialty section:
This article was submitted to Cardiovascular Biologics and Regenerative Medicine, a section of the journal Frontiers in Cardiovascular Medicine

***Received:** 01 March 2022*
***Accepted:** 21 April 2022*
***Published:** 19 May 2022*

Citation:
Knutsen RH, Gober LM, Kronquist EK, Kaur M, Donahue DR, Springer D, Yu ZX, Chen MY, Fu Y-P, Choobdar F, Nguyen M-L, Osgood S, Freeman JL, Raja N, Levin MD and Kozel BA (2022) Elastin Insufficiency Confers Proximal and Distal Pulmonary Vasculopathy in Mice, Partially Remedied by the K_{ATP} Channel Opener Minoxidil: Considerations and Cautions for the Treatment of People With Williams-Beuren Syndrome. Front. Cardiovasc. Med. 9:886813. doi: 10.3389/fcvm.2022.886813

Background: Williams Beuren syndrome (WBS) is a recurrent microdeletion disorder that removes one copy of elastin (*ELN*), resulting in large artery vasculopathy. Early stenosis of the pulmonary vascular tree is common, but few data are available on longer-term implications of the condition.

Methods: Computed tomography (CT) angiogram ($n = 11$) and echocardiogram ($n = 20$) were performed in children with WBS aged 3.4–17.8 years. Controls ($n = 11$, aged 4.4–16.8 years) also underwent echocardiogram. $Eln^{+/-}$ mice were analyzed by invasive catheter, echocardiogram, micro-CT (μCT), histology, and pressure myography. We subsequently tested whether minoxidil resulted in improved pulmonary vascular endpoints.

Results: WBS participants with a history of main or branch pulmonary artery (PA) stenosis requiring intervention continued to exhibit increased right ventricular systolic pressure (RVSP, echocardiogram) relative to their peers without intervention ($p < 0.01$), with no clear difference in PA size. Untreated $Eln^{+/-}$ mice also show elevated RVSP by invasive catheterization ($p < 0.0001$), increased normalized right heart mass ($p < 0.01$) and reduced caliber branch PAs by pressure myography ($p < 0.0001$). $Eln^{+/-}$ main PA medias are thickened histologically relative to $Eln^{+/+}$ ($p < 0.0001$). Most $Eln^{+/-}$ phenotypes are shared by both sexes, but PA medial thickness is substantially greater in $Eln^{+/-}$ males ($p < 0.001$). $Eln^{+/-}$ mice showed more acute proximal branching angles ($p < 0.0001$) and longer vascular segment lengths ($p < 0.0001$) (μCT), with genotype differences emerging by P7. Diminished PA acceleration time ($p < 0.001$) and systolic notching ($p < 0.0001$) were also observed in $Eln^{+/-}$ echocardiography. Vascular casting plus μCT revealed longer generation-specific PA arcade length ($p < 0.0001$), with increased PA branching detectable by P90 ($p < 0.0001$). Post-weaning minoxidil decreased RVSP ($p < 0.01$) and normalized PA caliber ($p < 0.0001$) but not early-onset proximal branching angle or segment length, nor later-developing peripheral branch number.

Conclusions: Vascular deficiencies beyond arterial caliber persist in individuals with WBS who have undergone PA stenosis intervention. Evaluation of $Eln^{+/-}$ mice reveals complex vascular changes that affect the proximal and distal vasculatures. Minoxidil, given post-weaning, decreases RVSP and improves lumen diameter, but does not alter other earlier-onset vascular patterns. Our data suggest additional therapies including minoxidil could be a useful adjunct to surgical therapy, and future trials should be considered.

Keywords: pulmonary, elastin, minoxidil, Williams syndrome, vasculopathy, pulmonary artery, sex as a biological variable

INTRODUCTION

Elastin insufficiency produces distinctive vascular abnormalities that include both focal stenosis in proximal elastic arteries and general large vessel arteriopathy consisting of narrow, stiff blood vessels throughout the body. People with elastin insufficiency, such as those with Williams Beuren syndrome [WBS; as reviewed by Kozel, Barak (1)] have prominent vascular features. The pathognomonic lesion for diseases of elastin insufficiency is a focal stenosis of the ascending aorta, also known as supravalvar aortic stenosis (SVAS), but long segment stenosis also occurs commonly. The proximal pulmonary arteries, descending aorta and its branches may also be impacted by stenosis (2). Estimates vary by study methodology, but show pulmonary vascular abnormalities in ∼40–60% of individuals with WBS (3, 4). They usually self-resolve in those with mild stenosis and some with "moderate" stenosis, but it's unclear whether those with resolving moderate stenosis were truly moderate (5, 6).

Less than half of individuals with pulmonary vascular abnormalities are thought to require surgical intervention. Catheter-based intervention has been successful in some cases, but surgical options are considered superior (7). Less is known about the impact and extent of peripheral pulmonary vascular lesions in WBS, as these vessels are more difficult to image with echocardiography and sometimes even with computed tomography (CT) angiography. Previous investigations in rodents showed potential for minoxidil, a K_{ATP} channel opener and vasodilator, to induce elastin production and generate remodeling that improved blood flow to organs in systemic circulation (8, 9). While a clinical trial with this medication did not show improvement in intima media thickness of the carotid artery, the primary endpoint for this study, an increase in lumen diameter was noted (10). Because pulmonary vascular abnormalities are particularly complex to treat through surgical intervention, we questioned whether minoxidil may add benefit to those receiving intervention for hemodynamically significant pulmonary vascular abnormalities.

To evaluate the impact of pulmonary vascular disease in elastin insufficiency, we examined elastin heterozygous ($Eln^{+/-}$) mice. In addition to expanding previously published findings in the proximal vasculature using *in vivo* and *ex vivo* methods, we also investigated the impact of elastin deficiency in more distal vasculature over a broad developmental window. In addition, we focused on sex as a biological variable, given the propensity for vascular disease in WBS to be more severe in males (11). Finally, we tested the impact minoxidil has on the proximal and distal pulmonary vasculature and discussed the possibilities and limitations for using minoxidil to treat pulmonary vascular disease in WBS patients.

MATERIALS AND METHODS

Human Subjects' Approvals and Inclusion

Oversight for the human subjects' research was provided by the Institutional Review Board of the National Institutes of Health. Data for all subjects and controls were obtained under the protocol 'Impact of Elastin Mediated Vascular Stiffness on End Organs' (ClinicalTrials.gov Identifier: NCT02840448). Legal guardians for the pediatric patients signed consent. Assent was obtained from participants as appropriate. This study recruits people with WBS, WBS-like conditions and controls. Here, we analyze data from controls and those with WBS aged 3.4–17.8 years. To be considered for this analysis, an individual with WBS must have clinical or research molecular testing that confirms deletion of one copy of the *ELN* gene, using one of several methods equivalent to the clinically used fluorescent *in situ* hybridization (FISH) test for WBS. Not all participants were able to complete all tests.

Human Echocardiographic Examination

Complete transthoracic echocardiograms ($n = 48$, 35 WS + 13 control) were performed using commercially available systems and measured according to American Society of Echocardiography guidelines. Portions of that data are reported elsewhere (12, 13). When available, tricuspid regurgitant (TR) peak velocity (TRV_{max}) was recorded. It can be transformed using the modified Bernoulli equation to estimate RV systolic pressure $RVSPe=4^*(TRV_{max})^2$ + right atrial (RA) pressure. However, for simplicity, we report only the TRV_{max}. If the initial research study failed to show a TR jet ($n = 20$, 18 WBS + 2 control), data from a second later research echocardiogram ($n = 2$ WBS) or concomitant clinical study (n=1 WBS) in which a jet was present were used instead, leading to 20 WBS and 11 control measures. In the past it has been assumed that most patients with clinically significant pulmonary hypertension would have a have measurable TRV jet (14, 15). As such, it may be safe to assume that RVSPe would not be significantly elevated in those participants ($N = 1$ WBS with history of PA intervention, $N = 14$ WBS with no history of PA intervention and $N = 2$ controls with no appreciable TR jet). Of note, the percentage of missing TRV_{max} was not different between the cases and controls and those with and without TRV_{max} measures were not statistically different in age, sex, and BMI distribution (data not shown).

CT Analysis of Proximal and Peripheral Lung Vasculature

Pediatric participants with WBS underwent a neck to pelvis vascular contrast enhanced CT scan (Canon Aquilion ONE, Tokyo, Japan) with iopamidol-370 (Isovue-370, Bracco Diagnostics, Monroe Township, NJ). Images were reconstructed with 2 mm slice thickness and 1 mm slice increments.

Vitrea Advanced Visualization 7.11.5.29 (Vital Images Inc., Minnetonka, MN) was used to post-process and analyze compiled CT data. Vascular aorta mode was used to generate vessel cross sections with multi-planar reformatting. The midpoint of each vessel segment was identified using the ruler tool and electronic calipers were used to collect short and long axis lumen diameter measurements of the main, left, and right PAs.

Due to concerns about radiation exposure, pediatric controls were not scanned. Thus, PA diameters were converted to standardized effective diameter Z-scores and compared to a published control population (16). Briefly, predicted diameters based on participant height and sex were calculated and used to establish a Z-score. Not all children were able to lay still for the unsedated study.

Animal Studies

All procedures described herein were approved by the Institutional Animal Care and Use Committee of the National Heart Lung and Blood Institute or Washington University School of Medicine. Institutional guidelines for animal experimentation and welfare were followed. The Eln^{tm1Dyl} mouse (17), was originally created in a 129x1/Sv; C57Bl/6 background but was further backcrossed to C57Bl/6 prior to these studies to remove 129x1/Sv genetic material that is known to influence phenotype (18). Studies were performed in male $Eln^{+/-}$ and $Eln^{+/+}$ mice ranging in age from postnatal (P) day ∼1–90. Females were studied at ∼P90. A subset of mice were treated with minoxidil (Sigma, St. Louis, MO) diluted in drinking water to provide ∼20 mg/kg/day (8) from approximately postnatal day 21 to ∼P90. Not all experiments could be performed in every mouse.

Right Ventricular Hemodynamic Measurements

Mice were restrained on a heated holder to maintain body temperature, while anesthesia was induced at 2.5% isoflurane (Florane, Baxter, San Juan, PR). After induction anesthesia was reduced to 1.5%. Upon achieving a level plane of anesthesia, a pressure catheter (1.4-Fr, model SPR671, Millar Instruments, Houston, TX) was inserted into the jugular vein and advanced into the right ventricle (RV). At the time of pressure collection, anesthesia was further reduced to 1% and pressures were recorded using Chart 5 software (AD Instruments, Colorado Springs, CO). By closely observing the hemodynamic trace for a standard ventricular waveform, and monitoring physical resistance during catheter advancement, we were able to advance the catheter comfortably beyond the tricuspid valve and avoid over-advancing into the apex. This allowed for optimal catheter placement within the ventricular chamber. Animals were monitored for discomfort or over-sedation.

Pressure-Diameter Testing

The left pulmonary artery (LPA), from the pulmonary trunk to just proximal to the first bifurcation, was excised post-euthanasia. Vessels were mounted on a pressure arteriograph (Danish Myotechnology, Copenhagen, Denmark) in balanced physiologic saline at 37°C, pressurized, and longitudinally stretched three times to *in vivo* length prior to data capture. Vessels were then transilluminated under a microscope connected to a charge-coupled device camera and computerized measurement system (Myoview, Danish Myotechnology) to allow for continuous recording of vessel diameters (further details on the pressure arteriography procedure can be found in (8). Intravascular pressure was increased from 0 to 70 mmHg in 10-mmHg steps. At each step, the outer diameter of the vessel was measured and manually recorded.

Histology

Main pulmonary trunk arteries (MPA) were collected and fixed (unloaded) in 10% buffered formalin (Fisher Scientific, Waltham, MA) overnight at 4°C, and then progressively dehydrated in ethanol. Vessels were embedded in paraffin and 5µm cross-sections cut. Sections were subsequently stained using Verhoeff van Gieson stain (k059, Poly Scientific R&D, Bay Shore, NY) to visualize elastin. Slides were scanned using the Hamamatsu NanoZoomer 2.0-RS digital slide scanner. Images were captured at 40x with embedded scale using the Hamamatsu NDP.view2 viewing software (Hamamatsu Photonics, Hamamatsu, Japan).

Lamellar number, circumference, and media wall thickness were measured as previously described (8).

Cardiac Mass Measurements

Prior to sacrifice, body mass (BM) was recorded for each mouse. Post euthanasia, the heart was dissected from the chest cavity and the auricles removed. The heart was then carefully rolled on an absorbent surface to remove excess blood without crushing the tissue/disturbing the interstitial fluid. The RV was then detached from the left ventricle/septum (LV) and each segment was weighed separately. Using digital calipers, tibia length (TL) was recorded from the tibia head (exposed after the patellar tendon is severed) to the space within the ankle exposed after severing the Achilles tendon. The ratios of right ventricular heart mass (RVHM) and left ventricular/septal heart mass (LVHM) normalized to both body mass (RVHM/BM; LVHM/BM) and tibia length (RVHM/TL; LVHM/TL) were then calculated to assess relative changes in heart size.

In vivo Murine Micro-Computed Tomography (CT) Imaging

Mice were placed in an induction chamber and anesthesia was induced using 4% isoflurane. Mice were transferred to a platform where a level plane of anesthesia at 2% isoflurane was achieved via nosecone. Ophthalmic ointment was applied and 80 microliters of Viscover^{TM} ExiTron^{TM} nano 12,000 contrast agent (Miltenyi Biotec, Bergisch-Gladbach, Germany) was delivered via standard tail vein injection. The platform with the secured mouse was transferred to the QuantumGX μCT chamber (PerkinElmer, Waltham, MA) and 4 min post-injection, the scan was initiated. A 4-min scan simultaneously capturing cardiac and respiratory rhythms was performed, and scans were reconstructed, gated to systole (19, 20).

Murine *in vivo* μCT Image Analysis

To evaluate PA caliber, μCT scans (cardiac gated to systole) were uploaded to Horos (Horosproject.org, Annapolis, MD) and arterial caliber of the MPA, right pulmonary artery (RPA) and LPA were assessed using the 3D multiplanar reformation tool on an oblique slice. The pulmonary trunk was assessed distal to the valves, where the vessel becomes most uniformly circular. The RPA and LPA were assessed just distal to the branch point from the MPA. For all segments, the lumen diameter was measured in four evenly spaced intervals around the circumference of the vessel and averaged to account for variations in the vessel shape. The angle of branching between the RPA and LPA was assessed in an oblique slice where the trunk and both branching vessels were in view using the Horos angle tool. For all measures, still images were captured, and measurements were recorded.

Pulmonary Artery and Left Ventricular Imaging by Echocardiogram

Cardiac imaging was performed using a high-frequency, high-resolution ultrasound system (Vevo2100, FUJIFILM VisualSonics Inc., Toronto, Canada) and a 40 MHz transducer probe (VisualSonics, MS-400). Mice were lightly anesthetized with isoflurane during the examination with HR maintained above 450 bpm. The mice were placed in a supine position over a heated imaging platform and rail system. Body temperature was maintained between 35 and 37 degrees Celsius as assessed by rectal probe. Color Doppler was applied to visualize PA flow from a modified long axis view; the parasternal long axis of the right ventricular outflow tract which visualizes the right ventricular outflow tract (RVOT), pulmonic valves and PA. Peak pulmonary artery velocity (mm/s), gradient (mm Hg), and pulmonary artery acceleration time (PAAT, s) were measured from the Pulsed Wave (PW) Doppler waveforms. PW Doppler samples were then taken parallel to MPA flow just distal to the pulmonic valve leaflets. Left ventricular measurements were made from the standard 2D and M mode images acquired from the parasternal long axis and mid-papillary short axis views.

Polymer Infusion and μCT Imaging of Young and Adult Mice

Microfil^{TM} (Flow Tech Inc., Carver, MA) injections were performed as previously described (21). Approximate postnatal day 1 (P1), 7 (P7), 30 (P30), and 90 (P90) mice were used for these experiments. Briefly, after removal of the anterior chest wall and diaphragm, the PA was catheterized via the RV. The pulmonary vasculature was then flushed with phosphate buffered saline containing sodium nitroprusside (10^{-4} M) to clear and dilate the vessel network. The lungs were then inflated to 20 mm Hg following tracheal cannulation, while still in the body cavity. At this point, Microfil^{TM} was slowly infused into the arterial vascular network. Once the infusion was complete, the polymer was allowed to cure before the heart lung block was fixed in 10% formalin at 4°C for 24 h. The heart and lungs were then removed from the thoracic cavity *en bloc* and scanned by uCT. It should be noted that the inability to statically control intraluminal pressure during the delivery and polymerization of the Microfil^{TM} precludes accurate vessel diameter measures.

Ex vivo μCT Imaging

Fixed mouse heart and lung samples were imaged using the Quantum GX μCT scanner (PerkinElmer, Waltham, MA). Based on field of view and specimen size, μCT scans were sub-reconstructed at 40μm (P90), 35μm (P30), 30μm (P7), or 25μm (P1). Both genotypes in each group were post-processed at the same resolution. Additional sub-reconstructions were used to achieve higher resolution for the left upper lobe with a focus on the left upper lobar feed artery (LULFA, see **Figures 7C,D**, arrowhead) at resolutions of 20μm (P90), 15μm (P30), 12μm (P7), and 10μm (P1), respectively.

Ex vivo μCT – Proximal Vascular Analysis

To extract the proximal vasculature, sub-reconstructed images of heart/lung samples were loaded into Amira 6.7.0 (ThermoFisher Scientific). Segmentation was performed using 'Magic Wand', a tool that connects all voxels within a manually denoted intensity range. A voxel at the center of the MPA was chosen as the "seed" and propagated to subsequent voxel connections of similar intensity. An upper threshold was then imposed on the reconstruction to simultaneously preserve the proximal conducting vasculature and exclude more distal vessels (see **Figures 7C,D**). Vessel length analysis was completed by selecting vessel segments stretching from the origin of the LPA or RPA and extending to the fourth branchpoint (Left Pulmonary Lobar Artery; LPLA) in the left lung and the sixth branchpoint (Right Pulmonary Lobar Artery; RPLA) in the right (see **Figures 7C,D** for details). "Graph Info" generated and compiled data for each vessel segment to measure path and Euclidean length along the extracted centerline. The ratio of path length to Euclidean length is defined as tortuosity. The branch angle formed between the LPA and RPA immediately as they branch off the MPA was also measured.

Ex vivo μCT – Distal Vascular Tree Analysis

The higher resolution sub-reconstructions were used to examine the smaller vasculature of the LULFA, chosen for its consistent size, branching pattern, and even filling across samples. A seed voxel was planted in the main proximal artery feeding the LULFA. After propagation of the vasculature using 'Magic Wand' and assignment of the volume to a material, the label image was created and skeletonized to find the centerline tree. To fully preserve the data from the smallest branches, the original vascular tree was not manually altered. Generation was assigned by selecting the LULFA's primary branch off the main artery and labeling it as the "root" of the tree, which allowed Amira to automatically assign increasing generations to the remainder of the tree. At each generation, the total length of vascular segments and total number of branches could then be quantified and compiled using "graph info." The subsequent output yielded a single cumulative vascular arcade length and branch number for each generation. Data was an average of several mice/genotype at each generation.

Statistics

Statistical analyses were performed using GraphPad Prism version 9 (GraphPad Software, San Diego, CA, www.graphpad.com.) One- or two-way ANOVA were employed as appropriate depending on the number of independent variables. The null hypothesis was rejected if ANOVA $p<0.05$ and multiple comparison testing was then performed with corrections for multiple testing by Tukey or Dunn (reported in figure legend for each graph). Comparison data are shown for pairwise testing based on genotype, sex, age or minoxidil treatment (Tx). Data for not scientifically relevant comparisons (e.g., $Eln^{+/+}$ male vs. $Eln^{+/-}$ female) were computed but not displayed.

For single variate analyses, unpaired *t*-tests were used for normally distributed data and Mann-Whitney testing was used with non-normally distributed data. Untreated $Eln^{+/-}$ males in the sex-based experiments were also utilized as the untreated cohort in the minoxidil experiments.

Chi-square analysis was used to evaluate the relationship between genotype and the presence of a mid-systolic notch.

RESULTS

Elevated RVSPe Persists in WBS Subjects Requiring Intervention

To further evaluate pulmonary vascular status in WBS, we performed echocardiograms and CT angiograms with IV contrast in subjects electing to undergo these procedures. See **Supplementary Table 1** for demographic information. Briefly, complete echocardiogram with doppler was performed on 35 children with WBS and 13 controls. Of those, 20 echocardiograms from WBS participants and 11 echocardiograms from controls exhibited a measurable TRV jet to approximate RVSPe (see methods) for analysis in Fig. 1A. The resulting groups were of similar age, sex at birth, and BMI. Thirty-five percent of those with WBS (7 children) had previously undergone a pulmonary intervention.

TRV_{max} was elevated among children with WBS who had undergone PA reconstruction, compared to those with WBS who hadn't had the procedure and healthy controls (**Figure 1A**, Kruskal-Wallis ANOVA $p < 0.01$, followed by multiple comparison testing by Dunn's, WBS with history of PA procedure median (interquartile range, IQR) = 3.1 (0.8) m/s; WBS without history of PA procedure = 2.0 (0.3) m/s; Control = 2.2 (0.2) m/s). In this respect, we saw a bi-modal distribution, with four WBS subjects with history of PA procedure having very significantly elevated TRV_{max}, including one subject who had undergone extensive PA reconstruction beyond the hilum and was planned for follow up surgical procedure. Following this study, that patient underwent clinically indicated cardiac catherization with balloon dilation angioplasty, which did result in significantly diminished MPA pressures (29/13/20 mmHg) with deliberate fracture of previously placed stents in the RPA and LPA, later reflected on echocardiogram by diminished TRV_{max} to 2.6 m/s. That subject's exertional fatigue symptoms resolved following intervention and planned follow up surgeries were delayed for 1–2 years. TRV_{max} measures for subjects who did not undergo PA reconstruction was not significantly different from matched control (Dunn).

Right and left branch pulmonary artery diameter was quantified from cardiac gated CT angiograms and converted to Z-score (9), and groups compared by two-way ANOVA (**Figure 1B**). No statistically significant pulmonary artery caliber dimension Z-score difference was seen between those who did or did not have PA reconstruction surgery.

Elastin Insufficiency Induces Increased RV Systolic Pressure in Male and Female Mice and Increased Right Heart Mass to Tibial Length That Is More Severe in Females

Pulmonary pressures were first assessed by invasive catheter measurement in untreated 3-month-old male and female mice. Right ventricular systolic pressure (RVSP) was higher in $Eln^{+/-}$; (two-way ANOVA, genotype effect, $p < 0.0001$; **Figure 2A**) and in males (sex effect: $p < 0.05$), with no sex X genotype interactive effect. Multiple comparison testing showed RVSP was significantly elevated in both male (9.9 mmHg higher, $p <$

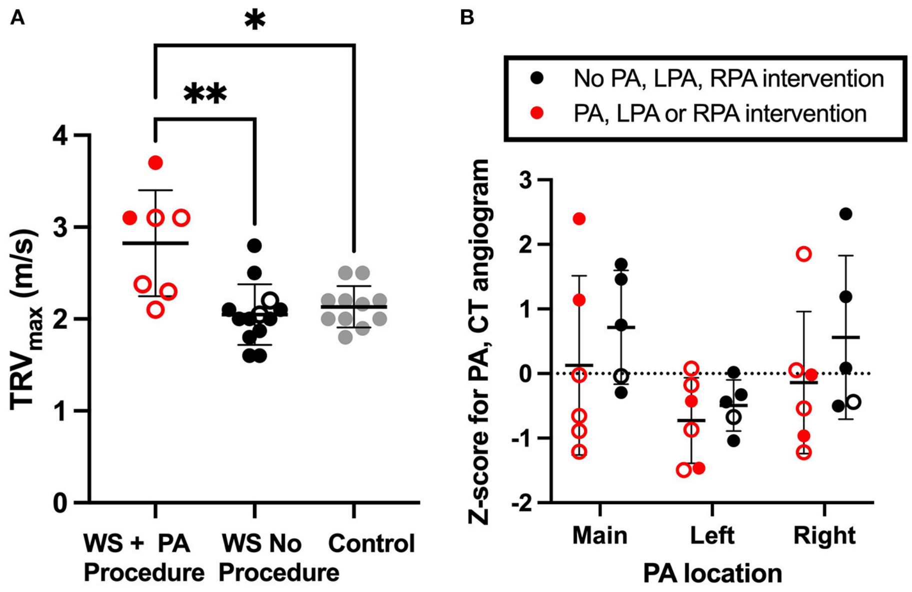

FIGURE 1 | Residual increased right ventricular pressure estimate in WBS participants with history of pulmonary artery intervention. **(A)** shows the TRV_{max} recorded by echocardiogram. RVSPe can be approximated from TRV_{max} using Bernoulli's equation as $RVSPe=4*(TRV_{max})^2$ + right atrial (RA) pressure. **(B)** illustrates Z-scored measures of main (MPA), left (LPA) and right (RPA) pulmonary artery lumen diameter. In both figures, WBS participants with a history of PA intervention are red, WBS participants with no PA intervention are black and controls are gray. A mean line +/- SD line is shown for each group. Open circles represent individuals who had SVAS repair. Closed circles are used for those not requiring SVAS repair. Multiple comparison testing (after ANOVA) by Tukey. * $p < 0.05$, ** $p < 0.01$.

0.0001) and female (7.1 mmHg higher, $p < 0.01$) $Eln^{+/-}$ mice as compared to same sex $Eln^{+/+}$ mice (**Figure 2A**). Additionally, RVSP was significantly elevated in male $Eln^{+/-}$ compared to female $Eln^{+/-}$ mice (4.5 mmHg higher, $p < 0.05$). There were no statistically significant differences between $Eln^{+/+}$ males and females. There were not statistically significant differences in right ventricular end-diastolic pressure (RVDP) by two-way ANOVA (**Figure 2A**).

Heart rate (HR) was higher in males (two-way ANOVA, sex effect, $p < 0.05$; **Figure 2B**) but was not different based on Eln genotype; no interactive effects were identified. Multiple comparison testing revealed no statistically significant differences between genotype or sex-based pairs.

The right ventricular heart mass to tibia length (RVHM/TL) ratio was higher in $Eln^{+/-}$ mice, (two-way ANOVA, genotype effect, $p <0.01$; **Figure 2C**), but there were no sex or sex X genotype interactive effects. On multiple comparisons testing, female $Eln^{+/-}$ mice exhibit elevated RVHM/TL ratios compared to female $Eln^{+/+}$ ($p < 0.05$; **Figure 2C**), but the male comparisons were not significantly different and there were no differences in male-female pairs of the same *Eln* genotype. The left heart, by comparison, showed higher heart mass to tibia length ratio (LVHM/TL) in males (two-way ANOVA, sex effect, p 0.0001; **Figure 2D**), but no genotype or sex X genotype interactive effect. In this case, both $Eln^{+/+}$ and $Eln^{+/-}$ males had larger LVHM/TL ratios than genotype matched females ($p < 0.0001$ for $Eln^{+/+}$ and $p < 0.001$ in $Eln^{+/-}$). Some of the cardiac differences may have been influenced by genotype-mediated differences in tibia length ($Eln^{+/-}$ had shorter TL p <0.001; **Figure 2E**; no sex or sex X genotype interactive effects for TL) in the normalization. Multiple-comparisons testing show male $Eln^{+/-}$ mice have significantly smaller tibias than male $Eln^{+/+}$ mice ($p < 0.05$), with the female comparison trending smaller, but not significant. When heart mass is instead normalized to body mass, RVHM/BM is again higher in $Eln^{+/-}$ mice (two-way ANOVA, genotype effect, $p < 0.01$; **Supplementary Figure 1A**), but no sex or sex X genotype interactive effects are seen. On multiple comparisons testing, female $Eln^{+/-}$ mice exhibit elevated RVHM/BM ratios compared to female $Eln^{+/+}$ ($p < 0.05$; **Supplementary Figure 1A**), but the male comparisons were not significantly different and there were no differences in male-female pairs of the same *Eln* genotype. LVHM/BM, in contrast, showed no effects by two-way ANOVA (**Supplementary Figure 1B**). Predictably, female mice weighed less than males (two-way ANOVA, $p < 0.0001$; **Supplementary Figure 1C**). There were no genotype or interactive effects. Multiple comparisons testing confirms male $Eln^{+/+}$ ($p < 0.001$) and $Eln^{+/-}$ ($p < 0.001$; **Supplementary Figure 1C**) are significantly larger than females of the same genotype.

Elastin Insufficiency Produces Decreased PA Diameter With Increased Wall Thickness That Is Most Severe in Male $Eln^{+/-}$ Mice

To assess PA diameter, LPAs were excised and evaluated on a pressure myograph. In male and female cohorts, multiple-comparisons testing following two-way ANOVA (group effect, pressure effect and pressure X group interactive effect all $p <$

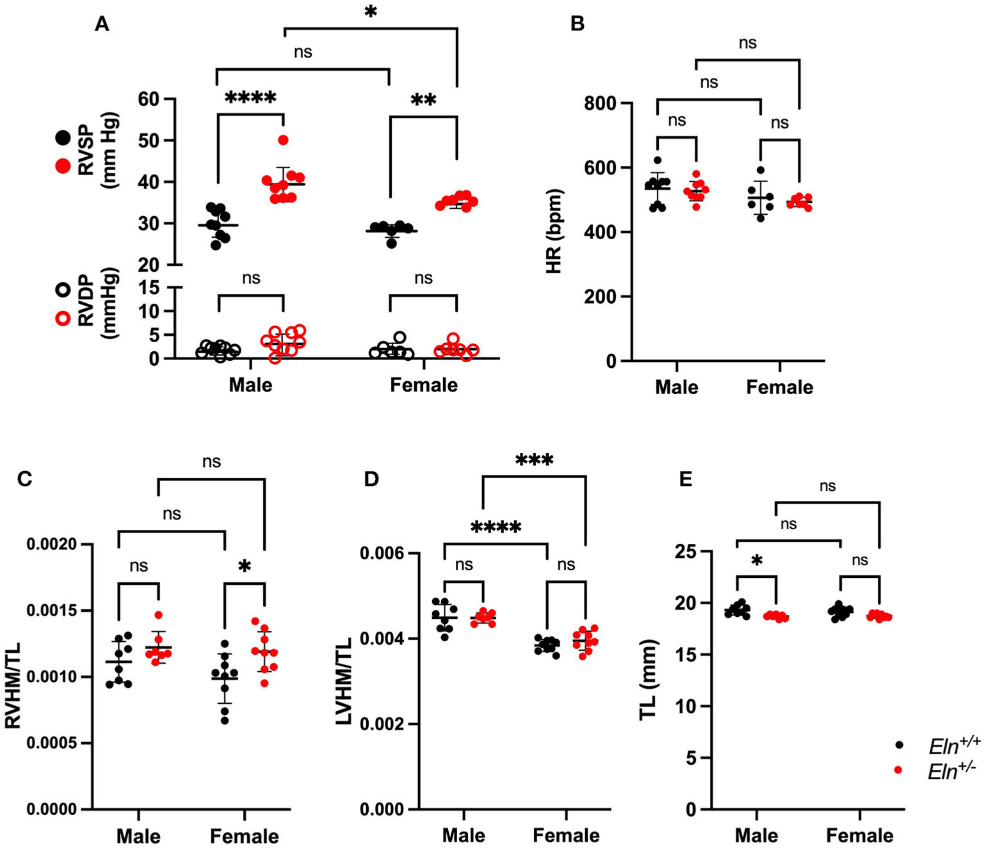

FIGURE 2 | Sex and Eln genotype differences in hemodynamic parameters. **(A)** shows RVSP in closed circles and RVDP in open circles in male and female $Eln^{+/+}$ and $Eln^{+/-}$ mice. **(B)** depicts HR in the same groups. **(C–E)** report heart mass as normalized to tibial length findings. **(C)**: RVHM/TL, **(D)**: LVHM/TL (this measure includes the interventricular septum and the LV in the LVHM measure), **(E)**: tibial length. $Eln^{+/+}$ data are presented in black and $Eln^{+/-}$ in red in all figures. A mean line +/- SD is shown for each sex/genotype combination. Multiple comparison testing (after ANOVA) by Tukey. * $p < 0.05$, ** $p < 0.01$, *** $p < 0.001$, **** $p < 0.0001$, and ns is not significant.

0.0001) showed consistently decreased $Eln^{+/-}$ outer diameters compared to $Eln^{+/+}$ (**Figure 3A**). There were no significant differences between sexes of the same genotype.

Histologic sections from unloaded male $Eln^{+/+}$ (**Figure 3B**), male $Eln^{+/-}$ (**Figure 3C**), female $Eln^{+/+}$ (**Figure 3D**), and female $Eln^{+/-}$ (**Figure 3E**) MPAs were assessed for structural differences. More elastic lamellae are seen in $Eln^{+/-}$ (two-way ANOVA, genotype effect, $p < 0.0001$; **Figure 3F**), but no sex or sex X genotype interactive effects were seen. Multiple-comparison testing confirmed male ($p < 0.0001$) and female ($p < 0.001$) $Eln^{+/-}$ have significantly more elastic lamellae than same sex $Eln^{+/+}$, but there were no statistically significant differences between genotype-based pairs.

MPA internal medial circumference, a proxy for unloaded lumen size, was smaller in $Eln^{+/-}$ mice (two-way ANOVA, genotype effect, $p < 0.0001$; **Figure 3G**), without sex or interactive effect. Multiple-comparison testing confirmed $Eln^{+/-}$ inner circumference is smaller than $Eln^{+/+}$ in both males ($p < 0.0001$) and females ($p < 0.001$, **Figure 3G**), but there were no statistically significant differences between genotype-based pairs.

Interestingly, media thickness was increased in $Eln^{+/-}$ as compared to $Eln^{+/+}$ (two-way ANOVA, genotype effect, $p < 0.0001$) and in males compared to females (sex effect $p < 0.001$) effects; no interactive effects were seen (**Figure 3H**). MPA wall thickness was increased in male $Eln^{+/-}$ ($p < 0.0001$, Fig 3H) and female $Eln^{+/-}$ ($p < 0.0001$) compared to their sex matched $Eln^{+/+}$ counterparts. However, male $Eln^{+/-}$ MPA medial wall thickness was also notably thicker than female $Eln^{+/-}$ ($p < 0.001$). A trend toward increased media thickness in male vs. female controls was noted as well ($p = 0.06$, males thicker).

Treatment With Minoxidil Increases *ex vivo* and *in vivo* Pulmonary Artery Caliber in $Eln^{+/-}$ Mice

To test minoxidil's therapeutic potential on the pulmonary vasculature, treatment (Tx) was initiated in $Eln^{+/-}$ mice immediately post-weaning (~P21) to ~P90. Because no interactive effect was seen for sex for any of the measures tested, Tx was evaluated in male mice only. Consistent with aortic

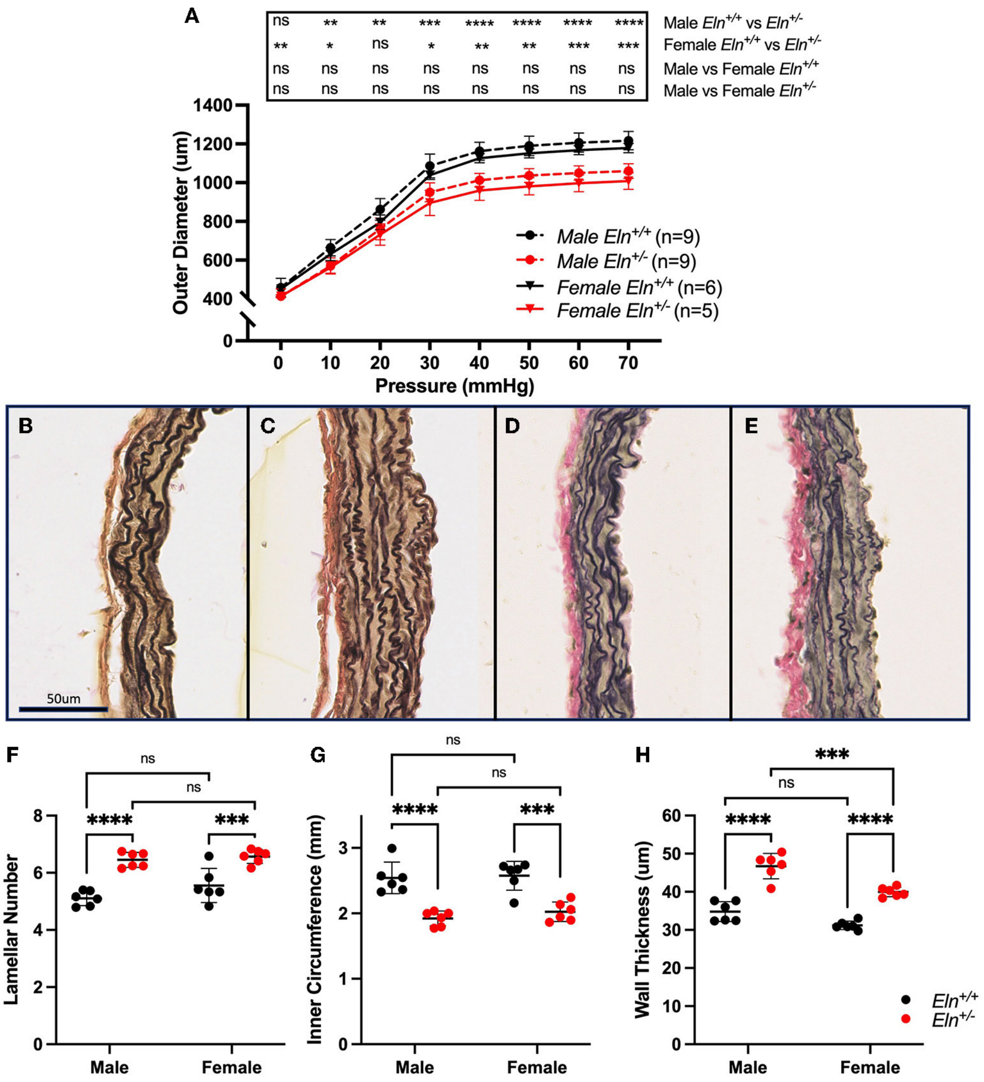

FIGURE 3 | Sex and Eln genotype differences in pulmonary artery morphology. **(A)** reports the relationship between intravascular pressure (x axis) and LPA diameter (y axis). **(B–E)** show VVG stained images of male *Eln*$^{+/+}$ **(B)**, male *Eln*$^{+/-}$ **(C)**, female Eln$^{+/+}$ **(D)**, and female *Eln*$^{+/-}$ **(E)** main pulmonary artery. **(F)** shows lamellar number. **(G)** is the MPA internal medial circumference and **(H)** shows the medial thickness for the various sex-genotype groups. *Eln*$^{+/+}$ data are presented in black and *Eln*$^{+/-}$ in red in all figures. In **(A)**, mean +/- SD are shown for all points. Males are shown as dashed lines and females as solid lines. For **(F–H)**, a mean line +/- SD is shown for each sex/genotype combination. Multiple comparison testing (after ANOVA) by Tukey. * $p < 0.05$, ** $p < 0.01$, *** $p < 0.001$, **** $p < 0.0001$, and ns is not significant.

studies, minoxidil appeared to increase PA outer diameter at all pressures as measured by pressure myography (two-way repeated measures ANOVA, treatment effect, $p < 0.0001$; **Figure 4A**). Higher pressure was associated with increased diameter in all groups (pressure effect, $p < 0.0001$). There was also a borderline interaction (p 0.06) between Tx and pressure for PA outer diameter, with higher pressures generating greater differences between the treated and untreated cohorts. Multiple-comparisons testing showed that the treated *Eln*$^{+/-}$ cohort had larger PAs compared to untreated *Eln*$^{+/-}$ mice, across all pressures (**Figure 4A**).

While histology confirmed increased internal circumference in treated male *Eln*$^{+/-}$ vessels compared to untreated *Eln*$^{+/-}$ (unpaired t-test, $p < 0.05$; **Figure 4B**), Tx did not alter the established lamellar number (**Figure 4C**) or medial thickness (**Figure 4D**).

In parallel with the *ex vivo* myography studies, we also performed *in vivo* analyses using cardiac gated μCT angiogram. Following confirmation of a statistically significant genotype effect by one-way ANOVA, (MPA: $p < 0.05$, LPA: $p < 0.01$ and RPA: $p < 0.01$), multiple comparisons confirmed smaller lumen diameter in untreated *Eln*$^{+/-}$ than *Eln*$^{+/+}$ PAs, across all three vessels (MPA: $p < 0.05$, **Figure 4E**; LPA: $p < 0.05$, **Figure 4F**; RPA: $p < 0.01$, **Figure 4G**). Tx results in PA lumen diameter increase in treated *Eln*$^{+/-}$ vessels compared to untreated *Eln*$^{+/-}$ across all three vessels (MPA: $p < 0.05$; LPA $p < 0.05$; RPA $p < 0.05$). No pairwise differences were seen between *Eln*$^{+/+}$ and treated *Eln*$^{+/-}$ in any vessel type.

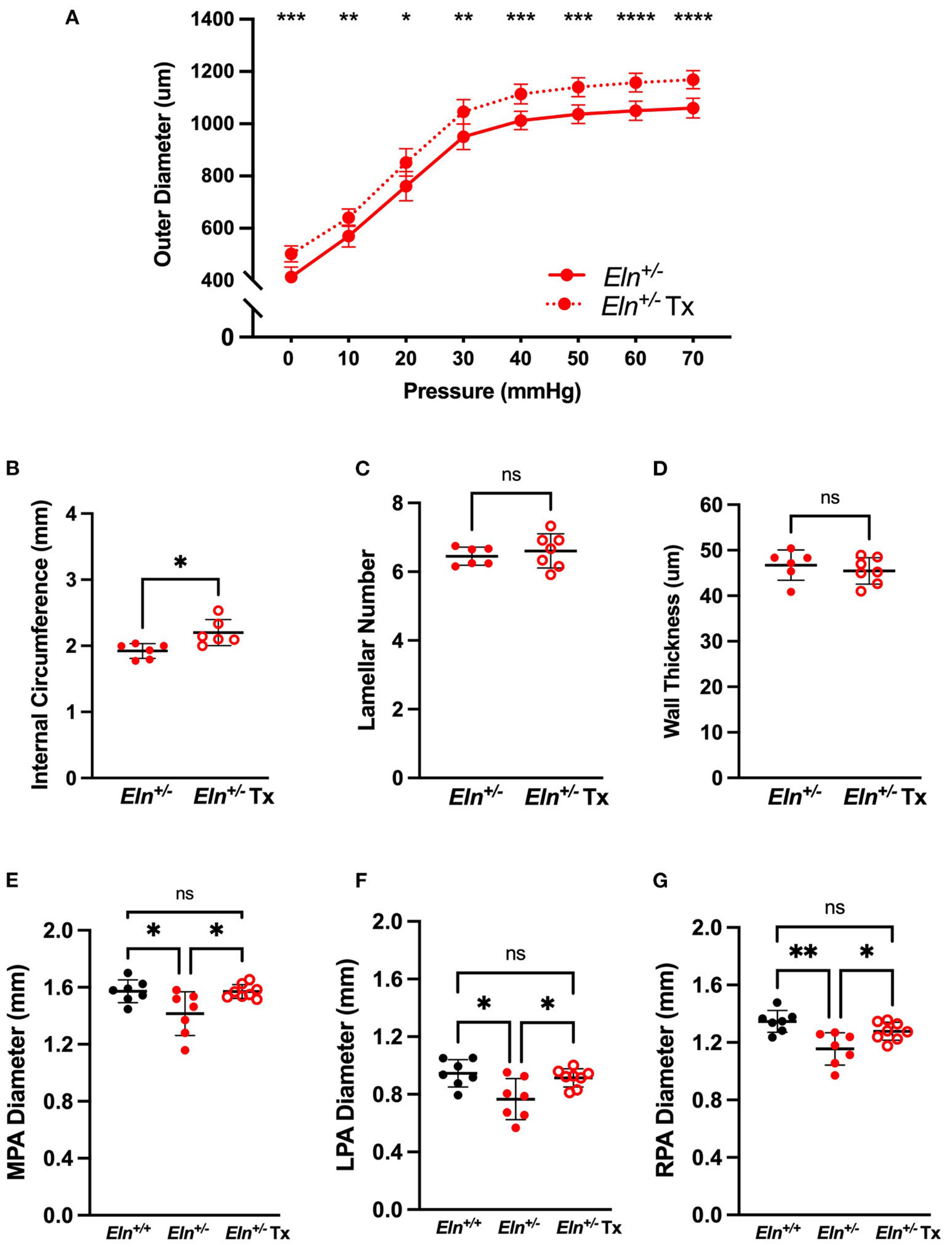

FIGURE 4 | Minoxidil increases pulmonary artery caliber. **(A)** reports the relationship between intravascular pressure (x axis) and LPA diameter (y axis) for treated and untreated *Eln*$^{+/-}$ mice. **(B–D)** depict measures collected from unloaded histological sections of main pulmonary arteries. **(B)** shows the internal medial circumference. **(C)** is lamellar number and **(D)** shows the medial thickness. **(E–G)** show *in vivo* arterial diameter measures for the main **(E)**, left **(F)** and right **(G)** pulmonary arteries. *Eln*$^{+/+}$ data are presented in black and *Eln*$^{+/-}$ in red. Untreated mice are depicted with closed circles and treated (Tx) mice are shown with open circles. In **(A)**, mean +/- SD are shown for all points. A mean line +/- SD is shown for each treatment/genotype combination in **(B–G)**. Unpaired *t*-tests were used in **(B–D)**. Multiple comparison testing (after ANOVA) by Tukey [**(A)** and **(E–G)**]. * $p < 0.05$, ** $p < 0.01$, *** $p < 0.001$, **** $p < 0.0001$ and ns is not significant.

Minoxidil Reduces RVSP as Measured by Invasive Pressure Catheterization in *Eln*$^{+/-}$ Mice

In the *Eln*$^{+/-}$ cohort, Tx reduced RVSP (6.1 mmHg difference, unpaired *t*-test, $p < 0.01$; **Figure 5A**) as measured by invasive pressure catheterization and yielded no difference in RVDP (**Figure 5A**). No Tx effect was detected in *Eln*$^{+/-}$ HR (**Figure 5B**).

Despite an apparent reduction of ventricular pressure and lumen size, minoxidil increased both RVHM/TL (Mann-Whitney; $p < 0.01$; **Figure 5C**) and LVHM/TL (Mann-Whitney, $p < 0.001$; **Figure 5D**) in *Eln*$^{+/-}$ mice. There

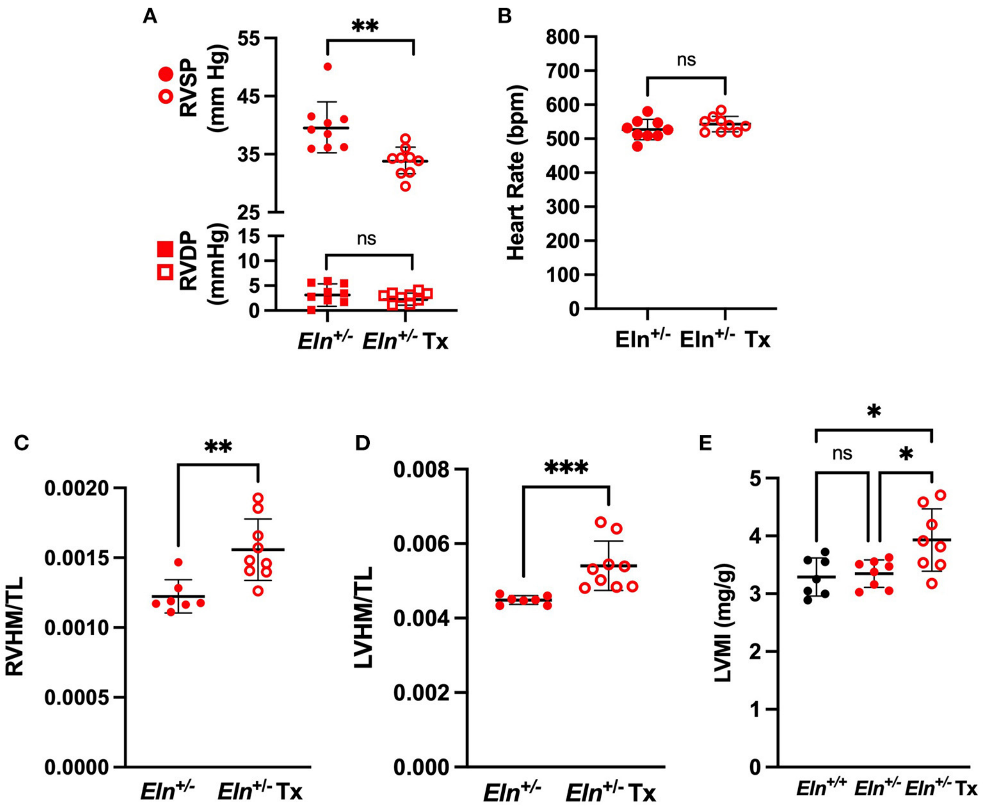

FIGURE 5 | Minoxidil reduces right ventricular pressure and increases heart size in *Eln*$^{+/-}$ mice. **(A)** shows RVSP in circles and RVDP in squares in treated and untreated *Eln*$^{+/-}$ mice. **(B)** depicts HR in the same groups. **(C,D)** report heart mass as normalized to tibial length findings. **(C)**: RVHM/TL and **(D)**: LVHM/TL (this measure includes the interventricular septum and the LV in the LVHM measure). **(E)** depicts Estimated Left Ventricular Mass Index (LVMI) assessed using echocardiogram. *Eln*$^{+/+}$ data are presented in black and *Eln*$^{+/-}$ are in red. Untreated mice are depicted with closed circles and minoxidil treated (Tx) mice are shown with open circles. A mean line +/- SD is shown for each Tx/genotype combination. Unpaired *t*-test was used for **(A)** and **(B)**, Mann-Whitney for **(C)** and **(D)**, and one-way ANOVA for **(E)**. Multiple comparison testing (after ANOVA) by Tukey. * $p < 0.05$, ** $p < 0.01$, *** $p < 0.001$, and ns is not significant.

was no difference in tibia length between male *Eln*$^{+/-}$ and *Eln*$^{+/-}$ Tx (Mann-Whitney; **Supplementary Figure 2A**). Similar effects were seen in RV with normalization to body mass: Tx increased both RVHM/BM (Mann-Whitney, $p < 0.01$; **Supplementary Figure 2B**) and LVHM/BM (Mann-Whitney, $p < 0.01$; **Supplementary Figure 2C**) in *Eln*$^{+/-}$ mice with no apparent difference in body mass identified between groups (Mann-Whitney; **Supplementary Figure 2D**).

Echocardiogram demonstrated similar findings. Following confirmation of statistically significant group effects for the echocardiogram measures by one-way ANOVA (data not reported), we performed pairwise comparisons. Echocardiogram estimated left ventricular heart mass indexed to body mass (LVMI) was indeed larger in the *Eln*$^{+/-}$ Tx group than in either the *Eln*$^{+/+}$ or the untreated *Eln*$^{+/-}$ groups (p<0.05 for both comparisons, **Figure 5E**). Individual measures of wall thickness (left ventricular posterior wall thickness at systole (LVPWs) and interventricular septal wall thickness at systole (IVSs)) were also detectably larger in the *Eln*$^{+/-}$ Tx group (See **Supplementary Table 2** for details). Left ventricular chamber end diastolic dimension (LVIDd) was also larger in the treated *Eln*$^{+/-}$ Tx mice as compared to *Eln*$^{+/+}$ ($p < 0.05$; **Supplementary Table**) but was not larger than untreated *Eln*$^{+/-}$.

Eln$^{+/-}$ Mice Exhibit Systolic Notching and Reduced Pulmonary Artery Acceleration Time (PAAT) by Echo Doppler; Neither Resolve With Minoxidil

Notching is thought to be caused by an abnormal wave reflection that occurs in the setting of elevated PA impedance (22). Compared to the traditional parabolic trace in the *Eln*$^{+/+}$ (**Figure 6A**), we see the emergence of systolic notching in the *Eln*$^{+/-}$. This observation consistently presents as either a distinct "shelf" (white arrow, **Figure 6B**) or a second inflection (red arrow, **Figure 6C**). A notch was present in 0 out of 7 *Eln*$^{+/+}$, 7 of 8 *Eln*$^{+/-}$, and 8 of 8 *Eln*$^{+/-}$ Tx echocardiograms (Chi-Square, $p < 0.0001$ χ^2; **Figure 6D**), suggesting increased PA impedence. Diminished echocardiogram-based PAAT is an indication of elevated pulmonary systolic blood pressure and may imply increased resistance (23). Multiple comparison testing following one-way ANOVA ($p < 0.001$) shows that untreated

Eln$^{+/-}$ mice have decreased PAAT relative to *Eln*$^{+/+}$ ($p < 0.001$; **Figure 6E**), but minoxidil does not rescue that decrease in the *Eln*$^{+/-}$ Tx group

Branching Patterns and Vessel Lengths of the Main Conducting Vessels Are Altered in the Eln+/-

To evaluate phenotypic features that might influence vascular resistance, we utilized a polymer casting technique we recently optimized (21) to visualize the length and branching pattern of the pulmonary architecture using μCT at several developmental timepoints. A representative *Eln*$^{+/+}$ (**Figure 7A**) and *Eln*$^{+/-}$ (**Figure 7B**) P90 volume rendering shows the entire PA vascular arcade. After thresholding to remove distal vasculature, the resulting rendering (*Eln*$^{+/+}$ **Figure 7C** and *Eln*$^{+/-}$ **Figure 7D**) was used for analysis. Previous investigation showed that alterations in branching patterns off the MPA trunk can affect hemodynamic performance altering both flow/pressure distribution and creating areas of high wall shear stress (24, 25). The angle formed between the RPA and LPA was more acute in *Eln*$^{+/-}$ mice compared *to Eln*$^{+/+}$ (two-way ANOVA, genotype effect, $p < 0.0001$; **Figure 7E**), but no age or interactive effect was present. Multiple-comparisons revealed a reduced *Eln*$^{+/-}$ branching angle at both P7 ($p < 0.05$) and P90 ($p < 0.01$), with a borderline difference noted at P30 ($p = 0.08$).

We know that, in addition to diminished lumen size, conduit length also increases resistance (26). Proximal pulmonary lobar arteries (see methods and **Figures 7C,D** for measurement boundaries) were all longer in *Eln*$^{+/-}$ mice as compared to *Eln*$^{+/+}$ (two-way ANOVA, genotype effect, LPLA: $p < 0.0001$, **Figure 7F** and RPLA: $p < 0.001$, **Supplementary Figure 3A**). All vessels lengthened with age (LPLA $p < 0.0001$ and RPLA $p < 0.0001$). However, *Eln*$^{+/-}$ proximal lobar artery segments appear to lengthen more over time compared to their *Eln*$^{+/+}$ counterparts [genotype X time interactive effect, LPLA ($p < 0.05$) and RPLA ($p < 0.05$)], suggesting another possible contributor to vascular resistance in *Eln*$^{+/-}$ mice. Multiple-comparison testing showed longer *Eln*$^{+/-}$ proximal arteries at P7 ($p < 0.01$), P30 ($p < 0.001$), and P90 ($p < 0.0001$) for the LPLA. Similarly, the RPLA showed an effect at P30 ($p < 0.05$) and P90 ($p < 0.001$).

Previous studies have shown increased tortuosity in systemic vessels affected by elastin insufficiency (27). The *Eln*$^{+/-}$ pulmonary arteries exhibit evidence of mild tortuosity. The LPLA was more tortuous in *Eln*$^{+/-}$ mice as compared to *Eln*$^{+/+}$ (two-way ANOVA, genotype effect, $p < 0.0001$, **Figure 7G**). Additionally, the LPLA exhibits more tortuosity at younger ages (two-way ANOVA, age effect, $p < 0.0001$). Multiple-comparison testing showed strong effects of *Eln* genotype at P1 ($p < 0.01$) and P7 ($p < 0.001$). Although the *Eln*$^{+/-}$ RPLA (**Supplementary Figure 3B**) trended toward increased tortuosity, it was not significant.

Eln$^{+/-}$ Mice Exhibit Early Delays in Peripheral PA Branching, With Later Recovery and Evidence of Increased Branches

For the peripheral analysis, we performed a higher resolution sub-reconstruction on the P1, P7, P30, and P90 LULFA (**Figures 7C,D** white arrow) and analyzed both generation specific arcade length (**Figures 8A–D**) and branch number (**Figures 8E–H**) for 15 generations. The pulmonary vascular bed can be seen as a tree that starts as a trunk (here we initiate measures in the LULFA) that then splits with successive generations. The generation-specific arcade length (GSAL) is the sum of the lengths of all the arterial segments in a given generation, while generation-specific branch number (GSBN) is the total number of branches in that generation in the vascular network supplied by the LULFA.

At P1, *Eln* genotype did not influence GSAL (two-way ANOVA repeated measures, genotype effect, $p =$ NS; **Figure 8A**). However, P1 GSAL did differ with generation number, as it does at all ages studied (generation effect, $p < 0.0001$ in all comparisons). At P7, *Eln*$^{+/-}$ GSAL is generally shorter than that of *Eln*$^{+/+}$mice (genotype effect, $p < 0.05$, **Figure 8B**), although multiple testing shows no significant pairwise comparisons. By P30, there is again no difference in GSAL based on *Eln* genotype (genotype effect, $p =$ NS, **Figure 8C**). However, by P90, the *Eln*$^{+/-}$ GSAL is markedly longer than the *Eln*$^{+/+}$ measure (genotype effect, $p < 0.0001$, **Figure 8D**) with an increased difference between the genotypes notable at more distal generation levels (genotype by generation interactive effect, $p < 0.05$). Pairwise comparisons are shown in the figure.

The increased GSAL could simply represent longer vascular segments (as noted in the proximal vasculature) or more branches per generation. As expected, GSBN varies by generation (two-way ANOVA repeated measures, generation effect, $p < 0.0001$ for all ages; **Figures 8E–H**). Decreased GSBN was noted in *Eln*$^{+/-}$ at P1 (genotype effect, $p < 0.05$; **Figure 8E**) and P7 (genotype effect, $p < 0.05$; **Figure 8F**). As with GSAL, there was no impact of *Eln* genotype on GSBN at P30 (genotype effect, $p =$ NS; **Figure 8G**), but a robust increase in branches noted by P90 (genotype effect, $p < 0.0001$; **Figure 8H**). Pairwise comparisons are shown in the figure. When the P90 GSAL is normalized to GSBL, we see that proximal segment lengths are longer in *Eln*$^{+/-}$ pulmonary trees. In the periphery where arteriolar mechanical function is less dependent on elastin, the segment lengths per branch are similar across genotypes (See **Supplementary Figure 4**).

Later Administration of Minoxidil Cannot Reverse Proximal Lobar Vessel Length, Tortuosity, LPA-RPA Angle or Generation Specific Peripheral Vascular Measures

As in humans with WBS and elastin insufficiency, typically diagnosed postnatally after the cardiovascular changes become apparent, we initiated Tx in mice post-weaning (∼P21–P90). As such, we only evaluated the Tx effect at P90

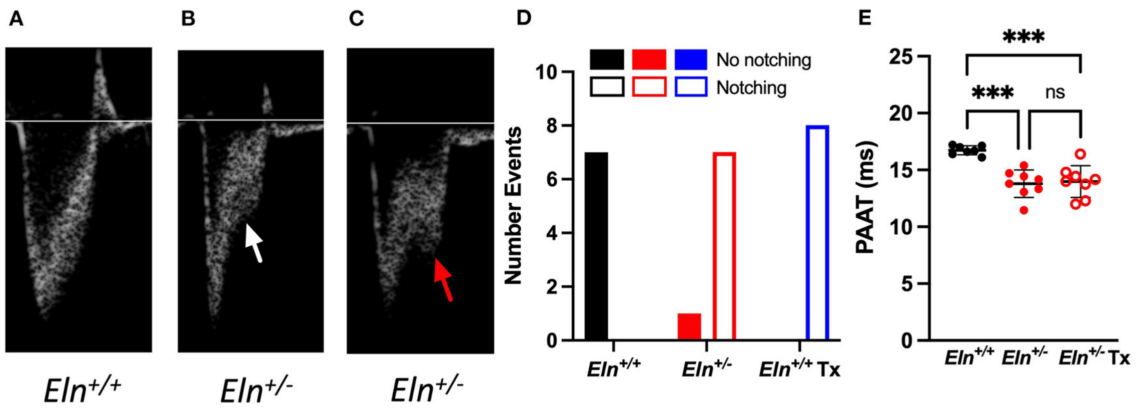

FIGURE 6 | *Eln*$^{+/-}$ mice display evidence of increased vascular resistance, not impacted by minoxidil. Panels A-C show pulmonary artery pulse wave Doppler. The typical parabolic trace is seen in the *Eln*$^{+/+}$ **(A)**, while a shelf-like systolic notch is present in the majority of treated and untreated *Eln*$^{+/-}$ mice **(B)** white arrow. In some cases, a second distinct systolic inflection, consistent with human systolic notching, becomes apparent **(C)** red arrow. Chi-square analysis **(D)** reports the frequency of notching in this cohort. **(E)** shows pulmonary artery acceleration time (PAAT). PAAT is associated with elevated pulmonary pressure and vascular resistance. In **(D)**, *Eln*$^{+/+}$ data are presented in black, untreated *Eln*$^{+/-}$ in red, and treated *Eln*$^{+/-}$ in blue. Mice without a notch are shown in solid bars and those with systolic notching have open bars. In **(E)**, *Eln*$^{+/+}$ data are presented in black and *Eln*$^{+/-}$ are in red. Untreated mice are depicted with closed circles and minoxidil treated (Tx) mice are shown with open circles. A mean line +/- SD is shown for each Tx/genotype combination. Multiple comparison testing (after ANOVA) by Tukey. *** $p < 0.001$ and ns is not significant.

using polymer injected lung mounts imaged by µCT. In this case, Tx did not reduce the length of any *Eln*$^{+/-}$ lobar arteries (unpaired *t*-test, p = NS; LPLA **Figure 9A** and RPLA **Supplementary Figure 5A**). Additionally, treatment had no impact on vessel tortuosity (unpaired *t*-test, p=NS; LPLA **Figure 9B** and RPLA **Supplementary Figure 5B**).

Similarly, post-weaning Tx did not widen the acute *Eln*$^{+/-}$ LPA-RPA angle (unpaired *t*-test, **Figure 9C**). Replication of LPA-RPA angle measurement using *in vivo* CT angiogram revealed similar findings across all genotypes (One way ANOVA, followed by pairwise comparisons, **Supplementary Figure 5C**), suggesting the findings are not just a byproduct of our casting process.

Finally, evaluation of the peripheral arcade in polymer injected lungs by two-way ANOVA repeated measures showed the previous patterns of generation-level GSAL and GSBN (**Figures 9D,E**, $p < 0.0001$ in both evaluations). However, there was no Tx effect.

DISCUSSION

Elastin haploinsufficiency causes significant morbidity and mortality in affected individuals. While SVAS is the most common vascular lesion in people with WBS (OMIM #194050) and *ELN*-related SVAS (OMIM #185500), ∼40–60% of individuals with these conditions have stenosis in the pulmonary tree (3, 4). The natural history for pulmonary vascular disease in elastin insufficiency is for eventual resolution in most mild cases, while moderate or severe disease usually requires surgical intervention (6). Smooth muscle cells in elastin insufficient vessels display abnormal circumferential growth (28) and fail to remodel appropriately with attempted percutaneous dilation (4, 29). Success rates for primary catheter-based palliation of branch PA disease have been reported at 51%, with frequent need for subsequent surgical intervention (30, 31). As such these procedures are now predominantly used as a temporizer before or between surgeries. Because the condition tends to impact multiple levels of the pulmonary vasculature from the hilum into the periphery, the surgery is exceedingly complex and the number of centers willing to attempt such approaches is vanishingly small. The reports of successful palliation in these centers, however, are encouraging (7, 32). Still, there is room for alternate approaches, if only because the availability of such specialized care is so limited. Additionally, data presented here show persistently elevated RVSPe in a subset of patients even after intervention. **Figure 1**, for example, includes one individual who benefited from extensive PA reconstruction beyond the hilum, but whose pressures remain high even though the proximal vascular measurements are relatively normal. Consequently, additional therapeutic options should be explored. The aim of this study was to characterize *Eln*$^{+/-}$ pulmonary vasculature structure from the branch pulmonary arteries to the periphery and to evaluate whether treatment with K_{ATP} channel opener, minoxidil, could mitigate pulmonary vascular abnormalities seen in *Eln*$^{+/-}$ mice. Minoxidil was initially developed as an anti-hypertensive owing to its inhibition of excitation-contraction coupling in muscle resulting in primary vasodilatory effect. However, subsequent studies showed that when given chronically, it induced expression of connective tissue genes that stabilize the vessel in its new dilated state.

Our analysis shows that *Eln*$^{+/-}$ mice display cardiovascular defects at all levels of the pulmonary vascular tree. RVSP is increased in the *Eln*$^{+/-}$, as assessed by both direct invasive catheterization (**Figure 2A**) and indirect echocardiographic assessment (**Figure 6E**). Furthermore, the right heart exhibits

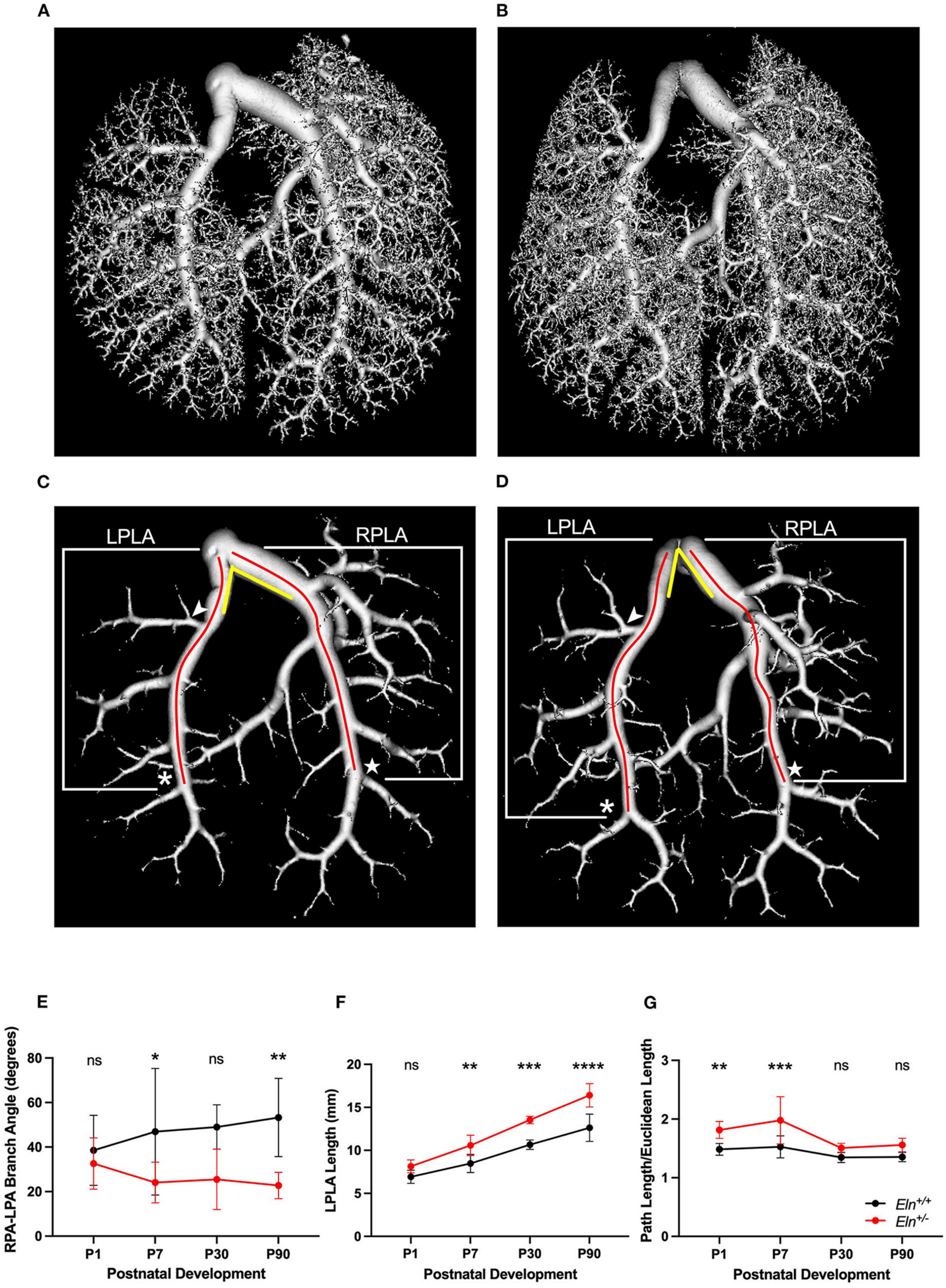

FIGURE 7 | Elastin insufficiency reduces PA branching angle and increases proximal arterial segment length. **(A)** (*Eln*$^{+/+}$) and **(B)** (*Eln*$^{+/-}$) contain a volume reconstruction of a lung set generated through *ex vivo* vascular casting and microCT. **(C)** (*Eln*$^{+/+}$) and **(D)** (*Eln*$^{+/-}$) are the same lung sets thresholded for large vessel analysis. The LPLA (asterisk denotes fourth branch) and RPLA (star marks the sixth branch) are noted with red lines to illustrate a typical path length measured by the software for each vessel. An arrowhead notes the position of the LULFA for small vessel analysis (see **Figure 8**) and yellow lines are an approximation of the angle formed between the LPA and RPA. This branch angle is evaluated in **(E)** at P1, P7, P30, and P90. The LPLA length **(F)** and tortuosity **(G)** are shown at the same time points. In **(E–G)**, *Eln*$^{+/+}$ data are presented in black and *Eln*$^{+/-}$ are in red. A mean line +/- SD are shown for each age/genotype combination. Multiple comparison testing (after ANOVA) by Sidak. * $p < 0.05$, ** $p < 0.01$, *** $p < 0.001$, **** $p < 0.0001$ and ns is not significant ($n = 5$–8/group).

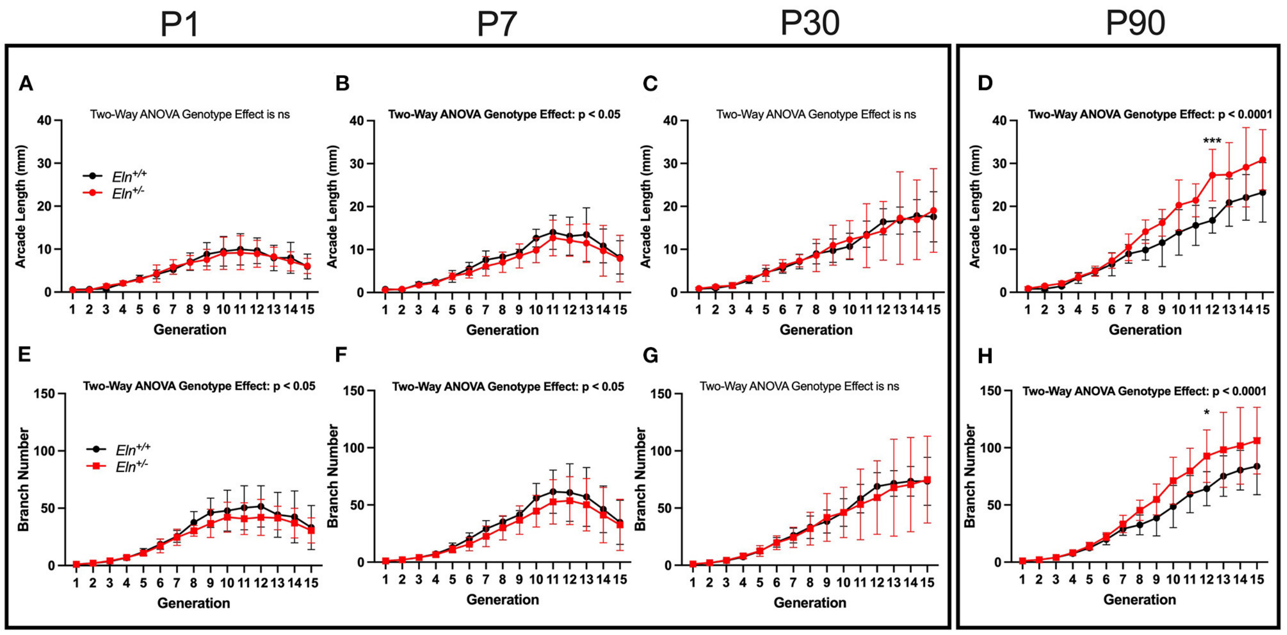

FIGURE 8 | Elastin insufficiency shows diminished vascular branching early in development giving rise to increased branching in adults. Generation-specific arcade length [GSAL; **(A–D)**] and generation-specific branch number [GSBN; **(E–H)**] were evaluated at P1, P7, P30, and P90. *Eln*$^{+/+}$ data are presented in black and *Eln*$^{+/-}$ are in red. Mean +/- SD are shown for each age/genotype combination. Multiple comparison testing (after ANOVA) by Sidak. * $p < 0.05$, *** $p < 0.001$, and ns is not significant ($n = 5$–8/group).

increased normalized mass (**Figure 2C**). Of note our data exhibit a smaller elastin insufficiency-associated increase in RVSP (9.94 (male) and 7.07 (female), and 8.62 (male and female combined) mmHg in this study, respectively vs. 34.8 mm Hg in Shifren et al. (33)). Reasons for this difference in magnitude may include genetic background, anesthetic choice, catheter characteristics, and general drift in mutant pressure over time. The initial publication of the *Eln*$^{+/-}$ model in 1998 showed an average systemic systolic blood pressure of 165 mmHg (34), while more recent publications report an average of 127 mmHg (8), potentially implicating epigenetic phenomena (35).

In vivo CT angiogram and *ex vivo* pressure-diameter testing by pressure myography confirm reduced *Eln*$^{+/-}$ inner and outer PA diameters, with the decreased slope of the myography-assessed pressure-diameter curve over the working range of the vessel (0–40 mm Hg in the *Eln*$^{+/-}$ mouse, **Figure 3A**) suggesting increased arterial stiffness. Likewise, histological analysis revealed medial hypertrophy in *Eln*$^{+/-}$ PAs (**Figure 3H**). Wall thickening such as this is commonly seen in humans with pulmonary vascular disease (36, 37) and may synergize with the primary elastin insufficiency defect to increase stiffness. Such features may suggest that the *Eln*$^{+/-}$ vasculopathy may limit vascular carrying capacity (both in the form of blood volume and oxygen/nutrient delivery). Indeed, previous studies evaluating the brain perfusion in the *Eln*$^{+/-}$ mouse also endorse reduced end organ flow (8).

In addition to the proximal caliber measures, our latex injection-μCT studies yielded evidence of abnormal proximal branching angles (**Figure 7E**), increased pulmonary arterial segment length (**Figure 7F**), increased tortuosity (**Figure 7G**) and evidence of altered peripheral branching (**Figure 8**). **Figure 10** illustrates the two notable developmental phases. Early in post-natal life (P1 and P7), the *Eln*$^{+/-}$ LULFA displays reduced branching. But then later, as the lungs grow and mature, the rate of branching increases, catching (P30) and eventually surpassing (P90) their *Eln*$^{+/+}$ counterpart. Reduced early branching was previously reported by Hilgendorff et al., who assessed pulmonary microvasculature in ventilated and unventilated P5-7 *Eln*$^{+/-}$ mice, showing an overall reduction in small vessel (<20μm) number, relative to their *Eln*$^{+/+}$ counterparts (38), with no change in alveolar number. The authors suggest that decreased arteriolar number may contribute to early pulmonary hypertension in their model. Indeed, many of the measures shown here may contribute to increased pulmonary pressure and possibly increased pulmonary vascular resistance in the *Eln*$^{+/-}$ pup. While we were unable to measure mouse pulmonary vascular resistance (PVR) directly, we did note several indirect measures suggestive of elevated PVR in mutant mice, including systemic notching and reduced PAAT, even at later ages after the branch number had normalized or surpassed the *Eln*$^{+/+}$ (39–41).

The phenomenon of altered branching remains unexplained. It is possible that early reduced vessel number represents a primary developmental abnormality of the *Eln*$^{+/-}$, with later vessel proliferation a compensatory response to decreased tissue perfusion. It is also possible that the later change in vascular patterning instead indicates a response to elastin mediated disease in the lung parenchyma. Recent studies have begun

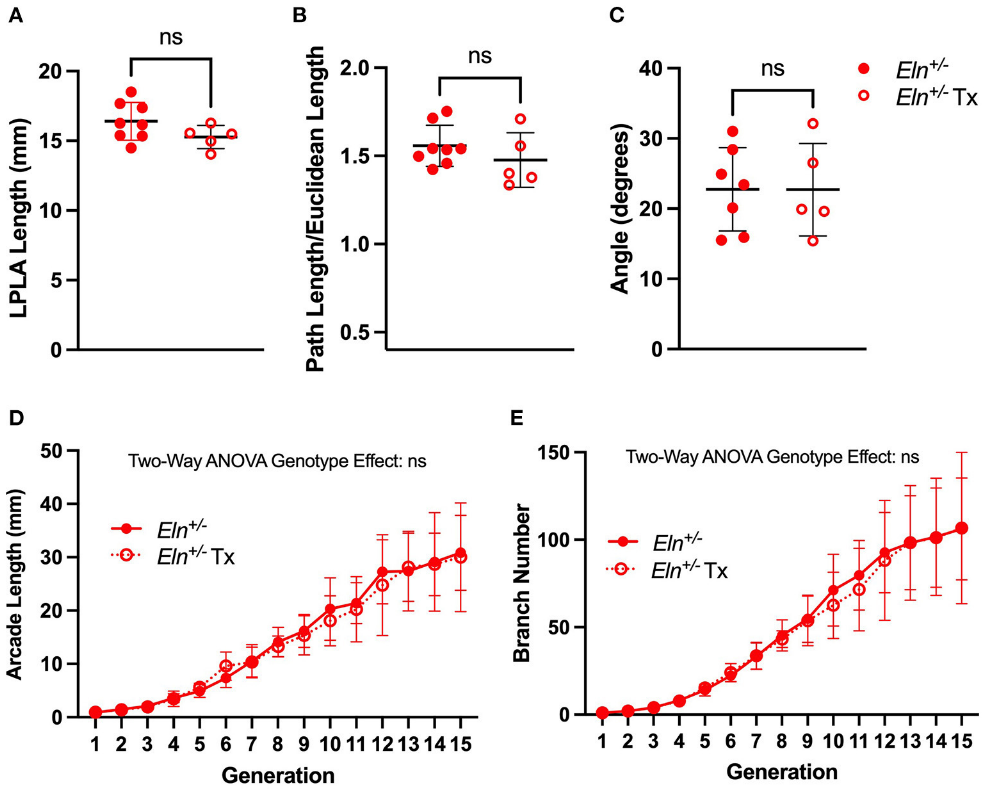

FIGURE 9 | Minoxidil does not impact post-natal branching patterns in *Eln*$^{+/-}$ mice. A lack of treatment effect for minoxidil is evident in P90 left pulmonary lobar artery (LPLA) length **(A)**, tortuosity **(B)** and LPA-RPA branching angle **(C)**. Similarly, no treatment differences are noted in generation-specific arcade length **(D)** or branch number **(E)**. Untreated *Eln*$^{+/-}$ values are in closed circles and treated *Eln*$^{+/-}$ values are depicted with open circles. In **(A–C)**, a mean line +/- SD are shown for each timepoint/genotype combination. In **(D,E)**, mean +/- SD are shown for all points. ns is not significant and *n* = 5–6/group for **(D,E)**.

to show evidence of air trapping and obstruction in humans with WBS and elastin insufficiency (42, 43) and altered lung compliance in the *Eln*$^{+/-}$ mouse (44, 45). More investigation is needed to understand this complex phenotype and how it may relate to the resolution of mildly elevated pulmonary artery pressures seen in many children with WBS over their first few years of life.

In this study, we also evaluated sex as a biological variable. In general, genotype X sex interactions were rare. The most notable exception was in medial thickness. While thickened abdominal aortic media has been reported in Wagenseil et al. (46), not all authors have reported thicker *Eln*$^{+/-}$ vessels, especially when using full wall, rather than media-only measures (33, 47, 48). Interestingly, our data showed more robust medial thickening in male *Eln*$^{+/-}$ pulmonary arteries than female, although both sexes exhibited this phenotype (**Figure 3H**). This sex effect is clinically relevant as males with elastin insufficiency as a result of WBS are reported to have more severe vascular disease than females (11). A recent genetic study confirmed this sex difference in SVAS outcomes (49), but it has not been specifically examined in terms of pulmonary vascular outcomes. Systemic arterial wall thickness, in general, has been reported as higher in adult and pediatric males, and increases with age (50). As noted above, medial thickening is often seen in PAs that have been chronically exposed to higher pulmonary pressures. Indeed, male *Eln*$^{+/-}$ do exhibit the highest RVSP of all groups. It is possible that there are certain pressure thresholds reached by male *Eln*$^{+/-}$, but not female *Eln*$^{+/-}$ mice that accelerate this outcome. Additional investigation of molecular signatures that differ between *Eln*$^{+/-}$ male and female pulmonary arteries is warranted as it may reveal factors that could serve as rational therapeutics for this condition.

Finally, and most importantly, we endeavored to evaluate minoxidil, a K_{ATP} channel opener and vasodilator (51, 52), as a treatment of pulmonary vasculopathy in people with WBS. Previous work with this drug showed that chronic administration increased arterial caliber in *Eln*$^{+/-}$ mice, decreased systemic blood pressure and led to systemic large artery remodeling, first by vasodilation and then with increased elastin and other connective tissue molecule deposition in the extracellular space (8). Moreover, these changes in vessel phenotype and composition persisted weeks after the drug had been removed. Similar functional improvements were seen in the treatment of wildtype mice who had experienced elastin loss due to age (9). A clinical study using minoxidil in a small number of individuals with WBS showed no improvement of the intima-media thickness in the carotid artery. The same study did, however show an increase in carotid lumen diameter in the same participants (10), suggesting that it may still prove

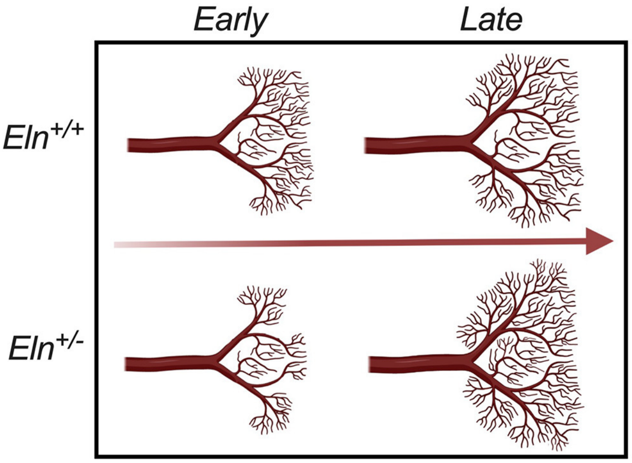

FIGURE 10 | Developmental time-course of Elastin haploinsufficient vasculature. Early (P1 and P7) in development, distal $Eln^{+/-}$ PAs exhibit less branching than the $Eln^{+/+}$. As the lungs grow and mature, the distal vasculature in the $Eln^{+/-}$ branch more - catching and eventually surpassing the $Eln^{+/+}$ counterpart later (P30 and P90) in development. This suggests a possible compensatory response to elastin insufficiency mediated changes in pulmonary physiology that occur over a wide developmental window.

useful in the treatment of elastin-mediated disease if used for different indications.

As such, we compared pulmonary vascular findings in $Eln^{+/-}$ mice administered minoxidil in their drinking water from weaning until 3 months of age to an untreated cohort. Encouragingly, we saw a drop in RVSP (**Figure 5A**) and an increase in proximal PA caliber by *in vivo* CT and *ex vivo* myography and histology (**Figure 4**) with minoxidil. However, markers suggestive of increased pulmonary vascular resistance in $Eln^{+/-}$ mice [PAAT and systolic notching, (41)] were not impacted by the drug (**Figures 6D–E**). The lack of improvement in these areas, underscores the multi-dimensional impact of elastin insufficiency on vessel physiology. Branching angle, arterial segment length, tortuosity, and differences in peripheral branching can all influence flow and vascular resistance patterns (24–26) and had already been established as abnormal in the $Eln^{+/-}$ as early as P7 (**Figures 7E–G** and **Figure 8**). While slight trends toward improvement of these measures were noted with Tx initiated at weaning (**Figures 9A–C**), the effect was not statistically significant, potentially because therapy was initiated too late. Earlier intervention should be prioritized in future trials.

In addition to the noted vascular features, minoxidil also increased heart mass. Given that minoxidil successfully decreased RVSP and increased lumen size, one would have predicted decreased RV mass to result from this. Interestingly, multiple authors do note cardiac hypertrophy as a common off-target effect of this drug, specifically in rodent models (53, 54). Review of those studies shows a trend toward larger cardiomyocyte cross-sectional area in treated WT animals, with more severe features noted in the RV. Subsequent work using K_{ATP} gain of function mutants suggest increased L-type calcium current accompanies increased K_{ATP} current, suggesting a possible mechanistic impetus underlying cardiac hypertrophy seen here (55–57). Regardless, we believe this to be an off-target effect of the medication that appears most pronounced in rodents. Of note, cardiac hypertrophy was not noted in the previous minoxidil trial in WBS (10), nor was it seen consistently in human subjects with Cantu Syndrome, which arises from K_{ATP} gain of function channel mutations (57).

Taken together, these findings suggest that elastin insufficiency produces a complex collection of vascular findings in the lung that are not limited to the proximal vasculature. Thus, optimal treatment for vascular disease in elastin insufficiency will require interventions which impact vessels at multiple levels and coincide with relevant developmental timelines. Our data show that minoxidil effectively improves proximal arterial caliber in elastin haploinsufficiency, but when delivered post-weaning in mice does not completely reverse vascular abnormalities. Consequently, to be used therapeutically, early diagnosis and treatment of elastin mediated pulmonary disease may yield more efficacious results. Our experience with treatment of mice in systemic circulation suggested that minoxidil could induce transcriptional changes that led to meaningful remodeling of $Eln^{+/-}$ vessels. As such, minoxidil could be considered for the treatment of younger children with severe pulmonary vascular disease as an adjunct to surgical intervention to improve lumen dimensions beyond the surgical field. Earlier treatment may influence other still developing contributors to vascular resistance such as branching angle and segment length. While it is likely that the hypertrophy seen here is a consequence of peculiarities of mouse physiology, cardiac size should be monitored and long-term use minimized to avoid off-target drug effects including hirsutism and skeletal bone remodeling.

DATA AVAILABILITY STATEMENT

The raw data supporting the conclusions of this article will be made available by the authors, without undue reservation.

ETHICS STATEMENT

The studies involving human participants were reviewed and approved by Institutional Review Board of the National Institutes of Health. Written informed consent to participate in this study was provided by the participants' legal guardian/next of kin. The animal study was reviewed and approved by Institutional Animal Care and Use Committee of the National Heart Lung and Blood Institute or Washington University School of Medicine.

AUTHOR CONTRIBUTIONS

BK, RK, and LG: conceptual/experimental design. RK, LG, EK, MK, DD, DS, ZY, MC, Y-PF, FC, M-LN, SO, JF, and NR: data collection. RK, LG, EK, MK, DD, DS, MC, Y-PF, FC, M-LN, ML, and BK: data analysis. RK, BK, and LG: wrote the manuscript. RK, BK, LG, EK, MK, DD, DS, ZY, MC, Y-PF, FC, M-LN, SO, JF, NR, and ML: edited the manuscript. All authors contributed to the article and approved the submitted version.

FUNDING

Funding for this work was provided by the Division of Intramural Research of the National Heart, Lung, and Blood Institute through grants ZIA HL006210 and ZIA HL-006247.

ACKNOWLEDGMENTS

We would like thank Michael Ricafort for his assistance in blood pressure acquisition and Olivia Kelada for her guidance in helping optimize the *in vivo* μCT experiments. This study used resources from the mouse imaging facility, murine phenotyping core, pathology core, and the NHLBI echocardiography laboratory. Biorender.com was used to construct **Figure 10**.

SUPPLEMENTARY MATERIAL

The Supplementary Material for this article can be found online at: https://www.frontiersin.org/articles/10.3389/fcvm.2022.886813/full#supplementary-material

REFERENCES

1. Kozel BA, Barak B, Kim CA, Mervis CB, Osborne LR, Porter M, et al. Williams syndrome. *Nat Rev Dis Primers.* (2021) 7:42. doi: 10.1038/s41572-021-00276-z
2. Wren C, Oslizlok P, Bull C. Natural history of supravalvular aortic stenosis and pulmonary artery stenosis. *J Am Coll Cardiol.* (1990) 15:1625–30. doi: 10.1016/0735-1097(90)92837-R
3. Collins RT II, Kaplan P, Somes GW, Rome JJ. Long-term outcomes of patients with cardiovascular abnormalities and williams syndrome. *Am J Cardiol.* (2010) 105:874–8. doi: 10.1016/j.amjcard.2009.10.069
4. Pham PP, Moller JH, Hills C, Larson V, Pyles L. Cardiac catheterization and operative outcomes from a multicenter consortium for children with williams syndrome. *Pediatr Cardiol.* (2009) 30:9–14. doi: 10.1007/s00246-008-9323-z
5. Giddins NG, Finley JP, Nanton MA, Roy DL. The natural course of supravalvar aortic stenosis and peripheral pulmonary artery stenosis in Williams's syndrome. *Br Heart J.* (1989) 62:315–9. doi: 10.1136/hrt.62.4.315
6. Wessel A, Pankau R, Kececioglu D, Ruschewski W, Bürsch JH. Three decades of follow-up of aortic and pulmonary vascular lesions in the Williams-Beuren syndrome. *Am J Med Genet.* (1994) 52:297–301. doi: 10.1002/ajmg.1320520309
7. Collins RT. 2nd, Mainwaring RD, MacMillen KL, Hanley FL. Outcomes of pulmonary artery reconstruction in Williams syndrome. *Ann Thorac Surg.* (2019) 108:146–53. doi: 10.1016/j.athoracsur.2019.02.013
8. Knutsen RH, Beeman SC, Broekelmann TJ, Liu D, Tsang KM, Kovacs A, et al. Minoxidil improves vascular compliance, restores cerebral blood flow, and alters extracellular matrix gene expression in a model of chronic vascular stiffness. *Am J Physiol Heart Circ Physiol.* (2018) 315:H18–32. doi: 10.1152/ajpheart.00683.2017
9. Coquand-Gandit M, Jacob MP, Fhayli W, Romero B, Georgieva M, Bouillot S, et al. Chronic treatment with minoxidil induces elastic fiber neosynthesis and functional improvement in the aorta of aged mice. *Rejuvenation Res.* (2017) 20:218–30. doi: 10.1089/rej.2016.1874
10. Kassai B, Bouye P, Gilbert-Dussardier B, Godart F, Thambo JB, Rossi M, et al. Minoxidil vs. placebo in the treatment of arterial wall hypertrophy in children with Williams Beuren Syndrome: a randomized controlled trial. *BMC Pediatr.* (2019) 19:170. doi: 10.1186/s12887-019-1544-1
11. Sadler LS, Pober BR, Grandinetti A, Scheiber D, Fekete G, Sharma AN, et al. Differences by sex in cardiovascular disease in Williams syndrome. *J Pediatr.* (2001) 139:849–53. doi: 10.1067/mpd.2001.118889
12. Carillo ML, Levin MD, Spurney CF, Kozel BA. Abstract 9063: global longitudinal strain and longitudinal early diastolic strain rate may identify those williams syndrome patients at risk of cardiomyopathy development. *Circulation*. (2021) 144(Suppl_1):A9063-A. doi: 10.1161/circ.144.suppl_1.9063
13. Diaz AE, Levin MD, Spurney CF, Kozel BA. Increased prevalence of diastolic dysfunction and vascular stiffness in Williams-beuren syndrome. ASE 31st annual scientific sessions: *J Am Soc Echocardiograp*. (2020) 33, 647–778. doi: 10.1016/S0894-7317(20)30281-9
14. Gladwin MT, Sachdev V, Jison ML, Shizukuda Y, Plehn JF, Minter K, et al. Pulmonary hypertension as a risk factor for death in patients with sickle cell disease. *N Engl J Med.* (2004) 350:886–95. doi: 10.1056/NEJMoa035477
15. Berger M, Haimowitz A, Van Tosh A, Berdoff RL, Goldberg E. Quantitative assessment of pulmonary hypertension in patients with tricuspid regurgitation using continuous wave Doppler ultrasound. *J Am Coll Cardiol.* (1985) 6:359–65. doi: 10.1016/S0735-1097(85)80172-8
16. Greenberg SB, Lang SM, Gauss CH, Lensing SY, Ali S, Lyons KA. Normal pulmonary artery and branch pulmonary artery sizes in children. *Int J Cardiovasc Imaging.* (2018) 34:967–74. doi: 10.1007/s10554-018-1303-7
17. Li DY, Faury G, Taylor DG, Davis EC, Boyle WA, Mecham RP, et al. Novel arterial pathology in mice and humans hemizygous for elastin. *J Clin Invest.* (1998) 102:1783–7. doi: 10.1172/JCI4487
18. Kozel BA, Knutsen RH, Ye L, Ciliberto CH, Broekelmann TJ, Mecham RP. Genetic modifiers of cardiovascular phenotype caused by elastin haploinsufficiency act by extrinsic non-complementation. *J Biol Chem.* (2011) 286:44926–36. doi: 10.1074/jbc.M111.274779
19. Kojonazarov B, Belenkov A, Shinomiya S, Wilchelm J, Kampschulte M, Mizuno S, et al. Evaluating systolic and diastolic cardiac function in rodents using microscopic computed tomography. *Circ Cardiovasc Imaging.* (2018) 11:e007653. doi: 10.1161/CIRCIMAGING.118.007653
20. Dinkel J, Bartling SH, Kuntz J, Grasruck M, Kopp-Schneider A, Iwasaki M, et al. Intrinsic gating for small-animal computed tomography: a robust ECG-less paradigm for deriving cardiac phase information and functional imaging. *Circ Cardiovasc Imaging.* (2008) 1:235–43. doi: 10.1161/CIRCIMAGING.108.784702
21. Knutsen RH, Gober LM, Sukinik JR, Donahue DR, Kronquist EK, Levin MD, et al. Vascular Casting of Adult and Early Postnatal Mouse Lungs for Micro-CT Imaging. *J Visualized Exp*: JoVE. (2020) 160:61242. doi: 10.3791/61242
22. Roberts JD, Forfia PR. Diagnosis and assessment of pulmonary vascular disease by Doppler echocardiography. *Pulm Circ.* (2011) 1:160–81. doi: 10.4103/2045-8932.83446
23. Levy PT, Patel MD, Groh G, Choudhry S, Murphy J, Holland MR, et al. Pulmonary artery acceleration time provides a reliable estimate of invasive pulmonary hemodynamics in children. *J Am Soc Echocardiogr.* (2016) 29:1056–65. doi: 10.1016/j.echo.2016.08.013
24. Zhang W, Liu J, Yan Q, Liu J, Hong H, Mao L. Computational haemodynamic analysis of left pulmonary artery angulation effects on pulmonary blood flow. *Interact Cardiovasc Thorac Surg.* (2016) 23:519–25. doi: 10.1093/icvts/ivw179
25. Boumpouli M, Danton MHD, Gourlay T, Kazakidi A. Blood flow simulations in the pulmonary bifurcation in relation to adult patients with repaired tetralogy of Fallot. *Med Eng Phys.* (2020) 85:123–38. doi: 10.1016/j.medengphy.2020.09.014
26. Klabunde RE. *Cardiovascular Physiology Concepts: Second edition*. Philadelphia, PA: Lippincott Williams & Wilkins/Wolters Kluwer, (2012).
27. Carta L, Wagenseil JE, Knutsen RH, Mariko B, Faury G, Davis EC, et al. Discrete contributions of elastic fiber components to arterial development and mechanical compliance. *Arterioscler Thromb Vasc Biol.* (2009) 29:2083–9. doi: 10.1161/ATVBAHA.109.193227
28. Jiao Y, Li G, Korneva A, Caulk AW, Qin L, Bersi MR, et al. Deficient circumferential growth is the primary determinant of aortic obstruction attributable to partial elastin deficiency. *Arterioscler Thromb Vasc Biol.* (2017) 37:930–41. doi: 10.1161/ATVBAHA.117.309079
29. Feltes TF, Bacha E, Beekman RH III, Cheatham JP, Feinstein JA, Gomes AS, et al. Indications for cardiac catheterization and intervention in pediatric cardiac disease: a scientific statement from the American heart association. *Circulation.* (2011) 123:2607–52. doi: 10.1161/CIR.0b013e31821b1f10

30. Cunningham JW, McElhinney DB, Gauvreau K, Bergersen L, Lacro RV, Marshall AC, et al. Outcomes after primary transcatheter therapy in infants and young children with severe bilateral peripheral pulmonary artery stenosis. *Circ Cardiovasc Interv.* (2013) 6:460–7. doi: 10.1161/CIRCINTERVENTIONS.112.000061
31. Geggel RL, Gauvreau K, Lock JE. Balloon dilation angioplasty of peripheral pulmonary stenosis associated with Williams syndrome. *Circulation.* (2001) 103:2165–70. doi: 10.1161/01.CIR.103.17.2165
32. Gandy KL, Tweddell JS, Pelech AN. How we approach peripheral pulmonary stenosis in Williams-Beuren syndrome. *Semin Thorac Cardiovasc Surg Pediatr Card Surg Annu.* (2009) 12:118–21. doi: 10.1053/j.pcsu.2009.01.012
33. Shifren A, Durmowicz AG, Knutsen RH, Faury G, Mecham RP. Elastin insufficiency predisposes to elevated pulmonary circulatory pressures through changes in elastic artery structure. *J Appl Physiol.* (2008) 105:1610–9. doi: 10.1152/japplphysiol.90563.2008
34. Faury G, Pezet M, Knutsen RH, Boyle WA, Heximer SP, McLean SE, et al. Developmental adaptation of the mouse cardiovascular system to elastin haploinsufficiency. *J Clin Invest.* (2003) 112:1419–28. doi: 10.1172/JCI19028
35. Rando OJ, Verstrepen KJ. Timescales of genetic and epigenetic inheritance. *Cell.* (2007) 128:655–68. doi: 10.1016/j.cell.2007.01.023
36. McLeod KA, Gerlis LM, Williams GJ. Morphology of the elastic pulmonary arteries in pulmonary hypertension: a quantitative study. *Cardiol Young.* (1999) 9:364–70. doi: 10.1017/S1047951100005151
37. Ivy DD, Neish SR, Knudson OA, Nihill MR, Schaffer MS, Tyson RW, et al. Intravascular ultrasonic characteristics and vasoreactivity of the pulmonary vasculature in children with pulmonary hypertension. *Am J Cardiol.* (1998) 81:740–8.
38. Hilgendorff A, Parai K, Ertsey R, Navarro E, Jain N, Carandang F, et al. Lung matrix and vascular remodeling in mechanically ventilated elastin haploinsufficient newborn mice. *Am J Physiol Lung Cell Mol Physiol.* (2015) 308:L464–78. doi: 10.1152/ajplung.00278.2014
39. Thibault HB, Kurtz B, Raher MJ, Shaik RS, Waxman A, Derumeaux G, et al. Non-invasive assessment of murine pulmonary arterial pressure: validation and application to models of pulmonary hypertension. *Circ Cardiovasc Imaging.* (2010) 3:157–63. doi: 10.1161/CIRCIMAGING.109.887109
40. Dabestani A, Mahan G, Gardin JM, Takenaka K, Burn C, Allfie A, et al. Evaluation of pulmonary artery pressure and resistance by pulsed Doppler echocardiography. *Am J Cardiol.* (1987) 59:662–8. doi: 10.1016/0002-9149(87)91189-1
41. Arkles JS, Opotowsky AR, Ojeda J, Rogers F, Liu T, Prassana V, et al. Shape of the right ventricular Doppler envelope predicts hemodynamics and right heart function in pulmonary hypertension. *Am J Respir Crit Care Med.* (2011) 183:268–76. doi: 10.1164/rccm.201004-0601OC
42. Pangallo E, Cianci P, Favuzza F, Milani D, Vimercati C, Moretti A, et al. Pulmonary function in Williams-Beuren syndrome: spirometric data of 22 Italian patients. *Am J Med Genet A.* (2021) 185:390–6. doi: 10.1002/ajmg.a.61966
43. Wan ES, Pober BR, Washko GR, Raby BA, Silverman EK. Pulmonary function and emphysema in Williams-Beuren syndrome. *Am J Med Genet A.* (2010) 152A:653–6. doi: 10.1002/ajmg.a.33300
44. Shifren A, Durmowicz AG, Knutsen RH, Hirano E, Mecham RP. Elastin protein levels are a vital modifier affecting normal lung development and susceptibility to emphysema. *Am J Physiol Lung Cell Mol Physiol.* (2007) 292:L778–87. doi: 10.1152/ajplung.00352.2006
45. Kronquist EK, Barochia A, Gober LM, Kaur M, Knutsen RH, Levin MD, et al. Baseline pulmonary function in Williams syndrome mimics the effects of mild COPD. Presented at the Annual Meeting of The American Society of Human Genetics; October 27–30 (2020). Virtual Meeting 2020.
46. Wagenseil JE, Knutsen RH Li DY, Mecham RP. Elastin-insufficient mice show normal cardiovascular remodeling in 2K1C hypertension despite higher baseline pressure and unique cardiovascular architecture. *Am J Physiol Heart Circ Physiol.* (2007) 293:H574–82. doi: 10.1152/ajpheart.00205.2007
47. Le VP, Knutsen RH, Mecham RP, Wagenseil JE. Decreased aortic diameter and compliance precedes blood pressure increases in postnatal development of elastin-insufficient mice. *Am J Physiol Heart Circ Physiol.* (2011) 301:H221–9. doi: 10.1152/ajpheart.00119.2011
48. Hawes JZ, Cocciolone AJ, Cui AH, Griffin DB, Staiculescu MC, Mecham RP, et al. Elastin haploinsufficiency in mice has divergent effects on arterial remodeling with aging depending on sex. *Am J Physiol Heart Circ Physiol.* (2020) 319:H1398–H408. doi: 10.1152/ajpheart.00517.2020
49. Parrish PCR, Liu D, Knutsen RH, Billington CJ, Mecham RP, Fu YP, et al. Whole exome sequencing in patients with Williams-Beuren syndrome followed by disease modeling in mice points to four novel pathways that may modify stenosis risk. *Hum Mol Genet.* (2020) 29:2035–50. doi: 10.1093/hmg/ddaa093
50. van den Munckhof I, Scholten R, Cable NT, Hopman MT, Green DJ, Thijssen DH. Impact of age and sex on carotid and peripheral arterial wall thickness in humans. *Acta Physiol (Oxf).* (2012) 206:220–8. doi: 10.1111/j.1748-1716.2012.02457.x
51. Hayashi S, Horie M, Okada Y. Ionic mechanism of minoxidil sulfate-induced shortening of action potential durations in guinea pig ventricular myocytes. *J Pharmacol Exp Ther.* (1993) 265:1527–33.
52. Campese VM. Minoxidil: a review of its pharmacological properties and therapeutic use. *Drugs.* (1981) 22:257–78. doi: 10.2165/00003495-198122040-00001
53. van der Velden J, Borgdorff P, Stienen GJ. Minoxidil-induced cardiac hypertrophy in guinea pigs. *Cell Mol Life Sci.* (1999) 55:788–98. doi: 10.1007/s000180050332
54. Moravec CS, Ruhe T, Cifani JR, Milovanovic M, Khairallah PA. Structural and functional consequences of minoxidil-induced cardiac hypertrophy. *J Pharmacol Exp Ther.* (1994) 269:290–6.
55. Koster JC, Knopp A, Flagg TP, Markova KP, Sha Q, Enkvetchakul D, et al. Tolerance for ATP-insensitive K(ATP) channels in transgenic mice. *Circ Res.* (2001) 89:1022–9. doi: 10.1161/hh2301.100342
56. Flagg TP, Charpentier F, Manning-Fox J, Remedi MS, Enkvetchakul D, Lopatin A, et al. Remodeling of excitation-contraction coupling in transgenic mice expressing ATP-insensitive sarcolemmal KATP channels. *Am J Physiol Heart Circ Physiol.* (2004) 286:H1361–9. doi: 10.1152/ajpheart.00676.2003
57. Levin MD, Singh GK, Zhang HX, Uchida K, Kozel BA, Stein PK, et al. K(ATP) channel gain-of-function leads to increased myocardial L-type Ca(2+) current and contractility in Cantu syndrome. *Proc Natl Acad Sci USA.* (2016) 113:6773–8. doi: 10.1073/pnas.1606465113

Conflict of Interest: The authors declare that the research was conducted in the absence of any commercial or financial relationships that could be construed as a potential conflict of interest.

GLOSSARY

WBS, Williams Beuren syndrome; CT, Computed Tomography; μCT, micro-CT; PA, Pulmonary Artery; RVSPe, Right Ventricular Pressure estimate; RVSP, Right Ventricular Systolic Pressure; SVAS, Supravalvar Aortic Stenosis; TR, Tricuspid Regurgitation; LPA, Left Pulmonary Arteries; MPA, Main Pulmonary trunk Arteries; BM, Body Mass; LV, Left Ventricle/septum; TL, Tibia Length; RVHM, Right Ventricular Heart Mass; LVHM, Left Ventricular Heart Mass; RPA, Right Pulmonary Artery; RVOT, Right Ventricular Outflow Tract; PAAT, Pulmonary Artery Acceleration Time; PW, Pulsed Wave; P, Postnatal; LULFA, Left Upper Lobe Feed Artery; LPLA, Left Pulmonary Lobar Artery; RPLA, Right Pulmonary Lobar Artery; Tx, Treatment; LVESV, Left Ventricular End Systolic Volume; LVEDV, Left Ventricular End Diastolic Volume; LVIDs, Left Ventricular Inner Diameter Systole; LVIDs, Left Ventricular Inner Diameter Diastole; LVAWs, Left Ventricular Anterior Wall Systole; LVAWd, Left Ventricular AnteriorWall Diastole; LVPWs, Left Ventricular Posterior Wall Systole; LVPWd, Left Ventricular Anterior Wall Diastole; IVSs, Intraventricular Septum Systole; IVSd, Intraventricular Septum Diastole; LVM, calculated Left Ventricular Mass; LVMI, calculated Left Ventricular Mass Indexed to body mass; LVEF, Left Ventricular Ejection Fraction; LVFS, Left Ventricular Fractional Shortening; LVOT, Left Ventricular Outflow Tract; RVDP, Right Ventricular Diastolic Pressure; HR, Heart rate; GSAL, Generation-Specific Arcade Length; GSBN, Generation-Specific Branch Number; COPD, Chronic Obstructive Pulmonary Disease, SD, Standard Deviation.

frontiers | Frontiers in Physics

ORIGINAL RESEARCH
published: 13 July 2022
doi: 10.3389/fphy.2022.915644

The Morphological Analysis of the Collagen Fiber Straightness in the Healthy Uninvolved Human Colon Mucosa Away From the Cancer

***Sanja Z. Despotović*[1]* and M. Ćosić*[2]

[1]Faculty of Medicine, Institute of Histology and Embryology, The University of Belgrade, Belgrade, Serbia, [2]Laboratory of Physics, Vinča Institute of Nuclear Sciences—National Institute of The Republic of Serbia, The University of Belgrade, Belgrade, Serbia

The *morphological method*—based on the topology and singularity theory and originally developed for the analysis of the scattering experiments—was extended to be applicable for the analysis of biological data. The usefulness of the topological viewpoint was demonstrated by quantification of the changes in collagen fiber straightness in the human colon mucosa (healthy mucosa, colorectal cancer, and uninvolved mucosa far from cancer). This has been done by modeling the distribution of collagen segment angles by the polymorphic beta-distribution. Its shapes were classified according to the number and type of critical points. We found that biologically relevant shapes could be classified as shapes without any preferable orientation (*i.e.* shapes without local extrema), transitional forms (*i.e.* forms with one broad local maximum), and highly oriented forms (*i.e.* forms with two minima at both ends and one very narrow maximum between them). Thus, changes in the fiber organization were linked to *the metamorphoses* of the beta-distribution forms. The obtained classification was used to define a new, shape-aware/based, measure of the collagen straightness, which revealed a slight and moderate increase of the straightness in mucosa samples taken 20 and 10 cm away from the tumor. The largest increase of collagen straightness was found in samples of cancer tissue. Samples of healthy individuals have a uniform distribution of beta-distribution forms. We found that this distribution has the maximal information entropy. At 20 cm and 10 cm away from cancer, the transition forms redistribute into unoriented and highly oriented forms. Closer to cancer the number of unoriented forms decreases rapidly leaving only highly oriented forms present in the samples of the cancer tissue, whose distribution has minimal information entropy. The polarization of the distribution was followed by a significant increase in the number of quasi-symmetrical forms in samples 20 cm away from cancer which decreases closer to cancer. This work shows that the evolution of the distribution of the beta-distribution forms—an abstract construction of the mind—follows the familiar laws of statistical mechanics. Additionally, the polarization of the beta-distribution forms together with the described change in the number of quasi-symmetrical forms, clearly visible in the parametric space of the beta-distribution and very difficult to notice in the observable space, can be a useful indicator of the early stages in the development of colorectal cancer.

Keywords: morphological analysis, pattern formation, type I collagen, collagen straightness, colorectal cancer

Edited by:
Rajprasad Loganathan,
Johns Hopkins Medicine,
United States

Reviewed by:
Massimiliano Galluzzi,
Shenzhen Institutes of Advanced Technology, (CAS), China
Guang-Kui Xu,
Xi'an Jiaotong University, China

Correspondence:
Sanja Z. Despotović
sanjadesp@gmail.com

Specialty section:
This article was submitted to Biophysics,
a section of the journal
Frontiers in Physics

Received: *08 April 2022*
Accepted: *30 May 2022*
Published: *13 July 2022*

Citation:
Despotović SZ and Ćosić M (2022) The Morphological Analysis of the Collagen Fiber Straightness in the Healthy Uninvolved Human Colon Mucosa Away From the Cancer.
Front. Phys. 10:915644.
doi: 10.3389/fphy.2022.915644

INTRODUCTION

Tumors are no longer considered an isolated population of cancer cells. It is now known that cancer cells widely interact with a surrounding environment and that these interactions are numerous and multidirectional. The cancer cells are interacting with a variety of tissue-resident cells, infiltrating host cells, and extracellular matrix proteins, which all together form the tumor microenvironment. These interactions between cancer cells and all components of the tumor microenvironment are influencing every step of tumor development, progression, and tumor response to different therapy modalities [1,2].

Extracellular matrix (ECM) is a dynamic network comprised of fibrous proteins and ground substance components. The most abundant component of ECM is a network made of collagen fibers, especially collagen type I. Both physical and chemical properties of collagen fibers are sensed by cancer cells and host cells from the tumor microenvironment and converted into downstream cellular responses which influence cell polarization, proliferation, migration, secretion, and survival [3,4]. On the other hand, all cells within the tumor microenvironment (including cancer cells), are involved in collagen fibers remodeling. The profound remodeling of collagen fibers (thus, change in synthesis, degradation, and cross-linking) accompanies all stages of tumor progression [5].

Colorectal cancer (CRC) is the third leading cause of cancer death in the world [6]. Like other solid tumors, CRC is a complex heterocellular system, in which mutated epithelial cells are constantly, from the very beginning, interacting with all components of the tumor microenvironment, including collagen fibers. In CRC, the remodeling of collagen fibers, including increased deposition, cross-linking, alignment, and straightness have been described [7]. The remodeling of collagen fibers, resembling that in cancer, has also been described in the uninvolved human colon mucosa, as far as 10 and 20 cm away from the CRC [8,9].

In the previous work, the identification of straight collagen segments was based on curvelet and Fourier transforms [10,11]. Each identified segment is associated with a phasor of unit length whose phase angle is equal to the angle between the corresponding collagen segment and some predetermined axis. The straightness of collagen fibers was expressed as the length of the phasor sum divided by the number of segments [10,11]. In simpler words, straightness is defined as a fraction of collagen segments sharing the same orientation.

Although straightforward to implement, this approach is unsatisfactory because any permutation of phasors will produce the same sum but will correspond to a completely different organization of collagen fibers. To elucidate further mechanisms of collagen remodeling, with potential application in CRC screening in mind, a new shape-aware method of characterization of collagen fibers is needed.

It can be said that the primary task of any experimentalist is to extract useful information out of the shape of the measured signal. In some cases, like in measuring the length or thickness of individual fiber, this task is straightforward and trivial. However, it can be very difficult when one tries to quantify the organization of the collagen fibers that form tissue. One of the main reasons for this is the large variation of the possible forms, that is, characteristic of any biological data. Because of this, scientists are never truly certain whether their hypothesis is merely a consequence of the statistical fluctuations and noise.

TABLE 1 | Demographic characteristics of patients included in the study.

Patients	Number	Age (years)	Gender	
			Male	Female
Cancer	10	72,5	5	5
Healthy	15	73,2	8	7

The standard approach to overcome this difficulty is to analyze a very large data set, to cover all possible cases. This method was successfully applied on numerous occasions and its validity is guaranteed by the laws of large numbers. However, it is very time-consuming, labor-intensive, and often challenging to implement. Additionally, population sizes of large statistical ensembles in biology and medicine are small compared to the sizes of statistical ensembles used in mathematics and physics, where population sizes of the Monte-Carlo simulations or the number of processed events in the CERN experiments are measured in billions. As a result, the standard approach requires the use of very advanced statistical methods, tailored for moderate sizes of the sample space, which can be also very difficult to implement.

Here we will investigate an alternative approach, inspired by topology and singularity theory. Note that topologists are not focused on one particular object, but on the whole family of objects that can be obtained from the original one by scaling, stretching, twisting, turning, or in general by applying certain kinds of allowed transformations. They group all objects sharing the same topological properties that are invariant on a specified set of transformations, regardless of how pronounced these properties are. In other words, topological classification should be highly immune/resistant to disturbing effects such as noise or statistical fluctuations since the exact shape of the object is not relevant at all.

A similar approach proved its usefulness in the scattering theory where the existence of the rainbow effect forces regular, abrupt metamorphoses (or in this case catastrophic changes [12]) of the angular distribution. The shape analysis was at the core of the newly developed *morphological method* [13], which was being used for the determination of the proton-graphene interaction potential and characterization of graphene samples [13,14].

It will be shown how to use *the morphological method* for the classification of collagen fiber samples that allows easy identification of the changes in its organization. Obtained distribution of shapes will be analyzed from the standpoint of the classical information theory. Determined classification will be used to define a shape-aware measure of the straightness of collagen fibers, which will be used to characterize collagen fibers in the healthy colon, CRC, and uninvolved human colon mucosa 10 and 20 cm away from the CRC. Finally, the obtained result will be compared with the results of previous studies. Although our focus is on collagen straightness, the presented model can be simply extended for the analysis of other collagen parameters such are fiber width, porosity, density, alignment, etc.

THEORETICAL AND EXPERIMENTAL METHODS

Tissue Samples

Tissue samples were obtained during diagnostic colonoscopy at the Department of gastrointestinal endoscopy, University Hospital Center "Dr. Dragiša Mišović-Dedinje", Belgrade, Serbia, as previously described [9]. Briefly, tissue samples from the colorectal carcinoma, and tissue samples from healthy-looking colon mucosa 10 and 20 cm away from the carcinoma in the caudal direction, were obtained from 10 patients (**Table 1**). The diagnosis of colorectal adenocarcinoma was confirmed by an experienced pathologist. For all patients, it was a newly discovered cancer, so they have not received any kind of treatment for the malignant disease before.

Samples of colon mucosa of 15 healthy patients of the corresponding age and gender (**Table 1**) were collected during colonoscopy in the same institution. In this group of patients, colonoscopy was indicated because of weight loss, rectal bleeding, or refractory anemia. Only patients in which colonoscopy didn't show any pathological findings or patients diagnosed with uncomplicated hemorrhoids were included in the study. Patients with inflammatory bowel disease, infections colitis, and diverticular disease of the colon were excluded from the study. Our study was approved by the Ethics Committee of University Hospital Center "Dr. Dragiša Mišović-Dedinje", Belgrade, Serbia (18/10/2017). All methods were carried out in the accordance with relevant guidelines and regulations.

Second-Harmonic Imaging of Collagen Fibers in Colon Tissue Samples

For the second harmonic imaging of collagen fibers in the label-free colon tissue samples, an original lab frame nonlinear laser-scanning microscopy (NLM) was used as previously described in [9,15,16]. In brief, the tunable mode-locked Ti: sapphire laser (Coherent's MIRA900) has been the source of the infrared femtosecond pulses. The laser light was directed onto the sample by a short-pass dichroic mirror (having a cut-off wavelength of 700 nm) and collected by the objective lens (Zeiss's EC Plan-Neofluar 40 × /1.3 NA Oil DIC M27). The laser wavelength was set to 840 nm. The second harmonic generation (SHG) was detected in the back-reflection arm, and recorded by the active-pixel CMOS-sensor camera (Canon, EOS 50D). The narrow bandpass filter at 420 nm (Thorlabs's FB420-10, FWHM 10 nm) blocks the scattered laser light and autofluorescence and passes only the second harmonic at 420 nm. The average laser power on the sample was 30 mW. The pulse duration (160 fs) and repetition rate (76 MHz) sets the peak laser power to be 2.5 kW.

Manual Segmentation of Collagen Fibers

On each SHG image three regions of interest (ROIs) with size 350 × 350 px were cropped. Each ROI was located near crypts and contained collagen fibers. To characterize the straightness of collagen fibers in ROIs, the following method was developed: On each image, the collagen fibers were identified by a histopathologist. Each fiber was additionally split into smaller segments and the relative frequency of its orientation with respect to the positive x-axis ware determined. In the final step, obtained distribution of the orientation angles was fitted by the appropriate statistical model.

Elements of the Singularity Theory

Let us consider a family of continuous, differentiable functions where each member is a map $\mathbb{R}^n \rightarrow \mathbb{R}$, that is parameterized by m continuous parameters. This family can be represented by a single continuous differentiable function

$$F(x_1,\ x_2, \ldots,\ x_n; c_1, c_2, \ldots, c_m), \tag{1}$$

where maps $\mathbb{R}^{n+m} \rightarrow \mathbb{R}$. In the singularity theory variables $x_1, \ldots,\ x_n \in \mathbb{R}$, are called state variables, $c_1, \ldots, c_m \in \mathbb{R}$ system parameters, while numbers n and m are known as corank and codimension, respectively [17]. The critical points of the family are points satisfying the following system of equations

$$\partial_{x_i} F(x_1, \ldots x_n; c_1, \ldots, c_m) = 0,\ \text{for}\ 1 \leq i \leq n, \tag{2}$$

while the degenerate critical points are critical points that additionally satisfy the following equation

$$\det\left[\partial^2_{x_i x_j} F(x_1, \ldots, x_n; c_1, \ldots, c_m)\right] = 0,\ \text{for}\ 1 \leq i,\ j \leq n, \tag{3}$$

here $[\partial^2_{x_i x_j} F]$ stands for the matrix of the second derivatives, i.e., for the Hessian matrix of the function F.

The singularity theory studies the behavior of the function family in the vicinity of its critical points and classifies members of the function family into structurally stable equivalence classes [12,17]. In simple words, the catastrophe theory lists inequivalent ways how a variation of the system parameters changes the number and type of the family member's critical points. The critical values of the parameters, for which redistribution occur, partition the parametric space into equivalence classes according to the number of the critical points the corresponding family members have.

If system dynamics force parameters of a certain family member to cross the boundary of its equivalence class and to enter into a subspace of another equivalence class, then that function undergoes the significant transformation that is called the metamorphose, or in V. I. Arnol'd's term perestroika [17]. Metamorphose is a more general term that includes bifurcations of the degenerate critical points and induction of unrelated isolated singularities.

Elements of the Multivariate Statistics

Let, $\boldsymbol{p}_1 = (x_1, y_1), \ldots, \boldsymbol{p}_N = (x_N, y_N)$ be arbitrary points in the plane. The center of the sampled data points is given by the arithmetic mean

$$\boldsymbol{\mu} = \left(\mu_x, \mu_y\right) = \frac{1}{N}\sum_{i=1}^{N}\boldsymbol{p}_i. \tag{4}$$

The unbiased covariance matrix of the sampled points is a matrix composed of the mean values of the products of marginal deviations of respective data points from its mean values, with Bassel's correction

$$\boldsymbol{\Sigma} = \frac{1}{N-1}\sum_{i=1}^{N}\begin{bmatrix} (x_i - \mu_x)(x_i - \mu_x) & (x_i - \mu_x)(y_i - \mu_y) \\ (y_i - \mu_y)(y_i - \mu_y) & (y_i - \mu_y)(y_i - \mu_y) \end{bmatrix} \tag{5}$$

The characteristic ellipse of the data point distribution is given by the equation

$$(\boldsymbol{p} - \boldsymbol{\mu})^T \cdot \frac{1}{2}\boldsymbol{\Sigma}^{-1} \cdot (\boldsymbol{p} - \boldsymbol{\mu}) = 1. \tag{6}$$

When the distribution of data is bivariate Normal, the characteristic ellipse encloses 63.21% of the data points. In the general case, the percentage of the enclosed data points can be different. Nevertheless, it represents a convenient measure of the spread of the data points.

The Beta-Distribution

The probability density function of the beta-distribution is given by the following expression [18].

$$f(\varphi; \alpha, \beta) = \frac{1}{2\pi B(\alpha, \beta)}\left(\frac{\varphi}{2\pi}\right)^{\alpha-1}\left(1 - \frac{\varphi}{2\pi}\right)^{\beta-1}, \; \alpha, \beta \geq 0. \tag{7}$$

The sample space of the state variable is $\varphi \in [0, 2\pi]$, α and β are shape parameters, while $B(\alpha, \beta)$ stands for the beta-function [19] and represents the normalization factor. The first and the second statistical moments of this distribution are

$$\bar{\varphi} = \int_0^{2\pi} \varphi f(\varphi; \alpha, \beta) \mathrm{d}\varphi = \frac{2\pi\alpha}{\alpha + \beta}; \; \sigma_\varphi^2 = \int_0^{2\pi} \varphi^2 f(\varphi; \alpha, \beta) \mathrm{d}\varphi - \bar{\varphi}^2 = \frac{4\pi^2\alpha\beta}{(\alpha + \beta)^2(\alpha + \beta + 1)}. \tag{8}$$

From the singularity theory perspective, **Eq. 7** defines the corank-one, codimension-two function family with the state variable φ, and parameters α and β which maps $[0, 2\pi] \to \mathbb{R}^+$. It will turn our advantageous to treat the $f(\varphi; \alpha, \beta)$ as a family of plane curves. In that case, the criticality condition simplifies to

$$\partial_\varphi f(\varphi; \alpha, \beta) = 0, \text{ or } \partial_\varphi f(\varphi; \alpha, \beta) = \infty. \tag{9}$$

In other words, critical points of curve f are points where the graph has a vertical or horizontal tangent. To distinguish between them we will call solutions of the equation $\partial_\varphi f = 0$ the *horizontal critical point*, while solutions of the equation $\partial_\varphi f = \infty$ will be called *vertical critical points*. Depending on the sign of the $\partial_\varphi f$ vertical critical point, the function f can be ascending or descending. Horizontal critical points are further classified as minima or maxima.

The partial derivative of the function f can be evaluated analytically and is given by the following expression

$$\partial_\varphi f(\varphi; \alpha, \beta) = \frac{1}{(2\pi)^2 B(\alpha, \beta)}\left(\frac{\varphi}{2\pi}\right)^{\alpha-2}\left(1 - \frac{\varphi}{2\pi}\right)^{\beta-2}\left[(\alpha - 1) - (\alpha + \beta - 2)\frac{\varphi}{2\pi}\right]. \tag{10}$$

Members of the family can have none, one, two, or three critical points. The two out of three possible critical points are the boundary points $\varphi = 0$ and $\varphi = 2\pi$ exist for $\alpha \neq 1$, and $\beta \neq 1$. The third $\varphi = 2\pi(\alpha - 1)/(\alpha + \beta - 2)$ exists only if parameters satisfy the constrains $\alpha \geq 1$, $1 \leq \beta$, $\alpha + \beta > 2$, and $\alpha \leq 1$, $1 \geq \beta$, $\alpha + \beta < 2$. The second partial derivative of the function f

$$\partial_\varphi^2 f(\varphi; \alpha, \beta) = \frac{\left(\frac{\varphi}{2\pi}\right)^{\alpha-3}\left(1 - \frac{\varphi}{2\pi}\right)^{\beta-3}}{(2\pi)^3 B(\alpha, \beta)(\alpha + \beta - 2)^2}\left\{\left[(\alpha - 1) - (\alpha + \beta - 2)\frac{\varphi}{2\pi}\right]^2 - \frac{(\alpha - 1)(\beta - 1)}{\alpha + \beta - 3}\right\}, \tag{11}$$

shows that only boundary points $\varphi = 0$ and $\varphi = 2\pi$ can be double degenerate critical points. In addition, family members can have at most two inflection points, and there can't be degenerate critical points of the higher-order.

RESULTS

When excited by a strong external electric field, the second harmonic generation happens only in materials for which a microscopic polarization field, generated by the local response of the material's microscopic constituents called harmonophores, averaged over all their positions and orientations produces anisotropic macroscopic polarization. In the case of collagen, the second-harmonic response originates in slight charge asymmetry between C=O and N-H groups, acting as a slight electron donor and acceptor, respectively, that favors oscillations of delocalized bond electrons along the collagen's backbone [20,21]. Since second harmonic generation happens coherently, an additional amplification of the effect occurs when all harmonophores are mutually aligned, as is the case for the harmonophores embedded in the rigid and compact collagen triple helix [19,21].

Figure 1 shows second-harmonic generation images of a human colon sample of a healthy mucosa (**Figure 1A**), colon mucosa taken 10 cm away from cancer (**Figure 1B**), and colon cancer sample (**Figure 1C**). In all examined cases, the distribution of the light intensity is dominantly determined by the density of collagen harmonophores coherently excited by the incoming laser beam. All other sources of second-harmonic interfere

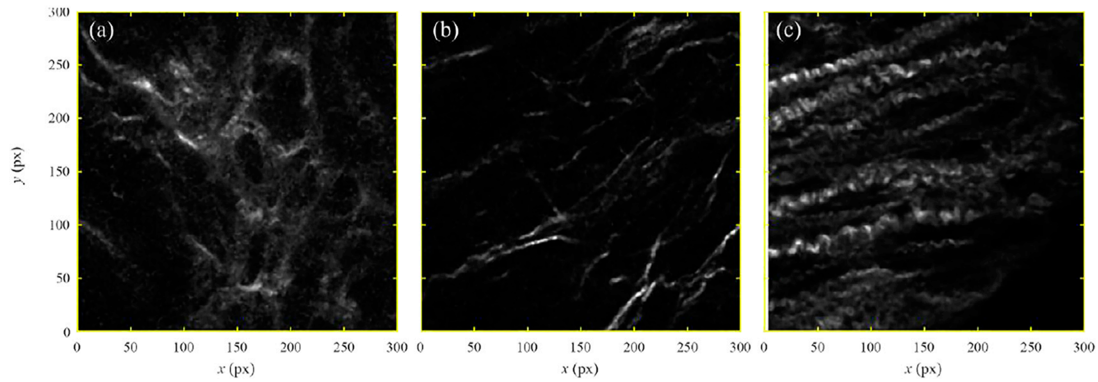

FIGURE 1 | (color online) The enlarged views of the recorded intensity distribution of second-harmonic light of **(A)** a healthy control sample (code name **K54S 5–1**); **(B)** a sample taken 10 cm away from cancer (code name **J10cm 4–2)**; **(C)** sample of cancer tissue (code name **JTU 2–2**).

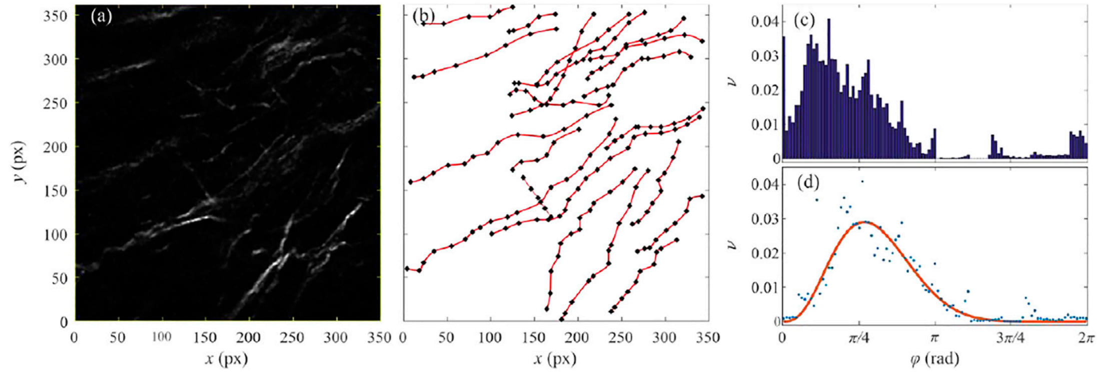

FIGURE 2 | (color online) **(A)** An image of the human colon mucosa 10 cm away from the tumor, code name **J10cm 4-2**, recorded by the non-linear second harmonic microscopy. **(B)** Black squares show the characteristic points of the identified collagen fibers. Red lines represent the cubic-spline fit of the characteristic points. **(C)** A relative frequency of the angles between a small segment of the collagen fiber and *x* axis. **(D)** The red line shows the optimal fit of the relative frequencies (blue points) with the beta-distribution.

destructively, producing small randomly fluctuating components of the measured light intensity. Thus, regions of the high intensity show a projection of the collagen network, located in the volume excited by the laser light, onto the image plane. As we have previously described [9] in the healthy colon mucosa collagen fibers are wavy, thin, and spreading in all directions throughout the lamina propria, around the crypts (**Figure 1A**). In the cancer tissue (**Figure 1C**) collagen fibers are thick and straight. The colon tissue samples 10 cm away from the cancer are somewhere in between, they contain regions resembling a healthy colon, but focally, straight, well-aligned collagen fiber could be observed (**Figure 1B**).

Each recorded image was inspected and collagen fibers were identified by an eye of the experienced histopathologist (Z. Despotović) using judgment, training, and experience. An example of the application of the already described manual segmentation procedure will be shown in the case of the image shown in **Figure 1B**.

Figure 2A shows the selected ROI selected in the second harmonic image of the colon mucosa sample taken 10 cm away from cancer (code name **J10cm 4–2**). The regions of high intensity (sufficiently above the random threshold) were only examined and the *ridge-like* maxima were identified. When there is no overlap between ridges, their route can be identified with the projection of the individual collagen fiber. In the case of the overlap between ridge-maxima, such identification is not unique because of multiple possibilities to connect collagen segments. To resolve the described ambiguity, the principle of the minimal curvature was established which states that correct linkage produces collagen fibers of minimal curvature.

On the backbone of each identified fiber, several control points were selected sufficient for fitting the fiber by a cubic-spline plane curve. Obtained collection of the control points and associated family of plane curves are shown in **Figure 2B** by the black squares and red lines, respectively. In the next step, each collagen fiber was subdivided into a large number of small segments of equal length and the relative frequency of angle φ measuring the angle between each spline segment and the positive x-axis was determined. The adopted resolution of the angular space was set to be 1 deg.

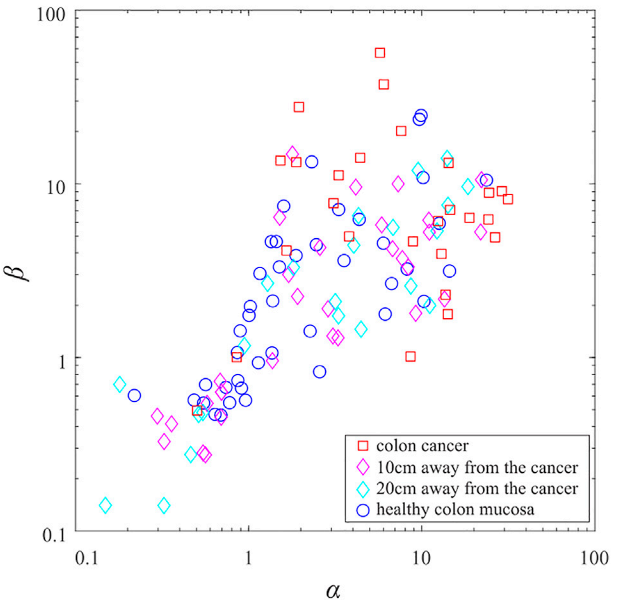

FIGURE 3 | (color online) The scatter plot of beta-distribution parameters. The blue circles correspond to the collagen fibers from the samples of the healthy colon mucosa. The cyan and magenta diamonds correspond to the samples taken 20 and 10 cm from the colorectal adenocarcinoma. The red squares correspond to the collagen fibers from the samples of colorectal cancer tissue.

The resulting distribution is shown in **Figure 2C**. Note that the reference direction for measuring angles was chosen arbitrarily. Any other choice of the reference direction, that is for example at an angle of θ with respect to the positive x-axis, induces the circular shift of the distribution from **Figure 2C** by an angle θ. This means that the domain of the angular variable φ is a circle and not a line. In the final step, obtained histograms were fitted with the beta-distribution given by **Eq. 7**, which is defined on the interval $[0, 2\pi]$. To take into account the periodic boundary conditions of the obtained distributions, the fitting of the beta-distribution was performed for all 360 different values of the circular shift, out of which those values of the beta-function parameters α and β were selected that correspond to the highest value of the goodness of the fit. In the case of the distribution shown in **Figure 2C**, the optimal fit is shown in **Figure 2D**. The optimal value of the circular shift was found to be $\theta = 19.6$ deg, which correspond to the parameters of the beta-distribution $\alpha = 4.15$ and $\beta = 9.57$. The distribution in **Figure 2D** has one large maximum at approximately $\pi/4$, corresponding to the most probable orientation of the collagen fiber segments from **Figure 2B**.

Applying the same procedure to all samples of the collagen fibers gives the distribution of the beta-distribution parameters shown in **Figure 3**. For better clarity, parameters of the beta-distribution are given in the logarithmic scale. Obtained data points occupy the rectangle in the parametric space whose lower left vertex is the coordinate origin, while its upper right vertex is the point ($\alpha = 37.4$, $\beta = 57.0$). The blue circles correspond to the colon mucosa samples in the healthy individuals, red squares correspond to CRC samples, while magenta and cyan diamonds correspond to tissue samples taken 10 cm (magenta) and 20 cm (cyan) away from cancer. The red data points (representing CRC samples) are located in an area far from the coordinate origin. On the contrary, most of the blue data points (healthy colon mucosa) are located in the region near the coordinate origin. The cyan and magenta data points (mucosa 20 and 10 cm away from cancer, respectively) have a wide distribution. Note that the distribution of cyan data points overlaps more with the distribution of the blue data points, while the distribution of magenta data points overlaps more with the distribution of the red data points. It could be said that distributions of cyan and magenta points capture the transition of collagen patterns from the healthy colon mucosa to the collagen patterns corresponding to the CRC. This result was expected and is in good agreement with previous findings [8,9].

DISCUSSION

The Shape Analysis

The straightforward approach for quantification of the fiber straightness would be to use the standard deviation σ_φ of the data from the mean value $\bar{\varphi}$, given in **Eq. 8**. The usefulness of these parameters stems from the fact that they are well-defined quantities that can be calculated for any kind of distribution. However, in this case, their use would be misleading for the following reasons. We have shown that the preferable orientation of the fiber segments corresponds to the maximum of the distribution and not to its mean value. Note that for different values of parameters α and β, beta-function does not necessarily have one maximum. The most important reason is that unlike parameters of the distribution α and β, the statistical moments $\bar{\varphi}$ and σ_φ carry no information about the shape of the distribution. For a completely disordered sample, the distribution of the fiber segments would be uniform. It is easy to show that in that case mean value of the angle segment is $\bar{\varphi} = \pi$, and the standard deviation is $\sigma_\varphi = \sqrt{3}\pi/3$. Obtained values are meaningless indications of the fiber straightness since in the case of the uniform distribution, there is no ordering of the segments at all.

Therefore, we have devised an alternative strategy that takes into account the shape of the beta-distribution. We have performed a detailed inspection of the beta-distribution parametric space to try to classify the corresponding members of the function family given in **Eq. 7** according to the number and type of critical points. **Figure 4** shows obtained partition of the relevant parametric subspace into desired equivalence classes. Note that beta-distribution is invariant to the simultaneous substitution $\alpha \to \beta$ and $\varphi/2\pi \to (1 - \varphi/2\pi)$. Therefore, the shapes of the family members corresponding to points (α, β) and (β, α) are mutually symmetric under the transformation $\varphi/2\pi \to (1 - \varphi/2\pi)$. The line $\alpha = \beta$ represents the bordering line splitting the parametric space into shape equivalent halves. In addition, this line corresponds to the symmetrical beta-distributions where the central critical point is located at the $\varphi = \pi$.

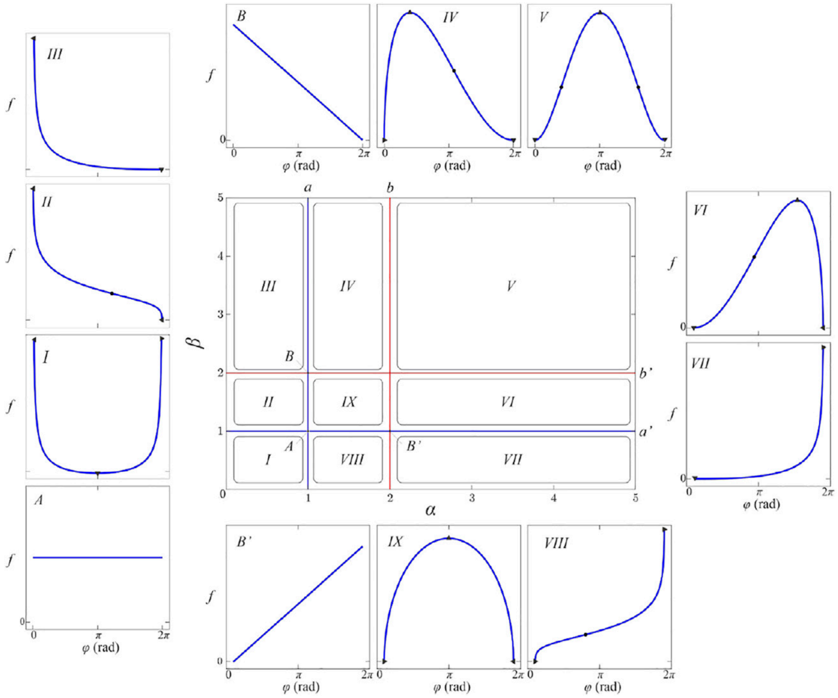

FIGURE 4 | (color online) The shape diagram of the beta-distribution. Insets labeled by Roman numerals *I-IX* show the shape of the beta-distribution for parameters from the corresponding subspaces labeled by the same symbol. The characteristic lines a, a', and b, b' are shown by the blue and red lines, respectively. Points A, B, B', correspond to the parameter values for which function f is proportional to the constant, and linear functions, respectively. Horizontal critical points of the function f were indicated by symbols ▲ and▼, while ascending and descending vertical critical points were denoted by symbols ► and ◄.

Equation 10 shows that for $0 < \alpha < 1$, regardless of the value of the parameter β, family members have descending vertical critical point at $\varphi = 0$, becomes ascending for $1 < \alpha < 2$. For $\alpha > 2$ ascending vertical critical point at $\varphi = 0$ transforms into ascending horizontal critical point. Because of the symmetry, the equivalent conclusion holds for the variation parameter β and boundary critical point at $\varphi = 2\pi$.

Blue lines, labeled as a and a' in **Figure 4**, show the characteristic line $\alpha = 1$, and its symmetrical image $\beta = 1$. In this subspace, beta-distribution is proportional to the simple power function. At their intersection is point $(1, 1)$ labeled A in **Figure 4** which corresponds to the constant function $1/2\pi$. Red lines labeled b and b' in **Figure 4** shows another pair of the mutually symmetric lines $\alpha = 2$, and $\beta = 2$. In the intersection of lines a and b' is the point $(1, 2)$, labeled B in **Figure 4**, for which function f is proportional to the linear function. Points A, B, and B' are the only points in the parametric space free from the critical points.

These four semi-lines divide parametric space into nine rectangular areas labeled $I, II, \ldots, IX$. In the region I function f has a descending vertical critical point at $\varphi = 0$, a horizontal critical point (minimum), and ascending vertical critical point at $\varphi = 2\pi$, while in the region IX ascending vertical critical point at $\varphi = 0$, descending vertical critical point at $\varphi = 2\pi$, and maximum. In region II, function f has two descending vertical critical points at $\varphi = 0$, and $\varphi = 2\pi$, and one inflection point. In the region III, function f has descending vertical critical point at $\varphi = 0$, minimum at $\varphi = 2\pi$, and one inflection point. In the region IV, function f has ascending vertical critical point at $\varphi = 0$, a maximum, and a minimum at $\varphi = 2\pi$, while in region V there are two minima at $\varphi = 0, 2\pi$, one maximum, and two inflection points. The shape of the function f for parameters in regions VI, VII, and $VIII$ is a symmetrical image of its shape for parameters in regions II, III, and IV.

Note that even infinitesimal changes of parameters $(1, 1) \rightarrow (1 + \epsilon,\ 1 + \epsilon)$ that correspond to the transition from the point A to the region IX, induces instantly three critical points at $\varphi = 0, \pi, 2\pi$, that are not formed by the splitting of the degenerate critical point. All other metamorphoses of the beta-distribution behave in the same manner and are of the induction type.

It should be said that singularities of the beta-distribution do not have biological relevance. They are mathematical artifacts of the beta-distribution introduced by our desire for the simplest normalizable polymorphic function family. Singular peaks do not exist in any finite segmentation of fibers, nor in our data. When inspected closely almost all samples whose parameters belong to regions I, II, III, VII, and $VIII$, it is very difficult to spot any particular preferable orientation of the collagen fibers. Therefore, the preferable orientation exists for beta-distribution parameters belonging to the regions IV, V, VI, and IX, where the beta-distribution has a single maximum. A useful measure for the level of the straightness, in this case, would be full-width-at-half-

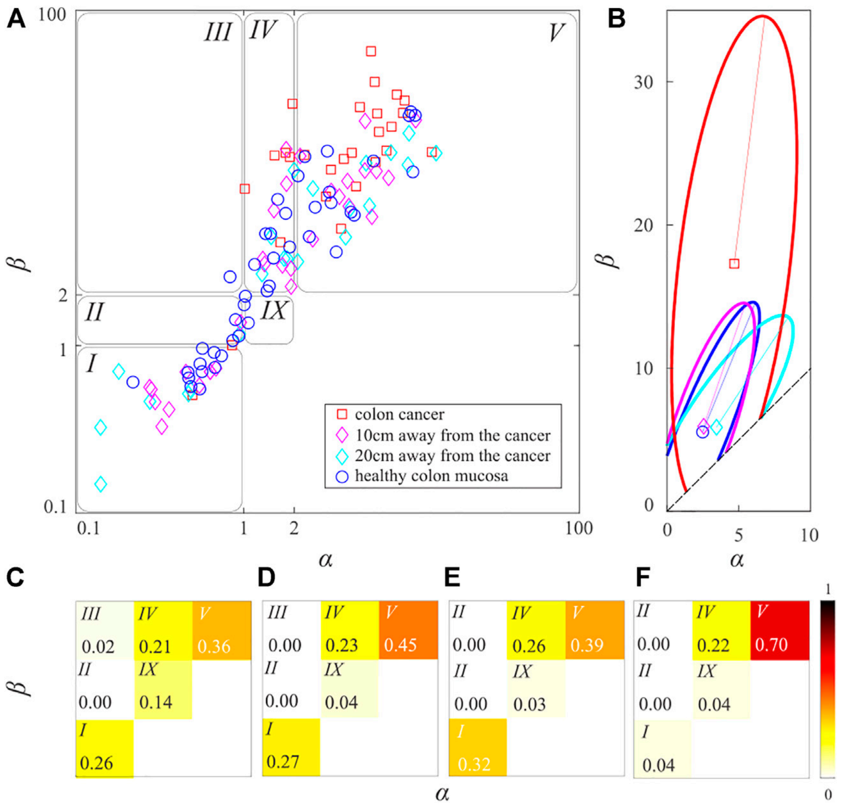

FIGURE 5 | (color online) **(A)** The scatter-plot of the irreducible beta-distribution parameters. **(B)** The characteristic ellipses of the healthy samples, samples were taken 20 and 10 cm from the cancer tissue, and samples of cancer tissue are shown by blue, cyan, magenta, and red lines, respectively. Parts of the curves outside the irreducible sample space were ignored. The shape distribution of **(C)** the healthy samples, **(D)** and **(E)** samples taken 20 and 10 cm far from the cancer tissue, and **(F)** samples of the cancer tissues. The relative frequency of the forms is shown by the different tones of the red color, according to the show colorbar.

maximum (FWHM) which is a well-defined quantity for finite maxima and undefined for the singular maxima of the distribution. The full-width-at-half-maximum is determined by the solutions of the equation

$$\frac{1}{2} f\left(\varphi_m; \alpha, \beta\right) = f\left(\varphi_m + \delta\varphi; \alpha, \beta\right), \tag{12}$$

where $\varphi_m = 2\pi(\alpha - 1)/(\alpha + \beta - 2)$ is a position of the maximum, and $\delta\varphi$ is a deviation from the maximum for which its amplitude reduces by half. This equation has two real solutions $(\delta\varphi)_1$ and $(\delta\varphi)_2$, where it is by convention $(\delta\varphi)_2 \geq (\delta\varphi)_1$. The full-width-at-half-maximum $\Delta\varphi$ of the maximum at φ_m is given by the difference $\Delta\varphi = (\delta\varphi)_2 - (\delta\varphi)_1$. By algebraic transformations, it is possible to transform **Eq. 12** into the following form

$$\frac{1}{2} = \left(1 + \frac{\delta\varphi}{\varphi_m}\right)^{\alpha-1} \left(1 - \frac{\delta\varphi}{2\pi - \varphi_m}\right)^{\beta-1}. \tag{13}$$

that is a transcendental equation without closed-form solutions. However, for small $\delta\varphi$, equivalently for large α and β, FWHM is given by the expression

$$\Delta\varphi = \frac{4\pi\sqrt{(\alpha-1)(\beta-1)\ln 2}}{(\alpha+\beta-2)^{3/2}}. \tag{14}$$

Therefore, for distribution parameters farther from the coordinate origin, the maximum of the distribution becomes narrower.

Note that the parameter $\Delta\varphi$ can have any value from the interval $[0, 2\pi]$. The value $\Delta\varphi = 0$ corresponds to the maximally possible level of straightness where all collagen segments have the same orientation, which is achievable for $\alpha, \beta \to \infty$. Value $\Delta\varphi = 2\pi$ is obtainable for $(\alpha, \beta) = (1, 1)$ and corresponds to no ordering at all since all possible orientation angles are equally represented. Parameter $\Delta\varphi$ correctly quantifies the level of straightness, however, its scale is inverted. Therefore, we will introduce an equivalent more intuitive measure of the straightness labeled s and defined by the following equation

$$s = 1 - \frac{\Delta\varphi}{2\pi}. \tag{15}$$

Parameter s, named self-alignment parameter, depends linearly on $\Delta\varphi$, thus it does not distort information contained in it, while it achieves the desired scale inversion. Thus, $s = 0$ corresponds to no alignment at all, while $s = 1$ corresponds to the maximal level of alignment where all collagen segments are parallel.

Now we will perform the analysis of shapes for the family of beta-distributions shown in **Figure 3**. To analyze only different shapes all data points that are located below the symmetry line $\alpha = \beta$ were substituted by their symmetrical images obtained by the transformation $(\alpha, \beta) \rightarrow (\beta, \alpha)$. **Figure 5A** shows obtained distribution of inequivalent parameters of the beta-distribution. For better visibility parameters of the beta-distribution are again shown in the logarithmic scale.

Centers of the distributions of the blue, cyan, magenta, and red data points are points $\boldsymbol{\mu}_b = (2.47, 5.54)$, $\boldsymbol{\mu}_c = (3.44, 5.87)$, $\boldsymbol{\mu}_m = (2.55, 5.94)$, and $\boldsymbol{\mu}_r = (4.67, 17.30)$, respectively. In the statistics, these points are understood as the most probable parameters of their corresponding beta-distributions. Therefore, we can say that the typical beta-distribution of each class has parameters $\boldsymbol{\mu}_b$, $\boldsymbol{\mu}_c$, $\boldsymbol{\mu}_m$, and $\boldsymbol{\mu}_r$, respectively. They all belong to the region V, where corresponding beta-distributions have one maximum. The respective widths of these maxima are $\Delta\varphi_b = 2.4777$, $\Delta\varphi_c = 2.4716$, $\Delta\varphi_m = 2.3714$, and $\Delta\varphi_r = 1.2709$, while their self-alignment parameters are $s_b = 0.6057$, $s_c = 0.6066$, $s_c = 0.6226$, and $s_r = 0.7977$.

Note that the typical straightness of the cyan data points (mucosa 20 cm away from the CRC) is only 0.16% larger than the typical straightness of the blue data points (healthy mucosa). The typical straightness of the magenta data points (mucosa 10 cm away from the CRC) is larger by 2.80% than the corresponding typical straightness of the healthy colon mucosa, whereas the typical straightness of the red data points (the CRC mucosa) is larger by 31.71%. Examination of their typical representatives implies that the distribution of cyan data points is more similar to the distribution of blue data points, whereas the distribution of magenta data points is more similar to the distribution of red data points. These findings are again in good agreement with previous findings [8,9].

Now we shall compare the sensitivity of the newly introduced procedure for measuring collagen straightness with the standard approach implemented in the software CT-FIRE used in the previous study [9]. Sensitivity of measurement quantifies the ability of the measuring apparatus, or measuring procedure, to amplify the detected signal and produce larger output. In technical terms, sensitivity is defined as a ratio of the output of the measuring apparatus and the corresponding measured input [22]. The direct application of the definition is impossible in this case since the input to both procedures are images of the collagen samples and outputs are numbers obtained by computation. Moreover, the new procedure determines the FWHM of the beta-distribution peak, while the standard measure gives a fraction of fiber segments sharing the common orientation.

However, if the straightness of the healthy samples is taken as a reference point it is possible to compare the relative sensitivities of both procedures since considered collagen samples 10 and 20 cm away from CRC, and healthy controls are the same as in [9]. The procedure which produces a larger relative change in the output has greater sensitivity. To have the test of maximal fairness we shall compare the relative sensitivity of the parameter s with CT-FIRE's straightness parameter because both of them have the same range. Note that the relative sensitivity of the parameter $\Delta\varphi$ is exactly $2\pi/\Delta\varphi_b - 1 \approx 1.54$ times larger.

In the case of the samples of colon mucosa 20 cm away from CRC relative variation of the s parameter is 0.16% while a relative variation of the parameter $\Delta\varphi$ is 0.25%. The corresponding relative variation of the CT-FIRE's straightness parameter was reported to be approximately 0.5% [9]. Thus, its sensitivity is larger than the relative sensitivity of the parameter s, while it is comparable to the relative sensitivity of the parameter $\Delta\varphi$. In the case of samples of colon mucosa 10 cm away from CRC relative variations of parameters s and $\Delta\varphi$ were 2.80% and 4.29%, respectively. Both of them are considerably larger than the relative variation of CT-FIRE's straightness parameter which was reported to be approximately 2% [9]. Therefore, the relative sensitivity of the new procedure is greater than the sensitivity of the standard procedure.

Whenever dealing with average values it is necessary to establish how typical these values are. To do so, we have used mean values $\boldsymbol{\mu}_b$, $\boldsymbol{\mu}_c$, $\boldsymbol{\mu}_m$, and $\boldsymbol{\mu}_r$ to calculate covariance matrices of blue, cyan, magenta, and red data points.

$$\boldsymbol{\Sigma}_b = \begin{bmatrix} \mathbf{7.81} & \mathbf{15.80} \\ \mathbf{15.80} & \mathbf{41.13} \end{bmatrix}, \quad \boldsymbol{\Sigma}_c = \begin{bmatrix} \mathbf{14.20} & \mathbf{17.89} \\ \mathbf{17.89} & \mathbf{30.56} \end{bmatrix}$$

$$\boldsymbol{\Sigma}_m = \begin{bmatrix} \mathbf{6.21} & \mathbf{11.88} \\ \mathbf{11.88} & \mathbf{37.07} \end{bmatrix}, \text{ and } \boldsymbol{\Sigma}_r = \begin{bmatrix} \mathbf{9.47} & \mathbf{16.90} \\ \mathbf{16.90} & \mathbf{149.57} \end{bmatrix},$$

and plotted corresponding blue, cyan, magenta, and red characteristic ellipses in **Figure 5B**. Note that in the definition of the characteristic ellipse it is assumed that sample space is an entire plane. In our case, the irreducible space of the semi-infinite and is bounded by the conditions α, $\beta \geq 0$, and $\beta \geq \alpha$. Therefore, parts of the characteristic ellipses below the lines $\alpha = \beta, \beta = 0$, and to the left of the line $\alpha = 0$ should be ignored.

Interestingly blue, cyan, and magenta ellipses have approximately the same area, while the red ellipse is considerably larger. It has been found that the blue ellipse contains 83.33% of blue data points, the cyan and magenta ellipses contain 72.73% and 90.62% of their respective data points, while the red ellipse encloses 74.07% of the red data points. Therefore, averages $\boldsymbol{\mu}_b$, $\boldsymbol{\mu}_c$, $\boldsymbol{\mu}_m$, and $\boldsymbol{\mu}_r$ are excellent representatives of their respective data. **Figure 5B** also shows the centers of the ellipses (mean values $\boldsymbol{\mu}_b$, $\boldsymbol{\mu}_c$, $\boldsymbol{\mu}_m$, and $\boldsymbol{\mu}_r$ labeled by blue circle, cyan and magenta diamonds, and red square), and lines joining the center ellipse with its vertex corresponding to the major semi-axes of the ellipse. Note that if an angle between the ellipse's major axis and the symmetry line $\alpha = \beta$ is small then the abundance of the quasi-symmetric forms (i.e., forms whose α and β parameters are very close to the symmetry line $\alpha = \beta$, and whose central crytical point is very close to π) is large. It has been found that angles between major semi-axes of the blue, cyan, magenta, and red ellipses and the symmetry axis are: $\theta_b = 67.87°$, $\theta_c = 56.91°$, $\theta_m = 71.22°$, and $\theta_r = 80.75°$, respectively. Moving closer to CRC, the number of the quasi-symmetrical forms increases at first and then starts decreasing steadily. Therefore, the described initial increase of quasi-symmetrical forms can be an indicator of an early stadium of CRC development.

All ellipses cover regions I to IX, however, the distribution of the points inside them is very different. The distribution of beta-distribution forms corresponding to the healthy colon mucosa is shown in **Figure 5C**. Note that forms without preferable direction (whose parameters belong to the regions *I*, to *III*) are almost equally represented as the transitional forms (whose parameters belong to regions IX, and IV), or forms with very pronounced preferable orientation (whose parameters belong to the region V). Distributions of the beta-distribution forms, corresponding to samples of the colon mucosa taken 10 and 20 cm away from the CRC, are shown in **Figures 5D,E**, respectively. In both cases the number of data points in the region IX is negligible (that corresponds to transitional forms of lower straightness). These points are redistributed into regions *I, IV*, and especially region V which corresponds to beta-distributions having very narrow central maximum (or equivalently to collagen samples of very high straightness). In the case of the cancer tissue, parameters of the beta-distribution almost exclusively belong to the highly oriented transitional form IV and highly oriented forms V. According to **Figures 5A,B** the level of the straightness of these forms is considerably larger than the straightness of the forms determined by the distribution of the blue, cyan, or magenta data points.

Collagen fibers are the most abundant component of extracellular matrix. Their biochemical and biomechanical properties influence all crucial processes in the tissues (morphogenesis, angiogenesis, cell's migration, proliferation, differentiation, and polarization) both in the health and disease [23].

It has been shown that cancer can induce changes in both biochemical and biomechanical properties of collagen fibers by different mechanisms: changes in production in enzymes which cross-link collagen fibers, like LOX, changes in synthesis and degradation of collagen fibers (via changes in number and activity of fibroblasts, myofibroblasts, and enzymes responsible from degradation of collagen fibers-matrix metalloproteinases) and by inducing biomechanical changes in the tumor microenvironment [7,9,23,24]. On the other hand, all cells, both cancer cells and host cells from the tumor microenvironment can sense these changes in collagen fibers and respond to them. It has been shown in many types of cancer that changes in collagen synthesis and degradation and collagen fibers remodeling, create a specific tumor microenvironment that promote tumor progression by influencing cell polarity, cell adhesions, and cell migration. In cancer, so-called "linearization" of collagen fibers has been described as an important parameter, with a significant impact of on tumor cell behavior-migration, proliferation and cell differentiation, and thus the ability of tumor cells to locally spread and form distant metastasis [23].

We have shown increase in straightness (increase in strongly oriented forms) in the cancer tissue, but, we have also shown increase in oriented forms in the healthy-looking tissue, far from the cancer. There are at least two explanations why we could expect changes this far from the cancer-systemic effects of tumor and filed carcinogenesis effect. It is known and believed that from the very early stages, tumor cells secrete growth factors, chemokines and cytokines which not only induce changes in the local environment, but acts on distant tissues, so from the very beginning tumors should be considered as a systemic disease [25]. On the other hand, according to field carcinogenesis theory, carcinogens act on the entire length of organ inducing a large altered field-filed of injury, and on this altered filed additional stochastic events could give rise to cancers [26]. Whatever the mechanism behind this changes in collagen fibers straightness is, we wanted a mathematical method that could detect and describe them, not only in cancer tissue, but also far from the cancer. The ability to detect them will be a good starting point in future studies to further characterize changes in collagen fibers, and investigate all the causes and consequences of these changes.

Observed behavior has also a simple interpretation in the terms of classical information theory and statistical mechanics where equal distribution of micro-states is associated with a long-lasting stable state, also known as thermodynamics equilibrium [27–29]. This state is special since for it the information entropy, defined by the weighted sum over the micro-states probabilities $p_i \ (i = 1, \ldots, N)$

$$S = -\sum_{i=1}^{N} p_i \log p_i, \tag{16}$$

is maximal [27–29]. Therefore, it is no surprise that equal distribution of forms corresponding to the blue data appoints is associated with the state of health, and has maximal detected information entropy $S_b = 1.3993$. Closer to the CRC, our data reveal a disturbance of the equilibrium state happening in two stages. In the first stage (at 20 and 10 cm away from the CRC) transitional forms of low straightness disappear producing states of lower entropies $S_c = 1.1796$ and $S_m = 1.1873$, respectively. Note that $S_c < S_m$ because the distribution of cyan data points has a larger number of quasi-symmetrical forms. In the final stage (very close to and in CRC itself) unoriented forms disappear and we are left with the distribution dominated by the highly oriented forms of very large straightness. By definition, this state corresponds to a state very far from the statistical equilibrium and has minimal observed information entropy $S_r = 0.8403$. Thus, observed polarization of the distribution of the beta-distribution forms happening at 10 cm 20 cm away from CRC can be another indicator of the early development of the CRC.

CONCLUSION

Increased straightness of collagen fibers has been detected in many cancers, including CRC [30–32]. It is believed that cancer cells use these linearized collagen fibers as "highways" for migration towards blood and lymphatic vessels [30,31,33].

To enhance our understanding of these processes we have modified *the morphological method* from condensed matter physics to be applicable for modeling biological data. To prove the usefulness of this *topological* viewpoint we have analyzed changes in the straightness of collagen fibers in the colon mucosa caused by the presence of the CRC. This was achieved by modeling the experimentally observed distribution of the collagen segment angles (in healthy colon mucosa, in mucosas taken 10 and 20 cm away from the CRC, and mucosa samples from CRC itself) by the polymorphic beta-distribution depending on two parameters. The parametric space of the beta-distribution was partitioned into subspaces according to the number and type of critical points of the beta-distribution. Each transition between subspaces, called metamorphoses, is abrupt and happens for the infinitesimal change of the critical values of parameters. Therefore, changes in the organization of the collagen fibers and their biological function were linked to the metamorphoses of the beta-distribution shapes. It should be stressed that described correspondence is a general feature of all topological models and it is by no means confined to modeling collagen orientation alone.

To give a biological interpretation of obtained mathematical classification, we have grouped the inequivalent shapes of the beta-distribution into three groups. The first group is formed by shapes without the local maximum, therefore without preferable orientation. The second group is formed by shapes with one less pronounced local maximum and at least one vertical critical point, called the transitional forms. The third group is formed by forms with pronounced local maximum and two inflection points that possess clear preferable orientation.

It has been found that samples of healthy colon mucosa contain an approximately equal amount of unoriented, transitional, and oriented forms of collagen fibers. Observed equal abundance of shapes is in perfect analogy with uniform distribution of microstates of the complex physical system necessary for the establishment of the thermodynamics equilibrium also known as a state of maximal entropy. In samples taken 10 and 20 cm away from CRC, the equilibrium distribution of forms is disturbed by the redistribution of less pronounced transitional forms increasing the fraction of unoriented and highly oriented forms. In the case of the mucosa samples taken from CRC, the distribution of forms is dominated by strongly oriented forms, corresponding to the thermodynamical state of low entropy, far from the equilibrium. We have also noticed the increase in the number of quasi-symmetrical forms in samples 10 cm away from CRC, while its number decreases steadily closer to CRC.

Our findings suggest that the abstract distribution of beta-distribution shapes follows the fundamental law of statistical mechanics, requiring that establishment of the long-lasting equilibrium is inextricably linked to the maximization of entropy. The described polarization of the distribution of beta-distribution forms, together with the evolution of the number of quasi-symmetrical forms can be an indicator of the early stage of CRC development.

We have introduced the shape-aware measure of collagen fiber straightness. The average straightness was measured by the FWHM of the pronounced maximum $\Delta\varphi$ (ranging from 0 up to 2π), which was rescaled to define a more intuitive mutual alignment parameter s ranging from 0 (for uniform distribution of the segment orientations), up to 1 (achievable when all collagen segments are parallel). Compared to the average straightness of collagen fibers in uninvolved colon mucosa, we have detected an increase of 0.16% and 2.80% of the parameter s in colon mucosa 20 cm, and 10 cm away from CRC, generated by the corresponding decrease of $\Delta\varphi$ parameters of 0.25% and 4.29%, respectively. The mutual-alignment parameter s of the CRC samples is larger by 31.71% than the corresponding straightness of fibers in the uninvolved colon mucosa, which corresponds to the variation of the $\Delta\varphi$ parameters of 48.71%.

In the previous work [9] we have used CT-FIRE, an open-source software package [10,11,34] for automatic extraction and analysis of collagen fibers. We have shown a statistically significant increase in collagen fiber straightness in the colon mucosa 10 and 20 cm away from cancer in comparison with collagen fibers in healthy mucosa. Using a novel approach, we have confirmed all findings of the previous study [9]. This study goes one step further by providing explicit criteria for detecting the changes in collagen fiber organization by the shape analysis of the corresponding beta distribution.

It should be said that the presented method is not ideal. Far from CRC relative sensitivity of the newly introduced straightness parameter s is smaller than the relative sensitivity of the straightness parameter given by the CT-FIRE software, while the relative sensitivity of the parameter $\Delta\varphi$ is comparable to it. Closer to CRC relative sensitivity of newly introduced straightness measures becomes superior. This means that the linearity of the parameter s is not uniform in the whole range [22].

There could be two possible explanations for this behavior. Our main goal was to show that *the morphological method* could be applied to a different type of biological data, so that the number of considered samples was relatively small. However, we are quite confident that analysis of the larger sample space will confirm all stated conclusions and improve the sensitivity and linearity of the proposed method. Another weakness was the manual segmentation of collagen fibers because it is time-consuming and subjective. It was done by an experienced histopathologist, but only collagen fibers clearly visible and possible to follow on the examined images were analyzed. So, some fibers from the image were omitted.

In future work, we would like to improve and automatize collagen fibers segmentation and extend the sample size and number of analyzed parameters.

DATA AVAILABILITY STATEMENT

The original contributions presented in the study are included in the article/Supplementary Material, further inquiries can be directed to the corresponding author.

ETHICS STATEMENT

The studies involving human participants were reviewed and approved by Ethics Committee of University Hospital Center "Dr. Dragiša Mišović-Dedinje", Belgrade, Serbia (18/10/2017). The patients/participants provided their written informed consent to participate in this study.

AUTHOR CONTRIBUTIONS

SD and MC contributed to conception and design of the study. SD collected the samples. MC performed the mathematical analysis. SD and MC wrote the manuscript. SD and MC contributed to manuscript revision, read, and approved the submitted version".

FUNDING

The research was funded by the Ministry of Education, Science, and Technological Development of the Republic of Serbia.

REFERENCES

1. Brassart-Pasco S, Brézillon S, Brassart B, Ramont L, Oudart J-B, Monboisse JC. Tumor Microenvironment: Extracellular Matrix Alterations Influence Tumor Progression. *Front Oncol* (2020) 10:397. doi:10.3389/fonc.2020.00397
2. Ming-Zhu J, Wei-Lin J. The Updated Landscape of Tumor Microenvironment and Drug Repurposing. *Sig Transuct Target Ther* (2020) 5:166.
3. Hynes RO. The Extracellular Matrix: Not Just Pretty Fibrils. *Science* (2009) 326:1216–9. doi:10.1126/science.1176009
4. Pickup MW, Mouw JK, Weaver VM. The Extracellular Matrix Modulates the Hallmarks of Cancer. *EMBO Rep* (2014) 15(12):1243–53. doi:10.15252/embr.201439246
5. Xu S, Xu H, Wang W, Li S, Li H, Li T, et al. The Role of Collagen in Cancer: from Bench to Bedside. *J Transl Med* (2019) 17:309. doi:10.1186/s12967-019-2058-1
6. Rawla P, Sunkara T, Barsouk A. Epidemiology of Colorectal Cancer: Incidence, Mortality, Survival, and Risk Factors. *pg* (2019) 14(2):89–103. doi:10.5114/pg.2018.81072
7. Le CC, Bennasroune A, Langlois B, Salesse S, Boulagnon-Rombi C, Morjani H, et al. Functional Interplay between Collagen Network and Cell Behavior within Tumor Microenvironment in Colorectal Cancer. *Front Oncol* (2020) 10:527. doi:10.3389/fonc.2020.00527
8. Despotović SZ, Milićević NM, Milošević DP, Despotović N, Predrag E, Petar S, et al. Remodeling of Extracellular Matrix if the Lamina Propria in the Uninvolved Human Rectal Mucosa 10 Cm and 20 Cm Away from the Malignant Tumor. *Tumour Biol* (2017) 39:1010428317711654. doi:10.1177/1010428317711654
9. Despotović SZ, Milićević ĐN, Krmpot AJ, Pavlović AM, Živanović VD, Krivokapić Z, et al. Altered Organization of Collagen Fibers in the Uninvolved Human colon Mucosa 10 Cm and 20 Cm Away from the Malignant Tumor. *Sci Rep* (2020) 10:6359. doi:10.1038/s41598-020-63368-y
10. Liu Y, Keikhosravi A, Mehta GS, Drifka CR, Eliceiri KW. Methods for Quantifying Fibrillar Collagen Alignment. *Methods Mol Biol* (2017) 1627:429–51. in L. Rittié (ed) Fibrosis(Humana Press, New York). doi:10.1007/978-1-4939-7113-8_28
11. Bredfeldt JS, Liu Y, Conklin MW, Keely PJ, Mackie TR, Eliceiri KW. Automated Quantification of Aligned Collagen for Human Breast Carcinoma Prognosis. *J Pathol Inform* (2014) 5:28. doi:10.4103/2153-3539.139707
12. Arnol'd VI. *Catastrophe Theory*. Springer-Verlag Berlin (2004). the second printing).
13. Ćosić M, Hadžijojić M, Petrović S, Rymzhanov R. Morphological Study of the Rainbow Scattering of Protons by Graphene. *Chaos* (2021) 31:093115. doi:10.1063/5.0059093
14. Hadžijojić M, Ćosić M, Rymzhanov R. Morphological Analysis of the Rainbow Patterns Created by Point Defects of Graphene. *J Phys Chem C* (2021) 125(38):21030. doi:10.1021/acs.jpcc.1c05971
15. Rabasović MD, Pantelić DV, Jelenković BM, Ćurčić SB, Rabasović MS, Vrbica MD, et al. Nonlinear Microscopy of Chitin and Chitinous Structures: a Case Study of Two Cave-Dwelling Insects. *J Biomed Opt* (2015) 20(1):016010.
16. Bukara K, Jovanic S, Drvenica IT, Stancic A, Ilic V, Rabasovic MD, et al. Mapping of Hemoglobin in Erythrocytes and Erythrocyte Ghosts Using Two Photon Excitation Fluorescence Microscopy. *J Biomed Opt* (2017) 22:26003. doi:10.1117/1.JBO.22.2.026003
17. Arnol'd VI. *The Theory of Singularities and its Applications*. Cambridge: PISA (1991).
18. Pearson K. *Tables of the Incomplete Beta-Function*. Cambridge: Cambridge Univ. Press (1932).
19. Abramowitz M, Stegun edt IA. *Handbook of Mathematical Functions, with Formulas, Graphs, and Mathematical Tables*. Washington, DC: National Bureau of Standards (1964).
20. Chen X, Nadiarynkh O, Plotnikov S, Campagnola PJ. Second Harmonic Generation Microscopy for Quantitative Analysis of Collagen Fibrillar Structure. *Nat Protoc* (2012) 7(4):654–69. doi:10.1038/nprot.2012.009
21. Marie-ClaireSchanne-Klein. SHG Imaging of Collagen and Application to Fibrosis Quantization. In: Pavone FS, Capagnola PJ, editors. *Second Harmonic Generation Imaging*. Boca Raton: Taylor & Francis (2014).
22. Usher MJ, Keating DA. *Sensors and Transducers: Characteristics, Applications, Instrumentation, Interfacing*. London: Macmillan Press LTD (1996).
23. Fang M, Yuan J, Peng C, Li Y. Collagen as a Double-Edged Sword in Tumor Progression. *Tumor Biol* (2014) 35:2871–82. doi:10.1007/s13277-013-1511-7
24. Sheieh AC. Biomechanical Forces Shape the Tumor Microenvironment. *Ann Biomed Eng* (2011) 39:1379–89. doi:10.1007/s10439-011-0252-2
25. McAllister SS, Weinberg RA. The Tumour-Induced Systemic Environment as a Critical Regulator of Cancer Progression and Metastasis. *Nat Cel Biol* (2014) 16:717–27. doi:10.1038/ncb3015
26. Backman V, Roy HK. Advances in Biophotonics Detection of Field Carcinogenesis for Colon Cancer Risk Stratification. *J Cancer* (2013) 4: 251–61. doi:10.7150/jca.5838
27. Kullback S. *Information Theory And Statistics*. Dover Publications (1978).
28. Jaynes ET. Information Theory and Statistical Mechanics. *Phys Rev B* (1957) 106:4. doi:10.1103/physrev.106.620
29. Landau LD, Lifshitz EM. *Course of Theoretical Physics: Statistical Physics*, 5. Oxford: Pergamon Press (1980).
30. Ouallette JN, Drifka CR, Pointer KB, Liu Y, Tyler JL, Kao WJ, et al. Navigation the Collagen Jungle: The Biomedical Potential of Fiber Organization in Cancer. *Bioengineering (Basel)* (2021) 8:17. doi:10.3390/bioengineering8020017
31. Provenzano PP, Eliceiri KW, Campbell JM, Inman DR, White JG, Keely PJ. Collagen Reorganization at the Tumor-Stromal Interface Facilitates Local Invasion. *BMC Med* (2006) 4:38. doi:10.1186/1741-7015-4-38
32. Nebuloni M, Albarello L, Andolfo A, Magagnotti C, Genovese L, Locatelli I, et al. Insight on Colorectal Carcinoma Infiltration by Studying Perilesional Extracellular Matrix. *Sci Rep* (2016) 6:22522. doi:10.1038/srep22522
33. Provenzano PP, Inman DR, Eliceiri KW, Trier SM, Keely PJ. Contact Guidance Mediated Three-Dimensional Cell Migration Is Regulated by Rho/ROCK-dependent Matrix Reorganization. *Biophysical J* (2008) 95:5374–84. doi:10.1529/biophysj.108.133116
34. Bredfeldt JS, Liu Y, Liu Y, Conklin CAMW, Szulczewski JM, Inman DR, et al. Computational Segmentation of Collagen Fibers from Second-Harmonic Generation Images of Breast Cancer. *J Biomed Opt* (2014) 19:016007. doi:10.1117/1.jbo.19.1.016007

Conflict of Interest: The authors declare that the research was conducted in the absence of any commercial or financial relationships that could be construed as a potential conflict of interest.

frontiers | Frontiers in Bioengineering and Biotechnology

ORIGINAL RESEARCH
published: 19 July 2022
doi: 10.3389/fbioe.2022.907611

Force-Bioreactor for Assessing Pharmacological Therapies for Mechanobiological Targets

Austin J. Scholp[1], *Jordan Jensen*[1], *Sathivel Chinnathambi*[1], *Keerthi Atluri*[2], *Alyssa Mendenhall*[1], *Timothy Fowler*[3], *Aliasger K. Salem*[2], *James A. Martin*[3] *and Edward A. Sander*[1,3]*

[1]*Roy J. Carver Department of Biomedical Engineering, College of Engineering, University of Iowa, Iowa City, IA, United States,* [2]*Division of Pharmaceutics and Translational Therapeutics, College of Pharmacy, University of Iowa, Iowa City, IA, United States,* [3]*Department of Orthopedics and Rehabilitation, Carver College of Medicine, University of Iowa, Iowa City, IA, United States*

Tissue fibrosis is a major health issue that impacts millions of people and is costly to treat. However, few effective anti-fibrotic treatments are available. Due to their central role in fibrotic tissue deposition, fibroblasts and myofibroblasts are the target of many therapeutic strategies centered primarily on either inducing apoptosis or blocking mechanical or biochemical stimulation that leads to excessive collagen production. Part of the development of these drugs for clinical use involves *in vitro* prescreening. 2D screens, however, are not ideal for discovering mechanobiologically significant compounds that impact functions like force generation and other cell activities related to tissue remodeling that are highly dependent on the conditions of the microenvironment. Thus, higher fidelity models are needed to better simulate *in vivo* conditions and relate drug activity to quantifiable functional outcomes. To provide guidance on effective drug dosing strategies for mechanoresponsive drugs, we describe a custom force-bioreactor that uses a fibroblast-seeded fibrin gels as a relatively simple mimic of the provisional matrix of a healing wound. As cells generate traction forces, the volume of the gel reduces, and a calibrated and embedded Nitinol wire deflects in proportion to the generated forces over the course of 6 days while overhead images of the gel are acquired hourly. This system is a useful *in vitro* tool for quantifying myofibroblast dose-dependent responses to candidate biomolecules, such as blebbistatin. Administration of 50 μM blebbistatin reliably reduced fibroblast force generation approximately 40% and lasted at least 40 h, which in turn resulted in qualitatively less collagen production as determined via fluorescent labeling of collagen.

OPEN ACCESS

Edited by:
Eileen Gentleman,
King's College London,
United Kingdom

Reviewed by:
Jeff Wolchok,
University of Arkansas, United States
Lauren Deems Black,
Tufts University, United States

***Correspondence:**
Edward A. Sander
edward-sander@uiowa.edu

Specialty section:
This article was submitted to Biomechanics, a section of the journal Frontiers in Bioengineering and Biotechnology

Received: *29 March 2022*
Accepted: *14 June 2022*
Published: *19 July 2022*

Citation:
Scholp AJ, Jensen J, Chinnathambi S, Atluri K, Mendenhall A, Fowler T, Salem AK, Martin JA and Sander EA (2022) Force-Bioreactor for Assessing Pharmacological Therapies for Mechanobiological Targets. Front. Bioeng. Biotechnol. 10:907611. doi: 10.3389/fbioe.2022.907611

Keywords: blebbistatin, collagen, fibrin, fibroblasts, fibrosis

INTRODUCTION

Tissue fibrosis is a major health issue that impacts millions of people and is costly to treat. It is estimated that fibrotic disorders contribute to 45% of deaths in the United States (Wynn, 2004). For example, idiopathic pulmonary fibrosis alone has a mortality rate of approximately 19 in every 100,000 people (Dove et al., 2019), with an estimated annual cost of about $20,000 per patient (Diamantopoulos et al., 2018). Increased tissue stiffness is also associated with cancer (Barton et al., 1999) and cardiovascular disease (Sidney et al., 2016), the top two leading causes of death in the

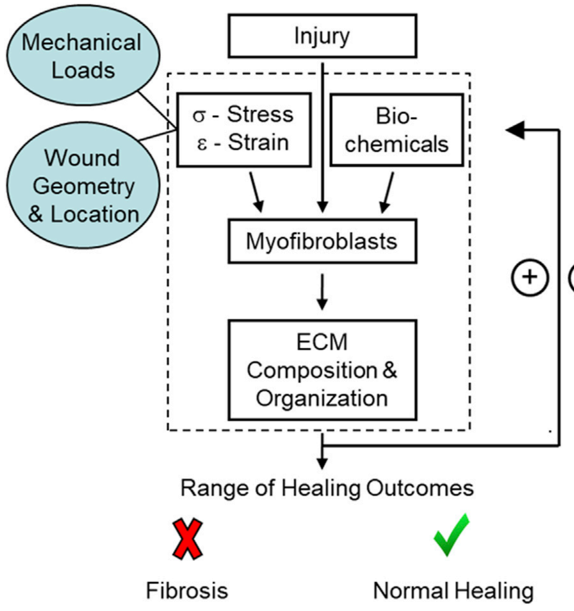

FIGURE 1 | Schematic of the mechano-chemical feedback loop present during healing. Initial conditions at the site of injury, such as the location, mechanical loads, and wound geometry, can affect myofibroblast differentiation and, in turn, healing outcomes.

United States (Lampi & Reinhart-King, 2018). Fibrosis can also occur following trauma to diarthrodial joints, such as the knee or elbow, which can lead to a reduced range of motion (Evans et al., 2009). Between 3% and 10% of patients who undergo total knee arthroplasty (Abdul et al., 2015) and about 8% of patients that receive surgical treatment of the elbow for trauma develop arthrofibrosis (Wessel et al., 2019). Despite the high prevalence of fibrosis and a broad understanding of injury-induced fibrogenesis, few effective anti-fibrotic treatments are available.

A common feature of fibrotic tissue is the chronic presence of activated myofibroblasts (Hinz et al., 2007, Hinz et al., 2012; Wynn, 2008; Klingberg et al., 2013). Myofibroblasts are a fibroblast phenotype often distinguished by the expression of alpha smooth muscle actin (α-SMA) in the cytoskeleton and their ability to generate large traction forces and deposit extracellular matrix (ECM) proteins such as collagen (Unterhauser et al., 2004). These cells are also highly responsive to their mechanical environment and the presence of biochemical factors, such as transforming growth factor beta (TGF-β1). Changes in the local mechanical environment are sensed primarily through focal adhesions and the auxiliary proteins that connect the actin cytoskeleton to the surrounding ECM (Geiger et al., 2009). These proteins can activate multiple signaling pathways, such as Rho/ROCK (Geiger & Bershadsky, 2002), Hippo (Ibar et al., 2018), ERK (Matsumoto et al., 2011), and YAP/TAZ (Dupont et al., 2011), which facilitate and reinforce actomyosin contractility, the transmission of force between the cell and the ECM, and the increased synthesis and deposition of collagen and other ECM proteins that further stiffen the tissue locally (Bolós et al., 2010; Guan, 2010). These processes, combined with biochemical signaling, stimulate and enhance a dynamic mechano-chemical feedback loop that can either resolve normally or lead to tissue dysfunction and disease (**Figure 1**).

Due to their central role in fibrotic tissue deposition, fibroblasts, and myofibroblasts have been the target of many therapeutic strategies centered primarily on either inducing apoptosis or blocking mechanical or biochemical stimulation. For example, Pirfenidone and Nintedanib are small-molecule drugs approved by the FDA for use in treating idiopathic lung fibrosis (Selvaggio & Noble, 2016). Pirfenidone acts by inhibiting TGF-β1 signaling and Nintedanib acts by inhibiting tyrosine kinase receptors for vascular endothelial growth factor (VEGF), fibroblast growth factor (FGF), and platelet-derived growth factor (PDGF) (Lampi & Reinhart-King, 2018). Rapamycin and sirolimus are also FDA-approved drugs that inhibit the kinase mTOR. Rapamycin also hinders macrophage and myofibroblast activation and TGF-β1 release in chronic kidney disease (CKD) (G. Chen et al., 2012; Tulek et al., 2011). The anti-inflammatory drug, sulfasalazine, promotes myofibroblast apoptosis by inhibiting κβ kinase and has been shown to reduce joint stiffness in a leporine model of arthrofibrosis (Atluri et al., 2020a). Additionally, small-molecule inhibition of focal adhesion kinase (FAK) can reduce scar formation in an *in vivo* murine model, thus indicating the potential for small-molecules to block mechanical signaling and reduce fibrosis at the level of the focal adhesion (Wong et al., 2011).

Part of the development of these drugs for clinical use involves *in vitro* prescreening. Typically, prescreening is done using simple high throughput assays on a cell monolayer (Astashkina et al., 2012). Although these assays can yield valuable information, such as drug effects on cell viability, proliferation, and metabolic function, the 2D testing environment is different from the 3D *in vivo* microenvironment, which can substantially impact cell behavior, function, and drug responsiveness (Fernandes & Vanbever, 2009). Crucially, these 2D screens are not ideal for discovering mechanobiologically significant compounds that impact functions like force generation, as force generation and other cell activities are highly dependent on the conditions of the microenvironment. Thus, higher fidelity models are needed to better simulate *in vivo* conditions and relate drug activity to quantifiable functional outcomes.

3D hydrogels can improve drug screening because they better mimic aspects of the tissue's mechanical and compositional environment. Collagen and fibrin gels are popular choices in this regard because collagen is the most abundant protein in soft tissue matrix and fibrin is the primary structural component of the provisional matrix of a clot (Tuan et al., 1996; Grinnell, 2000). For example, (Saito et al., 2012; Mastikhina et al., 2020) used collagen gels to test the effects of Pirfenidone on gel contraction. They found that Pirfenidone significantly reduced gel contraction in a dose-dependent manner. Along similar lines, Asmani et al. (2019) used a custom micropillar membrane-stretching system to examine how Nintedanib and Pirfenidone affect the response of lung fibroblasts under cyclic strain. Both drugs were shown to decrease forces generated by the fibroblasts.

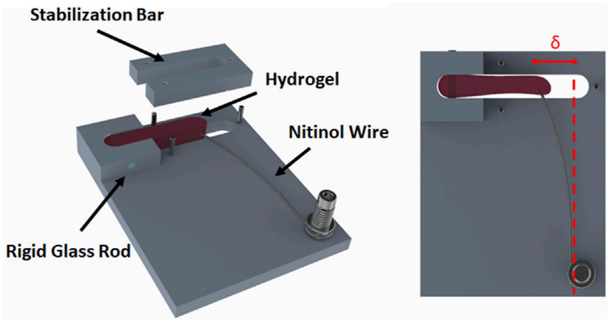

FIGURE 2 | Schematic of the force-bioreactor. A cell seeded fibrin gel (i.e., hydrogel) is polymerized in the cavity containing a rigid glass rod and a bendable Nitinol wire. The stabilization bar is only present during initial gel polymerization. Once polymerized, the stabilization bar is removed, and the hydrogel is free to contract. Force is determined by the amount of deflection (δ) the contracted gel produces in a calibrated wire.

We also have been investigating the therapeutic potential of different compounds to control the mechanobiology of myofibroblast activity, specifically in the context of fibrosis and contracture in injured joints (Atluri et al., 2016). In particular, we have been exploring the potential of blebbistatin for treating joint capsule fibrosis (Atluri et al., 2020b). Blebbistatin is a small, membrane-permeable biomolecule that reversibly inhibits non-muscle myosin II (NMMII) in a dose-dependent manner (Cheung et al., 2001; Straight et al., 2003; Kovács et al., 2004; Limouze et al., 2004; Allingham et al., 2005; Eddinger et al., 2007; Farman et al., 2008). This molecule limits the ability of the myosin head to discharge bound ADP, which prevents continuation of the power stroke and the generation of traction forces through the actin cytoskeleton. This process also interferes with mechanosensing and has the potential to interrupt the proposed mechanochemical feedback loop that contributes to tissue fibrosis (Atluri et al., 2020b). To provide some guidance on drug dosing strategies for blebbistatin and other drugs in our animal models, we are using fibroblast-seeded fibrin gels as a relatively simple mimic of the provisional matrix of a healing wound. These gels are maintained within a custom-built force-bioreactor that allows us to measure relationships between drug concentration, drug carrier composition, force generation, and downstream collagen production. In the bioreactor, fibroblasts are suspended homogeneously within a fibrin gel. The cells generate traction forces that reduce gel volume and deflect an embedded cantilever wire in proportion to the force generated. The force-bioreactor is coupled with a microcontroller-based imaging system that enables hourly imaging of multiple samples over extended periods of time. This system is a useful *in vitro* tool for quantifying myofibroblast dose-dependent responses to candidate biomolecules.

MATERIALS AND METHODS

Cell Culture

Rabbit joint capsule fibroblasts (RJCFs), obtained from ATCC (HIG-82/CRL-1832), were cultured in Dulbecco's modified Eagle medium (DMEM; Life Technologies Corporation, Grand Island, NY), supplemented with 10% fetal bovine serum (FBS; Life Technologies Corporation, Grand Island, NY), 0.1% amphotericin B (Life Technologies Corporation, Grand Island, NY) and 1% penicillin/streptomycin (Life Technologies Corporation, Grand Island, NY) in a humidified incubator at 37°C and 5% CO_2.

Force-Bioreactor

Six force-bioreactors (**Figure 2**) were machined from 3/8″ Teflon bar stock on a Haas TM-1 CNC mill. The bioreactor body has a 1–5/8″ by 1/4″ by 3/8″ rectangular cavity with a rigid 1.5 mm diameter glass rod and a bendable 0.008″ diameter Nitinol wire (Cat. # WSE000800000SG, Confluent Medical Technologies, Scottsdale, AZ) on either end. The base of a Nitinol (NiTi) wire was clamped to the device between two stainless steel washers and a 0.500″ long, 0.18″ OD, 0.144″ ID corrosion-resistant compression spring (Cat. # 9002T15, McMaster-Carr, Elmhurst, IL). The wire, spring, and washers were compressed with a 4–40 × 1/2″ stainless steel screw that threads into the Teflon base. The glass rod serves as a rigid constraint embedded within the polymerized fibrin gel and the wire acts as a cantilever. The top segment of the bioreactor, also referred to as the stabilization bar, is used to control the casting volume of the fibrin gel until it polymerizes. This was mated to the body with three 1/16″ stainless steel dowel pins. An additional 10 mm thick piece of polysulfone was machined to the diameter of the dish with a cutout for the bioreactor to reduce the volume of medium required to cover the gel. A schematic and parts list for the bioreactor can be found in the **Supplementary Materials**.

Nitinol Wire Calibration

Each NiTi wire was gripped at its base in a tensile testing machine (TMI Model 84-01) and incrementally displaced downward (**Figure 3**). The free end of the wire deflected against a Teflon block positioned on an analytical balance (Mettler-Toledo, Columbus, OH). The length of the wire between the grip and the block was set equal to the length of the wire used for the device. At each increment of displacement, the mass displayed on the balance was recorded and converted to force. These data were used to create a calibration curve from linear regression of the measurements from three wires. The resulting equation is $F = 0.1468\,mN/mm \times \delta$, where F is the force in mN and δ is the deflection in mm.

Cantilever Bioreactor Sterilization

The bioreactor components were placed in a 2% Alconox solution (Alconox, White Plains, NY) and sonicated for 1 h at 60°C. The components were thoroughly rinsed in deionized water and submerged in 70% ethanol overnight. Each piece was placed on a sterile drape within a biosafety cabinet and exposed to UV light for 30 min per side. The Teflon components and a disposable tissue culture dish (Falcon, 100 × 20 mm) were then soaked in a 2% Pluronic F-127 solution (Sigma, St. Louis, MO) for 2 h and allowed to dry for another 2 h. The device was then assembled under sterile conditions and was sealed to the dish using a sterile silicone-based grease (Dow Corning High Vacuum Silicon Grease).

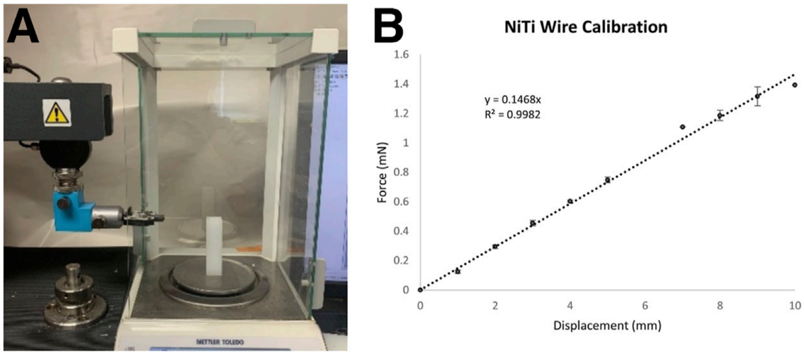

FIGURE 3 | (A) The tensile testing system and analytical balance used to generate force-deflection curves for each Nitinol wire. **(B)** A calibration curve generated from the average response of three Nitinol wires.

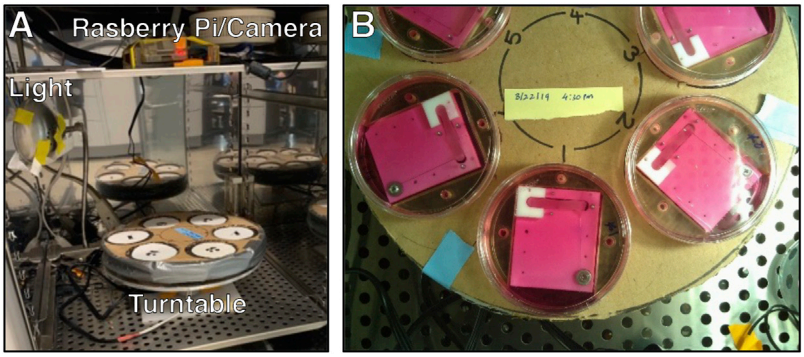

FIGURE 4 | (A) The bioreactor turntable and imaging system inside a dedicated incubator. **(B)** View of the turntable from the Raspberry Pi camera.

Fibrin Gel Polymerization

RJCFs were embedded in fibrin gels at a cell density of 1 million cells/ml. Gels were produced as described previously (Sander et al., 2011; El-Hattab et al., 2020) by combining cells with dissolved fibrinogen (F-8630, Sigma, St. Louis, MO), 20 mM HEPES buffered saline (H-0887, Sigma, St. Louis, MO), calcium chloride (Avantor, Center Valley, PA), and dissolved thrombin (T-4648, Sigma, St. Louis, MO). 2 ml of this solution were then added to the cavities of each bioreactor and allowed to polymerize at room temperature for 10 min before being transferred to the incubator for an additional 30 min of polymerization. After polymerization, the U-shaped stabilization bar was carefully removed, the gel was gently released from the side walls, and 25 ml of DMEM supplemented with 1 ng/ml of TGF-β1(PeproTech, Inc., Cranbury, NJ) and 50 μg/ml of ascorbic acid was added to the culture dishes. The bioreactors were maintained for up to 6 days. No media changes were made to prevent disruption of the gel-wire configuration during imaging.

Imaging and Quantification of Force Production

A Raspberry Pi, camera module (V2: 8 Megapixel, 1080p), and relay-triggered light source were used to acquire overhead images of the bioreactors inside the incubator (**Figure 4**). Six complete bioreactor assemblies were placed on a custom-built turntable that completed one revolution hourly. Images were acquired every 10 min so that an image of each bioreactor was acquired every hour. After image acquisition, NiTi wire deflection was quantified using a custom MATLAB program and converted to force using the calibration curve. Code for the imaging system can be found in the **Supplementary Materials**.

Confocal Imaging of Collagen Content

After the experiment, the gels were removed from the system and placed in a 6-well plate. Cells and collagen were labeled, respectively, using wheat-germ agglutinin conjugated with Alexa Fluor 647 and collagen-binding adhesion protein 35 (CNA35, a kind gift from Magnus Hooke, Texas A&M Health) conjugated with Alexa Fluor 488. Using a Nikon A1 confocal microscope (Nikon Instruments Inc., Melville, NY), representative z-stack images were taken and converted into a 3-D rendering.

Experimental Conditions

The normal contractile behavior of the myofibroblasts in the system was quantified and compared to the response of the

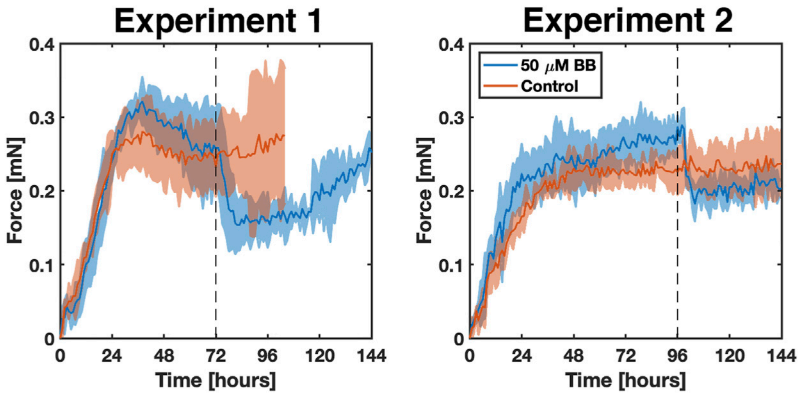

FIGURE 5 | Two experiments comparing the response and reproducibility of the bioreactor systems over 6 days in the presence (blue) and absence (red) of blebbistatin. Solid lines indicate the average of $n = 3$ replicates. The shaded areas correspond to the standard deviation. The grey dotted line marks the time at which 50 µm blebbistatin in 0.1% DMSO was added to the samples.

system to the addition of 50 µM blebbistatin (ab120425, Abcam, Waltham, MA) in 0.1% dimethyl sulfoxide (DMSO). Three samples for each condition were tested (*i.e.*, $n = 3$ control and $n = 3$ blebbistatin). Two separate experiments (also with n = 3 per group) were performed that differed in when the drug was added (*i.e.*, 72 or 96 h after the start of the experiment). Thus, the total number of samples was $n = 12$.

Statistical Analysis

Statistical analysis was carried out using GraphPad Prism version 9.31 (GraphPad, San Diego, CA). Paired t-tests were conducted to assess significance ($p < 0.05$) for differences in force before and after treatment. Unpaired t-tests were conducted to assess significant differences between treatment groups and controls.

RESULTS AND DISCUSSION

During 6 days of culture, untreated fibrin gels (*i.e.*, control) rapidly densified and decreased in length and volume from cell-generated traction forces, which were measured from the deflection of the embedded NiTi wires (**Figure 5**, **Supplementary Movie S1**). Treated gels followed the same trajectory but relaxed nearly instantly once blebbistatin was administered (**Figure 5**, **Supplementary Movie S2**). In the first experiment, the average rate of force increase in both control and treated gels remained nearly constant over the first 26 h at 0.010 mN/h. The control gels then reached an average steady-state force of 0.257 ± 0.012 mN for the remainder of the experiment. Starting around day four, gel compaction and thinning around the wire concentrated the stress such that the gel tore from the embedded wire. The treated gels reached a higher average force of 0.285 ± 0.021 mN between 26 and 72 h. At 72 h, when 50 µM blebbistatin in 0.1% DMSO was added, the average force rapidly decreased 40% from 0.257 ± 0.055 mN to a minimum of 0.154 ± 0.035 mN in 10 h ($p = 0.0199$). After approximately 40 additional hours, the force began to increase again.

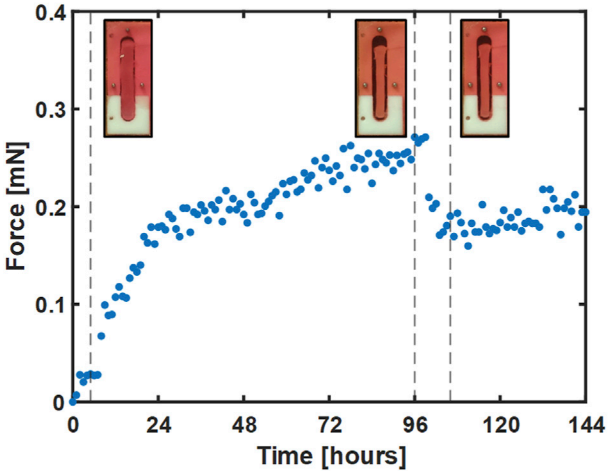

FIGURE 6 | A representative plot of the force response for a single gel treated with blebbistatin at 96 h. Images of gel deflection correspond to 5, 96, and 105 h and are marked with dotted lines.

A second set of experiments was conducted with two changes. First, to help address the issue of gel failure that occurred in the control gels in the first set of experiments, the surface area of each wire was increased by a factor of 8.5 by gluing a short segment (~5 mm) of a mylar wrapped hematocrit tube (OD ~ 1.7 mm) to each wire end. In addition, the pre-treatment period was extended by 24 h to help ensure that the gels had reached a steady-state level of tension. Consequently, 50 µM blebbistatin in 0.1% DMSO was added at 96 h to the treatment group. An example gel from this group is shown in **Figure 6**, where select images of the gel in the bioreactor accompany key parts of the force curve.

Compared to the first experiment, the average rate of force increase was slightly lower over the first 26 h at 0.009 mN/h and 0.007 mN/h for the treated and control gels, respectively. Average

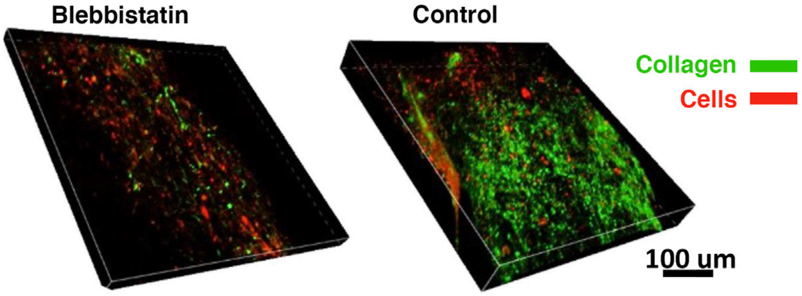

FIGURE 7 | Differences in collagen synthesis visualized on day 6. Collagen deposition (green) and cells (red) depicted in the confocal volume rendering for blebbistatin and control (i.e., no treatment), respectively.

forces between 27 and 96 h were also a little lower at 0.249 ± 0.018 mN and 0.220 ± 0.014 mN for treated and control gels, respectively. As before, administration of blebbistatin significantly reduced average gel force 37% from an average peak of 0.289 ± 0.022 mN at 98 h to 0.182 ± 0.024 mN at 104 h ($p = 0.0389$). Average gel force remained low for the remaining 48 h of the experiment, with signs of a slow increase in force beginning to develop near the conclusion of the experiment.

Taken together, our experiments show that administration of 50 μM blebbistatin in 0.1% DMSO reduced cell-generated tension within the gel by approximately 40% with effects that lasted at least 40 h. Small differences between the two independent sets of experiments were not significant and were likely due to the normal biological variation inherent in cell culture experiments.

To determine whether the decrease in gel force observed also impacted collagen production, both treated and control gels were also labeled with CNA35 (**Figure 7**). Qualitatively, less CNA35 labeling was observed in blebbistatin treated gels compared to controls, suggesting that collagen production was lower.

Several groups have used similar techniques to measure cell force generation within hydrogels (Kolodney & Wysolmerski, 1992; Eastwood et al., 1994; Freyman et al., 2001; Campbell et al., 2003). Most directly comparable to the present study, Eastwood *et al.* (Eastwood et al., 1994) measured the forces generated by human dermal fibroblasts in 1 mg/ml collagen gels over 48 h and found a linear increase in force followed by a plateau that started around 24 h. The average peak force per cell was reported as 100 ± 20 pN/cell. Our results using rabbit joint capsule fibroblasts in 6 mg/ml fibrin gels match these findings very closely. In addition to strong parallels in the force curves (*i.e.*, linear increase followed by a plateau around 24 h), our average force per cell ranged between 110 and 145 pN/cell.

It has been suggested that fibroblasts and other cell phenotypes regulate ECM tension according to a cell-specific setpoint in a process termed tensional homeostasis (Brown et al., 1998). At least over short periods of time (*i.e.*, hours to days), fibroblasts appear to regulate the forces they generate irrespective of the material properties of the hydrogel. The fact that we observed comparable force values in fibrin gels compared to collagen gels is supportive of this idea. However, long term adaptation of cells to their mechanical environment suggests that these setpoints can change and may be responsible for a host of fibrotic disorders and other diseases. One can modulate wire stiffness in the bioreactor by changing wire diameter and/or length. Different wire stiffness will impact the balance between cell traction forces and reorganization/realignment of the fibrin fibers in the gel, which might enable one to investigate these force set-points and other mechanobiological processes in more detail.

It is also possible that more subtle changes in gel stiffness from ECM adaptations could be revealed by this bioreactor system, but that requires knowing more about how much of the force remaining after administration of blebbistatin can be attributed to the cells versus forces supported by the gel. The 50 μM concentration of blebbistatin used in this study was chosen because it is not cytotoxic but still effective at reducing cell traction forces and collagen production (Atluri et al., 2016). This concentration, however, does not eliminate traction forces completely. To eliminate traction forces completely, one could try other compounds, such as cytochalasin D (Wakatsuki et al., 2000), or apply techniques that induce apoptosis (Roberts et al., 2004). The remaining deflection in the wire should then correspond to the force supported by ECM adaptations, a phenomenon reported in other hydrogel systems (Wakatsuki et al., 2000; Bidan et al., 2016; Brauer et al., 2019). More work will need to be done to explore this idea further.

This bioreactor was designed to monitor real-time changes in cell traction force in response to drugs that impact the force generating/sensing apparatus of the cell and downstream collagen production. We believe that there are metrics in the force curves that will be predictive of this downstream remodeling process, such as the percent reduction in peak force, the duration of this reduction, and the force magnitudes measured. However, additional experiments and biochemical quantification of collagen content will be necessary to firmly establish these relationships. One could also perform mechanical tests, such as uniaxial extension tests on the gels prior to assaying for collagen, to better relate the resulting collagen content to mechanical properties. This information, combined with the knowledge of how forces distribute among the cells and the gel, will provide additional insight on how the mechanical and biochemical environment influences tissue remodeling and how controlling that environment could be used to improve wound healing and tissue repair.

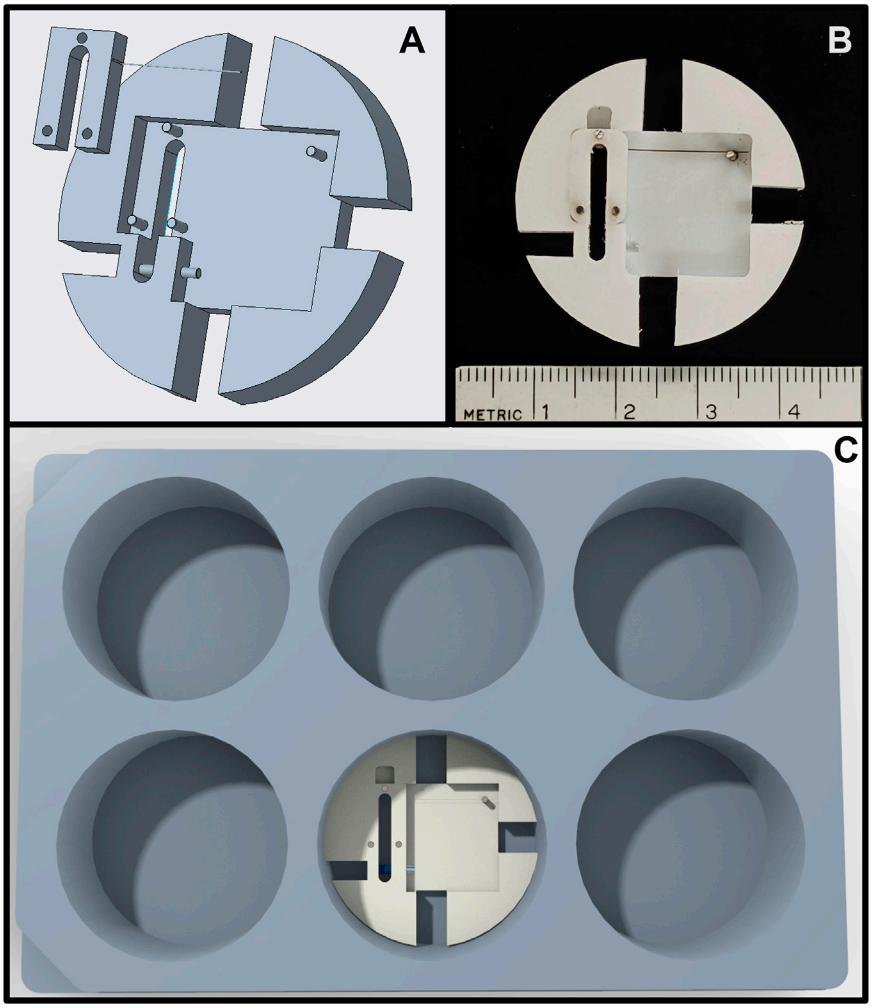

FIGURE 8 | (A) Rendering of the scaled-down force-bioreactor. **(B)** Image of a prototype bioreactor. **(C)** Rendering of the scaled-down bioreactor inside a standard 6-well tissue culture plate.

Our bioreactor system can help us better understand cell and ECM adaptations, particularly in the context of a mechanochemical feedback loop, and how compounds such as blebbistatin can be administered to control the healing response in a tissue. With respect to the latter, a balance must be struck between allowing fibroblasts to synthesize enough collagen and ECM proteins to repair the site of injury and limiting myofibroblast activity so that excessive collagen deposition is prevented. Our next steps are to use this bioreactor with drug delivery systems, such as biodegradable polymer microparticles or liposomes, to determine release kinetics and a therapeutic range of drug concentrations for normal healing.

Tomasek *et al.* (Tomasek et al., 2002) proposed that quiescent fibroblasts differentiate into a contractile, but α-SMA negative, proto-myofibroblast before transitioning to a fully activated α-SMA positive myofibroblast. Generally, it was thought that myofibroblast differentiation was irreversible, but several studies since have indicated that reversal can occur (Kisseleva et al., 2012; Garrison et al., 2013; Kollmannsberger et al., 2018). For example, Kollmannsberger *et al.* showed that myofibroblasts in a 3D microtissue reverted to α-SMA negative fibroblasts once tensile forces in the interior of the growing microtissue were offloaded to newly formed ECM, a process that occurred over a period of 2–3 weeks (Kollmannsberger et al., 2018). An even longer time scale of months was observed for myofibroblast reversal in a model of rat liver fibrosis (Kisseleva et al., 2012). In our experiments, it is highly likely that the duration of blebbistatin exposure was too short for myofibroblast reversal. Future experiments could be extended to examine whether blebbistatin can also cause reversal.

It has been known for decades that fibroblasts have tissue-specific properties that make, for example, the behavior of corneal fibroblasts differs from that of dermal fibroblasts (Doane & Birk, 1991). It is now clear that even within a specific tissue there is quite a bit of fibroblast heterogeneity. For example, genetic lineage tracing experiments in mice have found at least two distinct fibroblast populations in the peripapillary and reticular dermis, each with unique functions with respect to tissue repair

(Driskell et al., 2013; Rinkevich et al., 2015). Similarly, several genetically and biofunctionally distinct myofibroblast subpopulations have been identified in the healing wounds of mice (Shook et al., 2018, 2020), which suggests that each subpopulation has a unique role in the wound healing process. Heterogeneous tissue-specific fibroblast populations have also been recently identified in other tissues, such as the heart (Tallquist, 2020) and the lung (Xie et al., 2018). In this study, we used a relevant tissue-specific fibroblast population from the joint capsule in order to simplify our understanding of the relationships between drug dosing and joint capsule fibroblast behavior. As we develop this system further, it will be necessary to consider the effects and interactions of a more heterogenous cell population, particularly in the instance of a contracted joint, where additional cells, particularly immune cells, migrate into the capsule and impact the healing response (Qu et al., 2019). Building this additional complexity into our system has the potential to enable a deeper understanding of how joint contracture develops and how various treatment strategies might be developed in conjunction with animal studies.

The bioreactor sample size is well-suited for biochemical ECM quantification, mechanical testing, and for having sufficient cell numbers for conventional RNA or DNA analysis (*e.g.*, RNAseq or RT-qPCR). To accommodate this sample size, however, a large medium reservoir (*i.e.*, 25 ml) is needed to provide a sufficient source and sink for metabolites and waste products. A disadvantage to having a large reservoir is that the amount of drug needed can be costly. To address this issue, we have also designed a scaled-down version of the system that fits inside a 6-well plate (**Figure 8**) and uses a tenth of the reagents of the current system. Even smaller scale micropillar systems exist that easily fit within a 96-well plate (Vandenburgh et al., 2008; Boudou et al., 2012). These systems are well-suited for high-throughput drug screening and quantifying relationships between various drugs and force generation with minimal usage of reagents. However, the gel sizes generally preclude additional analysis for gene expression, protein quantification, and mechanical testing. Recent developments with single-cell RNA-seq (Luecken & Theis, 2019), new proteomics approaches for quantifying ECM proteins (Jacobson et al., 2020), and nanoindentation/atomic force microscopy (Xu et al., 2016) have the potential to enable one to work with much smaller samples, but these technologies are still being refined and not always available. Therefore, we envision the use of different sized-bioreactors, coupled with computational biochemical and biomechanical models, as the components of a multi-pronged approach to drug-screening for mechanobiologically significant compounds.

These bioreactors could also be used to study the contractile behavior of other mechanobiologically relevant cell phenotypes, particularly those that apply traction forces to their surrounding ECM, such as arterial smooth muscle cells (Chen et al., 1991), retinal epithelial cells (Smith-Thomas et al., 2000), or osteoblasts (Qi et al., 2007). Cells could be studied in the context of other diseases, such as ventilator induced lung injury (Bates & Smith, 2018) or cancer (Northcott et al., 2018), or in the context of development (Nelson & Gleghorn, 2012; Vianello & Lutolf, 2019), or other mechanobiologically relevant areas of investigation.

In conclusion, the force bioreactor system demonstrated that administration of 50 μM blebbistatin reliably reduces fibroblast force generation, which in turn resulted in qualitatively less collagen production as determined via fluorescent labeling. Quantification of collagen content (as well as the synthesis of other ECM proteins) via biochemical or proteomic analysis are needed to confirm these observations and to better understand the implications of temporarily and reversibly interrupting fibroblast/myofibroblast mechanosensing. In addition, tensile testing of the gels would be useful for relating compositional changes to mechanical changes.

DATA AVAILABILITY STATEMENT

The original contributions presented in the study are included in the article/**Supplementary Material**, further inquiries can be directed to the corresponding author.

AUTHOR CONTRIBUTIONS

ES, AS, JM, KA, and AM contributed to study conception and design. AS, JJ, SC, KA, and AM performed data collection. AS, JJ, SC, KA, AM, and ES contributed to data analysis. All authors contributed to drafting the manuscript.

FUNDING

Support for this work was provided by the University of Iowa, Department of Orthopedics and Rehabilitation and the National Institutes of Health NIAMS R21AR075137-01A1.

ACKNOWLEDGMENTS

We also wish to thank Tom Baer for his help constructing the bioreactor and turntable, Mariam El-Hattab for assistance with experiments, and Dr. Magnus Hooke, Texas A&M Health, for the CNA35.

SUPPLEMENTARY MATERIAL

The Supplementary Material for this article can be found online at: https://www.frontiersin.org/articles/10.3389/fbioe.2022.907611/full#supplementary-material

REFERENCES

Abdul, N., Dixon, D., Walker, A., Horabin, J., Smith, N., Weir, D. J., et al. (2015). Fibrosis Is a Common Outcome Following Total Knee Arthroplasty. *Sci. Rep.* 5 (1), 1–13. doi:10.1038/srep16469

Allingham, J. S., Smith, R., and Rayment, I. (2005). The Structural Basis of Blebbistatin Inhibition and Specificity for Myosin II. *Nat. Struct. Mol. Biol.* 12 (4), 378–379. doi:10.1038/nsmb908

Asmani, M., Kotei, C., Hsia, I., Marecki, L., Wang, T., Zhou, C., et al. (2019). Cyclic Stretching of Fibrotic Microtissue Array for Evaluation of Anti-fibrosis Drugs. *Cel. Mol. Bioeng.* 12, 529–540. doi:10.1007/s12195-019-00590-3

Astashkina, A., Mann, B., and Grainger, D. W. (2012). A Critical Evaluation of *In Vitro* Cell Culture Models for High-Throughput Drug Screening and Toxicity. *Pharmacol. Ther.* 134 (1), 82–106. doi:10.1016/J.PHARMTHERA.2012.01.001

Atluri, K., de Jesus, A. M., Chinnathambi, S., Brouillette, M. J., Martin, J. A., Salem, A. K., et al. (2016). Blebbistatin-Loaded Poly(d,l-Lactide-Co-Glycolide) Particles for Treating Arthrofibrosis. *ACS Biomater. Sci. Eng* 2 (7), 1097–1107. doi:10.1021/acsbiomaterials.6b00082

Atluri, K., Brouillette, M. J., Seol, D., Khorsand, B., Sander, E., Salem, A. K., et al. (2020a). Sulfasalazine Resolves Joint Stiffness in a Rabbit Model of Arthrofibrosis. *J. Orthop. Res.* 38 (3), 629–638. doi:10.1002/JOR.24499

Atluri, K., Chinnathambi, S., Mendenhall, A., Martin, J. A., Sander, E. A., Salem, A. K., et al. (2020b). Targeting Cell Contractile Forces: A Novel Minimally Invasive Treatment Strategy for Fibrosis. *Ann. Biomed. Eng.* 48, 1850–1862. doi:10.1007/s10439-020-02497-x

Barton, M. B., Harris, R., and Fletcher, S. W. (1999). Does This Patient Have Breast Cancer? *JAMA* 282 (13), 1270–1280. doi:10.1001/JAMA.282.13.1270

Bates, J. H. T., and Smith, B. J. (2018). Ventilator-induced Lung Injury and Lung Mechanics. *Ann. Transl. Med.* 6 (19), 378. doi:10.21037/ATM.2018.06.29

Bidan, C. M., Kollmannsberger, P., Gering, V., Ehrig, S., Joly, P., Petersen, A., et al. (2016). Gradual Conversion of Cellular Stress Patterns into Pre-stressed Matrix Architecture during *In Vitro* Tissue Growth. *J. R. Soc. Interface.* 13 (118), 20160136. doi:10.1098/RSIF.2016.0136

Bolós, V., Gasent, J. M., López-Tarruella, S., and Grande, E. (2010). The Dual Kinase Complex FAK-Src as a Promising Therapeutic Target in Cancer. *Ott* 3, 83. doi:10.2147/OTT.S6909

Boudou, T., Legant, W. R., Mu, A., Borochin, M. A., Thavandiran, N., Radisic, M., et al. (2012). A Microfabricated Platform to Measure and Manipulate the Mechanics of Engineered Cardiac Microtissues. *Tissue Eng. Part A* 18 (9–10), 910–919. doi:10.1089/TEN.TEA.2011.0341

Brauer, E., Lippens, E., Klein, O., Nebrich, G., Schreivogel, S., Korus, G., et al. (2019). Collagen Fibrils Mechanically Contribute to Tissue Contraction in an *In Vitro* Wound Healing Scenario. *Adv. Sci.* 6 (9), 1801780. doi:10.1002/ADVS.201801780

Brown, R. A., Prajapati, R., Mcgrouther, D. A., Yannas, I. V., and Eastwood, M. (1998). Tensional Homeostasis in Dermal Fibroblasts: Mechanical Responses to Mechanical Loading in Three-Dimensional Substrates. *J. Cell. Physiol.* 175, 323–332. doi:10.1002/(sici)1097-4652(199806)175:3<323::aid-jcp10>3.0.co;2-6

Campbell, B. H., Clark, W. W., and Wang, J. H.-C. (2003). A Multi-Station Culture Force Monitor System to Study Cellular Contractility. *J. Biomechanics* 36 (1), 137–140. doi:10.1016/S0021-9290(02)00325-1

Chen, G., Chen, H., Wang, C., Peng, Y., Sun, L., Liu, H., et al. (2012). Rapamycin Ameliorates Kidney Fibrosis by Inhibiting the Activation of mTOR Signaling in Interstitial Macrophages and Myofibroblasts. *PLOS ONE* 7 (3), e33626. doi:10.1371/JOURNAL.PONE.0033626

Chen, J.-K., Haimes, H. B., and Weinberg, C. B. (1991). Role of Growth Factors in the Contraction and Maintenance of Collagen Lattices Made with Arterial Smooth Muscle Cells. *J. Cell. Physiol.* 146 (1), 110–116. doi:10.1002/JCP.1041460115

Cheung, A., Dantzig, J. A., Hollingworth, S., Baylor, S. M., Goldman, Y. E., Mitchison, T. J., et al. (2001). A Small-Molecule Inhibitor of Skeletal Muscle Myosin II. *Nat. Cell Biol.* 4 (11), 83–88. doi:10.1038/ncb734

Diamantopoulos, A., Wright, E., Vlahopoulou, K., Cornic, L., Schoof, N., and Maher, T. M. (2018). The Burden of Illness of Idiopathic Pulmonary Fibrosis: A Comprehensive Evidence Review. *PharmacoEconomics* 36 (7), 779–807. doi:10.1007/S40273-018-0631-8

Doane, K., and Birk, D. E. (1991). Fibroblasts Retain Their Tissue Phenotype when Grown in Three-Dimensional Collagen Gels*1. *Exp. Cell Res.* 195 (2), 432–442. doi:10.1016/0014-4827(91)90394-A

Dove, E. P., Olson, A. L., and Glassberg, M. K. (2019). Trends in Idiopathic Pulmonary Fibrosis-Related Mortality in the United States: 2000-2017. *Am. J. Respir. Crit. Care Med.* 200 (7), 929–931. doi:10.1164/RCCM.201905-0958LE

Driskell, R. R., Lichtenberger, B. M., Hoste, E., Kretzschmar, K., Simons, B. D., Charalambous, M., et al. (2013). Distinct Fibroblast Lineages Determine Dermal Architecture in Skin Development and Repair. *Nature* 504 (7479), 277–281. doi:10.1038/nature12783

Dupont, S., Morsut, L., Aragona, M., Enzo, E., Giulitti, S., Cordenonsi, M., et al. (2011). Role of YAP/TAZ in Mechanotransduction. *Nature* 474 (7350), 179–183. doi:10.1038/nature10137

Eastwood, M., McGrouther, D., and Brown, R. (1994). A Culture Force Monitor for Measurement of Contraction Forces Generated in Human Dermal Fibroblast Cultures: Evidence for Cell-Matrix Mechanical Signalling. *Biochimica Biophysica Acta (BBA) - General Subj.* 1201 (2), 186–192. doi:10.1016/0304-4165(94)90040-X

Eddinger, T. J., Meer, D. P., Miner, A. S., Meehl, J., Rovner, A. S., and Ratz, P. H. (2007). Potent Inhibition of Arterial Smooth Muscle Tonic Contractions by the Selective Myosin II Inhibitor, Blebbistatin. *J. Pharmacol. Exp. Ther.* 320 (2), 865–870. doi:10.1124/JPET.106.109363

El-Hattab, M. Y., Nagumo, Y., Gourronc, F. A., Klingelhutz, A. J., Ankrum, J. A., and Sander, E. A. (2020). Human Adipocyte Conditioned Medium Promotes *In Vitro* Fibroblast Conversion to Myofibroblasts. *Sci. Rep.* 10 (1), 1–11. doi:10.1038/s41598-020-67175-3

Evans, P. J., Nandi, S., Maschke, S., Hoyen, H. A., and Lawton, J. N. (2009). Prevention and Treatment of Elbow Stiffness. *J. Hand Surg.* 34 (4), 769–778. doi:10.1016/J.JHSA.2009.02.020

Farman, G. P., Tachampa, K., Mateja, R., Cazorla, O., Lacampagne, A., and de Tombe, P. P. (2008). Blebbistatin: Use as Inhibitor of Muscle Contraction. *Pflugers Arch. - Eur. J. Physiol.* 455 (6), 995–1005. doi:10.1007/S00424-007-0375-3/FIGURES/7

Fernandes, C. A., and Vanbever, R. (2009). Preclinical Models for Pulmonary Drug Delivery. *Expert Opin. Drug Deliv.* 6 (11), 1231–1245. doi:10.1517/17425240903241788

Freyman, T. M., Yannas, I. v., Yokoo, R., and Gibson, L. J. (2001). Fibroblast Contraction of a Collagen-GAG Matrix. *Biomaterials* 22 (21), 2883–2891. doi:10.1016/S0142-9612(01)00034-5

Garrison, G., Huang, S. K., Okunishi, K., Scott, J. P., Kumar Penke, L. R., Scruggs, A. M., et al. (2013). Reversal of Myofibroblast Differentiation by Prostaglandin E2. *Am. J. Respir. Cell Mol. Biol.* 48 (5), 550–558. doi:10.1165/RCMB.2012-0262OC

Geiger, B., and Bershadsky, A. (2002). Exploring the Neighborhood. *Cell* 110 (2), 139–142. doi:10.1016/S0092-8674(02)00831-0

Geiger, B., Spatz, J. P., and Bershadsky, A. D. (2009). Environmental Sensing through Focal Adhesions. *Nat. Rev. Mol. Cell Biol.* 10 (11), 21–33. doi:10.1038/nrm2593

Grinnell, F. (2000). Fibroblast-collagen-matrix Contraction: Growth-Factor Signalling and Mechanical Loading. *Trends Cell Biol.* 10 (9), 362–365. doi:10.1016/S0962-8924(00)01802-X

Guan, J.-L. (2010). Integrin Signaling through FAK in the Regulation of Mammary Stem Cells and Breast Cancer. *IUBMB Life* 62 (4), 268–276. doi:10.1002/IUB.303

Hinz, B., Phan, S. H., Thannickal, V. J., Galli, A., Bochaton-Piallat, M.-L., and Gabbiani, G. (2007). The Myofibroblast. *Am. J. Pathology* 170 (6), 1807–1816. doi:10.2353/AJPATH.2007.070112

Hinz, B., Phan, S. H., Thannickal, V. J., Prunotto, M., Desmoulière, A., Varga, J., et al. (2012). Recent Developments in Myofibroblast Biology. *Am. J. Pathology* 180 (4), 1340–1355. doi:10.1016/J.AJPATH.2012.02.004

Ibar, C., Kirichenko, E., Keepers, B., Enners, E., Fleisch, K., and Irvine, K. D. (2018). Tension-Dependent Regulation of Mammalian Hippo Signaling Through LIMD1. *Journal of Cell Science* 131 (5), jcs214700.

Jacobson, K. R., Saleh, A. M., Lipp, S. N., Ocken, A. R., Kinzer-Ursem, T. L., and Calve, S. (2020). Extracellular Matrix Protein Composition Dynamically Changes during Murine Forelimb Development. *SSRN J.* 2020. doi:10.2139/SSRN.3634807

Kisseleva, T., Cong, M., Paik, Y., Scholten, D., Jiang, C., Benner, C., et al. (2012). Myofibroblasts Revert to an Inactive Phenotype during Regression of Liver Fibrosis. *Proc. Natl. Acad. Sci. U.S.A.* 109 (24), 9448–9453. doi:10.1073/PNAS.1201840109

Klingberg, F., Hinz, B., and White, E. S. (2013). The Myofibroblast Matrix: Implications for Tissue Repair and Fibrosis. *J. Pathol.* 229 (2), 298–309. doi:10.1002/PATH.4104

Kollmannsberger, P., Bidan, C. M., Dunlop, J. W. C., Fratzl, P., and Vogel, V. (2018). Tensile Forces Drive a Reversible Fibroblast-To-Myofibroblast Transition during Tissue Growth in Engineered Clefts. *Sci. Adv.* 4 (1), eaao4881. doi:10.1126/SCIADV.AAO4881

Kolodney, M., and Wysolmerski, R. (1992). Isometric Contraction by Fibroblasts and Endothelial Cells in Tissue Culture: a Quantitative Study. *J. Cell Biol.* 117 (1), 73–82. doi:10.1083/JCB.117.1.73

Kovács, M., Tóth, J., Hetényi, C., Málnási-Csizmadia, A., and Sellers, J. R. (2004). Mechanism of Blebbistatin Inhibition of Myosin II. *J. Biol. Chem.* 279 (34), 35557–35563. doi:10.1074/JBC.M405319200

Lampi, M. C., and Reinhart-King, C. A. (2018). Targeting Extracellular Matrix Stiffness to Attenuate Disease: From Molecular Mechanisms to Clinical Trials. *Sci. Transl. Med.* 10 (422), 475. doi:10.1126/SCITRANSLMED.AAO0475

Limouze, J., Straight, A. F., Mitchison, T., and Sellers, J. R. (2004). Specificity of Blebbistatin, an Inhibitor of Myosin II. *J. Muscle Res. Cell Motil.* 25 (4), 337–341. doi:10.1007/S10974-004-6060-7

Luecken, M. D., and Theis, F. J. (2019). Current Best Practices in Single-cell RNA-seq Analysis: a Tutorial. *Mol. Syst. Biol.* 15 (6), e8746. doi:10.15252/MSB.20188746

Mastikhina, O., Moon, B.-U., Williams, K., Hatkar, R., Gustafson, D., Mourad, O., et al. (2020). Human Cardiac Fibrosis-On-A-Chip Model Recapitulates Disease Hallmarks and Can Serve as a Platform for Drug Testing. *Biomaterials* 233, 119741. doi:10.1016/J.BIOMATERIALS.2019.119741

Matsumoto, T., Kuriwaka-Kido, R., Kido, S., Matsumoto, T., Kuriwaka-Kido, R., and Kido, S. (2011). "Mechanosensing and Signaling Crosstalks," in *Mechanosensing Biology* (Tokyo: Springer), 157–166. doi:10.1007/978-4-431-89757-6_11

Nelson, C. M., and Gleghorn, J. P. (2012). Sculpting Organs: Mechanical Regulation of Tissue Development. *Annu. Rev. Biomed. Eng.* 14, 129–154. doi:10.1146/ANNUREV-BIOENG-071811-150043

Northcott, J. M., Dean, I. S., Mouw, J. K., and Weaver, V. M. (2018). Feeling Stress: The Mechanics of Cancer Progression and Aggression. *Front. Cell Dev. Biol.* 6 (FEB), 17. doi:10.3389/FCELL.2018.00017/BIBTEX

Qi, J., Chi, L., Faber, J., Koller, B., and Banes, A. J. (2007). ATP Reduces Gel Compaction in Osteoblast-Populated Collagen Gels. *J. Appl. Physiology* 102 (3), 1152–1160. doi:10.1152/JAPPLPHYSIOL.00535.2006

Qu, F., Guilak, F., and Mauck, R. L. (2019). Cell Migration: Implications for Repair and Regeneration in Joint Disease. *Nat. Rev. Rheumatol.* 315 (3), 167–179. doi:10.1038/s41584-018-0151-0

Rinkevich, Y., Walmsley, G. G., Hu, M. S., Maan, Z. N., Newman, A. M., Drukker, M., et al. (2015). Skin Fibrosis. Identification and Isolation of a Dermal Lineage with Intrinsic Fibrogenic Potential. *Science* 348 (6232), aaa2151. doi:10.1126/SCIENCE.AAA2151

Roberts, K. M., Rosen, A., and Casciola-Rosen, L. A. (2004). Methods for Inducing Apoptosis. *Methods Mol. Med.* 102, 115–128. doi:10.1385/1-59259-805-6:115/COVER/

Saito, M., Yamazaki, M., Maeda, T., Matsumura, H., Setoguchi, Y., and Tsuboi, R. (2012). Pirfenidone Suppresses Keloid Fibroblast-Embedded Collagen Gel Contraction. *Archives of Dermatological Research* 304 (3), 217–222.

Sander, E. A., Barocas, V. H., and Tranquillo, R. T. (2011). Initial Fiber Alignment Pattern Alters Extracellular Matrix Synthesis in Fibroblast-Populated Fibrin Gel Cruciforms and Correlates with Predicted Tension. *Ann. Biomed. Eng.* 39 (2), 714–729. doi:10.1007/S10439-010-0192-2/FIGURES/8

Selvaggio, A. S., and Noble, P. W. (2016). Pirfenidone Initiates a New Era in the Treatment of Idiopathic Pulmonary Fibrosis. *Annu. Rev. Med.* 67, 487–495. doi:10.1146/ANNUREV-MED-120214-013614

Shook, B. A., Wasko, R. R., Rivera-Gonzalez, G. C., Salazar-Gatzimas, E., López-Giráldez, F., Dash, B. C., et al. (2018). Myofibroblast Proliferation and Heterogeneity Are Supported by Macrophages during Skin Repair. *Science* 362 (6417), eaar2971. doi:10.1126/SCIENCE.AAR2971

Shook, B. A., Wasko, R. R., Mano, O., Rutenberg-Schoenberg, M., Rudolph, M. C., Zirak, B., et al. (2020). Dermal Adipocyte Lipolysis and Myofibroblast Conversion Are Required for Efficient Skin Repair. *Cell Stem Cell* 26 (6), 880–895. e6. doi:10.1016/J.STEM.2020.03.013

Sidney, S., Quesenberry, C. P., Jaffe, M. G., Sorel, M., Nguyen-Huynh, M. N., Kushi, L. H., et al. (2016). Recent Trends in Cardiovascular Mortality in the United States and Public Health Goals. *JAMA Cardiol.* 1 (5), 594–599. doi:10.1001/JAMACARDIO.2016.1326

Smith-Thomas, L. C., Richardson, P. S. R., Rennie, I. G., Palmer, I., Boulton, M., Sheridan, C., et al. (2000). Influence of Pigment Content, Intracellular Calcium and Cyclic AMP on the Ability of Human Retinal Pigment Epithelial Cells to Contract Collagen Gels. *Curr. Eye Res.* 21 (1), 518–529. doi:10.1076/0271-3683(200007)2111-ZFT518

Straight, A. F., Cheung, A., Limouze, J., Chen, I., Westwood, N. J., Sellers, J. R., et al. (2003). Dissecting Temporal and Spatial Control of Cytokinesis with a Myosin II Inhibitor. *Science* 299 (5613), 1743–1747. doi:10.1126/SCIENCE.1081412

Tallquist, M. D. (2020). Cardiac Fibroblast Diversity. *Annu. Rev. Physiol.* 82, 63–78. doi:10.1146/ANNUREV-PHYSIOL-021119-034527

Tomasek, J. J., Gabbiani, G., Hinz, B., Chaponnier, C., and Brown, R. A. (2002). Myofibroblasts and Mechano-Regulation of Connective Tissue Remodelling. *Nat. Rev. Mol. Cell Biol.* 3 (55), 349–363. doi:10.1038/nrm809

Tuan, T.-L., Song, A., Chang, S., Younai, S., and Nimni, M. E. (1996). In VitroFibroplasia: Matrix Contraction, Cell Growth, and Collagen Production of Fibroblasts Cultured in Fibrin Gels. *Exp. Cell Res.* 223 (1), 127–134. doi:10.1006/EXCR.1996.0065

Tulek, B., Kiyan, E., Toy, H., Kiyici, A., Narin, C., and Suerdem, M. (2011). Anti-inflammatory and Anti-fibrotic Effects of Sirolimus on Bleomycin-Induced Pulmonary Fibrosis in Rats. *Cim* 34 (6), 341–E348. doi:10.25011/CIM.V34I6.15894

Unterhauser, F. N., Bosch, U., Zeichen, J., and Weiler, A. (2004). ?-Smooth Muscle Actin Containing Contractile Fibroblastic Cells in Human Knee Arthrofibrosis Tissue. *Arch. Orthop. Trauma Surg.* 124 (9), 585–591. doi:10.1007/S00402-004-0742-X/FIGURES/6

Vandenburgh, H., Shansky, J., Benesch-Lee, F., Barbata, V., Reid, J., Thorrez, L., et al. (2008). Drug-screening Platform Based on the Contractility of Tissue-Engineered Muscle. *Muscle Nerve* 37 (4), 438–447. doi:10.1002/MUS.20931

Vianello, S., and Lutolf, M. P. (2019). Understanding the Mechanobiology of Early Mammalian Development through Bioengineered Models. *Dev. Cell* 48 (6), 751–763. doi:10.1016/J.DEVCEL.2019.02.024

Wakatsuki, T., Kolodney, M. S., Zahalak, G. I., and Elson, E. L. (2000). Cell Mechanics Studied by a Reconstituted Model Tissue. *Biophysical J.* 79 (5), 2353–2368. doi:10.1016/S0006-3495(00)76481-2

Wessel, L. E., Gu, A., Richardson, S. S., Fufa, D. T., and Osei, D. A. (2019). Elbow Contracture Following Operative Fixation of Fractures about the Elbow. *JSES Open Access* 3 (4), 261–265. doi:10.1016/J.JSES.2019.09.004

Wong, V. W., Rustad, K. C., Akaishi, S., Sorkin, M., Glotzbach, J. P., Januszyk, M., et al. (2011). Focal Adhesion Kinase Links Mechanical Force to Skin Fibrosis via Inflammatory Signaling. *Nat. Med.* 18, 148–152. doi:10.1038/nm.2574

Wynn, T. A. (2004). Fibrotic Disease and the TH1/TH2 Paradigm. *Nat. Rev. Immunol.* 44 (8), 8583–8594. doi:10.1038/nri1412

Wynn, T. (2008). Cellular and Molecular Mechanisms of Fibrosis. *J. Pathol.* 214 (2), 199–210. doi:10.1002/PATH.2277

Xie, T., Wang, Y., Deng, N., Huang, G., Taghavifar, F., Geng, Y., et al. (2018). Single-Cell Deconvolution of Fibroblast Heterogeneity in Mouse Pulmonary Fibrosis. *Cell Rep.* 22 (13), 3625–3640. doi:10.1016/J.CELREP.2018.03.010

Xu, X., Li, Z., Cai, L., Calve, S., and Neu, C. P. (2016). Mapping the Nonreciprocal Micromechanics of Individual Cells and the Surrounding Matrix within Living Tissues. *Sci. Rep.* 6 (11), 1–9. doi:10.1038/srep24272

Conflict of Interest: The authors declare that the research was conducted in the absence of any commercial or financial relationships that could be construed as a potential conflict of interest.

frontiers | Frontiers in Cell and Developmental Biology

TYPE Original Research
PUBLISHED 07 September 2022
DOI 10.3389/fcell.2022.944126

Craniofacial tendon development—Characterization of extracellular matrix morphology and spatiotemporal protein distribution

Stefanie H. Korntner[1], Aniket Jana[1], Elizabeth Kinnard[1], Emily Leo[1], Timothy Beane[2], Xianmu Li[2], Rohit Sengupta[1], Lauren Becker[1] and Catherine K. Kuo[1,2,3,4]*

[1]Fischell Department of Bioengineering, University of Maryland, College Park, MD, United States, [2]Department of Biomedical Engineering, University of Rochester, Rochester, NY, United States, [3]Center for Musculoskeletal Research, University of Rochester Medical Center, Rochester, NY, United States, [4]Department of Orthopaedics, University of Maryland Medical Center, Baltimore, MD, United States

Craniofacial (CF) tendons are often affected by traumatic injuries and painful disorders that can severely compromise critical jaw functions, such as mastication and talking. Unfortunately, tendons lack the ability to regenerate, and there are no solutions to restore their native properties or function. An understanding of jaw tendon development could inform tendon regeneration strategies to restore jaw function, however CF tendon development has been relatively unexplored. Using the chick embryo, we identified the jaw-closing Tendon of the musculus Adductor Mandibulae Externus (TmAM) and the jaw-opening Tendon of the musculus Depressor Mandibulae (TmDM) that have similar functions to the masticatory tendons in humans. Using histological and immunohistochemical (IHC) analyses, we characterized the TmAM and TmDM on the basis of cell and extracellular matrix (ECM) morphology and spatiotemporal protein distribution from early to late embryonic development. The TmAM and TmDM were detectable as early as embryonic day (d) 9 based on histological staining and tenascin-C (TNC) protein distribution. Collagen content increased and became more organized, cell density decreased, and cell nuclei elongated over time during development in both the TmAM and TmDM. The TmAM and TmDM exhibited similar spatiotemporal patterns for collagen type III (COL3), but differential spatiotemporal patterns for TNC, lysyl oxidase (LOX), and matrix metalloproteinases (MMPs). Our results demonstrate markers that play a role in limb tendon formation are also present in jaw tendons during embryonic development, implicate COL3, TNC, LOX, MMP2, and MMP9 in jaw tendon development, and suggest TmAM and TmDM possess different developmental programs. Taken together, our study suggests the chick embryo may be used as a model with which to study CF tendon extracellular matrix development, the results of which could ultimately inform therapeutic approaches for CF tendon injuries and disorders.

EDITED BY
Rajprasad Loganathan,
Johns Hopkins Medicine, United States

REVIEWED BY
Dimitra Mangoura,
Biomedical Research Foundation of the Academy of Athens (BRFAA), Greece
Jeffrey A. Weiss,
The University of Utah, United States

*CORRESPONDENCE
Catherine K. Kuo,
ckk@umd.edu

SPECIALTY SECTION
This article was submitted to Cell Adhesion and Migration, a section of the journal Frontiers in Cell and Developmental Biology

RECEIVED 14 May 2022
ACCEPTED 10 August 2022
PUBLISHED 07 September 2022

CITATION
Korntner SH, Jana A, Kinnard E, Leo E, Beane T, Li X, Sengupta R, Becker L and Kuo CK (2022), Craniofacial tendon development—Characterization of extracellular matrix morphology and spatiotemporal protein distribution. *Front. Cell Dev. Biol.* 10:944126.
doi: 10.3389/fcell.2022.944126

KEYWORDS

tendon, craniofacial, jaw, tendon development, collagen, lysyl oxidase, matrix metalloproteinase, chick embryo

1 Introduction

Craniofacial (CF) tendons transfer muscle-generated forces to bones, thus enabling critical jaw movements such as mastication, talking, swallowing, and yawning. Over 3 million CF traumas occur each year in the U.S., involving injuries to the soft tissues and bones of the face and skull, caused by vehicle and sports accidents, assaults, and combat (Miura et al., 2006; Rocchi et al., 2007; Twigg and Wilkie, 2015; Luo et al., 2019; Su et al., 2021). Traumatic CF soft tissue injuries account for nearly 10% of all emergency department visits and up to $200 billion in medical costs (Kretlow et al., 2010; Su et al., 2021). Even though these injuries affect multiple CF tissues, including tendons, current treatment approaches to restore jaw function neglect tendons, and instead focus only on reconstructing bone despite failing to fully restore jaw function (Warren et al., 2003; Zhang and Yelick, 2018). CF tendons also experience painful disorders for which there are no effective treatments. Temporal tendinitis (tendinopathy) is a disorder or disease of the temporalis tendon that has been characterized by both inflammation and degeneration but is under-treated due to the anatomical complexity and incomplete understanding of temporal tendons (Dupont and Brown, 2012; Bressler et al., 2020). Taken together, there is a critical need to understand normal CF tendon formation in order to inform and develop treatment strategies to restore CF tendons and jaw function.

While a small number of studies have investigated CF tendon cell morphogenesis in zebrafish embryos (Chen and Galloway, 2014; McGurk et al., 2017; Subramanian et al., 2018), little is known about CF tendon development. Furthermore, animal models other than zebrafish have not been established for study of CF tendons. In contrast, limb tendon development has been studied in various animal models. We and others have used the chick embryo model to extensively to study limb tendon formation as it closely parallels that in mammals, making it an excellent model to study tendon formation with relevance to human (Fleischmajer et al., 1990; Ros et al., 1995; Birk et al., 1997; Birk and Mayne, 1997; Schweitzer et al., 2001; Edom-Vovard and Duprez, 2004; Canty et al., 2006; Banos et al., 2008; Kuo et al., 2008; Marturano et al., 2013; Marturano et al., 2014; Schiele et al., 2015; Havis et al., 2016; Marturano et al., 2016; Nguyen et al., 2018; Pan et al., 2018; Nguyen et al., 2021; Peterson et al., 2021). Furthermore, the chick embryo has previously been used to study embryonic craniofacial bone, muscle, and cartilage development (reviewed in Abramyan and Richman, 2018). Here, we propose the chick embryo as a model with which to study craniofacial tendon development.

In this study we focused on tendons that have similar jaw-opening and jaw-closing functions as the masticatory tendons in human. It has previously been described in pigeons, parakeets, finches, and tailor birds that the musculus Adductor Mandibulae Externus (mAME) is the principal jaw adductor that enables closing of the lower jaw, and that the musculus Depressor Mandibulae (mDM) is the principal jaw depressor that enables opening and sidewards rotation of the lower jaw (Bhattacharyya, 2013; Carril et al., 2015; Jones et al., 2019; To et al., 2021). We therefore focused on identifying and characterizing the tendons that attach the mAME and the mDM to the lower jaw, which we termed the TmAM (tendon attaching to the mAME) and TmDM (tendon attaching to the mDM). The jaw-closing TmAM and jaw-opening TmDM exhibit similar structure and function as tendons of the human jaw-closing muscles (masseter, temporalis, medial pterygoid) and jaw-opening muscles (lateral pterygoid), respectively (Van Eijden et al., 1997).

During embryonic development, limb tendons undergo drastic changes in cell density and extracellular (ECM) morphology (Kuo et al., 2008; Marturano et al., 2013; Schiele et al., 2015). The ECM of adult tendon is primarily composed of hierarchically organized collagen (Kastelic et al., 1978; Marturano et al., 2013). As the embryonic limb tendon develops, collagen content and organization continue to increase gradually until a functional tendon has formed (Kastelic et al., 1978; Marturano et al., 2013). Collagen type III (COL3) is present at various stages of limb tendon development, and has been implicated in regulating fibrillogenesis of collagen type I as well as fibril growth and assembly during embryonic limb tendon development (Fleischmajer et al., 1988; Fleischmajer et al., 1990; Ros et al., 1995; Birk and Mayne, 1997; Liu et al., 1997; Kuo et al., 2008). Another critical regulator of limb tendon development is lysyl oxidase (LOX), an enzyme that covalently crosslinks collagen to impart mechanical properties to the developing tendon (Marturano et al., 2013; Marturano et al., 2014). LOX mRNA, protein, and LOX-mediated collagen crosslink density increase over time during embryonic limb tendon development (Marturano et al., 2014; Pan et al., 2018). While its function during limb tendon development has been minimally studied, matrix metalloproteinase (MMP)-2 has been detected in chick embryo limb tendons and suggested to play a role in ECM remodeling during development (Jung et al., 2009). Tenascin-C (TNC), a matricellular protein that labels both tendon primordia and differentiated tendons, has been previously used as a marker to label limb tendons during development (Chiquet and Fambrough, 1984; Kardon, 1998; Edom-Vovard et al., 2002). It would be interesting to examine if these regulators and markers of limb tendon development are also present during CF tendon development.

TABLE 1 Developmental days (d) and corresponding Hamburger Hamilton stages (HH) of chick embryos used in this study.

Developmental day (d)	Hamburger Hamilton (HH) stage
d9	HH35
d11	HH37
d13	HH39
d15	HH41
d17	HH43
d19	HH45

The goal of this study was to characterize the chick embryo as a model with which to study jaw tendon development, with a particular focus on the TmAM and TmDM. We identified the TmAM and TmDM via a combination of functional, anatomical, and morphological features. Using histological and immunohistochemical (IHC) analyses, we characterized the TmAM and TmDM on the basis of cell and ECM morphology and spatiotemporal protein distribution from early to late embryonic development. We focused on ECM molecules implicated in embryonic limb tendon development, and also compared TmAM and TmDM with each other. Our data support the chick embryo as a model to study CF tendon ECM development, and presents morphological and protein characterizations that can serve as a foundation for future studies of CF tendon development.

2 Materials and methods

For all experiments chick embryos between developmental day (d) 9 through d19 were used, corresponding to Hamburger and Hamilton (Hamburger and Hamilton, 1951) stages (HH) 35 through HH45, respectively (Table 1). In this study, we refer to the different embryonic stages by developmental days (d). Image analyses of tendon cell density and cell morphology were performed by 3 reviewers in a blinded fashion.

2.1 Gross identification of CF tendon location

Freshly harvested chick embryo heads were used for dissection. After skin and superficial fat were removed, tendons were identified by gently pulling on tendons with forceps to show opening and closing of the beak.

2.2 Tissue harvest and processing

Fertilized White Leghorn chicken eggs (CBT Farms, Chestertown, MD) were incubated at 37°C in a humidified rocking incubator. On incubation d9 through d19, chick embryos were sacrificed by decapitation, staged, and heads were fixed in 10% neutral buffered formalin (Sigma-Aldrich, HT501128-4L, MO, United States) overnight at 4°C. After decalcification in Immunocal (StatLab Medical Products, TX, United States) heads were skinned and cut in half along the sagittal plane. Tissue specimens were dehydrated through serially graded ethanol washes, and then processed and embedded in paraffin, as previously described (Kuo et al., 2008; Brown et al., 2012; Navarro et al., 2022). Heads were oriented to section TmAM and TmDM longitudinally at 6 μm thickness. To orient paraffin blocks to obtain longitudinal sections of the TmAM, location and orientation of the eye, ear, and fossa temporalis of the squamosal bone were used as references. To orient paraffin blocks to obtain longitudinal sections of the TmDM, location and orientation of the lower mandible was used as a reference. Tissue sections were subsequently used for histological and immunohistochemical staining.

2.3 Histological identification of CF tendons

To identify CF tendons relative to muscle and bone, and visualize tendon morphology, tissue sections were stained with Mallory's trichrome, as previously described (Kuo et al., 2008; Kuo and Tuan, 2008; Marturano et al., 2013; Navarro et al., 2022), and brightfield images were acquired with a ZEISS Axioscan.Z1 slide scanning microscope with a 20x objective (Zeiss, Oberkochen, Germany).

2.4 Characterization of cell density and cell morphology

To assess tendon cell density and morphology, tissue sections were stained with hematoxylin and eosin (H&E), as previously described (Kuo et al., 2008; Kuo and Tuan, 2008; Brown et al., 2012; Marturano et al., 2013; Navarro et al., 2022), and brightfield images were acquired with a ZEISS Axioscan.Z1 slide scanner with a 40x objective. Three non-overlapping same-size (60 × 60 μm) regions of interest (ROIs), equally distributed along the mid-portion of the TmAM and TmDM and avoiding the myotendinous junction and enthesis, were selected for analysis. Brightfield images were deconvoluted into hematoxylin and eosin signals using the H&E macro in Fiji (Schindelin et al., 2012). Cell density was quantified by manually counting nuclei per unit area (mm^2). Aspect ratio (AR) and circularity of cell nuclei were characterized via image analysis using Fiji. Specifically, nuclei in hematoxylin images were manually selected using the wand tool, after which Fiji would automatically outline the nuclei. Measurements for AR and circularity were then performed automatically by Fiji. Nuclear AR was determined as the ratio of major axis to minor axis. Nuclear circularity was determined as 4 π x (area/perimeter^2).

2.5 Characterization of collagen content, organization, and fiber maturity

To assess collagen content, organization, and maturity, tissue sections were stained with picrosirius red (PSR) and imaged under brightfield and polarized light (POL), as previously described (Kuo and Tuan, 2008), using a ZEISS Axioscan.Z1 slide scanning microscope with a 20x objective. Three non-overlapping same-size (60 × 60 µm) regions of interest (ROIs) were selected equally distributed along the mid-portion of the TmAM and TmDM, avoiding the myotendinous junction and enthesis. Collagen content and organization were analyzed using Fiji. **Collagen content** was characterized by quantifying PSR-stained area in brightfield images. Specifically, images were converted into 8-bit binary images and thresholded to isolate PSR staining from background staining. Percentage area fraction of thresholded PSR staining was calculated. The same threshold was used for all technical and biological replicates for all embryonic stages. **Collagen organization** was characterized by quantifying birefringence signal of POL images, as higher birefringence signal is associated with more organized collagen (Kuo and Tuan, 2008). Specifically, POL images were converted into 8-bit binary images and thresholded to isolate birefringence signal from background. Percentage area fraction of thresholded birefringence signal was calculated. The same threshold was used for all technical and biological replicates for all embryonic stages. **Collagen maturity** was analyzed in POL images of PSR-stained sections using a custom MATLAB routine (version 2019b, Mathworks, Natick, MA). To identify collagen-rich regions of interest, a net intensity threshold was applied to all images as follows: $I_R + I_G + I_B \geq 140$, where I_R, I_G, and I_B represent the red, green, and blue intensity values of individual pixels, respectively. Within the thresholded region, individual pixels were classified as 1) red if $I_R/I_G \geq 1.8$; 2) green if $I_R/I_G \leq 1.1$; and 3) yellow if $1.1 < I_R/I_G < 1.8$. The classification limits were determined by calculating the I_R/I_G intensity ratio of individual pixels for green, yellow, and red. At least 10 pixels were analyzed per embryonic stage for determination of classification limits of each color. Using this classification strategy, area fractions occupied by green, yellow, and red fibers within each ROI were quantified. Relative content of green, yellow, and red regions were interpreted as areas of immature, intermediate, and mature collagen fibers, respectively (Dayan et al., 1989).

2.6 Immunohistochemical staining

Immunohistochemical staining was performed to detect TNC, COL3, LOX, MMP2 (gelatinase A), and MMP9 (gelatinase B), based on our previous protocols (Kuo et al., 2008; Brown et al., 2012) and with the following modifications. Briefly, antigen unmasking solution, BLOXALL® endogenous peroxidase blocking solution, normal horse serum (2.5%), ImmPRESS® HRP IgG polymers, and ImmPACT® DAB substrate (Peroxidase, HRP) were purchased from Vector Laboratories (CA, United States). Tissue sections were subjected to a citrate-based heat-mediated antigen retrieval, endogenous peroxidases were blocked for 10 min, and unspecific binding sites were blocked with 2.5% normal horse serum for 1 h. Sections were incubated over night with primary antibodies against TNC (M1-B4, Developmental Studies Hybridoma Bank (DSHB), Iowa, United States, 1:100), COL3 (3B2, DSHB, Iowa, United States, 1:100), LOX (ab31238, Abcam, 1:100), MMP2 (ab97779, Abcam, 1:100), and MMP9 (ab38898, Abcam, 1:100), or with normal horse serum as negative control. Hybridoma Product M1-B4 developed by Fambrough, D.M. and Hybridoma Product 3B2 developed by Mayne, R. were obtained from the DSHB, created by the NICHD of the NIH and maintained at the University of Iowa. After primary antibody incubation, slides were incubated for 1 h with either horse anti-mouse or horse anti-mouse IgG polymer. Subsequently, slides were developed with DAB substrate and counterstained with hematoxylin solution for 30 s (Gill No.1, Sigma, United States). Brightfield images were acquired with a ZEISS Axioscan. Z1 slide scanner with a 40x objective. Using ZEN lite software, three non-overlapping same-size (60 × 60 µm) regions of interest (ROIs) were selected equally distributed along the mid-portion of the TmAM and TmDM, avoiding the attachment zones to the muscle and the bone. Brightfield images were deconvoluted into DAB and hematoxylin signal using the H-DAB macro in Fiji. DAB-images were converted into 8-bit binary images and thresholded to isolate DAB-signal from background. Percentage area fraction of thresholded DAB signal was calculated. For each protein, the same threshold was used for all technical and biological replicates for all embryonic stages.

2.7 Statistical analysis

For all image analyses, a minimum of 3 biological replicates (N) were analyzed per embryonic stage. Per biological replicate (N), three ROIs, representing technical replicates ($n = 3$), were analyzed. Statistical analyses were performed using GraphPad Prism v.8.0.2 (La Jolla, CA, United States). Numerical data is presented as mean ± standard deviation. Each datapoint represents one biological replicate (N), which was determined by average values of 3 technical replicates (n) for that N. For comparison of cell density, cell morphology, collagen content,

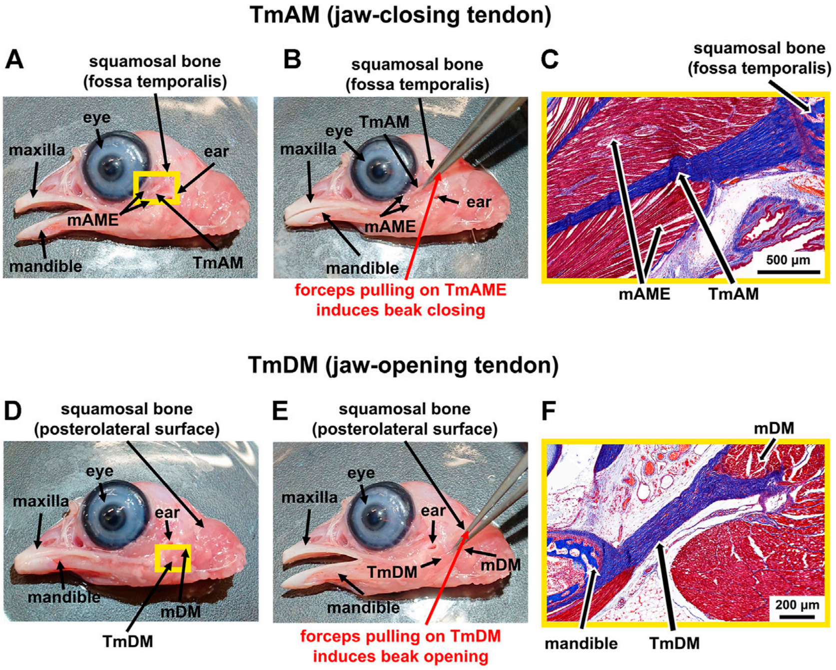

FIGURE 1
Identification of jaw-closing TmAM and jaw-opening TmDM in a d19 chick embryo. **(A)** Macroscopic view showing location of the jaw-closing TmAM with beak open. **(B)** Pulling the TmAM with a forceps induced closing of the jaw. **(C)** Mallory's trichrome staining of tissue regions highlighted by yellow rectangle in Figure 1A shows origin of TmAM (blue) at fossa temporalis of squamosal bone (dark blue) and attachment of mAME (red) along both sides of the TmAM. **(D)** Macroscopic view showing location of the jaw-opening TmDM with beak open. **(E)** Pulling the TmDM with a forceps induced opening of the jaw. **(F)** Mallory's trichrome staining of tissue regions highlighted by yellow rectangle in Figure 1D shows attachments at each end of the TmDM (blue) to mDM (red) and mandible (dark blue).

birefringence, collagen fiber maturity, and IHC-stained area fraction between d9 through d19 jaw tendons, one-way analysis of variance (ANOVA) for multiple comparisons was used followed by a Tukey's Post hoc test, after confirming normal distribution of the data (D'Agostino and Pearson omnibus normality test). When the above assumption was violated, non-parametric statistics and Kruskal–Wallis test for multiple comparisons was utilized. Statistical significance was set at $\alpha = 0.05$.

3 Results

3.1 Gross characterization of jaw-closing TmAM and jaw-opening TmDM

We grossly detected the TmAM as an intramuscular tendon that originates at the fossa temporalis of the squamosal bone and connects the mAME, a principal jaw adductor muscle, to the lower jaw (mandible) (Figure 1A). The TmAM is involved in rotating as well as lifting the lower jaw upwards and thus is a jaw-closing tendon (Figure 1B). We confirmed the TmAM by using forceps to gently pull on the tendon and showed a closing of the lower jaw (Figure 1B). The TmAM is a pennate tendon with muscle (mAME) attaching along the length of the TmAM on both sides and attachments at the squamosal bone and mandible (Figure 1C). We detected the TmDM as a prominent tendon that connects the mDM, a lower jaw rotator muscle, with the mandible at the posterior end of its medial surface (Figure 1D). The TmDM is involved in rotating the lower jaw as well as protracting the upper jaw (maxilla) and is thus a jaw-opening tendon (Figure 1E). We confirmed the TmDM by using forceps to gently pull on the tendon and demonstrated an opening of the lower jaw (Figure 1E). The TmDM is attached to muscle (mDM) on one end and to bone (mandible) on the other end (Figure 1F).

3.2 Histological characterization of jaw-closing TmAM and jaw-opening TmDM

TmAM and TmDM were first detected by embryonic d9 with histological stains. Tendon structures could not be identified histologically at d8 or earlier (not shown). In trichrome-stained sections, the TmAM was first detected at d9 via blue staining for collagen as well as via attachments to mAME which stained red

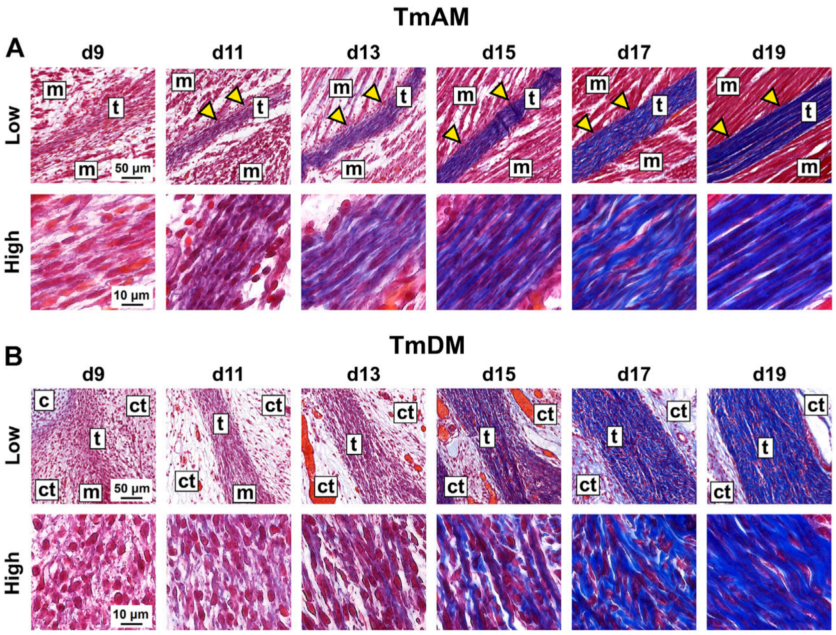

FIGURE 2
Collagen content appeared to increase and become more organized in jaw-closing TmAM and jaw-opening TmDM between d9 and d19. **(A)** Low and high magnification brightfield images of Mallory's trichrome staining of TmAM show collagen content (blue) increasing and becoming more organized between d9 and d19. Yellow arrows highlight muscles attaching along length of TmAM. **(B)** Low and high magnification brightfield images of Mallory's trichrome staining of TmDM show collagen content (blue) increasing and becoming more organized between d9 and d19. Tendon (t), muscle (m), cartilage (c), loose connective tissue (ct).

(Figure 2A). TmAM collagen content appeared to increase and become more organized between d9 and d19 (Figure 2A). Muscle fibers connecting to the TmAM were first detected at d11 (Figure 2A, yellow arrowheads). Similarly, the TmDM was first detected at d9 and distinguishable from surrounding tissue as a denser, more compact microstructure, unlike the surrounding loose connective tissue (Figure 2B). The collagenous matrix of the TmDM stained blue and the attached mDM stained red (Figure 2B). TmDM collagen content appeared to increase and become more organized between d9 and d19 (Figure 2B).

3.3 Characterization of tendon cell density and morphology

Quantitative image analysis of H&E-stained sections of the TmAM (Figure 3A) revealed a significant increase in cell density between d9 and d13 (Figure 3B). Cell density peaked at d13 in the TmAM and subsequently decreased significantly between d13 and d19 (Figure 3B). Nuclear aspect ratio increased significantly over time during development in the TmAM (Figure 3C). Nuclear circularity remained relatively constant between d9 and d13, decreased significantly after d13, and remained relatively constant between d15 and d19 in the TmAM (Figure 3D). Image analysis of H&E-stained sections of the TmDM (Figure 3A) showed cell density remained relatively constant between d9 and d17, and decreased significantly between d13 and d19 (Figure 3E). Nuclear aspect ratio increased significantly over time during development in the TmDM (Figure 3F). Nuclear circularity decreased significantly between d9 and d13 in the TmDM, and subsequently remained constant between d13 and d19 (Figure 3G). Based on these analyses, tendon cells in both the TmAM and the TmDM changed from a rounded to an elongated shape over time during development.

3.4 Characterization of collagen content, organization, and fiber maturity

TmAM collagen content, organization, and fiber maturity were analyzed in PSR-stained sections (Figure 4A). Image analysis revealed collagen content significantly increased from stage to stage between d9 and d13 in the TmAM and reached a plateau after d13 (Figure 4B). Analysis of collagen birefringence signal, a surrogate for collagen organization, revealed significant increases in the TmAM between d9 and d13 (Figure 4C). After d13, collagen birefringence signal reached a plateau in the TmAM (Figure 4C). Based on

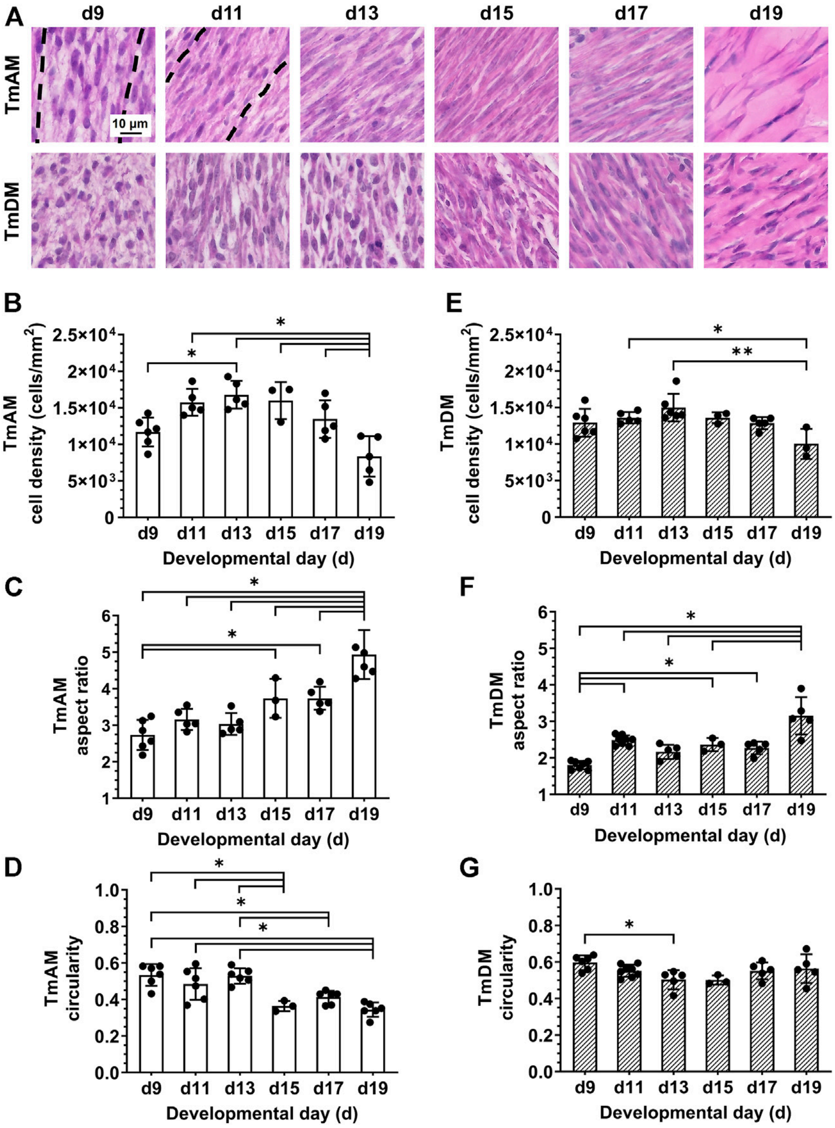

FIGURE 3

Cell density decreased and nuclei became more elongated in jaw-closing TmAM and jaw-opening TmDM between d9 and d19. **(A)** Representative brightfield images of H&E stained TmAM and TmDM. **(B)** Cell density increased significantly until d13 and subsequently decreased significantly until d19 in TmAM. **(C)** Nuclear aspect ratio increased significantly between d9 and d19 in TmAM. **(D)** Circularity decreased significantly between d9 and d19 in TmAM. **(E)** Cell density decreased significantly between d13 and d19 in TmDM. **(F)** Nuclear aspect ratio increased significantly between d9 and d19 in TmDM. **(G)** Circularity decreased significantly between d9 and d13 in TmDM.

these data, collagen content increased throughout development in the TmAM, and became more organized during early and intermediate developmental stages. Quantitative analysis of collagen fiber maturity in the TmAM revealed that the percentage of immature (green) fibers decreased significantly between d9 and d13 and remained consistently low after d11 (Figure 4D). Percentage of intermediate (yellow) fibers increased significantly in the TmAM between d9 and d13, peaked at d13, and decreased significantly between d13 and d19 (Figure 4E). Mature (red) fibers were first detected in the TmAM at d11 and percentage of mature fibers increased significantly between d11 and d19 (Figure 4F). Based on these data, collagen fibers in the TmAM progressed from mainly immature during early stages, to intermediate, and finally to mature during late stages of development.

TmDM collagen content, organization, and fiber maturity were also analyzed in PSR-stained sections (Figure 5A). Image analysis revealed collagen content in the TmDM increased significantly from stage to stage between d9 and d15 and reached a plateau after d15

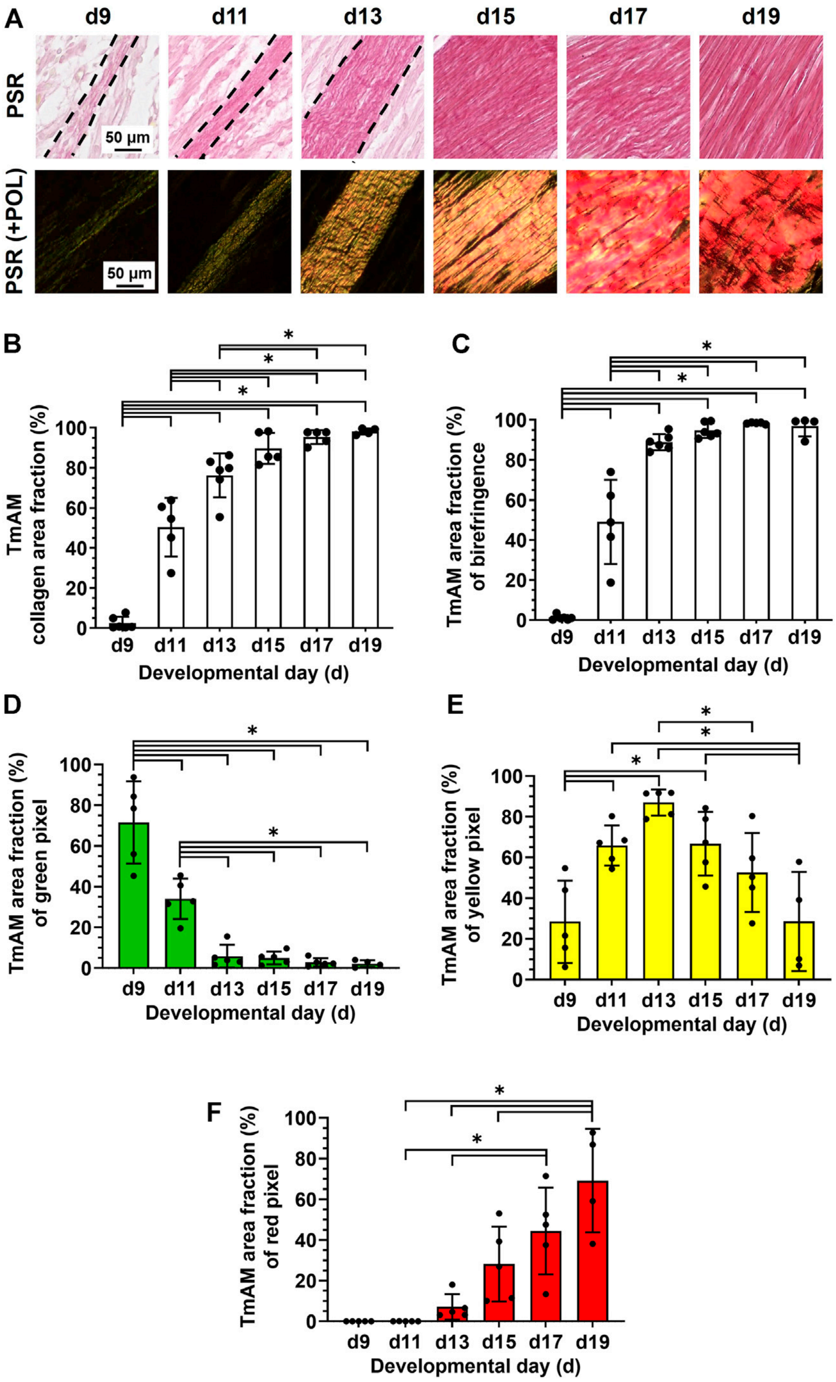

FIGURE 4
Collagen content increased, collagen became more aligned, and fiber maturity increased in jaw-closing TmAM between d9 and d19. **(A)** Representative brightfield and polarization (POL) images of PSR-stained TmAM. **(B)** Collagen content increased significantly over time and plateaued after d13 in TmAM. **(C)** In the TmAM, collagen birefringence signal increased significantly over time and reached a plateau after d13. **(D–F)** Collagen fibers progressed from mainly immature **(D)** during early stages, to intermediate **(E)**, and finally to mature **(F)** during late stages of development in TmAM.

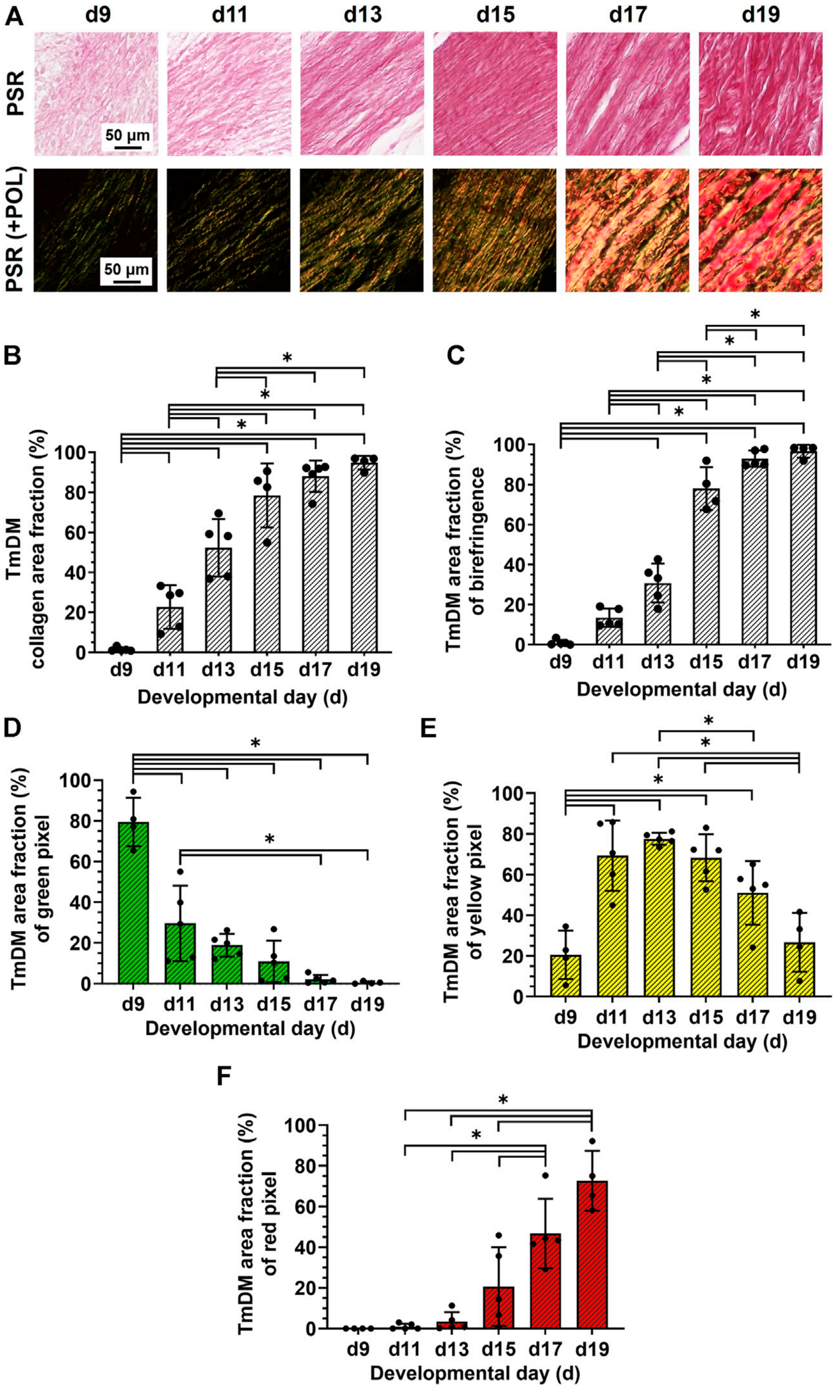

FIGURE 5
Collagen content increased, collagen became more aligned, and fiber maturity increased in jaw-opening TmDM between d9 and d19. **(A)** Representative brightfield and polarization images of PSR-stained TmDM. **(B)** Collagen content increased significantly over time and plateaued after d15 in TmDM. **(C)** In the TmDM, collagen birefringence increased significantly over time and reached a plateau after d17. **(D–F)** Collagen fibers in TmDM progressed from mainly immature **(D)** during early stages, to intermediate **(E)**, and finally to mature **(F)** during late stages of development.

(Figure 5B). Analysis of collagen birefringence signal revealed significant increases between d9 and d17 and then a plateau after d17 (Figure 5C). Based on this data, collagen content continued to increase in the TmDM throughout development, and became more organized during early and intermediate developmental stages. In the TmDM, percentage of immature (green) fibers decreased

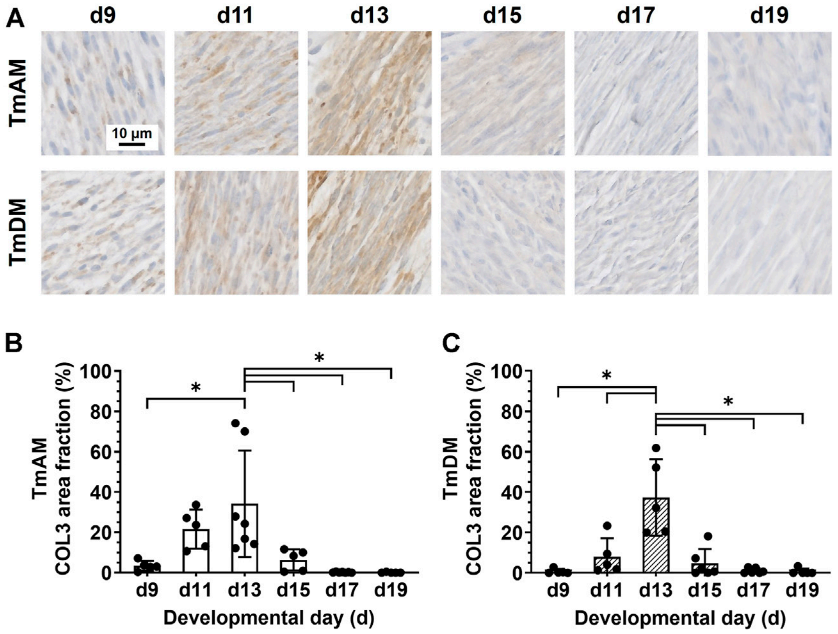

FIGURE 6
COL3 decreased after d13 in both jaw-closing TmAM and jaw-opening TmDM. **(A)** Representative brightfield images of COL3 IHC of TmAM and TmDM. **(B)** In TmAM, percentage area fraction positive for COL3 increased significantly until d13, and then decreased significantly in TmAM. **(C)** In TmDM, percentage area fraction positive for COL3 increased significantly until d13, and then decreased significantly after d13.

significantly between d9 and d11 (Figure 5D). Percentage of intermediate (yellow) fibers increased significantly in the TmDM between d9 and d13, peaked at d13, and subsequently decreased significantly between d13 and d19 (Figure 5E). Mature (red) fibers were first detected in the TmDM at d11 and increased significantly between d11 and d19 (Figure 5F). Based on these data, collagen fibers in the TmDM progressed from mainly immature during early stages, to intermediate, and finally to mature during late stages of development.

3.5 Spatiotemporal protein distribution of collagen type III (COL3)

Quantitative analysis of COL3 presence in the TmAM (Figure 6A) revealed that COL3 increased significantly between d9 and d13 (Figure 6B). COL3 peaked at d13 in the TmAM, decreased significantly after d13, and remained low until d19 (Figure 6B). Quantitative analysis of COL3 presence in the TmDM (Figure 6A) revealed that COL3 also increased significantly between d9 and d13 (Figure 6C). COL3 peaked at d13 in the TmDM, decreased significantly between d13 and d15, and remained low during later stages (Figure 6C).

3.6 Spatiotemporal protein distribution of tenascin-C (TNC)

Quantitative analysis of TNC presence in the TmAM (Figure 7A) revealed that TNC remained relatively high between d9 and d13, decreased significantly after d13, and remained low during later stages (Figure 7B). In contrast, quantitative analysis of TNC presence in the TmDM (Figure 7A) revealed that TNC was relatively low at d9 and d11, increased significantly between d9 and d13, and remained relatively constant between d13 and d19 (Figure 7C).

3.7 Spatiotemporal protein distribution of lysyl oxidase (LOX)

Quantitative analysis of LOX presence in the TmAM (Figure 8A) revealed that LOX was relatively constant during early and intermediate stages, and decreased significantly between d11 and d19 (Figure 8B). Quantitative analysis of LOX presence in the TmDM (Figure 8A) revealed that LOX levels were relatively constant between early and intermediate stages, decreased significantly between d11 and d17, and stayed constantly low until d19 (Figure 8C).

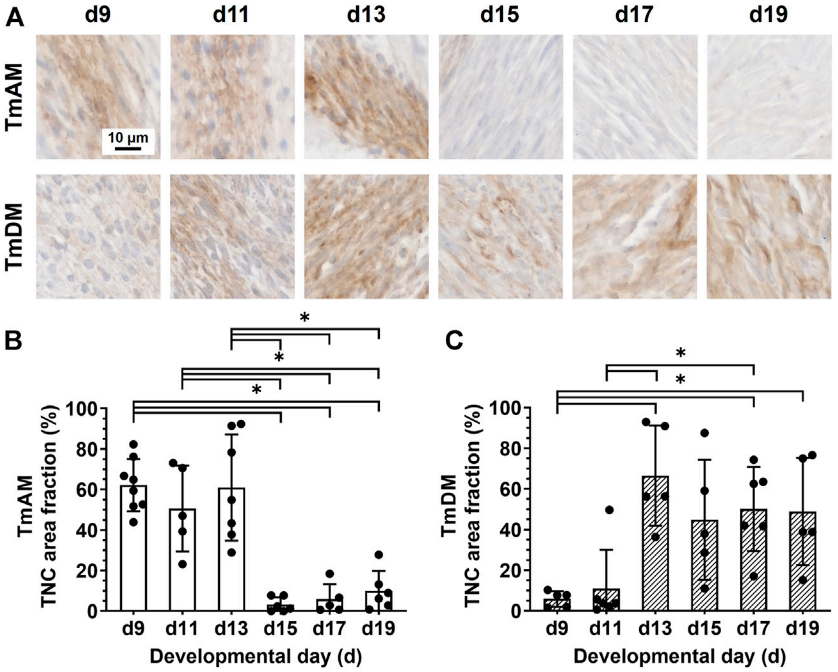

FIGURE 7
TNC showed different temporal patterns in jaw-closing TmAM and jaw-opening TmDM. **(A)** Representative brightfield images of TNC IHC of TmAM and TmDM. **(B)** In TmAM, percentage area fraction positive for TNC decreased significantly after d13. **(C)** In TmDM, percentage area fraction positive for TNC increased significantly until d13 and then plateaued.

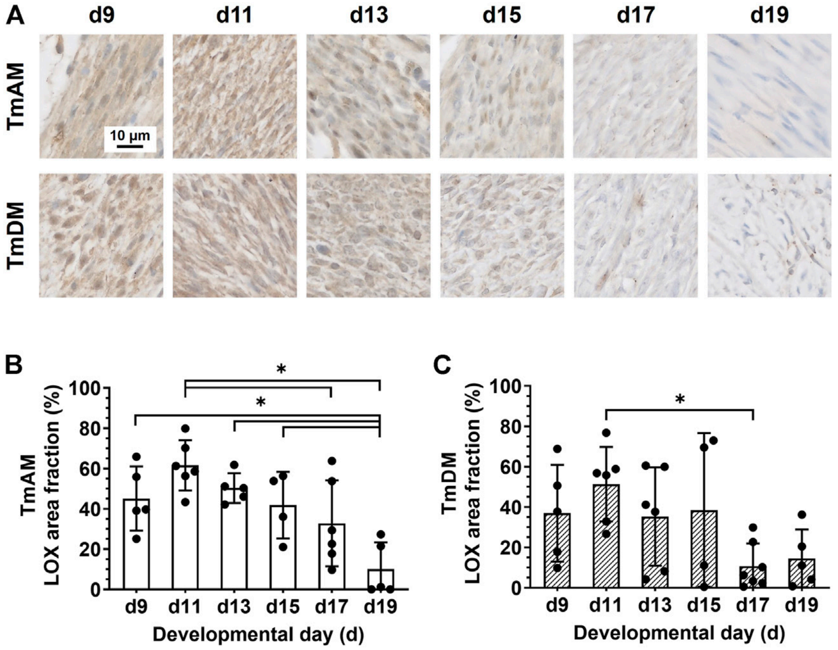

FIGURE 8
LOX decreased during late developmental stages in jaw-closing TmAM and jaw-opening TmDM. **(A)** Representative brightfield images of LOX IHC of TmAM and TmDM. **(B)** In TmAM, percentage area fraction positive for LOX decreased significantly from d15 to d19. **(C)** In TmDM, percentage area fraction positive for LOX decreased significantly between d11 and d17 in TmDM.

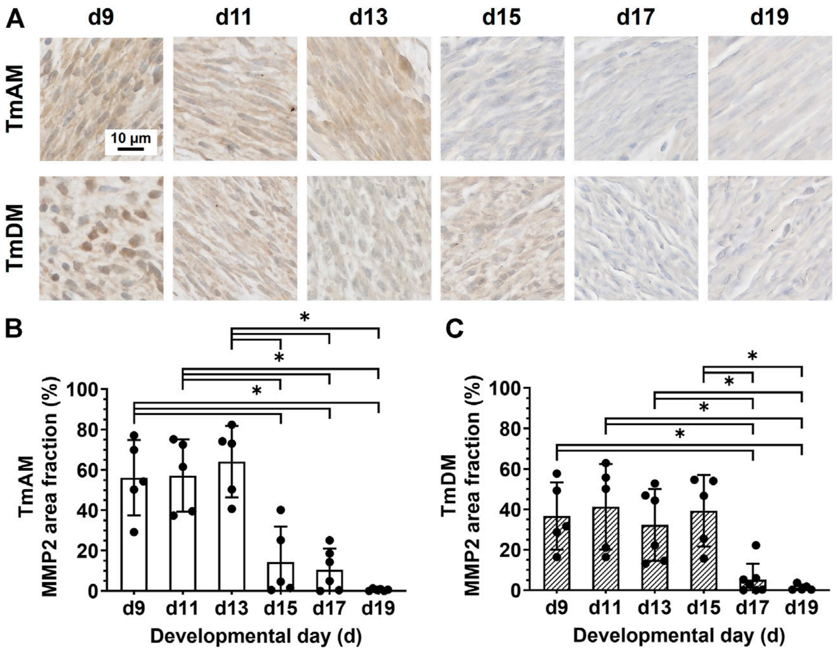

FIGURE 9
MMP2 decreased during mid-to-later stages in jaw-closing TmAM and jaw-opening TmDM. **(A)** Representative brightfield images of MMP2 IHC of TmAM and TmDM. **(B)** In TmAM, percentage area fraction positive for MMP2 decreased significantly after d13. **(C)** In TmDM, percentage area fraction positive for MMP2 decreased significantly after d15.

3.8 Spatiotemporal protein distribution of matrix metalloproteinase 2 (MMP2)

Quantitative analysis of MMP2 presence in the TmAM (Figure 9A) showed that MMP2 was relatively constant in the TmAM between d9 and d13, decreased significantly between d13 and d15, and remained constantly low until d19 (Figure 9B). Quantitative analysis of MMP2 presence in the TmDM (Figure 9A) showed that MMP2 remained relatively constant between d9 and d15 (Figure 9C). MMP2 decreased significantly between d15 and d17 and remained low until d19 (Figure 9C).

3.9 Spatiotemporal protein distribution of matrix metalloproteinase 9 (MMP9)

Quantitative analysis of MMP9 presence in the TmAM (Figure 10A) showed that MMP9 remained relatively constant between d9 and d17 and decreased significantly between d17 and d19 (Figure 10B). Quantitative analysis of MMP9 presence in the TmDM (Figure 10A) showed that MMP9 remained relatively constant between d9 and d19 (Figure 10C).

4 Discussion

CF tendon injuries and disorders can severely compromise jaw movements such as mastication, yet there are currently no treatments to regenerate and restore jaw function. Designing treatments for jaw tendon regeneration will require fundamental knowledge about jaw tendon development, which has been minimally studied. Here, we comprehensively characterized spatiotemporal patterns of cell and ECM morphology and protein distribution at distinct embryonic stages to provide markers for TmAM and TmDM development. Our results show markers that play a role in limb tendon formation are also present in jaw tendons during embryonic development, implicate COL3, TNC, LOX, MMP2, and MMP9 in jaw tendon development, and suggest TmAM and TmDM vary in their developmental programs. Our study supports the chick embryo as a novel model with which to study mechanisms of CF tendon development. This model, and the morphological and protein characterizations we present here, will enable future studies that could ultimately inform therapeutic approaches for CF tendon injuries and disorders.

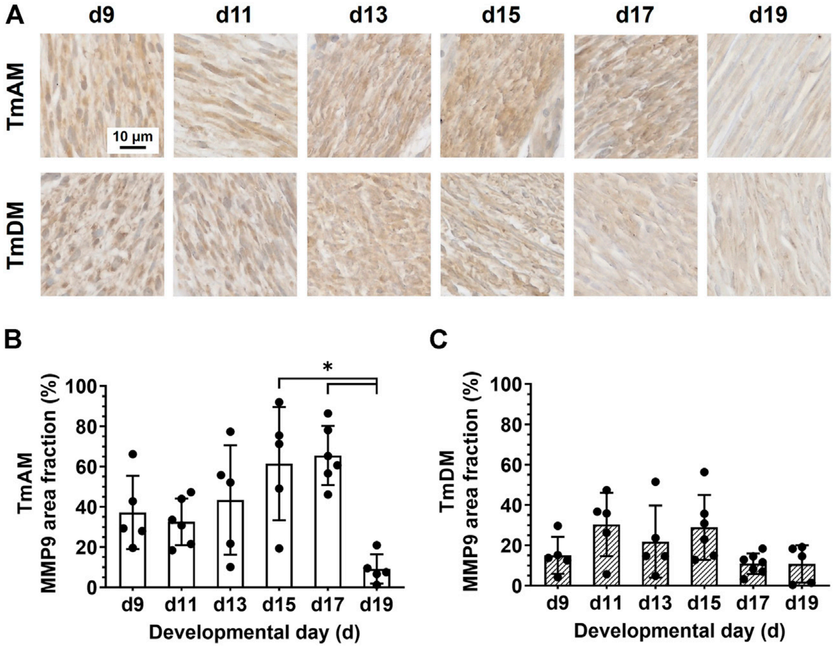

FIGURE 10
MMP9 was present in jaw-closing TmAM and jaw-opening TmDM between d9 and d19. **(A)** Representative brightfield images of MMP9 IHC of TmAM and TmDM. **(B)** In TmAM, percentage area fraction positive for MMP9 decreased significantly after d17. **(C)** In TmDM, percentage area fraction positive for MMP9 remained relatively constant between d9 and d19.

4.1 Chick embryos possess jaw-opening and jaw-closing tendons analogous to those in human

The TmAM is a multipennate tendon, as muscle fibers attach along the length of the tendon. Similar to our observations in the chick embryo, tendons of human jaw-closing muscles (masseter, temporalis, medial pterygoid) frequently exhibit a multipennate structure with muscle fibers inserting along the tendon length, which allows for transmission of high forces required for closing of the jaw (Van Eijden et al., 1997). Based on these findings, the TmAM could primarily be responsible for transmission of high forces during jaw-closing. In contrast, the jaw-opening TmDM is a non-pennate tendon, and attaches to muscle at the end of the tendon. Similar to our observations in the chick embryo, tendons of human jaw-opening muscles (lateral pterygoid, digastric, geniohyoid, mylohyoid) are also rarely pennate, and transmit forces to enable excursion and displacement of the jaw during opening (Van Eijden et al., 1997). Based on these findings, the TmDM could primarily be responsible for transmission of forces for excursion and displacement of the lower jaw during opening. These conclusions were corroborated by the jaw movements observed when gently pulling on the tendons (Figure 1).

4.2 Jaw tendons are detectable by d9

Both TmAM and TmDM could be first identified at d9, based on collagen presence, TNC labeling, and attachments to muscle and bone or cartilage (Figure 1C,F, Figure 2A,B, Figure 7A). TNC labels early distal tendon primordia between d5 and d7 as well as anatomically distinct tendons arising from these primordia after d7 (Chiquet and Fambrough, 1984; Chiquet-Ehrismann et al., 1986; Hurle et al., 1989; Hurle et al., 1990; Ros et al., 1995; Kardon, 1998). Previous studies by us and others have found that collagen matrix is first detectable via histological staining and second harmonic generation (SHG) imaging in chick embryo limb tendons at d9 (Ros et al., 1995; Marturano et al., 2013). Taken together, our results suggest TmAM and TmDM ECM development begin approximately at the same time as that of limb tendon during embryonic development.

4.3 TNC spatiotemporal distribution differs between TmAM and TmDM

TNC exhibited substantially different temporal patterns in the two jaw tendons. In particular, TNC protein distribution in the TmAM was relatively high until d13 and decreased afterwards, whereas in the TmDM it was relatively low during early stages and increased after d11 (Figure 7). TNC has been used as a marker for embryonic limb tendon (Chiquet and Fambrough, 1984; Hurle et al., 1989; Ros et al., 1995; Kardon, 1998; Edom-Vovard et al., 2002). However, even though TNC has been implicated in collagen fibrillogenesis during development of a range of tissues (Mackie, 1994; Riley et al., 1996; Chiquet-Ehrismann and Tucker, 2004), this role has not been definitively shown in tendon. To date, specific TNC functions during embryonic tendon development are largely unknown, yet our data confirms that jaw tendons possess TNC as well.

4.4 Jaw tendon cells shift from higher density and rounded morphology to lower density and elongated morphology during development

Cell density appeared constant in both TmAM and TmDM during early embryonic stages and decreased after d13 (Figures 3B,E). Our results here are similar to previously reported declines in tendon cell density during embryonic development based on quantitative DNA assays (Marturano et al., 2013). TmAM and TmDM cells became more elongated during development, reflected by increases in nuclear aspect ratio and decreases in circularity (Figures 3C,D,F,G). Similarly, limb tendon cells have been reported to switch from an initially round to a more elongated shape as embryonic development proceeds (Kannus, 2000). Previous studies have associated CF tendon cell elongation during embryonic development with major mechanical stimulatory events like the onset of muscle contractions in zebrafish (Subramanian et al., 2018). Interestingly, embryonic jaw movements such as “beak clapping”, the rapid opening and closing of the beak, has been observed as early as d9 (Kuo, 1932; Kuo, 1938), and is highest between d14 and d19 (Oppenheim, 1968). Our results on cell elongation in both jaw-opening and jaw-closing tendons demonstrate significant changes around these times (Figures 3C,D,F,G), potentially indicating that alterations in cell shape in the TmAM and TmDM could be possibly driven by beak clapping-induced mechanical stimulation.

4.5 Collagen content increases and becomes more organized during development

TmAM and TmDM both increased in collagen content (Figure 4B, Figure 5B), birefringence signal (Figure 4C, Figure 5C), and mature collagen fibers during embryonic development (Figure 4F, Figure 5F). Interestingly, TmAM and TmDM exhibited similar temporal patterns in the shift from predominately immature to intermediate to mature collagen fibers during development (Figures 4D–F, Figure 5D–F). Increases in birefringence during development suggested the ECM of both TmAM and TmDM were increasing in collagen fiber density, thickness, and alignment. Our observations in jaw tendons are consistent with our previous reports using SHG and biochemical analyses, which demonstrated that fibrillar collagen content, density, and alignment increase in limb tendons over time during development (Marturano et al., 2013; Marturano et al., 2014).

4.6 COL3 peaks when collagen content and birefringence start to plateau

COL3 is thought to be a critical regulator of collagen fibrillogenesis (Fleischmajer et al., 1988; Fleischmajer et al., 1990; Birk et al., 1997; Liu et al., 1997). COL3 is co-expressed with COL1 in limb tendon fascicles during chick embryonic development and appears to regulate the diameter of COL1 fibrils (Fleischmajer et al., 1988; Fleischmajer et al., 1990; Birk et al., 1997; Liu et al., 1997). Here, COL3 staining distribution increased until d13 in both TmAM and TmDM and decreased during subsequent stages (Figure 6). Similar temporal COL3 patterns have been reported in chick embryo limb tendons by us and others (Birk and Mayne, 1997; Kuo et al., 2008). Before d14, COL3 distribution is detected throughout limb tendon fascicles and is associated with smaller diameter collagen fibrils (Birk and Mayne, 1997; Kuo et al., 2008). After d14, COL3 decreases in limb tendon fascicles and collagen fibril diameter gradually increases (Fleischmajer et al., 1990; Birk et al., 1997; Liu et al., 1997; Kuo et al., 2008). Interestingly, COL3 continues to be detectable and associated with smaller diameter collagen fibrils in the regions surrounding the fascicles (Birk and Mayne, 1997; Kuo et al., 2008). In skin, COL3 deficient mice show abnormal collagen fibril diameter distribution (Liu et al., 1997). Taken together, the presence of COL3 in the TmAM and TmDM may suggest that COL3 contributes to regulation of collagen fibrillogenesis in CF tendons.

4.7 Presence of LOX during early and intermediate stages could imply that active collagen crosslinking is occurring

LOX staining was detected in both TmAM and TmDM throughout development and decreased during later stages (Figure 8). We previously showed that LOX activity and LOX-mediated crosslinking play critical roles in regulating the mechanical properties of embryonic limb tendon during development (Marturano et al., 2013; Pan et al., 2018). In particular, inhibition of LOX activity prevented increases in limb tendon elastic modulus by inhibiting the formation of new collagen crosslinks (Marturano et al., 2013). In another study, induction of paralysis during development led to lower LOX activity levels and elastic modulus in limb tendon as compared to controls (Pan et al., 2018). On the other hand, increase in movement frequency led to increases in elastic modulus, whereas inhibition of LOX activity during enhanced movement abrogated the increases in modulus (Pan et al., 2018). Notably, LOX-mediated crosslink density increases during limb tendon development, and these increases correlate with increases in proLOX and LOX activity levels (Marturano et al., 2014; Pan et al., 2018). Based on these data, it is possible that LOX-mediated crosslinking of collagen occurs during early and mid-developmental stages of TmAM and TmDM development. However, because the antibody in this study detects both proLOX and active LOX, future analyses would be needed to confirm formation of LOX-mediated collagen crosslinks.

4.8 MMP2 and MMP9 may be involved in tendon development

During embryonic development MMPs are involved in ECM remodeling of various tissues including blood vessels, bone, cartilage, skeletal muscle, lungs, and skin (Birkedal-Hansen et al., 1993; Ravanti and Kähäri, 2000; Page-McCaw et al., 2007; Krane and Inada, 2008), but have been minimally examined in tendon development. Here, we detected MMP2 (Figure 9) and MMP9 (Figure 10) protein in both TmAM and TmDM, suggesting roles in ECM remodeling during development. MMP-2 and MMP-9 show activity against denatured collagen type I and type III molecules and native non-fibrillar collagens (Birkedal-Hansen et al., 1993; Aimes and Quigley, 1995; Allan et al., 1995; Bigg et al., 2007; Baldwin et al., 2019). Additionally, MMP2 cleaves soluble and reconstituted fibrillar collagen type I, whereas MMP9 cleaves soluble collagen types I and III (Aimes and Quigley, 1995; Bigg et al., 2007). MMP2-deficient mice are smaller at birth, have slower growth rate, and exhibit distinct phenotypes of limb, trunk, and head bones, compared to wild-type littermates (Itoh et al., 1997; Inoue et al., 2006). During chick embryonic limb tendon development, MMP2 activity is highest prior to and during collagen fibril growth, implicating a role of MMP2 in fibril growth and matrix assembly (Jung et al., 2009). Similarly, MMP2 was relatively high in TmAM and TmDM during early and mid-developmental stages, and decreased significantly during later stages (Figure 9). Thus, it is possible that MMP2 is involved in remodeling the tendon ECM during early and mid-developmental stages. While little is known about MMP9 in tendon development, MMP9 is expressed at other sites of active tissue remodeling in the developing embryo (Reponen et al., 1994; Alexander et al., 1996), and MMP9 deletion leads to abnormal bone development (Vu et al., 1998). Here, MMP9 levels were relatively high until late developmental stages in TmAM, whereas they remained relatively consistent throughout development in TmDM (Figure 10). Considering the remodeling roles of MMP9 in other embryonic skeletal tissues, presence of MMP9 could indicate stage-specific roles in ECM remodeling in TmAM and TmDM during embryonic development.

4.9 TmAM and TmDM may follow different developmental programs

Despite many similarities, the developing TmAM and TmDM also exhibited distinct differences in temporal patterns of specific markers, potentially reflecting different developmental processes. The TmAM reaches a maximum collagen content and birefringence level earlier than TmDM during development, attributed in part to the slightly slower decrease in immature collagen fibers in the TmDM (Figures 4, 5). Differences in cell morphology (Figure 3) could imply differences in developmental processes between the TmAM and TmDM considering regulation of cell shape may be important for limb tendon development (Richardson et al., 2007). In particular, TmAM exhibited greater decreases in nuclear circularity together with greater increases in nuclear aspect ratio over time compared to TmDM, suggesting that TmAM cells elongate to a greater extent compared to TmDM cells. Pennate tendons accumulate muscle forces from varying angles arising from muscle attachments along the length of the tendon. Compared to non-pennate tendons, pennate tendons are functionally stiffer (Farris et al., 2013; Brukner et al., 2018). Based on the differences in how they each attach to muscle, it is likely that the TmAM and TmDM experience different mechanical stimuli during embryonic development. Different mechanical microenvironments experienced by the pennate TmAM and the non-pennate TmDM could be responsible for different temporal patterns in TNC, LOX, and MMP protein distribution (Figures 7–10), as TNC, LOX, MMP2, and MMP9 have each been reported to be regulated by mechanical loading. In particular, TNC expression levels decreased with limb immobilization but increased with treadmill running in Achilles tendons of rats (Järvinen et al., 1999; Järvinen et al., 2003). We have previously shown that paralysis of embryos reduces LOX activity levels in limb tendons compared to controls, suggesting LOX is regulated by mechanical loading of tendon during development (Pan et al., 2018). During late developmental stages, LOX decreases relatively earlier in TmDM compared to TmAM (Figure 8), which may suggest differences in LOX-mediated collagen crosslinking due to differences in mechanical loading of the two jaw tendons. Both MMP2 and MMP9 have been reported to be regulated by mechanical loading in tendon (Koskinen et al., 2004; Huisman et al., 2016). It would be interesting to investigate if earlier decreases in MMP2 (Figure 9) and later decreases in MMP9 (Figure 10) in the TmAM compared to the TmDM are regulated by differences in mechanical loading of the two jaw tendons. The differences in their muscle attachments could also expose TmAM and TmDM differently to muscle-secreted growth factors (Eloy-Trinquet et al., 2009; Wang et al., 2010; Subramanian and Schilling, 2015), which could also have contributed to the differences between TmAM and TmDM outlined above. Taken together, the effects of muscle-induced loading and muscle-secreted factors would be interesting to examine in future studies.

4.10 Limitations and future perspectives

The aim of this study was to characterize the chick embryo as a model to study CF tendon formation and to provide distinct morphological and immunohistochemical markers to describe ECM formation of jaw-opening and jaw-closing tendons. To further characterize specific roles of LOX and MMPs in CF tendon development, perturbation of protein and activity levels would be needed. Future studies could also employ additional methods to characterize different aspects of collagen matrix formation in greater detail. The antibodies available for immunohistochemistry at the time of this study could not differentiate between pro-form and active-form of the proteins, and thus future studies should assess LOX and MMP activity levels as well as protein levels of their respective pro-forms.

5 Conclusion

This report identified the jaw-closing TmAM and jaw-opening TmDM in the chick embryo that have similar functions as masticatory tendons in human and provided a detailed histological and immunohistochemical characterization of these tissues from early to late embryonic development. Our data implicate TNC, COL3, LOX, MMP2, and MMP9 in CF tendon formation and demonstrated that the two antagonistic tendons develop at different rates with respect to ECM formation and spatiotemporal distribution of tendon-associated and matrix remodeling molecules. Taken together, our study supports the chick embryo as a model with which to study CF tendon ECM development, the results of which could ultimately inform therapeutic approaches for CF tendon injuries and disorders.

Data availability statement

The original contributions presented in the study are included in the article/Supplementary Material, further inquiries can be directed to the corresponding author.

Ethics statement

The animal study was reviewed and approved by Institutional Animal Care and Use Committee at the University of Maryland, College Park.

Author contributions

SK and CK designed the experiments. AJ wrote the MATLAB routine for PSR image analyses, contributed intellectually to collagen imaging methods and analyses, and provided scientific and manuscript writing contributions. SK, EK, EL, TB, XL, RS and LB performed experiments and data analysis. SK and CK wrote the manuscript. CK conceived the project. All authors gave final approval for publication.

Funding

This study was supported in part by the National Institutes of Health under grant no. NIAMS/NIH R01AR072886 (to CK).

Conflict of interest

The authors declare that the research was conducted in the absence of any commercial or financial relationships that could be construed as a potential conflict of interest.

Publisher's note

References

Abramyan, J., and Richman, J. M. (2018). Craniofacial development: Discoveries made in the chicken embryo. *Int. J. Dev. Biol.* 62, 97–107. doi:10.1387/ijdb.170321ja

Aimes, R. T., and Quigley, J. P. (1995). Matrix metalloproteinase-2 is an interstitial collagenase. Inhibitor-free enzyme catalyzes the cleavage of collagen fibrils and soluble native type I collagen generating the specific 3/4- and 1/4-length fragments. *J. Biol. Chem.* 270, 5872–5876. doi:10.1074/jbc.270.11.5872

Alexander, C. M., Hansell, E. J., Behrendtsen, O., Flannery, M. L., Kishnani, N. S., Hawkes, S. P., et al. (1996). Expression and function of matrix metalloproteinases and their inhibitors at the maternal-embryonic boundary during mouse embryo implantation. *Development* 122, 1723–1736. doi:10.1242/dev.122.6.1723

Allan, J. A., Docherty, A. J., Barker, P. J., Huskisson, N. S., Reynolds, J. J., and Murphy, G. (1995). Binding of gelatinases A and B to type-I collagen and other matrix components. *Biochem. J.* 309 (1), 299–306. doi:10.1042/bj3090299

Baldwin, S. J., Kreplak, L., and Lee, J. M. (2019). MMP-9 selectively cleaves non-D-banded material on collagen fibrils with discrete plasticity damage in mechanically-overloaded tendon. *J. Mech. Behav. Biomed. Mat.* 95, 67–75. doi:10.1016/j.jmbbm.2019.03.020

Banos, C. C., Thomas, A. H., and Kuo, C. K. (2008). Collagen fibrillogenesis in tendon development: Current models and regulation of fibril assembly. *Birth Defects Res. C Embryo Today.* 84, 228–244. doi:10.1002/bdrc.20130

Bhattacharyya, B. (2013). Avian jaw function: Adaptation of the seven–muscle system and a review. *Proc. Zoological Soc.* 66, 75–85. Springer. doi:10.1007/s12595-012-0056-x

Bigg, H. F., Rowan, A. D., Barker, M. D., and Cawston, T. E. (2007). Activity of matrix metalloproteinase-9 against native collagen types I and III. *Febs J.* 274, 1246–1255. doi:10.1111/j.1742-4658.2007.05669.x

Birk, D. E., and Mayne, R. (1997). Localization of collagen types I, III and V during tendon development. Changes in collagen types I and III are correlated with changes in fibril diameter. *Eur. J. Cell Biol.* 72, 352–361.

Birk, D. E., Zycband, E. I., Woodruff, S., Winkelmann, D. A., and Trelstad, R. L. (1997). Collagen fibrillogenesis *in situ*: Fibril segments become long fibrils as the developing tendon matures. *Dev. Dyn.* 208, 291–298. doi:10.1002/(SICI)1097-0177(199703)208:3<291::AID-AJA1>3.0.CO;2-D

Birkedal-Hansen, H., Moore, W. G., Bodden, M. K., Windsor, L. J., Birkedal-Hansen, B., Decarlo, A., et al. (1993). Matrix metalloproteinases: A review. *Crit. Rev. Oral Biol. Med.* 4, 197–250. doi:10.1177/10454411930040020401

Bressler, H. B., Markus, M., Bressler, R. P., Friedman, S. N., and Friedman, L. (2020). Temporal tendinosis: A cause of chronic orofacial pain. *Curr. Pain Headache Rep.* 24, 18. doi:10.1007/s11916-020-00851-1

Brown, J. P., Lind, R. M., Burzesi, A. F., and Kuo, C. K. (2012). Elastogenic protein expression of a highly elastic murine spinal ligament: The ligamentum flavum. *PLoS One* 7, e38475. doi:10.1371/journal.pone.0038475

Brukner, P., Cook, J. L., and Purdam, C. R. (2018). Does the intramuscular tendon act like a free tendon? *Br. J. Sports Med.* 52, 1227–1228. doi:10.1136/bjsports-2017-098834

Canty, E. G., Starborg, T., Lu, Y., Humphries, S. M., Holmes, D. F., Meadows, R. S., et al. (2006). Actin filaments are required for fibripositor-mediated collagen fibril alignment in tendon. *J. Biol. Chem.* 281, 38592–38598. doi:10.1074/jbc.M607581200

Carril, J., Degrange, F. J., and Tambussi, C. P. (2015). Jaw myology and bite force of the monk parakeet (Aves, Psittaciformes). *J. Anat.* 227, 34–44. doi:10.1111/joa.12330

Chen, J. W., and Galloway, J. L. (2014). The development of zebrafish tendon and ligament progenitors. *Development* 141, 2035–2045. doi:10.1242/dev.104067

Chiquet, M., and Fambrough, D. M. (1984). Chick myotendinous antigen. I. A monoclonal antibody as a marker for tendon and muscle morphogenesis. *J. Cell Biol.* 98, 1926–1936. doi:10.1083/jcb.98.6.1926

Chiquet-Ehrismann, R., Mackie, E. J., Pearson, C. A., and Sakakura, T. (1986). Tenascin: An extracellular matrix protein involved in tissue interactions during fetal development and oncogenesis. *Cell* 47, 131–139. doi:10.1016/0092-8674(86)90374-0

Chiquet-Ehrismann, R., and Tucker, R. P. (2004). Connective tissues: Signalling by tenascins. *Int. J. Biochem. Cell Biol.* 36, 1085–1089. doi:10.1016/j.biocel.2004.01.007

Dayan, D., Hiss, Y., Hirshberg, A., Bubis, J. J., and Wolman, M. (1989). Are the polarization colors of picrosirius red-stained collagen determined only by the diameter of the fibers? *Histochemistry* 93, 27–29. doi:10.1007/BF00266843

Dupont, J. S., Jr., and Brown, C. E. (2012). The concurrency of temporal tendinitis with TMD. *Cranio.* 30, 131–135. doi:10.1179/crn.2012.019

Edom-Vovard, F., and Duprez, D. (2004). Signals regulating tendon formation during chick embryonic development. *Dev. Dyn.* 229, 449–457. doi:10.1002/dvdy.10481

Edom-Vovard, F., Schuler, B., Bonnin, M. A., Teillet, M. A., and Duprez, D. (2002). Fgf4 positively regulates scleraxis and tenascin expression in chick limb tendons. *Dev. Biol.* 247, 351–366. doi:10.1006/dbio.2002.0707

Eloy-Trinquet, S., Wang, H., Edom-Vovard, F., and Duprez, D. (2009). Fgf signaling components are associated with muscles and tendons during limb development. *Dev. Dyn.* 238, 1195–1206. doi:10.1002/dvdy.21946

Farris, D. J., Trewartha, G., Mcguigan, M. P., and Lichtwark, G. A. (2013). Differential strain patterns of the human Achilles tendon determined *in vivo* with freehand three-dimensional ultrasound imaging. *J. Exp. Biol.* 216, 594–600. doi:10.1242/jeb.077131

Fleischmajer, R., Perlish, J. S., Burgeson, R. E., Shaikh-Bahai, F., and Timpl, R. (1990). Type I and type III collagen interactions during fibrillogenesis. *Ann. N. Y. Acad. Sci.* 580, 161–175. doi:10.1111/j.1749-6632.1990.tb17927.x

Fleischmajer, R., Perlish, J. S., Timpl, R., and Olsen, B. R. (1988). Procollagen intermediates during tendon fibrillogenesis. *J. Histochem. Cytochem.* 36, 1425–1432. doi:10.1177/36.11.3049791

Hamburger, V., and Hamilton, H. L. (1951). A series of normal stages in the development of the chick embryo. *J. Morphol.* 88, 49–92. doi:10.1002/jmor.1050880104

Havis, E., Bonnin, M. A., Esteves De Lima, J., Charvet, B., Milet, C., and Duprez, D. (2016). TGFβ and FGF promote tendon progenitor fate and act downstream of muscle contraction to regulate tendon differentiation during chick limb development. *Development* 143, 3839–3851. doi:10.1242/dev.136242

Huisman, E., Lu, A., Jamil, S., Mousavizadeh, R., Mccormack, R., Roberts, C., et al. (2016). Influence of repetitive mechanical loading on MMP2 activity in tendon fibroblasts. *J. Orthop. Res.* 34, 1991–2000. doi:10.1002/jor.23207

Hurle, J. M., Hinchliffe, J. R., Ros, M. A., Critchlow, M. A., and Genis-Galvez, J. M. (1989). The extracellular matrix architecture relating to myotendinous pattern formation in the distal part of the developing chick limb: An ultrastructural, histochemical and immunocytochemical analysis. *Cell Differ. Dev.* 27, 103–120. doi:10.1016/0922-3371(89)90740-5

Hurle, J. M., Ros, M. A., Gañan, Y., Macias, D., Critchlow, M., and Hinchliffe, J. R. (1990). Experimental analysis of the role of ECM in the patterning of the distal tendons of the developing limb bud. *Cell Differ. Dev.* 30, 97–108. doi:10.1016/0922-3371(90)90078-b

Inoue, K., Mikuni-Takagaki, Y., Oikawa, K., Itoh, T., Inada, M., Noguchi, T., et al. (2006). A crucial role for matrix metalloproteinase 2 in osteocytic canalicular formation and bone metabolism. *J. Biol. Chem.* 281, 33814–33824. doi:10.1074/jbc.M607290200

Itoh, T., Ikeda, T., Gomi, H., Nakao, S., Suzuki, T., and Itohara, S. (1997). Unaltered secretion of beta-amyloid precursor protein in gelatinase A (matrix metalloproteinase 2)-deficient mice. *J. Biol. Chem.* 272, 22389–22392. doi:10.1074/jbc.272.36.22389

Järvinen, T. A., Józsa, L., Kannus, P., Järvinen, T. L., Hurme, T., Kvist, M., et al. (2003). Mechanical loading regulates the expression of tenascin-C in the myotendinous junction and tendon but does not induce de novo synthesis in the skeletal muscle. *J. Cell Sci.* 116, 857–866. doi:10.1242/jcs.00303

Järvinen, T. A., Jozsa, L., Kannus, P., Järvinen, T. L., Kvist, M., Hurme, T., et al. (1999). Mechanical loading regulates tenascin-C expression in the osteotendinous junction. *J. Cell Sci.* 112, 3157–3166. doi:10.1242/jcs.112.18.3157

Jones, M. E. H., Button, D. J., Barrett, P. M., and Porro, L. B. (2019). Digital dissection of the head of the rock dove (*Columba livia*) using contrast-enhanced computed tomography. *Zool. Lett.* 5, 17. doi:10.1186/s40851-019-0129-z

Jung, J. C., Wang, P. X., Zhang, G., Ezura, Y., Fini, M. E., and Birk, D. E. (2009). Collagen fibril growth during chicken tendon development: Matrix metalloproteinase-2 and its activation. *Cell Tissue Res.* 336, 79–89. doi:10.1007/s00441-009-0755-4

Kannus, P. (2000). Structure of the tendon connective tissue. *Scand. J. Med. Sci. Sports* 10, 312–320. doi:10.1034/j.1600-0838.2000.010006312.x

Kardon, G. (1998). Muscle and tendon morphogenesis in the avian hind limb. *Development* 125, 4019–4032. doi:10.1242/dev.125.20.4019

Kastelic, J., Galeski, A., and Baer, E. (1978). The multicomposite structure of tendon. *Connect. Tissue Res.* 6, 11–23. doi:10.3109/03008207809152283

Koskinen, S. O., Heinemeier, K. M., Olesen, J. L., Langberg, H., and Kjaer, M. (2004). Physical exercise can influence local levels of matrix metalloproteinases and their inhibitors in tendon-related connective tissue. *J. Appl. Physiol.* 96, 861–864. doi:10.1152/japplphysiol.00489.2003

Krane, S. M., and Inada, M. (2008). Matrix metalloproteinases and bone. *Bone* 43, 7–18. doi:10.1016/j.bone.2008.03.020

Kretlow, J. D., Mcknight, A. J., and Izaddoost, S. A. (2010). Facial soft tissue trauma. *Semin. Plast. Surg.* 24, 348–356. doi:10.1055/s-0030-1269764

Kuo, C. K., Petersen, B. C., and Tuan, R. S. (2008). Spatiotemporal protein distribution of TGF-betas, their receptors, and extracellular matrix molecules during embryonic tendon development. *Dev. Dyn.* 237, 1477–1489. doi:10.1002/dvdy.21547

Kuo, C. K., and Tuan, R. S. (2008). Mechanoactive tenogenic differentiation of human mesenchymal stem cells. *Tissue Eng. Part A* 14, 1615–1627. doi:10.1089/ten.tea.2006.0415

Kuo, Z. Y. (1932). Ontogeny of embryonic behavior in Aves. I. The chronology and general nature of the behavior of the chick embryo. *J. Exp. Zool.* 61, 395–430. doi:10.1002/jez.1400610304

Kuo, Z. Y. (1938). Ontogeny of embryonic behavior in Aves. XII. Stages in the development of physiological activities in the chick embryo. *Am. J. Psychol.* 51, 361–378. doi:10.2307/1415660

Liu, X., Wu, H., Byrne, M., Krane, S., and Jaenisch, R. (1997). Type III collagen is crucial for collagen I fibrillogenesis and for normal cardiovascular development. *Proc. Natl. Acad. Sci. U. S. A.* 94, 1852–1856. doi:10.1073/pnas.94.5.1852

Luo, E., Liu, H., Zhao, Q., Shi, B., and Chen, Q. (2019). Dental-craniofacial manifestation and treatment of rare diseases. *Int. J. Oral Sci.* 11, 9. doi:10.1038/s41368-018-0041-y

Mackie, E. J. (1994). Tenascin in connective tissue development and pathogenesis. *Perspect. Dev. Neurobiol.* 2, 125–132.

Marturano, J. E., Arena, J. D., Schiller, Z. A., Georgakoudi, I., and Kuo, C. K. (2013). Characterization of mechanical and biochemical properties of developing embryonic tendon. *Proc. Natl. Acad. Sci. U. S. A.* 110, 6370–6375. doi:10.1073/pnas.1300135110

Marturano, J. E., Schiele, N. R., Schiller, Z. A., Galassi, T. V., Stoppato, M., and Kuo, C. K. (2016). Embryonically inspired scaffolds regulate tenogenically differentiating cells. *J. Biomech.* 49, 3281–3288. doi:10.1016/j.jbiomech.2016.08.011

Marturano, J. E., Xylas, J. F., Sridharan, G. V., Georgakoudi, I., and Kuo, C. K. (2014). Lysyl oxidase-mediated collagen crosslinks may be assessed as markers of functional properties of tendon tissue formation. *Acta Biomater.* 10, 1370–1379. doi:10.1016/j.actbio.2013.11.024

Mcgurk, P. D., Swartz, M. E., Chen, J. W., Galloway, J. L., and Eberhart, J. K. (2017). *In vivo* zebrafish morphogenesis shows Cyp26b1 promotes tendon condensation and musculoskeletal patterning in the embryonic jaw. *PLoS Genet.* 13, e1007112. doi:10.1371/journal.pgen.1007112

Miura, M., Miura, Y., Sonoyama, W., Yamaza, T., Gronthos, S., and Shi, S. (2006). Bone marrow-derived mesenchymal stem cells for regenerative medicine in craniofacial region. *Oral Dis.* 12, 514–522. doi:10.1111/j.1601-0825.2006.01300.x

Navarro, J., Korcari, A., Nguyen, P., Bah, I., Alkhalifa, A., Fink, S., et al. (2022). Method development and characterization of chick embryo tendon mechanical properties. *J. Biomech.* 133, 110970. doi:10.1016/j.jbiomech.2022.110970

Nguyen, P. K., Deng, F., Assi, S., Paco, P., Fink, S., Stockwell, C., et al. (2021). Phenotype stability, expansion potential, and senescence of embryonic tendon cells *in vitro*. *J. Orthop. Res.* 40, 1584–1592. doi:10.1002/jor.25180

Nguyen, P. K., Pan, X. S., Li, J., and Kuo, C. K. (2018). Roadmap of molecular, compositional, and functional markers during embryonic tendon development. *Connect. Tissue Res.* 59, 495–508. doi:10.1080/03008207.2018.1511710

Oppenheim, R. W. (1968). Light responsivity in chick and duck embryos just prior to hatching. *Anim. Behav.* 16, 276–280. doi:10.1016/0003-3472(68)90009-2

Page-Mccaw, A., Ewald, A. J., and Werb, Z. (2007). Matrix metalloproteinases and the regulation of tissue remodelling. *Nat. Rev. Mol. Cell Biol.* 8, 221–233. doi:10.1038/nrm2125

Pan, X. S., Li, J., Brown, E. B., and Kuo, C. K. (2018). Embryo movements regulate tendon mechanical property development. *Philos. Trans. R. Soc. Lond. B Biol. Sci.* 373, 20170325. doi:10.1098/rstb.2017.0325

Peterson, B. E., Rolfe, R. A., Kunselman, A., Murphy, P., and Szczesny, S. E. (2021). Mechanical stimulation via muscle activity is necessary for the maturation of tendon multiscale mechanics during embryonic development. *Front. Cell Dev. Biol.* 9, 725563. doi:10.3389/fcell.2021.725563

Ravanti, L., and Kähäri, V. M. (2000). Matrix metalloproteinases in wound repair (review). *Int. J. Mol. Med.* 6, 391–407. doi:10.3892/ijmm.6.4.391

Reponen, P., Sahlberg, C., Munaut, C., Thesleff, I., and Tryggvason, K. (1994). High expression of 92-kD type IV collagenase (gelatinase B) in the osteoclast lineage during mouse development. *J. Cell Biol.* 124, 1091–1102. doi:10.1083/jcb.124.6.1091

Richardson, S. H., Starborg, T., Lu, Y., Humphries, S. M., Meadows, R. S., and Kadler, K. E. (2007). Tendon development requires regulation of cell condensation and cell shape via cadherin-11-mediated cell-cell junctions. *Mol. Cell. Biol.* 27, 6218–6228. doi:10.1128/MCB.00261-07

Riley, G. P., Harrall, R. L., Cawston, T. E., Hazleman, B. L., and Mackie, E. J. (1996). Tenascin-C and human tendon degeneration. *Am. J. Pathol.* 149, 933–943.

Rocchi, G., Fadda, M. T., Marianetti, T. M., Reale, G., and Iannetti, G. (2007). Craniofacial trauma in adolescents: Incidence, etiology, and prevention. *J. Trauma* 62, 404–409. doi:10.1097/01.ta.0000197627.05242.a4

Ros, M. A., Rivero, F. B., Hinchliffe, J. R., and Hurle, J. M. (1995). Immunohistological and ultrastructural study of the developing tendons of the avian foot. *Anat. Embryol.* 192, 483–496. doi:10.1007/BF00187179

Schiele, N. R., Von Flotow, F., Tochka, Z. L., Hockaday, L. A., Marturano, J. E., Thibodeau, J. J., et al. (2015). Actin cytoskeleton contributes to the elastic modulus of embryonic tendon during early development. *J. Orthop. Res.* 33, 874–881. doi:10.1002/jor.22880

Schindelin, J., Arganda-Carreras, I., Frise, E., Kaynig, V., Longair, M., Pietzsch, T., et al. (2012). Fiji: An open-source platform for biological-image analysis. *Nat. Methods* 9, 676–682. doi:10.1038/nmeth.2019

Schweitzer, R., Chyung, J. H., Murtaugh, L. C., Brent, A. E., Rosen, V., Olson, E. N., et al. (2001). Analysis of the tendon cell fate using Scleraxis, a specific marker for tendons and ligaments. *Development* 128, 3855–3866. doi:10.1242/dev.128.19.3855

Su, P., Paquet, C., O'dell, K., Reinstadler, D., Kokot, N., Granzow, J., et al. (2021). Trends in operative complex middle and upper maxillofacial trauma: A 17-year study. *Laryngoscope* 131, 1985–1989. doi:10.1002/lary.29442

Subramanian, A., Kanzaki, L. F., Galloway, J. L., and Schilling, T. F. (2018). Mechanical force regulates tendon extracellular matrix organization and tenocyte morphogenesis through TGFbeta signaling. *Elife* 7, e38069. doi:10.7554/eLife.38069

Subramanian, A., and Schilling, T. F. (2015). Tendon development and musculoskeletal assembly: Emerging roles for the extracellular matrix. *Development* 142, 4191–4204. doi:10.1242/dev.114777

To, K. H. T., O'brien, H. D., Stocker, M. R., and Gignac, P. M. (2021). Cranial musculoskeletal description of black-throated finch (aves: Passeriformes: Estrildidae) with DiceCT. *Integr. Org. Biol.* 3, obab007. doi:10.1093/iob/obab007

Twigg, S. R., and Wilkie, A. O. (2015). New insights into craniofacial malformations. *Hum. Mol. Genet.* 24, R50–R59. doi:10.1093/hmg/ddv228

Van Eijden, T. M., Korfage, J. A., and Brugman, P. (1997). Architecture of the human jaw-closing and jaw-opening muscles. *Anat. Rec.* 248, 464–474. doi:10.1002/(sici)1097-0185(199707)248:3<464::aid-ar20>3.3.co;2-4

Vu, T. H., Shipley, J. M., Bergers, G., Berger, J. E., Helms, J. A., Hanahan, D., et al. (1998). MMP-9/gelatinase B is a key regulator of growth plate angiogenesis and apoptosis of hypertrophic chondrocytes. *Cell* 93, 411–422. doi:10.1016/s0092-8674(00)81169-1

Wang, H., Noulet, F., Edom-Vovard, F., Tozer, S., Le Grand, F., and Duprez, D. (2010). Bmp signaling at the tips of skeletal muscles regulates the number of fetal muscle progenitors and satellite cells during development. *Dev. Cell* 18, 643–654. doi:10.1016/j.devcel.2010.02.008

Warren, S. M., Fong, K. D., Chen, C. M., Loboa, E. G., Cowan, C. M., Lorenz, H. P., et al. (2003). Tools and techniques for craniofacial tissue engineering. *Tissue Eng.* 9, 187–200. doi:10.1089/107632703764664666

Zhang, W., and Yelick, P. C. (2018). Craniofacial tissue engineering. *Cold Spring Harb. Perspect. Med.* 8, a025775. doi:10.1101/cshperspect.a025775

frontiers | Frontiers in Cardiovascular Medicine

TYPE Original Research
PUBLISHED 28 November 2022
DOI 10.3389/fcvm.2022.993310

EDITED BY
Rajprasad Loganathan,
Wichita State University, United States

REVIEWED BY
Yoshito Yamashiro,
National Cerebral and Cardiovascular Center, Japan
Abhijit Deb Roy,
Johns Hopkins Medical Institute,
United States

*CORRESPONDENCE
Lauren D. Black III
lauren.black@tufts.edu

[†]PRESENT ADDRESSES
Corin Williams,
Draper, Cambridge, MA, United States

Raymond M. Wang,
Department of Bioengineering,
University of California, San Diego, La Jolla, CA, United States

Kelly E. Sullivan,
Vertex Pharmaceuticals, Boston, MA,
United States

Whitney L. Stoppel,
Department of Chemical Engineering,
University of Florida, Gainesville, FL,
United States

[‡]These authors have contributed equally to this work

SPECIALTY SECTION
This article was submitted to Cardiovascular Biologics and Regenerative Medicine,
a section of the journal
Frontiers in Cardiovascular Medicine

RECEIVED 13 July 2022
ACCEPTED 10 October 2022
PUBLISHED 28 November 2022

CITATION
Watson MC, Williams C, Wang RM, Perreault LR, Sullivan KE, Stoppel WL and Black LD III (2022) Extracellular matrix and cyclic stretch alter fetal cardiomyocyte proliferation and maturation in a rodent model of heart hypoplasia.
Front. Cardiovasc. Med. 9:993310.
doi: 10.3389/fcvm.2022.993310

Extracellular matrix and cyclic stretch alter fetal cardiomyocyte proliferation and maturation in a rodent model of heart hypoplasia

Matthew C. Watson[1,2‡], Corin Williams[1†‡], Raymond M. Wang[1†], Luke R. Perreault[1], Kelly E. Sullivan[1†], Whitney L. Stoppel[1†] and Lauren D. Black III[1,3*]

[1]Department of Biomedical Engineering, Tufts University, Medford, MA, United States, [2]Department of Mechanical Engineering, Tufts University, Medford, MA, United States, [3]Cellular, Molecular, and Developmental Biology Program, Sackler School for Graduate Biomedical Sciences, Tufts University School of Medicine, Boston, MA, United States

Introduction: Birth defects, particularly those that affect development of the heart, are a leading cause of morbidity and mortality in infants and young children. Babies born with heart hypoplasia (heart hypoplasia) disorders often have a poor prognosis. It remains unclear whether cardiomyocytes from hypoplastic hearts retain the potential to recover growth, although this knowledge would be beneficial for developing therapies for heart hypoplasia disorders. The objective of this study was to determine the proliferation and maturation potential of cardiomyocytes from hypoplastic hearts and whether these behaviors are influenced by biochemical signaling from the extracellular matrix (ECM) and cyclic mechanical stretch.

Method: Congenital diaphragmatic hernia (CDH)-associated heart hypoplasia was induced in rat fetuses by maternal exposure to nitrofen. Hearts were isolated from embryonic day 21 nitrofen-treated fetuses positive for CDH (CDH+) and from fetuses without nitrofen administration during gestation.

Results and discussion: CDH+ hearts were smaller and had decreased myocardial proliferation, along with evidence of decreased maturity compared to healthy hearts. In culture, CDH+ cardiomyocytes remained immature and demonstrated increased proliferative capacity compared to their healthy counterparts. Culture on ECM derived from CDH+ hearts led to a significant reduction in proliferation for both CDH+ and healthy cardiomyocytes. Healthy cardiomyocytes were dosed with exogenous nitrofen to examine whether nitrofen may have an aberrant effect on the proliferative ability of cardiomyocyte, yet no significant change in proliferation was observed. When subjected to stretch, CDH+ cardiomyocytes underwent lengthening of sarcomeres while healthy cardiomyocyte sarcomeres were unaffected. Taken together, our results suggest that alterations to environmental cues such as ECM and stretch may be important factors in the pathological progression of heart hypoplasia.

KEYWORDS

cardiomyocytes, proliferation, heart hypoplasia, extracellular matrix (ECM), mechanical stretch

Introduction

Congenital diaphragmatic hernia (CDH) is a serious birth defect that occurs in ∼1 in 2,500–3,000 live births. Only ∼16% of prenatally diagnosed CDH patients are expected to survive past the first year of life (1). Failure of the diaphragm to close permits intrusion of visceral organs into the thoracic cavity and subsequent compression of the developing heart and lungs. Heart and/or lung hypoplasia is associated with a particularly poor prognosis in CDH (2). Interestingly, patients born with mild to moderate heart hypoplasia exhibit restored heart growth after surgical repair of CDH (3); however, the underlying mechanisms are unknown. A better understanding of the factors that influence heart growth during development is not only critical for improving therapies for children with heart defects but would also be invaluable to the field of cardiac regeneration as a whole.

Cardiomyocyte proliferation plays a key role in cardiac growth during fetal development (4) and may provide an explanation for restored heart growth in repaired CDH. In other forms of heart hypoplasia, such as Hypoplastic Left Heart Syndrome, there is evidence that cardiomyocyte proliferation is severely diminished (5), although this has not been established in CDH-associated heart hypoplasia. Cardiomyocyte behavior can be regulated by a variety of biochemical and biophysical cues, such as the extracellular matrix (ECM) (6, 7), growth factors (6, 8), cell-cell contacts (9), substrate stiffness (10, 11), and mechanical stretch (12). Although current data is limited, studies suggest that at least some of these signals may be altered in the developing hypoplastic heart (13).

It is intriguing to consider the possibility that cardiomyocyte proliferation can be recovered in heart hypoplasia if pathological conditions are removed, or healthy biochemical/biophysical environments are restored. The experimental manipulation of mechanical loading in embryonic zebrafish (14) and chick hearts (15) motivated the use of fetal aortic annuloplasty in severe HLHS in an attempt to restore normal blood flow and, subsequently, left heart growth (16). In this study, we hypothesized that cardiomyocyte proliferation is reduced in CDH-associated heart hypoplasia, but that the cells retain the ability to proliferate if they are removed from the hypoplastic environment. We used the nitrofen model of CDH in rats, which is thought to be similar in etiology and phenotype to human CDH (17–19). In addition to studying proliferation in native hearts, we isolated cardiac cells and assessed their response to two external cues that have been implicated in heart hypoplasia defects: the biochemical signaling of the ECM, which is thought to be structurally immature in heart hypoplasia (20, 21), and cyclic stretch, which is diminished in heart hypoplasia (12). Our *in vitro* culture systems allowed us to systematically study these cues independently, which would not be possible *in vivo*. We found that CDH+ cardiomyocytes were more proliferative than healthy cardiomyocytes when placed in culture, and that ECM and cyclic stretch (1 Hz, 5% amplitude) differentially regulated proliferation and maturation.

Materials and methods

Nitrofen model of congenital diaphragmatic hernia

All animal procedures were performed in accordance with the Institutional Animal Care and Use Committee at Tufts University and the NIH Guide for the Care and Use of Laboratory Animals. Pregnant Sprague-Dawley rats at gestational day E10 (purchased from Charles River Laboratories, Wilmington, MA) were subjected to short Isoflurane anesthesia and immediately gavaged with a single dose of 100 mg nitrofen (Wako Pure Chemical Industries, Japan) dissolved in 2 ml olive oil. Control animals received olive oil alone, similar to previously described methods (13). Pregnancy then progressed until E21, at which point the dams were sacrificed by CO_2 inhalation. E21 was chosen as the time point as this was immediately pre-birth and it has been previously shown that the defects caused by CDH are postnatally lethal. The fetuses were harvested for the studies described below.

Fetal heart harvest

Immediately after harvest, fetuses were placed on ice, and euthanized by decapitation. The chest wall was carefully opened above the diaphragm and the heart and lungs were removed. The diaphragm was then checked for the presence of CDH. Nitrofen treatment at E10 resulted in CDH in ∼80–85% of the fetuses, similar to what others have found (22). As so few nitrofen-treated CDH negative hearts were found (~2–4 out of 12–16 hearts per litter), they were not included in the present study. CDH was never detected in control fetuses. Nitrofen-treated CDH positive (CDH+) and control ("healthy") hearts were weighed prior to further characterization.

Histology and imaging of native heart sections

Whole hearts were fixed by immersion in 4% paraformaldehyde at 4°C overnight. After washing with phosphate buffered saline (PBS), the samples were cryo-protected in sucrose solution (30% wt/vol), and then embedded in Tissue Tek optimum cutting temperature (OCT) compound. The hearts were sectioned (thickness of 7 μm) on a Leica CM 1950 CryoStat. Heart slices were stored at −20°C until use. OCT compound was removed by washing with PBS prior to staining with hematoxylin and eosin (H&E) to visualize gross heart structure. Hearts were imaged on a Keyence BZ-X700 fluorescent microscope using a color camera. The thickness of the compact zone of the left ventricular free wall was measured with ImageJ using H&E stained sections.

ECM composition

A subset of CDH+ and healthy hearts were used to determine extracellular matrix (ECM) composition by liquid chromatography tandem mass spectrometry (LC-MS/MS), similar to our previous studies of cardiac ECM (7). Immediately after weighing, freshly isolated whole hearts were decellularized in 0.1% sodium dodecyl sulfate (SDS) for 48 h at room temperature with agitation on an orbital shaker. The resulting ECM was then incubated in 0.1% TritonX-100 (Amresco, Solon, OH) for ~3–4 h, washed with distilled water, frozen, and lyophilized overnight (Labconco, Kansas City, MO). The ECM of individual fetal hearts was solubilized in 200 μl urea solution (5 M urea, 2 M thiourea, 50 mM DTT, 0.1% SDS) (23) for 20 h with agitation. Finally, the ECM was precipitated in acetone and analyzed *via* LC-MS/MS within 24 h at the Beth Israel Deaconess Medical Center Mass Spectrometry Core Facility. Among the samples ($N = 3$ for each condition), 34 unique ECM components were identified and their relative percentages in the total ECM composition was determined from spectrum counts.

Immunocytochemistry

To study proliferation and sarcomere development in the native healthy and CDH+ hearts, sections were stained for nuclei (Hoechst 33258), Ki67 (Abcam, rabbit polyclonal), and sarcomeric α-actinin (Sigma, mouse monoclonal). Briefly, the samples were washed with PBS, then blocked with 5% donkey serum and 1% bovine serum albumin (BSA) for 1 h at room temperature. Incubation with primary antibodies was for 1 h, followed by 3 PBS washes, then incubation with secondary antibodies (AlexaFluor 488 donkey anti-rabbit IgG, AlexaFluor 555 donkey anti-mouse IgG; Invitrogen) for 1 h. After washing with PBS, the samples were imaged on an Olympus IX8I microscope with Metamorph Basic software (version 7.7.4.0, Molecular Devices). Image analysis to determine cardiomyocyte proliferation and sarcomere length was carried out as described below in sections Cell proliferation measurements and Cardiac cell culture with exogenous nitrofen.

Cardiac gene expression by quantitative PCR

A panel of cardiac genes was analyzed by PCR. RNA was isolated from fetal hearts using the RNeasy® Mini Kit (Qiagen Sciences, Germantown, MD) per the manufacturer's instructions. RNA concentration was determined using a Nanodrop 2000 Spectrophotometer (Thermo Scientific, Waltham, MA) and purity was assessed by the ratio of the 260/280 absorbance readings. Samples with high purity were then used to make cDNA using the High Capacity cDNA Reverse Transcription Kit (Applied Biosystems, Foster City, CA) per the manufacturer's instructions. cDNA was loaded into the wells of a MicroAmp® Optical 96-well reaction plate with 10 μl of 2× TaqMan® Gene Expression Master Mix and 1 μl of predesigned 20× TaqMan® Gene Expression Assay primers for the specific gene of interest (Applied Biosystems, Foster City, CA) diluted in nuclease-free water to a final volume of 20 μl. Samples were probed for gene expression related to contractile function (MYH6, MYH7, TNNT2, TNNI3, ACTN2, ATPA2), gap junction signaling (GJA1, CDH2) and early markers of the cardiac lineage (GATA4, GATA6, NKX2-5). Expression of each gene was normalized to GAPDH values. Quantitative RT-PCR was performed using the Mx3000P QPCR System (Agilent Technologies, Lexington, MA) with incubation parameters of 2 min at 50°C, 10 min at 95°C and 40 cycles of 15 s at 95°C followed by 1 min at 60°C. Ct values were determined by the software provided with the Mx3000P QPCR System and differences in mRNA expression were calculated by the $2^{-\Delta\Delta ct}$ method (24) based on validation tests performed by Applied Biosystems.

Cardiac cell isolation and culture

Cells from CDH+ and healthy control hearts were isolated according to our previously described methods (25). Briefly, hearts were isolated from euthanized fetal pups at E21, the ventricles were minced, and the tissue underwent 7 × 7 min digestions in collagenase type II (Worthington Biochemical Corp, Lakewood, NJ) and sterile PBS supplemented with 20 mM glucose. Cells were counted with a hemocytometer and seeded at a density of 100,000 cells/cm^2 into tissue culture polystyrene 48-well plates. The culture medium contained 15% fetal bovine serum (FBS) in Dulbecco's Modified Eagle Medium (DMEM) with 1% penicillin-streptomycin and was changed every 2 days. The cells were fixed and stained with Hoechst, Ki67, and α-actinin at various time points, imaged, and analyzed as described below in sections Cell proliferation measurements and Cardiac cell culture with exogenous nitrofen.

Cell proliferation measurements

Cell numbers and proliferation were determined using custom pipelines in CellProfiler (release 11710, the Broad Institute). Total cell nuclei were determined from the Hoechst stain and proliferating cells (Ki67+ nuclei) were determined from the Ki67 stain. The α-actinin stain used to label cardiomyocytes was used as a "mask" to identify cardiomyocyte-specific nuclei and proliferation. Total cell and cardiomyocyte density was calculated using the total imaged area (converted to mm^2) for each sample. Cardiomyocyte-specific proliferation was measured as the percentage of proliferating cells that were also positive for sarcomeric α-actinin [(Ki67+ α-actinin+)/Ki67+].

Cardiac cell culture with exogenous nitrofen

To determine whether nitrofen would affect the behavior of healthy cardiomyocytes, cardiomyocytes freshly isolated from neonatal hearts were seeded onto 12 well plates at a density of 50,000 cells/cm^2. Cells were cultured in serum containing medium until beating was observed. Once beating was observed, cells were treated with medium containing nitrofen at 50 and 100 ug/ml. Dosages were determined by estimating the concentrations of nitrofen delivered to each rat fetus. Serum containing medium was used as a control. For normalization purposes, a subset of each group was fixed at Cells were treated on days 1 and 2, and wells from each group were fixed on either 1 day prior to the first nitrofen treatment or 3 days after the beginning of nitrofen treatment. Cells were stained, imaged, and analyzed for proliferation as described above in section Cell proliferation measurements.

Sarcomere measurements

Sarcomere length has been used as a measure of cardiomyocyte maturation (10, 26, 27). To adequately visualize sarcomeres, images of α-actinin staining at 40× magnification were acquired. Analysis was performed using ImageJ software (NIH, version 1.45s). When organized sarcomeres were observed, a line was manually drawn across multiple sarcomeres perpendicular to alignment. The "Plot Profile" function was used to display the staining intensity across the line. The number of sarcomeres in a given length was counted and the average measured sarcomere length was calculated. Sarcomeres were also categorized according to the following definitions: "developing" (sarcomeres measuring $<1.8\,\mu m$ in length); and "mature" ($\geq 1.8\,\mu m$) (28).

Cardiac cell culture on ECM

ECM from healthy and CDH+ hearts was obtained as described above and solubilized at a concentration of 10 mg/ml in a solution containing 1 mg/ml pepsin and 0.1 M HCl (7, 29). The ECM solution was neutralized with NaOH, immediately coated onto 48-well plates at a density of 50 µg/cm^2 and allowed to dry in a sterile tissue culture cabinet overnight. Prior to cell seeding, the ECM was washed three times with sterile PBS. Cells freshly isolated from healthy and CDH+ hearts were then seeded onto the coated plates at a density of 100,000 cells/cm^2. To avoid the potential confounding effects of serum on proliferation, cells were cultured in a serum-free medium that contained the following: 50/50 mixture of DMEM and Ham's F12 Nutrient Mix (Invitrogen), 0.2% (wt/vol) bovine serum albumin (BSA) (Sigma), 0.5% (vol/vol) insulin–transferrin–selenium-X (Invitrogen) and 1% penicillin–streptomycin (Invitrogen), with 10 mM L -ascorbic acid (Sigma) added fresh at every feeding (30). Cells were fed on days 1 and 3, and wells from each group were fixed on either day 1 or day 4 in culture. Cells were stained, imaged, and analyzed for proliferation as described above in section Cell proliferation measurements.

Cardiac cell culture with cyclic mechanical stretch

To determine the effects of cyclic mechanical stretch on cardiomyocyte behavior, cells were cultured on a custom-built cell culture membrane stretching device (31). Fetal cardiac cells isolated at E21 from healthy and CDH+ hearts were seeded at 1 × 10^6 cells per well in 6-well Bioflex® culture plates. The experimental set-up was similar to previously described methods with slight modifications (31). The Bioflex® culture plate membranes were pre-coated with collagen type I by the manufacturer. We found that an additional surface treatment of 4 µg/cm^2 human plasma Fibronectin (Millipore, Billerica MA) in DMEM applied overnight at 37°C with mild orbital plate agitation was necessary to create a consistent surface coating for cell adhesion. Cells were initially cultured under static conditions for 4 days post-isolation to ensure strong adhesion to the membrane and then stretched for 3 days on the custom-built system. Membranes were deformed based on a standard left ventricular volumetric loading waveform with 1 Hz frequency and 5% amplitude. Control samples were not subjected to stretching ("static"). The underside of the Bioflex® culture membranes was lubricated with a silicone lubricant (Loctite, Düsseldorf, Germany) to minimize friction with the plunger during stretch. Cells were fed culture medium containing 10% horse serum, 2% FBS, and 1% penicillin-streptomycin in DMEM. Medium was changed and lubricant was reapplied every 2 days. At the end of the experiment, samples were fixed, stained, and imaged as described above. Analysis included proliferation and sarcomere measurements as described above in sections Cell proliferation measurements and Cardiac cell culture with exogenous nitrofen. In addition, subset of wells was subjected to gene expression analysis as described in section Cardiac gene expression by quantitative PCR.

Statistical analysis

Statistical analysis was performed using analysis of variance (ANOVA) and Tukey's *post-hoc* test or the unpaired Student's t-test, as appropriate. Differences were considered statistically significant for $p < 0.05$. Statistical testing was carried out using GraphPad Prism 9 (GraphPad Software, San Diego, CA).

Results

Altered gross morphology in CDH+ hearts

Upon isolation at E21, we found that CDH+ hearts were smaller and had significantly decreased mass compared to healthy controls (Figures 1A,B). Qualitatively, H&E staining suggested that the CDH+ hearts were morphologically immature, with many still exhibiting the ventricular groove, thinner/less compacted ventricular walls, and more trabeculation compared to healthy hearts (Figure 1C). Measurements of the compact zone of the left ventricular free wall (Figure 1C, inset denoted by arrows) indicated that CDH+ hearts had thinner compact myocardium compared to healthy hearts (400 ± 96 vs. 580 ± 48 µm; Figure 1D, $p < 0.01$). ECM was also altered in CDH+ hearts as determined by LC-MS/MS (Figure 1E), particularly in some of the lower abundance components. Specifically, significant increases in the relative abundance of Collagen IV ($p < 0.01$) and nearly significant increases in Collagen VI peptides and decreased Collagen XIV ($p < 0.1$ in all cases) were found in CDH+ vs. healthy hearts (Figure 1F, Table 1). High abundance proteins such as Collagen I, Fibrillin-1, and Fibronectin were not significantly different.

CDH+ hearts exhibit reduced cell proliferation and cardiomyocyte maturity

To determine whether CDH+ hearts exhibited reduced proliferation, native heart sections were stained for Ki67 to identify proliferating cells and sarcomeric α-actinin to label cardiomyocytes (Figure 2A). Cell proliferation was significantly decreased in CDH+ hearts compared to healthy controls (Figure 2B). Particularly in CDH+ hearts, many non-myocytes appeared to be Ki67+ (Figure 3A, *yellow arrows*). Therefore we determined whether proliferation was decreased specifically in the cardiomyocyte population. Although cardiomyocyte proliferation (as determined by Ki67 + α-actinin + cells) showed a decreasing trend in CDH+ hearts, it was not statistically significant ($p = 0.07$) (Figure 2C).

To assess cardiomyocyte maturity, we analyzed sarcomere lengths and gene expression in native hearts. Average sarcomere length was significantly lower in CDH+ hearts compared to healthy (Figures 3A,B). In line with this data, a greater proportion of measured sarcomeres were "mature" (≥1.8 µm) in healthy vs. CDH+ hearts (∼80 vs. ∼50%, respectively; Figure 3C). Taken together, the sarcomere measurements imply that cardiomyocytes were less mature in CDH+ hearts compared to healthy. We also investigated a panel of cardiac genes (Figure 3D) and found that *mhc6*, the gene for myosin heavy chain α which is more abundant in the maturing or adult rat heart (32, 33), was significantly down-regulated in CDH+ hearts relative to healthy (Figure 3E). Furthermore, the ratio of mhc6 to mhc7, which has been used to assess cardiomyocyte maturity (34), was significantly decreased in CDH+ hearts (Figure 3F).

CDH+ cardiomyocytes in culture remain immature and become proliferative

To determine whether proliferation remained low or could be recovered upon removal from the hypoplastic environment, we isolated cells from CDH+ and healthy hearts and cultured on standard tissue culture plastic. After 1 day cardiomyocyte density was similar for both conditions, but after 6 days there were significantly more cardiomyocytes in the CDH+ population compared to the healthy population (Figure 4A). Whereas the healthy cardiomyocytes did not significantly increase in number from

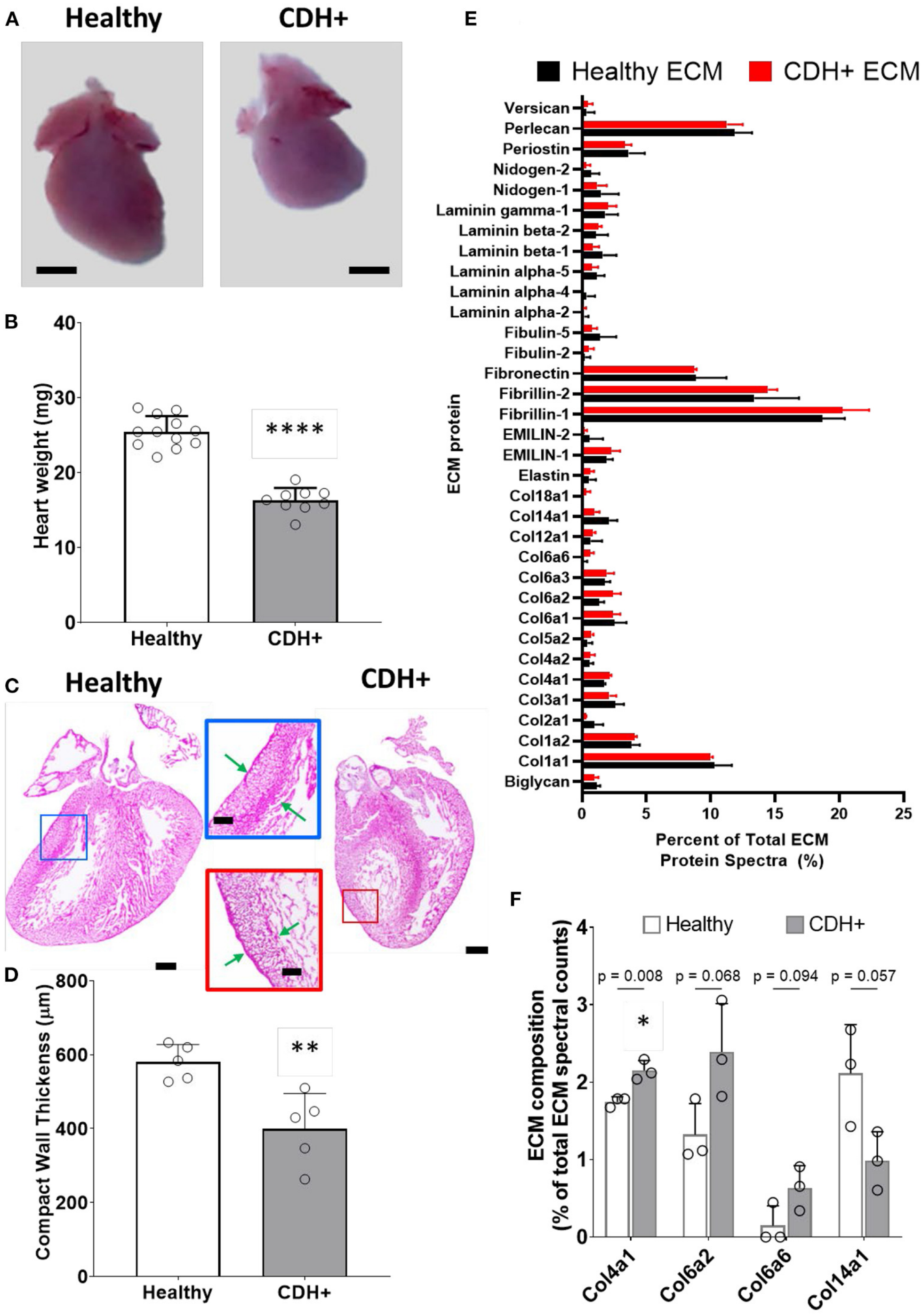

FIGURE 1

Altered heart morphology in the rat model of CDH. **(A)** Representative images of E21 hearts from healthy controls and nitrofen-treated CDH+ fetuses. Scale bar represents 1 mm. **(B)** Heart mass measurements (mean ± S.D.). **** Denotes $p < 0.0001$ from unpaired t-test. **(C)** Representative H&E stained sections of healthy and CDH+ hearts. Insets show measurements of LV compacted free wall thickness (green arrows). Scale bars = 500 µm for whole heart sections and 200 µm for insets. **(D)** Measurements of left ventricle (LV) free wall thickness ($n = 5$) (mean ± S.D.). ** Denotes $p < 0.01$ from unpaired t-test. **(E)** All proteins detected during LC-MS/MS proteomics analysis of healthy and CDH+ heart ECM. Data are presented as the percent of total ECM protein spectra (mean ± S.D.). **(F)** Data for proteins that are significantly different or close to it between healthy and CDH+ hearts. *p*-values for each comparison between healthy and CDH+ hearts using an unpaired t-test are shown above the grouped bars. Again, data is presented as percent of total ECM protein spectra.

TABLE 1 Relative ECM composition.

ECM protein	Healthy		CDH+		*p*-value	CDH+ fold change w.r.t. Healthy	
	Mean	±	Mean	±		Mean	±
Biglycan	1.15	0.27	0.97	0.32	0.50	0.84	0.28
Col1a1	10.30	1.34	10.01	0.15	0.73	0.97	0.01
Col1a2	3.86	0.63	4.09	0.16	0.57	1.06	0.04
Col2a1	0.98	0.66	0.32	0.02	0.16	0.33	0.02
Col3a1	2.58	0.67	2.13	0.53	0.42	0.83	0.21
Col4a1	1.75	0.06	2.15	0.13	0.01	1.23	0.07
Col4a2	0.60	0.27	0.66	0.34	0.84	1.09	0.57
Col5a2	0.42	0.38	0.75	0.14	0.23	1.76	0.33
Col6a1	2.53	0.93	2.38	0.59	0.83	0.94	0.23
Col6a2	1.32	0.40	2.39	0.63	0.07	1.81	0.47
Col6a3	1.78	0.41	1.93	0.57	0.73	1.08	0.32
Col6a6	0.15	0.26	0.63	0.29	0.09	4.27	1.92
Col12a1	0.68	0.88	0.86	0.19	0.74	1.27	0.28
Col14a1	2.11	0.63	0.98	0.38	0.06	0.47	0.18
Col18a1	0.00	0.00	0.32	0.33	0.17	Inf	Inf
Elastin	0.54	0.54	0.64	0.29	0.80	1.18	0.54
EMILIN-1	1.91	0.49	2.29	0.67	0.47	1.20	0.35
EMILIN-2	0.60	1.03	0.21	0.18	0.56	0.35	0.31
Fibrillin-1	18.68	1.74	20.25	2.06	0.37	1.08	0.11
Fibrillin-2	13.38	3.47	14.45	0.71	0.63	1.08	0.05
Fibronectin	8.83	2.39	8.71	0.19	0.94	0.99	0.02
Fibulin-2	0.24	0.41	0.54	0.38	0.40	2.28	1.61
Fibulin-5	1.39	1.27	0.77	0.40	0.46	0.55	0.29
Laminin alpha-2	0.19	0.32	0.11	0.20	0.76	0.61	1.05
Laminin alpha-4	0.37	0.65	0.00	0.00	0.37	0.00	0.00
Laminin alpha-5	1.14	0.62	0.75	0.50	0.45	0.66	0.44
Laminin beta-1	1.62	1.07	0.85	0.47	0.32	0.53	0.29
Laminin beta-2	1.07	0.94	1.28	0.25	0.73	1.20	0.23
Laminin gamma-1	1.81	0.99	2.03	0.64	0.76	1.13	0.35
Nidogen-1	1.49	1.36	1.17	0.76	0.74	0.79	0.51
Nidogen-2	0.68	0.67	0.32	0.33	0.44	0.47	0.48
Periostin	3.63	1.25	3.32	0.52	0.71	0.91	0.14
Perlecan	11.86	1.35	11.26	1.22	0.60	0.95	0.10
Versican	0.36	0.62	0.45	0.39	0.84	1.25	1.08

Determined from spectral counts, data are percentages of total ECM spectra. Last column is fold change of CDH+ ECM components with respect to Healthy. Those in red show down regulation below 0.5-fold while those in green show upregulation greater than 1.5-fold.

1 to 6 days (fold change of 1.45), the CDH+ cardiomyocytes increased 2.4-fold ($p = 0.0025$). At 2 days, Ki67 was detected in 24% of the CDH+ cardiomyocytes, compared to only 12% in the healthy, demonstrating that the CDH+ cells were indeed more proliferative ($p < 0.02$, Figure 4B). We also found that sarcomeres were significantly smaller in the CDH+ cardiomyocytes after 6 days, suggesting that these cells remained less mature than healthy cells (Figure 4C).

Culture with exogenous nitrofen does not affect proliferation in healthy cardiomyocytes

In order to determine whether alterations in cardiomyocyte proliferation in the CDH+ animals were due to a direct effect of nitrofen, we treated cardiomyocytes with nitrofen and assessed proliferation over the course of 3 days. For these studies, freshly isolated cardiomyocytes were cultured

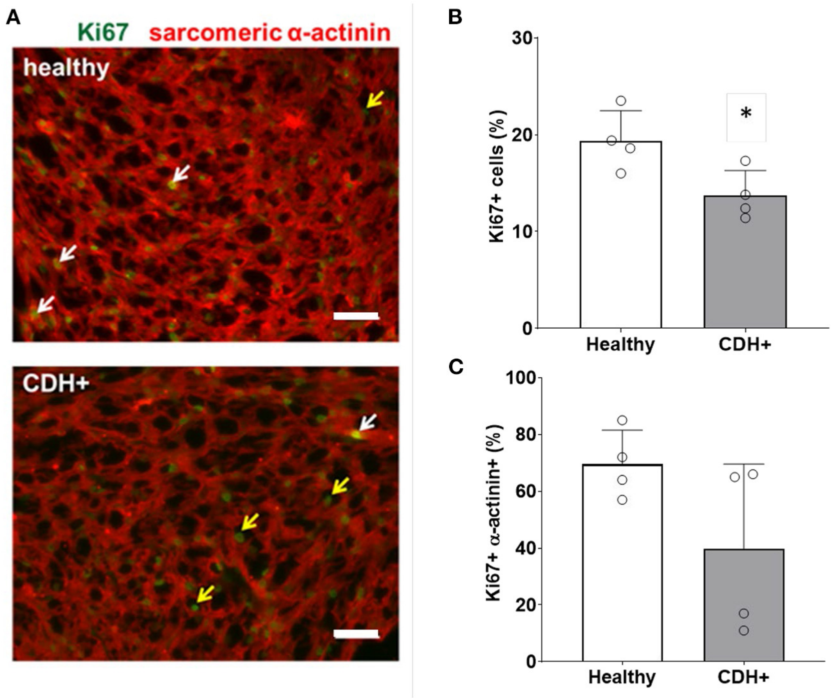

FIGURE 2
Proliferation measurements in healthy and CDH+ hearts. **(A)** E21 heart sections stained for Ki67 (green) and sarcomeric α-actinin (red); examples of Ki67+ cardiomyocytes (white arrows), Ki67+ non-myocytes (yellow arrows), scale bars = 50 µm. **(B)** Total cell proliferation shown as percent of cells expressing Ki67. * Denotes $p < 0.05$. **(C)** Cardiomyocyte-specific proliferation (the percentage of Ki67+ cells that were also α-actinin+).

with 0 mg, 50 mg, and 100 mg of nitrofen. After 72 h of culture, we observed no significant differences in in ki-67+ cardiomyocytes that were treated with exogenous nitrofen compared to cardiomyocytes cultured without nitrofen (Figure 4D), indicating that the responses of the cardiomyocytes from the CDH+ hearts were likely the result of alterations to the biochemical and biophysical properties of the ECM.

CDH+ cardiac ECM inhibits cardiomyocyte proliferation

Given that ECM composition was altered in CDH+ hearts (Figures 1E,F), we hypothesized that the ECM plays a role in the decreased proliferation observed in CDH-associated heart hypoplasia. Healthy and CDH+ cardiomyocytes were seeded onto healthy and CDH+ heart-derived ECM and cultured with serum-free medium. After 4 days, cardiomyocyte numbers were significantly higher on healthy ECM compared to CDH+ ECM for both healthy and CDH+ cardiomyocytes (Figures 5A,B). CDH+ cardiomyocytes were generally more proliferative than their healthy counterparts on either ECM. However, culture on CDH+ ECM resulted in significantly decreased cardiomyocyte proliferation for both healthy and CDH+ populations (Figure 5C). This data suggests that changes in ECM composition present in CDH+ hearts inhibits cardiomyocyte proliferation in CDH-associated heart hypoplasia.

Cyclic mechanical loading promotes maturation of CDH+ cardiomyocytes

Compression of the heart likely impedes the ability of the heart to undergo normal stretch in CDH (20). We hypothesized that mimicking physiological stretch *ex vivo* could promote CDH+ cardiomyocyte proliferation and maturation. For these studies, we used a frequency of 1 Hz at 5% amplitude. After 3 days of stretching (7 days in culture), we assessed sarcomere lengths (Figure 6A) and proliferation and we did see a significant decrease in cardiomyocyte specific proliferation in CDH+ cells ($p < 0.05$, Figure 6B). In addition, CDH+ cardiomyocytes had significantly longer sarcomeres after stretching compared to static controls ($p < 0.001$), while sarcomere lengths in healthy cells were unaffected by stretch (Figure 6C). Gene expression analysis of a panel of genes (Figure 6D), showed that CDH+ cells cultured under static conditions had lower expression of MHC6 and MHC7 than Healthy cells cultured statically

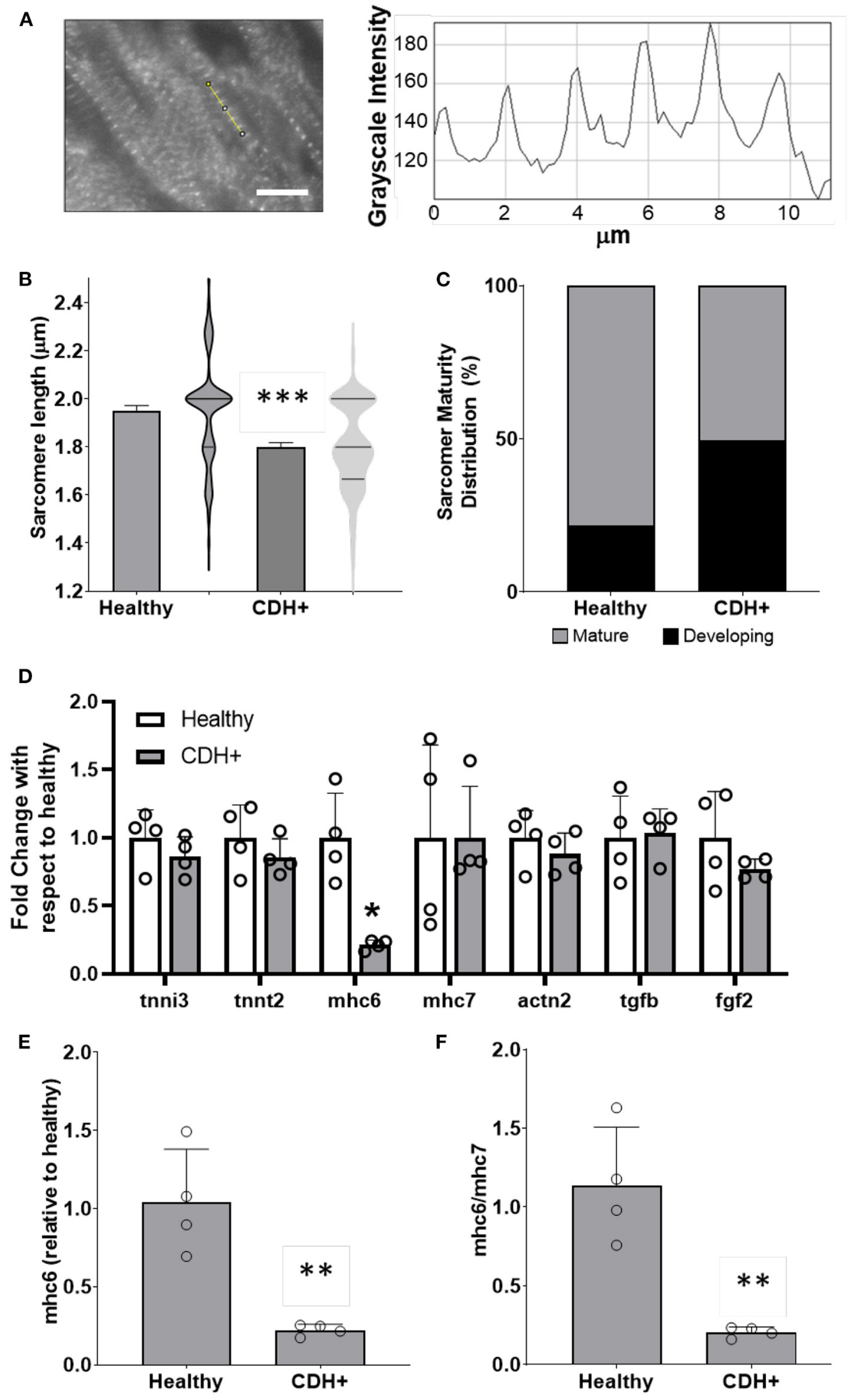

FIGURE 3
Maturation assessments in healthy and CDH+ hearts. **(A)** Example of sarcomere staining and measurement in native heart sections. A line is drawn perpendicular to the sarcomeres (yellow) and the profile is plotted in ImageJ. Peak-to-peak distances represent sarcomere lengths. Scale bar represents 10 µm. **(B)** Average sarcomere length measurements (mean ± S.E.M. on left, violin plots showing the distribution of the data on right, $n > 80$ individual cells per condition). *** Denotes $p < 0.001$. **(C)** A greater percentage of sarcomeres were mature (≥1.8 µm) in healthy vs. CDH+ hearts. **(D)** Gene expression data for panel of genes investigated. * $p < 0.05$ w.r.t. healthy. **(E)** Gene expression of αMHC (mhc6) as well as the ratio of α to β isoforms (mhc6/mhc7) and **(F)** was decreased in CDH+ hearts ($n = 4$). In both cases ** denotes $p < 0.01$.

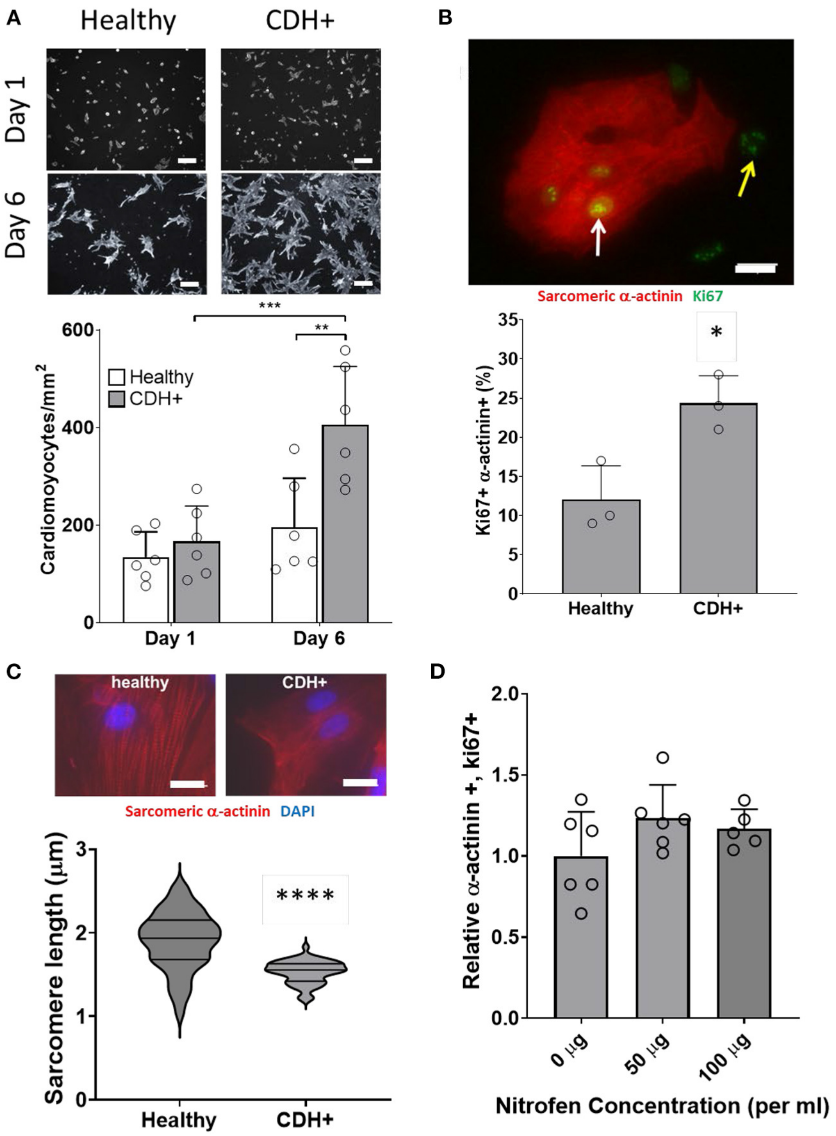

FIGURE 4
Characterization of CDH+ cardiomyocytes in culture. **(A)** Representative images of cardiomyocytes (α-actinin stain in gray scale) after 1 day or 6 days in culture (top). Cardiomyocyte density at 1 and 6 days (bottom). Graph shows mean ± SD ($n = 6$). ** Denotes $p < 0.01$ w.r.t. Healthy cells at Day 6. *** Denotes $p < 0.001$ w.r.t. CDH+ at 24 h. **(B)** Cardiomyocyte proliferation (Ki67+ α-actinin+) at 2 days. Inset shows example of Ki67+ cardiomyocyte (white arrow) and non-myocyte (yellow arrow). Graph shows mean ± SD ($n = 3$). * Denotes $p < 0.05$. **(C)** Representative images of sarcomere staining in healthy and CDH+ cardiomyocytes where Red is cardiac α-actinin and blue is the nuclear marker DAPI (top). Sarcomere length measurements (bottom). **** Denotes $p < 0.001$. **(D)** Proliferative cardiomyocytes at 72 h post-treatment with exogenous nitrofen. Data is normalized by relative expression of α-actinin+ and Ki67+ at 24 h pre-treatment. Graph shows mean ± SD ($n = 5$).

($p < 0.1$ for both). In addition, while MHC6 was lower in statically cultured cells, the addition of stretch led to a nearly significant increase in MHC6 in CDH+ cells ($p < 0.1$), which also indicated increased maturity in CDH+ cells subjected to stretch. p-values for all comparisons of the gene expression data are shown in Table 2. Taken together, these results show that cyclic mechanical stretch promoted sarcomere maturation in CDH+ cardiomyocytes.

Discussion

The nitrofen model of CDH in rats is a valuable tool for studying molecular and cellular alterations in heart hypoplasia which are difficult in humans. Although a few groups have looked at changes in growth factors (20, 35, 36), and cardiac and ECM genes (20, 37, 38) in the nitrofen model of CDH, CDH+ cardiac cells have not been cultured or subjected to specific

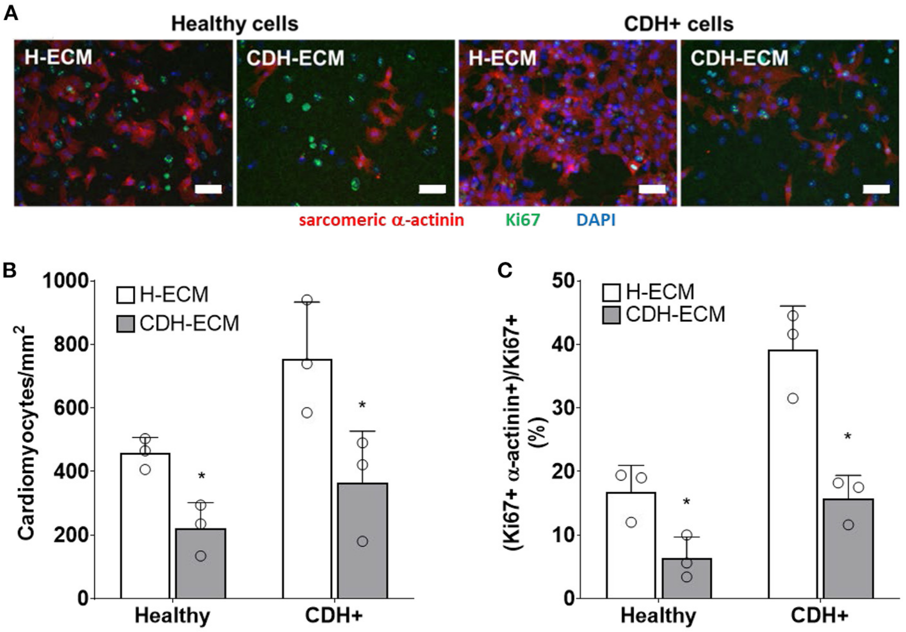

FIGURE 5
Cardiomyocyte response to ECM. **(A)** Representative images of cells on ECM derived from healthy hearts (H-ECM) and CDH+ hearts (CDH-ECM), stained for Hoechst (blue), Ki67 (green), and cardiac α-actinin (red). **(B)** Cardiomyocyte density and **(C)** cardiomyocyte proliferation were significantly decreased in both healthy and CDH+ populations on CDH-ECM after 4 days in culture. Graphs show mean ± SD ($n = 3$). In all cases * denotes $p < 0.05$.

engineered environments to study their response to biochemical or biophysical cues. The key novel findings of this study are: (1) cell proliferation and cardiomyocyte maturity were decreased in CDH+ hearts compared to healthy; (2) in culture, CDH+ cardiomyocytes remained immature with increased proliferative potential compared to healthy cardiomyocytes; (3) ECM derived from CDH+ hearts significantly reduced both healthy and CDH+ cardiomyocyte proliferation compared healthy cardiac ECM; and (4) cyclic mechanical stretch promoted sarcomere maturation in CDH+ cardiomyocytes.

Given that the healthy heart undergoes a transition from hyperplastic to hypertrophic growth soon after birth (39, 40), cardiomyocyte proliferation and maturation are usually considered to be inversely correlated. However, we found that CDH+ hearts had smaller sarcomeres and reduced *mhc6* expression, suggesting a less mature state, while also having decreased proliferation compared to healthy controls-importantly these effects were not caused by a direct effect of nitrofen on cardiomyocytes in the developing hearts. Numerous external factors can influence cell behavior, such as growth factor signaling, the ECM, tissue stiffness, and the dynamic mechanical environment (6–12). While some of these cues are known to be altered in heart hypoplasia, it is unclear how their complex interactions could lead to concurrent decreased proliferation and maturity in the CDH+ heart. It was initially surprising to find that in culture the proliferation of CDH+ cardiomyocytes significantly exceeded that of healthy cardiomyocytes. It appears that the immature state of CDH+ cardiomyocytes is advantageous for recovered growth, as the removal of the hypoplastic environment allowed the cells to undergo a proliferative “burst” that would not be achievable by more mature myocytes. A similar mechanism may exist in young patients who undergo CDH repair, as recovery of heart dimensions have been observed in patients with mild to moderate heart hypoplasia (3). Given recent studies of young human hearts (8, 41), therapeutic strategies which promote cardiomyocyte proliferation will likely be most effective during early life.

Cardiac ECM influences cardiomyocyte proliferation (6, 7) but has not been well studied in the context of heart hypoplasia disorders. We found that culture on CDH+ ECM led to reduced proliferation of both healthy and CDH+ cardiomyocytes. This was intriguing since there were significant changes in only a small fraction of ECM components (Collagens IV, VI, and XIV, which were each < 3% of the ECM) relative to total composition. However, these proteins have important roles that could affect how cells sense and respond to the ECM (42–46). In CDH-associated heart hypoplasia and HLHS, two studies suggest that the ECM in hypoplastic hearts is less mature compared to healthy hearts (20, 21, 46). Specifically, Guarino et al. found reduced procollagen and tropoelastin in CDH+ fetal rat hearts and Davies et al. observed increased fibronectin

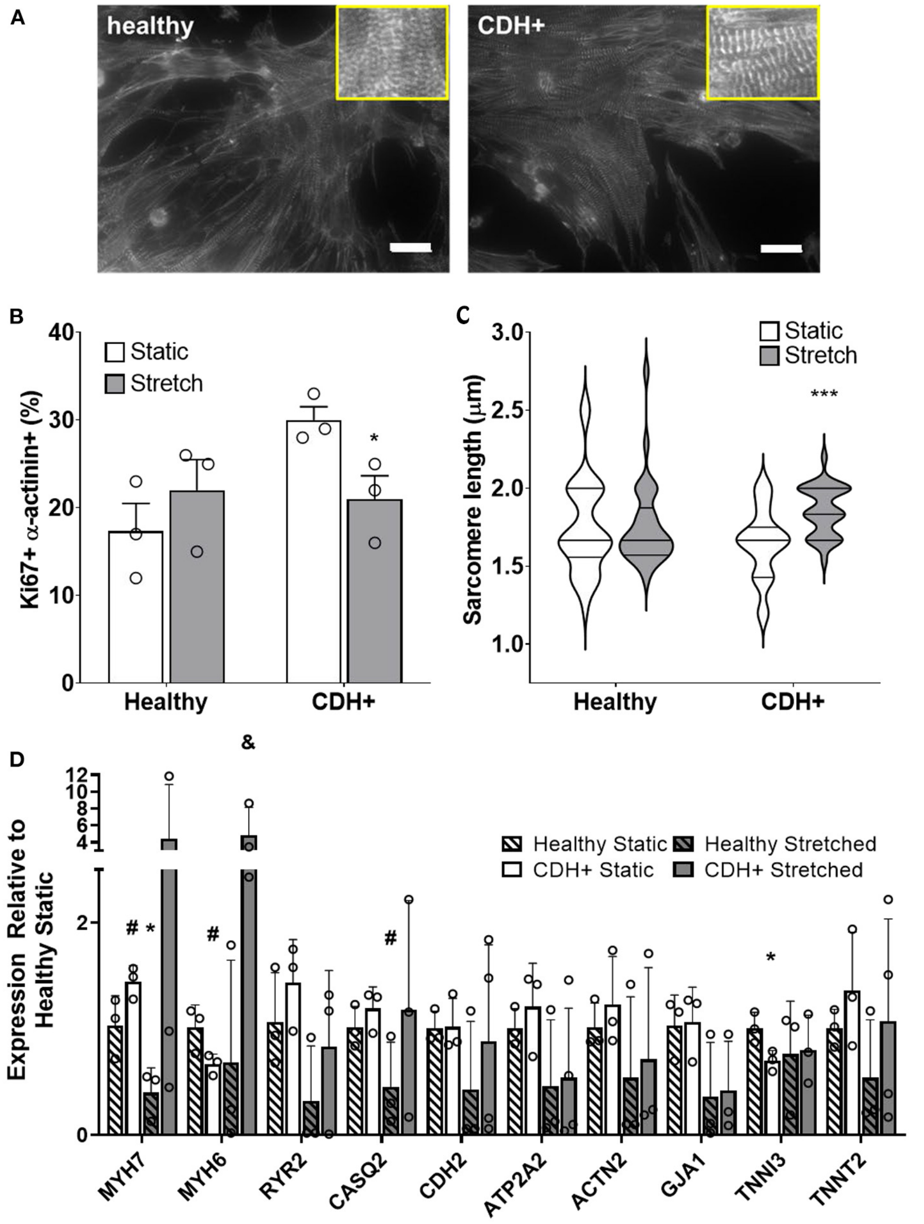

FIGURE 6
Cardiomyocyte responses to stretch. **(A)** Representative images of stretched cardiomyocytes (α-actinin stain). Insets show sarcomeres. Scale bars = 25 μm. **(B)** Cardiomyocyte proliferation was not significantly affected by stretch in healthy cells but was significantly decreased in CDH+ cells with stretch. Graph shows mean ± SD ($n = 3$). * Denotes $p < 0.05$. **(C)** CDH+ cardiomyocytes underwent lengthening of sarcomeres in response to stretch. Graph shows mean ± SEM ($n \geq 23$). *** Denotes $p < 0.001$. **(D)** Panel of genes measured in healthy and CDH+ cells during both static conditions and following stretch. * Denotes $p < 0.05$ w.r.t Healthy Static, # denotes $p < 0.1$ w.r.t Healthy Static, and & denotes $p < 0.1$ w.r.t CDH+ Static.

and decreased collagen in HLHS hearts compared to non-HLHS patients. Tao et al. found that Col14a null mice displayed defects in ventricular morphogenesis and had significantly increased cardiomyocyte proliferation postnatally but a similar trend as in our CDH model toward decreased cardiomyocyte proliferation at E11.5 (45). Similarly, a recent study by Bousalis et al. observed increased expression of fibronectin, collagen IV, and integrin β-1 within *Nkx2-5* mutant embryonic mouse hearts compared to wild type hearts (46). Interactions between fibronectin and integrins can lead to downstream signaling cascades that control cell spreading, migration, and proliferation (47, 48). Our findings are counter-intuitive, as immature ECM has generally been found to promote proliferation (6–8, 49). The role of the ECM is more complex; future studies should explore the roles

TABLE 2 Gene expression with stretch.

	Static to static	Healthy static to stretch	CDH+ static to stretch	Stretch to stretch
MYH7	0.09	0.04	0.47	0.34
MYH6	0.06	0.59	0.10	0.11
RYR2	0.36	0.14	0.27	0.37
CASQ2	0.33	0.10	0.99	0.31
CDH2	0.95	0.21	0.82	0.50
ATP2A2	0.48	0.22	0.18	0.88
Actn2	0.50	0.36	0.41	0.81
GJA1	0.88	0.12	0.12	0.89
TNNI3	0.04	0.46	0.63	0.92
TNNT2	0.36	0.23	0.67	0.44

p-values for t-tests between various groups for all genes measured in Figure 6D. Green denotes $p < 0.05$ while yellow denotes $p \leq 0.10$.

of specific peptides or interactions among ECM components to elucidate the nuances of the ECM in heart hypoplasia pathology and cardiomyocyte proliferation.

Normal stretching of the heart wall is diminished in CDH due to compression by visceral organs (20). We found that CDH+ cardiomyocytes had decreased proliferation and lengthened sarcomeres when stretched using a custom flexible membrane apparatus compared to static conditions; healthy cells, which were already relatively mature, did not further lengthen their sarcomeres under these cyclic loading conditions. Cyclic stretch has been used as a strategy to drive cardiomyocyte maturation in a number of tissue engineering applications (12, 50). Diminished mechanical movement experienced by cardiomyocytes within CDH+ hearts could be a potential mechanism of arrested cardiomyocyte maturity in CDH-associated heart hypoplasia and has also been implicated in hypoplastic left heart syndrome due to reduced blood flow in the left side of the heart (51). The role of mechanical forces is intriguing when contrasting CDH-associated heart hypoplasia and hypoplastic left heart syndrome. Although these two heart hypoplasia defects share some similar features such as reduced growth factors, altered ECM, and decreased cardiac transcription factors (5, 13, 20, 21, 52, 53), the outcomes after surgical repair are vastly different. Repair of CDH leads to removal of the compressive forces on the heart by intruding organs, and thus cardiac growth often normalizes (3). This is not the case for hypoplastic left heart syndrome: restoration of blood flow *via* fetal aortic valvuloplasty does not lead to recovered left ventricular growth (16). A deeper understanding of the specific underlying pathological mechanisms of these different forms of heart hypoplasia is needed.

Future direction related to this work could include a more detailed mechanistic study that attempts to dissect the specific ECM proteins or peptides that result in the reduction of proliferation in CDH+ hearts. For example, Yamashiro et al. found that stretch stimulation induces thrombospondin-1 secretion, which acts on cell adhesion plaques (54). While thrombospondin was not evident in our initial proteomics screen of heart ECM, it is possible that it is present in small amounts and it is also possible that it may be more expressed by the cells upon stretch in our system as well. Another potential avenue of future work related to this study would involve the study of samples taken from human hypoplastic heart patients. While these discarded samples that come from surgical repair often come from atrial tissue, it may still be a valuable source of tissue to assess changes in cardiomyocyte proliferation and ECM expression in the context of human congenital heart defects.

In conclusion, we have found that cardiomyocytes from CDH+ hearts are capable of robust proliferation, likely a result of their immature phenotype maintained during heart development. Our studies also point to altered ECM and mechanical forces as important environmental regulators of cardiomyocyte state in heart hypoplasia. Future work aimed at understanding these mechanisms could lead to novel biomechanical signaling-based therapies to improve cardiac growth and function in children born with hypoplastic hearts.

Data availability statement

The original contributions presented in the study are included in the article/supplementary material, further inquiries can be directed to the corresponding author.

Ethics statement

The animal study was reviewed and approved by Institutional Animal Care and Use Committee (IACUC) Tufts University.

Author contributions

MW and CW designed and carried out the bulk of the experiments and wrote the manuscript. RW carried out the experiments and analysis related to cyclic stretch. LP assisted with cell isolations and experimental procedures for *in vitro* culture. KS and WS assisted with experimental design and analysis. LB assisted with experimental design, data interpretation and analysis, and writing/editing of the manuscript. All authors contributed to the article and approved the submitted version.

Funding

This work was supported by an NIH/NHLBI postdoctoral fellowship (F32 HL112538) to CW, an American Heart Association Predoctoral Fellowship (14PRE19960001) to KS, NIH Institutional Research and Academic Career Development Awards (IRACDA) fellowship (K12GM074869), Training in Education and Critical Research Skills (TEACRS) to WS, and NIH/NHLBI (R21 HL115570), NSF (Award#: 1351241), DoD-CDMRP (Award#: W81XWH1610304), and American Heart Association (AHA, Award#: 20TPA35500082) to LB.

Acknowledgments

The authors thank Professor John Asara and the Mass Spectrometry Core Laboratory (Beth Israel Deaconess Medical Center) for running LC-MS/MS on ECM samples.

Conflict of interest

The authors declare that the research was conducted in the absence of any commercial or financial relationships that could be construed as a potential conflict of interest.

Publisher's note

References

1. Colvin J, Bower C, Dickinson JE, Sokol J. Outcomes of congenital diaphragmatic hernia: a population-based study in Western Australia. *Pediatrics.* (2005) 116:e356–63. doi: 10.1542/peds.2004-2845

2. Graziano JN. Cardiac anomalies in patients with congenital diaphragmatic hernia and their prognosis: a report from the congenital diaphragmatic hernia study group. *J Pediatr Surg.* (2005) 40:1045–50. doi: 10.1016/j.jpedsurg.2005.03.025

3. Vogel M, McElhinney DB, Marcus E, Morash D, Jennings RW, Tworetzky W. Significance and outcome of left heart hypoplasia in fetal congenital diaphragmatic hernia. *Ultrasound Obstet Gynecol.* (2010) 35:310–7. doi: 10.1002/uog.7497

4. Soonpaa MH, Field LJ. Survey of studies examining mammalian cardiomyocyte DNA synthesis. *Circ Res.* (1998) 83:15–26. doi: 10.1161/01.RES.83.1.15

5. Gaber N, Gagliardi M, Patel P, Kinnear C, Zhang C, Chitayat D, et al. Fetal reprogramming and senescence in hypoplastic left heart syndrome and in human pluripotent stem cells during cardiac differentiation. *Am J Pathol.* (2013) 183:720–34. doi: 10.1016/j.ajpath.2013.05.022

6. Ieda M, Tsuchihashi T, Ivey KN, Ross RS, Hong TT, Shaw RM, et al. Cardiac fibroblasts regulate myocardial proliferation through beta1 integrin signaling. *Dev Cell.* (2009) 16:233–44. doi: 10.1016/j.devcel.2008.12.007

7. Williams C, Quinn KP, Georgakoudi I, Black LD 3rd. Young developmental age cardiac extracellular matrix promotes the expansion of neonatal cardiomyocytes in vitro. *Acta Biomater.* (2014) 10:194–204. doi: 10.1016/j.actbio.2013.08.037

8. Kuhn B. del Monte F, Hajjar RJ, Chang YS, Lebeche D, Arab S, et al. Periostin induces proliferation of differentiated cardiomyocytes and promotes cardiac repair. *Nat Med.* (2007) 13:962–9. doi: 10.1038/nm1619

9. Tirziu D, Giordano FJ, Simons M. Cell communications in the heart. *Circulation.* (2010) 122:928–37. doi: 10.1161/CIRCULATIONAHA.108.847731

10. Jacot JG, McCulloch AD, Omens JH. Substrate stiffness affects the functional maturation of neonatal rat ventricular myocytes. *Biophys J.* (2008) 95:3479–87. doi: 10.1529/biophysj.107.124545

11. Engler AJ, Carag-Krieger C, Johnson CP, Raab M, Tang HY, Speicher DW, et al. Embryonic cardiomyocytes beat best on a matrix with heart-like elasticity: scar-like rigidity inhibits beating. *J Cell Sci.* (2008) 121(Pt 22):3794-802. doi: 10.1242/jcs.029678

12. Banerjee I, Carrion K, Serrano R, Dyo J, Sasik R, Lund S, et al. Cyclic stretch of embryonic cardiomyocytes increases proliferation, growth, and expression while repressing Tgf-beta signaling. *J Mol Cell Cardiol.* (2015) 79:133–44. doi: 10.1016/j.yjmcc.2014.11.003

13. Guarino N, Shima H, Puri P. The hypoplastic heart in congenital diaphragmatic hernia: reduced expression of basic fibroblast growth factor and platelet-derived growth factor. *Pediatr Surg Int.* (2000) 16:243–6. doi: 10.1007/s003830050737

14. Bartman T, Hove J. Mechanics and function in heart morphogenesis. *Dev Dyn.* (2005) 233:373–81. doi: 10.1002/dvdy.20367

15. Miller CE, Wong CL, Sedmera D. Pressure overload alters stress-strain properties of the developing chick heart. *Am J Physiol Heart Circ Physiol.* (2003) 285:H1849–56. doi: 10.1152/ajpheart.00384.2002

16. McElhinney DB, Lock JE, Keane JF, Moran AM, Colan SD. Left heart growth, function, and reintervention after balloon aortic valvuloplasty for neonatal aortic stenosis. *Circulation.* (2005) 111:451–8. doi: 10.1161/01.CIR.0000153809.88286.2E

17. Clugston RD, Klattig J, Englert C, Clagett-Dame M, Martinovic J, Benachi A, et al. Teratogen-induced, dietary and genetic models of congenital diaphragmatic hernia share a common mechanism of pathogenesis. *Am J Pathol.* (2006) 169:1541–9. doi: 10.2353/ajpath.2006.060445

18. Noble BR, Babiuk RP, Clugston RD, Underhill TM, Sun H, Kawaguchi R, et al. Mechanisms of action of the congenital diaphragmatic hernia-inducing teratogen nitrofen. *Am J Physiol Lung Cell Mol Physiol.* (2007) 293:L1079–87. doi: 10.1152/ajplung.00286.2007

19. Mahood TH, Johar DR, Iwasiow BM, Xu W, Keijzer R. The transcriptome of nitrofen-induced pulmonary hypoplasia in the rat model of congenital diaphragmatic hernia. *Pediatr Res.* (2016) 79:766–75. doi: 10.1038/pr.2015.277

20. Guarino N, Shima H, Puri P. Structural immaturity of the heart in congenital diaphragmatic hernia in rats. *J Pediatr Surg.* (2001) 36:770–3. doi: 10.1053/jpsu.2001.22957

21. Davies B. d'Udekem Y, Ukoumunne OC, Algar EM, Newgreen DF, Brizard CP. Differences in extra-cellular matrix and myocyte homeostasis between the neonatal right ventricle in hypoplastic left heart syndrome and truncus arteriosus. *Eur J Cardiothorac Surg.* (2008) 34:738–44. doi: 10.1016/j.ejcts.2008.06.037

22. Baglaj M, Dorobisz U. Late-presenting congenital diaphragmatic hernia in children: a literature review. *Pediatr Radiol.* (2005) 35:478–88. doi: 10.1007/s00247-004-1389-z

23. Ngoka LC. Sample prep for proteomics of breast cancer: proteomics and gene ontology reveal dramatic differences in protein solubilization preferences of radioimmunoprecipitation assay and urea lysis buffers. *Proteome Sci.* (2008) 6:30. doi: 10.1186/1477-5956-6-30

24. Schmittgen TD, Livak KJ. Analyzing real-time PCR data by the comparative CT method. *Nat Protoc.* (2008) 3:1101–8. doi: 10.1038/nprot.2008.73

25. Ye K, Sullivan K, Black L. Encapsulation of cardiomyocytes in a fibrin hydrogel for cardiac tissue engineering. *J Vis Exp.* (2011) 55:e3251. doi: 10.3791/3251-v

26. Williams C, Sullivan K, Black LD 3rd. Partially digested adult cardiac extracellular matrix promotes cardiomyocyte proliferation in vitro. *Adv Healthcare Mater.* (2015) 4:1545–54. doi: 10.1002/adhm.201500035

27. Ronaldson-Bouchard K, Ma SP, Yeager K, Chen T, Song L, Sirabella D, et al. Advanced maturation of human cardiac tissue grown from pluripotent stem cells. *Nature.* (2018) 556:239–43. doi: 10.1038/s41586-018-0016-3

28. Young JL, Engler AJ. Hydrogels with time-dependent material properties enhance cardiomyocyte differentiation in vitro. *Biomaterials.* (2011) 32:1002–9. doi: 10.1016/j.biomaterials.2010.10.020

29. Singelyn JM, DeQuach JA, Seif-Naraghi SB, Littlefield RB, Schup-Magoffin PJ, Christman KL. Naturally derived myocardial matrix as an injectable scaffold for cardiac tissue engineering. *Biomaterials.* (2009) 30:5409–16. doi: 10.1016/j.biomaterials.2009.06.045

30. Engel FB. Cardiomyocyte proliferation: a platform for mammalian cardiac repair. *Cell Cycle.* (2005) 4:1360–3. doi: 10.4161/cc.4.10.2081

31. Lau JJ, Wang RM, Black LD 3rd. Development of an arbitrary waveform membrane stretcher for dynamic cell culture. *Ann Biomed Eng.* (2014) 42:1062–73. doi: 10.1007/s10439-014-0976-x

32. Scuderi GJ, Butcher J. Naturally engineered maturation of cardiomyocytes. *Front Cell Dev Biol.* (2017) 5:50. doi: 10.3389/fcell.2017.00050

33. Siedner S, Kruger M, Schroeter M, Metzler D, Roell W, Fleischmann BK, et al. Developmental changes in contractility and sarcomeric proteins from the early embryonic to the adult stage in the mouse heart. *J Physiol.* (2003) 548(Pt 2):493–505. doi: 10.1113/jphysiol.2002.036509

34. Panguluri SK, Tur J, Fukumoto J, Deng W, Sneed KB, Kolliputi N, et al. Hyperoxia-induced hypertrophy and ion channel remodeling in left ventricle. *Am J Physiol Heart Circ Physiol.* (2013) 304:H1651–61. doi: 10.1152/ajpheart.00474.2012

35. Teramoto H, Yoneda A, Puri P. Gene expression of fibroblast growth factors 10 and 7 is downregulated in the lung of nitrofen-induced diaphragmatic hernia in rats. *J Pediatr Surg.* (2003) 38:1021–4. doi: 10.1016/S0022-3468(03)00183-0

36. Makanga M, Dewachter C, Maruyama H, Vuckovic A, Rondelet B, Naeije R, et al. Downregulated bone morphogenetic protein signaling in nitrofen-induced congenital diaphragmatic hernia. *Pediatr Surg Int.* (2013) 29:823–34. doi: 10.1007/s00383-013-3340-6

37. Burgos CM, Uggla AR, Fagerstrom-Billai F, Eklof AC, Frenckner B, Nord M. Gene expression analysis in hypoplastic lungs in the nitrofen model of congenital diaphragmatic hernia. *J Pediatr Surg.* (2010) 45:1445–54. doi: 10.1016/j.jpedsurg.2009.09.023

38. Baptista MJ, Nogueira-Silva C, Areias JC, Correia-Pinto J. Perinatal profile of ventricular overload markers in congenital diaphragmatic hernia. *J Pediatr Surg.* (2008) 43:627–33. doi: 10.1016/j.jpedsurg.2007.08.044

39. Laflamme MA, Murry CE. Heart regeneration. *Nature.* (2011) 473:326–35. doi: 10.1038/nature10147

40. Li F, Wang X, Capasso JM, Gerdes AM. Rapid transition of cardiac myocytes from hyperplasia to hypertrophy during postnatal development. *J Mol Cell Cardiol.* (1996) 28:1737–46. doi: 10.1006/jmcc.1996.0163

41. Bersell K, Arab S, Haring B, Kuhn B. Neuregulin1/ErbB4 signaling induces cardiomyocyte proliferation and repair of heart injury. *Cell.* (2009) 138:257–70. doi: 10.1016/j.cell.2009.04.060

42. Rozario T, DeSimone DW. The extracellular matrix in development and morphogenesis: a dynamic view. *Dev Biol.* (2010) 341:126–40. doi: 10.1016/j.ydbio.2009.10.026

43. Poschl E, Schlotzer-Schrehardt U, Brachvogel B, Saito K, Ninomiya Y, Mayer U. Collagen IV is essential for basement membrane stability but dispensable for initiation of its assembly during early development. *Development.* (2004) 131:1619–28. doi: 10.1242/dev.01037

44. Klewer SE, Krob SL, Kolker SJ, Kitten GT. Expression of type VI collagen in the developing mouse heart. *Dev Dyn.* (1998) 211:248–55. doi: 10.1002/(SICI)1097-0177(199803)211:3<248::AID-AJA6>3.0.CO;2-H

45. Tao G, Levay AK, Peacock JD, Huk DJ, Both SN, Purcell NH, et al. Collagen XIV is important for growth and structural integrity of the myocardium. *J Mol Cell Cardiol.* (2012) 53:626–38. doi: 10.1016/j.yjmcc.2012.08.002

46. Bousalis D, Lacko CS, Hlavac N, Alkassis F, Wachs RA, Mobini S, et al. Extracellular matrix disparities in an Nkx2-5 mutant mouse model of congenital heart disease. *Front Cardiovasc Med.* (2020) 7:93. doi: 10.3389/fcvm.2020.00093

47. Valiente-Alandi I, Schafer AE, Blaxall BC. Extracellular matrix-mediated cellular communication in the heart. *J Mol Cell Cardiol.* (2016) 91:228–37. doi: 10.1016/j.yjmcc.2016.01.011

48. Watson MC, Cherry-Kemmerling EM, Black LD. Cell-matrix interactions in cardiac development and disease. In: Zhang Y, editor. *Multi-scale Extracellular Matrix Mechanics and Mechanobiology. Studies in Mechanobiology, Tissue Engineering and Biomaterials.* Cham, Switzerland: Springer International Publishing (2020), p. 311–42. doi: 10.1007/978-3-030-20182-1_10

49. Wu CC, Jeratsch S, Graumann J, Stainier DYR. Modulation of mammalian cardiomyocyte cytokinesis by the extracellular matrix. *Circ Res.* (2020) 127:896–907. doi: 10.1161/CIRCRESAHA.119.316303

50. Mihic A, Li J, Miyagi Y, Gagliardi M, Li SH, Zu J, et al. The effect of cyclic stretch on maturation and 3D tissue formation of human embryonic stem cell-derived cardiomyocytes. *Biomaterials.* (2014) 35:2798–808. doi: 10.1016/j.biomaterials.2013.12.052

51. Gobergs R, Salputra E, Lubaua I. Hypoplastic left heart syndrome: a review. *Acta Med Litu.* (2016) 23:86–98. doi: 10.6001/actamedica.v23i2.3325

52. Takayasu H, Sato H, Sugimoto K, Puri P. Downregulation of GATA4 and GATA6 in the heart of rats with nitrofen-induced diaphragmatic hernia. *J Pediatr Surg.* (2008) 43:362–6. doi: 10.1016/j.jpedsurg.2007.10.047

53. Mahle WT, Spray TL, Wernovsky G, Gaynor JW, Bernard J. Clark I. Survival after reconstructive surgery for hypoplastic left heart syndrome: a 15-year experience from a single institution. *Circulation.* (2000) 102:III-136–III-141. doi: 10.1161/01.CIR.102.suppl_3.III-136

54. Yamashiro Y, Thang BQ, Ramirez K, Shin SJ, Kohata T, Ohata S, et al. Matrix mechanotransduction mediated by thrombospondin-1/integrin/YAP in the vascular remodeling. *Proc Natl Acad Sci USA.* (2020) 117:9896–905. doi: 10.1073/pnas.1919702117

Frontiers in
Cell and Developmental Biology

Explores the fundamental biological processes of life, covering intracellular and extracellular dynamics.

The world's most cited developmental biology journal, advancing our understanding of the fundamental processes of life. It explores a wide spectrum of cell and developmental biology, covering intracellular and extracellular dynamics.

Discover the latest Research Topics

See more →

Frontiers

Avenue du Tribunal-Fédéral 34
1005 Lausanne, Switzerland
frontiersin.org

Contact us

+41 (0)21 510 17 00
frontiersin.org/about/contact

frontiers | Research Topics